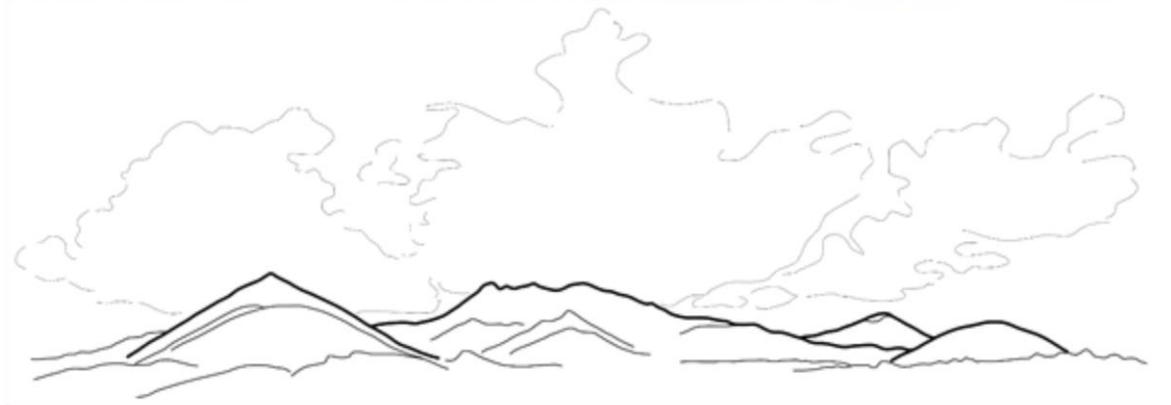


Critical Eruptive Controls of an Intra-plate Volcano: Ascension Island, South Atlantic

Bridie Verity Davies



Student Registration Number: 100212641

Thesis submitted for the degree of Doctor of Philosophy

School of Environmental Sciences

University of East Anglia

July 2022

University of East Anglia

This copy of the thesis has been supplied on condition that anyone who consults it is understood to recognise that its copyright rests with the author and that use of any information derived therefrom must be in accordance with current UK Copyright Law. In addition, any quotation or extract must include full attribution.

Abstract

Understanding what drives transitions in eruptive style is an important challenge in volcanology. Existing descriptions of small-volume trachytic eruptions often record transitions in eruptive behaviour, including and outwith explosive-effusive transitions, but detailed ascent and eruption dynamics reconstructions are rare. Historically, poor deposit preservation and exposure and unconstrained trachytic melt physical properties have contributed to a dearth of relevant literature. Here, I first make use of recent advances in understanding trachytic melt properties to reconstruct ascent and eruption dynamics of a particularly well-preserved and -exposed small-volume eruption on Ascension Island, South Atlantic - the Echo Canyon eruption (EC). Forensic stratigraphy, petrographic analysis, reconstruction of bulk magma properties and quantitative textural analysis reveal: the EC eruption underwent several transitions in eruptive behaviour, driven by rapid ascent, decompression and vesiculation. Further, peak explosion intensity equivalent to volcanic explosivity index (VEI) 6 eruptions was transiently achieved before transition to effusive activity by rapid evolution of permeable vesicle networks in conduit margin shear zones. Next, I use 2D and 3D textural analyses of a stratigraphically and compositionally well-constrained basalt-rhyolite 'Mingled Fall' deposit to assess how mingling impacts vesiculation during ascent. I find vesiculation in mingled clasts' basaltic and rhyolitic regions progressed independently with little–no shear. In the basaltic regions, connectivity development was only slightly inhibited relative to scoriaceous clasts. I show 2D and 3D studies in texturally complex samples return different vesiculation histories. The 3D vesicle size distribution studies are more reliable for complex clasts, whereas 2D shape descriptors are better constrained and more useful for inter-eruption comparisons. Finally, I demonstrate how frameworks developed throughout offer insights into the evolution of the volumetrically comparable La Soufrière St Vincent, 2020-21 eruption. This thesis makes a useful contribution to understanding ascent and eruption dynamics of small-volume, but potentially high-impact events, common to isolated ocean island settings.

Access Condition and Agreement

Each deposit in UEA Digital Repository is protected by copyright and other intellectual property rights, and duplication or sale of all or part of any of the Data Collections is not permitted, except that material may be duplicated by you for your research use or for educational purposes in electronic or print form. You must obtain permission from the copyright holder, usually the author, for any other use. Exceptions only apply where a deposit may be explicitly provided under a stated licence, such as a Creative Commons licence or Open Government licence.

Electronic or print copies may not be offered, whether for sale or otherwise to anyone, unless explicitly stated under a Creative Commons or Open Government license. Unauthorised reproduction, editing or reformatting for resale purposes is explicitly prohibited (except where approved by the copyright holder themselves) and UEA reserves the right to take immediate 'take down' action on behalf of the copyright and/or rights holder if this Access condition of the UEA Digital Repository is breached. Any material in this database has been supplied on the understanding that it is copyright material and that no quotation from the material may be published without proper acknowledgement.

Contents

Abstract	2
List of figures:.....	9
Chapter 1:.....	9
Chapter 2:.....	9
Chapter 3:.....	10
Chapter 4:.....	12
Chapter 5:.....	13
Appendix 1:	13
Appendix 2:	14
Appendix 3:	14
Appendix 4:	14
List of Tables:.....	15
Chapter 2:.....	15
Chapter 3:.....	15
Chapter 4:.....	16
Appendix 1:	17
Appendix 2:	17
Appendix 3:	17
List of accompanying material:	18
Acknowledgements:.....	19
Chapter 1: Introduction.....	23
1.1 Reconstructing eruptive transitions.....	25
1.2 Ascension Island as an exemplar of small volume hazardous eruptions.....	30
1.3 The contribution from the Chapters in this Thesis	31
Chapter 2: Reconstructing dynamics of the Echo Canyon explosive – effusive eruption ...	33

2.1 Introduction	33
2.2 Deposits and Products of the Echo Canyon Eruption.....	37
2.3 Methods.....	41
2.3.1 Stratigraphy and sampling.....	41
2.3.2 Density measurements & Textural Categorisation	42
2.3.4 Geochemical analyses.....	44
2.3.5 SEM imagery	45
2.4 Stratigraphy of the Echo Canyon Eruption Deposits	45
2.4.1 Stratigraphic Summary	45
2.4.2 Pumice cone stratigraphy	51
Lower cone	51
Middle Cone.....	54
Upper Cone – Proximal PDC deposits.....	59
Distal Deposits	63
2.4.3 Post cone units.....	71
2.5 Vesicularity and vesicle textures	73
2.6 Whole Rock Compositions and Viscosity.....	73
2.7 Petrography:	79
2.8 Discussion:	80
2.8.1 Stratigraphy and Eruptive Style	81
2.8.2 Evolution and Variability of Vesicle Textures	82
2.8.3 Bulk Vesicularity, Fragmentation and Explosivity.....	85
2.8.4 Obsidian Breccia, Tuffisite Formation and Degassing Pathways.....	90
2.8.5 Melt Composition, Viscosity, and Eruption Dynamics.....	91
2.8.6 Eruption Sequence and Dynamics Summary.....	93
2.9 Conclusions / future work	96

Chapter 3: Forensic reconstruction of the Echo Canyon Eruption using quantitative textural and petrological microanalysis	97
3.1 Introduction:	97
3.2 Methods:	100
3.2.1 Sampling and petrology:	100
3.2.2 BSE Imaging, calculation of shape factors and generation of VSDs.	104
3.3 Results:	111
3.3.1 Crystal populations & glass compositions:	111
3.3.1a Macrocryst phases:	114
3.3.1b Groundmass phases:.....	120
3.3.2 Vesicle Size Distributions (VSD)	124
3.3.3 Inferred T & H ₂ O from crystal populations	129
<i>Plagioclase – melt thermometry & hygrometry</i>	130
<i>K-feldspar – melt thermometry & hygrometry</i>	131
3.3.4 Variations in vesicle shape	138
Macro-vesicular Equant (842A_63 – Unit 1).....	139
Micro-vesicular Equant (843A_4 – Unit 2).....	144
Dense (844C_10 – Unit 4)	144
Macro-vesicular Elongate (829A_29a – Unit 9)	147
Dense LX (827C_6_LX – OBP)	147
Dense HX (827C_6_HX – OBP)	151
Macro-vesicular Equant (827C_3 – OBP)	151
Summary – comparison of textural groups and Cone vs OBP Deposits	153
3.3.5 Shape parameter Ω & Capillary number.....	153
3.4 Discussion:.....	158
3.4.1 Reconstructing T, H ₂ O & viscosity – plagioclase-melt vs K-spar-melt pairs	159
Feldspar populations, Temperatures & H ₂ O.....	161

Melt vs Magma viscosity in the cone & post-cone deposits	163
Summary.....	166
Vesiculation & ascent - Cone deposits	168
Implications.....	169
Vesiculation & ascent – Post-cone deposits.....	170
Implications.....	171
3.4.3 Relating vesicle shape to capillary number, viscosity & overpressure.....	171
Applying models of bubble shape, capillary number & overpressure	172
Implications for the EC eruption.....	174
3.4.4 Using bubble number density to reconstruct decompression & ascent rate ..	175
3.4.5 Reconstructing the ascent of the Echo Canyon magma (summary)	179
Magma source and crustal interaction:.....	180
Early eruptive phase – cone deposits	180
Late eruptive phase – post-cone deposits.....	181
3.5 Conclusions & implications:.....	181
Chapter 4: Textural analysis of the Mingled Fall Deposit in 2D & 3D	183
4.1 Introduction	183
4.2 The Mingled Fall deposit.....	187
4.3 Methods 1 – sampling & clast selection	191
4.3.1 Stratigraphy & sampling	191
4.3.2 Density measurements & clast selection	192
4.4 Methods 2 - 3D data collection & processing.....	193
4.4.1 XCT data collection	194
4.4.2 Segmentation – HRES	198
4.2.2a Creating a binary melt field:	200
4.2.2b Add thicker melt films and crystals	202
4.4.3 Extracting bubbles – single composition	205

4.4.3a Bubble separation	205
4.4.3b Removing edge-touching vesicles – single composition	208
4.4.4 Extracting bubbles - two compositions.....	209
4.4.4a Sub-dividing the volume by composition & applying separation algorithms	210
4.4.4b Removing edge-touching bubbles – two compositions.....	212
4.4.5 Quantitative analysis of the bubble populations.....	214
4.4.6 Extracting crystal volumes	214
4.5 Methods 3 - 2D textural analysis	217
4.5.1 Thin sectioning & SEM imaging.....	217
4.5.2 2D Vesicle shape analysis.....	219
4.6 Results	220
4.6.1 2D VSDs	220
4.6.2 2D shape parameters	227
4.6.3 3D VVDs & VSDs	231
4.6.4 3D shape parameters	237
4.6.4a Larger bubble populations 3D trends	242
4.6.4b Smaller bubble populations	244
4.7 Discussion.....	245
4.7.1 Initial interpretations for ascent dynamics of the Mingled Fall.....	245
4.7.2 Impact of excluding partial bubbles from VVD and VSD analysis.....	247
4.7.3 Considerations from XCT data processing	249
Limitations of resolution – error on bubble volumes & preservation of thin films	250
Impact of other constraints	252
4.7.4 Comparing 2D and 3D textural studies	252
VVD and VSD	253
Shape parameters	256

4.7.5 Future work	258
4.8 Conclusions & implications.....	258
Chapter 5: Synthesis	260
5.1 Introduction	260
5.2 Value of forensic volcanology and petrology	261
5.3 Importance of small-volume trachytic eruptions.....	263
5.4 Insights from 2D and 3D textural studies	265
5.5 Application of principles to the 2020 – 21 volcanic crisis at La Soufrière St Vincent	267
5.5.1 Background to La Soufrière St Vincent and the 2020-21 eruption	269
5.5.2 Time & resource constrained characterisation of complex crystal populations	270
5.5.2 Forensic fieldwork producing insights for specific eruption phases & textures informing geochemical studies.....	274
5.5.3 Reflections and learning from 2020-21 workflows:	279
5.6 Future work	282
5.7 Conclusions	283
Trachytic eruption styles and the Echo Canyon eruption	283
Strategies for reconstructing past eruptions:.....	283
2D vs 3D textural studies and the Mingled Fall:.....	284
Appendices:	286
Appendix1 – Echo Canyon eruption deposits.....	286
1.1 – Echo Canyon localities	286
1.2 – Original logs and sketches	290
1.21 – Logs from Echo Canyon units 1 – 10.....	290
1.22 – logs and sketches from Unit 11	294
1.23 original logs of Unit 12.....	297
1.24 – Log of coastal distal PDC deposits	299

1.25 – logs of distal PDC deposits in and around the Ariane Site Quarry and NE Bay	300
1.26 – log of distal PDC deposits at Spire Beach	303
1.3 – XRF standards data	305
1.4 – Stratigraphic data used for Fig. 2.9	306
1.5 – Clast Bulk Vesicularity Data	307
1.6 Textural group abundance data used in Fig. 2.9	314
Appendix 2 – quantification of vesicle textures	314
2.1: microlite crystallinities	314
2.2: Machine learning image segmentation	314
2.3: Regularity and Solidity descriptors	316
2.4: Additional vesicle shape plots	316
Appendix 3: 2D and 3D studies of the Mingled Fall	322
Appendix 3.1: XRF data for the Mingled Fall used to calculate DRE from Chamberlain <i>et al.</i> , (2020)	322
Appendix 3.2: Detail on separation algorithms between basalt and rhyolite regions.	323
Appendix 4 – Initial Petrography of the 2020-21 La Soufrière Dome rocks	328
List of References:	344

List of figures:

Chapter 1:

Fig. 1.1 – Geological map and location of Ascension Island	30
---	----

Chapter 2:

Fig. 2.1 – Geological map of Ascension Island with Echo Canyon (EC) location	37
---	----

Fig. 2.2 – Geological map of the EC eruption deposits	38
--	----

Fig. 2.3 – Annotated overview photos of the EC eruption deposits.....	39
Fig. 2.4 – Interpretive cross-sections of the EC eruption deposits.....	40
Fig. 2.5 – Apparatus for pyroclast density measurements.....	43
Fig. 2.6 – Composite log of the EC eruption deposits.....	47
Fig. 2.7 – Pumice clast types found in the EC deposits.....	48
Fig. 2.8 – Other common clasts in the EC deposits.....	49
Fig. 2.9 – Summary of stratigraphic variations in the EC deposits.....	50
Fig. 2.10 – Outcrop photos of the lower cone deposits.....	53
Fig. 2.11 – Outcrop photos of the middle cone deposits.....	58
Fig. 2.12 – Outcrop photos of the upper cone deposits.....	61
Fig. 2.13 – Outcrop photos of distal PDC deposits (coastal).....	64
Fig. 2.14 – Outcrop photos of distal PDC deposits (NE-Bay Quarry).....	68
Fig. 2.15 – Outcrop photos of distal PDC deposits (Spire Beach).....	70
Fig. 2.16 – Outcrop photos of post-cone deposits.....	72
Fig. 2.17 – Plots of whole rock major and trace element data.....	75
Fig. 2.18 – Characteristic crystal populations of the EC deposits.....	80
Fig. 2.19 – Schematic showing development of textures in pyroclasts.....	84
Fig. 2.20 – Bulk vesicularity distributions for EC units and other eruptions.....	87
Fig. 2.21 – Summary figure showing progression of the EC eruption.....	94

[Chapter 3:](#)

Fig. 3.1 – Summary of unit characteristics determining clast selection.....	101
Fig. 3.2 – Method of crystal identification and image segmentation.....	103
Fig. 3.3 – Manual image correction for VSD analysis.....	107
Fig. 3.4 – TAS diagram of melt inclusion and matrix glass compositions.....	112

Fig. 3.5 – Triangular diagrams of pyroxene compositions.....	113
Fig. 3.6 – Triangular diagrams of feldspar compositions.....	113
Fig. 3.7 – SEM images of euhedral – subhedral anorthoclase phenocrysts.....	116
Fig. 3.8 – SEM images of subhedral plagioclase antecrysts.....	117
Fig. 3.9 – SEM images of subhedral albite macrocrysts.....	118
Fig. 3.10 – SEM images of sieve textured feldspar macrocrysts.....	119
Fig. 3.11 – SEM images of clinopyroxene macrocryst populations.....	120
Fig. 3.12 – SEM images of feldspar microlite populations.....	121
Fig. 3.13 – SEM images of groundmass populations of clinopyroxene.....	123
Fig. 3.14 – SEM images of crystal clots / clusters.....	124
Fig. 3.15 – Plots of $\log(Nv>L)$ vs $\log(L)$ and $\log(Nv)$ vs L	127
Fig. 3.16 – Vesicle volume distribution plots.....	129
Fig. 3.17 – Measured vs predicted Kd_{Or-Ab} for feldspar-melt equilibrium.....	135
Fig. 3.18 – Shape parameters for vesicles from sample 842A_63.....	143
Fig. 3.19 – Shape parameters for vesicles from sample 843A_4.....	145
Fig. 3.20 – Shape parameters for vesicles from sample 844C_10.....	146
Fig. 3.21 – Shape parameters for vesicles from sample 829A_29a.....	148
Fig. 3.22 – Shape parameters from low microlite (LX) regions of 827C_6.....	149
Fig. 2.23 – Shape parameters from high microlite (HX) regions of 827C_6.....	150
Fig. 3.24 – Shape parameters from 827C_3.....	152
Fig. 3.25 – Cumulative frequency plots of Ω and $1 - \Omega$	156
Fig. 3.26 – Capillary number against $1 - \Omega$	157
Fig. 3.27 – BSE images of high and low vesicularity in the lava and dome.....	166
Fig. 3.28 – Bubble number density against SiO_2 (ascent rate meter).....	178
Fig. 3.29 – Formation of bubble textures across the conduit.....	179

Chapter 4:

Fig. 4.1 – Geological map of Ascension showing Mingled Fall localities.....	188
Fig. 4.2 – Generalised stratigraphic log of the Mingled Fall.....	189
Fig. 4.3 – Bulk vesicularity and texture variations to guide clast selection.....	193
Fig. 4.4 – Correlative microscopy workflow.....	194
Fig. 4.5 – Textural features from low resolution XCT full clast scans.....	196
Fig. 4.6 – Feature matching between high- and low-resolution scans.....	197
Fig. 4.7 – Parts 1 and 2 of XCT data processing workflow.....	199
Fig. 4.8 – Testing membrane enhance algorithm parameters.....	201
Fig. 4.9 – Checking for edge-effects in enhanced sub-volumes.....	202
Fig. 4.10 – Schematic of greyscale histogram for auto thresholding limits.....	203
Fig. 4.11 – Process for removing disconnected noise.....	204
Fig. 4.12 – Separation algorithm <i>neighborhood count</i> schematic.....	205
Fig. 4.13 – Comparison of output from varying separation parameters.....	205
Fig. 4.14 – Method of re-combining over-split large bubbles.....	207
Fig. 4.15 – Manual labelling of partial bubbles.....	209
Fig. 4.16 – SEM images of basaltic and rhyolitic regions of mingled clasts.....	210
Fig. 4.17 – Parts 3 and 4 of XCT data processing workflow.....	211
Fig. 4.18 – Part 5 of XCT data processing workflow.....	212
Fig. 4.19 – Manual labelling of partial bubbles for multiple compositions.....	213
Fig. 4.20 – Method of targeted thin-sectioning.....	218
Fig. 4.21 – Segmentation quality between basalt and rhyolite regions.....	219
Fig. 4.22 – Vesicle volume distributions (VVD) from 2D data.....	223
Fig. 4.23 – Vesicle size distributions from 2D data.....	225

Fig. 4.24 – SEM images of vesicle textures in Mingled Fall regions/clasts.....	226
Fig. 4.25 – Plots of 2D shape data for Mingled Fall regions/clasts.....	228
Fig. 4.26 – VVDs from 3D data.....	234
Fig. 4.27 – Cumulative volume fraction against log(EqD) from 3D data.....	235
Fig. 4.28 – Plot of ln(n) against equivalent diameter from 3D data.....	235
Fig. 4.29 – Plot of log(Nv > L) against log(L) from 3D data.....	236
Fig. 4.30 – Elongation vs Anisotropy from 3D data.....	239
Fig. 4.31 – Volume3d vs anisotropy from 3D data.....	240
Fig. 4.32 – Volume3d vs elongation from 3D data.....	241
Fig. 4.33 – VVDs with partial bubbles overlaid from 3D data.....	248
Fig. 4.34 – Plot of ln(n) vs EqD with partial bubbles from 3D data.....	249
Fig. 4.35 – Comparison of ln(n) vs L for 2D and 3D data (rhyolite regions).....	254
Fig. 4.36 – Comparison of ln(n) vs L for 2D and 3D data (scoria clast).....	256

[Chapter 5:](#)

Fig. 5.1 – Crystal populations and textures in La Soufrière rocks.....	272
Fig. 5.2 – Microlite populations in the La Soufrière rocks.....	276
Fig. 5.3 – Crystal size distributions from La Soufrière rocks.....	278

[Appendix 1:](#)

Fig. 1.21 – Logs from Echo Canyon units 1 – 10.....	290-293
Fig. 1.22 – Logs and Sketches from Echo Canyon Unit 11.....	294-296
Fig. 1.23 – Original Logs from Echo Canyon Unit 12.....	297-298
Fig. 1.24 – Log of Coastal PDC deposits.....	299
Fig. 1.25 – logs of distal PDC deposits in and around the Ariane Site Quarry and NE Bay.....	300-302

Fig. 1.26 – Log of distal PDC deposits at Spire Beach.....	303-304
---	---------

[Appendix 2:](#)

Fig. 2.1 – Snapshot of Trainable Weka Segmentation (TWS) window.....	315
Fig. 2.2 – examples of poor segmentation in TWS output.....	316
Fig 2.3 – Regularity and Solidity Descriptors.....	316
Fig. 2.4 – Density plots of regularity vs solidity for EC units.....	317
Fig. 2.5 – Density plots of roundness vs circularity for EC units.....	318
Fig. 2.6 – Density plots of regularity vs circularity for EC units.....	319
Fig. 2.7 – Density plots of roundness vs circularity for EC units.....	320
Fig. 2.8 – Density plots of particle area vs aspect ratio for EC units.....	321

[Appendix 3:](#)

Fig. 3.1 – Parts 3 and 4 of the XCT data processing workflow.....	325
Fig. 3.2 – Part 5 of the XCT data processing workflow.....	327
Fig. 3.3 – Removing overlap at basalt-rhyolite boundary.....	328

[Appendix 4:](#)

Fig. 4.1 – degraded rims on clinopyroxene.....	329
Fig. 4.2 – Extreme degradation between oxides and clinopyroxenes.....	330
Fig. 4.3 – Less extreme degradation at clinopyroxene rims.....	330
Fig. 4.4 – Extreme breakdown of Fe-Ti oxide.....	331
Fig. 4.5 – Immiscibility textures in melt inclusions.....	332
Fig. 4.6 – Healed fracture in feldspar.....	333
Fig. 4.7 – Clinopyroxene macro-phenocryst with degraded rims.....	334
Fig. 4.8 – Clinopyroxene with melt inclusions.....	334
Fig. 4.9 – Symplectic forsterite.....	335

Fig. 4.10 – Complex zoning in feldspar.....	336
Fig. 4.11 – Feldspar microlite populations.....	336
Fig. 4.12 – Zoning in feldspar microlite populations.....	337
Fig. 4.13 – Feldspar microlite populations.....	338
Fig. 4.14 – Oxides in the groundmass and degraded orthopyroxenes.....	339
Fig. 4.15 – Needle-like Fe-Ti oxides in the groundmass.....	339
Fig. 4.16 – Degradation of orthopyroxene microlite.....	340
Fig. 4.17 – Degraded larger and smaller groundmass orthopyroxenes.....	341
Fig. 4.18 – Devitrification of glass.....	342
Fig. 4.19 – Growth of orthopyroxene at vesicle edges.....	342

List of Tables:

Chapter 2:

Table 2.1 – Comparison of explosive small-volume eruptions from the literature.....	35-36
Table 2.2 – Sample numbers and locations.....	42
Table 2.3 – Whole rock major element data (in %) for Echo Canyon units and different textural groups.....	76
Table 2.4 – Whole rock trace element data for Echo Canyon samples, measured via XRF at the University of East Anglia.....	77
Table 2.5 – Trace element data for Echo Canyon samples, measured via LA-ICPMS at the University of Granada by J H Scarrow.....	78
Table 2.6 – Calculated viscosity for EC units and comparison magma compositions.....	79

Chapter 3:

Table 3.1 – Clasts analysed for VSD and vesicle shapes from the EC eruption.....	106
Table 3.2 – Symbols, shape parameters & eruption parameters used in Ch. 3.....	110-111

Table 3.3 – Vesicle free relative abundances of mineral phases in units of the EC eruption deposits.....	115
Table 3.4 – Output values from VSD analyses.....	126
Table 3.5 – Output from iterative calculation of T & H ₂ O using Eq. 23 from Putirka (2008) & Eq. 23 of Waters and Lange (2015), for plagioclase-melt pairs.....	132-134
Table 3.6 – Modelled temperatures from Putirka (2008) and H ₂ O contents using the Mollo <i>et al.</i> , (2015) K-feldspar-melt hygrometer.....	136-137
Table 3.7 – Summary of vesicle shape data from Figs. 3.18 – 3.24.....	140-142
Table 3.8 – parameters from images analysed for shape analysis.....	155
Table 3.9 – calculated bubble overpressures for the EC sampled units based on measured Ω values and modelled capillary numbers from Moitra <i>et al.</i> , (2013).....	158
Table 3.10 – Viscosities calculated from plagioclase and alkali-feldspar crystal-melt equilibrium pairs for the Echo Canyon eruption deposits.....	164
Chapter 4:	
Table 4.1 – Studied and sampled outcrops of the Mingled Fall from this study.....	191
Table 4.2 – Details of clasts selected for further analysis from the Mingled Fall.....	193
Table 4.3 – pixel size for x-ray computed microtomography scans.....	195
Table 4.4 – Parameters measured for bubbles in the Mingled Fall dataset from x-ray computed tomography data using Avizo®.....	215-216
Table 4.5 – details of processed and analysed volumes used in vesicle analysis.....	217
Table 4.6 – Parameters extracted from 2D VSDs and shape analysis.....	221
Table 4.7 – 2D shape parameters from the Mingled Fall.....	229
Table 4.8 – Parameters from 3D studies of vesicle texture.....	232
Table 4.9 – Description of variations in shape parameters in 3D, larger* vesicle populations from the Mingled Fall.....	243

[Appendix 1:](#)

Table 1.1 – All Echo Canyon deposit localities & sample sites from 2018 – 2020.....	286-289
Table 1.2 – Data for standards used in XRF analyses – University of East Anglia.....	305
Table 1.3 – Trace element standards used in XRF Analyses – University of East Anglia.....	305
Table 1.4 – Echo Canyon stratigraphic data used to produce Fig. 2.9.....	306
Table 1.5 – Vesicularity of clasts from Unit 1 of the Echo Canyon deposits used to generate Figs. 2.9 and 2.20.....	307
Table 1.6 – Vesicularity of clasts from Unit 2 of the Echo Canyon deposits used to generate Figs. 2.9 and 2.20.....	308
Table 1.7 – Vesicularity of clasts from Unit 3 of the Echo Canyon deposits used to generate Figs. 2.9 and 2.20.....	309
Table 1.8 – Vesicularity of clasts from Unit 4 of the Echo Canyon deposits used to generate Figs. 2.9 and 2.20.....	310
Table 1.9 – Vesicularity of clasts from Unit 9 of the Echo Canyon deposits used to generate Figs. 2.9 and 2.20.....	311
Table 1.10 – Vesicularity of clasts from Unit 11 of the Echo Canyon deposits used to generate Figs. 2.9 and 2.20.....	312
Table 1.11 – Vesicularity of clasts from the Orange-Brown Pumice (OBP) of the Echo Canyon deposits used to generate Figs. 2.9 and 2.20.....	313
Table 1.12 – Abundance of textural groups in the Echo Canyon Eruption Deposits. Used to generate Fig. 2.9.....	314

[Appendix 2:](#)

Table 2.1 – Crystal data for high and low crystallinity regions in sample 827C_6.....	314
--	-----

[Appendix 3:](#)

Table 3.1 – Whole rock data for the Mingled fall from Chamberlain et al., (2020) used to calculate dense rock equivalent density.....	322
--	-----

List of accompanying material:

Electronic appendix 1_1: Compositional and stratigraphic data for the Echo Canyon eruption products

Electronic Appendix 2_1: Electron microprobe mineral and glass data, standard calibration and error calculations.

Electronic Appendix 2_2: Images from 829A_29a, all raw data and code used for shape analysis

Electronic Appendix 2_3: Images used in VSD analysis (and shape analysis) and raw VSD outputs

Electronic Appendix 2_4: Images used to collect crystal percentages.

Electronic Appendix 2_5: Raw thermometry and hygrometry output from *Thermobar*

Electronic Appendix 3_1: R-code and 3D bubble data used to plot VVD and VSD curves

Electronic Appendix 3_2: Raw XCT data for 5_102 and 7_50

Electronic Appendix 3_4: 2D shape data from the Mingled Fall clasts

Electronic Appendix 3_5: 2D VVD and VSD data and images used.

Acknowledgements:

Although on paper, this thesis took “only” 5 years to complete – courtesy of a global pandemic, countless analytical delays and one extraordinarily technologically cursed student (me) – it is the culmination of a 15-year obsession. When at the age of 13, I told my geography teacher Mr Garcia I wanted to study volcanoes, he told me I would have to get a geography GCSE, take Geology A-Level, do a Geology degree to master’s level, and finally, complete a PhD in volcanology.

So, I did.

To Mr Garcia, I would like to say thank you...and any ideas for the next 15?

Over the last 5 years, my whole supervisory team has provided me with a wealth of knowledge, support and advice. Chiara Petrone and Kate Dobson were always willing to answer a panicked email, participate in an emergency Zoom or help me get those last few bits of data (again, and again, and again). Closer to home, Ricky Herd’s attention to detail and consistent reminders that everything I write is too long...kept me focussed and provided timely and light-hearted nudges in the right direction – not to mention inspiring me to start my own “how did you get that in your suitcase?!” rock collection. I want to thank Rich Brown for making my time in the field a joy (mostly). Spending 8 weeks on a tiny island with my supervisor and his family after only meeting twice could have been a disaster, but his sense of humour, general good-eggedness and complete acceptance that I’d rather spend the morning meetings playing LEGO with his toddlers - Basti and Arianna - than looking at satellite photos, meant I didn’t lose my mind. That, and he never once complained when I refused to dig laterally on my shift in the scoria pit. Finally, there’s Jenni. It is hard to describe all the ways Jenni has helped me on this journey. Her enthusiasm, encouragement, and ability to ask the right questions at the right moment have pushed me forward – even when I really *really* didn’t want to. Under Jenni’s supervision I have felt valued and cared for every step of the way, she has inspired me to make sure that whatever comes next, I keep pushing myself and those around me to make things better for those who come behind. Through the pandemic, and my countless delays and mishaps, Jenni has been there to put things in perspective, recommend a good volcano movie and assure me I’ll get there in the end. The opportunities Jenni has given me outside of my thesis work have shaped me as a researcher, and a human. Whether I was participating in Norwich

Science Festival every year, attending Volcano Awareness week in St Vincent, or contributing to her other research projects, Jenni reminded me not to feel guilty for taking time away from my thesis - it was all part of my training. From very early on, my friends (and other supervisors) have joked that I get more and more like Jenni every day – I consider this to be a *HUGE* compliment.

The fieldwork and analyses that underpinned this PhD would not have been possible without an army of people. EnvEast have supported me every step of the way, even when my fieldwork budget tripled overnight with the news that instead of one flight and a two week stay, I would have to take three flights and stick around for 8. The team at the Ascension Island Government Conservation dept., namely Laura, Sophie, Dee and Dan facilitated so much of my work, gave advice, transported rocks and kept our spirits up towards the end of our second season. Everyone on Ascension made me feel welcome, but special mentions go to Al who provided us with whatever tool we needed, took us on walks and ultimately, soaked us with beer. And Hugh, who gave up his free time to scrabble about in the pumice with me and used a bin bag to keep me in the shade on Letterbox – a true hero. I'd like to thank Becca Winstanley for choosing to do a PhD on Ascension, thus giving me the chance to go back as her field partner for 8 glorious weeks – my last chance to catch some sea and sun before COVID-19 struck. We laughed, we cried, we broke beds...I'll never watch Moana without thinking of her. Here at UEA, I'd like to thank Bertrand Lézé for all his help with sample prep, XRF analyses and his endless willingness to try *just a little bit harder* to get good contrast between feldspar microlites and glass.

The wider Ascension Island volcanology team is a huge part of why I made it this far. Katie Preece and Katy Chamberlain (K²) provided a wealth of tips for surviving Ascension, answered all the questions I deemed too stupid to take to Jenni, and offered encouragement throughout. An especially huge thanks is owed to Jane Scarrow, who was my field partner for my first season. We shared a VERY small room for 8 weeks, made a lot of questionable crumble and sampled half the rocks on the island. Jane made sure I took care of myself and didn't grumble *too much* when I was stingy with my Percy Pigs. Since then, Jane has been the supervisor who isn't *technically* a supervisor. We've compared field notes 1000's of times, puzzled over Echo Canyon, and spent many hours silently working over Zoom. Jane has been so generous with her time and wisdom and is always ready to send doughnuts when required. I couldn't have done it without her. Another special mention has to go to the volcano community on twitter, they've helped me find references,

located obscure spreadsheets, and sent snippets of code. Not to mention providing endless inspiration in the form of volcano pics.

As well as my academic cheerleaders and support network I have had an incredible bunch of friends without whom I wouldn't have survived the PhD. My fellow housemates at Fort Speedwell and the Household Formerly Known as Speedwell - here's to the nuggs, the Netflix binges and the Roy's muffins. We survived the Beast from the East, TWO bathroom floods, and one global pandemic...it was a TIME but we survived it all relatively intact. My most cringe-inducing, heartfelt thanks go to Claire Buchan, the queen of *my* hea-R-t, without whom, my thesis would only contain hand-drawn graphs. She patiently taught me the mysteries of R, despite the fact that everything I wanted to do broke all the rules. I also want to thank my pal Willow, and her parents Gabriela and Chris. Every time I headed to London for analysis, they put me up in their family home, made me feel welcome and insisted I ate three square meals. I will be forever grateful!

The last few months have been a slog and I wouldn't have gotten through them without Emma and Richmal. They put up with my *supernatural* ability to fixate on the same tv show for 6 months...sat with me (in-person and virtually) through late-night campus dinners and assured me its normal to hate **Every. Single. Word.** you've ever written. The other 2 thirds of volcano-tears, Jade and James, have been with me from the start (I think...I think it's been...84 years?) and I can't imagine it any other way. From the lows of getting blisters from excessive use of gaffa tape, to the highs of La Soufrière St Vincent, Jade and James have been there for me. Arguably, James has been there too much...but we survived sharing a house for a year, an office for 4, and 4 years of joint birthdays so I guess neither of us is too annoying to be around? My friends have been my rock (pun intended), they've listened, we've laughed, we've cried, and they've been some of the best parts of my time here in Norwich. I am sure we will be pals for life.

Last, but by no means least, I need to thank my family and partner. My parents and sister have been there every step of the way. Stopping to let me pick up my 1000th rock on the beach on as a toddler, telling me I can do anything I put my mind to, and generally encouraging me in every possible way. They never doubted I would get to the end, and they let me know it repeatedly. They put up with my complete inability to commit to any plan until it was about to happen, my grumpiness when things weren't working (which was A LOT) and even let me mooch off them for 7 months during COVID. My social worker

parents managed to raise a child who is very much a scientist, but they also made sure I would use my “powers” for good. It is from them that I learned that the relationships you build with people are what will help you make a difference in the world. Something that I know has helped me no end during my PhD and will serve me well as I continue bothering rocks for years to come. Finally, I want to say thank you to my partner Thomas, we’ve lived apart for most of the 10 years we’ve been together, but he never made me choose between him and volcanoes! Thomas is a part of my family, he’s been patient, sympathetic, and willing to drive across the country when I was too overwhelmed by my PhD to book a train ticket. Now that I’ve *finally* written my thesis, I’m looking forward to wasting our evenings watching people drop stuff on stuff...totally guilt-free.



From the top left, Katy Chamberlain, me, Becca Winstanley, Basti and Rich Brown, Jane Scarrow, Jade Eyles, James Christie, and me. From AIG Conservation: Lucie Machin and Will Wood. Hugh Carville, Al and Bex, James (also AIG Conservation) and Rob (AIG), me and Becca Winstanley. Bottom right, Jenni Barclay and me.

Chapter 1: Introduction

Volcanic eruptions are the spectacular surface expression of magma's journey from the interior of the Earth. At a single volcanic centre, eruptive episodes can vary dramatically in intensity and scale, controlled by processes acting across timescales ranging from more than 1000's of years, to minutes. Eruptive transitions happen when there is a shift in the style of activity during the course of an eruptive episode. Amongst the most explosive eruptions worldwide, > 60% include an explosive-effusive transition (Cassidy *et al.*, 2018) but transitions can also include a shift from phreatic – magmatic activity or fluctuations in explosion intensity (e.g., fountaining/ discrete blasts/ production of a stable plume) and column stability. The nature and timescales of such transitions has a significant impact on the type and severity of the hazards faced by populations near and far. As such, it is vital that we gain a better understanding of eruptive transitions in all settings, to ensure more effective monitoring and hazard assessment in volcanically active regions across the globe.

Much of the literature on eruptive transitions to date has focussed on the characterisation and modelling of eruption and ascent dynamics for large-volume, high intensity events (e.g., Polacci *et al.*, 2001; Sparks and Young 2002; Houghton *et al.*, 2010; Rotella *et al.*, 2014; Pappalardo *et al.*, 2018;). Typically, these are eruptions of calc-alkaline arc magmas or those located at high magma-production rate centres such as Hawaii and Iceland (Parcheta *et al.*, 2013; Shea *et al.*, 2017; Janebo *et al.*, 2016; Schmith *et al.*, 2018). Eruptions with a volcanic explosivity index (VEI) of 4 or more are highly explosive, produce large volumes of material and occur over hours to days at a single volcanic centre (e.g., Novarupta 1912 – Adams *et al.*, (2006) and Taupo 1.8 ka – Houghton & Wilson *et al.*, (2010)). Such eruptions are demonstrably high impact events (e.g., cause dramatic changes to the landscape and would pose a significant risk to life and or property) and are usually more readily preserved in the geological record than smaller volume eruptions (e.g., Mt St Helens 1980 – Carey *et al.*, (1990), Vesuvius 79AD – Carey & Sigurdsson (1987)). Further, the physical properties of calc-alkaline melts and their responses to changing conditions during ascent have been investigated through experiments and modelling (e.g., Huppert *et al.*, 1982; Robert *et al.*, 2013; Giordano *et al.*, 2008; Gardner and Ketcham 2011) allowing constraints to be placed on ascent rate, bubble overpressure and fragmentation mechanism. Through these studies, several factors controlling eruptive transitions have been identified including ascent rate, volatile content and degassing, magma rheology and magma-conduit interactions (Cassidy

et al., 2018) but our understanding of how these translate to recognising monitoring signals that can be used in anticipating these transitions is still incomplete.

In contrast, despite being relatively common across a range of settings (e.g., Pico Teide – Pico Viejo, Tenerife – intraplate, Pantelleria – back-arc rifting, Tarvurur and Vulcan, Papua New Guinea – Arc (Davies *et al.*, 2022)), the ascent and eruption dynamics of small-volume alkali-rich magmas are relatively understudied. We know small-volume eruptions are important in the rock record as many trachytic examples have been identified in association with larger volcanic structures, their volumes estimated, and stratigraphy recorded to reconstruct the long-term evolution of volcanic centres (e.g., Katsui and Katz 1967; Cole *et al.*, 1995; Pistolesi *et al.*, 2015). However, only a few studies have interrogated deposits in more detail to begin to reconstruct and understand the drivers behind the ascent and eruption dynamics of these events (e.g., Houghton *et al.*, (1985) – Mayor Island pumice cones, Shea *et al.*, 2017 – Hawaii, and Clarke (2020) - Aluto). This is in part due to the poor preservation of small-volume eruptions in ocean island settings (Preece *et al.*, 2021) (where such eruptions are common) and the lack of adequate exposure (e.g., Hernando *et al.*, 2019). Shea *et al.*, (2017) used detailed stratigraphic observations from a few key outcrops as a framework on which to trace changes to clast texture, vesicularity and ultimately eruption dynamics in the Pu’u Wa’awa’a pumice cone in Hawaii. This study demonstrated how a unified approach can produce high-resolution insights into eruptive processes for small-volume eruptions, but remains one of very few examples to do so for these eruptions. In this thesis I will expand upon the approach of Shea *et al.*, (2017) to increase our understanding of the dynamics of small-volume eruptions worldwide.

It is accepted that magma composition and rheology (and variations thereof) exert a strong control on ascent and eruption dynamics (Cassidy *et al.*, 2018). However, our understanding of the properties of trachytic magmas and their behaviour during ascent is still surprisingly limited. Attempts to reproduce subsurface conditions experimentally have been hindered by the challenges associated with alkali-feldspar crystallisation in experiments (Arzilli *et al.*, (2013). However, some of the more extreme alkali compositions such as phonolites have been the focus of much investigation (e.g., Sulpizio *et al.*, 2005; Larsen and Gardner 2004; Arzilli *et al.*, 2016; Mongrain *et al.*, 2008). Recent advances in experimental, modelling, and textural studies have begun to provide vital constraints on the physical properties of trachytic magmas (Giordano *et al.*, 2004; Arzilli and Carroll 2013; Fanara *et al.*, 2013; Shea *et al.*, 2017), identifying them as “kinetically reactive” in response

to perturbations during ascent (Shea *et al.*, 2017). We now know that trachytic melts can hold more water at a given pressure and have a higher H₂O diffusivity than their calc-alkaline equivalents, this facilitates rapid volatile exsolution and can cause extensive microlite crystallisation during ascent (Shea *et al.*, 2017; Deniel *et al.*, 2020). This new understanding of the behaviour of trachytic magmas during ascent helps identify processes underpinning the changing eruptive styles recorded in the stratigraphy of these small-volume trachytic eruptions.

The catalogue of studies that use high-resolution reconstructions of transitions in eruptive style and calculated physical melt properties to place constraints on – and understand the drivers of – the explosivity and associated hazards of small-volume trachytic eruptions is limited. This study aims to expand our knowledge and understanding of these eruptions by interrogating deposits from small-volume trachytic eruptions on Ascension Island in the South Atlantic.

In doing so I will answer the following research questions:

1. What evidence (and tools) can we use to identify eruptive transitions in small-volume eruptions at a high resolution that can be applied even where exposure is limited?
2. What is the nature of transitioning eruption style in small-volume trachytic eruptions (e.g., explosive-effusive and variations in explosion intensity)?
3. What *controls* the nature of transitioning eruption style for these eruptions?

Finally, I will consider the implications of the answers to questions 1 – 3 for ongoing hazard assessment at these eruption centres.

[1.1 Reconstructing eruptive transitions](#)

Reconstructions of the ascent and eruption dynamics of ancient eruptions rely on the interrogation of preserved eruption products. Transitions in eruptive behaviour are thus usually identified by tracing changes to deposit characteristics (e.g., Buck *et al.*, 1981; Houghton *et al.*, 1985; Miyabuchi 2011; Chamberlain *et al.*, 2016; Martí *et al.*, 2018). The most obvious of these transitions is an explosive-effusive transition that produces a lava flow or dome that can be directly linked to explosive stratigraphy through deposit geometry, crystal populations and composition or direct observations (e.g., Preece *et al.*, 2016). However, explosive-effusive (and vice versa) transitions are not the only important

variations in eruptive activity (Cassidy *et al.*, 2018). Fluctuations in column height, partial and total column collapse (producing pyroclastic density currents – PDCs) and changing explosion intensities all have important implications for volcanic hazard and can also be identified in the rock record. Changes in grain size, clast componentry, unit thicknesses, their internal structures and lateral extents are all used to infer mechanisms of emplacement and hence changing eruption style (e.g., Newhall and Self, 1982; Pyle *et al.*, 2015; Biass *et al.*, 2019). Further, calculated erupted volumes and reconstruction of column heights for eruption phases are used to trace changes in eruption magnitude and intensity during and between events (Pyle 2015).

These field-based investigations represent a critical first step in reconstructing eruption dynamics. However, when used in isolation, these techniques only provide descriptions of changing eruption style rather than elucidating the underlying causes of these transitions. Further, measures of magnitude and intensity that rely on accurate reconstructions of deposit volumes are unreliable for eruptions where deposits are poorly preserved – common for small-volume eruptions – and thus full grain size studies, or the production of isopach maps are challenging. To understand the drivers of transitions identified through interrogation of the rock record several approaches are used that examine a range of processes from deep in the storage region, to the shallow sub-surface. The most effective studies are those where processes occurring in different parts of the system can be linked together to explain the eruptive styles recorded in the stratigraphy (Colucci *et al.*, 2014).

As volatile content is a key factor influencing both the triggering and ascent rate of magma, some studies focus on reconstructions of deep initial magmatic volatile concentrations and the extent of magma degassing during ascent (e.g., Barclay *et al.*, 1996). This is done via analysis of melt and volatile inclusions in deeper sourced phenocryst populations (Blundy and Cashman 2008), alongside analyses of matrix glass and microlite populations that record volatile concentrations during shallow ascent (e.g., Edmonds *et al.*, 2001; Harford *et al.*, 2003). Phenocryst populations must be carefully identified via crystal textures and composition and related to their host melt through reconstruction of crystallisation pathways and their classification as an equilibrium phase (e.g., Clyne 1999; Chamberlain *et al.*, 2019). This becomes more complex in crystal poor systems, or those where crystals from multiple batches of compositionally similar melt may be incorporated into the crystal cargo. Further, there is no guarantee that melt/volatile inclusions will be preserved in analysed samples (e.g., lack of inclusions in phenocryst phases in the rhyolite melt of the

mingled fall – Chamberlain *et al.*, 2020). Calculating volatile concentrations in the late-stage, shallowly ascending melt can be challenging, particularly for alkali-rich melts where alkali-phases are susceptible to ion migration during electron microprobe analysis (Humphreys *et al.*, 2006), or where glass regions of sufficient size are rare (e.g., microlite rich or highly vesicular samples). Reconstructions of volatile contents are often coupled with temperatures, melt compositions and crystallinities to establish melt rheology (e.g., Vona *et al.*, 2013; Mader *et al.*, 2013) as this exerts a control on the development of overpressure and volatile migration, ultimately influencing fragmentation mechanism and explosion intensity (Cassidy *et al.*, 2018).

Models of magma ascent and conduit processes are also used to explain changes in eruptive style (e.g., Suzuki & Koyaguchi 2012) and intensity as factors both internal and external to the ascending magma exert an influence (Cassidy *et al.*, 2018). Such models require considerations of conduit geometry (and changes to that indicated by deposit componentry), calculations of magma ascent and decompression rate, development of shear zones, magma rheology and erupted volumes to reproduce the erupted stratigraphy. Such models can be powerful in identifying factors that lead to transitions in eruptive style (e.g., Carr *et al.*, 2010; Degruyter *et al.*, 2012), but they require detailed knowledge of parameters such as initial magma composition, rheology and volatile content, volatile diffusivity, crustal properties etc. (Pinkerton *et al.*, 2002). Even when many of these things are known, these models are often computationally expensive and rely on various assumptions and system constraints that must first be established via experimental work or other models (e.g., Polacci *et al.*, 2004).

One of the main controls on eruption style is the efficiency with which volatiles escape and the subsequent impact on melt rheology, interlinked with changes associated with ascending magma (Cassidy *et al.*, 2018). These processes are preserved in erupted rocks as permeability, residual volatiles, crystal populations and bubble-melt geometries. Thus, for larger eruptions, field-based studies are often coupled with measurements of bulk pyroclast vesicularity, quantification of vesicle textures and experimental data to gain insights into ascent dynamics and vesiculation processes (e.g., Blower *et al.*, 2003; Shea *et al.*, 2010b; Houghton *et al.*, 2010; Rotella *et al.*, 2014).

Several studies of vesicle texture have been used to elucidate controls on eruptive behaviour where reconstructions of changing intensity and style have already been

established using stratigraphic observations and calculations of deposit volumes and/or column height (Polacci *et al.*, 2003; Houghton *et al.*, 2010; Shea *et al.*, 2011; Shea *et al.*, 2017; Colombier *et al.*, 2017 and Shea *et al.*, 2019). These studies traced changes in bubble nucleation and growth processes, resulting outgassing pathways and fragmentation mechanisms via studies of clast density distributions, vesicle size distributions and qualitative descriptions of bubble shape to reconstruct the ascent processes that led to changes in eruption style. Any study that makes use of quantitative and/or qualitative analysis of vesicle size and/or shape relies on several assumptions. First, that the vesicle textures being examined are representative of the magma at the point of fragmentation and thus only represent the vesiculation history of the magma up until that point. Second, that any 2D-3D conversion of bubble shape (used to calculate bubble number densities and vesicle size distributions) is valid, and finally, that the clasts analysed capture the dominant and extreme processes that control changes in eruptive behaviour.

The first is commonly dealt with by selecting clasts within the 16-32 mm size range as these are deemed most likely to have quench times of less than that needed for significant post-fragmentation relaxation and so pre-fragmentation bubble shapes are inferred to be preserved (Houghton and Wilson 1989). The second relies on an appropriate choice of stereological conversion for the analysed samples. Most studies use the conversions of Sahagian and Proussevitch (1998) which assumes a spherical bubble geometry and precludes the incorporation of clasts where vesicle elongation is significant (Shea *et al.*, 2010). While this allows quick and easy reconstruction of key parameters for many clasts and comparison between many datasets from eruptions worldwide, use of this conversion means key processes associated with extensive shear e.g., development of permeable networks and bubble collapse are excluded from such analyses and must be accounted for in another way. Some studies e.g., Mitchell *et al.*, (2019) apply different stereological conversions for more elongate clasts to counter this. The third assumption can only be countered by a thorough examination of the clast textures present in the studied deposits. Each of the studies referenced at the start of this section produced clast density distributions and categorised clasts based on their macro-scale textures prior to selecting clasts for micro-scale textural studies. This meant clasts with representative densities and textures could be sampled as well as more extreme endmembers via an analytically feasible number of clasts.

When these assumptions are addressed appropriately, studies of vesicle texture can provide powerful insights into transitions in eruptive behaviour. Vesicle size distributions in Houghton *et al.*, (2010) revealed non-steady-state bubble growth and similarities in small size classes for different stages of the eruption revealed consistent nucleation and early growth processes for all stages of the eruption. However, changes to the proportions of clasts with different microtextural characteristics showed that shallow processes changed throughout the eruption. The initial phase had a slower ascent, allowing more extensive coalescence to be recorded in vesicle populations. Later, more rapid ascent resulted in smaller bubble populations which are not overprinted by coalescence and were interpreted to represent development of a stable plume (Houghton *et al.*, 2010). Later stages showed more diverse textures representative of varied vesiculation histories and degrees of outgassing. By tracing these changes and mapping them to the deposit characteristics Houghton *et al.*, (2010) were able to reconstruct the drivers for progressive changes to eruptive style – changes in vent position magma storage, conduit geometry and ascent history. Polacci *et al.*, (2003) used a similar approach to establish how shear at conduit margins impacted conduit dynamics that led to a transition from fall to flow emplacement for the Plinian phase of the Campanian Ignimbrite and Shea *et al.*, (2011) showed how changing clast densities promoted column collapse during the 79AD eruption of Vesuvius. These studies provide a good framework on which to interrogate small-volume eruptions with transitioning eruptive style, however, as explosion intensity cannot be constrained through traditional techniques for these smaller eruptions, other strategies will be explored in Chapters 2 and 3 that take advantage of the relationships between bubble size and shape, and eruptive processes.

Volcanic eruptions can be global in their reach but processes governing eruption style typically arise from microscopic variations in conditions within the magma. Thus, a key aim of this thesis is to combine deposit-scale interpretations of eruptive transitions with the microscopic investigation of the changing physical processes that drive them to elucidate processes controlling transitioning eruptive behaviour for a small-volume eruption on Ascension Island for the first time.

1.2 Ascension Island as an exemplar of small volume hazardous eruptions

Ascension Island is an intraplate volcano located ~90km west of the Mid-Atlantic Ridge (MAR) (Fig. 1.1). There have been no observed eruptions on Ascension Island. Recent $^{40}\text{Ar}/^{39}\text{Ar}$ dating by Preece *et al.*, (2018) puts the most recent eruption at 0.51 ± 0.18 ka, with several other lava flows dated in the Holocene period, meaning that this is an active or potentially active volcano (Global Volcanism Program, 2023. Ascension (385050)). The products of eruptions on Ascension follow an alkaline trend ranging from basaltic through to rhyolitic (Weaver *et al.*, 1996; Kar *et al.*, 1998; Paulick *et al.*, 2010; Chamberlain *et al.*, 2019), and exhibit a wide range of eruption styles. Work to date has largely focussed on mapping, dating and characterising eruptive materials geochemically (e.g., Daly, 1925; Nielson and Sibbett 1996; Kar *et al.*, 1998; Jicha *et al.*, 2013), and understanding the islands origins and crustal structure (Evangelidis *et al.*, 2004; Montelli *et al.*, 2006; Paulick *et al.*, 2010).

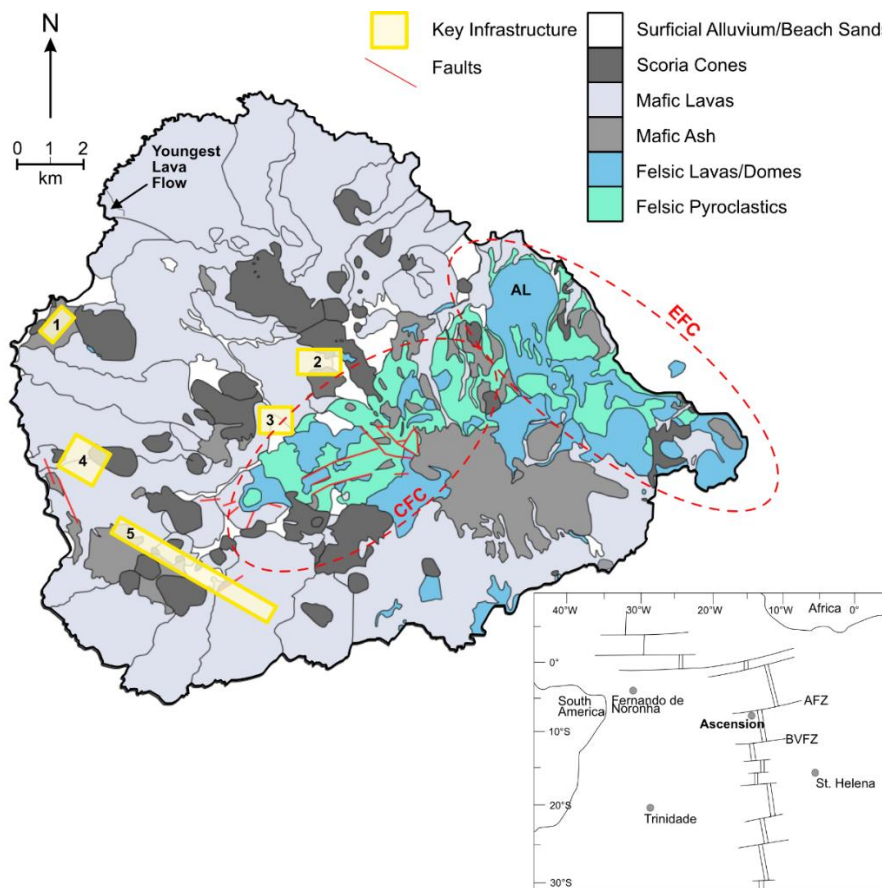


Fig. 1.1 Simplified geological map of Ascension Island, adapted from Chamberlain *et al.*, (2016) showing distribution of mafic and felsic effusive and explosive products, key infrastructure, and key deposits. 1: Georgetown, 2: Two Boats Village, 3: Travellers Hill Royal Air Force station, 4: US air force base, 5: Wideawakes airfield. AL: Ariane Lava flow. EFC: Eastern felsic complex, CFC: Central Felsic Complex. Extent of EFC and CFC denoted by dashed red ellipses. Inset: Location of Ascension Island relative to the Mid-Atlantic ridge in the South Atlantic.

However, recent field campaigns (2014 – 2018) re-focussed on the eruptive histories of the volcanic systems on the island (Preece *et al.*, 2021) and have also integrated petrological with volcanological fieldwork to understand the relationships between eruptions and their inferred plumbing system (Chamberlain *et al.*, 2016; Chamberlain *et al.*, 2019). Over its 1 Myr subaerial history more than 80 explosive felsic eruptions have occurred, (Preece *et al.*, 2021) as well as a series of effusive domes and flows (Chamberlain *et al.*, 2019, Preece *et al.*, 2018). Any one of these eruptions would have a profound impact not only on the island community and environment, but would also generate eruptive plumes that would have significant disruptive potential in busy shipping lanes and airspace. Individual eruptions are difficult to trace across the island due to poor preservation (Preece *et al.*, 2021) but this work identified three eruptions that were sufficiently preserved and exposed to enable further exploration of ascent and eruption dynamics. Two of these eruptions will be explored in detail in the coming chapters to improve our understanding of ascent and eruption dynamics of small-volume trachytic melts at low magma production rate settings.

The two studied eruptions represent archetypes of eruptive behaviour of this type of magma in ocean island settings. The first is the Echo Canyon eruption (Chapters 2 and 3), an exceptionally well preserved and exposed small-volume trachytic pumice cone and lava flow that exhibits multiple transitions in eruptive behaviour. The second is a macroscopically mingled basalt-rhyolite pumice fall deposit, (the Mingled Fall) which was characterised in Chamberlain *et al.*, (2020). This deposit is the only such example of compositional mingling found on Ascension to date and records rapid ascent from approximately 10 km depth (approximately 24 hours after mingling) (Chamberlain *et al.*, 2020). Eruptions that exhibit multiple transitions in eruptive behaviour, and those triggered by compositional mingling, are both typical of trachytic eruptions in ocean island settings (e.g., Dellino and La Volpe 1995; Cole *et al.*, 1995; Jeffery *et al.*, 2018 and Sbrana *et al.*, 2018). As such, exploring controls on the ascent dynamics of these examples from Ascension will offer vital insights into the progression of many trachytic eruptions worldwide.

[1.3 The contribution from the Chapters in this Thesis](#)

This brief introduction details the gap in knowledge around the documentation and attribution of cause to transitions in small volume alkaline eruptions and the state-of-the-art in the reconstruction of ascent dynamics and eruptive behaviour using microscopic

investigation of erupted products. Each chapter provides a wider relevant introduction but in sum, the following chapters make a new contribution to our understanding of the ascent and eruption dynamics of small-volume trachytic eruptions, by combining careful field-based volcanology, petrology and 2 and 3D textural characterisation.

In Chapter 2 the Echo Canyon eruption sequence is described for the first time and then used as a framework upon which to reconstruct changes to bulk magma properties during identified transitions in eruptive style by incorporating evidence from clast textures and bulk vesicularity (also see Davies *et al.*, 2021). In Chapter 3 qualitative and quantitative studies of vesicle textures of pyroclasts in 2D and key intensive parameters calculated using forensic examination of the crystal cargo will be used to elucidate controls on eruptive transitions for the Echo Canyon eruption. In Chapter 4 the impact of basalt-rhyolite mingling on vesiculation processes and magma ascent will be evaluated using 2D and 3D studies of vesicle texture, and the limitations / benefits of these tools for elucidating controls on ascent dynamics discussed. In Chapter 5 I reflect on the value of this work in furthering understanding of eruptive transitions. The case studies used here represent small volume alkali eruptions typical of ocean islands, so in the synthesis I return to a recent (and thus well constrained physically) eruption of a calc-alkaline system. Here, petrological textures helped to rapidly understand the broad eruptive system (Joseph *et al.*, 2022) but in this Chapter I consider the further insights to be gained from my further study of these eruptive products and their value. In linking this work to the main thesis results on an alkali OIB systems I suggest a framework through which to study the deposits of small-volume eruptions - highlighting the importance of a forensic, multi-scale approach to reconstructions of eruption and ascent dynamics.

Chapter 2: Reconstructing dynamics of the Echo Canyon explosive – effusive eruption

2.1 Introduction

Small-volume silicic eruptions are common across a range of settings and exhibit the diverse eruption styles shown in table 2.1. Relative to large-volume calc-alkaline eruptions the ascent dynamics of often alkali-rich small-volume eruptions are relatively understudied. Small-volume silicic eruptions typically occur as late-stage activity associated with larger volcanic features e.g., calderas (e.g., Cole *et al.*, 1995; Hernando *et al.*, 2019), shield volcanoes (e.g., Shea *et al.*, 2017) and flank fissures (e.g., Katsui and Katz 1967; Pistolesi *et al.*, 2015) (table 2.1). The evolution and eruption of these small volume magmas may be governed by the low flux of incoming eruptible melt and crustal heterogeneity (Chamberlain *et al.*, 2019). Scarcity of eruptible melt can be attributed to long-term, low magma-production rates, such as at Ascension (Chamberlain *et al.*, 2019), and/or significant reservoir depletion by earlier activity, such as often leads to caldera formation (e.g., Capaldi *et al.*, 1976) (table 2.1).

Direct observations, and inferences from preserved deposits show small-volume silicic eruptions are capable of intense short-lived explosive phases with few precursory signals, important transitions in eruption style, and pulsatory activity capable of generating pyroclastic density currents (PDCs) (table 2.1). Thus, a critical challenge for volcanic hazard assessment is to recognise the fingerprint and drivers of such variability in eruptive style through the interrogation of remaining deposits; set against challenges from the poor preservation (Preece *et al.*, 2021) or minimal exposure (e.g., Hernando *et al.*, 2019) typical of these eruptions, a consequence of low initial eruptive volumes, ash/pumice fall offshore (for small ocean islands) and destruction by subsequent eruptions and erosion. To complement stratigraphic investigations of erupted deposits, studies of juvenile clast texture have provided key insights into eruption dynamics of larger silicic eruptions (e.g., Polacci *et al.*, 2003; Alfano *et al.*, 2012; Preece *et al.*, 2014). Such textures represent an integrated history of melt-gas-crystal-strain interactions in ascending magma (Houghton and Wilson 1989), for the most part preserved at the point of fragmentation. Microscopic changes to vesicle textures can occur post-fragmentation, particularly where viscosities are low, and vesicles well connected (e.g., Gardner *et al.*, 2017). However, here the focus is on

bulk vesicularity and macro-scale clast textures in hand specimen. Post-fragmentation modifications should, therefore, have a minimal impact on the dominant clast textures and resulting interpretations discussed here. For more detailed quantification of vesicle textures e.g., vesicle size distributions (e.g., Shea *et al.*, 2010), these modifications must be accounted for, see chapter 3. The bulk properties of deposits identified from differing stratigraphic horizons in the field can be used to interpret the drivers of changing eruption dynamics such as the development of heterogeneous pressure gradients, shear zones or plug formation and destruction (e.g., Schipper *et al.*, 2013; Saubin *et al.*, 2016; Shea *et al.*, 2017). Analysis of juvenile clast texture is thus a powerful tool for reconstructing ascent and eruption dynamics of un-observed eruptions.

Trachytic melts have a lower viscosity than their calc-alkaline equivalents (Whittington *et al.*, 2001; Giordano *et al.*, 2004) which influences bubble structure and outgassing. Investigations of clast texture are thus particularly important for reconstructing and understanding the dynamics of these lesser-studied eruptions. Experimentation, modelling, and textural studies have recently improved our understanding of the physical properties and ascent dynamics of alkali-rich melts (Giordano *et al.*, 2004; Arzilli and Carroll 2013; Fanara *et al.*, 2013; Shea *et al.*, 2017). The idea that trachytic melts are “kinetically reactive” facilitating complex ascent and eruption dynamics is gaining traction. The basis for this is their low viscosity, high H₂O diffusivity, rapid degassing and vesiculation, and tendency to crystallise microlites rapidly in response to perturbation (Shea *et al.*, 2017; Deniel *et al.*, 2020).

To date, reconstruction of small-volume alkali-rich eruptions has largely focussed on longer-term volcanic histories rather than individual episodes (Buck *et al.*, 1981; Mahood and Hildreth 1986; Rotolo *et al.*, 2007; Singer *et al.*, 2008; Vezzoli *et al.*, 2009; Hutchison *et al.*, 2016; Sbrana *et al.*, 2018). In this chapter we present new insights into the eruptive transitions and dynamics of an unusually well-preserved and exposed eruption on Ascension Island, South Atlantic – the Echo Canyon Eruption. We combine detailed eruption stratigraphy and mapping of field relationships with analysis of individual and bulk clast textures to reconstruct transitions in eruption styles, understand their drivers and the resulting implications for future activity in this and similar settings.

Table 2.1: Comparison of explosive small volume silicic eruptions from the literature									
Pumice cone/small volume eruption	Eruptive vol. (km ³)	Cone height (m)	Max cone diameter (km)	Associated effusive	Larger volcanic structure	Eruption style	Magma Composition	Tectonic setting	
Echo Canyon eruption, Ascension Island	0.01 – 0.3	Approx. 50	0.5 – 1	Dome & lava	EFC, not caldera.	Strombolian – Plinian (transient)	Trachyte	Ocean Island	
Payún Matrú, Argentina ¹		100 – 150	0.35 – 1.5	Dome & lava	Post-caldera	Strombolian (possible sub-Plinian)	Trachyte	Back-arc	
Pu'u Wa'awa'a, Hawai'i ²	< 5.5	250 – 300	1.6		Post-shield	Strombolian-Vulcanian	Trachyte	Intra-plate	
Wendo Koshe, Ethiopia ³	1.7	6	~10	Lava	Post-caldera	Weakly Plinian	Per. rhyolite	Rift	
Aluto cones, Ethiopia ^{4,5}	0.01-0.25	10-100	1	Domes & lavas	Post-caldera	Violent Strombolian sub-Plinian	Per. rhyolite	Rift	
Monte Pilato, Lipari, Italy ^{6,7}		450	1	Lava	Dome	Vulcanian	Per. rhyolite	Arc	
Aso pumice cones, Japan ⁸	0.11-2.21		1 – 5*		Post-caldera	Max VEI 5	Dacite	Back-arc	
Milos, Greece ⁹	2-3 (DRE)	300 – 450		Crypto domes & sills	Ocean Island		Dacite	Arc	
PT-PV Tenerife ¹⁰		1370 (PT)	4.5 – 6	Lavas domes &	Post-caldera	Max VEI 4	Phonolite	Intra-plate	
Pantelleria cones, Italy ^{11,12,13}		25 – 100	100 – 350	Lavas domes &	Post-caldera	Strombolian sub-Plinian	Trachyte, pantellerite	Back-arc rifting	

Table 2.1 continued: Comparison of explosive small volume silicic eruptions from the literature										
Pumice cone/small volume eruption	Eruptive vol. (km ³)	Cone height (m)	Max cone diameter (km)	Associated effusive	Larger volcanic structure	Eruption style	Magma Composition	Tectonic setting		
Mayor Island cones, NZ ^{14, 15}	~0.01-0.1	34 – 50	-	Lavas & domes	& Post-caldera	Strombolian sub-Plinian	-	Per. rhyolite		Arc
Cordon Caulle, Chile (CCIV) ¹⁶	1.5**	100	-	Lavas & dome	Fissure	-	Rhyolite			Arc (fissure)
Cordon Caulle, Chile (1960) ¹⁷	0.016	-	-	Lavas (0.2 km ³)	Fissure	VEI 3	Dacite			Arc (fissure)
Cordon Caulle, Chile (2011) ^{18, 19}	0.8	50	-	Lavas	Fissure	VEI 5 (GVP)	Rhyolite/dacite			Arc (fissure)
1630 AD Furnas, Sao Miguel ^{20, 21, 22}	2.903	200	500	Dome (0.2km ³)	Post-caldera	Sub-Plinian	Trachyte			EAFZ
Caldeira do Alferes, Sete Cidades ^{23, 24}	0.09	-	~1.2	Domes***	Post-caldera	VEI3	Trachyte			EAFZ
Ischia, Italy ^{25, 26}	-	-	-	Domes	Post-caldera	Strombolian/sub-Plinian	Trachyte			Arc
Tavurvur & Vulcan, Papua New Guinea ^{27, 28, 29, 30}	0.3	200, 160	1.3 – 1.5	-	Post-caldera	VEI 4 (1994)	Dacite			Arc

*Measured directly from Google Earth, **total bulk volume for pumice, lavas & domes, ***Not associated with cone, Per. Rhyolite is peralkaline rhyolite. EAFZ is Eastern Azores Fracture Zone

References: ¹Hernando *et al.*, (2019), ²Shea *et al.*, (2017), ³Rapprich *et al.*, (2016), ⁴Hutchison *et al.*, (2016), ⁵Clarke & Calder (2019), ⁶Dellino & La Volpe (1995), ⁷Davì *et al.*, (2011), ⁸Miyabuchi (2011), ⁹Stewart & McPhie (2006), ¹⁰Ablay & Martí (2000), ¹¹Orsi *et al.*, (1989), ¹²Orsi *et al.*, (1991), ¹³Rotolo *et al.*, (2007), ¹⁴Houghton & Wilson (1985), ¹⁵Houghton *et al.*, (1992), ¹⁶Singer *et al.*, (2008), ¹⁷Katsui & Katz (1967), ¹⁸Pistolesi *et al.*, (2015), ¹⁹Castro *et al.*, (2014), ²⁰Croasdale, *et al.*, (1978), ²¹Cole *et al.*, (1995), ²²Jeffery *et al.*, (2016), ²³Moore (1991), ²⁴Queiroz *et al.*, (2008), ²⁵Capaldi *et al.*, (1976), ²⁶Sbrana *et al.*, (2018), ²⁷McKee *et al.*, (1985), ²⁸Blong (1994), ²⁹McKee & Duncan (2016), ³⁰Google Earth, (2016).

2.2 Deposits and Products of the Echo Canyon Eruption

The EC eruption deposits crop out over $\sim 3.4 \text{ km}^2$ in the Eastern Felsic Complex and have an $^{40}\text{Ar}/^{39}\text{Ar}$ age of $59 \pm 4 \text{ ka}$ (Preece *et al.*, 2021) (see Figs. 2.1 and 2.2). They consist of a partially preserved and exposed proximal pumice cone, pumice fall deposits, a lava dome and a brecciated lava (Fig. 2.3). There is no evidence for a significant time break between the EC deposits (e.g., paleosols or erosional surfaces), and all the eruption products have a unique phenocryst population, we therefore consider them to be products of a single eruption. This distinct EC phenocryst population comprises 3–8 mm diameter feldspar and clinopyroxene macrocrysts (discussed in detail in section 2.7). Pumice clasts typically contain $< 3\%$ feldspar microlites from $< 10 - 750 \mu\text{m}$, with the exception of some clasts within the uppermost pumice fall. The geometry of the volcanic edifice, apparently elongated towards NW, results from both the paleo-topography and prevailing wind direction (Fig. 2.4). The pumice cone has a maximum preserved thickness of 50 m (Fig. 2.3a), and it thins rapidly to the E-SE (Fig. 2.3e) and W-NW (Fig. 2.4b and c).

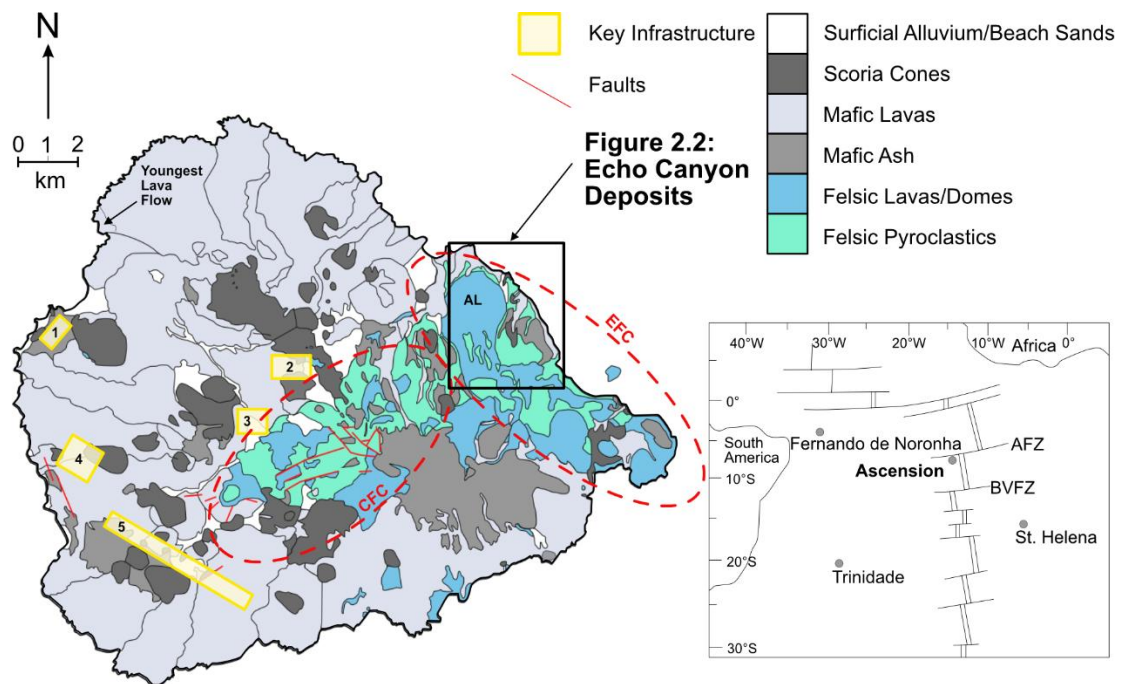


Fig. 2.1 Simplified geological map of Ascension Island, adapted from Chamberlain *et al.* (2016) showing distribution of mafic and felsic effusive and explosive products, key infrastructure, and key deposits. **1:** Georgetown, **2:** Two Boats Village, **3:** Travellers Hill Royal Air Force station, **4:** US air force base, **5:** Wideawakes airfield. **AL:** Ariane Lava flow. **EFC:** Eastern felsic complex, **CFC:** Central Felsic Complex. Extent of EFC and CFC denoted by dashed red ellipses. Black rectangle denotes location of Fig. 2. **Inset:** Location of Ascension Island relative to the Mid-Atlantic ridge in the South Atlantic.

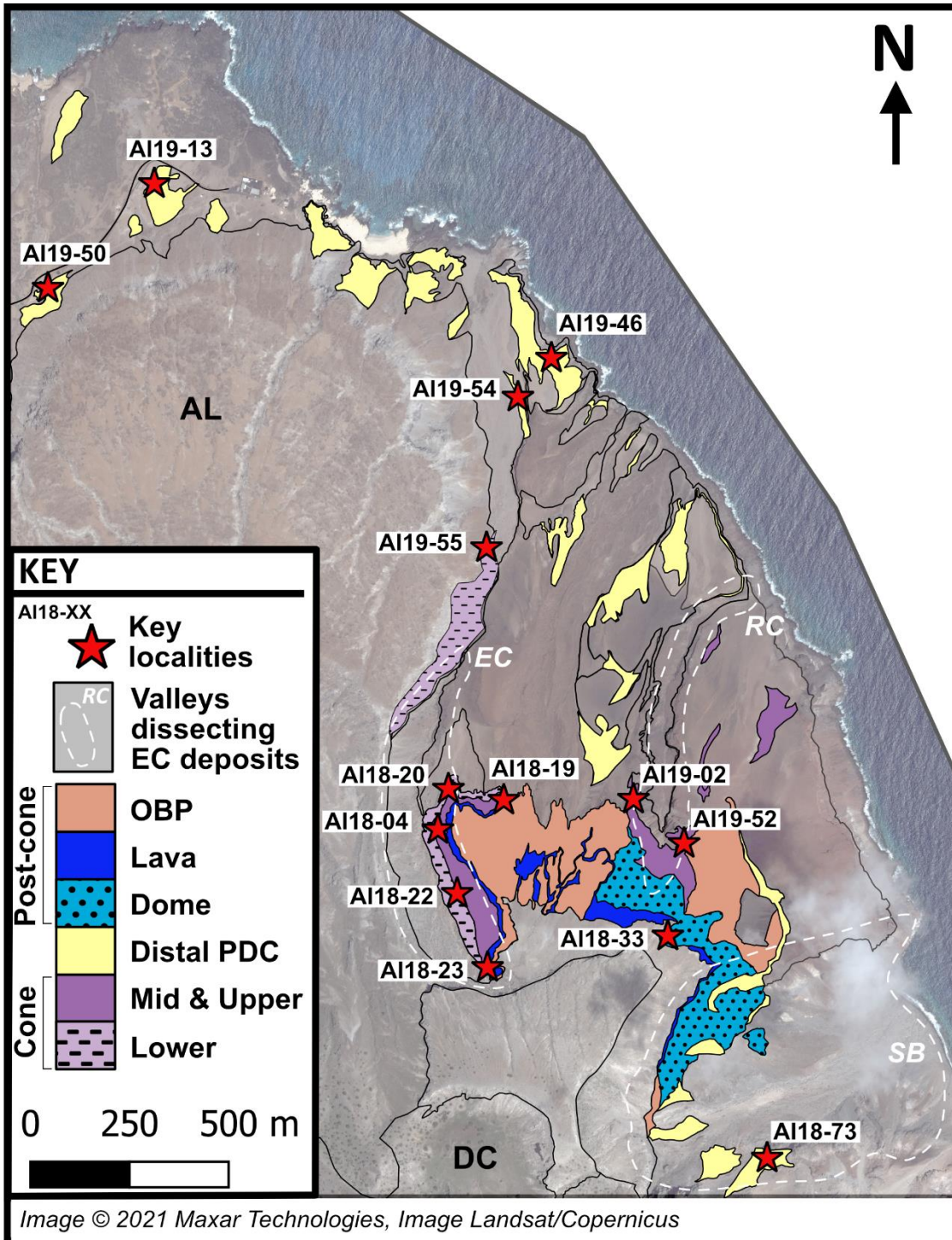


Fig. 2.2 Geological map of the Echo Canyon (EC) deposits – black box in Fig. 2.1. OBP is orange-brown pumice. Distal pyroclastic density current deposits (PDC) mark furthest extent of EC deposits north of the Ariane lava flow (AL). White dashed lines mark footprint of valleys EC – Echo Canyon, RC – Rainbow Canyon and SB – Spire Beach. Geology overlaid on Google Satellite image for Ascension Island (Google, Earth 2006). EC deposits are overlain by AL, which is likely sourced from Devil’s Cauldron (DC).

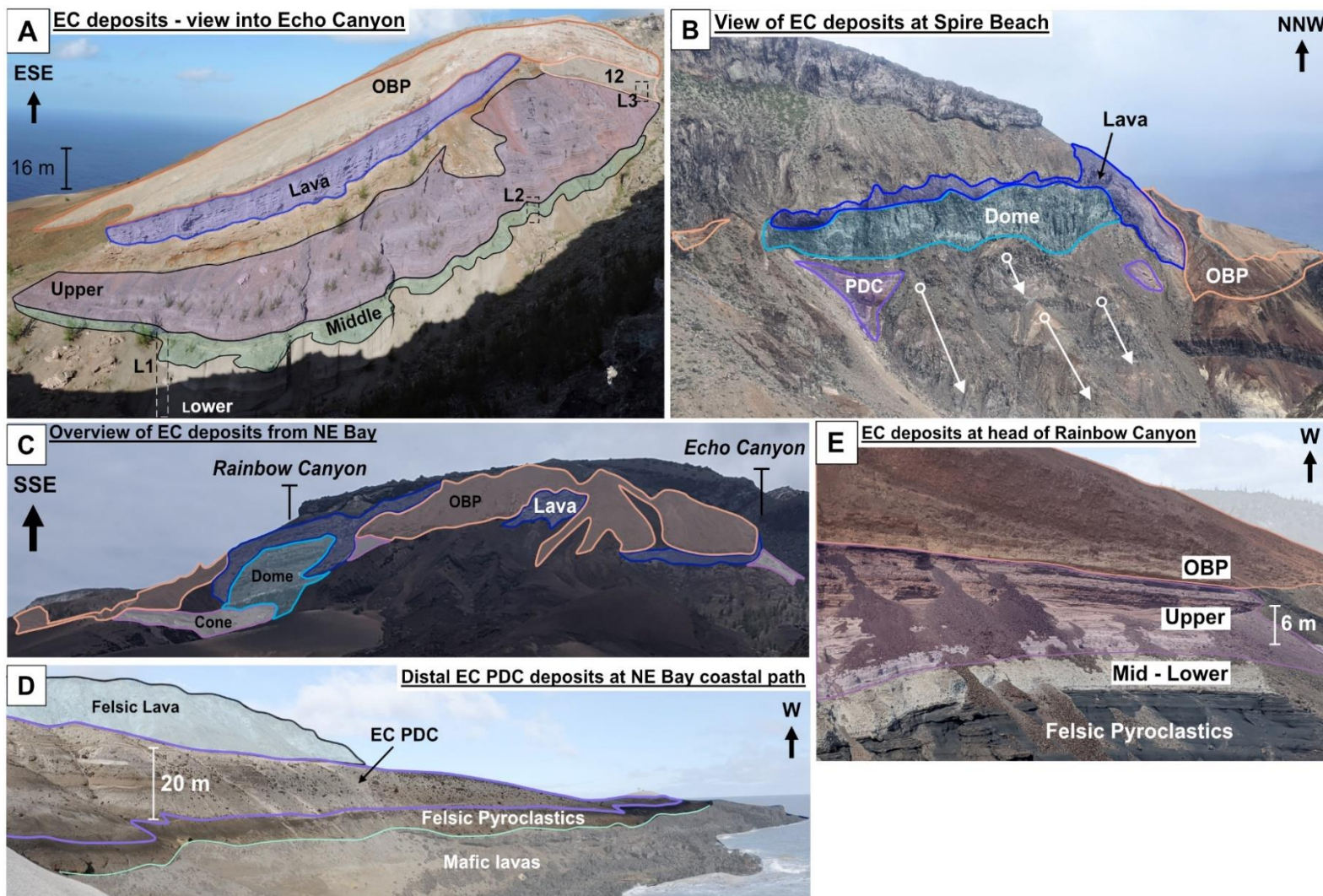


Fig. 2.3 Overview photos of Echo Canyon (EC) eruption deposits. **A:** view into Echo Canyon showing dissected cone, relates to Fig. 2.4a box 1. Black dashed boxes L1, L2 and L3 show logged sections (see [Appendix 1.2]). Lower, Middle and Upper cone, Unit 12 and orange-brown pumice (OBP) are defined by lithologic characteristics. **B:** section at Spire Beach (see Fig. 2.4d), white arrows from circles show slump directions, with distal pyroclastic density current deposits (PDC), the dome, lava and OBP indicated by shaded outlined regions. **C:** view of EC deposits looking SSE from NE Bay coastal path. Valleys EC and Rainbow Canyon (RC) are marked. **D:** Relationship between distal PDC deposits of EC eruption, felsic pyroclastics and coastal lavas, taken from the NE-Bay lower coastal path. **E:** view into western face of RC showing relationships between the OBP, cone deposits and felsic pyroclastics. EC Units logged at 6 m scale bar location.

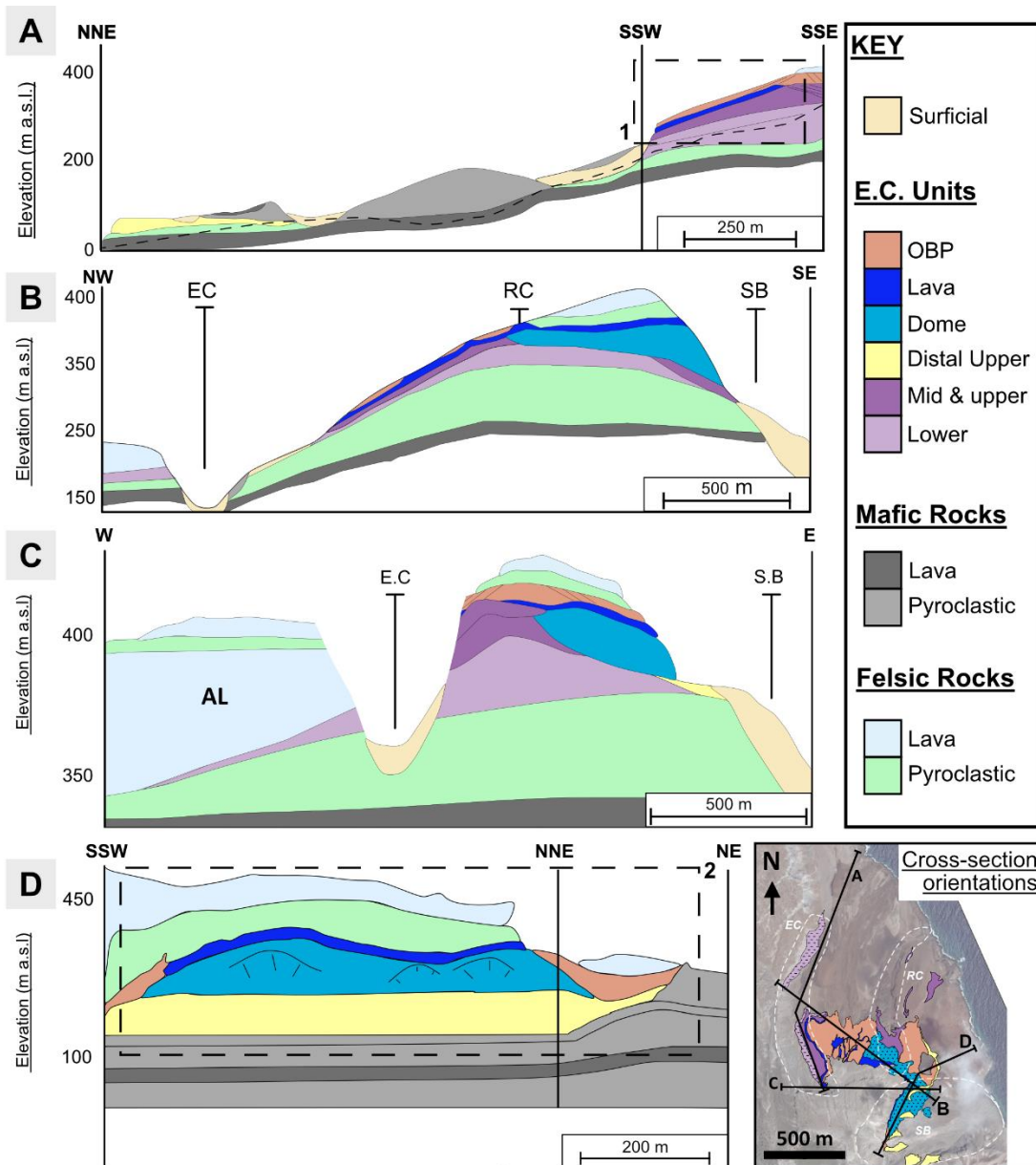


Fig. 2.4 Interpretive cross-sections through the Echo Canyon (EC) eruption deposits corresponding to lines of section A-D on inset. OBP is orange-brown pumice, “upper”, “mid” and “lower” refer to upper, middle and lower cone defined by lithologic characteristics **A:** section down Echo Canyon to the coast with underlying felsic pyroclastics and mafic lavas projected below the land surface (dashed black line). **B:** section from EC to Spire Beach (SB) shows rapid thinning of pumice cone deposits, locations of the three canyons that cut the EC deposits are marked; Rainbow Canyon (RC), EC and SB. **C:** approximated more proximal section W-E showing dome to the east and thinning of cone stratigraphy beneath the Ariane Lava (AL) to the west. **D:** Spire Beach section showing how OBP mantles pyroclastic density current (PDC) deposits, lava and dome. **Inset map:** shows orientations of cross-sections with EC deposits annotated onto satellite imagery of NE-Bay from Google Earth. Dashed lines denote extent of key valleys dissecting EC deposits, EC, RC, and SB.

2.3 Methods

2.3.1 Stratigraphy and sampling

Stratigraphy of the EC volcanic edifice was determined over two 7-week field seasons in 2018 and 2019/20. Stratigraphic logs through eruption deposits were carried out at localities AI18-04, 22 and 23 in 2018 and AI19-02, 46 and 13 in 2019 (Fig. 2.2). Locations for stratigraphic logging of deposits were chosen based on exposure, accessibility and relationship to overall geometry and deposit extent. A geological map of the region (Fig. 2.2) was produced using data from field observations, photographs and Google Earth imagery (Google Earth, 2006).

The EC edifice is divided into pumice cone and post-pumice cone deposits: the pumice cone is divided into three parts, lower, middle and upper, based on lithologic characteristics. The lower, middle and upper parts of the cone were sub-divided into 12 Units comprising one or more beds. Each Unit was distinguished from stratigraphic neighbours via either componentry and juvenile clast texture, or the identification of a repeated sequence of distinct lithologic characteristics. Average maximum clast size was calculated by measuring the 5 largest clasts in outcrop and taking the average long axis. Modal clast size was qualitatively estimated in the field by measuring several clasts deemed to be representative based on careful examination of the wider outcrop; modal clast size values quoted henceforth are qualitative estimates only as a full grain size study was not completed. The sheer cliff face of the outcrop made access to upper units difficult and precluded excavation of sufficient material from each unit.

Six Units from the pumice cone were sampled, one from each Unit in the lower cone, one from the middle cone and one from the upper cone - at AI18-04, AI18-22 and AI19-02 respectively (Fig. 2.2). The sampling targeted each eruptive phase identified using lithologic observations. Sampling of the middle and upper cone was restricted due to outcrop accessibility in the steep cliffs of Echo Canyon and Rainbow Canyon. Bulk samples of explosive products of the cone and post-cone Units containing clasts of 16 – 32 mm were collected by excavating a region up to 10 cm thick, extending laterally across the Unit until enough material was acquired for density measurements and whole rock analyses as outlined in Shea *et al.*, (2010). Samples of Units 1–4, and 9 were collected from Echo Canyon at localities AI18-04 and AI18-22 respectively. Unit 11 was sampled at AI19-52 in

Rainbow Canyon, the lavas at AI18-20 and AI18-33, and the post-cone pumice fall (the Orange-brown pumice, OBP) at AI18-19, as shown in Fig. 2.2. Grid references for key field localities and sample sites are listed in table 2.2, a full list of locations of field observations can be found in [Appendix 1.12 Table 1.1].

Table 2.2: Sample numbers and locations			
Sample Number	Locality	Grid Reference (UTM, zone 28S)	Sample Description
AI18-842A	AI18-04	-7.930696, -14.328462	Unit 1 pumice
AI18-843A	AI18-04	-7.930696, -14.328462	Unit 2 pumice bed
AI18-843C	AI18-04	-7.930696, -14.328462	Unit 2 vesicular end member of VVLP clasts
AI15-602B	2015 EC	-7.930677, -14.328498	Unit 2 dense endmember VVLP clasts
AI18-844A	AI18-04	-7.930696, -14.328462	Unit 3 pumice
AI18-844C	AI18-04	-7.930696, -14.328462	Unit 4 pumice
AI18-844E	AI18-04	-7.930696, -14.328462	Unit 4 lapilli tuff block example
AI18-829A	AI18-22	-7.931708, -14.328216	Unit 9 pumice
AI18-845B	AI18-04	-7.930696, -14.328462	Unit 9 equivalent, breadcrust bombs
AI18-845C	AI18-04	-7.930696, -14.328462	Unit 9 equivalent, angular banded bombs
AI19-006	AI19-02	-7.930211, -14.323915	Unit 11 obsidian breccia
AI19-137	AI19-52	-7.930808, -14.322408	Unit 11 pumice rich layer
AI18-871B	AI18-33	-7.933265, -14.323332	Post cone dome lava
AI18-828C	AI18-20	-7.930233, -14.327792	Post-cone brecciated lava
AI18-827C	AI19-19	-7.93025, -14.326757	Post-cone OBP

VVLP = Variably Vesicular Lava – Pumice clasts, **EC** = Echo Canyon, **OBP** = Orange-Brown Pumice

2.3.2 Density measurements & Textural Categorisation

In the laboratory, bulk samples were passed through an 8 mm sieve. Clasts in the >8 mm size fraction were ordered by size and each axis measured to remove clasts > 32 mm and <16 mm. From the remaining clasts the 100 largest were selected following Shea *et al.*, (2010), for the OBP, all 16–32 mm clasts were selected. Clasts which have undergone significant post-fragmentation textural alteration often have expanded cores and dense rims, fluidal morphologies and breadcrust exteriors (e.g., Polacci 2005). None of the clasts used in producing bulk vesicularity distributions (BVDs) exhibited breadcrust exteriors or fluidal morphologies. Clasts of the same morphology, colour and size as those selected for density measurements from each Unit were broken open to check for internal textures indicative of significant post-fragmentation vesicle expansion, none were found. Analysed clasts from the cone deposits lacked evidence of thermal alteration e.g., discoloration or formation of rims and care was taken to select the freshest looking clasts from the OBP where such discoloration was more common. Density of the 16–32 mm juvenile clasts was

determined using the Archimedes principle following the suspension method detailed in Houghton and Wilson (1989) and Shea *et al.*, (2010), see Fig. 2.5. Each cleaned and dried clast was weighed then waterproofed by wrapping in a known mass of parafilm and attached to a ballast of known mass and volume. Clast and ballast were then immersed in water suspended below a balance. The film was then removed, and the clast weighed again to ensure no water had penetrated the waterproofing. Finally, ballast and removed parafilm were weighed in water. The temperature of the water was routinely checked to ensure consistency in density calculations.

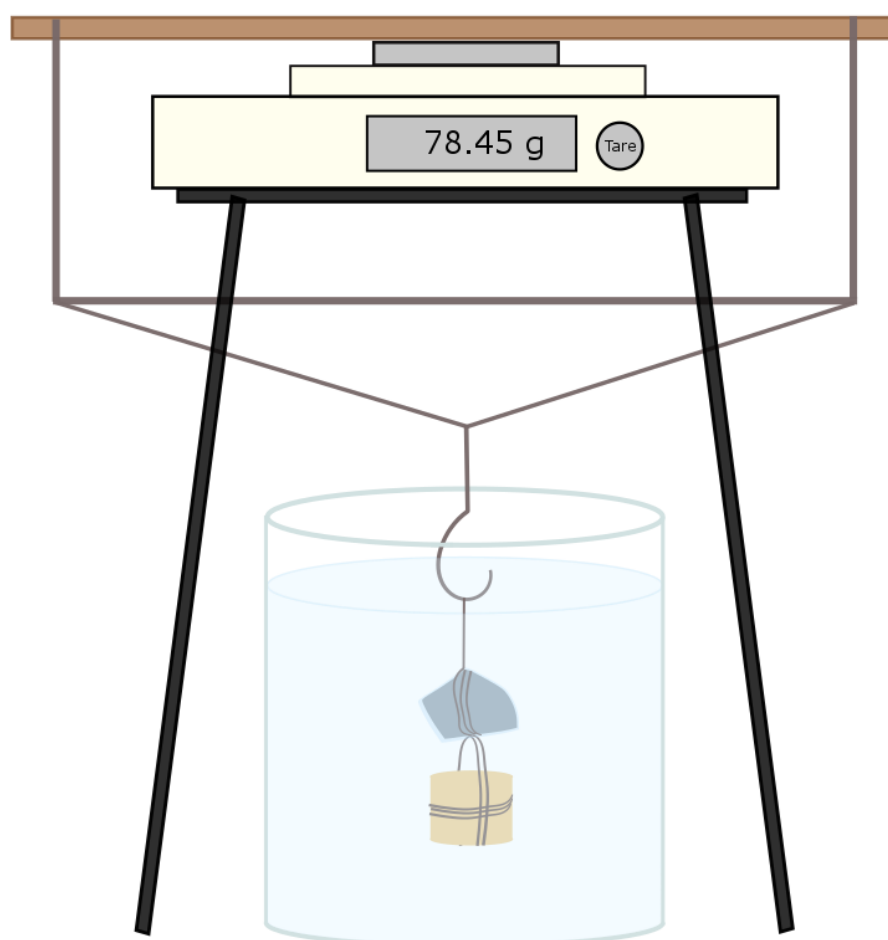


Fig. 2.5 apparatus set up for density measurements. A balance is elevated (using a tripod) and a wooden bar placed on the scale with a hook suspended below the balance and tripod that is able to swing freely. The wrapped clast and ballast are attached to the hook and immersed in a beaker of water of known temperature and the weight recorded.

For Units 1, 2, 3, 4, 6 and 11, 100 clasts were measured. For the OBP, 43 clasts were measured as the bulk sample acquired contained a high proportion of clasts > 32 mm diameter. Clast vesicularities were calculated using the following equations from Shea *et al.*, (2010) after Houghton and Wilson (1989):

$$\rho_{BULK} = \frac{\omega_{AIR}}{\omega_{AIR} - (\omega_{WATER} - \omega_{WATER}^{FILM} - \omega_{WATER}^{BALLAST})} \quad [1]$$

$$\phi = \frac{\rho_{DRE} - \rho_{BULK}}{\rho_{DRE}} \quad [2]$$

$$Bulk\ Vesicularity = \phi \times 100 \quad [3]$$

Where ρ is density, ω is weight, ϕ is porosity and DRE is dense rock equivalent. Dense rock equivalent values were calculated using the method of Lange and Carmichael (1987) from whole rock compositions attained using X-ray fluorescence (XRF) analysis (see below for details of XRF method) which gave values of 2.51 g/cm³ for Units 1 – 11 and 2.55 g/cm³ for the OBP. Measured clasts were categorised based on pervasive vesicle textures observed in hand specimen.

2.3.4 Geochemical analyses

For geochemical analysis of pyroclastic units, a 20 cm x 30 cm bag of juvenile clasts was collected and cleaned. For the lavas, several fist-sized samples were collected from the least altered regions of the flow and dome. Lavas were then trimmed to expose less altered portions and several 3-4 cm sized chunks selected from each unit for analysis. Pumice clasts and lava samples were prepared for X-ray fluorescence (XRF) analyses following Chamberlain *et al.*, (2016). Each sample was soaked in Milli RO water for 24 hours and cleaned for 15 minutes in a sonic bath, this process was repeated 5 – 7 times until the water remained clear after sonication. All pumice clasts and lava samples were dried at 60°C for 72 hours. Several handfuls of prepared pumice clasts and all prepared lava samples were then crushed, and an aliquot of each sample milled in a tungsten carbide container before XRF analyses were carried out on a Bruker-AXS S4 Pioneer at the University of East Anglia. For major elements, analyses of multiple international standards yielded accuracies $\leq \pm 0.18$ wt% when compared with certified values.

Trace element concentrations were measured by Jane H Scarrow by ICP-mass spectrometry after HNO₃+HF digestion of 0.1000 g of sample powder at ~180 °C and 200 psi for 30 min, evaporation to dryness, and dissolution in 100 ml of 4 vol.% HNO₃. Measurements were done with a PE SCIEX ELAN- 5000 spectrometer (rhodium internal standard). Precision, as determined from international standards was better than $\pm 2\%$ and $\pm 5\%$ for concentrations of 50 and 5 ppm, respectively. Raw major and trace element data and XRF standards data are given in [Appendix 1.3, tables 1.2 and 1.3]

2.3.5 SEM imagery

A total of 27 clasts were selected for thin section from the explosive eruption products. In order to attain a representative sample, we considered; 1) the textural heterogeneity of each Unit 2) the bulk vesicularity of each selected clast relative to the BVD of the Unit 3) how each textural group influences the BVD and 4) unusual textural features. The selected clasts represent a spread of textural type and bulk density within and between each sampled Unit as well as textural extremes. One thin section was taken from each of the post-cone lavas. Polished thin sections were then carbon coated and backscattered and secondary electron images collected on an FEI Quanta 650 FEG at the Natural History Museum, London, UK, and a Zeiss Gemini sigma 300 VP at the Zeiss facility in Cambridge, UK.

2.4 Stratigraphy of the Echo Canyon Eruption Deposits

2.4.1 Stratigraphic Summary

The EC deposits comprise a pumice cone, brecciated lava dome and flow, and an overlying pumice fall deposit, outlined in Fig. 2.6. The pumice cone is here divided into three parts: the lower, middle and upper cone. Across the explosive deposits several common clast types were identified. Key clast types are described below in Figs. 2.7 and 2.8, these clast types are referenced in the detailed stratigraphy below. Variations in clast size, lithic abundance, bulk vesicularity and juvenile clast texture are summarised in Fig. 2.9. Though a full investigation of the obsidian breccia clasts (Fig 2.8) found in the EC eruption deposits is beyond the scope of this thesis there are some additional key features which need to be highlighted here. The obsidian breccia clasts contain a mixture of mm and cm-scale obsidian and lava clasts, the latter containing the distinct EC crystal population. Ashy matrix-supported channels exist between the larger fragments and contain whole and fragmented crystals (also from the EC population), rounded and angular fragments of pumice as well as the smaller angular obsidian and lava fragments. These features are typical of those observed in tuffisites, e.g., Saubin *et al.*, (2016), Tuffen *et al.*, (2003) and so these clasts are interpreted incomplete fragments of tuffisite veins (e.g., missing the walls of the fracture pathway).

The lower cone is composed of massive, clast-supported pumice fall deposits and is subdivided into 4 Units, one of which contains three thin ash beds (Fig. 2.10a). A

conspicuous layer of lithic clasts containing syenite and granite blocks marks the boundary between Units 3 and 4 (Fig. 2.6). The middle cone is more heterogeneous than the lower cone (Fig. 2.9) and comprises interbedded matrix- and clast-supported beds (Fig. 2.11) of variable grain size. Clast-supported beds contain angular pumice clasts whereas the matrix-supported beds contain rounded pumice clasts. These are interpreted as pumice fall deposits and PDC deposits, respectively (see “emplacement mechanism” interpretation sections throughout the stratigraphic description below). Erosional surfaces have not been observed between Units of the lower and middle cone. The upper cone comprises a sequence of matrix- and clast-supported PDC deposits containing sub-angular to rounded pumice clasts (Unit 11 Fig. 2.6, Fig 2.3e and Fig. 2.12c). The upper cone is distinguished by the appearance of obsidian and obsidian breccia clasts (Fig. 2.8) that constitute 10 % of the Unit. Distal outcrops of Unit 11 occur at distances of 2 km from the cone, and reach ~30 m thick (Figs. 2.13 - 15). The uppermost Unit in the cone (Unit 12) is a coarse-grained clast-supported, proximal fall deposit composed of pumice spatter - some of which exceed 70 cm in diameter – and dense juvenile clasts that closely resemble the overlying lava flow (Fig. 2.12d – h). Unit 12 drapes an unconformity on top of the PDC deposits of the upper cone and some of the middle cone (Fig. 2.3a), a possible result of erosion by PDCs that did not leave any deposits, or partial cone collapse, reflecting the proximity of the likely vent to this location.

Two trachytic lavas post-date the pumice cone. The lower lava is a 30–40 m thick, variably altered and brecciated trachyte lava dome, 3–4 times thicker than the overlying lava (see Fig. 2.3b, Fig. 2.4b – d and Fig 2.16a – c). It contains distinctive 3–8 mm feldspar and clinopyroxene macrocrysts (3–5%) often associated with vesicles up to 1 cm. Groundmass crystallinity is heterogeneous in thin section with regions up to 70% feldspar microlites. The overlying lava is a 7.5–10 m thick brecciated porphyritic trachyte lava flow of similar composition to the older lava, but with lower overall groundmass crystallinity – up to 30% feldspar microlites. Feldspar and clinopyroxene macrocrysts comprise 3–5% of the lava. The lava has a vesicularity of up to 10 percent, with vesicle diameters up to 0.5 cm. Sub-parallel, discontinuous layering is defined by lenses of unaltered lava and brecciated regions altered to clays (Fig 2.16d – f). The uppermost Unit, the OBP, is a massive, coarse-grained, clast-supported pumice fall deposit that thickens from 3–10 m over 450 m from the top of the cliff above AI18-04 towards the SE to locality AI18-23, and mantles underlying topography (Fig. 2.3a, c, e and 2.4a, c, d). It is composed of angular pumice (~95 vol. %) and

obsidian (~5 vol. %) lapilli and blocks (Fig. 2.16h). In thin section, pumice clasts contain discrete microlite-rich regions within homogenous glass (see section 2.7 and Fig. 2.18).

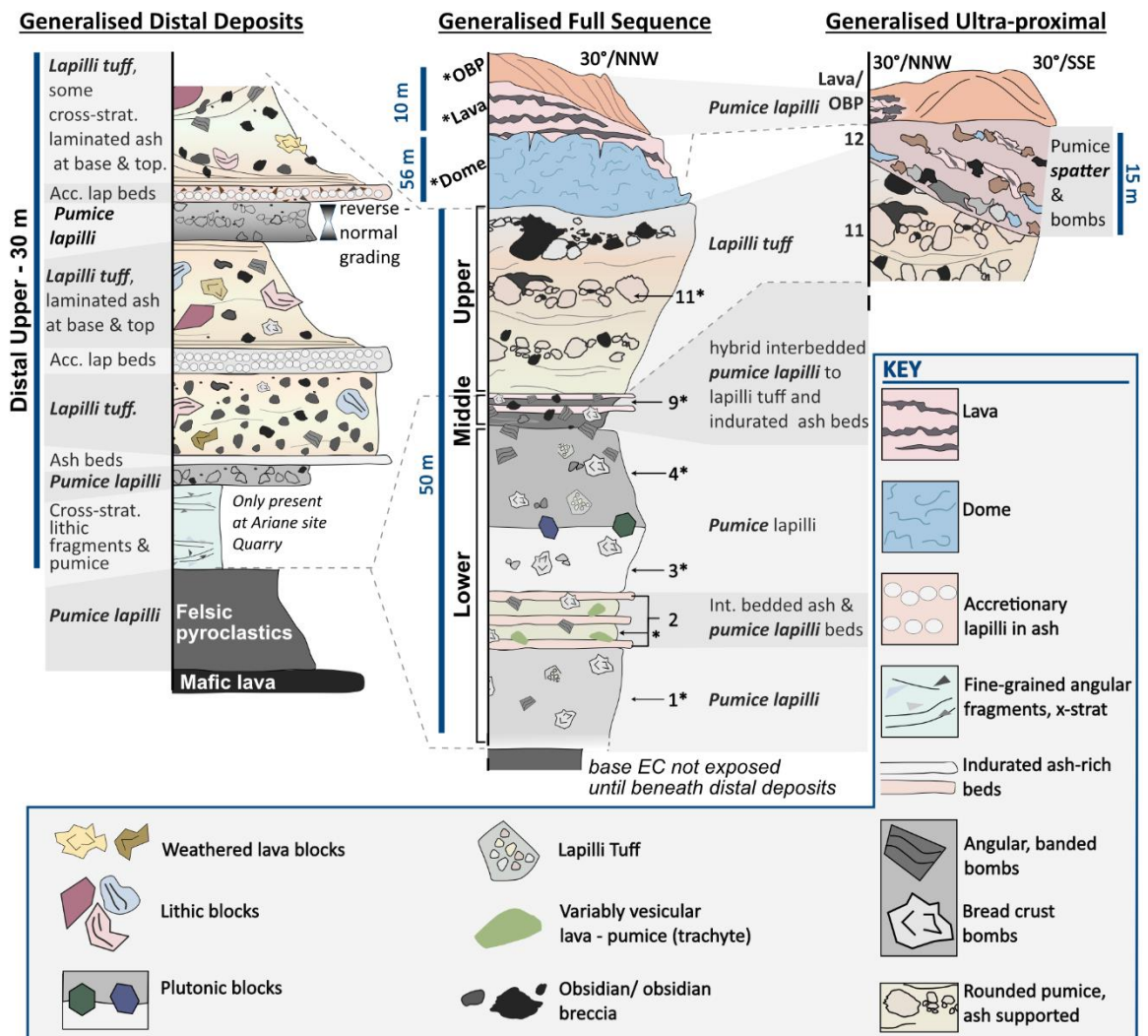


Fig. 2.6 Composite log of the Echo Canyon (EC) eruption deposits. Beds represented by a solid fill are clast supported; beds with a gradient fill are variably matrix and clast supported as detailed in the main text. Dashed grey lines indicate stratigraphic relationships between distal, generalised sequence and ultra-proximal deposits. Dashed black lines indicate contact not always exposed. Clast types and key bed characteristics are detailed in the key. Unit numbers as referred to in text are marked in black, asterisks indicate sampled Units. Maximum exposed thickness of cone deposits is 50 m.

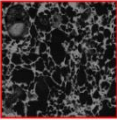

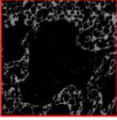

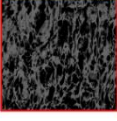

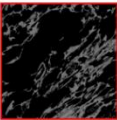

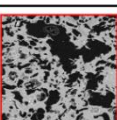

		Vesicle Texture	Appearance	Bulk Ves. ¹	Image
Main Pumice Lapilli Types	Type 1	Micro-vesicular, equant Sub-spherical - colloform vesicles rare. < 5% vesicles in <i>H.S.</i> > 1 mm	Pale grey Angular Friable	<u>Modal:</u> 75 - 79% <u>Range:</u> 55 - 84%	 2 
	Type 2	Macro-vesicular, equant Sub-spherical - colloform vesicles. 30% vesicles in <i>H.S.</i> > 0.1 cm < 5% are >2 cm	Pale grey - white Angular Foam-like Friable	<u>Modal:</u> 80 - 84% <u>Range:</u> 64 - 92%	 1 
	Type 3	Micro-vesicular, elongate Elongate - tube vesicle networks. Dominantly < 1 mm Approx. 5% > 1 mm	Mid-grey, angular Not easily friable Some mm-scale banding // vs ⊥ elongation = glassy vs saccharoidal texture.	<u>Modal:</u> 75 - 79% <u>Range:</u> 58 - 83%	 4 
	Type 4	Macro-vesicular, elongate Elongate - tube vesicle networks. <i>H.S.</i> many > 1mm Max vesicle diameter: 1.5 cm	Pale grey, angular Not easily friable Some mm-scale banding // vs ⊥ elongation = glassy vs saccharoidal texture.	<u>Modal:</u> 74 - 79% <u>Range:</u> 58 - 82%	 3 
	Type 5	Dense Range of rounded & complex sheared networks Few vesicles visible in <i>H.S.</i> Visible vesicles mostly < 1 mm	Dark grey Angular Dark, mm-scale banding common Not easily friable	<u>Modal:</u> 60 - 70% <u>Range:</u> 49 - 84%	 5 

Fig. 2.7 Description of five pumice clast textural types identified in the Echo Canyon deposits. *H.S.* indicates in hand specimen, // is parallel to elongation orientation, ⊥ indicates perpendicular to elongation direction. Superscripts: ¹Bulk vesicularity as measured from at least 100 clasts of each textural group. Black scale bars represent 1 cm. Red boxes 1-5 are backscattered electron images of representative vesicle textures from each identified pumice type, boxes are 1mm². SEM images 1-4 collected on a FEI Quanta 650 FEG at the Natural History Museum, London, UK, image 5 collected on a Zeiss Gemini sigma 300 VP at the Zeiss facility in Cambridge, UK.

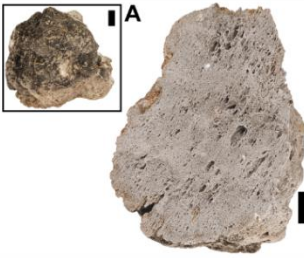

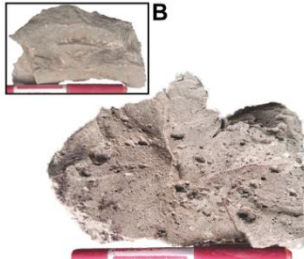
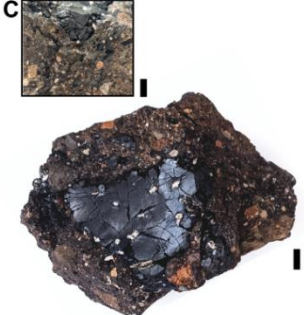

		Internal Texture	Appearance	Bulk Ves.	Image
Bombs	Bread-crust bombs	<p>Equant vesicles dominant in H.S.</p> <p>Exception, coarse core vesicles, w/colloform structure present in some clasts.</p> <p>Variably vesicular, core - rim.</p>	<p>Exterior bread-crust texture</p> <p>Sub-spherical w/ angular fractures.</p> <p>Outer rims grey-black & pink</p> <p>Diameter 7 - 25 cm</p>	Avg. of 4 measurable typical bombs: 78%	
	Angular banded bombs	<p>Dense w/dark grey & pink banding (P.B)</p> <p>PB's > vesicular than dense grey bands.</p> <p>Vesicles >1 mm rare, typically in cores or pink bands.</p>	<p>Smooth, curved fracture faces</p> <p>Dark grey & pink exteriors.</p> <p>Diameter: 6.4 - >25 cm</p>	Avg. of 2 measurable typical bombs: 58%	
		Internal Texture	Appearance & Typical Ves.		Image
Other Clast Types	VVLP clasts¹ (Juvenile)	<p>Spectrum from dense lava - vesicular pumice within clasts & bombs.</p> <p>Highly vesicular portions contain colloform vesicle geometries > 1 cm.</p>	<p>Grey-green</p> <p><u>Dense</u> end-member 0.4 - 25 cm</p> <p><i>Typical Ves²: 25%</i></p> <p><u>Vesicular</u> spectrum: 3 - 15 cm</p> <p><i>Typical Ves³: 62%</i></p>		
	Obs & Obs-breccia (Juvenile)	<p>Black obsidian w/ 3 - 5% E.C. phenocrysts⁴.</p> <p>Clasts: <1 - >10 cm.</p> <p>Angular fragments:</p> <p>Red lithic, dense VVLP, crystals, vesiculated melt, ash matrix.</p>	<p>Forms:</p> <p>Angular clasts within breccia & in isolation.</p> <p>Glassy portions of dense pumice bombs (group C strat.)</p> <p>Ductilely deformed around pumice/ onto breccia</p> <p><i>Typical Ves⁵: 19%</i></p>		
	Lapilli Tuff (Non-juvenile)	<p>Matrix supported</p> <p>70% grey ash matrix.</p> <p>25% well-rounded yellow & grey pumice clasts.</p> <p>5 % angular lithic fragments.</p>	<p>Pinkish-grey</p> <p>Angular - sub-rounded</p> <p>Diameter: ~3 cm - 30 cm</p> <p>Grey ~0.5 cm rim on larger blocks.</p> <p><i>Typical Ves⁶: 72%</i></p>		

Fig. 2.8 Descriptions of clasts commonly found in the Echo Canyon deposits. ¹VVLP = Variably Vesicular Lava-Pumice clasts, ²Dense end-member average determined from three typical clasts, ³vesicular end-member average from four typical clasts, ⁴See *Petrography* and Fig. 2.18 for petrography of EC phenocrysts. ⁵Obsidian breccia determined from three typical clasts, ⁶average lapilli tuff bulk vesicularity taken from one measurable representative clast. **A:** breadcrust bomb exterior view. **B:** dense end-member equivalent of VVLP clasts, red pen is 14 cm. **C:** side view of obsidian breccia clast showing relationship between obsidian and other brecciated material. Black bars are 1 cm for scale.

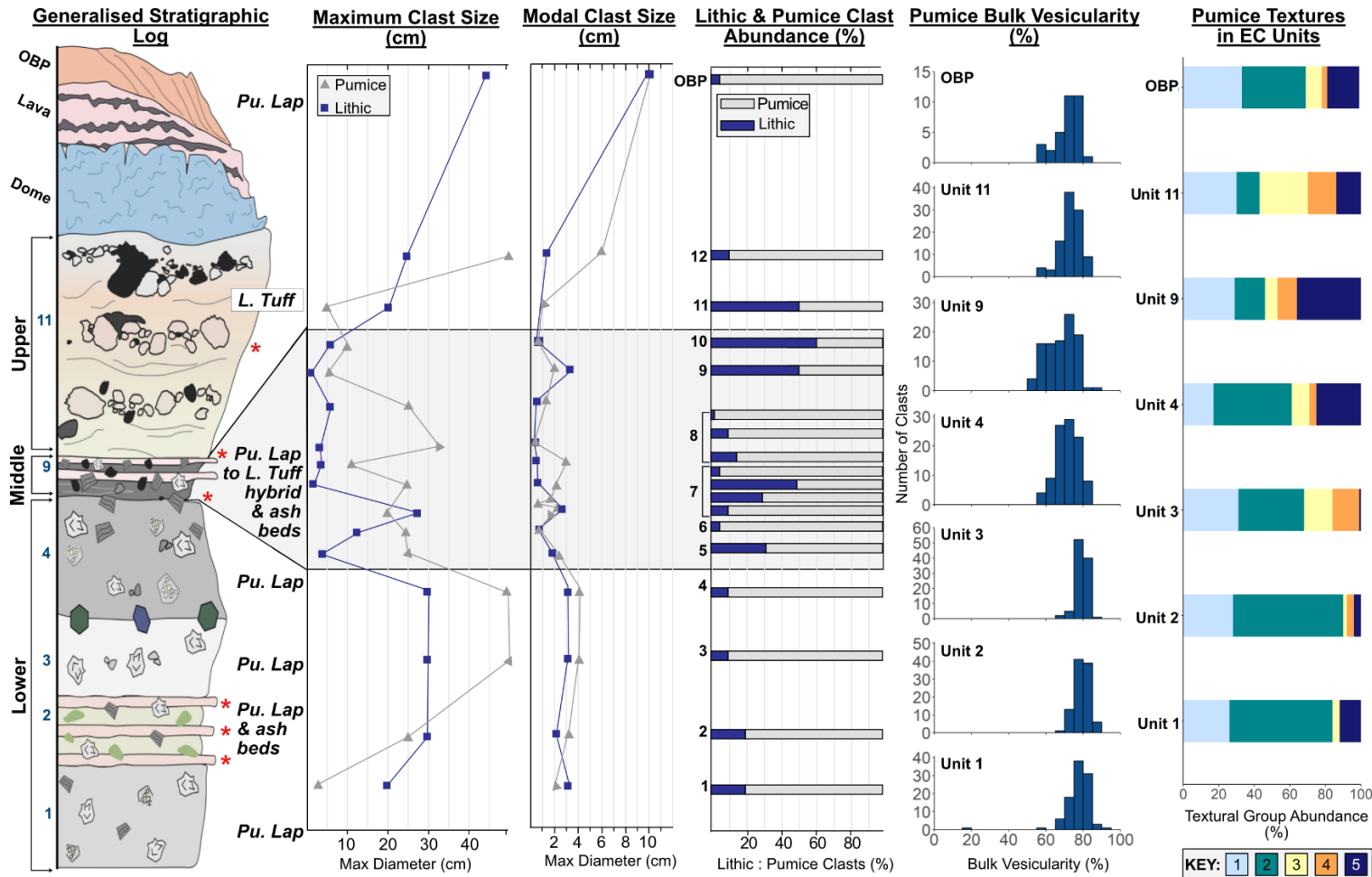


Fig. 2.9 Generalised vertical section from Fig. 2.6, red asterisks mark stratigraphic locations where fine ash was identified in outcrop; the ash beds of Unit 2, Units 5– 10 of the middle cone and Unit 11. Maximum and modal lithic and pumice clast data measured in the field are shown – max OBP pumice is 1.2m (proximal spatter – unit 12). The grey shaded region represents data for beds in Units 5–10. Measured modal and average maximum lithic and clast size are smallest in middle and upper cone Units. Lithic clast proportions increase in middle and upper Units relative to the lower cone. Bulk vesicularity distributions for each sampled Unit are presented, the number of clasts analysed for each Unit is quoted in brackets next to the Unit number/name. Abundance of pumice clast textures are displayed as a percentage of analysed clasts for each Unit. Numbers 1–5 in the key correspond to the five main textural types identified: type 1: micro-vesicular equant, type 2: macro-vesicular equant, type 3: micro-vesicular elongate, type 4: macro-vesicular elongate, type 5: dense.

2.4.2 Pumice cone stratigraphy

Units 1-10 of the lower and middle cone and Unit 12 of the upper cone were logged in detail at localities AI18-04, AI18-22 (unit 10 – not accessible at AI18-04) and AI18-23 in Echo Canyon. Unit 11 was observed from a distance at locality AI18-22 and logged in detail at locality AI19-02 and 52 in Rainbow Canyon. The generalised full sequence and generalised ultra-proximal stratigraphy reflect the units as observed at these locations but the original logs from each locality can be found in [Appendix 1.2]. Localities and deposits are shown on Fig. 2.2, sample numbers and locations are given in table 2.3 / [Appendix 1.1, table 1.1]. Changes to the modal and maximum clast sizes of units in the middle and upper cone between AI18-04 – 823 (e.g., moving from more distal to more proximal) could not be obtained due to poor outcrop accessibility. However, modal and maximum clast size variations for unit 4 and the OBP however, were recorded across this transect.

Lower cone

Unit 1 is a 4 m thick, massive, clast supported pumice lapilli unit dipping $\sim 20^\circ$ north (Fig. 2.10a). Juvenile clasts comprise 85 % of the unit, < 10% of which are bombs and $\sim 5\%$ are dense endmember VVLP clasts: lithic clasts make up 15% of the unit. Pumice lapilli are angular with a modal clast size of 2–3 cm and contain $\leq 1\%$ feldspar and clinopyroxene crystals of 2–5 mm (Fig. 2.10b). Abundances of the five types of vesicle texture within pumice lapilli are: macro-vesicular equant, 58%; micro-vesicular equant, 26%; macro-vesicular elongate, 4% and dense, 12%. Bombs are 50:50 breadcrust and angular fragmented types, maximum diameter is 10 cm. Lithic clasts are angular, common types in decreasing abundance are grey-black aphyric lava, red scoria and purple-black aphyric vesicular lava. Modal lithic clast size is 3–4 cm and maximum clast size is 20 cm. Clasts of lapilli tuff are rare, angular and less than 3 cm.

The upper contact with the basal ash bed of unit 2 is sharp, planar and continuous. The base of Unit 1 is not exposed here but approximately 10 m below the outcrop down-canyon to the north, underlying lavas crop out. Unit 1 is laterally continuous with consistent dip; the outcrop extends approximately 100 m SSW up-canyon until obscured by alluvial canyon debris which means any potential thickening of this unit up-canyon is hidden.

Unit 2 is 1.6 m thick and comprises three ~10 cm thick ash beds interbedded with two clast supported, massive pumice lapilli beds. The lower and upper pumice beds are 90 cm and 40 cm thick respectively. Unit 2 lies conformably on unit 1, dipping approximately 20° north (Fig. 2.10a).

Ash beds are indurated and contain 80% ashy matrix, ~ 10% pumice and 8–10% lithic clasts (Fig. 2.10c). Pumice lapilli clasts are sub-angular, range from < 0.1–4 cm and contain the same macrocryst population as those in Unit 1. Pumice bombs are rare, dominantly breadcrust type and have a maximum diameter of 25 cm. Lithic clasts are angular and the same population as described for Unit 1. Modal and maximum lithic clast sizes are < 1 cm and 4 cm respectively. Ash beds are laterally continuous, mantle the irregular surface of underlying pumice clasts, have consistent thickness and dip, and lack stratification.

Pumice beds comprise 80% pumice clasts, of which < 10% are bombs; 5–10% VVLP clasts and ~10% lithic clasts (Fig. 2.10c). Pumice lapilli are angular, have modal diameter of 3–4 cm and contain the same macrocryst population as those in Unit 1. Abundances of the five types of vesicle texture within pumice lapilli are: macro-vesicular equant, 62%; micro-vesicular equant, 28%; macro-vesicular elongate, 4%; micro-vesicular elongate, 2% and dense, 4%. Pumice bombs are dominated by breadcrust type but angular fragmented types are present, maximum bomb diameter is 25 cm. VVLP clasts occur across the spectrum from vesicular to dense, clast diameters range from ~ 2 cm to 30 cm, larger clasts tend to be more vesicular. Lithic clasts are angular, and the same population as described for Unit 1. Modal and maximum lithic clast diameters are 2–3 cm and 10 cm respectively.

Contacts between ash and pumice beds within Unit 2 are sharp, planar and continuous, as are the lower and upper contacts of the Unit 2 ash beds with the pumice beds of Unit 1 and Unit 3. Unit 2 is laterally continuous with consistent dip; the outcrop extends approximately 120 m SSW, up-canyon until obscured by alluvial canyon debris, no thickening is observed along this distance.

Unit 3 is a 2 m thick massive, clast supported pumice lapilli unit that lies conformably on Unit 2, dipping approximately 20° north (Fig. 2.10a). Juvenile clasts comprise 95% of the unit, < 5% of which are bombs and < 5 % are VVLP clasts: lithic clasts make up 5 % of the unit. Pumice lapilli are angular with a modal clast size of 4 cm and contain the same macrocryst population as units 1 and 2 (Fig. 2.10d). Abundances of the five types of vesicle texture within pumice lapilli are: macro-vesicular equant, 37%; micro-vesicular equant,

31%; macro-vesicular elongate, 15%; micro-vesicular elongate, 16% and dense, 1%. Bombs are dominantly breadcrust type and have a maximum diameter of 50 cm, larger bombs tend to be angular-fragmented type. VVLP clasts tend to be the dense endmember and have a modal diameter of 0.5 cm. Lithic clasts are angular and comprise the same population as units 1 and 2. Modal lithic clast size is 3–4 cm, maximum diameter is 30 cm.

The upper contact with Unit 4 is also sharp and planar, marked by a change in unit colour – from pale grey to dark grey associated with a change in juvenile clast texture – and a concentrated layer of 10–30 cm lithic clasts including granite and syenite. The lower contact with Unit 2 is sharp and planar, outcropping continuously for approximately 200 m to the SSW, where it becomes intermittently obscured by alluvial canyon debris, which frequently obscures the base of this unit and precludes identification of thickening.

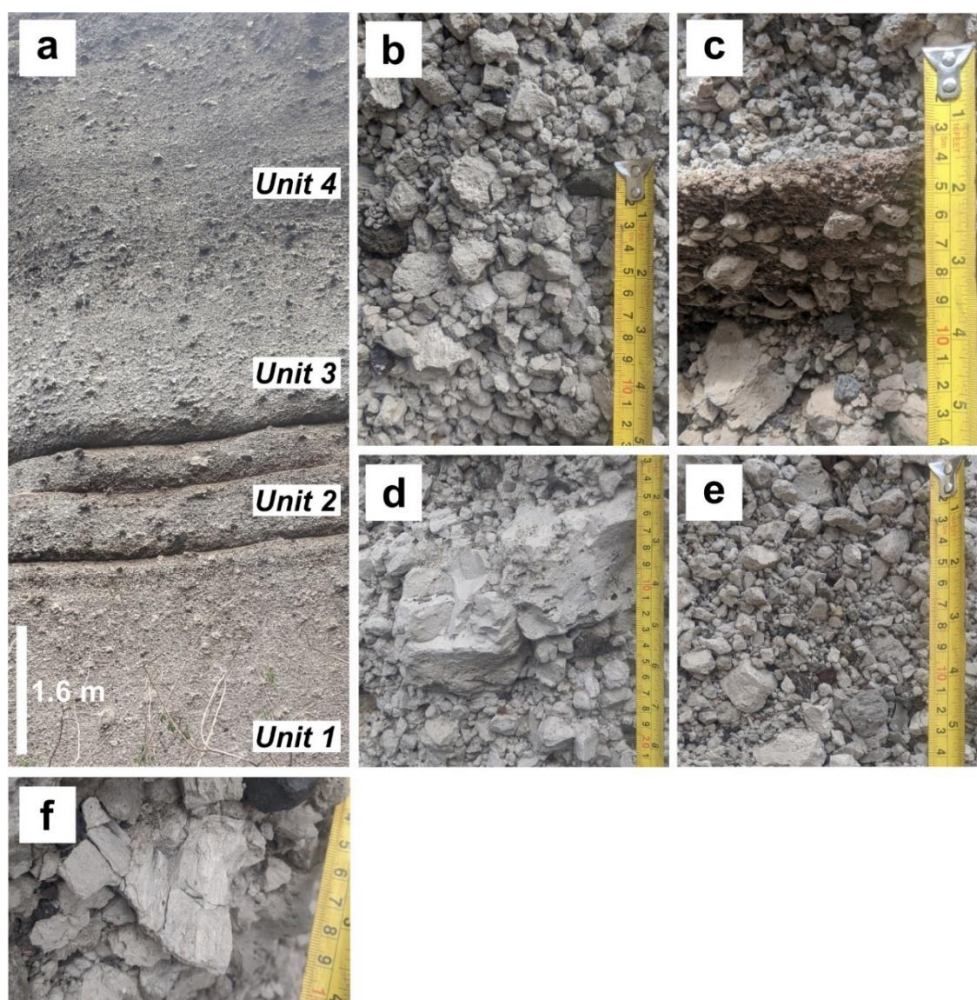


Fig. 2.10 Outcrop photos of the lower cone taken at AI18-04. **A** – Units 1–4 of the lower cone, dominated by massive pumice fall deposits with three minor ash beds within Unit 2. Subtle colour change from light to dark grey marks the boundary between Units 3 and 4. **B** – angular clast-supported pumice lapilli bed of Unit 1. **C** – Ash-rich bed and clast supported pumice beds of Unit 2. **D** – pumice bomb within clast supported pumice lapilli bed of Unit 3. **E** – Clast supported pumice lapilli bed of Unit 4 with angular pumice lapilli and 10% lithic clasts. **F** – example of an angular fragmented type bomb within Unit 4.

Unit 4 is a 4 m thick massive, clast supported pumice lapilli unit that lies conformably on Unit 3, dipping approximately 20° north (Fig. 2.10a). Juvenile clasts comprise ~90% of the unit, < 5% of which are bombs: lithic clasts make up 10% of the unit, of which < 5% are lapilli tuff. Pumice lapilli are angular with a modal clast size of 4 cm and contain the same macrocryst population as the underlying units (Fig. 2.10e). Abundances of the five types of vesicle texture within pumice lapilli are: macro-vesicular equant, 44%; micro-vesicular equant, 17%; macro-vesicular elongate, 4%; micro-vesicular elongate, 10% and dense, 25%. Bombs are dominantly the angular-fragmented type (Fig. 2.10f) and have a maximum diameter of 50 cm. Lithic clasts are angular and comprise the same population as the units below with the addition of clasts and blocks of lapilli tuff. Modal lithic clast size is 3–4 cm, maximum diameter is 30 cm for lava and scoria clasts, 50 cm for lapilli tuff.

The contact between units 4 and 5 marks the start of the middle cone. The boundary is marked by a gradational decrease in modal clast size from 4–2 cm, this gradation spans ~ 40 cm. The boundary between units 3 and 4 is sharp and planar, marked by the darker grey colour of unit 4 and the concentrated layer of 10–30 cm lithic clasts, the only place where plutonic clasts were found within the cone stratigraphy. Unit 4 is laterally continuous with consistent dip; the outcrop extends approximately 200 m SSW, up-canyon until intermittently obscured by alluvial canyon debris. At Locality AI19-36 unit 4 is 10m thick, and modal and maximum pumice clast sizes are 4 cm and 26.5 cm respectively.

Emplacement Mechanism: The stratigraphy of the lower cone is dominated by clast-supported lapilli units containing angular clasts and lacking any cross-stratification or lensing of material – even within the ash beds of unit 2. These features of the lower-cone stratigraphy indicate deposition via fall rather than flow (Cas and Wright 1996).

Middle Cone

Unit 5 is a 50 cm thick, clast supported pumice lapilli unit that lies conformably on Unit 4, dipping approximately 20° north (Fig. 2.11a). Proportions of juvenile and lithic clasts changes vertically throughout the unit. Juvenile clasts comprise ~80–70% of the unit from base to top, 10% are dense endmember VVLP clasts and < 5 % are bombs. Lithic clasts make up 20–30% of the unit from base to top. Pumice lapilli are angular, modal diameter grades from 2–0.5 cm vertically and contain the same macrocryst population as the underlying units. Abundances of the five pumice lapilli types were not quantified for this unit but

pumice lapilli tend towards denser vesicle textures: macro-vesicular textures are only observed in clasts > 4 cm. Bombs are dominated by the angular-fragmented type, have a maximum diameter of 25 cm and occur throughout, regardless of grading. Dense endmember VVLP clasts are angular and modal clast size grades from 1.5–0.5 cm vertically. Lithic clasts are angular, common types in decreasing abundance and size are purple-black aphyric vesicular lava, grey-black lava with 1–2 mm feldspar phenocrysts and red scoria. Modal lithic clast size grades from 1.5–0.5 cm vertically, maximum lithic clast diameter is 4 cm. Unit 5 is normally graded with finest particles of < 0.2 cm at the top of the unit.

The upper contact with Unit 6 is sharp, planar and continuous, disrupted only by larger bombs protruding from Unit 5 into the base of Unit 6. The lower contact with Unit 4 is gradational as described above. Unit 6 is continuous with consistent dip for approximately 300 m up-canyon to the SSW, where it is obscured by alluvial canyon debris.

Emplacement mechanism: As in the lower-cone, the clast-supported angular nature of the pumice lapilli of unit 5 is indicative of fall rather than flow as an emplacement mechanism (Cas and Wright 1996).

Unit 6 is a 10 cm thick partially welded pumice and ash bed that lies conformably on Unit 5 dipping approximately 20° north (Fig. 2.11a upper white bed, Fig. 2.11b white bed at base). The unit is dominantly matrix supported with cm-scale clast supported lenses. Juvenile pumice comprises 95% of the unit, lithic clasts the remaining 5%. Pumice lapilli are angular and have a modal diameter of 0.5 cm, in larger clasts the same macrocryst population as the other EC units is visible. Abundances of the five pumice lapilli types were not quantified for this unit but pumice lapilli tend to be dense with dark banding. Both breadcrust and angular-fragmented type bombs are present with a maximum diameter of 28 cm. Lithic clasts of the purple-black aphyric vesicular lava and grey-black lava with 1–2 mm feldspar phenocrysts are angular with a modal and maximum diameter of 0.5 and 12 cm respectively. The upper contact is sharp and continuous disrupted only by larger bombs protruding from Unit 6 into the base of Unit 7, as is the lower contact with Unit 5. Unit 6 is continuous with consistent dip for approximately 300 m up-canyon to the SSW, where it is obscured by alluvial canyon debris.

Unit 7 is a 90 cm thick sequence of clast supported beds that lies conformably on Unit 6 dipping approximately 20° north. Proportions of pumice and lithic clasts and modal clast sizes vary vertically through the unit (Fig. 2.11b). Juvenile clast abundance decreases from

90 – 50% over the first 70 cm of the unit, increasing to 95% in the upper 20 cm, < 5% of juvenile clasts are dense VVLP clasts. Lithic clasts make up the remainder of the unit. Pumice lapilli change from angular – sub-angular over the first 70 cm, returning to angular in the upper 20 cm of the unit. Juvenile material contains the same macrocryst population as the other EC units. Abundances of the five pumice lapilli types were not quantified for this unit but pumice lapilli are typically micro-vesicular with dark millimetre-scale banding. Modal juvenile clast diameter increases from 1.5–2 cm over the first 50 cm of the unit, maximum diameter increases from 5–20 cm over the same range. Above this is a 20 cm thick section with modal and maximum juvenile clast sizes of 0.3 cm and 1 cm respectively, clasts here are the most rounded – possibly due to abrasion during transport. The uppermost 20 cm of the unit has modal and maximum clast sizes of 1.5 and 20 cm respectively (Fig. 2.11c). Bombs are consistently < 10 % of the pumice population and show both breadcrust and angular-fragmented types, with a visible continuum between the two, maximum bomb diameter is 20 cm. Three different lithic clast types were observed, in decreasing abundance these are purple-red vesicular aphyric lava, red scoria and grey-black aphyric lava. The lithic clast population is consistent throughout the unit and contains the same clast types observed in the other EC units, modal and maximum clast size are < 3 cm and 28 cm respectively. Throughout the unit, lithic clasts are angular and have modal and maximum clast diameters of < 3 cm and 28 cm respectively. Within the lower 50 cm, variations in clast size and proportions do not occur with consistent thickness, pinching and swelling laterally. Clast sizes and proportions observed in the upper 40 cm however, are laterally continuous.

The upper contact with Unit 8 is sharp and planar disrupted only by large pumice bombs and lithic clasts, as is the lower contact with Unit 6. Unit 7 is continuous with consistent dip for approximately 300 m up-canyon to the SSW, where it is obscured by alluvial canyon debris.

Unit 8 is an 18 cm thick matrix supported lapilli-tuff, it lies conformably on Unit 7 dipping ~20° north (Fig. 2.11d). Ashy matrix accounts for 70% of the unit and clasts 30% - split 50:50 juvenile and lithic clasts. Juvenile clasts are sub-rounded to sub-angular and occur in discontinuous centimetre-scale lenses. Pumice lapilli have a modal clast size of 2 cm and contain the same macrocryst population as observed in other EC units. Abundances of the five pumice lapilli types were not quantified for this unit but pumice lapilli are often dense and contain glassy obsidian bands and patches. Pumice bombs comprise < 2% of juvenile

material and have a maximum diameter of 25 cm. The lithic population is angular and contains black-grey lava with 1–2 mm feldspar phenocrysts, red scoria and purple-black aphyric lava. Lithic clasts have modal and maximum clast diameters of 0.3 cm and 5 cm respectively, larger clasts are concentrated in lenses alongside pumice lapilli. Unit 8 marks the upper portion of the logged section at locality AI18-04 but the stratigraphy continues an additional ~15 m, units are correlated across to locality AI18-22 (see [Appendix 1.21]). The contact with the overlying units is sharp, planar and laterally continuous, disrupted only by larger bombs at the boundary with the overlying unit as is the lower contact with Unit 7.

Unit 9 is a 40 cm thick clast supported pumice lapilli unit that lies conformably on unit 8 dipping ~20° north. Juvenile clasts comprise 90% of the unit, inclusive <10% bombs and dense endmember VVLP clasts: lithic clasts comprise 10% of the unit (Fig. 2.11e). Pumice lapilli are angular and modal diameter increases from 5 mm in the basal 4 cm, to 6 cm in the upper 6 cm of the unit. Abundances of the five types of vesicle texture within pumice lapilli are: macro-vesicular equant, 17%; micro-vesicular equant, 29%; macro-vesicular elongate, 11%; micro-vesicular elongate, 7% and dense, 36%. Bombs are dominantly the angular banded type, with a maximum diameter of 33 cm, bombs coarsen upwards in the unit. Vesicles up to 2 cm diameter occur in the largest bombs. Obsidian chips are rare and < 3 mm in diameter. All juvenile material contains the EC macrocryst population as observed in the units below. Lithic clasts are angular, the population comprises a phenocryst bearing purple-red lava and grey phenocryst bearing lava. Modal lithic clast diameter increases from 0.2–3.5 cm up through the unit.

The upper contact with unit 10 is sharp, planar and continuous, disrupted only by large pumice bombs protruding from the upper part of unit 9. The lower contact with Unit 8 is the same. Unit 9 is continuous from AI18-04 to AI18-22 – where it was logged [Appendix 1.21 (log at AI18-04 units 1 – 10) and 1.22 (Log at AI18-022 units 7 – 10)]: unit 9 extends SSW for another 70 m until covered by alluvial canyon debris.

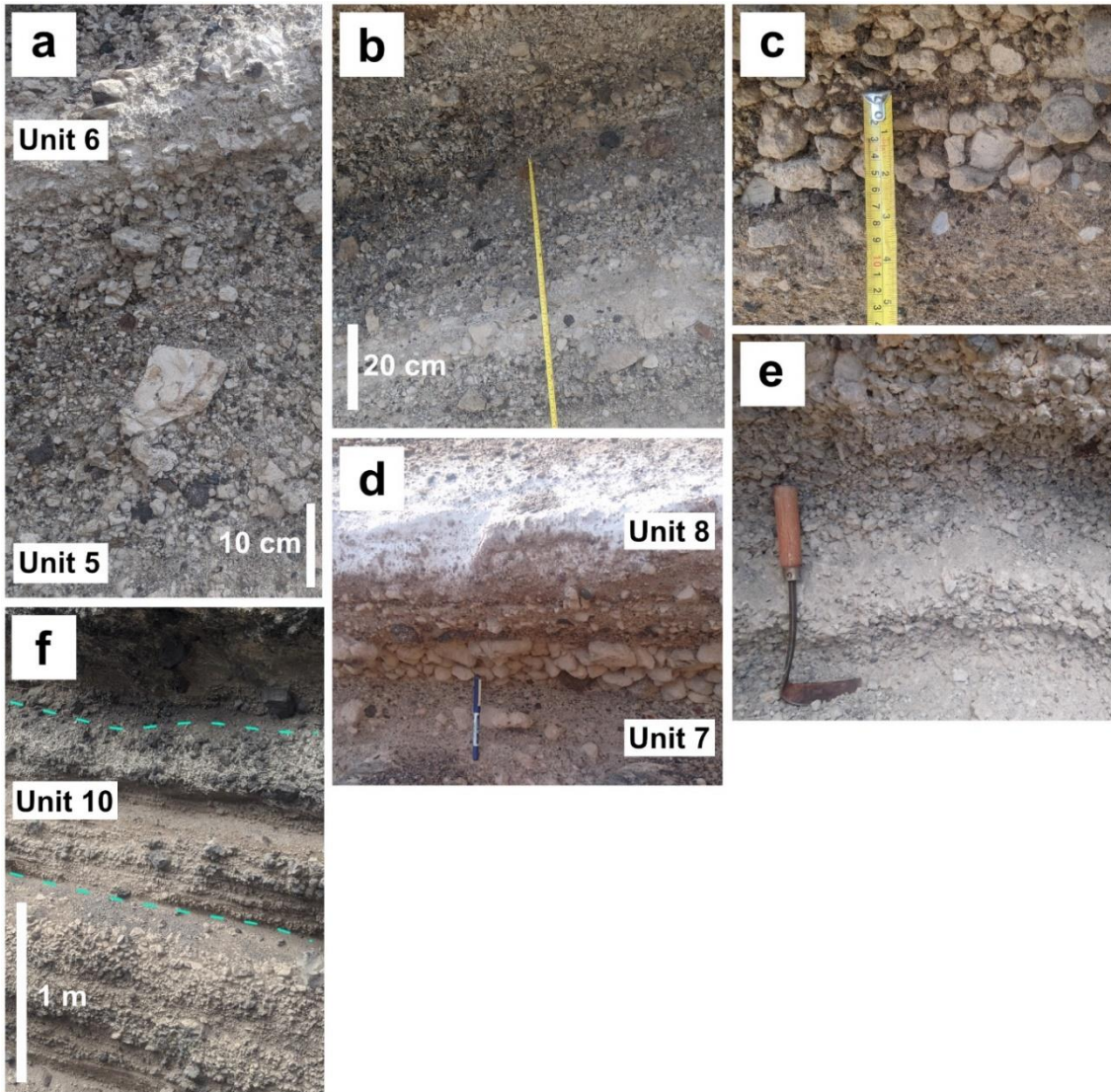


Fig. 2.11 Units of the middle cone stratigraphy, A – D taken at AI18-04, E and F taken at AI18-22. **A:** clast-supported, pumice dominated Unit 5 with graded bedding and a higher proportion of bombs near the boundary with Unit 6. **B:** Units 6 (white ash unit) and 7 showing rapid changes in clast size and ash content within Unit 7. **C:** upper portion of unit and with rounded pumice clasts as shown in D. **D:** upper part of Unit 7 and ash-rich, indurated Unit 8. Pen 14 cm for scale. **E:** excavated pumice rich bed from Unit 9 sampled for density measurements. **F:** showing transition between middle and upper cone with Unit 10 denoted by dashed line.

Unit 10 was described from locality AI18-22 but was difficult to access in the steep cliff face (Fig. 2.11f), and so observations were brief, and no samples collected. This unit marks the uppermost part of the middle cone, the overlying stratigraphy continues for another 20 m to the base of the brecciated lava and is best described at locality AI19-02 in Rainbow Canyon—see Unit 11 description.

Unit 10 is 90 cm thick, comprising interbedded matrix and clast supported beds that lie conformably on unit 9, dipping ~20° north. Matrix supported beds consist of >95% ash and < 5% 2 mm pumice and lithic clasts. Matrix supported beds are indurated and the outer

surface stained reddish-brown. Clast supported beds comprise 90% juvenile material including < 3% bombs: lithic clasts constitute 10% of the unit. Pumice lapilli are generally angular sub-angular to sub-rounded with a modal diameter of 1 cm, but some clast-supported beds contain clasts up to 4 cm diameter. Abundances of the five pumice lapilli types were not quantified for this unit but pumice lapilli tend towards denser vesicle textures. Angular banded and breadcrust bomb types are present: maximum bomb diameter is 33 cm. Lithic clasts are angular, comprising a phenocryst bearing purple-red lava and grey phenocryst bearing lava. Modal lithic clast diameter is 0.5 cm but clasts up to 4 cm diameter occur in beds containing the 4 cm pumice clasts.

The upper contact with a thick clast supported unit is slightly undulating (Fig. 2.11f) but sharply defined while the lower contact is sharp and planar only disrupted by larger bombs protruding into the base of unit 10 from Unit 9. Unit 10 is continuous across the exposed EC canyon wall, extending another ~70 m SSW until covered by alluvial canyon debris.

Emplacement mechanism: Units 6 – 10 of the middle-cone comprise a mixture of (pumice) clast- and matrix-supported beds, where lenses of clast-supported material pinch and swell along some horizons and are laterally continuous in others. Pumice clasts range from angular to sub-rounded and modal clast size is varied. These features suggest primary simultaneous deposition of fall and flow deposits, or “hybrid activity” (Dowey and Williams, 2022 and Valentine and Giannetti, 1995). This marks a transition in eruptive style away from the simpler fall deposits recorded in the lower cone stratigraphy and unit 5 of the middle cone.

Upper Cone – Proximal PDC deposits

Unit 11 is a 12 m thick exposure of interbedded matrix (lapilli-tuff) and clast supported (pumice lapilli) beds sitting conformably on clast supported pumice lapilli units exposed in the cliff face at the head of Rainbow Canyon (Fig. 2.12a) (locality AI19-02 and 52). This unit is a condensed section equivalent to the inaccessible upper stratigraphy that thickens from 16–30 m, approximately N – S above unit 10 in the eastern face of Echo Canyon. At the Rainbow Canyon locality, the underlying clast supported pumice lapilli units are interpreted to be the condensed equivalent of units 1–10.

Matrix supported beds contain 70–90% ash, <20% pumice, ~10% obsidian and <10% lithics (Fig. 2.12b). Pumice lapilli clasts are sub-rounded to rounded and have a modal clast size of

5 cm (Fig. 2.12c). Obsidian and obsidian breccia clasts (Fig. 2.12c) range from <1–15 cm in diameter and, like the pumice clasts, contain the same macrocryst population as the other EC units. Lithic clasts are comprised of a grey-black aphyric lava, red scoria and purple-black aphyric vesicular lava. The exteriors of these clasts are altered red. Lithic clasts are concentrated in lenses and have a modal diameter of <1 cm. Matrix supported beds are stratified, ash and fine lithic clasts define cm-scale cross-stratification and pumice lapilli define decimetre-scale cross-stratification (most easily observed in Fig. 2.12A from across the canyon due to the sheer nature of the outcrop making photographing the structures close-up more challenging) see [Appendix 1.22 for original logs and sketches].

Clast-supported beds are massive and contain <30% ash, 60% pumice, 10% obsidian and 10% lithic clasts. Pumice lapilli are sub-angular to sub-rounded and have a modal clast size of 5 cm. Abundances of the five types of vesicle texture within pumice lapilli are: macro-vesicular equant, 13%; micro-vesicular equant, 30%; macro-vesicular elongate, 16% micro-vesicular elongate, 27% and dense, 12%. Juvenile obsidian and obsidian breccia clasts have a maximum diameter of 20 cm. Lithic clasts have a modal diameter of 3 cm and are comprised of a grey-black aphyric lava, red scoria and purple-black aphyric vesicular lava. The exteriors of these clasts are altered red. Across both matrix and clast supported beds, breadcrust bombs, often with a black exterior constitute ~30% of all juvenile material: black interiors were observed in some bomb fragments. Maximum bomb diameter is 40 cm.

In Rainbow canyon, Unit 11 is directly overlain by both the dome and the OBP, which mantles the exposed stratigraphy of the upper cone beyond the domes' extent. In Echo Canyon, Unit 11 is directly overlain by the brecciated lava, apart from at the head of the canyon where Unit 12 cuts across Unit 11 and the middle cone.

Emplacement mechanism: This unit defines a marked transition in emplacement mechanism relative to the lower cone. The poor sorting of the unit, dominance of matrix supported beds and rounded pumice clasts indicate emplacement by pyroclastic density currents. Evidence of lateral movement is recorded in cross-stratification on the decimetre scale within the most matrix rich beds.

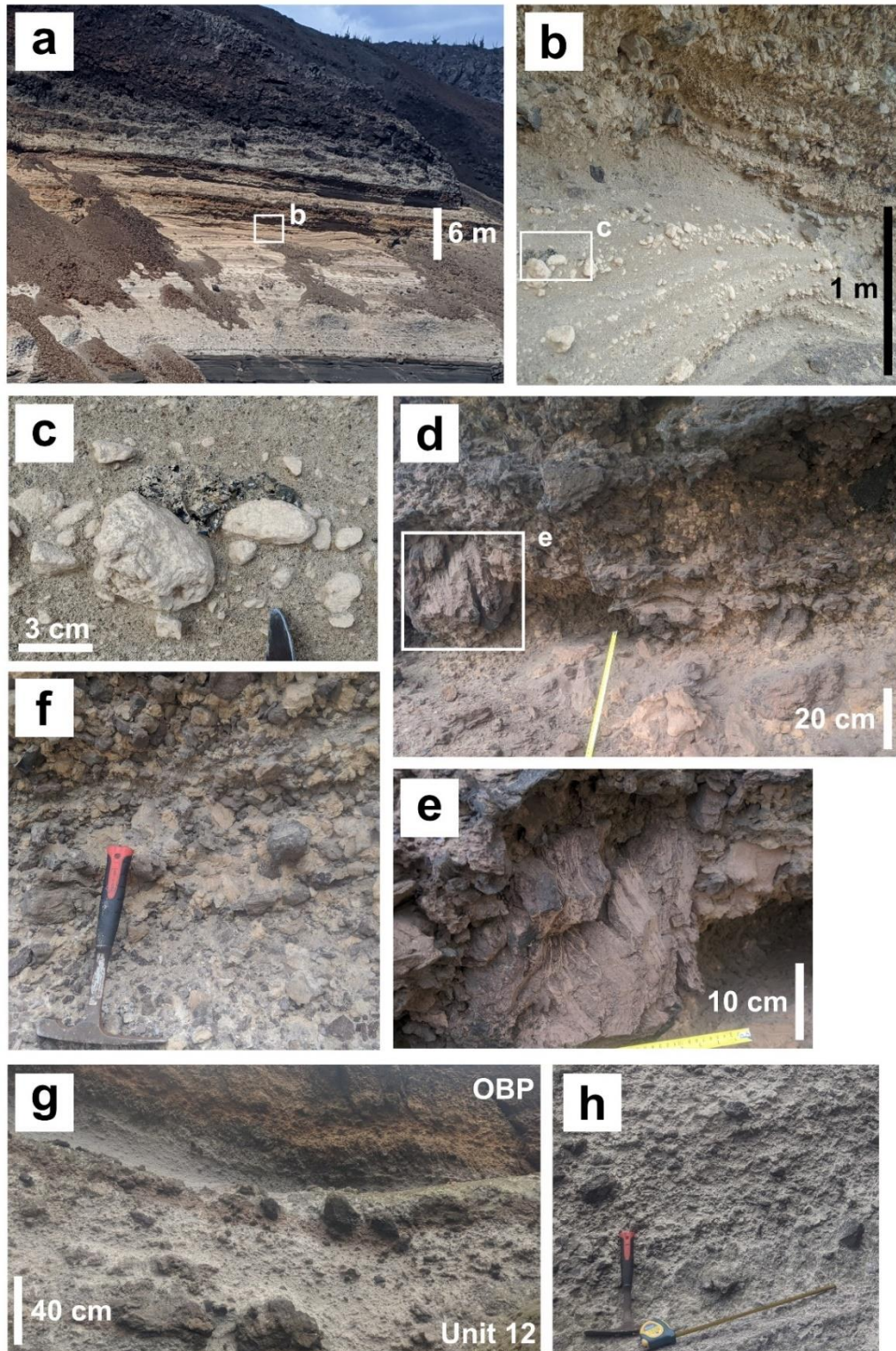


Fig. 2.12 Field photos of upper cone deposits. **A:** view towards AI19-02 looking approximately west at pale grey – yellow upper cone deposits (Unit 11) overlying felsic pyroclastics (black unit below) with OBP above. **B:** stratified ash-dominated portions of Unit 11, pumice clasts are rounded and obsidian clasts can be deformed around pumice, **C. D:** view of spatter-like portion of Unit 12 taken at AI19-23. **E:** close-up of dense, banded pumice spatter. **F:** clast supported coarse pumice and lava clasts within Unit 12, hammer length 23 cm for scale. **G and H:** upper portion of Unit 12, highly altered pumice clasts with large blocks of lava and pumice bombs standing out from surface. Orange unit at the top of G is the OBP.

Unit 12 is 15 m thick, clast supported and dips $\sim 20^\circ$ SW crosscutting the middle cone in the head of Echo Canyon (see Fig. 2.12d). Ninety-five percent of clasts are juvenile - 55% pumice lapilli/bombs and 40% lava fragments. Lithic clasts make up the remaining 5%. Juvenile clasts are angular and contain the EC feldspar macrocryst population. All juvenile material is angular and modal pumice and lava clast diameters decrease from 12 cm to 4.5 cm over the lower 7 m of the stratigraphy. In the middle of Unit 12 is a 3 m thick concentration of elongate pumice bombs up to 70 cm wide, here lava blocks are up to 1 m in diameter (Fig. 2.12e). Large pumice blocks have the appearance of “spatter”. Their long axes are aligned horizontally, clasts are often banded and have black and orange altered exteriors and interiors. Where pumice clasts are largest individual clasts are difficult to distinguish as they are often deformed around each other. The upper 7 m of Unit 12 is altered to white-grey, traces of pumice clasts show a modal diameter of 6 cm, maximum 50 cm (Fig. 2.12 g, h). Juvenile lava clasts are less altered, angular and show banding, they range from 3–120 cm in diameter. The lithic clast population consists of a grey-black aphyric lava, red scoria and purple-black aphyric vesicular lava, modal lithic clast mirrors that of the juvenile pumice population throughout the unit. The unit has a chaotic appearance, lacking well-defined internal stratification apart from where “spatter” becomes more dominant than lava clasts in the middle of the unit.

Unit 12 is laterally restricted, cropping out for approximately 35 m in the eastern face of Echo Canyon. In Echo Canyon, the lower contact of Unit 12 is a sharp angular unconformity where it cuts across the underlying stratigraphy of the upper cone while the upper contact with the OBP appears conformable, although was difficult to distinguish in outcrop due to high levels of alteration (Fig. 2.12g). The upper portions of the OBP appear to dip the same way as Unit 12 when viewed at a distance. See [Appendix 2.23] for original log.

Emplacement mechanism: The presence of pumice blocks > 50 cm, their morphology, high degrees of alteration and the presence of large clasts of juvenile lava in this unit indicate that Unit 12 is the most proximal deposit observed in Echo Canyon. The unconformity at the base, prevalence of spatter and lack of internal structure is interpreted to record vent proximal hybrid explosive-effusive activity where erupted products are a combination of vent-accumulations of lava, pre-existing pumice clasts and newly forming pumice spatter before the deposition of the overlying OBP.

Distal Deposits

The distal EC deposits are described below, the units at these localities are classified as distal due to a) their distance from the head of Echo Canyon – where the presence of pumice spatter, juvenile and lithic clast size and alteration all indicate highly proximal deposition, b) clasts in these units contain the distinct EC crystal population and c) units often contain obsidian correlating them to the upper cone deposits but the middle and lower cone stratigraphy is absent, indicating the distance from the likely vent region is greater considering the lower and middle cone stratigraphy is interpreted as pumice fall deposits.

The NE-Bay coastal distal deposits have a thickness of approximately 25–30 m and dip from 8–22°, approximately east (Fig. 2.13a). The units lie conformably on the scoriaceous component of a compositionally zoned pumice – scoria fall that thickens eastwards, as described by Chamberlain *et al.*, (2016). All pumice and obsidian clasts in the distal deposits contain the distinct EC feldspar crystal population observed in proximal stratigraphy. The distal stratigraphy is composed of three main bed types (A, B, C) which form a repeating sequence A-B-C from top to bottom. Each bed type is described below.

Type A beds are massive lapilli-tuff units. They are between 3 and 7 m thick, matrix supported and generally massive with a very weathered exposed surface (Fig. 2.13a and b). The matrix comprises 30–40% of each bed and is a medium sand grade mixture of black lithic clasts, ash and tiny pumice fragments. Pumice lapilli comprises 50–60% of each bed, are rounded, have a modal clast size of 3 cm and a maximum diameter of 4 cm. Less than 10% of pumice clasts are bombs > 40 cm. Abundances of the five pumice lapilli types were not quantified for this unit but pumice lapilli are typically dense with dark banding. The lithic clast population is comprised of obsidian, purple-black lava, green-blue finely crystalline lava and a yellow, highly-altered trachyte containing 1 mm feldspar phenocrysts. Lithic clasts have a modal diameter of 1 cm, but large, sub-angular blocks of the lavas have a modal diameter of 30 cm and a maximum of 110 cm.

Type A beds form the lower contact with the underlying zoned pumice-scoria fall (felsic pyroclastics in Fig. 2.6 and 2.13), a sharp, planar boundary that is clearly visible all along the coastal outcrop (Fig. 2.13a). They are also the uppermost beds in the distal stratigraphy, overlain by re-worked alluvial material. There are 5 beds of this type in the NE-Bay distal stratigraphy.

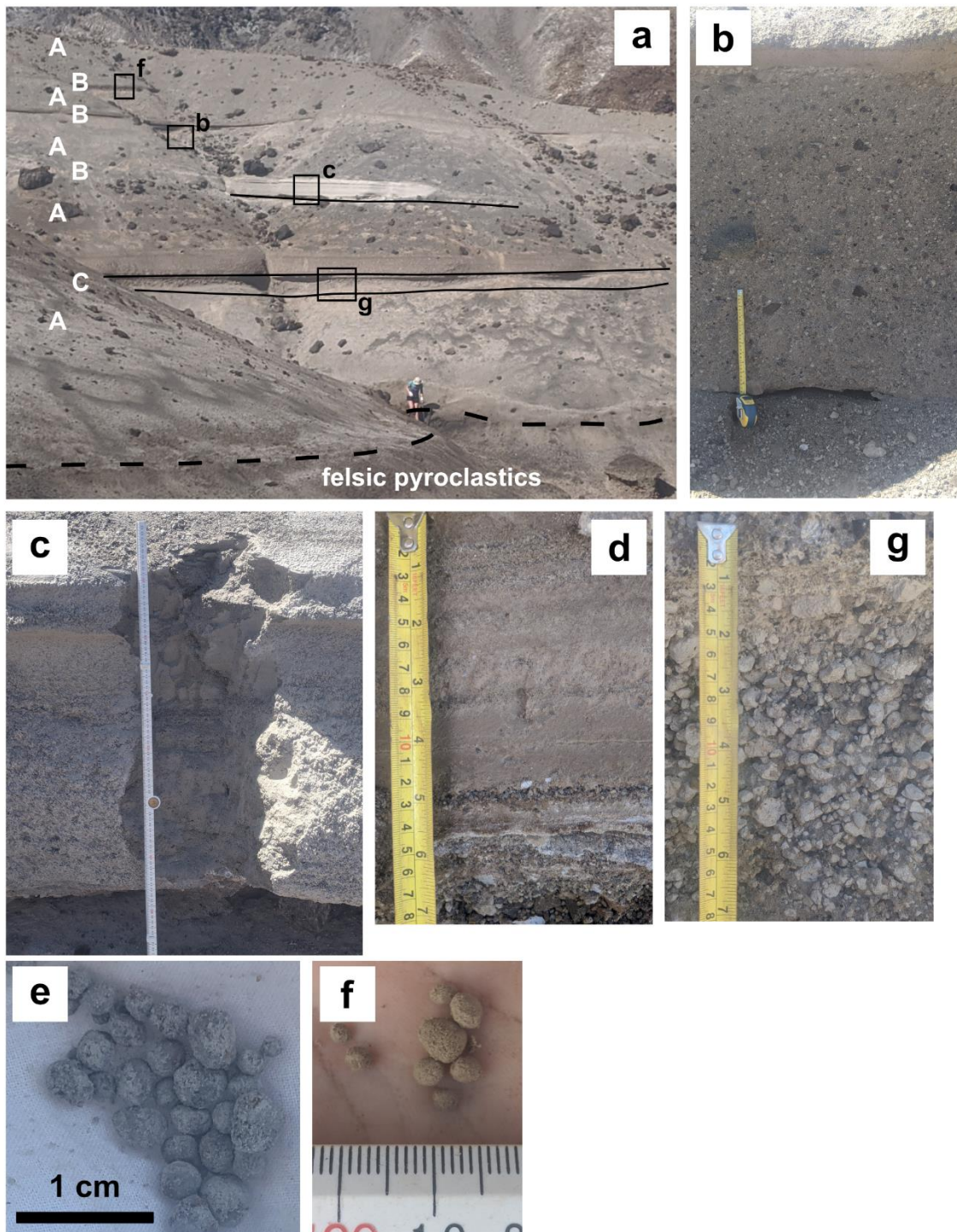


Fig. 2.13 Field photos of EC distal PDC deposits at NE-Bay AI19-46. **A:** overview of distal PDC deposits at the outcrop, approximately 25 m thick and showing contact with underlying felsic pyroclastics – zoned pumice – scoria fall (dashed line). Person 175 cm for scale. White text “A, B, C” refers to typical stratigraphy as described in text. **B:** type A units, tape measure extended to 30 cm for scale. **C and D:** type B units, **C:** white accretionary lapilli bed, **D:** ash rich bed with lenses of lithic fragments and accretionary lapilli. **E and F:** accretionary lapilli from C and D respectively. **G:** clast supported type C beds.

Type B beds sit above and beneath type A in the stratigraphy and range from 20 – 64 cm thick: type B beds are pinkish-white and indurated (Fig. 2.13a, c and d). Ash is generally the dominant component, but beds have varying proportions of 2–4 mm accretionary lapilli

and 0.3–1 cm angular lithic fragments (Fig. 2.13 c – f). Accretionary lapilli compose 90–10% of beds, concentrated in cm-scale layers at lower concentrations. Rounded 2 mm pumice clasts comprise < 5% of each bed, as do lithic clasts, concentrated in 1–2 cm layers. Lithic clasts are made up of black obsidian and blue-grey lavas. The base of type B beds is always marked by a distinct pink 1–2 cm, fine ash layer. Thickness of these beds is continuous, and they extend along the full coastal exposure, there are 6 beds of this type in the Ne-Bay distal stratigraphy.

Type C beds are 20–60 cm thick, massive, and clast supported. Pumice lapilli make up 50% of the beds, lithics < 30% and an ashy matrix comprises 10–30% of the beds (Fig. 2.13 a and g). Beds are reversely graded. Pumice clasts are rounded and typically dense with banding, modal clast size grades from 0.3–4 cm up through each bed. Lithic clasts are sub-rounded with modal diameter grading upwards from 0.2–1 cm. The fine, base of the bed is matrix rich and more welded than the coarse upper part. Contacts between type C units and the under/overlying beds are sharp, planar and continuous across the coastal exposure.

The occurrence of obsidian, rounded pumice clasts containing the EC crystal population and their stratigraphic relationship to the underlying zoned pumice – scoria fall ties these units to the upper portion of proximal EC sequence logged in Echo Canyon and Rainbow Canyon (Unit 11). In type A units, the high matrix content, poor sorting and presence of large blocks precludes deposition via air-fall at this distance from the likely vent location for the EC deposits. The presence of accretionary lapilli in type B beds is interpreted to be most likely due to the interaction of ash and sea water/ atmospheric moisture as there is no other evidence for magma-water interactions and seawater-ash interaction is likely at locations so close to the coast. Welding at the matrix-rich base coupled with rounding and reverse grading of pumice clasts in type C units suggests these are not pumice fall deposits. Taken together, the characteristics of this sequence of ash rich and poorly sorted massive units suggests the distal EC deposits were emplaced via pyroclastic density currents. See [Appendix 1.24] for original log.

Ariane Site Quarry & NE-Bay Road distal deposits are exposed close to the Ariane ESA site (see Fig. 2.2 AI19-50 and AI19-13). Here the distal deposits are composed of several beds that are the equivalent of the type A, B and C beds observed in the NE-Bay deposits with only a few minor differences – outlined below. The quarry face is approximately 6 m thick with the base covered by slumped material (Fig. 2.14a). Digging into this material revealed

an approximately 55 cm thick fine-grained bed consisting of blueish-grey lithic fragments and rounded pumice clasts up to 1 cm in size (Fig. 2.14b). This bed has complex cross-stratification and lenses of fine material. At the base of the bed is a layer of > 20 cm lithic blocks, the base of this was not excavated. The top of this bed is marked by a 1 cm thick pale grey-brown fine-sand grade layer which has a sharp upper contact with the overlying stratigraphy. The fine-grained cross-stratified bed is also observed at localities AL19-54 and AL19-55 (see Fig 2.2) in deposits at the mouth of Echo Canyon where pumice cone stratigraphy is also absent.

The distal EC deposits are approximately 3 m thick in both the quarry and roadside exposure and dip approximately 10–20° towards the N/NNW. At the roadside exposure (AL19-50), the contact with underlying compositionally zoned pumice – scoria fall is observed by digging down less than 30 cm. In the quarry exposure there are 3 type B beds, 3 type C beds and 1 type A bed in a sequence B, A, C, B, C, B, C from top to bottom (Fig. 2.14a).

The type A bed at the Ariane site quarry is approximately 1 m thick, matrix supported and massive with a heavily weathered surface – essentially the same as those in the coastal deposits. The matrix contains ash and < 1 mm black lithic fragments. As in the coastal deposits, pumice clasts are rounded and have a modal diameter of 2–3 cm. The main difference to the coastal Type A beds is the presence of an additional pumice population which is very dense, yellow in colour and contains 1 mm feldspar phenocrysts, these clasts are up to 6 cm in diameter. Lithic clasts are angular – sub-angular and include a black lava and a purple-red lava as seen in the coastal deposits. Lithic clasts are typically 2–3 cm in diameter but also occur as large blocks with a maximum diameter of 102 cm, these comprise less than 5% of the unit (Fig. 2.14c). The lower 40 cm of this bed is more welded than the upper part (not observed in the coastal equivalents), but this effect pinches out round the quarry outcrop. The upper and lower contacts are sharp and planar. Above the type A bed is a 30 cm accretionary lapilli-rich type B bed, below it is a type C bed.

Type B beds are 12–30 cm thick pink-brown indurated ash beds as seen in the coastal deposits. They lie conformably in the sequence (Fig. 2.14d). Within each bed, rounded pumice and lithic clasts from 0.1–1 cm diameter are concentrated in 1 cm thick layers, usually 1 or 2 per bed. The uppermost type B bed, at the top of the sequence contains >

90% 3 mm accretionary lapilli. We correlate this approximately to the accretionary lapilli bed observed in the coastal PDC deposits.

Type C beds are 10–60 cm thick, clast supported and exhibit reverse grading as seen in the coastal equivalent units (Fig. 2.14e). These beds contain 90% pumice, which is rounded and has a modal diameter ranging from 0.1–3 cm from the base to the top of the unit. Vesicle textures in pumice clasts include macro-vesicular equant, elongate and densified. Angular, dense, yellow pumice clasts containing 1 mm feldspar phenocrysts comprises 20% of the pumice population and reaches 4 cm diameter, only found in the upper portions of the beds. Lithic clasts comprise 10% of the unit and include a black-grey lava and a red vesicular lava, modal diameter is typically 0.1–3 cm with finest clasts in the base. In the coarser upper portion of the beds, mm-diameter rounded clasts form discontinuous irregular lenses up to 1 cm thick. See [Appendix 1.25] for original log and sketch.

Spire Beach distal EC deposits that crop out at locality (AI18-73) are heavily weathered, the exposure is gently sloping with several steps that cut into the stratigraphy where harder units stand out from the face (Fig. 2.15a). The composition of units in the weathered flat surface was difficult to define and so key descriptions were limited to cut faces. The dominant lithologic characteristics are very similar to that of the matrix supported (type A) beds observed at the NE-Bay coastal and quarry outcrops, with clast supported (type C) beds forming a minor constituent in the stratigraphy, no accretionary lapilli are found here. The units dip approximately 20° towards the ENE: the exposed sequence is approximately 7 m thick.

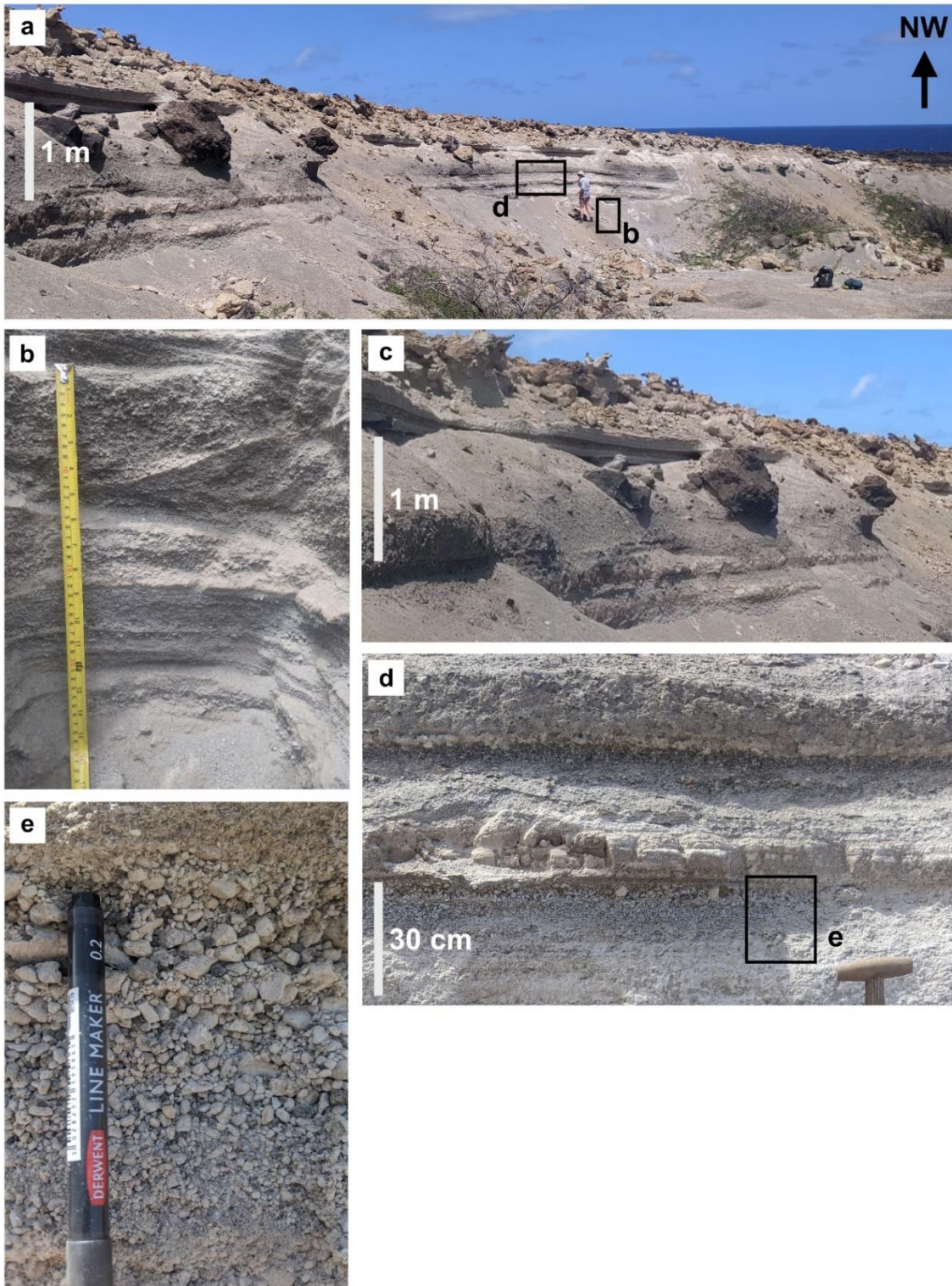


Fig. 2.14 Field photographs of Echo Canyon (EC) distal Pyroclastic density current (PDC) deposits at the Ariane Site Quarry AI19-13. **A:** overview of exposure at the quarry site, person 175 cm tall for scale. **B:** close-up of cross-stratified units at the base of the EC deposits. **C:** type A beds containing large blocks and boulders, heavily weathered. **D:** close-up of type B and C beds, type B beds are pale competent ash beds, type C beds contain pumice and are reversely graded as shown in **E**.

Approximately 2–3 m thick matrix supported (type A) beds dominate the stratigraphy: the matrix is a brown-purple ash which weathers to pale grey. The beds are comprised of 80% matrix, 10% pumice clasts, 5% obsidian breccia and dense endmember VVLP clasts

approximately and 5% lithic clasts. Pumice clasts are sub-angular – rounded with a modal diameter of 1 cm: pumice bombs and fragments can be greater than 7 cm (Fig. 2.15b and c). Pumice clasts are generally dense and micro-vesicular, while pumice bombs are the angular banded type. The dense clasts - obsidian breccia, dense VVLP clasts and other lithic clasts, range from angular 3 mm fragments and rounded 2–3 cm clasts, to sub-angular – angular blocks from 0.3–1 m in diameter. The obsidian in obsidian breccia clasts is heavily altered and easily friable, a variety of lithic and pumice clasts which range from 1 cm–10's of cm in diameter are held together by the obsidian. Lithic clasts include a purple vesicular lava with altered 3 mm feldspar phenocrysts and a red non-vesicular lava. Discontinuous pumice rich lenses, 4–10 cm thick pinch in and out across the beds. Matrix supported beds appear to be more strongly welded than clast supported beds, contacts between beds are marked by a 1–2 cm ash layer and are sharp and planar as a result.

Clast supported beds are typically 10–30 cm thick, best exposed in steps in the outcrop where outer surfaces are broken away. The beds are made up of 75% pumice lapilli, 10% pumice bombs, 10% obsidian breccia, and 5% other lithic clasts (Fig. 2.15d). Pumice clasts are angular with a modal diameter of 3 cm and a maximum of 6 cm. Dense, banded pumice bombs are up to 40 cm in diameter (Fig. 2.15e). Obsidian fragments are as fine as 3 mm, but obsidian breccia blocks are typically 20–30 cm in diameter (Fig. 2.15f). Other lithic clasts are of the same types as described in matrix-supported units and can be up to 70 cm in diameter. Clast supported beds show some subtle reverse grading amongst the pumice lapilli, slightly overprinted by the bomb population. See [Appendix 1.26] for original log and sketch.

Emplacement mechanism: The NE-Bay coastal section, Ariane site Quarry and Spire Beach distal deposits all record a similar mechanism of emplacement, with slight variations in componentry that likely reflect the different spatial and temporal distributions of these pyroclastic density currents. The presence of larger obsidian breccia clasts in the Spire Beach deposits indicates these flows may not have travelled as far from their source as those seen at the Coast and at the Ariane Quarry and/or formed later in the eruptive sequence where obsidian was more abundant (e.g., correlating to the upper portions of unit 11 – proximal PDCs). The lack of stratification in the massive lapilli tuffs of all the distal deposits (type A beds) indicates turbulent shear was suppressed at distal localities – possibly due to the low slope of the paleo-topography onto which these flows were deposited (particularly at the coastal and Ariane Quarry localities) (Branney *et al.*, 2002).

The cross-stratified nature of the bed seen at the base of the Ariane Site logs and at localities AI19-54 and AI19-55 could be interpreted to represent the presence of a dilute cloud that surges ahead of the arrival of the higher concentration pyroclastic density current (Hoblitt, 1986). Ash rich beds containing accretionary lapilli are absent in the proximal PDC deposits (Unit 11), accretionary lapilli are likely limited to the distal deposits due to their increased proximity to the sea and thus greater interaction with seawater.

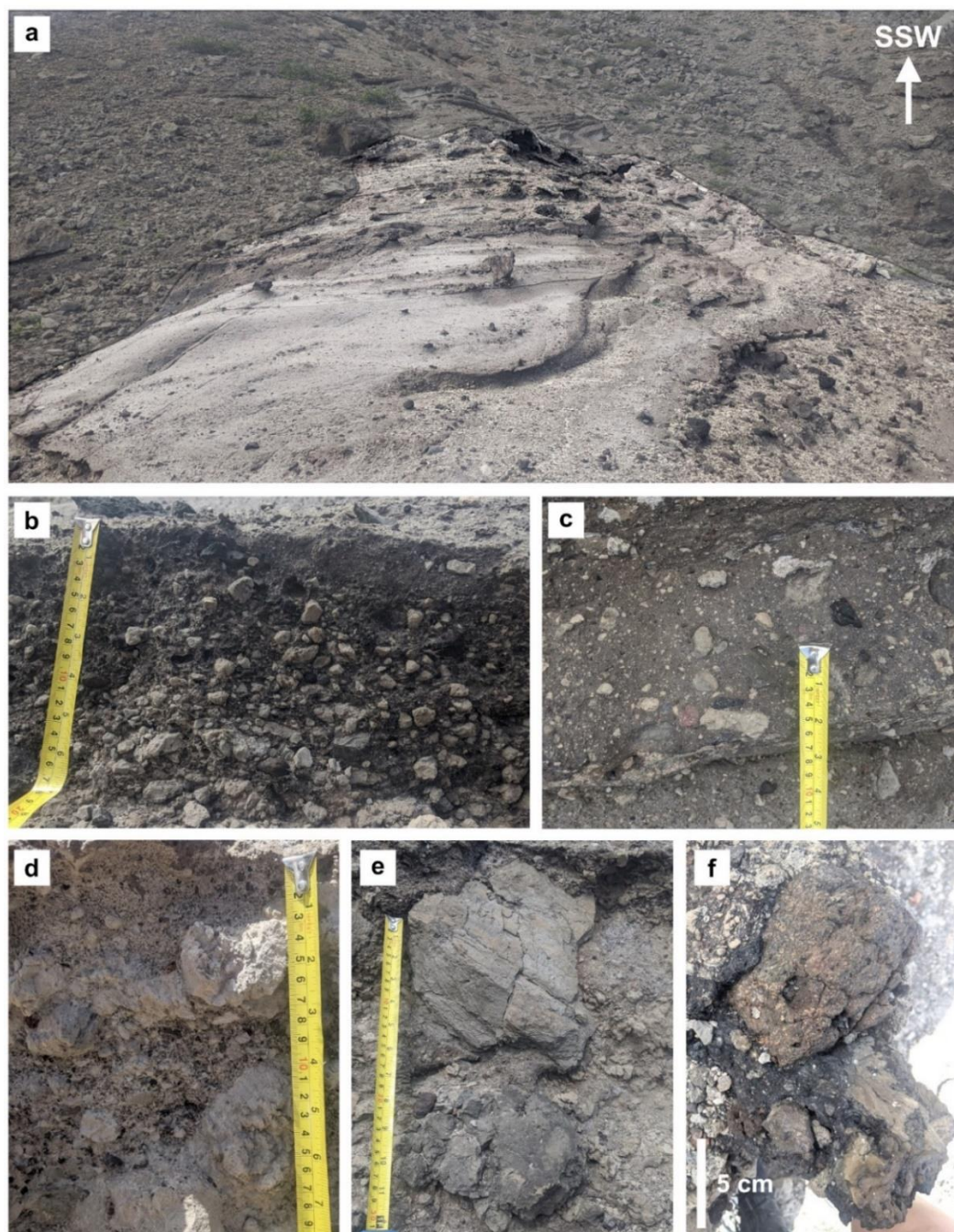


Fig. 2.15 Photos of distal PDC deposits at Spire Beach, AI18-73. **A:** Exposure of heavily weathered PDC deposits at AI18-73. **B:** fresh cut face through type A beds showing matrix supported pumice clasts and lithic fragments. **C:** weathered top surface of type A beds shown in B. **D & E:** altered type C clast supported beds with pumice bombs. **F:** example of obsidian breccia at Spire Beach, lithic clasts and pumice fragments within banded obsidian.

2.4.3 Post cone units

The dome is a blue-grey, 30–40 m thick brecciated porphyritic trachyte lava cropping out in direct contact with PDC deposits at Rainbow Canyon, and Spire Beach (Fig. 2.16a). The crystal population is as described for all EC eruption deposits (see *Petrography* and Fig. 2.18): feldspar and clinopyroxene macrocrysts constitute 3–5% of the dome. Groundmass crystallinity is heterogeneous in thin section but up to 70%. Vesicles up to 1 cm diameter comprise < 10% of the dome and often contain macrocrysts. The dome is extensively brecciated and heterogeneously altered to white clays (Fig. 2.16b): un-altered blocks are usually ≤1 m in diameter and exhibit mm – cm flow banding (Fig. 2.16c).

The lava flow is a purple-grey, 7.5–10 m thick brecciated porphyritic trachyte lava (Fig. 2.16d). The lava overlies the pumice cone at Echo Canyon (AI18-20), and the dome at Rainbow Canyon (AI19-02, 52) and Spire Beach (AI18-73). The macrocryst population is the same as that of the dome. Groundmass crystallinity in thin section is heterogeneous with regions of >30% crystals. Vesicles up to 0.5 cm diameter comprise < 10 % of the lava flow. The lava flow is brecciated but clays produced by alteration are pink. Coherent, un-altered regions are aligned parallel to flow direction, which is approximately north (Fig. 2.16e and f). In thin section, complex mm – cm scale banding is observed.

The OBP is a 3–10 m thick clast supported pumice fall that thickens to the SE. The dip of the OBP is typically ~30°, the direction varying from SSE to NNW depending on the underlying topography of the EC sequence (Fig. 2.16g). Juvenile material comprises > 95% of the unit, including approximately 5% obsidian, pumice clasts are dominated by bombs. Pumice clasts are angular with a modal diameter of 10 cm. Abundances of the five types of vesicle texture within pumice lapilli are: macro-vesicular equant, 36%; micro-vesicular equant, 33%; macro-vesicular elongate, 3% micro-vesicular elongate, 9% and dense, 18%. Breadcrust bombs are dominant with a maximum diameter of 45 cm. Many pumice clasts are pale orange/pink and have dark thermally altered cores. Obsidian fragments range from 2–45 cm in diameter, larger clasts/blocks are often rounded – sub-rounded (Fig. 2.16h). Contacts between the upper pumice fall and underlying lavas are sharp. The contact with Unit 12 of the upper cone, however, is gradational and difficult to discern due to alteration of clasts and outcrop accessibility (Fig. 2.12g).

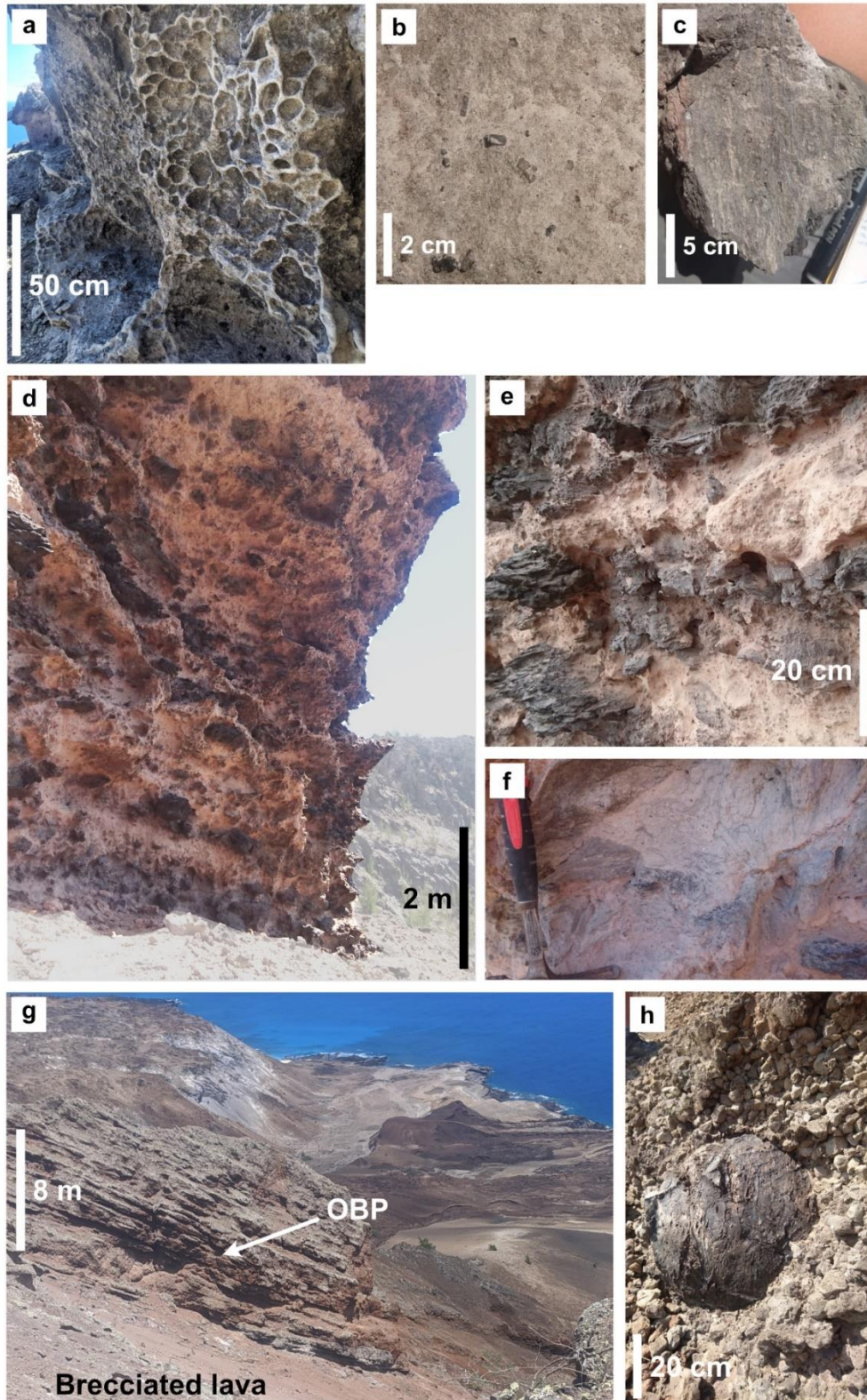


Fig. 2.16 Images of Echo Canyon (EC) post-cone deposits. **A:** outcrop of the dome at Al18-33. **B:** close-up of weathered regions with EC macrocrysts of clinopyroxene and plagioclase. **C:** Sampled fragment of less altered dome lava showing mm-cm banding, macrocrysts and vesicles. **D:** the brecciated lava in outcrop showing brecciation and alteration to pink clays and banding of unaltered blocks. **E and F:** close-up of banding picked out by altered and unaltered regions in brecciated lava, in F, hammer handle is 20 cm for scale. **G:** view overlooking NE bay showing OBP dipping approximately 30° towards the NE overlying the brecciated lava. **H:** obsidian bomb within coarse pumice of the OBP.

[2.5 Vesicularity and vesicle textures](#)

Bulk vesicularity distributions (BVDs) and the abundance of each of the five identified textural types (Fig. 2.7) in the pumice population of each sampled Unit are displayed relative to their stratigraphic position in Fig. 2.9.

From Units 1–3, BVDs progressively narrow about a mode of 75–80%. Clasts in Units 1 and 2 are both dominated by macro-vesicular equant vesicles and < 5% are sheared. In Unit three, 31% of clasts are sheared and the BVD is the narrowest of all the Units. Whereas Unit 4 has similar lithologic characteristics to Unit 3, the pumice population is texturally distinct and the BVD is broader: 64% of clasts fall outside the modal range – 70–75%. The proportion of dense clasts increases by 24%, and sheared and micro-vesicular equant clast abundance is halved.

The abundance of dense clasts peaks at 36% in Unit 9. Vesicle texture heterogeneity is reflected in the BVD, which is broad with 37% of clasts with a vesicularity lower than 65%, compared to none in Unit 3. In Unit 11, the five textural types are more evenly represented and the BVD narrower than Unit 9, modal vesicularity is 70–75%. The proportion of dense clasts is 22% lower than in Unit 9 but 43% of clasts are sheared. In the OBP, modal vesicularity increases and broadens to 70–80% and 16% of clasts have a vesicularity of < 65%. Less than 10% of clasts are sheared and 23% are dense. Full bulk vesicularity data and textural groups can be found in [Appendices 1.4 and 1.5].

[2.6 Whole Rock Compositions and Viscosity](#)

Average whole-rock compositions of bulk samples from representative Units are shown in Fig. 2.17, major and trace element data are presented in tables 2.3, 2.4 (XRF) and 2.5 (La-ICPMS). Table 2.3 also shows additional XRF analyses of the major textural types present in each unit. All juvenile material is trachytic: between Units 1 and 9, $K_2O + Na_2O$ variation is <0.5 wt% and SiO_2 <1 wt%. The lavas are ~3 wt% poorer in silica with the same range in alkalis. The overlying OBP composition sits between the lavas and the cone pumices. There was no significant difference in major element composition between textural groups from the same Unit (see table 2.3). All the EC Units have a peralkalinity index (PI) of 1–1.04 [PI = Molar $(Na_2O + K_2O)/Al_2O_3$]. Generally, major and trace element data for the proximal cone pumices reflect a slightly more evolved composition than the overlying lavas and post-cone deposits – distal deposits were not analysed for whole rock due to lab closures during the

COVID-19 pandemic. Cone units have lower Al_2O_3 , MgO, Sr, Eu and Ba than the post cone Units, see Fig. 2.17. Proximal cone pumices have Zr concentrations > 1080 ppm whereas the lava, dome and OBP have Zr concentrations <900 ppm.

Whole-rock major element data was used to calculate estimated melt viscosity across a range of H_2O concentrations (table 2.6). Samples are only mildly peralkaline so the model of Giordano *et al.*, (2008) was applied. For comparison, calculated viscosities of a typical calc-alkaline basalt, dacite and rhyolite from Le Maitre (1976), and peralkaline rhyolite from Clarke (2020) are orders of magnitude higher (table 2.6)

Several previous studies indicate Ascension Island magmas are wet: 2–4 wt% for a trachyte and 8 wt% for a mingled basalt-rhyolite scoria-pumice fall (Kar *et al.*, 1998; Chamberlain *et al.*, 2016, 2019, 2020). Volatile data for the EC eruption will be reconstructed during Chapter 3, but volatile contents captured in different erupted glasses were not constrained. Here, the EC melt viscosity is calculated across a range of volatile concentrations. At 4 wt% (representing a likely pre-eruptive water content), EC melts would have a viscosity of 103.3 – 103.6 Pas at a reasonable eruptive temperature of 900°C. This is only one order of magnitude greater than a basalt erupting at 1000°C with 1 wt% water (Table 2.6) but with lower water contents or following degassing viscosity would rise, our calculations demonstrate that this is highly unlikely even then to generate melt with viscosities equivalent to normal rhyolite.

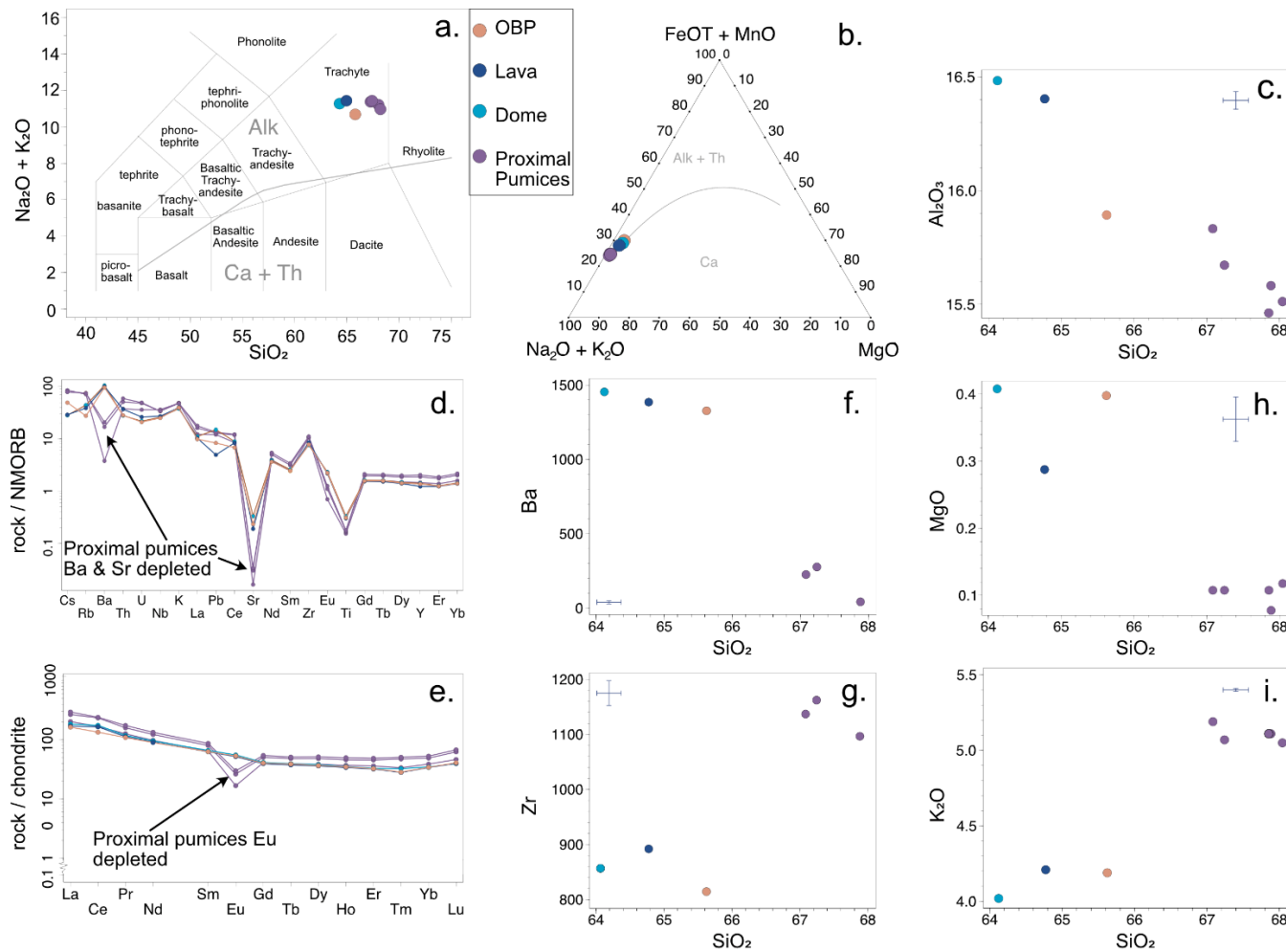


Fig. 2.17 Bulk unit average whole-rock major and trace element data of pumice and lavas from the Echo Canyon (EC) deposits. Proximal pumices are from the lower – upper cone. In **C, F, G, H and I**, blue crosses represent maximum analytical error for each element, ± 0.18 for SiO_2 , ± 0.03 for MgO, ± 0.04 for Al_2O_3 and ± 0.1 for K_2O . **A:** Total alkalis-silica diagram showing EC deposits plot in the trachyte field with proximal pumices slightly more evolved than the lavas and orange-brown pumice (OBP), symbols are larger than analytical error. **B:** Ternary plot of total Fe + MnO against MgO, and total alkalis. Calc-alkaline (Ca), alkaline (Alk) and tholeiitic (Th) fields denoted. **C:** Plot of Al_2O_3 vs SiO_2 . **D:** Trace element data normalised against normal mid-ocean ridge basalt (NMORB) showing proximal pumices depleted in Ba and Sr relative to the lavas and OBP. Trace element data is from LA-ICPMS analyses apart from Zr, from whole rock XRF data, normalization values from Hofmann (1988). **E:** Trace elements normalised to chondrite showing proximal pumices are depleted in Eu relative to the lavas and OBP, normalization values from McDonough and Sun (1995). **F:** plot of Ba vs SiO_2 . Barium from La-ICPMS and SiO_2 from whole-rock XRF analysis. **G:** plot of Zr vs SiO_2 . **H:** plot of MgO vs SiO_2 . **I:** plot of K_2O vs SiO_2 . **C, F, G, H and I** show proximal pumices are compositionally more similar to each other than to the lavas and OBP.

Table 2.3: Whole rock major element data (in %) for Echo Canyon units and different textural groups.

Unit	Sample N°	Sample Type/ group	SiO ₂	TiO ₂	Al ₂ O ₃	MnO	MgO	Fe ₂ O ₃	CaO	P ₂ O ₅	K ₂ O	Na ₂ O	Total
Unit 1	842A	Prox.Pum (bulk)	67.86	0.25	15.59	0.16	0.08	3.59	0.73	0.02	5.12	6.20	99.61
Unit 2	843B	Prox.Pum (bulk)	67.83	0.26	15.47	0.16	0.11	3.67	0.76	0.02	5.12	6.20	99.60
Unit 3	844A	Prox.Pum (bulk)	68.02	0.27	15.52	0.17	0.12	3.64	0.77	0.02	5.06	6.01	99.60
Unit 4	844D	Prox.Pum (bulk)	67.06	0.28	15.84	0.17	0.11	3.79	0.81	0.03	5.20	6.29	99.58
Unit 9	829B1	Prox.Pum (bulk)	67.22	0.29	15.68	0.17	0.11	3.76	0.80	0.02	5.08	6.46	99.59
Dome	871B	Lava	64.10	0.54	16.49	0.24	0.41	4.74	1.44	0.12	4.03	7.36	99.48
Lava	828C	Lava	64.75	0.49	16.41	0.21	0.29	4.57	1.13	0.09	4.22	7.33	99.50
OBP	827C	Pumice (bulk)	65.55	0.50	15.88	0.22	0.37	4.76	1.31	0.10	4.17	6.62	99.48
Unit 1	842A	Macro Equant	67.30	0.25	15.91	0.16	0.07	3.95	0.74	0.02	5.21	6.38	100
		Micro Equant	67.26	0.25	15.92	0.16	0.08	3.95	0.75	0.02	5.2	6.39	100
		Dense	67.17	0.27	15.84	0.16	0.16	4.00	0.81	0.02	5.12	6.45	100
Unit 2	843A	Macro Equant	67.17	0.27	15.99	0.16	0.07	3.96	0.76	0.03	5.20	6.40	100
		Micro Equant	67.13	0.27	15.99	0.16	0.09	4.04	0.77	0.02	5.19	6.36	100
Unit 3	844A	Macro Equant	67.19	0.28	15.99	0.17	0.11	4.06	0.78	0.02	5.19	6.22	100
		Micro Equant	67.16	0.28	16.00	0.16	0.13	4.05	0.77	0.03	5.20	6.23	100
		Macro Elongate	67.86	0.27	15.62	0.17	0.11	4.11	0.75	0.02	5.13	5.95	100
		Micro Elongate	67.73	0.27	15.76	0.16	0.12	4.11	0.76	0.02	5.12	5.95	100
Unit 4	844C	Macro Equant	67.16	0.29	15.79	0.17	0.12	4.16	0.81	0.03	5.23	6.25	100
		Micro Equant	66.90	0.29	15.84	0.17	0.12	4.21	0.85	0.03	5.22	6.38	100
		Dense	68.12	0.28	15.31	0.16	0.12	4.05	0.80	0.02	2.04	6.09	100
Unit 9	829A	Macro Equant	67.25	0.29	15.72	0.17	0.10	4.21	0.78	0.02	5.07	6.38	100
		Micro Equant	66.48	0.29	15.98	0.17	0.10	4.13	0.80	0.03	5.17	6.85	100
		Dense	66.68	0.30	15.99	0.17	0.10	4.12	0.82	0.03	5.08	6.70	100
OBP	827C	Macro Equant	65.87	0.49	15.78	0.21	0.36	5.21	1.27	0.09	4.18	6.55	100
		Micro Equant	65.36	0.51	15.91	0.23	0.36	5.37	1.31	0.10	4.19	6.67	100
		Dense	65.42	0.50	15.95	0.22	0.39	5.27	1.34	0.10	4.14	6.66	100

Table 2.4: Whole rock trace element data for Echo Canyon samples, measured via XRF at the University of East Anglia. Reported in ppm.

Unit	Sample N°	Sample Type/ group	Zr	Sc	Ni	Zn	As	Rb	Sr	Y	Nb	Mo	Ba	La	Ce	Th
Unit 1	842A	Prox.Pum (bulk)	1099	-	-	126	-	105	-	77	129	10	113	98	158	15
Unit 2	843B	Prox.Pum (bulk)	-	-	19	125	-	101.5	-	74.5	124.5	10	164	95	152.5	14.5
Unit 3	844A	Prox.Pum (bulk)	-	-	16	124	-	99	-	72	121	10	197	9+7	151	15
Unit 4	844D	Prox.Pum (bulk)	1139	-	-	122	-	96	-	71	117	-	242	95	146	14
Unit 9	829B1	Prox.Pum (bulk)	1165	-	29	121	-	93	-	70	116	-	282	91	142	12
Dome	871B	Lava	795	-	-	109	-	65	48	60	91	-	1645	64	100	-
Lava	828C	Lava	895	11	-	119	-	68	27	59	94	-	1592	72	101	-
OBP	827C	Pumice (bulk)	817	10.7	14.5	119	-	66.3	35.3	61.7	90.7	-	1562.3	70.3	110.3	9.7
Unit 1	842A	Macro Equant	995	-	-	126	10	103	-	76	126	10	121	106	157	15
		Micro Equant	998	-	-	127	10	103	-	77	127	10	124	100	161	15
		Dense	990	-	-	127	10	104	-	77	130	10	108	110	162	15
Unit 2	843A	Macro Equant	1009	-	-	125	11	99	-	73	122	11	178	100	155	15
		Micro Equant	1014	-	-	125	11	99	-	72	121	10	172	93	155	16
Unit 3	844A	Macro Equant	1021	-	-	124	11	97	-	71	119	-	204	94	151	15
		Micro Equant	1020	-	-	123	10	98	-	72	120	10	188	97	155	15
		Macro Elongate	1024	-	-	124	10	98	-	71	120	10	196	96	152	14
		Micro Elongate	1020	-	19	124	10	98	-	72	120	-	191	95	153	13
Unit 4	844C	Macro Equant	1025	-	-	121	-	95	-	70	116	-	257	93	146	13
		Micro Equant	1019	-	20	123	-	95	-	70	117	-	246	87	148	14
		Dense	1031	-	25	123	-	96	-	72	119	-	237	94	144	13
Unit 9	829A	Macro Equant	1039	-	-	122	10	94	-	70	117	-	282	93	142	14
		Micro Equant	1030	-	-	125	10	95	-	71	118	10	261	94	150	14
		Dense	1038	-	26	122	-	93	-	70	116	-	286	91	147	13
OBP	827C	Macro Equant	768	10	15	119	-	67	34	62	92	-	1545	71	116	10
		Micro Equant	760	11	-	121	-	67	35	62	91	-	1576	69	104	10
		Dense	742	11	14	117	-	65	37	61	89	-	1566	71	111	9

Table 2.5: Trace element data for Echo Canyon samples, measured via LA-ICPMS at the University of Granada by J H Scarrow. Reported in ppm.

Unit	Sample N°	Sample Type/ group	Li	Rb	Cs	Be	Sr	Ba	Sc	V	Cr	Co	Ni	Cu	Zn
Unit 1	842A	Prox.Pum (bulk)	1099	-	-	126	-	105	-	77	129	10	113	98	158
Unit 2	843B	Prox.Pum (bulk)	-	-	19	125	-	101.5	-	74.5	124.5	10	164	95	152.5
Unit 3	844A	Prox.Pum (bulk)	-	-	16	124	-	99	-	72	121	10	197	9+7	151
Unit 4	844D	Prox.Pum (bulk)	1139	-	-	122	-	96	-	71	117	-	242	95	146
Unit 9	829B1	Prox.Pum (bulk)	1165	-	29	121	-	93	-	70	116	-	282	91	142
Dome	871B	Lava	795	-	-	109	-	65	48	60	91	-	1645	64	100
Lava	828C	Lava	895	11	-	119	-	68	27	59	94	-	1592	72	101
OBP	827C	Pumice (bulk)	817	10.7	14.5	119	-	66.3	35.3	61.7	90.7	-	1562.3	70.3	110.3
Unit	Sample N°	Sample Type/ group	Ga	Y	Nb	Ta	Hf	Mo	Sn	Tl	Pb	U	Th	La	Ce
Unit 1	842A	Prox.Pum (bulk)	15	52.53	127.84	8.77	21.42	10.52	6.37	0.16	5.92	2.57	7.07	47.99	102.61
Unit 2	843B	Prox.Pum (bulk)	14.5	-	-	-	-	-	-	-	-	-	-	-	-
Unit 3	844A	Prox.Pum (bulk)	15	-	-	-	-	-	-	-	-	-	-	-	-
Unit 4	844D	Prox.Pum (bulk)	14	67.57	119.46	8	20.95	9.82	5.56	0.15	6.33	3.43	9.57	63.09	143.27
Unit 9	829B1	Prox.Pum (bulk)	12	73.33	119.46	8.03	21.17	9.69	5.63	0.14	6.59	3.52	1.11	69.64	146.96
Dome	871B	Lava	-	50.60	91.09	6.53	14.73	1.36	1.25	0.07	7.36	1.56	5.23	43.47	107.27
Lava	828C	Lava	-	44.19	95.44	6.80	15.91	1.70	1.97	-	2.43	1.87	6.93	40.31	101.18
OBP	827C	Pumice (bulk)	9.7	49.28	88.19	5.84	14.55	7.00	3.69	0.12	4.11	1.5	5.28	38.55	82.28
Unit	Sample N°	Sample Type/ group	Pr	Nd	Sm	Eu	Gd	Tb	Dy	Ho	Er	Tm	Yb	Lu	
Unit 1	842A	Prox.Pum (bulk)	11.69	44.52	9.52	0.94	8.14	1.42	9.46	2.01	5.76	0.83	6.23	1.14	
Unit 2	843B	Prox.Pum (bulk)	-	-	-	-	-	-	-	-	-	-	-	-	
Unit 3	844A	Prox.Pum (bulk)	-	-	-	-	-	-	-	-	-	-	-	-	
Unit 4	844D	Prox.Pum (bulk)	14.72	56.05	11.82	1.48	10.04	1.73	11.83	2.50	7.27	1.17	7.88	1.53	
Unit 9	829B1	Prox.Pum (bulk)	16.14	60.93	12.83	1.68	10.80	1.84	12.64	2.71	7.78	1.25	8.51	1.66	
Dome	871B	Lava	10.97	43.61	9.75	3.12	8.23	1.42	9.32	1.92	5.27	0.80	5.60	0.97	
Lava	828C	Lava	10.45	41.61	9.24	2.92	7.82	1.35	8.85	1.85	5.12	0.69	5.45	0.98	
OBP	827C	Pumice (bulk)	10.14	40.86	9.29	2.97	7.98	1.37	9.00	1.88	5.19	0.70	5.51	0.99	

Unit/ Erupted composition	Peralkalinity Index (PI)	Temperature (°C)*	H ₂ O (wt%)	Viscosity (Pa s)**
EC Unit 1 (PF)	1.01	900	1 – 4	10 ^{5.5} – 10 ^{3.6}
EC Unit 9 (PDC)	1.04	900	1 – 4	10 ^{5.4} – 10 ^{3.6}
EC Dome	1	900	1 – 4	10 ^{5.1} – 10 ^{3.3}
EC Lava	1.01	900	1 – 4	10 ^{5.1} – 10 ^{3.4}
Basalt ¹	0.38	1000	1 – 4	10 ^{2.5} – 10 ^{1.8}
Unzen Dacite ²	0.57	800	1 – 4	10 ^{6.9} – 10 ^{4.8}
Rhyolite ³	0.78	800	1 – 4	10 ^{7.7} – 10 ^{5.3}
Aluto Per.Rhy ⁴	1.63	750	1 - 4	10 ^{4.9} - ~10 ^{2.5}

PF = Pumice fall unit, PDC = pyroclastic density current deposits, Per.Rhy = peralkaline rhyolite.¹Basalt composition from Le Maitre (1975). ²Unzen Dacite composition from Giordano *et al.*, (2005). ³Rhyolite composition from Le Maitre (1975) oxide data in supplementary data. ⁴From Clarke (2020). *Temperatures quoted are approximate eruptive temperatures from Giordano *et al.*, (2004)
 **Viscosities calculated using Giordano *et al.*, (2008) apart from peralkaline rhyolite, Clarke (2020) used the model of Di Genova *et al.*, (2013) for peralkaline rhyolites.

2.7 Petrography:

The juvenile components of the EC eruption contain 3–8 mm alkali feldspar and pyroxene crystal intergrowths: individual crystals are 2–4 mm and, in places, fragmented (Figs. 2.18a and d). Within pumice clasts, crystals ≥ 2 mm comprise < 1 modal %, in lavas up to 5 modal %: intact intergrowths and > 3 mm crystals are most abundant in lavas and obsidian. Euhedral – subhedral alkali-feldspar crystals of 1–2 mm are present, alongside 150–700 μm fragmented and whole alkali-feldspar, quartz, orthopyroxene, clinopyroxene and olivine (Fig. 2.18a – e): these crystals constitute <2% of all juvenile material. Alkali-feldspar microlites of < 10–200 μm generally have abundances of 1-2% in pumice clasts, 70% in the dome and 30% in the lava flow. Some OBP clasts however, contain clearly defined regions of up to 30% alkali-feldspar microlites (Fig. 2.18f). Microlites are distorted by large vesicles in pumice clasts and can be aligned parallel to banding in lavas. Disequilibrium textures are rare (Fig. 2.18 a – e, g – i) but some pumice clasts contain fragments of crystal rich material containing crystal remnants.

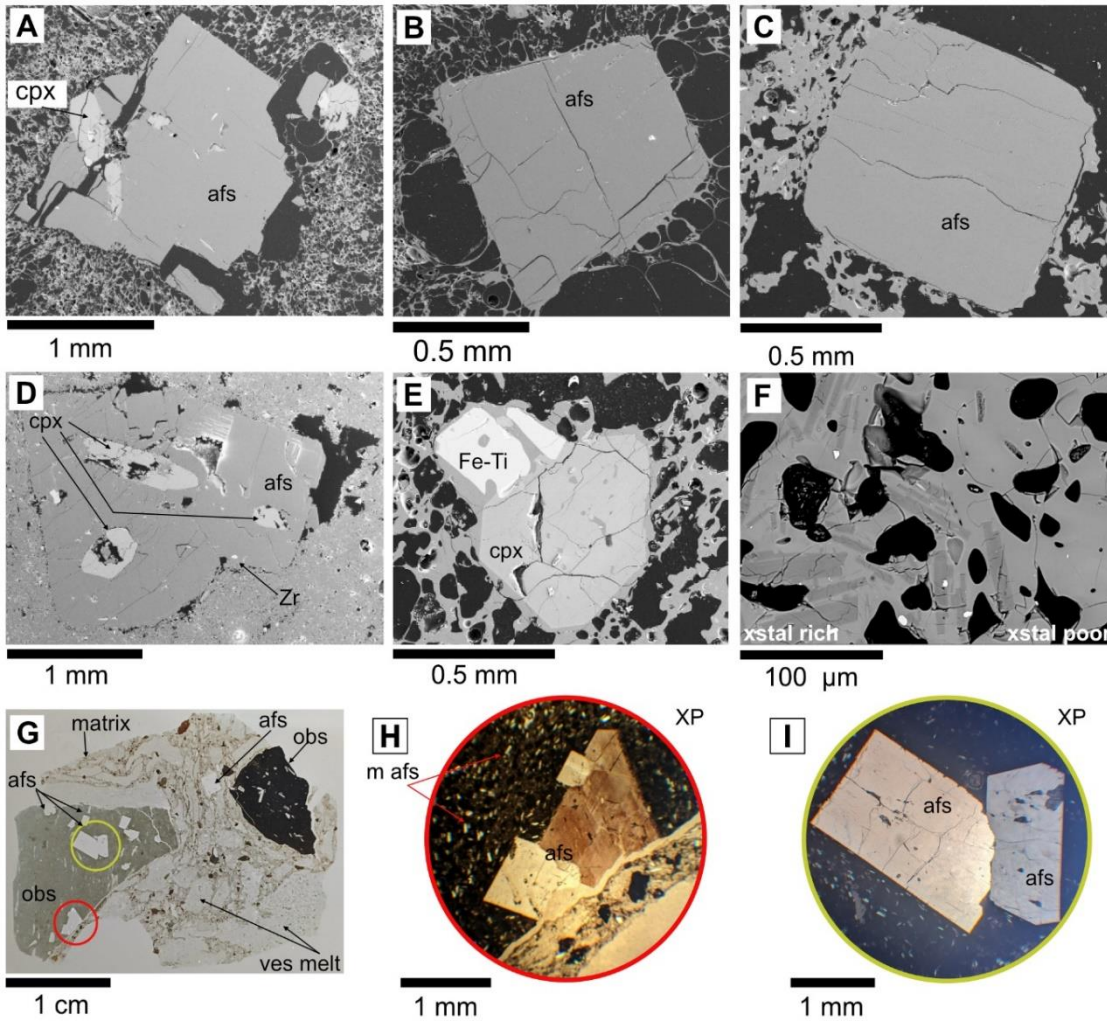


Fig. 2.18 Characteristic crystal population of Echo Canyon (EC) products. **A & D**: 3 mm alkali-feldspar (afs) crystal clots with clinopyroxene (cpx) and zircon (Zr) inclusions. **A**: from pumice sample with sharp edges, **D** within lava – more rounded edges, groundmass is highly microcrystalline. **B & C**: smaller euhedral afs population ~500 μm (**B** from Unit 3 pumice), **C** with rounded edges (from orange-brown pumice (OBP)) **A-E**: Secondary electron images collected on a Zeiss Gemini 300 SEM at the University of East Anglia, UK. **F**: Regions of high and low afs microlite abundance within clast from the OBP. Backscattered electron image collected on a FEI quanta 650 FEG SEM at the Natural History Museum, London, UK. **G**: thin section of obsidian breccia (obs) with clasts of obsidian, ashy matrix and fragments of pumice (ves melt). EC afs present in clasts and matrix. **H & I**: Images of EC 3 mm afs crystals within obsidian in cross-polarised light (XP).

2.8 Discussion:

Stratigraphy, juvenile clast textures and bulk vesicularity distributions (BVDs) are discussed below and used to interpret eruption dynamics, place constraints on explosivity and understand the influence of magma composition on the progression of the EC eruption.

2.8.1 Stratigraphy and Eruptive Style

Deposit characteristics of the EC stratigraphy reveal multiple transitions in eruptive style. Initial explosive activity generated persistent pumice fall (Unit 1) followed by intermittent dominance of ash production (Unit 2) which was followed by a longer period of pumice fall out during the peak of the eruption (Units 3 and 4). In the middle cone, pumice fall out gave way to hybrid activity (intermittent fountaining) producing a mixture of pumice fall and pyroclastic density current deposits (Units 6 – 10). In the upper cone, collapse and PDC formation became the dominant eruptive process (Unit 11 and distal deposits). An effusive phase followed (lava and dome), before a final, short-lived explosive phase which generated further pumice fall out (OBP). The deposits are linked to a single eruptive period through the absence of erosional surfaces between explosive and effusive phases, deposit geometry and the presence of a distinct phenocryst population not seen in other Ascension Island deposits (Fig. 2.18). The slightly less evolved compositions of the post-cone units may reflect slight compositional zonation of the magma storage region resulting in initial eruption of lower density, more evolved compositions as is often seen for trachytic melts (e.g. Chamberlain *et al.*, 2016; Jeffery *et al.*, 2018).

Cone deposit similarities in estimated modal lithic and pumice clast size, within each Unit and abundance of pumice and lithic clasts > 64 mm, indicates they are proximal (cf., Cas and Wright 1996). Deposits thin rapidly, lack matrix and have modal bulk vesicularity >70%. Characteristics of Units 1 and 2 indicate proximal pumice fall out, similar to strombolian pumice cones described by Houghton and Wilson (1985) on Mayor Island, New Zealand (table 2.1). The thickness, lack of stratification and low lithic clast abundances in Units 3 and 4 reflect progression to an established column with little input of conduit material (c.f. Cioni *et al.*, 2008; Cioni, *et al.*, 2015). Conversely, the sequence of pumice vs matrix supported units, lenses of pumice clasts, and variability in modal pumice clast sizes in units 6 – 10 suggest a transition to hybrid fall out and PDC activity in the middle cone (Dowey and Williams 2022). This may suggest waning eruption intensity and increased column instability, as is often associated with pulsatory sub-plinian activity (Cioni *et al.*, 2015; Andrews *et al.*, 2018) or partial fountaining as suggested as a mechanism for hybrid activity by Dowey and Williams (2022). In the upper cone, the dominance of metres thick, stratified ash rich beds containing lenses of pumice clasts records a significant phase of partial/total column collapse or sustained fountaining which generated PDCs (cf., Scott *et al.*, 1996; Cole

et al., 1999; Houghton *et al.*, 2004; Cioni *et al.*, 2008; Andrews *et al.*, 2018; Dowe and Williams, 2022).

The brecciated nature of both the dome and (to a greater extent) the lava and the close association of these units with the metre-scale pumice spatter in the proposed vent-proximal locations suggests the “effusive” products may have been fed by low-explosivity fountaining making them clastogenic in origin, as has also been seen in pumice cone associated lavas on Pantelleria (e.g., Stevenson and Wilson, 1997 and Gottsman and Dingwell, 2002). The crystallinities of the dome and lava, 30–70% and vesicularities < 5%, indicate significant degassing prior to effusion (cf., Deniel *et al.*, 2020) which could explain the reduced explosivity of this phase. The OBP represents the final, volumetrically subordinate, explosive phase of the EC eruption. Angular pumice clasts contain discrete microlite rich regions which may represent incorporation of accumulated degassed melt from the conduit margins (cf., Mitchell *et al.*, 2019). Evidence for persistence of conduit accumulations of densified melt is provided by the abundance of obsidian bombs in the upper cone and OBP. A late-stage explosive magmatic eruption may be linked to shallow pressurisation from the closure of degassing pathways beneath the flow and dome (e.g., Deniel *et al.*, 2020), continued deep evolution of the final eruptible melt leading to increased overpressures (e.g., Chamberlain *et al.*, 2016), or a combination of the two.

2.8.2 Evolution and Variability of Vesicle Textures

For lapilli with little to no post-fragmentation textural alteration, crystallinity, bulk vesicularity, and vesicle shape and size are all controlled by conditions in the magma prior to and during ascent (Cashman and Mangan 1994). Viscosity, volatile content and ascent rate of the melt all influence vesicle and crystal nucleation and growth (Cashman and Mangan 1994). The textural fingerprint of a lapilli population is thus the outcome of spatial and temporal variations in these parameters. Hence, even qualitative comparison of these features can identify key step-changes in ascent dynamics that lead to transitions in eruptive style.

By considering how vesicle textures develop prior to fragmentation, the relative influence of bubble growth, coalescence and shear on the melt for each stage of an eruption can be discerned. This principle is used to interpret characteristic vesicle textures of type 1–5 lapilli clasts and their relative abundance throughout the eruption to understand changes in eruptive style. Figure 2.19 shows how polydisperse vesicle textures evolve under sheared

and non-sheared conditions and the dominant processes acting at each stage, as recorded in type 1–5 lapilli clasts. Immature vesicle populations forming in the absence of shear are recorded by type 1 clasts: maturation of vesicle textures through continued growth promotes bubble interference and coalescence (Sparks 1978; Klug and Cashman 1996) – type 2 clasts. However, ascending melt is subject to transverse velocity gradients: drag at conduit margins reduces ascent velocity relative to the centre of the flow, creating zones of intense shear associated with rapidly changing velocity (Polacci *et al.*, 2003; Shea *et al.*, 2012; Cassidy *et al.*, 2018). If an immature vesicle population is sheared, small elongate vesicles will result (type 3). If a mature population is sheared, coarse elongate vesicles result (e.g. type 4) and shear induced coalescence hastens development of permeable networks. When a permeability threshold is reached, outgassing occurs: if gas flux is insufficient bubble collapse ensues (Shea *et al.*, 2012). Resultant textures are heterogeneous: clasts have irregular vesicles, thick glass walls and lower bulk vesicularities (type 5, Fig. 2.19) (Polacci *et al.*, 2003; Shea *et al.*, 2012). Shea *et al.*, (2012) showed that shear induced vesicle collapse can increase the density of the eruption column sufficiently to induce column collapse and PDC formation.

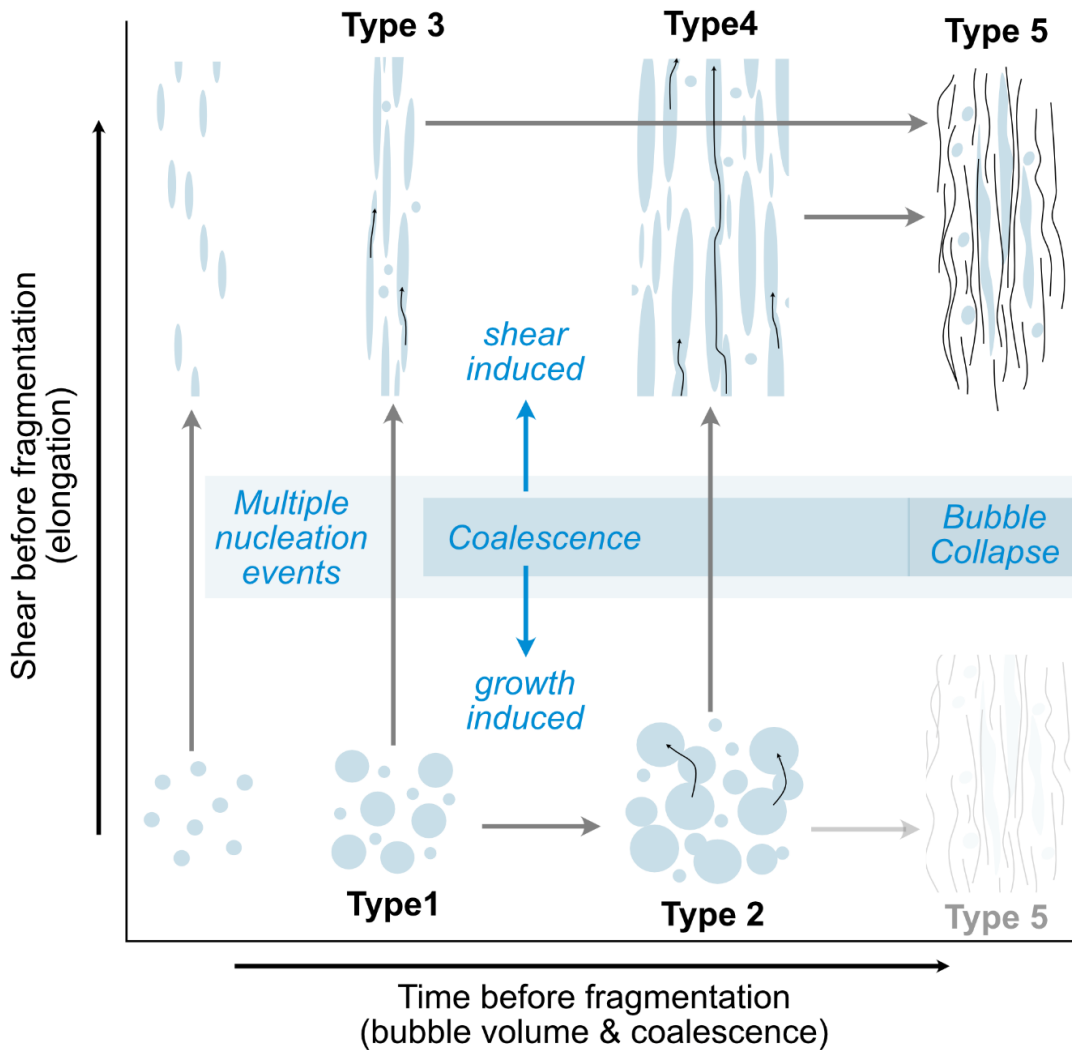


Fig. 2.19 Diagram showing bubble nucleation, growth and coalescence processes in the absence and presence of shear to form the five textural types observed in the Echo Canyon (EC) lapilli population. Types 1 and 2 record multiple nucleation events and progressive vesicle growth without shear. Types 3 and 4 show how shear impacts vesicle shape and coalescence. Type 5 occurs after coalescence leading to outgassing through permeable networks and bubble collapse. Black arrows show movement of volatiles through permeable networks. Shaded rectangles show initiation of main processes during textural evolution. Greyed-out type 5 represents this process in the absence of shear – a lesser contributor to EC clast textures.

Whether a juvenile clast population has immature or mature vesicle textures depends on when fragmentation occurs relative to growth, coalescence and relaxation (τ) timescales (Moitra *et al.*, 2013). As such, when magma properties of the rising melt column vary laterally, interaction with the fragmentation surface/threshold produces texturally heterogeneous pumice populations (Polacci *et al.*, 2003). In the EC pumices, fragmentation captures vesicle populations; i) before extensive bubble growth (type 1, and 3 if sheared); ii) after coalescence is initiated but within τ (type 2); iii) after shearing and some coalescence, but before outgassing and vesicle collapse (types 3 and 4); and iv) after outgassing and vesicle collapse (type 5). Changing proportions of sheared and dense clasts

may then, be associated with development of low velocity shear zones, and the extent to which outgassing could progress before fragmentation. Conduit modification and changes in fragmentation depth and magma flux may have influenced the proportion of melt and maturity of vesicle populations within shear zones and hence the density profile at the point of fragmentation (cf., Klug and Cashman 1996; Shea *et al.*, 2012; Cassidy *et al.*, 2018).

The influx of sheared clasts in Unit 3 (Fig. 2.9) is interpreted to reflect a widening of marginal shear zones within the conduit. The lack of dense clasts indicates outgassing and vesicle collapse was not extensive prior to fragmentation. In contrast, dense clasts make up 25% of Unit 4, reflecting onset of bubble collapse and densification of the eruption column. Further densification of the column occurred during eruption of Unit 9 (middle cone) with an even higher proportion of dense and sheared clasts marking a tipping point, beyond which column collapse and PDC formation dominated. Obsidian clasts in PDC deposits may reflect continued densification of melt in marginal shear zones - the source region for type 5 clasts - explaining the low abundance of type 5 clasts in Unit 11 (cf., Shea *et al.*, 2017).

[2.8.3 Bulk Vesicularity, Fragmentation and Explosivity](#)

When reconstructing explosive volcanic eruptions, it is important to characterise the explosivity/intensity/magnitude of individual phases, as this informs our understanding of the associated hazards, transitioning eruption styles and timescales for change. The volcanic explosivity index (VEI) as defined by Newhall and Self (1982) has been widely used to semi-quantitatively categorise and compare eruptions based on relationships between magnitude, intensity and rate of energy release. Continuous scales of magnitude and intensity relate closely to VEI, and better describe observed extremes in eruptive style (Pyle 2015). However, each of these classification systems require accurate calculation of eruption mass, mass eruption rate or plume height (Pyle 2015), which is often precluded in small-volume eruptions by poor preservation, or minimal exposure. Houghton *et al.*, (2013) extended the VEI to better capture explosivity of small-volume basaltic eruptions on Hawaii but this also requires accurate determination of eruption volumes. Standard scales of magnitude and intensity also fail to correctly capture the explosive potential, transient nature and associated hazards of individual phases of an eruption, or the timescales over which they may occur. Despite the coarseness of the VEI, its widespread use in volcanology and the media make it valuable when identifying and communicating potential hazards

from future eruptions as they are often quoted in hazard assessments (e.g. Mastrolorenzo *et al.*, 2017, Campi Flegrei and Sieron *et al.*, 2019, Ceboruco volcano), and so careful comparisons - with caveats – can be worthwhile. In order to make interpretations of changing bulk processes in the ascending magma and link these to changing eruptive style for unobserved and poorly preserved eruptions Mueller *et al.*, (2011) compared clast bulk vesicularities of several eruptions with well constrained eruption styles, dynamics and intensities. By doing so, they showed how such studies allow reconstruction of fragmentation mechanisms and eruption style. This is a useful approach, as the physical processes controlling a vesicle population also influence the explosivity and nature of fragmentation which are preserved in easily sampled juvenile clasts. By comparing vesicularity data of individual phases from the EC eruption to eruption data collated by Mueller *et al.*, (2011), we identify step-changes in fragmentation mechanism and explosivity that would otherwise be masked, or inappropriately categorised using bulk properties of the deposits. Mueller *et al.*, (2011) preferentially sampled clasts from phases that represented the peak intensity for the VEI assigned to the eruption e.g., only the Plinian fallout phases of the Novarupta 1912 eruption. This means that direct comparisons can be made between these eruptions and the EC Units as both datasets represent specific eruption phases rather than an integral of bulk deposit vesicularity for the eruption as a whole. For simplicity and consistency with their study, in the following sections we describe phases of the EC eruption in terms of the classifications given to the eruptions to which their distributions most closely match as used by Mueller *et al.*, (2011) (e.g., Strombolian – Vulcanian – Sub-plinian – Plinian etc). However, the implication is not that each phase of the EC eruption is the direct equivalent to the compared eruption style (for example it is not implied that a “Plinian-comparable” phase produces the volumes seen in Plinian eruptions), but that the intensity of the explosive processes (fragmentation etc.) during a singular point in the eruption and some of the potential associated hazards are comparable. In section 2.8.6, I will discuss the implications of these findings in the context of processes occurring during these small-volume, trachytic eruptions.

Figure 2.20 is adapted from Mueller *et al.*, (2011) and shows the BVDs (lines) and variance (bracketed numbers) of each EC pyroclastic Unit alongside BVDs for several other eruptions. Shaded fields on Fig. 2.20 are the BVDs of several explosive eruptions of well constrained eruption style and intensity. Explosive felsic eruptions represent sub-Plinian to ultra-Plinian peak activity. Mafic eruptions represent Hawaiian – Strombolian activity.

Variance of BVDs can be used to infer fragmentation mechanism. Low variance BVDs reflect fragmentation by bubble interference and rupture (Sparks 1978). In contrast, high variance reflects transient fragmentation controlled by decompression processes where bubble overpressure exceeds the strength of the melt (Fowler *et al.*, 2010).

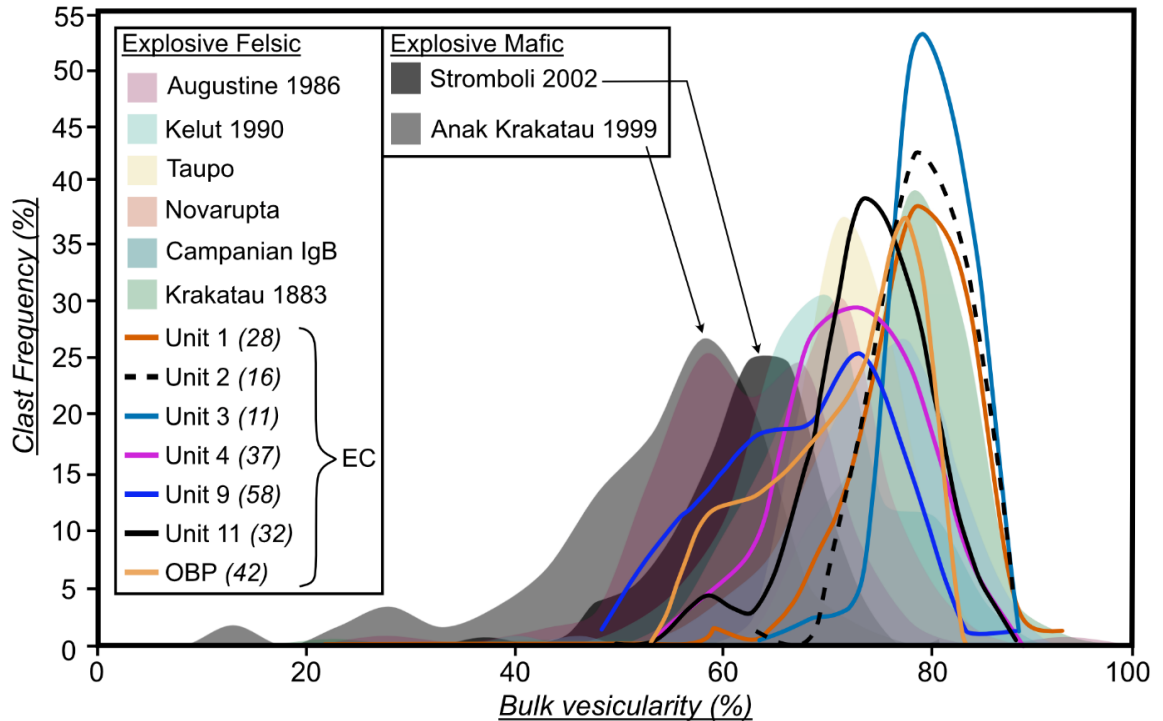


Fig. 2.20 comparison of Echo Canyon (EC) vesicularity distributions with eight eruptions of well-constrained eruption style and intensity. Non-EC bulk vesicularity curves (shaded regions) are adapted from Mueller *et al.*, (2011) Fig. 2. Bulk vesicularity distributions of EC Units are plotted as solid and dashed lines. Variance of clast vesicularity for each EC Unit is displayed in brackets.

For the EC eruption, variance decreases between Units 1 and 3, then increases by a factor of 3 in Unit 4 and peaks in Unit 9. Variance in the PDC deposits and overlying OBP are lower than that of Unit 9 but remain high. We suggest therefore, that the dominant fragmentation mechanism shifted during the eruption. Fragmentation controlled by bubble-interference became increasingly important as early activity progressed. From Unit 4 onwards, transient fragmentation controlled by decompression processes became increasingly dominant. This coincides with the onset of vesicle collapse, PDC formation and ultimately the explosive-effusive transition. Bulk vesicularity distributions of pumice fall Units 1–3 progressively narrow, closely matching the dacitic – rhyodacitic, Plinian eruption of Krakatau in 1883. Units 4, 9 and 11, have broader distributions and lower modal bulk vesicularities than Units 1–3 but neither their shape nor modal vesicularities match closely with those of the mafic explosive eruptions. Bulk vesicularity distributions are shifted to higher vesicularities in systems with poly-disperse and deformed vesicles that have not yet

undergone collapse (Mueller *et al.*, 2011). The position of the porosity distribution thus relates to magmatic volatile content and degree of outgassing at the point of fragmentation (Mueller *et al.*, 2011): BVDs of Units 1–3 suggest higher magmatic volatile content for early phases. Later stages e.g., Units 4 and 9 were more outgassed, displaying lower bulk vesicularities and supporting our interpretation of clast densification through progressive development of connectivity and outgassing.

The trachytic Campanian ignimbrite is classified as Plinian, as is Krakatau 1883, showing that low viscosity trachytic melts are capable of highly intense explosive activity comparable to that which would produce a stable plume given sufficient magma supply (volumes and rates), as is seen in larger volume eruptions. As the BVDs for Unit 3 and the Krakatau 1883 eruption are similar, we infer that Unit 3 may record a comparable *transient* peak explosion intensity during the EC eruption. The low lithic content, thickness, and massive, clast-supported nature of this Unit supports the interpretation of a column that was effectively stable (lacking fountaining) for at least the duration of the deposition of that unit. Units 1 and 2 have very similar BVDs to Unit 3 but contain more lithic clasts, include the dense transitional pumice-lava clasts and are interbedded with ash beds, indicating greater input of conduit material (possibly associated with vent clearing) than in Unit 3 and periods of cyclic plug formation and rupture via discrete blasts. Unit 4 is unusual as it has very similar deposit characteristics to Unit 3 but the BVD (Fig. 2.20) and juvenile clast population for Unit 4 (Fig. 2.9) indicate significant changes to fragmentation mechanism, vesicle connectivity and outgassing. The mismatch between deposit characteristics, BVD and the lapilli population indicates some lag between the onset of densification processes and changing eruption style. Oscillation of the column / partial fountaining becomes more prevalent (with explosion intensities equivalent to sub-Plinian eruptions cited in Mueller *et al.*, (2011)) until the Units 6 - 10 of the middle cone (analysed unit – 9). Column collapse / dominance of persistent fountaining does not occur until the upper cone (analysed unit - 11). For Unit 9, the BVD (Fig. 2.20), lapilli population (Fig. 2.9) and lithologic characteristics (Figs. 2.6, 2.11b and 2.9) are all consistent with a transition to a destabilising plume (or hybrid fall-flow activity as described in 2.8.1 and c.f. Dowe and Williams 2022) ultimately transitioning to the dominance of PDC formation producing Unit 11.

Bulk vesicularity distributions, when combined with careful interpretation of deposit characteristics can provide insights into the bulk behaviour of ascending magmas, changing

conduit dynamics, and resulting eruptive style (Mueller *et al.*, 2011). This is vital for reconstruction of unobserved eruptions. However, there are limitations to this approach. While important interpretations of volcanological processes and the associated hazards can be made, quantification of degassing, water exsolution and discharge rates, and hence column heights require further analyses. Quantification of textures using vesicle and crystal size distributions (VSD and CSD) and microlite number densities allow modelling of these parameters (e.g., Toramaru *et al.*, 2006 and Toramaru *et al.*, 2008). However, such textural analyses, particularly VSDs require careful assessment of coalescence, bubble relaxation and elongation prior to analysis (e.g., Mitchell *et al.*, 2019; Houghton *et al.*, 2010; Shea *et al.*, 2010). In addition, intensive parameters e.g., initial and eruptive melt volatile concentrations and temperatures must be first established to produce reliable model results (Toramaru *et al.*, 2006). While quantification of textures in this manner are beyond the scope of this chapter (see Chapter 3), interrogation of the deposit characteristics, pervasive clast textures and BVDs provide a volcanological framework onto which quantitative modelling of eruption dynamics using micro-scale textures can later be applied.

The geometry, extent and proximal nature of the preserved EC fall and PDC deposits, lava and dome, suggest an eruptive volume of approximately 0.01–0.3 km³ comparable to Mayor Island and Aluto (Table 2.1). In isolation, the volume would yield an approximate VEI of 2 for this eruption, suggesting low intensity, fountaining eruptive styles. The deposit componentry, clast textures and BVDs however, reveal explosions occurring as part of this “fountaining” can have peak intensities reminiscent of those recorded in the vesicularity distributions of Plinian and sub-Plinian eruptions. While a VEI 6 classification is precluded by the small eruptive volumes, it’s clear that explosion intensities, equivalent to those observed during *individual* phases of VEI 6 eruptions can be achieved, if only transiently (aka without development of a persistent, stable plume > 10-25 km in height), in the course of events like the Echo Canyon eruption. Pyle (2015) plotted the relationship between eruption magnitudes calculated using erupted masses of well constrained eruptions, to eruption intensities calculated using mass eruption rates. Considering a VEI 6 eruption has a magnitude of around 6 (Pyle, 2015), the intensities of the EC eruption phases can be estimated. Eruptions with a magnitude of 6 relate to eruption intensities of approximately 12, products of high mass eruption rates (around 10⁹ kg m/s) – comparable to units 3 and 4 representative of the peak of the EC eruption. Sub-plinian activity or VEI’s of 5 relate to

intensities of around 10-11, associated with a lower mass eruption rate of around 10^{7-8} kg/s (Pyle, 2015) – comparable to phases in the middle – upper cone.

Rapid evolution of vesicle textures during ascent and promotion of outgassing combined with almost complete degassing of the melt increased the dominance of transient, and then persistent fountaining /column collapse. The highly degassed magma promoted a transition to low-intensity, fountaining-fed effusive activity, which produced the clastogenic texture of the highly brecciated lava and dome. Similar complex eruption dynamics are preserved in other alkaline pumice cones e.g. Pu'u Wa'awa'a, Hawaii (Shea *et al.*, 2017), Aluto (Clarke 2020) and Mayor Island (Houghton *et al.*, 1985; Houghton *et al.*, 1992) indicating rapid transitions in eruptive style and intensity are common for eruptions of this composition and volume. The role of obsidian and tuffisite formation in accelerating these transitions is discussed in the following section.

2.8.4 Obsidian Breccia, Tuffisite Formation and Degassing Pathways

Fragments of homogenous, banded and brecciated obsidian are first observed in PDC deposits, Unit 11, of the upper cone stratigraphy, coincidental with destabilisation of the plume and transition to lower eruption intensity. Eruption of obsidian may evidence processes underpinning transitioning eruptive style. Obsidian pyroclasts can form via densification of melt during bubble collapse due to permeable outgassing (Shea *et al.*, 2017), or through sintering and relaxation of ash particles (Gardner *et al.*, 2017): both can occur at varying depths within the conduit. Crystallinity of the EC obsidian is varied, some clasts contain <<1% microlites, while others have >40%. Cracks and small rounded – elongate vesicles in crystal-poor obsidian may suggest formation by sintering (Gardner *et al.*, 2017). However, irregular vesicles aligned parallel to microlites visible in thin sections of crystal-rich obsidian, and vesicular banding seen in hand specimen, indicate formation by vesicle collapse (Shea *et al.*, 2017). Similarities in macro-scale textures between the EC clasts and the Shea *et al.*, (2017) obsidian lead me to favour vesicle collapse as the dominant formation process, further evidence of extensive degassing prior to effusive activity.

Observations made during the eruptions of Chaitén (2008-2009) and Cordón Caulle in Chile (2011-2012) and subsequent work on tuffisites (Alfano *et al.*, 2012; Castro *et al.*, 2014; Pistolesi *et al.*, 2015; Heap *et al.*, 2019) have highlighted the complexity of degassing processes during eruptions of silica-rich melt. Brecciated obsidian tuffisites have been

shown to record processes of magmatic auto-brecciation and explosive degassing via the influx of hot gas, ash and rock mixtures at the conduit margins (Rust *et al.*, 2004; Saubin *et al.*, 2016; Heap *et al.*, 2019). The obsidian breccia clasts exhibit classic tuffisite characteristics (as described in Tuffen *et al.*, 2002 and Saubin *et al.*, 2016) but no clasts observed in this study capture a complete section across a vein (e.g., from wall to wall with the infilled pathway between). They do however, often also contain abundant obsidian and may also have obsidian attached to the exterior of their fractured surface, indicating fractured tuffisite veins (clasts) came into contact with bubble- and microlite-free melt in the conduit.

The occurrence of tuffisite fragments in the PDC deposits suggests accumulation of outgassed melt on the conduit walls and brittle development of permeable pathways prior to the explosive-effusive transition. Castro *et al.*, (2014) showed that tuffisites extending 10's–100's of metres into the conduit can act as a transient degassing system shifting activity from explosive to effusive. Strongly bimodal porosity/bulk vesicularity distributions are inferred to represent sampling of material with multiple degassing histories, for example, dome growth or plug formation (Mueller *et al.*, 2011). Units 9 and 15 have BVDs that very weakly tend towards bimodality which indicates material with a different degassing history may have been sampled. This second degassing history does not however, exert as strong a control on the shape of the BVD as one might expect for a period of dome/plug formation. Tuffisites however, are a record of transient, explosive degassing within the volcanic system (Castro *et al.*, 2014). A secondary degassing pathway which is transient, may exert a weaker control on the BVD, resulting in the weakly bi-modal BVDs of Units 9 and 15 of the EC eruption. If tuffisites intersected with deeper magmatic foams, they may have also contributed to densification of ascending melt prior to effusive activity (Saubin *et al.*, 2016). Obsidian and tuffisite formation, therefore, may have had an important role in facilitating rapid transitions from explosive to effusive activity during the EC eruption.

2.8.5 Melt Composition, Viscosity, and Eruption Dynamics

There is now a wealth of evidence that trachytic eruptions can exhibit a similar range in eruptive style as larger calc-alkaline eruptions (table 2.1). However, the question of how the physical properties of trachytic melts influence eruption dynamics, particularly in the case of small-volume events, remains. Bubble growth, coalescence, melt relaxation and

collapse have a key influence on eruption dynamics and are all strongly controlled by the viscosity and volatile content of the melt (Cashman and Mangan 1994). Calculation of water contents for individual EC eruption units is beyond the scope of this Chapter and will be calculated via water contents for the EC eruption deposits will be calculated via feldspar-melt hygrometry in Chapter 3. Instead, here a reasonable estimate of 1–4 wt % water (e.g. those seen for other eruption on Ascension cf., Kar *et al.*, 1998; Chamberlain *et al.*, 2016, 2019, 2020)) is used to give a range of likely melt viscosities. This range yields an estimated viscosity of 105.5–103.5 Pas for the EC eruption products, two orders of magnitude lower than a calc-alkaline rhyolite with the same water content at a reasonable eruptive temperature (table 2.6). For the EC trachytes, low viscosity and high H₂O diffusivity mean high bubble overpressures are unlikely to be maintained (Shea *et al.*, 2017). Under such conditions, brittle fragmentation and high intensity explosive activity is more difficult to achieve with reasonable ascent rates and conduit geometries (Hughes *et al.*, 2017). Nevertheless, localisation of strain within the melt column changes melt-rheology at multiple length and timescales during ascent and can facilitate brittle fragmentation in peralkaline melts (Hughes *et al.*, 2017). Inter and intra-clast textural heterogeneity suggests strain localisation was prevalent in the melt column during the EC eruption. Furthermore, Hughes *et al.*, (2017) suggested that high initial magmatic H₂O concentrations and low viscosity may promote rapid decompression within peralkaline melts. With an estimated 1–4 wt% initial H₂O content in the EC melt, the tendency of trachytes to vesiculate rapidly during decompression (Shea *et al.*, 2017) and evidence of strain localisation may explain the high intensity of early explosive phases. In addition, the water content at the point of fragmentation may be lower than the peak pre-eruptive value, increasing the viscosity and further easing fragmentation to some degree. Low viscosities also reduce timescales of melt re-organisation, allowing vesicle networks to respond rapidly to shear strain and outgassing, pushing eruptions towards effusive activity - which may explain why these high intensity explosive phases seem to be so short-lived. Although beyond the scope of this chapter, quantification of pre-eruptive and late-stage H₂O concentrations would provide further constraints on the evolution of trachytic melt viscosity during the eruption and will be the focus of future work.

Degassing-induced crystallisation is another contributing factor in the transition from explosive to effusive activity, as increasing viscosity induces shear stress in the conduit promoting construction of spines and lobes (Deniel *et al.*, 2020). In calc-alkaline dome-

forming eruptions, groundmass crystallinities rarely exceed 50% locally and PDCs are regularly triggered by Vulcanican blasts due to gas overpressure in the dome (Deniel *et al.*, 2020). In contrast, the trachytic Puy de Dôme in France is glass-poor and only a few syn-dome explosions are recorded (Deniel *et al.*, 2020). The Puy de Dôme eruption closed with an explosive magmatic phase with a volume subordinate to the main edifice - similar to the final, OBP, phase of the EC eruption (Deniel *et al.*, 2020). Deniel *et al.*, (2020) argued that high crystallinities reflect efficient and near-complete degassing of the magma prior to and during dome construction. The intrinsic properties of trachyte melts, and high dome permeability due to extensive fracturing facilitating this process (Deniel *et al.*, 2020). For the effusive products of the EC eruption, high crystallinities may also record extensive degassing. As argued by Deniel *et al.*, (2020) the physical properties of trachytic melts help to facilitate this process. In this instance however, the additional high permeability may have been achieved via the presence of transient open fracture networks, evidence for which is the tuffsite fragments, transiently increasing conduit permeability at the explosive-effusive transition (e.g., Castro *et al.*, 2014). The explosive post-dome eruption of the OBP mirrors that of the Puy de Dome eruption: so, significantly, dome formation does not preclude further explosive magmatic activity during short-lived, small-volume eruptions.

The physical behaviour of trachytic melts during ascent can produce high intensity explosive phases and swift explosive-effusive transitions. High intensity phases are short-lived as bubble overpressures are not maintained, rapidly evolving vesicle textures promote outgassing and extensive degassing induced crystallisation occurs. The “*kinetic reactivity*” (Shea *et al.*, 2017) of trachytic melts explains the varied eruption dynamics of these small-volume eruptions, as recorded in their diverse juvenile clast populations.

2.8.6 Eruption Sequence and Dynamics Summary

Interpretations of stratigraphic observations, juvenile clast populations and textures, and BVDs are integrated, and evolution of EC eruption dynamics reconstructed and summarised below and in Fig. 2.21. Where possible, we draw comparisons between the EC eruption and other small-volume trachytic eruptions from table 2.1 to show how the EC eruption enhances our understanding of these events worldwide.

Strombolian Fountaining and discrete blasts

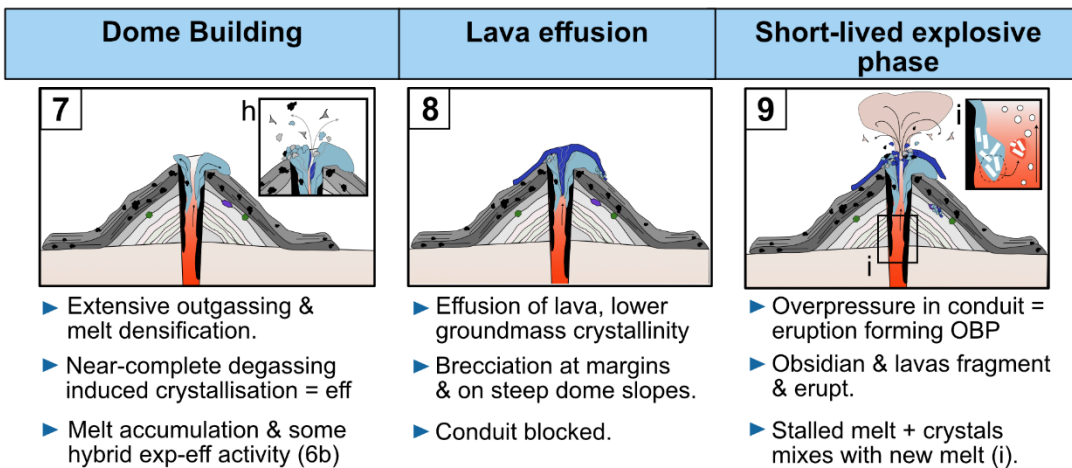
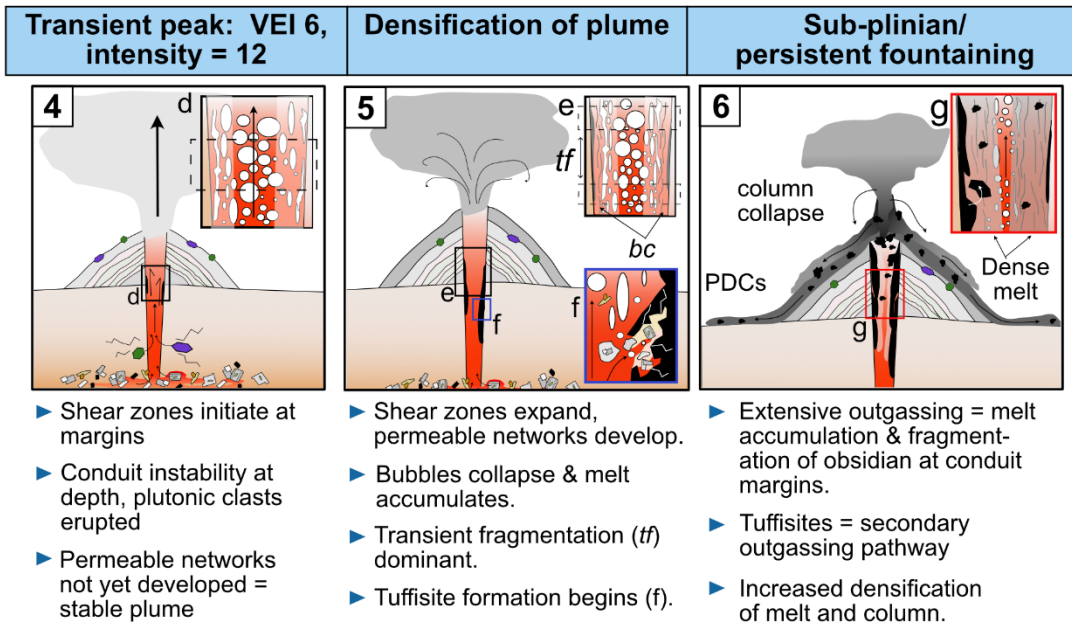
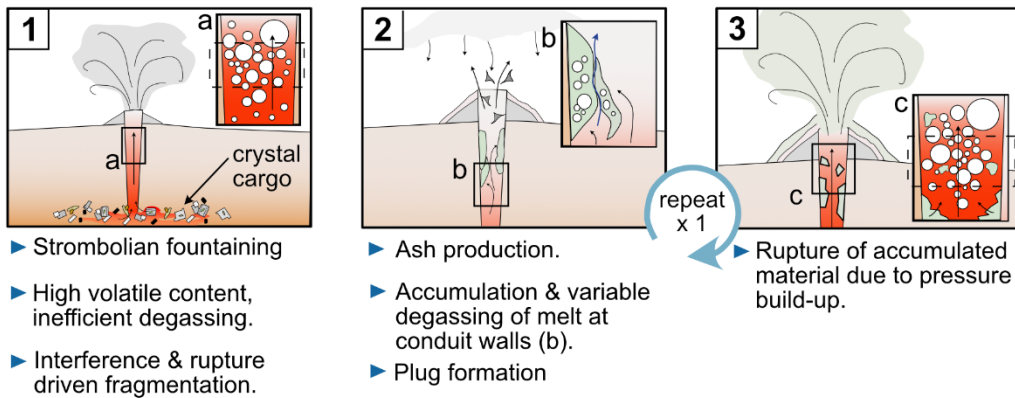


Fig. 2.21 Boxes A – I represent key phases in the Echo Canyon eruption, as discerned from eruption stratigraphy and analyses of juvenile clasts. An idealised cone is presented with stratigraphic Units as described in main text accumulating after each phase. Underlying topography and wind direction are not reflected here – *eff* = effusive. Numbered inset boxes show schematics of processes of vesicle evolution as interpreted from juvenile clast texture, from **1-7** show increasing importance of marginal shear zones on bubble structure, connectivity and outgassing. **Box 8** shows a detailed view of hybrid explosive effusive activity that formed Unit 12 at the projected vent region. **Box 9** shows a possible mechanism for production of clasts with crystalline regions in the orange-brown pumice.

Early low intensity Strombolian fountaining is recorded by Units 1 and 2 (Fig. 2.21a– c), common for these small-volume trachytic events, e.g. the non-welded pumice fall facies at Payún Matrú, Argentina (Hernando, *et al.*, 2019) (Table 2.1). A volumetrically subordinate cycle of accumulation and disruption of dense melt in the conduit then produced the VVLP clasts and ash beds of Unit 2 (Fig. 2.21b and c). Bulk vesicularity distributions (Fig. 2.20) and lapilli populations (Fig. 2.9) for Units 1–3 indicate during early phases, volatile-rich melt vesiculated rapidly during ascent and decompression, fragmenting by bubble interference and rupture (Fig. 2.21a – d). Lithologic characteristics of Units 3 and 4 indicate the subsequent formation of a relatively more stable column with a transient peak intensity of 10-12 (comparable to the intensities calculated for Plinian eruptions), supported by the BVD of Unit 3 (Fig. 2.20). Initiation of marginal shear zones in the conduit introduced sheared clasts to the juvenile population in Unit 3. Unit 4 juvenile clasts record propagation of marginal shear zones, enhanced connectivity of vesicle networks and initiation of melt densification and accumulation: the BVD of Unit 4 shows transient fragmentation became more dominant (Fig. 2.21d and e-5). The contradiction between the juvenile clast population and the BVD (Fig. 2.9 and 2.20) of Unit 4, and its lithologic characteristics, indicate a lag between the initiation of melt densification and destabilisation of the plume. Heterogeneous clast textures and obsidian formation are common in trachytic eruptions (e.g., Houghton *et al.*, 1985; Shea *et al.*, 2017) suggesting trachytic melts support multiple complex degassing histories in the conduit even for small eruptive volumes (Shea *et al.*, 2017). Tuffisite formation on the conduit walls provided an additional outgassing pathway (Fig. 2.21e-6) as continued melt densification initiated partial column collapse and PDC formation (Fig. 2.21e). Subsequent conduit destabilisation sampled accumulated obsidian and tuffisites during deposition of Unit 11 (Fig. 2.21e and f). In late stages, near-complete degassing resulted in high crystallinities and aided a transition to effusive activity forming the dome and brecciated lava, with hybrid activity likely at the initial transition (Fig. 2.21g and h). Pressurisation beneath the dome produced a final magmatic explosive eruption, the OBP, incorporating accumulations of degassed melt from the conduit walls producing heterogeneously microcrystalline clasts (Fig. 2.21i). The excellent exposure of the EC eruption deposits provides a near-complete record of the eruption and shows that many of the processes identified across the eruptions in table 2.1 can occur within a single eruption period and may even be the norm for events of this type.

[2.9 Conclusions / future work](#)

We use unusually well preserved and exposed deposits on Ascension Island, South Atlantic to reconstruct a small-volume explosive-effusive-explosive trachytic eruption. By combining the detailed eruption stratigraphy with analysis of individual and bulk clast densities we demonstrate that eruptions of this type are capable of short-lived periods of high intensity explosions, and rapid transitions in eruptive style. In particular, we show that:

(1) The Echo Canyon eruption had multiple transitions in eruptive style controlled by bulk regimes which transitioned from that controlled by rapidly vesiculating magma to one controlled by the development of shear zones and networks that allowed transient fragmentation to dominate, initiating column collapse.

(2) Magmas of trachytic composition can produce explosive phases with a transient peak intensity equivalent to that seen in Plinian eruptions (intensity values of 12) without the establishment of a stable plume with heights >10-25 km. The global record suggests these intense explosive phases are unlikely to be sustained for long periods, as a consequence of relatively easier outgassing. Ultimately, this and degassing controlled crystallisation in these '*kinetically reactive*' magmas encourages the development of effusive activity.

(3) Our detailed analysis reveals that these rapid transitions (occurring over relatively small volumes of ascending and erupted melt) could be characteristic of these low-volume silicic magmas which are found worldwide. The varied eruption styles and rapid transitions exhibited by small-volume trachytic eruptions have significant implications for our understanding of volcanic hazard, particularly in remote ocean island settings.

(4) Combined analysis of BVDs, macro-scale clast textures and deposit characteristics allows reconstruction of the bulk characteristics of ascending melts revealing changes to conduit and eruption dynamics. Quantification of micro-scale vesicle and crystal textures and changing volatile content and viscosity will enable modelling of useful parameters such as degassing and discharge rates and will be the focus of future work.

Textural studies of other preserved deposits are vital to identify patterns in eruption style and further investigation of fragmentation in trachytes is required to understand how high intensity eruptive periods initiate. Recognising signals of these processes in monitoring data will be critical for ongoing hazard assessment in regions that produce small-volume trachytic eruptions.

Chapter 3: Forensic reconstruction of the Echo Canyon Eruption using quantitative textural and petrological microanalysis

3.1 Introduction:

In Chapter 2 I used field-based stratigraphy and macroscopic characteristics to establish the stratigraphy and eruptive sequence of the Echo Canyon eruption. A small-volume trachytic pumice cone formed via early strombolian – vulcanian fountaining which progressed to a short-lived peak eruption intensity equivalent to that of a Plinian explosion before the dominance of column collapse/ persistent fountaining and PDC formation (Fig. 2.21a – c, Units 1 – 11 Fig. 3.1). A period of low intensity fountaining-fed effusive activity produced a brecciated clastogenic lava dome and overlying flow (Fig. 2.21g, h) before the eruption terminated with a smaller explosive phase (Fig. 2.21i and Fig. 3.1 - OBP). Bulk vesicularity distributions demonstrated a transition from fragmentation via bubble interference and rupture in the early phases, to transient fragmentation at the peak of the eruption (Fig. 2.20). Simultaneously, the onset and expansion of shear zones at the conduit margins (recorded in increasing abundances of sheared clasts – Fig. 3.1) enabled development of permeable networks, outgassing and melt densification (evidenced by dense pumice clasts and obsidian fragments), facilitating the explosive – effusive transition. Transitions in fragmentation mechanism and eruption dynamics have been reconstructed for the Echo Canyon deposits - controlled by variations in gas-melt-crystal-conduit interactions - providing a framework for the forensic analysis of vesicle textures and melt properties.

As demonstrated in chapter 2, the fingerprints of changing stress and strain along with variations in magmatic intensive properties can be established to some extent in the bulk properties of clasts, but further clues arise from detailed analysis of the crystal cargo, their inferred conditions of entrainment and the quantitative analysis of vesicle size and shape. Their detailed interpretation within the context of our stratigraphy generates clues as to dominant controls on eruption style and changes in intensity. Linking quantitative textural studies to petrological analysis provides additional constraints on eruption dynamics and establishes whether changing intensive parameters (e.g., melt temperature and composition) are responsible for the eruptive behaviour preserved in the EC deposits.

Even for observed eruptions, constraining the underlying controls on ascent dynamics is hampered by our inability to see inside the conduit (Toramaru, 2006). This problem is

exacerbated for unobserved eruptions where we cannot rely on seismic evidence, observations of changing column height, gas measurements and first-hand accounts to place constraints on ascent rates, explosivity and magma movement. Quantitative studies of pyroclast size, shape and texture have long been used to reconstruct the behaviour of melt and volatile phases during ascent (e.g., Houghton and Wilson 1989; Polacci *et al.*, 2003, Houghton *et al.*, 2010; Shea *et al.*, 2010b; Alfano *et al.*, 2012 and Mitchell *et al.*, 2019), whereas petrologic studies are used to place constraints on magma storage depth, temperature, volatile content, viscosity and even ascent rates (e.g., Storey *et al.*, 1989; Blundy and Cashman 2001; Neave *et al.*, 2012; Chamberlain *et al.*, 2016 and Costa *et al.*, 2020).

Quantification of vesicle textures can be done via construction of vesicle volume (VVD) and size distributions (VSD) or analysis of vesicle shapes, both approaches provide insights into processes that control the development of permeable pathways and can be used to calculate key eruption parameters.

VVDs and VSDs can be used to constrain a range of parameters. Their shapes reflect the number of nucleation events and the relative dominance of bubble growth, coalescence, ripening and collapse within a vesicle population (e.g., Shea *et al.*, 2010) giving insight into melt-gas interactions prior to fragmentation. Blower *et al.*, (2001) showed that the mathematical expressions that describe natural VSD curves can be compared with experimental data to infer degassing processes to reconcile bubble growth and conduit flow models during rapid ascent. Toramaru (2006) used bubble number densities calculated via VSD analysis to generate a decompression rate meter which can place constraints on magma ascent rate without the need for complex analytical techniques or the presence of clear diffusion profiles in crystals. Shea *et al.*, (2010) described a framework for the construction of VSDs and developed the software FOAMS in order to standardise data collection in 2D. Careful selection of representative clasts, consideration of magnification choice and consistency in segmentation and image correction ensure generated curves are representative of vesicle textures and allow comparison between eruption phases. Limitations of this approach stem from difficulties in converting irregular 2D shapes into 3D bubble volumes. FOAMS uses the 2D – 3D stereological conversion of Sahagian and Proussevitch (1998) which assumes spherical objects and uses geometric binning to calculate the abundance of objects in a given size range across several orders of magnitude. Where vesicles are significantly impacted by shear, an assumption of spherical

98

geometry is not appropriate, and so sheared clasts cannot be analysed in this way. For un-sheared clasts however, these techniques and models can be applied to constrain changing bubble-melt interactions during the EC eruption and elucidate the underlying controls on eruptive transitions identified in chapter 2.

Moitra *et al.*, (2013) used the relationships between bubble shape, melt properties and capillary number to provide constraints on key eruption parameters e.g., overpressure and fragmentation threshold for non-sheared pyroclasts. They used a model for diffusive bubble growth, calculated parameters such as surface tension and melt viscosity and existing models of magma ascent for well-constrained eruptions to define a relationship between vesicle shape and capillary number. Again, this model is not appropriate for intensely sheared clasts, where nucleation and growth exert a smaller control on overall bubble shape. The applicability of the Moitra *et al.*, (2013) model to the trachytic melts of the EC eruption will be evaluated to examine whether eruption parameters derived from un-sheared EC clasts can be accepted as realistic estimates.

Interpretation of textural data and application of the above models relies on effectively constraining key magmatic parameters such as melt temperature and volatile content as they exert a strong control on melt rheology (Cassidy *et al.*, 2018). This is particularly challenging in crystal poor magmas where equilibrium mineral pairs are scarce. Further, as petrologic models rely on substitution of cations between mineral/melt phases they are usually strongly dependent on composition and volatile content (Putirka 2008). Thus, selected models must be applicable to the compositional space of the sampled material. As plagioclase is almost ubiquitous in igneous rocks, plagioclase-plagioclase and plagioclase-melt thermometers and hygrometers have been refined repeatedly over the years (e.g., Barth 1951, 1962, 1968; Stormer 1975; Putirka 2008; Lange *et al.*, 2009 and Waters and Lange 2015). For alkali-rich melts however, k-feldspar can be more abundant, and so k-feldspar – melt thermometers and hygrometers have also been developed (e.g., Putirka 2008 and Mollo *et al.*, 2015). The Putirka (2008) plagioclase and k-feldspar – melt thermometers were developed and tested against a wide range of melt compositions (SiO₂ from 42 – 73 wt%) and pressures (0.001 – 27 kbar) and the Mollo *et al.*, (2015) hygrometer was specifically calibrated to trachytic – phonolite compositions. Both models include tests for equilibrium between mineral-melt pairs based on the exchange of Ab-An and Or-Ab in plagioclase and k-feldspar respectively. Once melt temperatures and H₂O concentrations have been established, melt viscosities can be calculated. Like thermometers and

99

hygrometers, viscosity models must be calibrated against a suitable dataset for the input composition. The model of Giordano *et al.*, (2008) was calibrated using compositions that range from calc-alkaline - peralkaline, and volatile contents from 0 – 8 wt% and temperatures from 245 - 1580°C meaning it can be reasonably applied to the trachytic melts of the EC eruption to place constraints on evolving (crystal free) viscosities.

In this chapter, shapes of vesicles from each macro-scale textural group identified in Chapter 2 will be quantified on the micro-scale and compared to identify dominant controls on vesicle shape. Existing models discussed above will be applied to this data to place constraints on the dominant processes acting on each textural type and combined with clast type abundance data from chapter 2 (see Fig. 3.1) to assess changing controls on eruption style throughout the EC deposits. Forensic examination of crystal cargo and micro-analysis of matrix glass and melt inclusions will be used to calculate intensive variables and constrain variations in melt viscosity using the models of Putirka (2008), Mollo *et al.*, (2015) and Giordano *et al.*, (2008). The influence of crystal-bubble-melt interactions on viscosity will be discussed and the influence of melt composition on the applicability of thermometers, hygrometers and the relationship presented by Moitra *et al.*, (2013) evaluated. This will inform a model for the origin and ascent of the EC magma that explains the eruption sequence recorded in the EC deposits, characterised in chapter 2.

3.2 Methods:

3.2.1 Sampling and petrology:

Twenty-nine samples of the Echo Canyon eruption deposits previously classified based on their macro-scale textures in chapter 2 were chosen for thin-sectioning and inspected under the petrographic microscope to identify microlites, phenocryst phases and microscopic vesicle textures. These included twenty-four pumice lapilli from units 1 – 4, 9 and the OBP one dome sample and one lava sample. Stratigraphic positions of samples are marked with an asterisk next to unit names/numbers on the stratigraphic log in Fig. 3.1. Each section was further examined using backscattered (BSE) and secondary electron (SE) imaging on a Zeiss Gemini 300 at the University of East Anglia, an FEI Quanta 650 FEG at the Natural History Museum, London, UK, and a Zeiss Gemini sigma 300 VP at the Zeiss facility in Cambridge, UK. Analyses of crystal populations, matrix glasses and melt inclusion compositions were carried out on the Cameca SX100 microprobe at the Natural History Museum, London using a 20 Kev and 20 nA beam with a spot size of 10 µm for glass and 5

μm for crystals. For glasses, only analyses with totals $\geq 93\%$ were used and for crystals only analyses with totals $\geq 98\%$ were used. Percentage error on electron microprobe analyses of Na, Al, Si, Mg, Ca, O and Fe was < 0.4 , relative to standards, for K error was less than 0.8%, standards used and their compositions can be found in [electronic appendix 1_1].

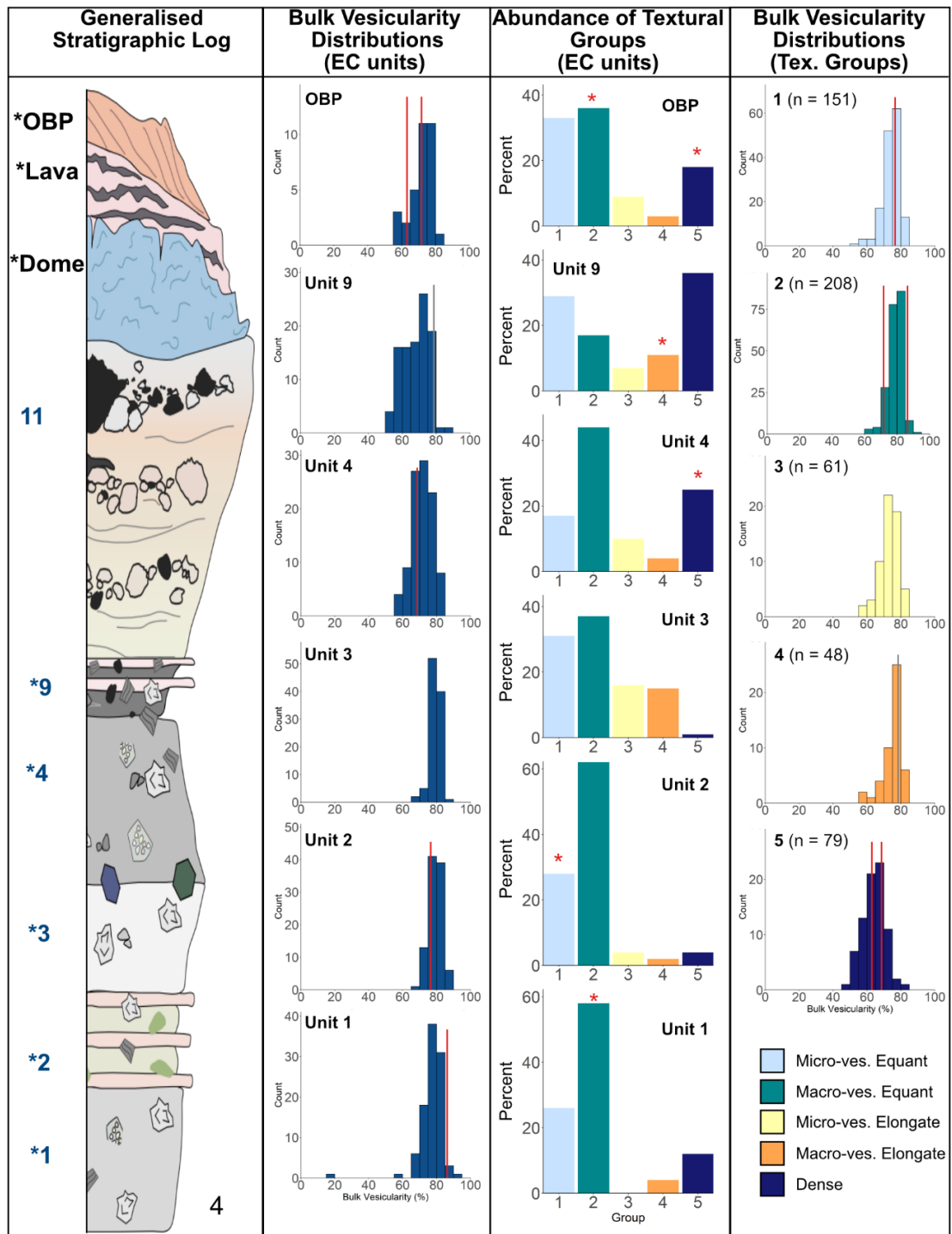


Fig. 3.1: Plots showing how clasts were selected for vesicle size distribution and vesicle shape analysis. Left: Bulk vesicularity distributions (BVDs) for Echo Canyon (EC) units (presented in chapter 2) from which clasts were sourced. Middle: abundance of textural groups in each unit. Right: BVDs for each textural group across all units. Lines in red mark location of clasts selected for VSD and shape analysis, grey lines are clasts selected for just shape analysis (due to their elongate vesicle textures). Red and grey asterisks show groups selected clasts were sourced from. Asterisks next to unit names/numbers indicate sampled horizons.

Abundance of mineral phases and macrocryst textures of the dome (871B) and the lava (828C) were estimated via point counting of high-resolution full thin section BSE images generated on the Sigma 300 SEM at the British Geological Survey, Keyworth by Jeremy Rushton. At least 500 points were counted on each thin section, with a spacing of 1 mm. Where a point lay on the intersection between a crystal and its inclusion, a value of 0.5 was given for each phase. In microlite and microphenocryst populations alkali feldspar (Afs) vs plagioclase feldspar (Pfs) cannot be discerned by greyscale, where e-probe analyses are available microlite compositions are stated. Where e-probe data was collected for specific macrocrysts this was used to determine the feldspar phase present. For all cone samples total crystal content was < 5% and so phase abundances were estimated via inspection of full thin section BSE images and high magnification BSE images of smaller regions.

For samples in the OBP where microlites are more abundant, microlite crystallinities were quantified to assess the impact of crystallisation on melt viscosity and eruptive style. High resolution BSE images were generated using the Zeiss Gemini 300 SEM at the University of East Anglia (e.g., Fig 3.2a). Care was taken to maximise the contrast between microlites and matrix glass, both during data collection and in post processing using *Affinity Photo*. Nonetheless greyscale values (a function of compositional similarity) overlapped to the extent that the automated *Trainable Weka Segmentation* (TWS) plugin in ImageJ did not provide effective segmentation. Instead, each crystal was outlined by hand using *Affinity Designer* to generate multi-phase greyscale images of crystals, glass and crystals touching the edges of the image/ fractured crystals. Fractured crystals and those at the edges were excluded and removed from the total analysed area as their true shape and size are unknown, see Fig 3.2b – d. When using this method, larger crystals are preferentially excluded from analyses as they are more likely to intersect the edge. This impact of this was lessened by using a single large image at a high resolution as a source for crystal measurements reducing the opportunity for large crystals to be cut off at image margins. At least 600 crystals were analysed from both HX and LX regions. Crystal, image, and vesicle areas were then measured via greyscale thresholding in ImageJ (Fig 3.2e) and microlite crystallinities calculated for HX and LX regions individually. For microlite crystallinity calculations and raw SEM images, binary image input see [Appendix 2.1] and [Electronic Appendix 2_4].

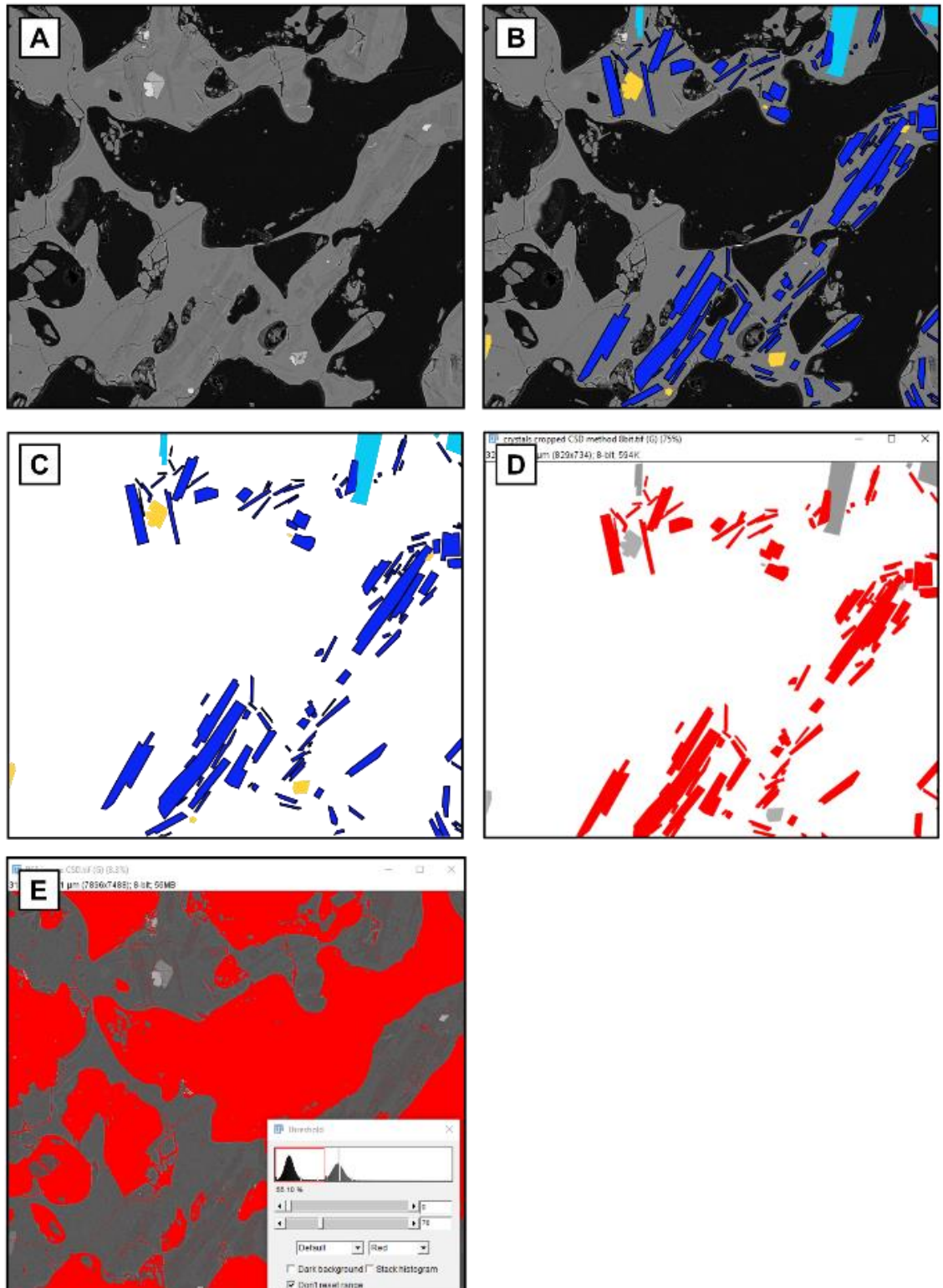


Fig 3.2: Method of crystal identification and image segmentation for quantification of crystal abundance. **A:** Sub-section from a BSE image used for crystallinity analysis, very little contrast between feldspars and glass. **B:** Crystals are outlined by hand. Dark blue are feldspars which are fully represented (in the larger image), pale blue are feldspars which are cut by the edge of the image and are excluded from analysis, yellow are oxides. **C:** crystals isolated from BSE image imported into ImageJ. **D:** crystals image converted to grey scale the threshold set to select feldspars only (highlighted red) **E:** thresholding of BSE image to obtain % vesicles (red region).

3.2.2 BSE Imaging, calculation of shape factors and generation of VSDs.

Quantification of vesicle textures via the production of vesicle size distributions (VSDs) is now common practice (e.g., Giachetti *et al.*, 2011; Shea *et al.*, 2010b Cross *et al.*, 2012; Polacci *et al.*, 2012) since Shea *et al.*, (2010) developed FOAMS - software which automatically applies the 2D – 3D stereological conversion of Sahagian and Prousevitich (1998) to 2D cross-sections of vesicles extracted from binary input images at a range of magnifications. Users can account for the presence of phenocrysts using shades of grey, control the minimum pixel size of an object and adjust the overlap in analysed vesicle diameter at each magnification. FOAMS then calculates vesicle size and volume distributions, various shape parameters, 3D vesicularities and bubble number densities. Vesicle volume and size distributions can be used to interpret degassing processes (Blower *et al.*, 2001), bubble number densities have been used to estimate decompression rates (Toramaru 2006) and the relationship between bubble shape and capillary number has been used to reconstruct bubble overpressures and fragmentation thresholds (Moitra *et al.*, 2013). As with all studies of vesicle size and shape in 2D, the main limitation stems from the unreliability of 2D – 3D stereological conversions. The conversion of Sahagian and Prousevitich (1998) assumes a spherical bubble geometry which works reasonably well when analysing clasts that have undergone little shear, and where bubble connectivity is low (Shea *et al.*, 2010). Where bubbles are intensely sheared, vesiculation and outgassing no longer control bubble shape, meaning standard models (e.g., Moitra *et al.*, 2013 and Toramaru 2006) no longer hold.

Direct measurement of bubble volume and shape in 3D more accurately capture the complex nature of bubble networks. The application of x-ray computed tomography (XCT) in studies of pyroclast texture is becoming more widespread (e.g., Gualda and Rivers 2006; Hughes *et al.*, 2017; Colombier *et al.*, 2018) thanks to the increasing resolution of datasets, more effective data processing packages (e.g., Avizo™ and Dragonfly™) and better constraints on the sources of uncertainty in XCT analyses (Lin *et al.*, 2015). Studies of vesicle and clast texture in 3D have elucidated processes of formation of fluidal pyroclasts at Aluto, Ethiopia (Clarke *et al.*, 2020), vesiculation and cooling processes in Surtseyan eruptions at Hunga Tonga-Hunga Ha'apai volcano (Colomiber *et al.*, 2018) and provided constraints on fragmentation processes in peralkaline rhyolites (Hughes *et al.*, 2017). Limitations of vesicle studies in 3D stem from interactions between object size, data resolution and applied

segmentation algorithms (Ketcham 2005; Lin *et al.*, 2015). These must be minimised where possible and where they cannot (e.g., reaching resolution limits) accounted for when interpreting 3D VSDs. Examination of vesicle textures in 3D will be discussed in Chapter 4. Care must also be taken to ensure interpretations of process from micro-scale features are representative of the bulk conditions in and ascending magma – an issue that also applies to studies in 2D and was addressed using the methods outlined below.

From the 27 EC samples selected for thin sectioning, six pumice clasts from across four of the five dominant textural groups identified in chapter 2 were chosen for quantitative textural analysis - micro-vesicular equant, macro-vesicular equant, macro-vesicular elongate and dense (see. Fig. 3.1 asterisks denote chosen clasts by textural group and sampling locations). To ensure representative sampling of vesicle textures and eruption phases, the modes and extremes in bulk vesicularity for each unit from chapter 2 *and* of each textural group across the deposit were considered. The samples selected for thin section, their textural group, stratigraphic unit, and corresponding eruption phase are listed in table 3.1. The bulk vesicularity of each clast is marked on the plots of bulk vesicularity distribution (BVD) for the units and textural groups alongside the proportions of each clast type in each unit throughout the sequence in Fig. 3.1. Thin sections of micro and macro-vesicular elongate clasts were qualitatively compared, on the microscopic scale their textures were very similar. While not every unit was sampled for quantitative textural analysis in thin section, care was taken to capture modes and extremes in texture that can be extrapolated throughout the deposit. Clasts from the PDC deposits (upper cone) were not used for quantitative textural analysis due to the timing of their collection (January 2020) and subsequent lab closures due to the COVID-19 pandemic restricting thin section production. The bulk vesicularity and macro-scale textures of Unit 11 clasts are reported in chapter 2 (Fig. 2.9) and indicate this phase was more texturally heterogeneous than Unit 9. By not analysing micro-scale textures for this unit, eruption parameters for this very last stage prior to the explosive-effusive transition cannot be quantified - this should be a priority for future studies. Nevertheless, deposit characteristics are sufficient to infer column collapse in Unit 11 and textural analyses in preceding units give an indication of the dominant processes that led to this transition.

Backscattered electron (BSE) images of each pumice clast were acquired and processed for vesicle size distribution (VSD) and shape analysis following Shea *et al.*, (2010). After inspection of each thin section on the SEM, the following imaging strategy was adopted, 8
105

images at x250 – smallest resolvable object (with 5.1% error, Shea *et al.*, 2010) 2 μm diameter, 4 images at x100 – smallest resolvable object of 4.6 μm and 2 images at x25 – smallest resolvable object of 18.55 μm . Images were binarized using the TWS plugin in *ImageJ* (for details of parameters used see [Appendix 2.2]). In pumice clasts, melt films are often so thin that they are not effectively resolved during segmentation due to a) overlapping greyscale values and b) thickness being less than 1 pixel in diameter and so missed by *ImageJ*. In other instances, melt films are broken during mounting, impregnation and polishing – broken films are easily identified in BSE images, but are not preserved during segmentation. It is important to preserve these melt films as their absence impacts the apparent permeability of the sample and alters measured vesicle size and shape. Thus, any such films were manually re-drawn by overlaying the binarized image with 40 – 50% transparency on the BSE image in *Affinity designer* as the human eye more readily identifies these features. Walls were only re-drawn where either complete films or obvious protrusions associated with broken walls were clearly visible in the BSE image as shown in Fig. 3.3. Debris and partially preserved 3D vesicle surfaces, associated with broken vesicle walls and inconsistent polishing were also manually removed to ensure magma porosity at the point of fragmentation was accurately represented.

Table 3.1: Clasts analysed for VSD and vesicle shapes from the Echo Canyon Eruption

Sample_Clast Number	Textural group	Bulk Vesicularity (%)	Unit	Eruption Phase
842A_63	Macro-equant	86	1	Early pumice cone - base, strombolian
843A_4	Micro-equant	76	2	Early pumice cone - vulcanian blasts
844C_10	Dense	69	4	Transient peak densification initiated
829A_29a	Macro-elongate (perpendicular to primary elongation)	79	9	Densification of the plume / initiation of collapse
871B	Crystalline	31	Dome	Post-cone effusive
828C	Crystalline	28	Lava	Post-cone effusive
827C_3	Macro-equant	71	OBP	Post-cone explosive
827C_6	Dense	63	OBP	Post-cone Explosive

OBP = Orange-Brown Pumice

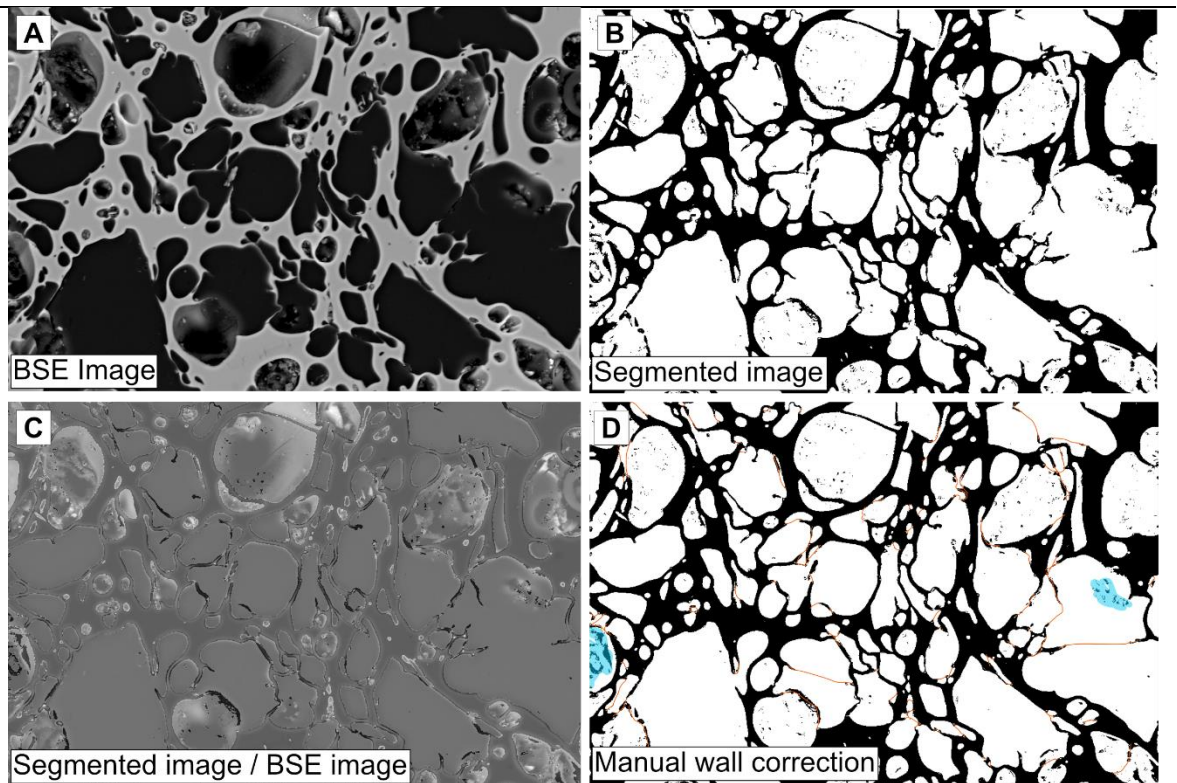


Figure 3.3: images showing vesicle wall reconstruction in *Affinity Designer* and before and after manual debris removal. **A:** original Backscattered electron (BSE) image **B:** image after segmentation in ImageJ, **C:** segmented image overlaid with opacity of 40% onto BSE image **D:** segmented image with manually drawn walls in orange and spots of debris due to poor segmentation of 3D effects highlighted in blue, these regions were also manually removed from the image. Debris is comprised of noise from poor segmentation of partially infilled vesicles, or broken bubble walls.

The “*Analyze Particles*” tool in *ImageJ* was used to extract vesicle area, perimeter, major and minor axes of the best fit ellipse, Feret diameter, aspect ratio of the best fit ellipse, roundness (form factor – Liu *et al.*, 2015) and solidity (Liu *et al.*, 2015). From these measurements other shape parameters were calculated (see below). All symbols and parameters are listed in table 3.2 along with the equations and parameters used and descriptions of what each variable represents. ImageJ calculates roundness (Rd) and solidity (S) using equations 1 and 2. Equivalent diameter (EqD), circularity (C) (Liu *et al.*, 2015) and regularity (Rg) (Mitchell *et al.*, 2019) were then calculated using equations 3 – 5. Where A is particle area, M is major axis of the best fit ellipse, A_c is the area of the convex hull, P is particle perimeter and D_f is the ferret diameter.

$$Rd = \frac{4A}{\pi \times M^2} \quad [1]$$

$$S = \frac{A}{A_c} \quad [2]$$

$$EqD = 2 \times \sqrt{\frac{A}{\pi}} \quad [3]$$

$$C = 4\pi \frac{A}{P^2} \quad [4]$$

$$Rg = \frac{M}{Df} \quad [5]$$

$$\Omega = \frac{A}{\pi \lambda_l \lambda_s} \quad [6]$$

The shape descriptors defined above were chosen to give the most comprehensive description of vesicles in 2D, largely to consider their deviation from a perfect sphere:

Roundness describes the closeness of the particle to a circular cross-section and is less sensitive to protrusions on the vesicle walls (Liu *et al.*, 2015).

Regularity considers the distance between points on the vesicle perimeter, making it more sensitive to protrusions/irregularities in the vesicle walls aka textural roughness (Mitchell *et al.*, 2019). Vesicles with surface protrusions that increase the maximum distance between two points on the particle surface (Feret Diameter) without contributing significant additional area to the particle (and so do not significantly extend the long axis of the best-fit ellipse) will have a lower regularity [see Appendix 2.3 Fig 2.3 for diagram].

Solidity is a measure of morphological roughness aka the spatial distribution of the particle area and thus is more sensitive to particle-scale concavities (Liu *et al.*, 2015). The convex hull of a shape acts like an elastic band stretched around its limits, the greater the concavity, the greater the reduction in particle area relative to the area of the convex hull and so the lower the solidity [see Appendix 2.3 Fig 2.3 for diagram].

Circularity allows a relative measure of the deviation of the particle from a perfect sphere resulting from a change in elongation *or* surface roughness. If elongation is the dominant factor causing deviation from a circle, then circularity values will plot closer to roundness values. If morphological roughness is the dominant factor, circularity will be closer to values

of solidity; if textural roughness is the main factor, circularity values will plot closer to regularity (Liu *et al.*, 2015). In addition, the shape parameter Ω - see Eq. 6 - (termed *regularity* by Shea *et al.*, (2010) but here referred to as “*shape factor*” to avoid confusion with regularity as defined in Eq. 5 as used by Mitchell *et al.*, 2019) was calculated for vesicles with a circular diameter of 9 – 100 μm (as calculated from the particle area). Where λ_l is the semi-long axis of the best fit ellipse and λ_s is the semi-short axis of the best fit ellipse. The chosen size range includes the median vesicle size of each sample analysed while staying as close as possible to the range selected for analysis by Moitra *et al.*, (2013) to allow later comparison. For raw SEM images *only* used in shape analysis (829A_29a), all raw shape data and all calculated shape parameters see [electronic appendix 2_2], all other images used in shape analysis are found in [electronic appendix 2_3] as they were also used for VSD analysis.

Table 3.2 Symbols, shape parameters and eruption parameters used in Chapter 3

VSD analysis		
Symbol / parameter	Unit	Description
L	mm (FOAMS output)	Equivalent diameter of sphere of with the same volume as the particle (after 2D – 3D conversion in FOAMS)
n	-	Number density absolute
Na	-	Number density 2D: number of objects per unit area.
Nv	-	Number density 3D: number of objects per unit volume.
V	mm ³ (FOAMS output)	Particle volume
Shape analysis		
Symbol / parameter	Unit / equation	Description
A	μm ² / mm ² (FOAMS)	Particle area
Ac	μm ²	Area of the convex hull
P	μm	Particle perimeter
Df	μm	Feret Diameter
Best Fit ellipse (ImageJ)	-	An ellipse generated by fitting the second order central moments of the ellipse to the distribution of data points on the particle. Long and short axes adjusted to produce an ellipse of the same area. Aka SXM ellipse (c.f. Heilbronner and Barrett 2014)
M	μm	Major axis best fit ellipse (ImageJ)
Best-fit ellipse (FOAMS)	-	An ellipse generated by fitting the second order central moments of the ellipse to the distribution of data points on the particle (Mathworks UK, 2022).
λ _l	mm (FOAMS output)	Semi-major axis of best fit ellipse (Mathworks UK, 2022)
λ _s	mm (FOAMS output)	Semi-minor axis of best fit ellipse (Mathworks UK, 2022)
Rd	$Rd = \frac{4A}{\pi \times M^2}$	Roundness (ImageJ): relative smoothness of vesicle overall, morphological roughness (Liu <i>et al.</i> , 2015).
S	$S = \frac{A}{A_c}$	Solidity (ImageJ): spatial distribution of the particle area, morphological roughness – particle scale concavities.
EqD	μm $EqD = 2 \times \sqrt{\frac{A}{\pi}}$	Equivalent diameter of circle with area equal to particle area (A).
C	$C = 4\pi \frac{A}{P^2}$	Circularity: deviation from spherical resulting from elongation or surface roughness (as defined by Liu <i>et al.</i> , (2015))
Rg	$Rg = \frac{M}{Df}$	Regularity as defined by Mitchell <i>et al.</i> , (2019). Distance between points on the vesicle perimeter, textural roughness.
Ω	- $\Omega = \frac{A}{\pi \lambda_l \lambda_s}$	Shape parameter Ω used by Moitra <i>et al.</i> , (2013) originally termed “regularity” by Shea <i>et al.</i> , (2010). Most sensitive to shapes produced by the coalescence of two or more vesicles.
Table 3.2 contd.		
For calculating eruption parameters		
Symbol / parameter	Unit / equation	Description

Ca	-	Capillary number
ϕ	-	Magma/clast porosity
σ	Nm ⁻¹	Surface tension
R	μm	Bubble radius
ΔP	MPa	Bubble overpressure
	$\Delta P = \frac{2\sigma}{R} \left(1 + 2\phi^{-2/3} Ca \right)$	
ΔP_f	$\Delta P_f = \frac{2.4}{\phi}$	Fragmentation threshold. For Plinian and Hawaiian eruptions with a characteristic permeability of $\sim 10^{-12} \text{ m}^2$.

VSD analysis was performed in FOAMS (Shea *et al.*, 2010) using binary images after manual film reconstruction. Minimum object size was set to 5 pixels, associated with a 5.1% error on the smallest vesicle population at each magnification (Shea *et al.*, 2010). The outputs were examined, and appropriate cut-off values chosen manually as per Shea *et al.*, (2010) before the final VSD curves were generated (for images, raw FOAMS output and manually assigned cut-off values see [electronic appendix 2_3]).

[3.3 Results:](#)

3.3.1 Crystal populations & glass compositions:

Careful characterisation of crystal populations and analysis of glass compositions is vital to elucidate the storage and ascent history of a magma (e.g., Clyne 1999; Chamberlain *et al.*, 2016 and Costa *et al.*, 2020), as well as enable reconstruction of physical melt properties key to reconstructing ascent dynamics and understanding eruptive behaviour. Melt and crystal compositions and textures are forensically examined below to identify pheno/antecryst populations and trace any changes across the EC eruption deposits.

Whole rock analyses of the EC deposits show broadly trachytic compositions, with small differences in bulk rock composition with stratigraphic position recognised in chapter 2. Bulk rock and glass compositions do show some similarities, the electron microprobe analyses of various forms of glass from the EC deposits are plotted in Fig. 3.4 alongside a summary of whole rock data from chapter 2. The explosive deposits are generally crystal poor (< 1% crystals > 500 μm in all units and \sim 1% microlites in the cone – units 1 – 11 Fig. 3.1), excepting some regions in the OBP where microlites comprise up to 31% (Figs. 2.18F and 3.12F). In contrast, the lava and dome are more crystal rich with up to 90% groundmass crystallinity and 2.5% crystals > 500 μm . Several crystal populations were identified across the EC deposits, these are sub-divided into a) groundmass phases – microlites (< 100 μm

long-axis) and microcrysts (150 – 300 μm), and b) macrocryst phases – including phenocrysts and antecrysts (0.5 – 3 mm). Here, the term *macrocryst* is used to make an initial distinction between microlites and coarser crystals without simultaneously implying a genetic relationship between larger populations and the host melt. Estimated abundances of different crystal populations (obtained through point counting in effusive products and BSE image inspection for explosive deposits) are reported in table 3.3. Variations in macrocryst and groundmass crystal textures, composition and stratigraphic occurrence are described in detail in sections 3.3.1a and b and phenocrysts/antecrysts identified. Crystal, melt inclusion and matrix glass electron microprobe data are presented in full in [Electronic Appendix 2_1].

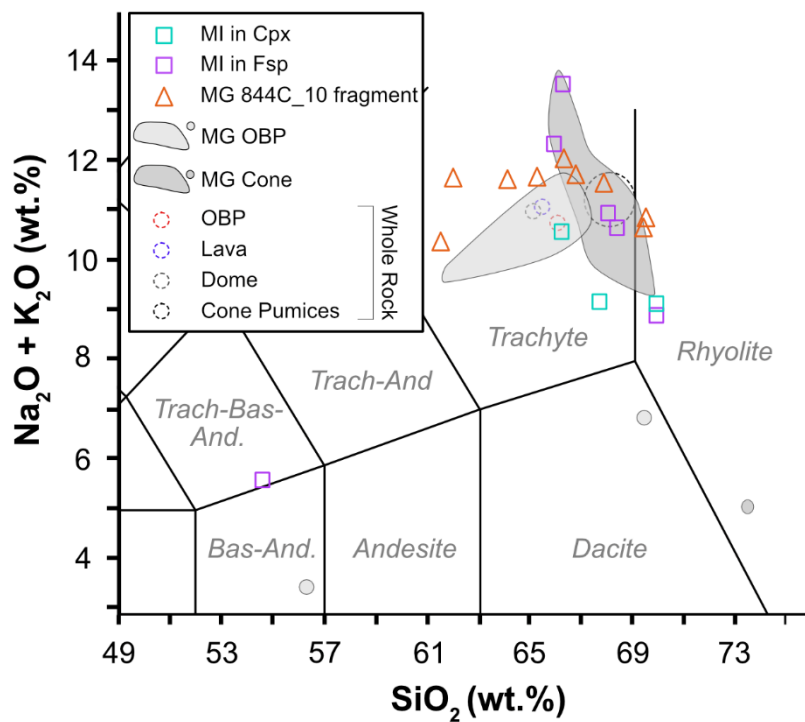


Fig. 3.4 TAS diagram showing matrix glass compositions (MG) from the cone deposits and Orange-Brown Pumice (OBP) (fields) and melt inclusion (MI) data from feldspar phenocrysts in the lava, dome and cone (purple squares) and clinopyroxenes in the OBP and dome (teal squares). Matrix glass compositions from a fragment within a clast from Unit 4 are also shown (orange triangles). Whole rock data as detailed in Ch. 2 displayed as fields denoted by dashed circles.

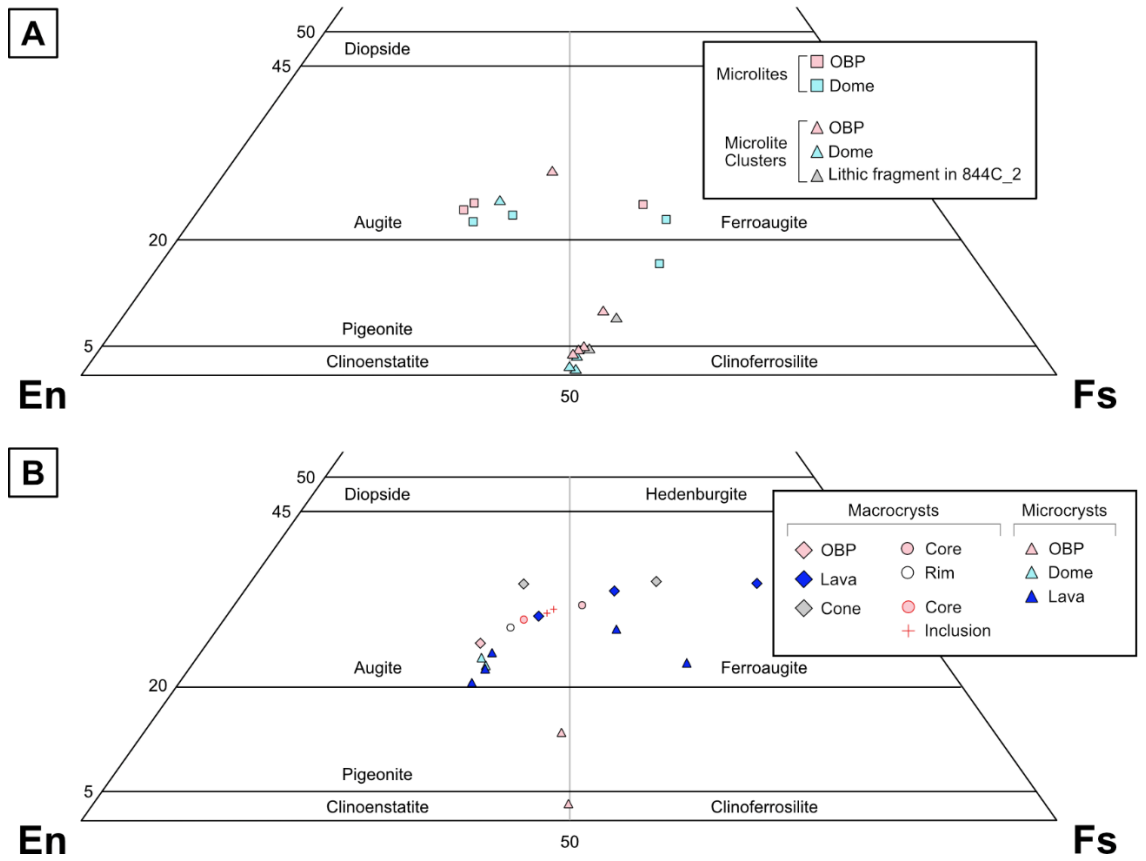


Figure 3.5: plots of crystal population compositions from electron micro-probe data. **A:** pyroxene microlites **B:** pyroxene macrocrysts.

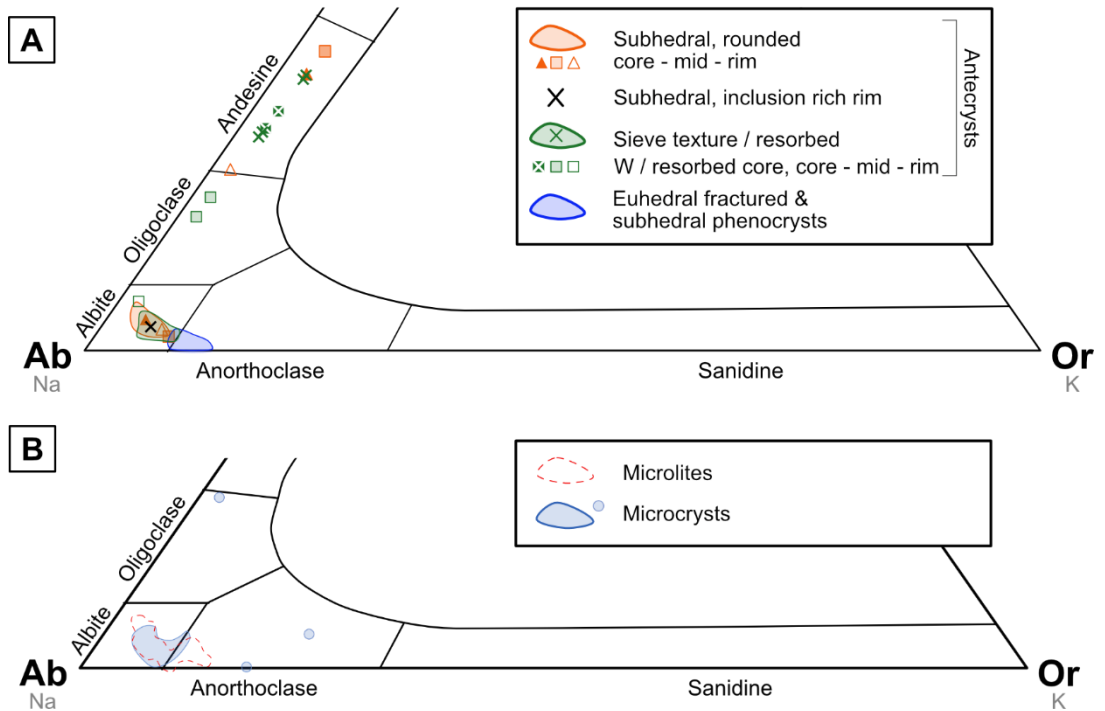


Figure 3.6 Plots of feldspar crystal populations from electron micro-probe data. **A:** feldspar macrocrysts **B:** feldspar microlites and microcrysts.

3.3.1a Macrocryst phases:

The macrocryst population described here in thin section corresponds to the distinct 3 – 8 mm EC phenocryst population observed in hand specimen and reported in chapter 2 though macrocrysts captured in these thin sections of cm-scale clasts rarely exceed 3 mm. Further to the descriptions in chapter 2, distinctions are now made between phenocrysts and antecrysts based on textural and compositional characteristics. More broadly, macrocrysts include: (a) four texturally and compositionally distinct feldspar pheno/antecryst populations, (b) euhedral clinopyroxene antecrysts and (c) Fe-Ti oxides with and without preserved exsolution lamellae. In cone and post-cone pumices macrocrysts are rare, with only a couple of examples of each type observed across all 25 pumice thin sections, partly a function of their high vesicularity. Across all units, feldspars are the most common macrocryst phase, with a maximum abundance of 2.35% observed in the lava. The macrocryst population is described below, sub-divided by texture and composition to identify phenocryst vs antecryst phases present in the EC eruption deposits.

Table 3.3: Vesicle free relative abundances of mineral phases in units of the EC eruption deposits.											
	Macrocrysts			Groundmass phases							
Deposit/ unit	Feldspar¹ (%)	Fe-Ti Oxides² (%)	Clino- pyroxene (%)	Fsp microcrysts (%)	Quartz microcrysts (%)	Cristobalite microcrysts (%)	Fsp microlites ³ (%)	Fe-Ti Oxides (%)	Cpx microlites ⁴ (%)	Apatite (%)	Glass (%)
<i>Lower Cone</i>	<1	<1	<1	<<1	-	-	<1	0.03	-	-	95
<i>Middle Cone</i>	<1	<1	<1	0.15	-	-	1.15	0.04	0.32	-	98
<i>Dome</i>	1.7	-	<1	5.3	1.7	3.3	83.1	2.8	2.2	-	-
<i>Lava</i>	2.35 ⁵	-	<1	6.9	3.18	4.5	76	4.2	1.1	0.2	1.42
<i>OBP (LX)</i>	<0.1	-	-	-	-	-	3.9	0.91	-	-	95.2
<i>OBP (HX)</i>	<0.1	-	-	-	-	-	31.2	0.8	-	-	68

¹Plagioclase antecrysts and anorthoclase phenocrysts, ²with exsolution lamellae, ³Albite dominant, Anorthite secondary. ⁴Anhedral / rounded. ⁵Andesine and Albite. Lower, middle and Upper cone % estimated values based on inspection of whole thin section maps and high-resolution BSE images. Macrocrysts are defined as crystals > 300 µm long axis, microcrysts as 150 – 300 µm long axis and microlites <150 µm long axis.

Euhedral-subhedral Feldspar phenocrysts:

Euhedral anorthoclase feldspar crystals (Fig. 3.6a) with long axes ranging from 0.5 – 3 mm are present in the explosive deposits but not the dome or lava. They are typically fractured and can contain Fe-Ti oxide inclusions (Fig. 3.7a – e). One subhedral crystal contains a 1 mm long pyroxene inclusion and a 70 μm apatite (Fig. 3c). All examples lack zoning or significant signs of disequilibrium (e.g., sieve texture, dissolution, embayment). One fractured subhedral 2 mm long-axis anorthoclase crystal containing pyroxene inclusions and one zircon was found in the lava Fig. 3.7F. As well as presenting equilibrium textures/ limited indicators of disequilibrium, these crystals fall within bounds of chemical equilibrium when tested against their host melts (see section 3.3.3) and so are classified as phenocrysts.

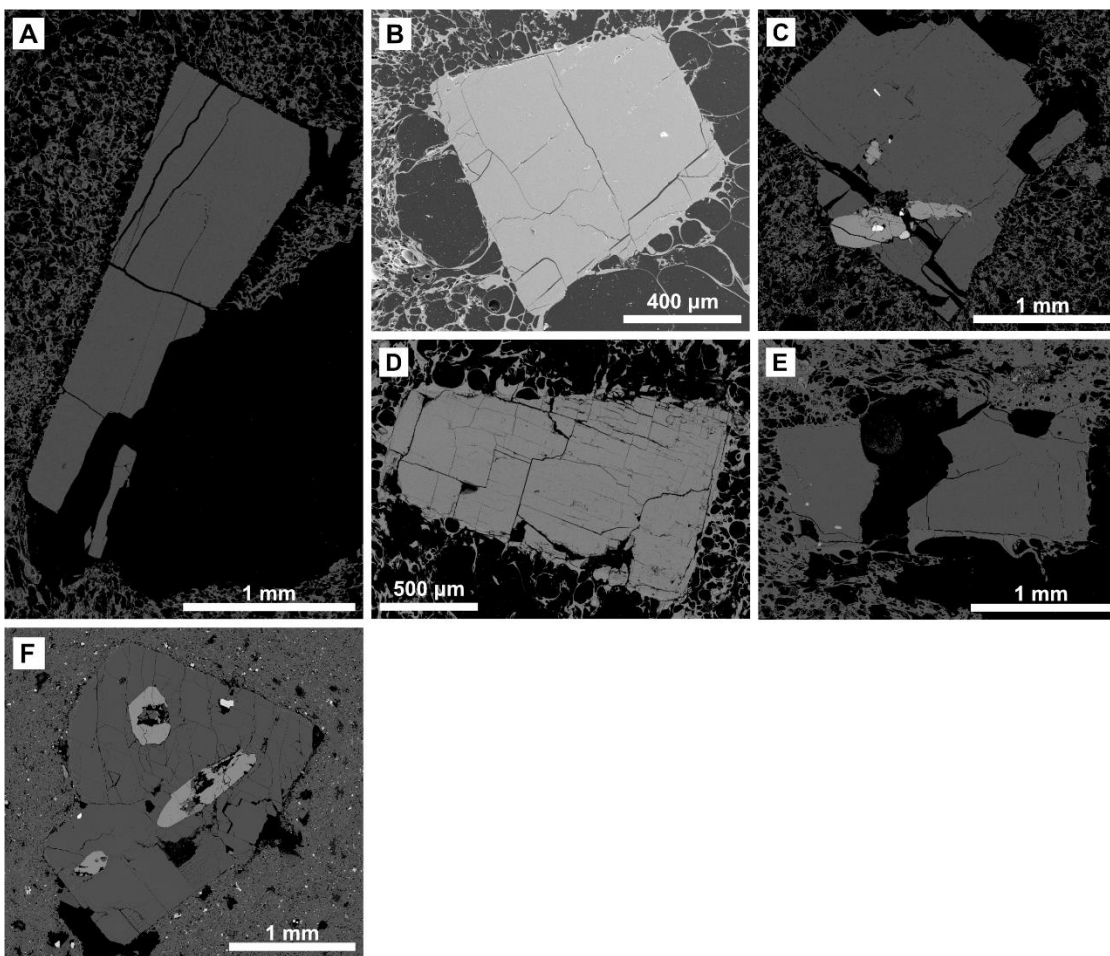


Figure 3.7: Euhedral – subhedral anorthoclase phenocryst population. **A and B:** Fractured euhedral anorthoclase crystals from lower cone pumice. **C:** euhedral anorthoclase crystal with a pyroxene inclusion from lower cone pumice. **D:** fractured anorthoclase crystal from lower cone pumice. **E:** anorthoclase crystal fractured apart in pumice from the middle cone. **F:** subhedral anorthoclase with pyroxene (mid-grey) and zircon (bright upper white in right of phenocryst) inclusions.

Subhedral plagioclase antecrysts:

Subhedral plagioclase crystals with long axes ranging from 0.5 – 1 mm are found in all the EC eruption products (Fig. 3.8). They are often fractured, though not always, lack any distinctive zoning, have rounded crystal faces and can have Na-enriched rims up to 10 μm thick. Most are albitic (Fig. 3.6a) but one andesine crystal with a 40 μm thick oligoclase rim was found in the lava (Fig. 3.8F). Rounded crystal faces indicate mild textural disequilibrium, but crystals lack extensive dissolution and so are classified as antecrysts, sourced from a melt of similar composition to the host.

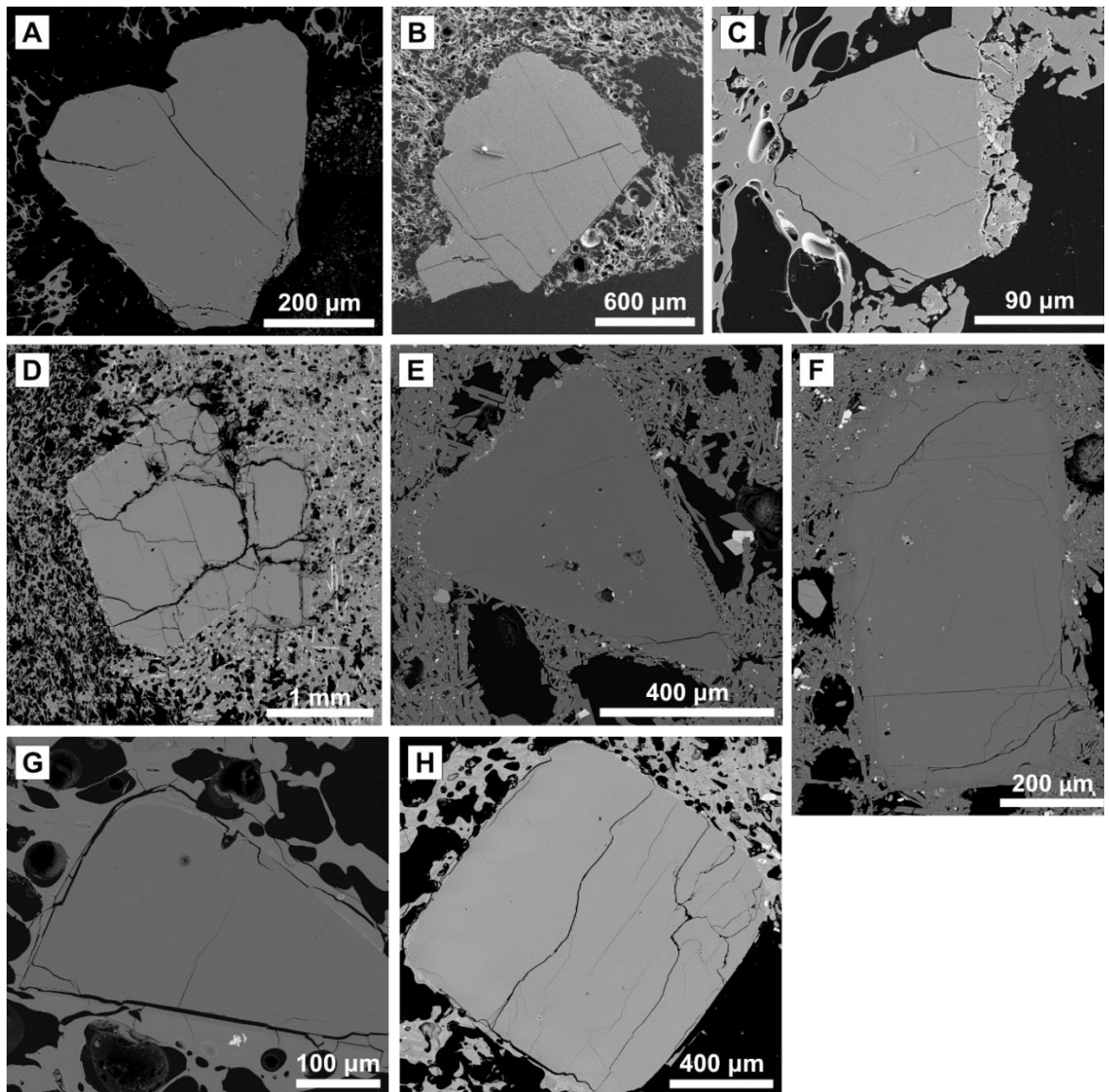


Figure 3.8: Examples of subhedral/rounded feldspar macrocrysts in the Echo Canyon eruption products. A – E and G – H are albitic and F is Andesine with a rim that plots on the andesine-oligoclase boundary (darker grey).

Subhedral plagioclase antecrysts with inclusion rich rims:

Subhedral albite crystals with inclusion rich rims and long axes ranging from 500 – 800 μm were observed in Unit 3, the dome and the lava: they are most abundant in the effusive products (Fig. 3.9). Inclusion rich rims vary in thickness from $<10 - 100 \mu\text{m}$. Inclusions are dominantly Fe-Ti oxides and clinopyroxene.

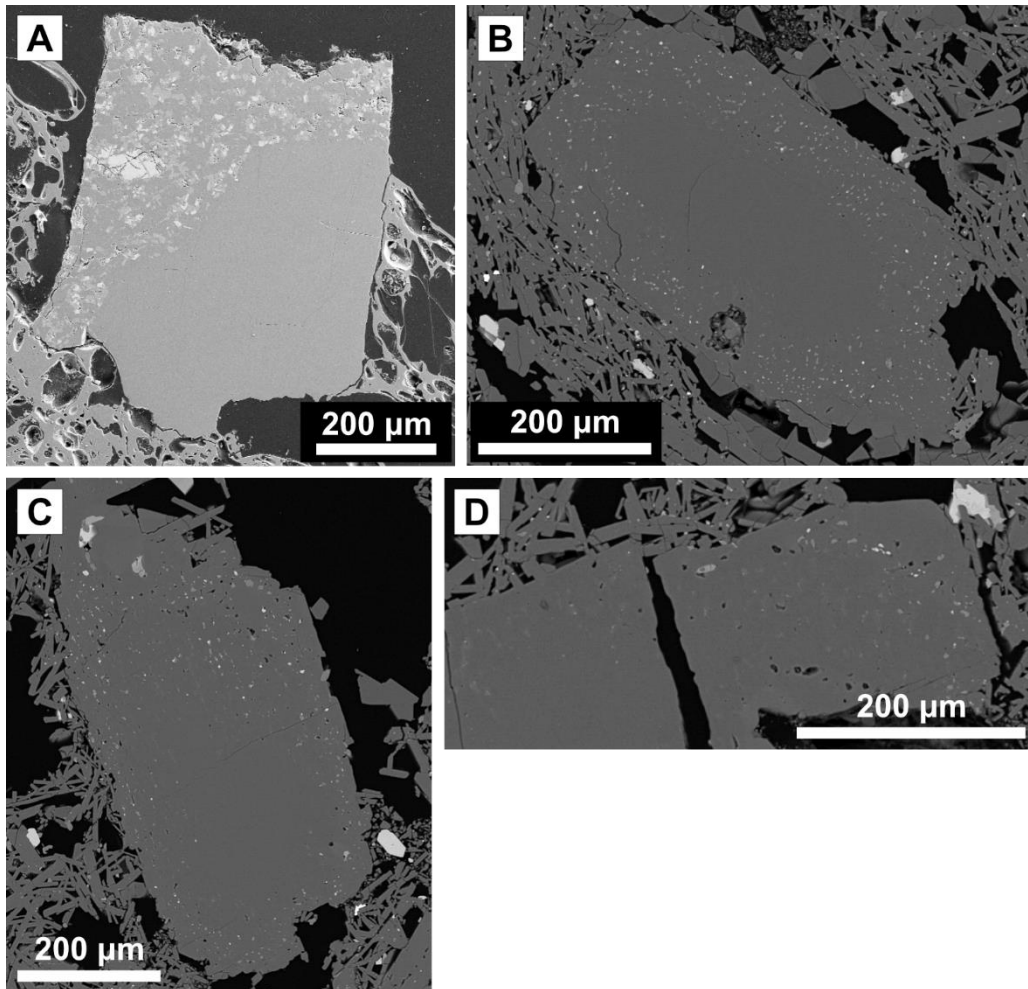


Figure 3.9: Subhedral albite macrocrysts with inclusion rich rims from Unit 3 of the pumice cone (A) and the lava dome (B – D). Inclusions comprise Fe-Ti oxides and clinopyroxene. Image A was produced using secondary electron imaging, B – D were produced using backscattered electron imaging.

Sieve textured / resorbed feldspars:

Sieve textured and resorbed plagioclase crystals were found in the cone and post-cone deposits (Fig. 3.10). Intact crystals typically have long-axes $> 2 \text{ mm}$ while fragments are $0.5 - 1 \text{ mm}$. This population is often fractured and can contain melt inclusions. The few melt inclusions large enough to be analysed via electron microprobe ranged from $65 - 70 \text{ wt\% SiO}_2$ and $8.9 - 12 \text{ wt\% K}_2\text{O} + \text{Na}_2\text{O}$. These compositions are very similar to the surrounding

glass and so it is likely these are connected to the external melt and do not reflect less evolved melt compositions. In the lower pumice (Fig. 3.10a) the sieve textured albite is compositionally very close to the albite/anorthoclase boundary and passed the equilibrium tests applied however, such distinct textural disequilibrium and shared morphological characteristics with other more albitic examples suggest it is part of the same antecryst population as Fig. 3.10b-e.

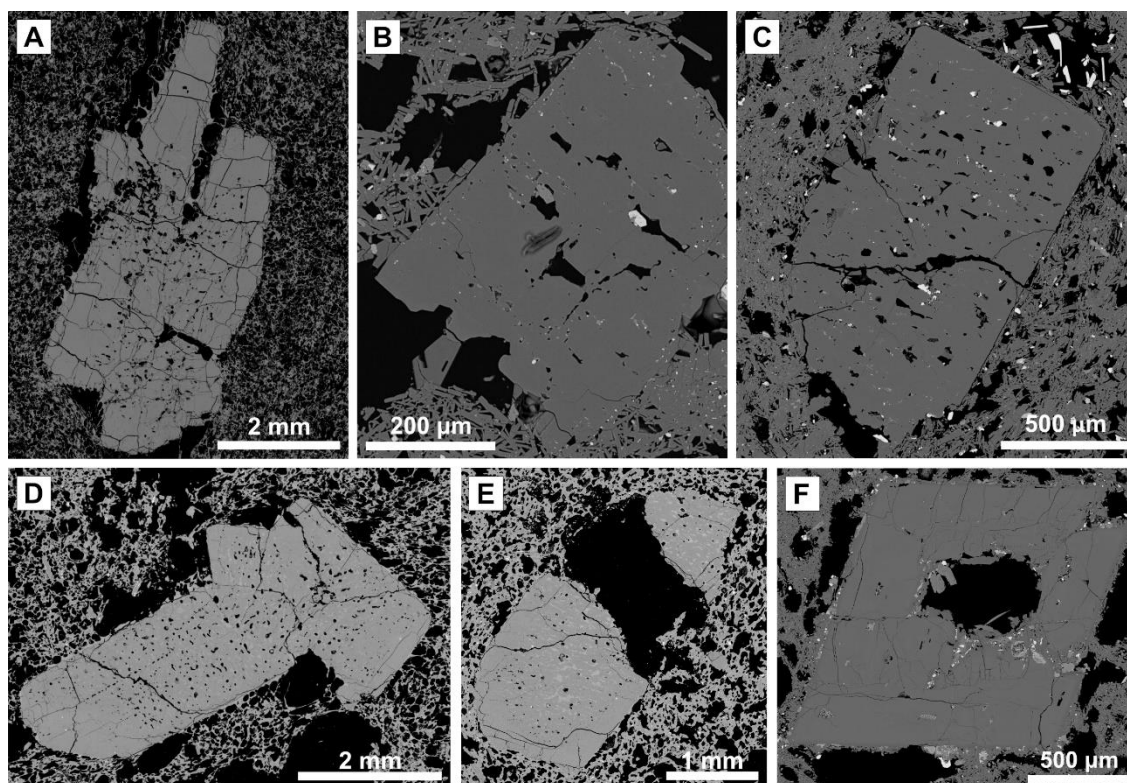


Figure 3.10: **A:** sieve textured albite crystal from lower cone pumice. **B and C:** sieve textured albite crystals with Fe-Ti oxide inclusions from the post-cone lavas. **D and E:** sieve textured albite crystals from the overlying baked pumice (OBP). **F:** oligoclase crystal with well-developed crystal faces, andesine rim and a resorbed core from the lava.

Clinopyroxenes:

Euhedral augite crystals of approximately 0.5 – 1 mm were observed in thin sections of the EC eruption deposits (though up to 3 mm clinopyroxenes were observed across hand specimens and in the field). Augites are often fractured and contain inclusions of apatite (Fig. 3.11a and b). Melt inclusions (MI) have Mg#'s similar to the matrix glass (MI = 8.56 and 11.35, matrix glass = 11.78) and vastly different to their host crystal (Mg# = 95 – 100) (see [Electronic Appendix 2_1] for full compositional data) and so are likely connected to the crystal exterior. Augites are usually associated with subhedral Fe-Ti oxides with or without preserved exsolution lamellae. One augite with a more Ca-rich rim was observed in the

post-cone pumice fall, this rim had some evidence of resorption on one crystal face (Fig. 3.11b). This sample also contained a skeletal augite with an apatite inclusion (Fig. 3.11d and e). Resorption evidenced by connected melt inclusions, and Mg#’s indicate this augite population is antecrystic.

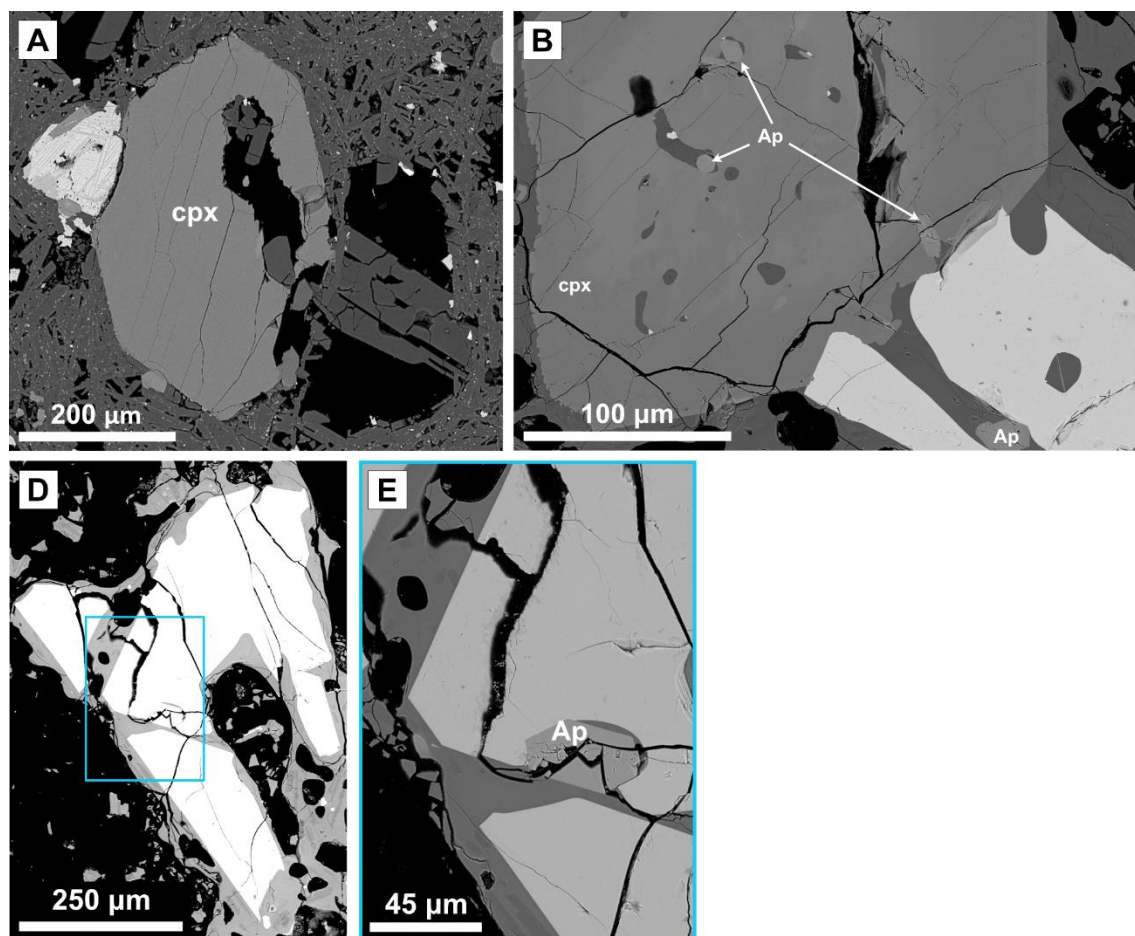


Figure 3.11: Clinopyroxene macro/microcryst populations and associated Fe-Ti oxides. **A** and **B**: euhedral augites (cpx) associated with Fe-Ti oxide microcrystals (brighter greyscale), **B** contains inclusions of melt and apatite (Ap). **C**: Skeletal augite containing an apatite (ap) inclusion (**D**).

3.3.1b Groundmass phases:

Feldspar microlites:

All eruptive products contain albite – anorthoclase microlites which are here defined as crystals from 5 – 100 µm long-axis, see Fig. 3.12. Microlite abundance ranges from < 1% in the cone pumices to > 70% (vesicle free) in the lava and dome. As described in chapter 2 the OBP clasts contain regions of high (HX) and low (LX) microlite crystallinity with up to 31% of the vesicle free area comprising feldspar microlites in HX regions (Fig. 3.12f).

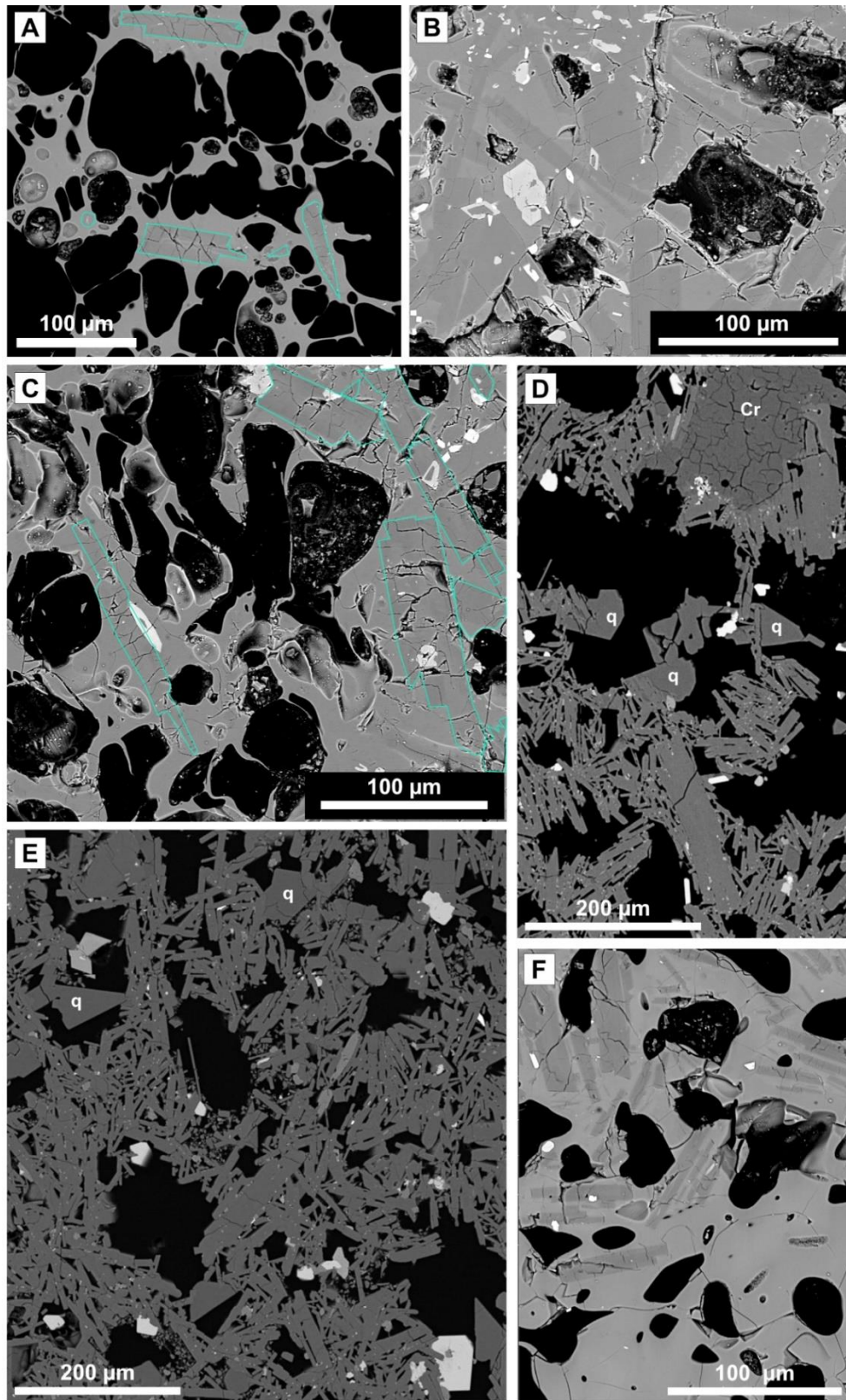


Figure 3.12 showing feldspar microlite and microcryst populations in the Echo Canyon eruption products. **A:** microlites from a Unit 2 pumice clast (843A_4). **B:** microlite and microcrysts within a crystal rich fragment within a pumice clast from Unit 4 of the cone (844C_2). **C:** Microlites from within pumice region of the same clast as B. **D:** groundmass in the lava (828C) showing feldspar microlites and microcrysts along with cristobalite (Cr) and angular quartz fragments (q). **E:** groundmass in the lava (871B), brighter phases are Fe-Ti oxides and apatite. **F:** A crystal rich/poor boundary in orange-brown pumice clast (827C_6).

Microcryst populations:

Feldspar microcrysts from 150 – 300 μm (Fig. 3.12d and e) are present throughout the sequence but are most common in the post-cone eruptive products, up to 6.9% in lavas. More than 90% of feldspar microcrysts are albite with some anorthoclase and one oligoclase microlite analysed (see Fig. 3.6).

Anhedral, rounded augite microcrysts show evidence of disequilibrium, with resorption and embayment common (Figs. 3.13a and b). They commonly contain Fe-Ti inclusions and can be associated with subhedral – euhedral Fe-Ti oxides up to 300 μm (long-axis).

Remaining groundmass and crystal clots:

Other groundmass phases include < 10 μm Fe-Ti oxides– concentrated in dense regions of the lava and dome (Fig. 3.13c), equant and anhedral Fe-Ti oxides from < 10 – 130 μm (oxides > 100 μm may contain exsolution lamellae) (Fig. 3.13 d and e), subhedral – anhedral clinopyroxenes < 100 μm (as seen in Fig. 3.13a and b, but smaller) and skeletal fayalite crystals (Fig 3.13f and g). The lava and dome also contain up to 4.5% 30 – 300 μm fractured cristobalite crystals (Fig. 3.12d and 3.13a) and ~3% 100 μm quartz fragments (Fig. 3.12e).

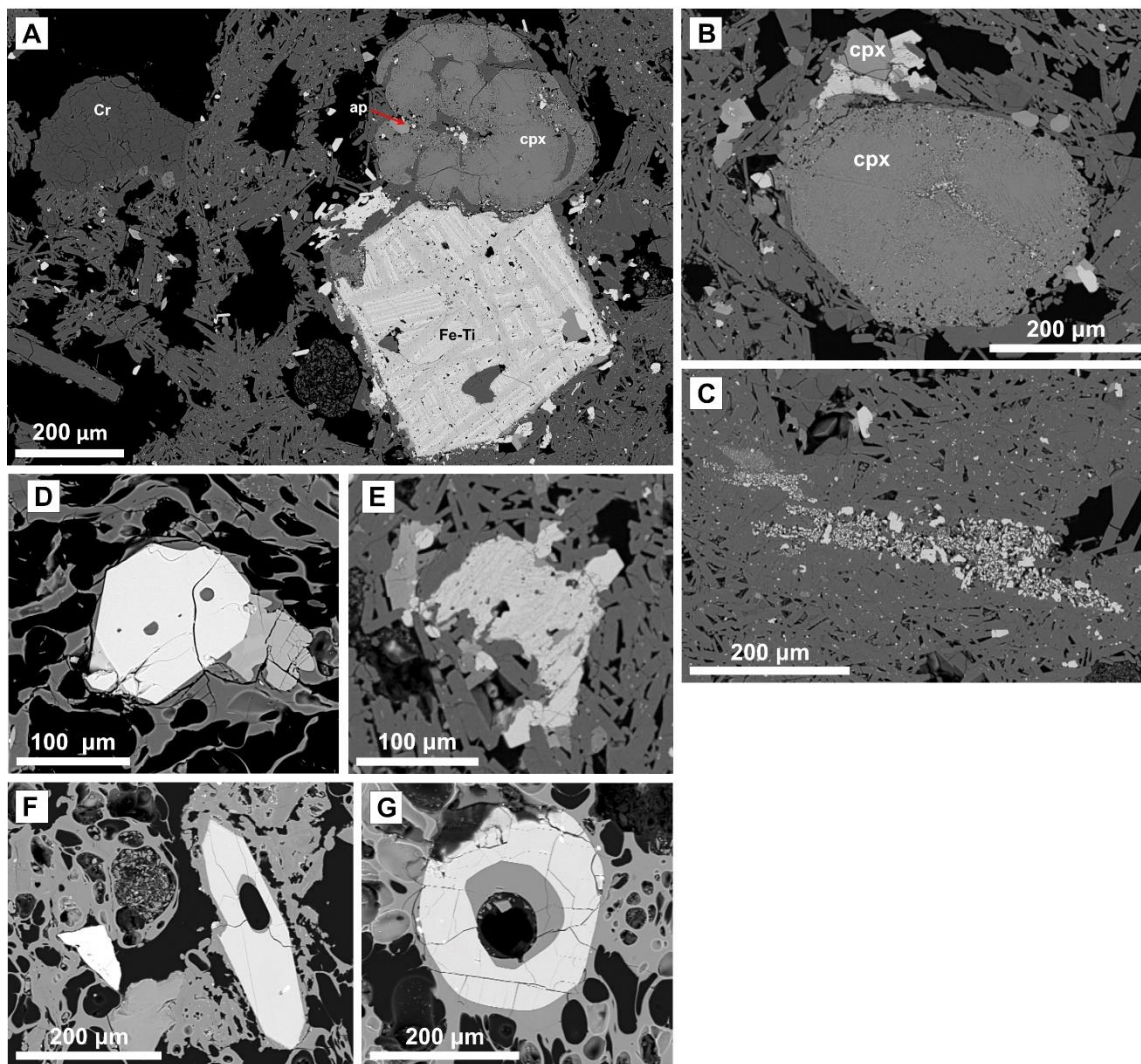


Figure 3.13: **A:** anhedra, rounded clinopyroxene with embayment and inclusions of apatite and Fe-Ti oxides. Associated with a larger Fe-Ti oxide containing exsolution lamellae. Cristobalite (Cr) microcrystals are present in the groundmass. **B:** another example of an anhedra clinopyroxene crystal and associated clusters of Fe-Ti oxides. **C:** Examples of Fe-Ti oxide concentrations in the dome. **D and E:** examples of larger oxides with and without exsolution lamellae from explosive (A) and effusive (B) deposits. **F:** rounded pyroxene with resorbed core from the upper cone, **G:** typical fayalite crystal from the middle cone pumice.

In addition to the above groundmass phases, clots of crystals are found in several of the erupted units, examples are given in Fig. 3.14. Some of these clots are clearly entrained fragments of other rocks in a solid state e.g., Figs 3.14a and b. Others appear to be either partially vesiculated (Fig. 3.14c) or better incorporated into the melt e.g., Fig 3.14g and h. All crystal clots contain crystals that compositionally match the microlite and microcryst populations seen elsewhere in the groundmass. The clot in Fig. 3.14c even contains an albite macrocryst that matches the composition and texture of the other plagioclase antecrysts.

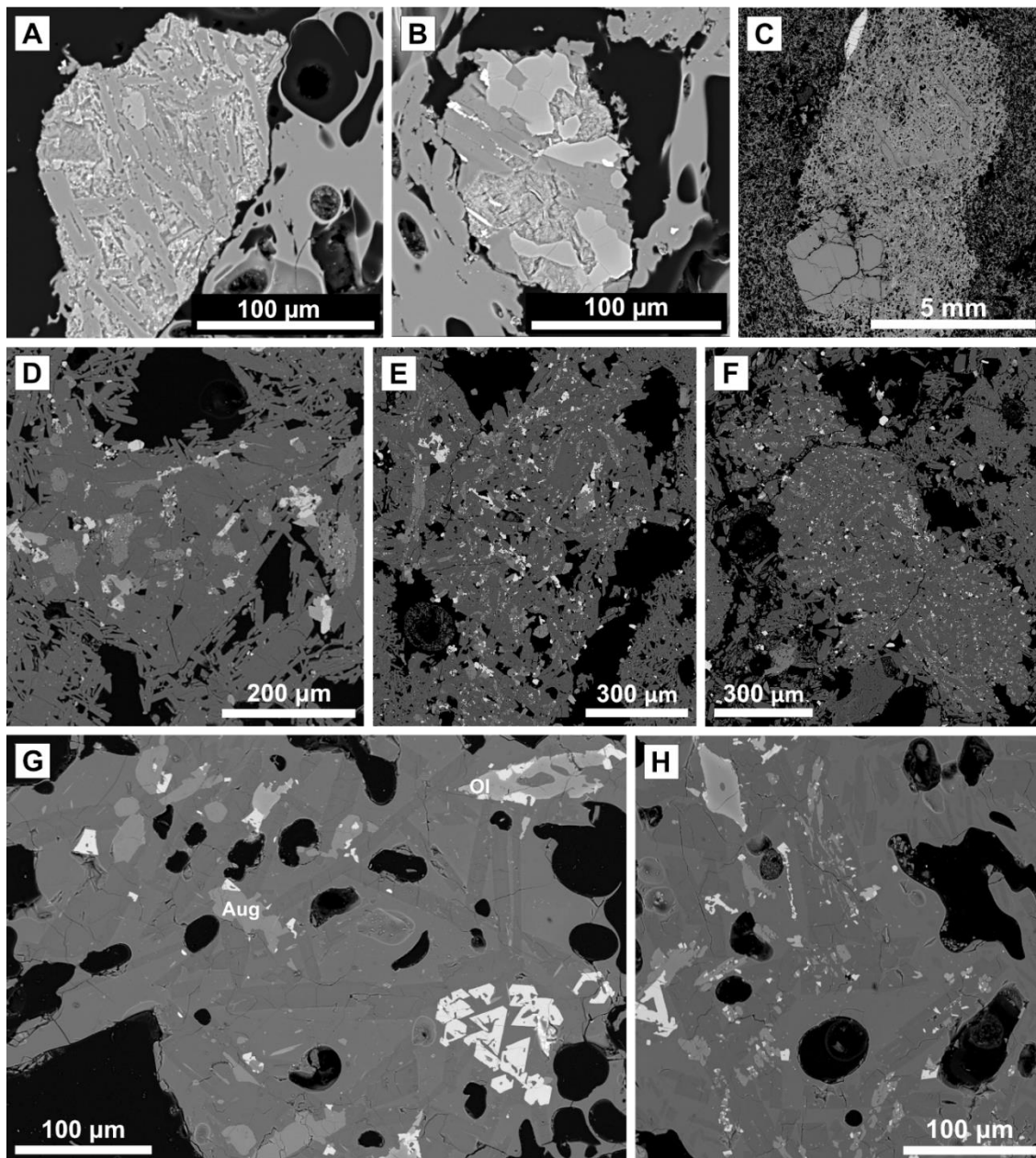


Figure 3.14: Crystal clusters from the Echo Canyon eruption products. **A and B:** brittle fragments of crystalline rocks entrained in pumice clasts from Units 4 and 9 respectively (samples 844C_2 and 829a_29b). **C:** crystal cluster and macrocryst entrained in Unit 4 clast (844C_2), partially vesiculated. **D:** example of crystal cluster in the dome (871B). **E and F:** examples from the lava (828C) which are partially vesiculated/ fragmented. **G and H:** examples of more dispersed crystal clots from the orange-brown pumice (827C_3 and 827C_6), augite indicated by *Aug*, fayalite labelled *Ol*. Crystals in C – H are all similar to those seen more dispersed in the broader groundmasses of their respective samples.

3.3.2 Vesicle Size Distributions (VSD)

Vesicle volume (VVD) and vesicle size (VSD) distributions can be used to identify the dominant processes operating on an ascending package of melt in the build-up to fragmentation. Vesiculation, bubble growth, coalescence, ripening and collapse all produce vesicle populations with different characteristics (e.g., Shea *et al.*, 2010) and offer insights

into melt-gas interactions prior to fragmentation. Below, VVDs and VSDs are generated for textural groups that have not been extensively sheared (e.g., not the macro-vesicular elongate clast) to identify the dominant process controlling vesicle textures in each clast type.

Vesicle size distribution analysis was performed on binarized and manually corrected images for 5 samples from the EC eruption deposits. Two sets of images from 827C_6 were analysed, one set from regions of high microlite crystallinity (HX) and a second from regions with low microlite crystallinity (LX). Table 3.4 reports the samples, their textural group, measured 3D vesicularity and calculated output values from FOAMS. Calculated 3D vesicularities in FOAMS are typically lower than measured whole clast vesicularities apart from sample 842A_63 (table 3.4). It is inferred that this is due to (A) the relatively weak capture of the largest vesicle populations in thin section as they are typically excluded due to intersections with the image boundaries, and (B) potential slight over-estimation of vesicularities during manual measurement. Over-estimation of vesicularities during density measurements can stem from tiny pockets of air being trapped between the parafilm and irregular clast surface despite best efforts to minimise this effect. Measured and calculated 3D vesicularities for clast 827C_6 are the least consistent, this clast is the most texturally heterogeneous on the macro-scale. Similarly, our calculated measurement represents a localised area of the sample whereas values in 3D are a whole clast average – the variance between these two values is within sample variance reported for bulk samples from this unit (43%).

Plots of $\log(N_{v>L})$ (population density (N_v) of vesicles greater than a given length (L)) vs $\log(L)$ (see Fig. 3.15) were used to calculate the exponent d for a line of best-fit following a power law of the form $N_{v(>L)} \sim f(L^{-d})$ and plots of $\log(N_v)$ vs L were used to calculate the exponent a for a line of best-fit following an exponential law of the form $N_v \sim f(e^{-aL})$.

Table 3.4: Output values from VSD analyses										
Sample_clast	Tex. Group	Nv (mm ⁻³)	NvCorr (mm ⁻³)	2D Ves. (%)	3D Ves. (%)	Whole clast Ves. (%)	N° included	L - Major mode	L - minor mode	D. type*
842A_63	2	4.815x10 ⁵	1.94x10 ⁶	75	89	86	771	0.046	0.361	<i>p</i> (2.83)
843A_4	1	1.15x10 ⁶	2.96x10 ⁶	61	68	76	1903	0.056	0.112	<i>p</i> (2.84)
844C_10	5	8.88x10 ⁵	1.81x10 ⁶	51	56	69	1517	0.045	0.09	-
827C_3	2	3.85x10 ⁵	1.02x10 ⁶	62	69	73	596	0.091	0.045, 0.361	<i>p</i> (2.70) / <i>e</i> (13.17)
827C_6_LX	5	7.25x10 ⁵	1.31x10 ⁶	45	46	65	602	0.055	0.344	<i>p</i> (2.81)
827C_6HX	5	1.44x10 ⁶	2.25x10 ⁶	36	38	65	725	0.091	0.182	<i>p</i> (2.71)

*Type of distribution: *p* = power law distribution of the form $Nv(>L) \sim f(L^{-d})$ with exponent *d* in parentheses, *e* = exponential of the form $Nv \sim f(e^{-aL})$ with corresponding exponents *a* in parenthesis, *p/e* = undetermined / both show a good fit. Best-fit functions were calculated in R using a linear regression and have an $R^2 > 0.95$. Power law exponents were calculated using a plot of $\log(Nv>L)$ vs $\log(L)$, exponential fit exponents were calculated using a semi-log plot of $\log(Nv>L)$ vs L .

Several samples from the explosive OBP and cone deposits (842A_63, 843A_4 and 827C_6) are classified as power law distributions but sample 827C_3 from the OBP shows a good fit ($R^2 > 0.95$) for both best-fit lines and so is classed as power law / exponential. Vesicle number densities (per mm^3) were calculated in FOAMS (Nv) and corrected for clast vesicularity (NvCorr) (Shea *et al.*, 2010) (see table 3.4). Corrected vesicle number densities were of the same order of magnitude across all the EC eruption deposits. The macro-vesicular equant clast from the base of the pumice cone (842A_63) had an NvCorr value almost double that of the equivalent texture clast from the OBP, 1.94×10^6 and 1.02×10^6 mm^{-3} respectively. The micro-vesicular equant clast from Unit 2 of the pumice cone had the highest NvCorr of 2.96×10^6 , closely followed by the HX regions of the dense clast from the OBP (827C_6_HX) – 2.25×10^6 mm^{-3} . The dense sample from the cone deposits (844C_10) has an NvCorr of 1.81×10^6 mm^{-3} , the lowest of the cone deposits.

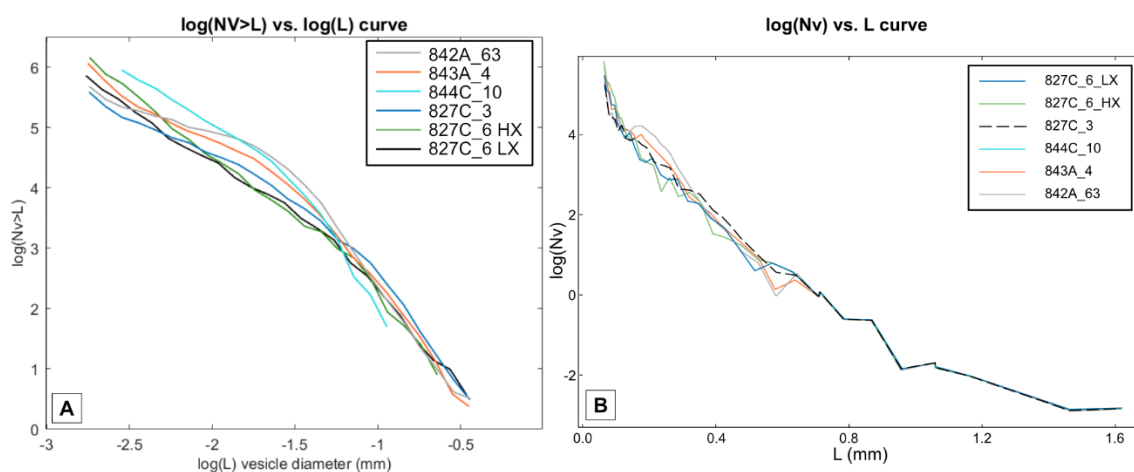


Fig 3.15: A: $\log(Nv>L)$ vs $\log(L)$ plot for all samples from the Echo Canyon eruption deposits as used to calculate power law exponents using linear regression lines of best-fit. B: $\log(Nv)$ vs L plot for all samples from the EC eruption deposits as used to calculate exponential law exponents using linear regression lines of best-fit. Nv is vesicle number density and L is characteristic length, aka the diameter of a volume equivalent sphere.

Vesicle volume distributions (VVDs) produced by FOAMS are shown in Fig. 3.16, displayed as half-bins for clarity. Clast 842A_63 (macro-vesicular equant) has a distribution closest to normal, a slight right-skew, major mode of 0.046 mm and a secondary mode at the largest vesicle size class. Clast 843A_4 (micro-vesicular equant) has a broader flatter distribution with the major and minor modes representing similar volume fractions: the presence of two distinct vesicle populations is more convincing than in 842A_63. Sample 844C_10 (dense) has a similar modal vesicle diameter to 842_63 but is more heavily skewed towards lower equivalent diameters and has a small secondary population distributed around the minor-mode at 0.09 mm. The vesicle volume distribution for 827C_3 is shifted to larger

vesicle diameters with a major mode at 0.091 mm and a minor at 0.361 mm. There is a second minor mode at 0.045 which appears to be associated with a smaller secondary population skewed towards smaller diameters. The VVD for 827C_6_HX (dense, OBP) is shifted to larger vesicle sizes and has hints of a normal distribution about a vesicle diameter of 0.109 mm but is overprinted by major and minor modes at 0.344 and 0.055 mm respectively. The VVD for the high microlite crystallinity regions in 827C_6 does not extend to equivalent vesicle diameters > 0.229 and has a major mode of 0.091, as in 827C_3. The VVD has a more irregular shape with a long tail towards the smaller vesicle diameters. The minor mode at 0.182 hints at a secondary larger vesicle population.

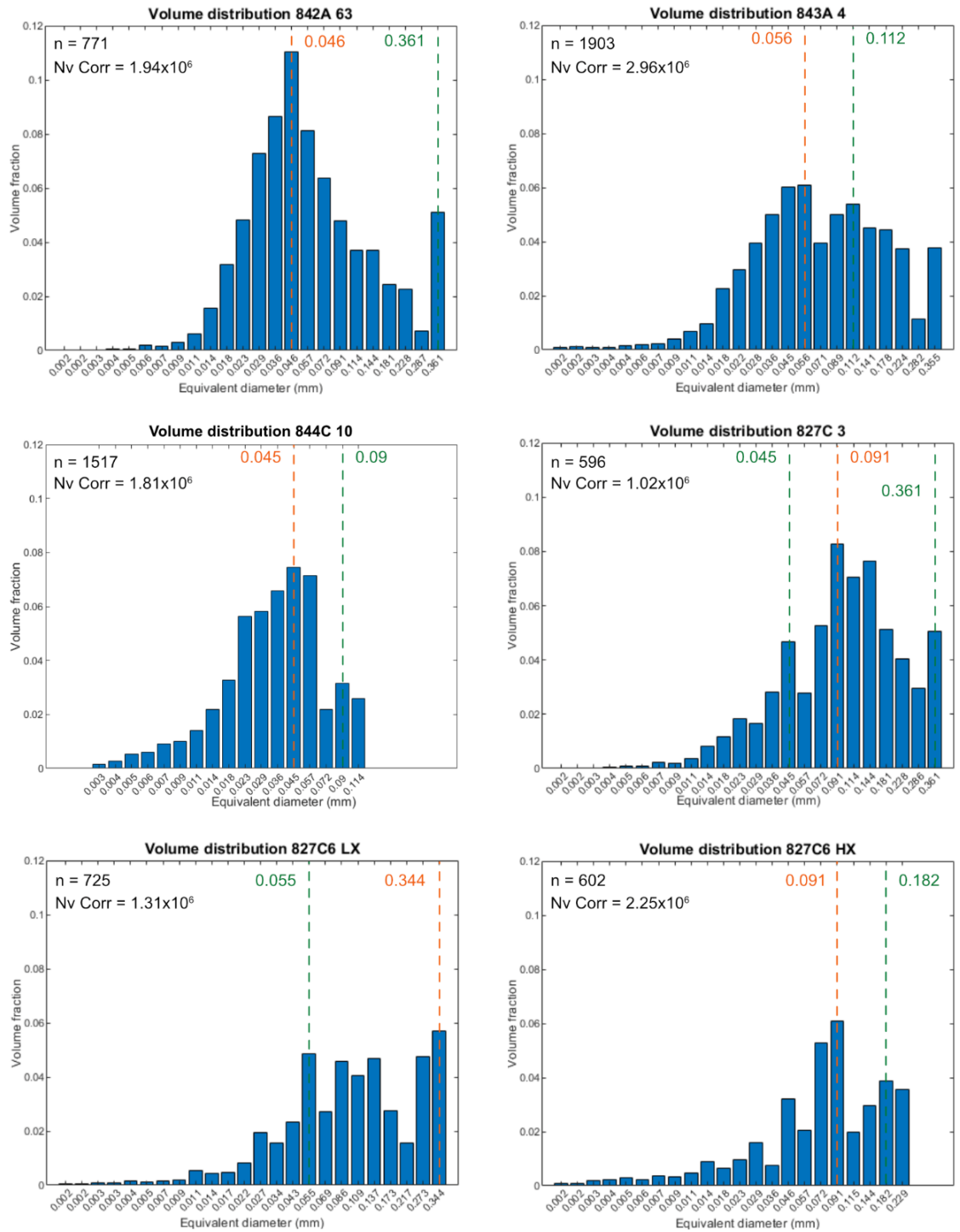


Fig. 3.16: VVD plots of Echo Canyon samples. Orange dashed line marks dominant modal diameter, green dashed line marks secondary modal equivalent diameter. Number of included vesicles (n) and vesicle number density corrected for clast vesicularity (NV Corr) are indicated for each sample. Exact values of bins vary per sample, but x and y-axes are set to the same overall range to allow comparison.

3.3.3 Inferred T & H₂O from crystal populations

A critical issue with a limited crystal cargo and wide variance in texture was to identify any mineral populations that could represent a state of equilibrium with either melt or one

another in the run up to eruption in order to reconstruct the critical changes that led to changes in eruptive style or infer the key drivers.

Electron microprobe analyses of groundmass, microcryst and macrocryst (including phenocryst/antecryst) phases were used to identify potential equilibrium Fe-Ti oxide and feldspar-melt pairs for reconstruction of melt temperature and H₂O. No equilibrium oxide pairs were identified in the samples despite their abundance in the lava and dome sections. Clinopyroxenes were tested for equilibrium with their host melts and potential melt inclusions via Mg# but no equilibrium pairs were identified (Mg#'s for all crystal and glass analyses are listed in [Electronic Appendix 2_1]). Instead, feldspar-melt pairs were used for both thermometry and hygrometry using equations from Putirka (2008) and Mollo *et al.*, (2015) respectively.

Plagioclase – melt thermometry & hygrometry

Plagioclase-melt thermometry was performed on plagioclase microlite- and macrocryst-melt pairs by applying equation 23 of Putirka (2008) in *Thermobar* – an open source thermobarometry tool created by Wieser *et al.*, (2021). A pressure of 250 MPa was used as measured from melt inclusions in the trachy-basalt – trachytic zoned fall deposit by Chamberlain *et al.*, (2016) and in agreement with entrapment pressures of 200 – 300 MPa from felsic plutonic bodies by Webster and Rebbert (2001). In *Thermobar*, the high/ low temperature equilibrium test of Putirka (2008) was applied for plagioclase-melt analyses. Eight micro/macrocryst-melt and 4 microlite-melt pairs passed the high temperature test, but most pairs passed the low temperature test - 117 macro/microcrysts, 7 microlites. Only 5 pairs failed both equilibrium tests, all were microlite-melt pairs. Modelled temperatures from plagioclase-melt thermometry are listed in table 3.5. Modelled temperatures range from 968 – 1069°C for micro/macrocryst-melt pairs and 1014 – 1067°C for microlite-melt pairs. Analyses that passed the low-T equilibrium test produced temperatures ranging from 968 - 1049°C and those passing the high-T test ranged from 1053 – 1069°C.

In *Thermobar*, equation 23 of the Waters and Lange (2015) plagioclase-melt hygrometer was then applied iteratively to calculate the most likely H₂O content for a best-fit temperature using the plagioclase-melt thermometry of Putirka (2008) as an initial input as quoted for the hygrometer only model of Waters and Lange (2015), this model incorporates the ±4.3°C error of the Putirka model and yields an error (calculated vs the calibration dataset) of ±0.35 wt% H₂O. For micro/macrocryst-melt pairs that passed the

low-T equilibrium test, calculated H₂O values ranged from -0.27 – 4.89 wt%: all micro/microcryst pairs that passed the high-T test returned negative H₂O values. For microlite-melt pairs that passed the low-T equilibrium test, calculated H₂O values ranged from -0.95 – 2.77 wt %: all microlite-melt pairs that passed the high-T test returned negative H₂O values. Modelled H₂O values for each apparent equilibrium pair can be found alongside the associated temperature in table 3.5, full *Thermobar* output from the iterative T-H₂O calculation can be found in [Electronic Appendix 2_5]. Pairs resulting in negative H₂O values were excluded from further analysis.

K-feldspar – melt thermometry & hygrometry

Alkali-feldspar-melt thermometry was performed on all identified K-feldspar microlite-, microcryst- and phenocryst-melt pairs using equation 24b from Putirka (2008) at 250 MPa in *Thermobar*. There is no inbuilt equilibrium for alkali-feldspar-melt pairs equivalent to the Putirka (2008) plagioclase-melt test and so all resulting temperatures are reported in table 3.6. Microlite-melt pairs gave temperatures from 745 – 1046°C, microcryst-melt pairs gave temperatures ranging from 749 – 800°C and phenocryst-melt pairs gave temperatures ranging from 751 – 892°C. One microlite-melt pair returned a temperature of -273°C, only one analysis exceeded 900°C (1046°C from a fractured 150µm long microlite in 842A_35b). Mean and median temperatures for all analyses are 802°C and 821°C respectively. These are slightly lower than a temperature of 993°C reported by Chamberlain *et al.*, (2019) using the same model, but consistent with temperatures modelled for other trachytes in the Eastern Felsic Complex (EFC) (White Horse, effusive = 837°C, Cricket Valley, explosive = 886°C) (Chamberlain *et al.*, 2019).

Table 3.5: Output from iterative calculation of T & H ₂ O using Eq. 23 from Putirka (2008) & Eq. 23 of Waters and Lange (2015), for plagioclase-melt pairs.								
Unit / Sample	Type	Site	Point	Crystal Comp.	Putirka T (°C)	Pass Eqbm?	Iterative T (°C)	H ₂ O (wt%)
OBP / 827C_6	Microlite-melt	9	1 / 3	An ₆ Ab ₈₅ Or ₉	1015	Low T: Yes	1050	-0.95
	Microlite-melt	11	1 / 2	An ₄ Ab ₈₄ Or ₁₂	1049	Low T: Yes	1070	-0.55
	Microlite-melt	9	1 / 4	An ₃ Ab ₈₆ Or ₁₁	1068	High T: Yes	1016	1.38
	Microcryst-melt	3	1 / 3	An ₃ Ab ₈₄ Or ₁₂	1035	Low T: Yes	1122	-2.19
	Microcryst-melt	7	1 / 1	An ₁₂ Ab ₇₅ Or ₁₃	1044	Low T: Yes	978	1.86
	Microcryst-melt	14	1 / 2	An ₃ Ab ₈₆ Or ₁₁	1049	Low T: Yes	Didn't pass Eqbm test	
	Microcryst-melt (core)	17	1 / 1	An ₆ Ab ₈₈ Or ₇	1001	Low T: Yes	977	0.72
	Repeat with other nearby glass	17	1 / 7	An ₆ Ab ₈₈ Or ₇	994	Low T: Yes	1003	-0.27
	Macrocryst-melt	3	1 / 1	An ₃ Ab ₈₂ Or ₁₅	1063	High T: Yes	1164	-2.42
OBP / 827C_3	Microlite cluster-melt	6	1 / 11	An ₁₄ Ab ₇₆ Or ₁₀	1048	Low T: Yes	1005	1.19
	Microlite cluster-melt	6	1 / 13	An ₂₂ Ab ₇₆ Or ₁₀	1029	Low T: Yes	941	2.56
	Microcryst-melt	1	1 / 1	An ₅ Ab ₈₇ Or ₈	1045	Low T: Yes	1044	0.01
	Microcryst-melt (resorbed)	8	1 / 1	An ₄ Ab ₈₈ Or ₈	1025	Low T: Yes	1009	0.45
	Repeat different part of crystal	8	1 / 2	An ₄ Ab ₈₈ Or ₈	1023	Low T: Yes	1002	0.58
	Repeat different part of crystal	8	1 / 3	An ₅ Ab ₈₈ Or ₇	1013	Low T: Yes	967	1.33
Lava / 828C	Microcryst-melt	1	1 / 3	An ₁₇ Ab ₈₁ Or ₂	999	Low T: Yes	882	3.69
	Microcryst-melt	5	1 / 5	An ₄ Ab ₈₅ Or ₁₀	1037	Low T: Yes	1024	0.35
	Macrocryst-melt	5	1 / 7	An ₄ Ab ₈₆ Or ₁₀	1038	Low T: Yes	1032	0.17
	Macrocryst-melt (rim)	5	1 / 8	An ₄ Ab ₈₅ Or ₁₁	1044	Low T: Yes	1050	-0.15
	Microcryst clot-melt	6	1 / 3	An ₁₄ Ab ₈₃ Or ₃	998	Low T: Yes	886	3.51
	Microcryst clot-melt	6	1 / 4	An ₁₃ Ab ₈₄ Or ₃	996	Low T: Yes	887	3.44
	Macrocryst-melt (rim)	7	1 / 2	An ₅ Ab ₈₆ Or ₁₀	1031	Low T: Yes	1089	-0.84
	Microcryst-melt (fragment)	8	1 / 8	An ₆ Ab ₈₅ Or ₉	1022	Low T: Yes	1008	0.64
	Microcryst-melt	12	1 / 7	An ₄ Ab ₈₆ Or ₁₀	1038	Low T: Yes	975	1.36
	Macrocryst-melt (resorbed)	13	1 / 1	An ₄ Ab ₈₆ Or ₁₀	1040	Low T: Yes	1032	0.18
	Macrocryst-melt (resorbed)	13	1 / 4	An ₄ Ab ₈₇ Or ₁₀	1039	Low T: Yes	1038	0.05
	Macrocryst-melt (resorbed)	15	1 / 1	An ₄ Ab ₈₆ Or ₁₀	1038	Low T: Yes	1039	0

Table 3.5 contd. Output from iterative calculation of T & H ₂ O using Eq. 23 from Putirka (2008) & Eq. 23 of Waters and Lange (2015), for plag-melt pairs.								
Unit / Sample	Type	Site	Point	Crystal Comp.	Putirka T (°C)	Pass Eqbm?	Iterative T (°C)	H ₂ O (wt%)
Lava / 828C	Microcryst-melt	15	1 / 3	An ₃ Ab ₈₆ Or ₁₁	1048	Low T: Yes	1032	0.15
	Macrocryst-melt (resorbed)	17	1 / 1	An ₄₀ Ab ₅₉ Or ₁	1027	Low T: Yes	912	3.43
	Macrocryst-melt (resorbed)	17	1 / 2	An ₃₇ Ab ₆₁ Or ₁	1025	Low T: Yes	910	3.44
	Macrocryst-melt	18	1 / 5	An ₇ Ab ₈₈ Or ₅	1000	Low T: Yes	919	2.47
	Macrocryst-melt	19	1 / 3	An ₇ Ab ₈₈ Or ₅	1001	Low T: Yes	921	2.45
	Macrocryst-melt	20	1 / 1	An ₄ Ab ₈₇ Or ₈	1025	Low T: Yes	994	0.85
	Macrocryst-melt (core)	21	1 / 1	An ₄ Ab ₈₅ Or ₁₁	1045	Low T: Yes	1052	-0.2
	Macrocryst-melt (rim)	21	1 / 2	An ₅ Ab ₈₅ Or ₉	1028	Low T: Yes	997	0.87
	Microcryst-melt	22	1 / 4	An ₄ Ab ₈₇ Or ₉	1030	Low T: Yes	1008	0.6
	Microcryst-melt	22	1 / 5	An ₆ Ab ₈₅ Or ₉	1023	Low T: Yes	977	1.3
	Macrocryst-melt (rim)	23	1 / 1	An ₃₀ Ab ₆₉ Or ₁	1016	Low T: Yes	899	3.58
	Macrocryst-melt (mid)	23	1 / 2	An ₅₀ Ab ₄₉ Or ₁	1034	Low T: Yes	921	3.36
	Macrocryst-melt (core)	23	1 / 3	An ₄₆ Ab ₅₃ Or ₁	1032	Low T: Yes	918	3.37
	Macrocryst-melt (core)	24	1 / 1	An ₄₃ Ab ₅₆ Or ₁	1030	Low T: Yes	916	3.39
	Macrocryst-melt (mid)	24	1 / 2	An ₅₃ Ab ₄₆ Or ₁	1036	Low T: Yes	922	3.36
	Microcryst-melt	7	1 / 1	An ₃ Ab ₈₅ Or ₁₂	1056	High T: Yes	1089	-0.84
	Macrocryst-melt (resorbed)	16	1 / 1	An ₅ Ab ₈₆ Or ₉	1061	High T: Yes	923	4
Microcryst-melt	21	1 / 6	An ₃ Ab ₈₄ Or ₁₃	1058	High T: Yes	1094	-0.9	
Dome / 871B	Microlite-melt	2	1 / 8	An ₈ Ab ₈₇ Or ₄	1016	Low T: Yes	946	2.06
	Microlite-melt	5	1 / 9	An ₇ Ab ₈₅ Or ₉	1034	Low T: Yes	993	1.14
	Microlite cluster-melt	11	1 / 3	An ₂₀ Ab ₇₅ Or ₅	1028	Low T: Yes	934	2.77
	Microlite-melt	3	1 / 10	An ₄ Ab ₈₅ Or ₁₁	1058	High T: Yes	1076	-0.46
	Microcryst-melt	4	1 / 7	An ₆ Ab ₈₄ Or ₁₀	1045	Low T: Yes	1029	0.43
	Macrocryst-melt (rim)	12	1 / 3	An ₄ Ab ₈₆ Or ₉	1045	Low T: Yes	1039	0.17
	Microcryst-melt	12	1 / 8	An ₅ Ab ₈₆ Or ₉	1042	Low T: Yes	1027	0.4
	Microcryst-melt	12	1 / 9	An ₆ Ab ₈₅ Or ₁₀	1043	Low T: Yes	1023	0.53
	Macrocryst-melt (core)	13	1 / 1	An ₅ Ab ₈₅ Or ₉	1043	Low T: Yes	1027	0.42

Table 3.5 Contd. Output from iterative calculation of T & H ₂ O using Eq. 23 from Putirka (2008) & Eq. 23 of Waters and Lange (2015), for plag-melt pairs.								
Unit / Sample	Type	Site	Point	Crystal Comp.	T (°C)	Pass Eqbm?	Iterative T (°C)	H ₂ O (wt%)
Dome / 871B	Microcryst-melt	14	1 / 10	An ₄ Ab ₈₇ Or ₉	1042	Low T: Yes	1031	0.29
	Microcryst-melt	16	1 / 1	An ₄ Ab ₈₅ Or ₁₁	1034	Low T: Yes	928	3.11
	Macrocryst-melt	17	1 / 2	An ₃₄ Ab ₆₅ Or ₁	1037	Low T: Yes	932	3.07
	Microcryst-melt	17	1 / 11	An ₂₉ Ab ₇₀ Or ₂	1028	Low T: Yes	921	3.18
	Microcryst-melt	3	1 / 4	An ₅ Ab ₈₄ Or ₁₁	1054	High T: Yes	1060	-0.14
	Macrocryst-melt (resorbed)	10	1 / 1	An ₄ Ab ₈₅ Or ₁₁	1054	High T: Yes	1065	-0.29
Unit 9 / 829A_6b	Macrocryst-melt (fragment)	7	1 / 1	An ₄₆ Ab ₅₄	1006	Low T: Yes	905	3.1
	Macrocryst-melt (fragment)	7	1 / 8	An ₄₆ Ab ₅₃	1006	Low T: Yes	905	3.1
Unit 4 / 844C_2	Microlite-melt	4	1 / 2	An ₃ Ab ₈₆ Or ₁₁	1058	High T: Yes	1044	0.37
	Macrocryst-melt	1	1 / 1	An ₄ Ab ₈₄ Or ₁₂	1014	Low T: Yes	1061	-1.27
	Macrocryst-melt	1	1 / 2	An ₄ Ab ₈₅ Or ₁₁	1001	Low T: Yes	1057	-1.51
	Macrocryst-melt (resorbed)	3	1 / 1	An ₃ Ab ₈₆ Or ₁₀	1012	Low T: Yes	1020	-0.2
	Macrocryst-melt (in lithic)	4	1 / 1	An ₅ Ab ₈₆ Or ₉	1035	Low T: Yes	972	1.79
	Microlite-melt (in lithic)	6	1 / 4	An ₄ Ab ₈₆ Or ₁₀	1041	Low T: Yes	991	1.4
	Microlite-melt (in lithic)	6	1 / 6	An ₄ Ab ₈₇ Or ₉	1035	Low T: Yes	976	1.68
	Macrocryst-melt (resorbed, lithic)	8	1 / 1	An ₁₂ Ab ₈₆ Or ₂	997	Low T: Yes	851	4.69
	Macrocryst-melt (resorbed, lithic)	8	1 / 2	An ₂₆ Ab ₇₃ Or ₁	1015	Low T: Yes	862	4.84
	Macrocryst-melt (resorbed, lithic)	8	1 / 3	An ₂₁ Ab ₇₇ Or ₂	1009	Low T: Yes	855	4.89
	Macrocryst-melt (resorbed, lithic)	8	1 / 4	An ₂₂ Ab ₇₇ Or ₂	1009	Low T: Yes	856	4.89
	Macrocryst-melt (resorbed, lithic)	8	1 / 6	An ₇ Ab ₈₆ Or ₇	1016	Low T: Yes	912	3.15
	Macrocryst-melt (resorbed, lithic)	8	1 / 8	An ₂₆ Ab ₇₃ Or ₁	1015	Low T: Yes	862	4.82
	Macrocryst-melt (core)	9	1 / 1	An ₂₂ Ab ₇₆ Or ₂	977	Low T: Yes	860	3.8
	Macrocryst-melt (rim)	9	1 / 2	An ₈ Ab ₈₈ Or ₄	968	Low T: Yes	877	2.94
	Microcryst-melt	9	1 / 3	An ₄ Ab ₈₂ Or ₄	1029	Low T: Yes	1058	-0.77
	Macrocryst-melt	1	1 / 3	An ₄ Ab ₈₄ Or ₁₂	1056	High T: Yes	1032	0.66
Unit 3 / 844A_6	Microlite-melt	12	1 / 1	An ₃ Ab ₈₂ Or ₁₅	1064	High T: Yes	1079	-0.39

The Mollo *et al.*, (2015) feldspar-melt hygrometer was then applied to all K-feldspar-melt pairs to model H₂O content in the Echo Canyon eruption deposits. In the dome and lava samples matrix glass was absent or the area too small to be analysed by electron microprobe so averaged whole rock compositions from XRF analyses were used as a substitute for melt compositions. As total micro/macrocryst content is <5% this is assumed to be a reasonable approximation. Pressure was kept consistent at 250 MPa and each pair was run with their modelled Putirka (2008) temperature. To check for equilibrium between crystals and melt, the measured $K_{\text{Or-Ab}}$ was plotted against the predicted value as presented in Mollo *et al.*, (2015) – see Fig. 3.17. The data are compared to a line of $\text{measured } K_{\text{Or-Ab}} = \text{predicted } K_{\text{Or-Ab}}$ with upper and lower bounds of “equilibrium” set at $\pm 5\%$, this is within the % error on electron microprobe analyses for minerals and glass. To account for the error associated with the Putirka (2008) thermometer for alkali-feldspars ($\pm 23^\circ\text{C}$), the input temperature for each pair was varied by $\pm 23^\circ\text{C}$ and checked against the upper and lower “equilibrium” bounds of $\pm 5\%$. This temperature change did not push any analyses that were already classed as in equilibrium outside of the equilibrium range.

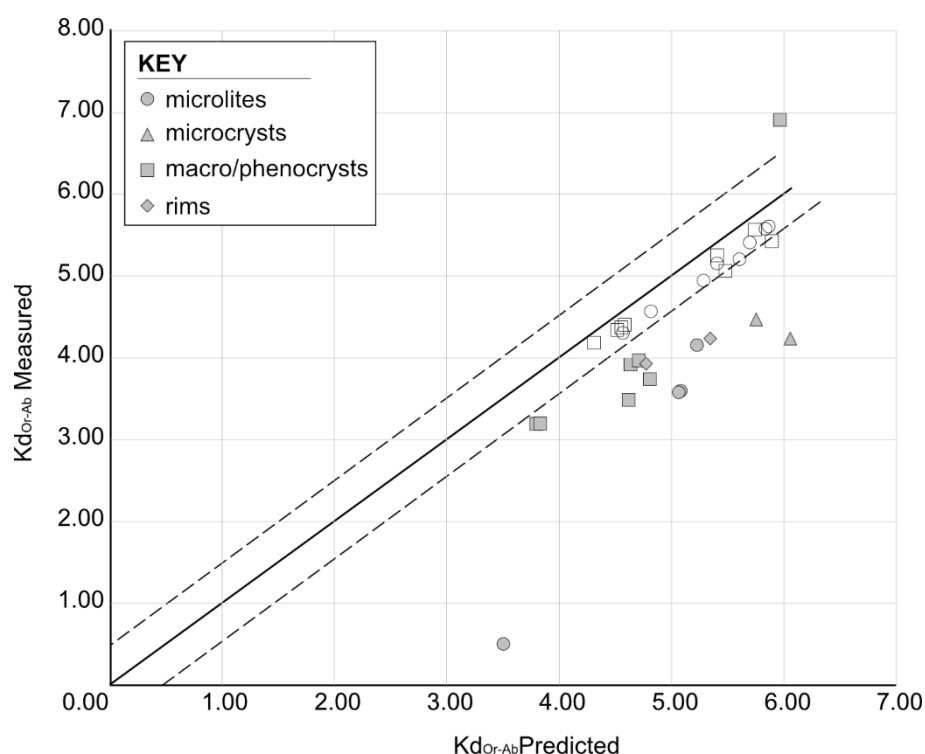


Fig 3.17: Plot showing predicted vs measured $K_{\text{Or-Ab}}$ for crystal and glass pairs from the Echo Canyon eruption deposits. Solid black line shows predicted = measured, upper and lower dashed lines show limits for equilibrium (set at $\pm 5\%$) based on upper and lower error limits of electron microprobe data and calculated temperatures. Data points on or within dashed lines are classified as equilibrium analyses – open symbols.

Table 3.6: Modelled temperatures from Putirka (2008) and H ₂ O contents using the Mollo <i>et al.</i> , (2015) K-feldspar-melt hygrometer							
Unit / Sample	Type	Site	Point	Crystal Comp	T (°C)	H ₂ O (wt%)	Eqbm?
OBP / 827C_6	Microlite-melt	5	1/7	An ₄ Ab ₇₅ Or ₂₁	746	2.81	No
	Microcryst-melt	7	1/5	An ₅ Ab ₇₇ Or ₁₈	750	2.86	No
	Macrocryst-melt	13	1/1	Ab ₇₈ Or ₂₂	751	6.86	No
	Microlite-melt	17	1/6	An ₄ Ab ₇₅ Or ₂₁	746	2.87	No
Lava / 828C	Macrocryst-melt	9	1/1	An ₁ Ab ₇₈ Or ₂₂	821	6.38	No
	repeat of above	9	1/2	Ab ₇₄ Or ₂₆	811	6.84	No
	repeat of above	9	1/8	An ₁ Ab ₇₈ Or ₂₂	821	6.37	No
	Macrocryst-melt	10	1/1	Ab ₇₄ Or ₂₆	812	6.78	No
	Macrocryst-melt (rim)	24	1/3	An ₂ Ab ₇₇ Or ₂₂	818	4.10	No
Dome / 871B	Macrocryst-melt	1	1/2	An ₁ Ab ₇₇ Or ₂₁	795	6.07	No
	Macrocryst-melt (rim)	13	1/3	An ₁ Ab ₈₀ Or ₂₀	802	4.72	No
	Microlite-melt	16	1/2	An ₁ Ab ₈₀ Or ₂₀	801	2.83	No
	Microcryst-melt	16	1/8	An ₂ Ab ₇₉ Or ₁₉	801	5.40	No
Unit 9 / 829A_6b	Macrocryst-melt	1	1/1	An ₂ Ab ₇₉ Or ₁₉	875	5.77	Yes
	Macrocryst-melt	1	1/2	An ₁ Ab ₇₅ Or ₂₃	865	6.46	Yes
Unit 4 / 844C_2	Macrocryst-melt inclusion	14	1/2	An ₂ Ab ₈₂ Or ₁₆	858	8.23	No
	Macrocryst-melt inclusion 2	14	1/2	An ₂ Ab ₈₀ Or ₁₈	887	5.37	Yes
	Macrocryst-melt	15	1/1	An ₂ Ab ₈₀ Or ₁₈	887	5.34	Yes
	Macrocryst-melt	15	1/2	An ₂ Ab ₇₉ Or ₁₉	865	5.83	Yes
Unit 3 / 844A_6	Macrocryst-melt	1	1/1	An ₁ Ab ₇₇ Or ₂₂	853	6.87	Yes
	Macrocryst-melt (fragment)	1	1/2	An ₁ Ab ₇₇ Or ₂₂	852	6.60	Yes
	Macrocryst-melt	2	1/1	An ₁ Ab ₇₆ Or ₂₂	852	6.79	Yes
	Microlite-melt	11	1/1	An ₂ Ab ₇₉ Or ₁₉	861	4.51	Yes
	Microlite-melt	11	1/2	An ₃ Ab ₇₇ Or ₂₀	920	2.46	Yes
	Macrocryst-melt	11	1/3	An ₂ Ab ₈₀ Or ₁₈	811	6.52	Yes

Table 3.6 Contd. Modelled temperatures from Putirka (2008) and H ₂ O contents using the Mollo <i>et al.</i> , (2015) K-feldspar-melt hygrometer							
Unit / Sample	Type	Site	Point	Crystal Comp	T (°C)	H₂O (wt%)	Eqbm?
Unit 3 / 844A_6. 1.9	Macrocryst-melt	11	1/4	An ₂ Ab ₈₀ Or ₁₈	892	5.56	Yes
	Microlite-melt	12	1/2	An ₃ Ab ₇₈ Or ₁₉	867	3.13	Yes
	Microlite-melt	12	1/3	An ₂ Ab ₇₇ Or ₂₁	885	5.03	Yes
	Microlite-melt	14	1/1	An ₂ Ab ₇₉ Or ₁₉	835	5.79	Yes
	Microlite-melt	14	1/2	An ₂ Ab ₇₅ Or ₂₂	886	3.12	Yes
Unit 1 / 842A_35b	Microlite-melt	4	1/1	Ab₇₃Or₂₆	1047	4.58	No

All modelled H₂O values are listed alongside Putirka (2008) temperatures in table 3.6. Crystal-melt pairs that fall within upper and lower limits of error are deemed to be in equilibrium and are highlighted. Equilibrium phenocryst- and microcryst-melt pairs produced modelled H₂O contents of 5.34 – 6.87wt% and equilibrium microlite-melt pairs gave H₂O contents of 2.46 – 5.79wt%. One phenocryst (844C_2 sites 14 and 15) was run twice (for temperature and H₂O), once with a melt composition from the matrix glass and once with melt composition from apparent melt inclusion measurements. Both plotted within the equilibrium range with H₂O values within 0.3wt% of each other. The range seen in the micro/phenocryst-melt pairs is consistent with K-feldspar-melt hygrometry for other trachytic melts in the EFC (White Horse = 5.5wt%, Cricket Valley = 5.2wt%) (Chamberlain *et al.*, 2019).

3.3.4 Variations in vesicle shape

By quantitatively describing the vesicle shapes within each textural group we can more robustly identify the relative dominance of various factors affecting a population than via qualitative inspection of images. This can then be used to interpret how physical conditions in the ascending melt impacted the formation and evolution of vesicle textures as the eruption progressed.

Density plots of regularity vs solidity, roundness/regularity/solidity vs circularity and particle area vs aspect ratio of the best fit ellipse were generated for each of the six samples analysed. The results for each unit are plotted side by side grouped by parameter type in [Appendix 2.4, Figs. 2.4 – 2.8] to allow comparison between the units for each set of interacting shape factors. Variations in trends in each plotted pair of shape parameters, organised by textural group and stratigraphic location, are displayed in Figs. 3.18 – 3.24 and are summarised in table 3.7. For sample 827C_6 of the OBP, two sets of images were collected and analysed. One from high microlite crystallinity regions (HX – 31%), and one from low microlite crystallinity regions (LX – 1.3%). The density plots show variation in dominant and extreme vesicle shape characteristics between stratigraphic units and macro-textural groups identified within the Echo Canyon Deposits. Table 3.8 shows the vesicularities, number of vesicles, total area analysed, median circular particle diameter,

median shape factor (Ω) and median $1 - (\Omega)$ for each set of analyses. In the following sections, vesicle shapes are described in the context of these parameters to identify relationships between elongation, morphological roughness and textural roughness for each textural group at a given stratigraphic location. This information is correlated with the abundance of each textural group across the EC units reported in Chapter 2 - and Fig. 3.1 - to extrapolate and infer the major and minor controls on vesicle shape within each unit of the EC eruption deposits.

Macro-vesicular Equant (842A_63 – Unit 1)

Plots of vesicle shape from the macro-vesicular equant clast from Unit 1 (Fig. 3.18A – E and table 3.7) show a population of near-circular cross-sections with limited particle-scale protrusions (morphological roughness) and very few finer-scale irregularities (e.g., those formed by preservation of retracting vesicle walls – textural roughness) as shown in the binarized image in Fig. 3.18F. Most vesicles have an area of $100 - 1000 \mu\text{m}^2$ with an aspect ratio of 1:1 – 1.5. Few vesicles extend to a ratio of 1:2 and there is a very minor population of vesicles with an area of $<10 \mu\text{m}^2$ (Fig. 3.18E). There is no obvious connection between vesicle size and elongation. Where particles deviate from circular, elongation is the dominant factor, though generally not extreme, in keeping with the macro-textural observations for this clast.

Table 3.7: Summary of vesicle shape data from Figs.3.18 – 3.24.

Textural Group / Unit (Fig.)	Density plot results					Major / minor controls on vesicle shape
	Regularity vs Circularity (Re/C)	Roundness vs Circularity (Ro/C)	Solidity vs Circularity (S/C)	Solidity vs Regularity (S/Re)	Area vs Aspect ratio (A/AR)	
<p>Macro-Equant / Unit 1</p> <p>(Fig. 3.18)</p>	<ul style="list-style-type: none"> Data densest at high values Low textural roughness 	<ul style="list-style-type: none"> Data densest at moderate – high values At low values roundness ≈ circularity 	<ul style="list-style-type: none"> Data densest at high values At low values, solidity ≠ circularity 	<ul style="list-style-type: none"> Data densest at high values Low morphological & Textural roughness 	<ul style="list-style-type: none"> Major population at 100 – 1000 μm² & AR 1:1 – 1.5 Minor population at <10 μm & AR 1:2 	<p>Major: Elongation though elongation not extreme (Ro/C)</p> <p>Minor: Morphological roughness not as significant as elongation (S/Re & S/C). Low abundance, more elongate population (A/AR). Negligible textural roughness (Re/C)</p>
<p>Micro-Equant / Unit 2</p> <p>(Fig. 3.19)</p>	<ul style="list-style-type: none"> Generally, very high regularity No strong textural roughness 	<ul style="list-style-type: none"> Densest regions extend to high and low values. Population at low circularity – high roundness At low values circularity ≈ roundness 	<ul style="list-style-type: none"> High data density across wide range of values At low values, solidity ≈ circularity 	<ul style="list-style-type: none"> Higher proportion extending to lower values than Macro Eq. Data densest at high values Morph/textural roughness = minor 	<ul style="list-style-type: none"> Major population at ~100 – 1000 μm² & AR 1:1 – 1:2 Minor population at < 100 μm² & AR 1:3 	<p>Major: Elongation though elongation not extreme (Ro/C)</p> <p>Minor: Minor population of small, more elongate vesicles (A/AR). Morphological roughness exerts a minor control (Ro/C & S/C) Textural roughness negligible (Re/C)</p>

Table 3.7 contd.: Summary of vesicle shape data from Figs. 3.18 – 3.24.						
Textural Group / Unit (Fig.)	Density plot results					Major / minor controls on vesicle shape
	Regularity vs Circularity (Re/C)	Roundness vs Circularity (Ro/C)	Solidity vs Circularity (S/C)	Solidity vs Regularity (S/Re)	Area vs Aspect ratio (A/AR)	
Dense / Unit 4 (Fig. 3.20)	<ul style="list-style-type: none"> Data densest at high circularities Low circularity ≠ low regularity 	<ul style="list-style-type: none"> High proportion of data across wide range of values Roundness ≈ circularity Minor population at low circularity, high roundness 	<ul style="list-style-type: none"> At low values, solidity less similar to circularity than in micro-equant sample 	<ul style="list-style-type: none"> Data densest at high values Lacking textural /morphological roughness 	<ul style="list-style-type: none"> Greater proportion with AR > 1:2 than equant samples. AR up to 1:5 Highest AR in vesicles with area 10 – 1000 μm² 	<p>Major: Elongation main factor (Ro/C) Elongation more extensive than in Macro/micro equant samples (A/AR).</p> <p>Minor Morphological roughness less important than in micro-equant clast (S/C). Textural roughness least important (Re/C & S/Re).</p>
Macro-Elongate / Unit 9 (Fig. 3.21)	<ul style="list-style-type: none"> Data densest at high regularity. Low regularity ≠ low circularity 	<ul style="list-style-type: none"> Data densest at ~0.5 and lower. Roundness ≈ circularity 	<ul style="list-style-type: none"> Solidity ≠ circularity Morphological roughness less important than elongation 	<ul style="list-style-type: none"> Data densest at high values Lacking textural / morphological roughness 	<ul style="list-style-type: none"> Maximum AR is 1:5, high density data with AR > 1:2 Vesicles at area ≈ 100 μm² have higher ARs 	<p>Major: Elongation is dominant, and significant proportion are elongate (Ro/C) More vesicles are elongate than dense sample.</p> <p>Minor: Morphological roughness less important than elongation (S/C) but more important than textural roughness (Re/C)</p>

Table 3.7contd.: Summary of vesicle shape data from Figs. 3.18 – 3.24.

Textural Group / Unit (Fig.)	Density plot results					Major / minor controls on vesicle shape
	Regularity vs Circularity (Re/C)	Roundness vs Circularity (Ro/C)	Solidity vs Circularity (S/C)	Solidity vs Regularity (S/Re)	Area vs Aspect ratio (A/AR)	
Dense LX / OBP (Fig. 3.22)	<ul style="list-style-type: none"> Data densest at high regularity values Regularity ≠ circularity at low circularity values 	<ul style="list-style-type: none"> One group: roundness ≈ circularity at low values One group: roundness > circularity at low values 	<ul style="list-style-type: none"> Solidity correlates with but ≠ circularity. 	<ul style="list-style-type: none"> Data extends to lower values (except micro-equant) Densest at high values 	<ul style="list-style-type: none"> Data dense at area ≈ 1000 μm² and ≈ 10,000 μm² AR 1:1.5 dominant, smaller population at AR > 1:3 	<p>Major: In one group elongation = dominant factor (Ro/C). More complex vesicle shapes (S/Re). Smaller population more elongate (A/AR)</p> <p>Minor One population where morphological roughness is the dominant factor, though not as dominant as elongation (Ro/C & S/C). Textural roughness least important (Re/C)</p>
Dense HX / OBP (Fig. 3.23)	<ul style="list-style-type: none"> Densest at high regularity, low circularity Regularity correlates with but ≠ circularity 	<ul style="list-style-type: none"> Dominant population at low circularity with higher roundness 	<ul style="list-style-type: none"> Densest at moderate – high solidity, low circularity 	<ul style="list-style-type: none"> Higher proportion at low values than other samples Densest at high values Lower low values than LX 	<ul style="list-style-type: none"> Data dense at area ≈ 1000 μm² and ≈ 10,000 μm² Smaller population extends to higher AR, max ~1:5 	<p>Major: More complex vesicle shapes (S/C) & greater influence of morphological & textural roughness than in cone (Re/C & S/Re). Small vesicles = most elongate (A/AR).</p> <p>Minor: Elongation has small impact but not main factor (Ro/C)</p>
Macro-Equant / OBP (Fig. 3.24)	<ul style="list-style-type: none"> Data dense at high regularity. Regularity ≠ circularity at low circularity. 	<ul style="list-style-type: none"> Roundness ≈ circularity Minor population at high roundness, low circularity. 	<ul style="list-style-type: none"> Densest at high solidity. Second population at lower solidity, correlates with but ≠ circularity 	<ul style="list-style-type: none"> Data densest at high values 	<ul style="list-style-type: none"> Area values larger than in cone. Highest AR at ~ 100 μm² & ~ 1000 μm². More vesicles have AR > 1:2 than in cone Eq.Macro 	<p>Major: Lacks complex vesicle networks (S/Re). Elongation a dominant factor. Two size populations of high AR vesicles. Heterogenous population.</p> <p>Minor: Morphological roughness impacts some vesicles (Ro/C). Textural roughness negligible (Re/C).</p>

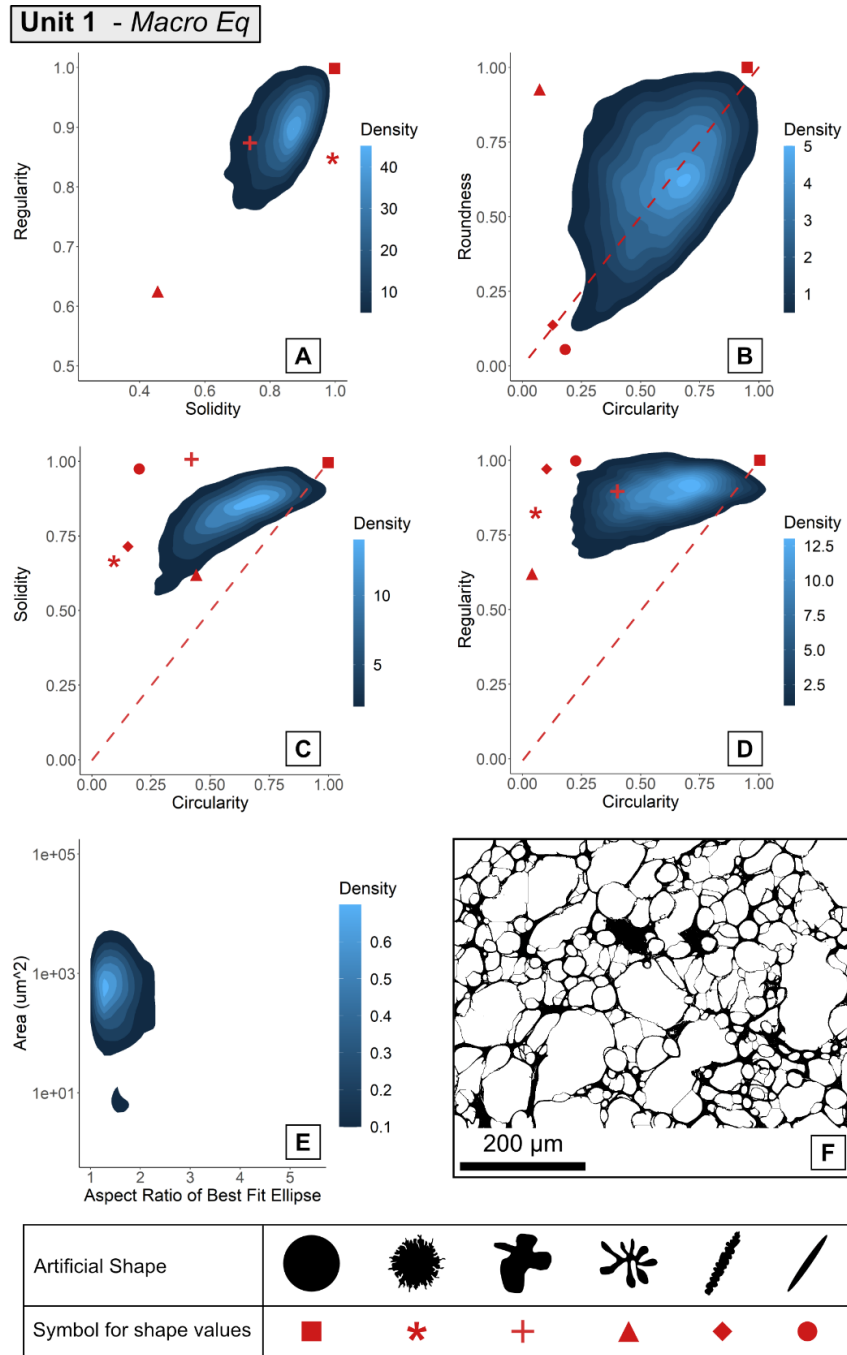


Fig. 3.18 – Density plots of shape parameters for vesicles from sample 842A_63, a macro-vesicular equant (Macro – Eq) clast from Unit 1 of the Echo Canyon deposits. **A:** regularity data plotted against solidity with values plotted (red symbols) for four artificially generated vesicle shapes as displayed in the key. **B:** roundness data plotted against circularity with values plotted (red symbols) for four artificially generated vesicle shapes as displayed in the key, red dashed line represents circularity = roundness. **C:** solidity data plotted against circularity data with values plotted (red symbols) for six artificially generated vesicle shapes as displayed in the key, red dashed line represents solidity = circularity. **D:** regularity data plotted against circularity with values plotted (red symbols) for six artificially generated vesicle shapes as displayed in the key, red dashed line represents regularity = circularity. **E:** particle area data plotted against aspect ratio of the best fit ellipse as calculated using ImageJ. **F:** example binarized image post-correction for missing / broken vesicle walls showing vesicle textures for this sample.

Micro-vesicular Equant (843A_4 – Unit 2)

Plots of vesicle shape from the micro-vesicular equant clast from Unit 2 (Fig. 3.19A – E and table 3.7) reflect a much more heterogeneous vesicle population than in the macro-vesicular equant sample (842A_63), as displayed in Fig. 3.19F. Vesicle elongation and particle-scale protrusions (morphological roughness) are both responsible for deviations from perfectly circular cross-sections. Morphological roughness has a greater influence on vesicle shape than in the macro-vesicular equant sample, but elongation is still the dominant factor. Again, high regularity values associated with low circularities indicates textural roughness is not an important factor contributing to vesicle shape (Fig. 3.19D). The maximum aspect ratio in the micro-vesicular equant sample is 1:3 showing that in a small subset of vesicles, elongation is more pronounced than in the macro-vesicular equivalent. These more elongate vesicles are typically an order of magnitude smaller than the dominant vesicle population (Fig. 3.19E).

Dense (844C_10 – Unit 4)

For the dense clast from Unit 4, the data presented in Fig. 3.20A – E and table 3.7 reflect a vesicle population strongly impacted by more extreme elongation than in the macro and micro-vesicular equant samples from units 1 and 2. Aspect ratios extend to 1:5, higher than in macro and micro-vesicular equant clasts and the highest aspect ratios are seen in vesicles with areas of 10 – 1000 μm^2 (Fig. 3.20E). Elongation is the most dominant factor impacting vesicle shape, though morphological roughness also exerts an influence - though to a lesser degree - as reflected in the particle scale protrusions visible in parts of Fig. 3.20F.

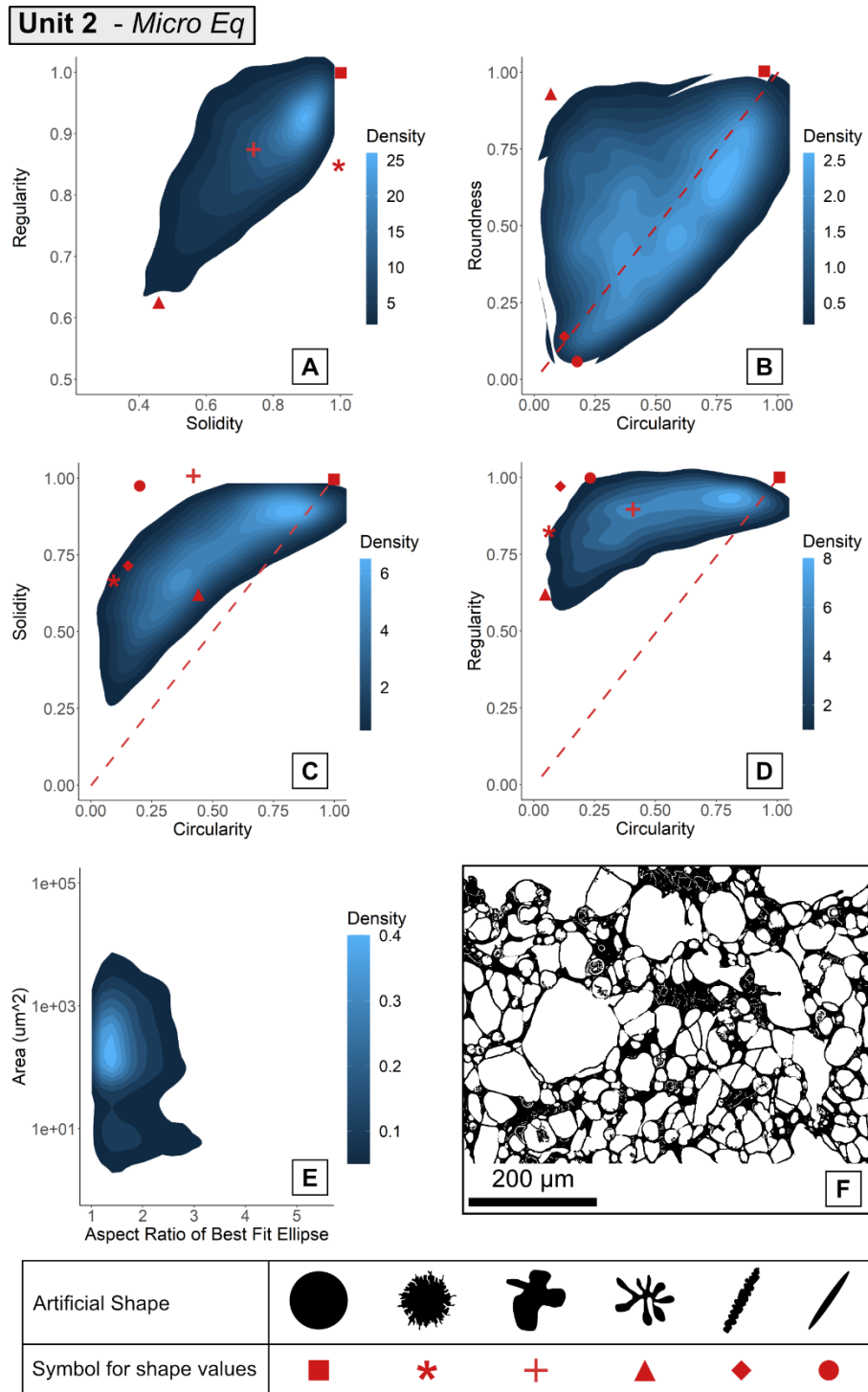


Fig. 3.19 – Density plots of shape parameters for vesicles from sample 843A_4, a micro-vesicular equant (Micro – Eq) clast from Unit 2 of the Echo Canyon deposits. **A:** regularity data plotted against solidity with values plotted (red symbols) for four artificially generated vesicle shapes as displayed in the key. **B:** roundness data plotted against circularity with values plotted (red symbols) for four artificially generated vesicle shapes as displayed in the key, red dashed line represents circularity = roundness. **C:** solidity data plotted against circularity data with values plotted (red symbols) for six artificially generated vesicle shapes as displayed in the key, red dashed line represents solidity = circularity. **D:** regularity data plotted against circularity with values plotted (red symbols) for six artificially generated vesicle shapes as displayed in the key, red dashed line represents regularity = circularity. **E:** particle area data plotted against aspect ratio of the best fit ellipse as calculated using ImageJ. **F:** example binarized image post-correction for missing / broken vesicle walls showing vesicle textures for this sample.

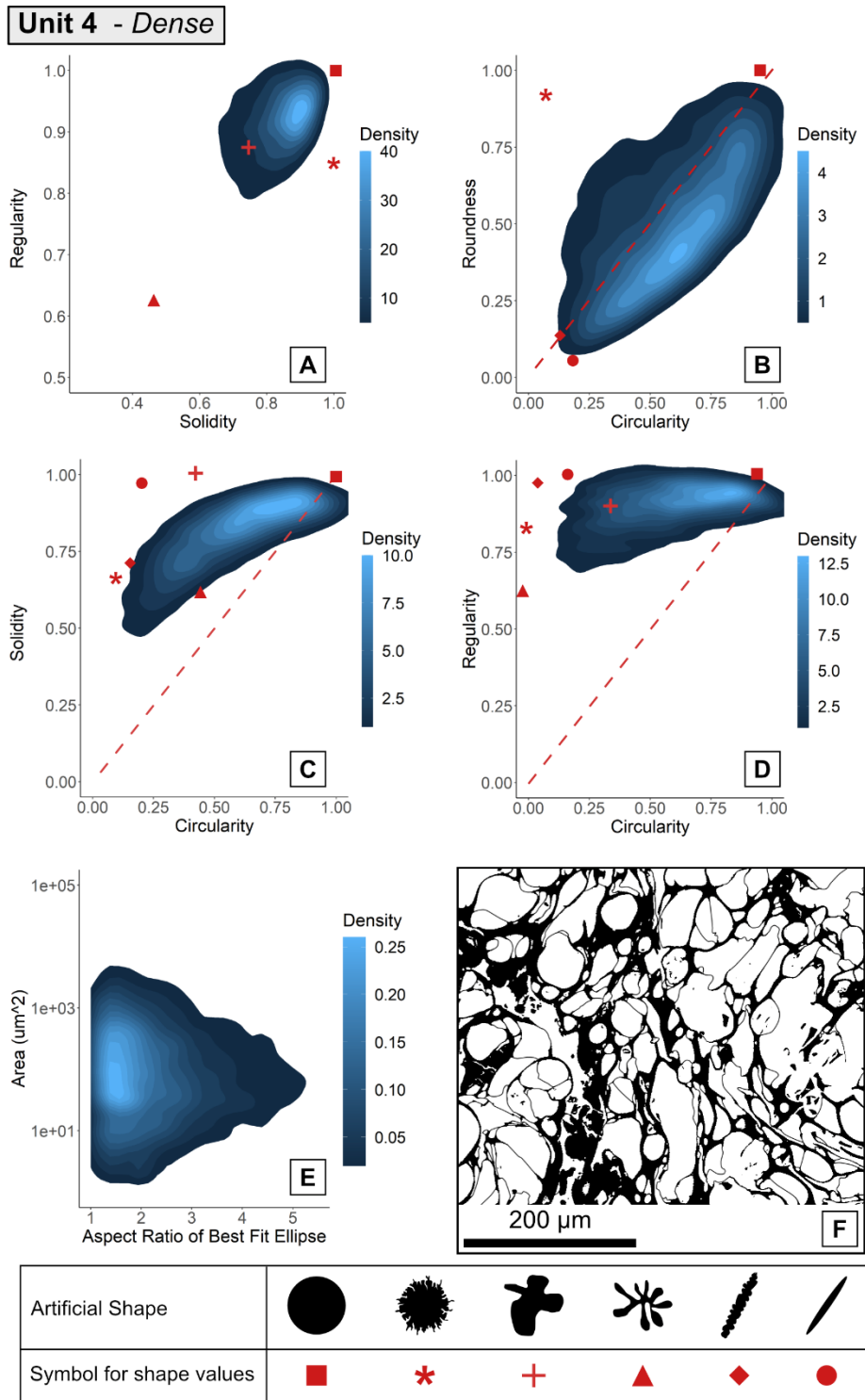


Fig. 3.20 – Density plots of shape parameters for vesicles from sample 844C_10, a dense clast from Unit 4 of the Echo Canyon deposits. **A:** regularity data plotted against solidity with values plotted (red symbols) for four artificially generated vesicle shapes as displayed in the key. **B:** roundness data plotted against circularity with values plotted (red symbols) for four artificially generated vesicle shapes as displayed in the key, red dashed line represents circularity = roundness. **C:** solidity data plotted against circularity data with values plotted (red symbols) for six artificially generated vesicle shapes as displayed in the key, red dashed line represents solidity = circularity. **D:** regularity data plotted against circularity with values plotted (red symbols) for six artificially generated vesicle shapes as displayed in the key, red dashed line represents regularity = circularity. **E:** particle area data plotted against aspect ratio of the best fit ellipse as calculated using ImageJ. **F:** example binarized image post-correction for missing / broken vesicle walls showing vesicle textures for this sample.

Macro-vesicular Elongate (829A_29a – Unit 9)

Shape data for the macro-vesicular elongate sample from Unit 9 (Fig. 3.21A – E and table 3.7) show a vesicle population strongly impacted by high degrees of elongation across all vesicle sizes (Fig. 3.21E). However, maximum elongation (aspect ratio 1:5) is restricted to vesicles with an area around 100 μm^2 . High values of solidity and regularity reflect a lack of morphologically complex vesicle networks within the sample, vesicle walls are still generally “smooth”. This is similar to the dense sample, where morphological roughness, aka particle-scale protrusions have lesser but discernible impact on vesicle shape than elongation, while textural roughness has a negligible impact. These features are reflected in the intensely elongated vesicles visible in Fig. 3.21F.

Dense LX (827C_6_LX – OBP)

In low crystallinity regions of the OBP dense clast, vesicle shape data (Figs. 3.22A – E and table 3.7) reveals a vesicle population quite different to that seen in the dense clast from the EC cone deposits (844C_10). Vesicles are more irregular and there is a more complex relationship between the influence of morphological and textural roughness and elongation (Figs, 3.22C and D). Particle-scale protrusions exert more of an influence over vesicle shape than small-scale protrusions (Fig. 3.22C vs D). Two vesicle populations are distinguishable, one just below 1000 μm^2 and a second at $\sim 10,000 \mu\text{m}^2$. Both populations are dominated by vesicles with an aspect ratio around 1:1.5 but the smaller population is more heterogeneous, containing a small number of vesicles with aspect ratios greater than 1:3. While the OBP LX regions have a lower microlite abundance than the HX regions of this sample, feldspar microlite content is higher (3.9%) than that of the dense sample from Unit 4 (< 1%). Vesicles in the OBP LX sample are larger but glass walls are thicker as can be seen when comparing Figs. 3.22E and F with 3.20E and F.

Unit 9 - Macro EI

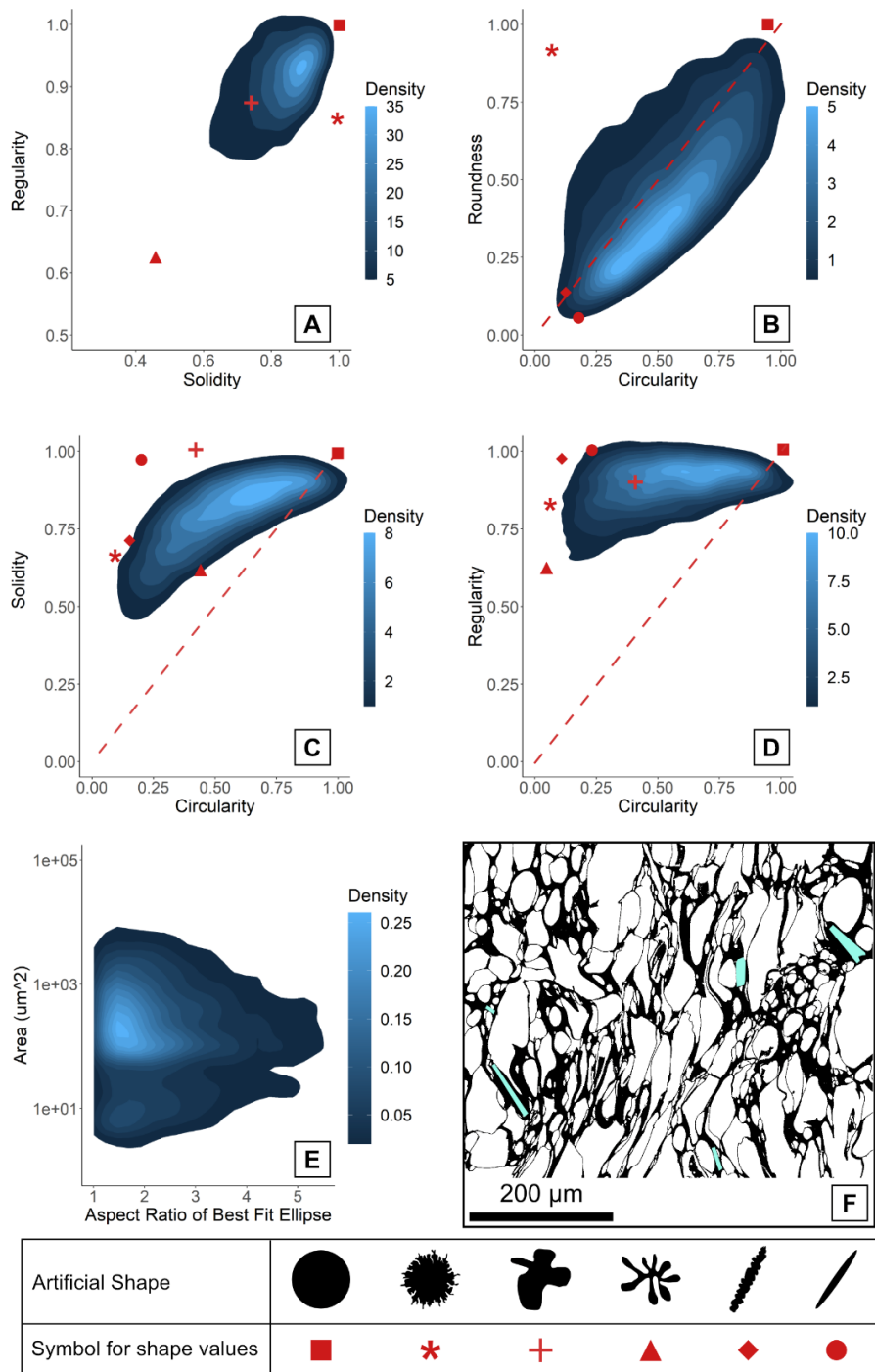


Fig. 3.21 – Density plots of shape parameters for vesicles from sample 829A_29a, a macro-vesicular elongate clast from Unit 9 of the Echo Canyon deposits. **A**: regularity data plotted against solidity with values plotted (red symbols) for four artificially generated vesicle shapes as displayed in the key. **B**: roundness data plotted against circularity with values plotted (red symbols) for four artificially generated vesicle shapes as displayed in the key, red dashed line represents circularity = roundness. **C**: solidity data plotted against circularity data with values plotted (red symbols) for six artificially generated vesicle shapes as displayed in the key, red dashed line represents solidity = circularity. **D**: regularity data plotted against circularity with values plotted (red symbols) for six artificially generated vesicle shapes as displayed in the key, red dashed line represents regularity = circularity. **E**: particle area data plotted against aspect ratio of the best fit ellipse as calculated using ImageJ. **F**: example binarized image post-correction for missing / broken vesicle walls showing vesicle textures for this sample, blue rectangles are feldspar crystals.

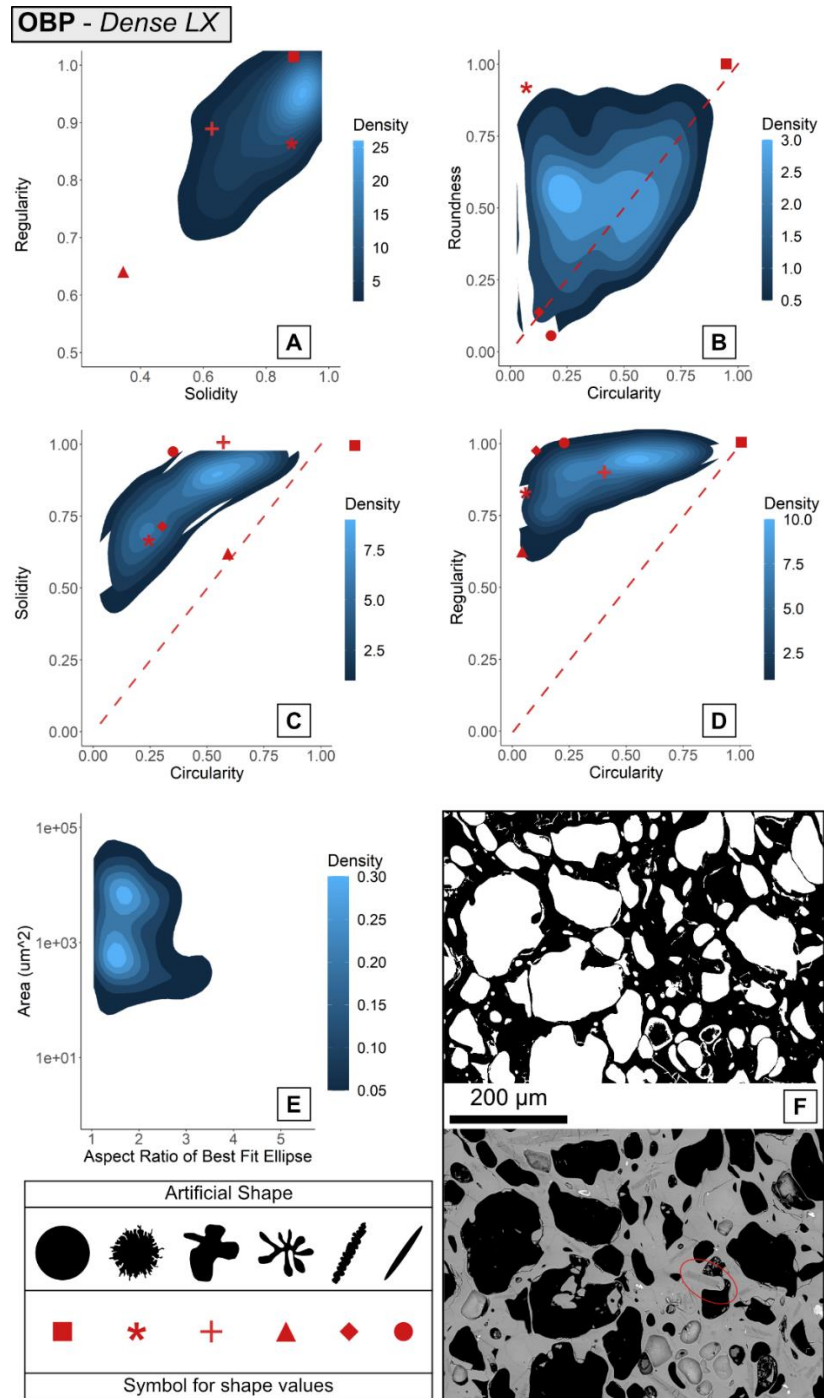


Fig. 3.22– Density plots of shape parameters for vesicles from low microlite content (LX) regions of sample 827C_6, a dense clast from the orange-brown pumice fall (OBP), the post-lava explosive phase of the Echo Canyon deposits. **A**: regularity data plotted against solidity with values plotted (red symbols) for four artificially generated vesicle shapes as displayed in the key. **B**: roundness data plotted against circularity with values plotted (red symbols) for four artificially generated vesicle shapes as displayed in the key, red dashed line represents circularity = roundness. **C**: solidity data plotted against circularity data with values plotted (red symbols) for six artificially generated vesicle shapes as displayed in the key, red dashed line represents solidity = circularity. **D**: regularity data plotted against circularity with values plotted (red symbols) for six artificially generated vesicle shapes as displayed in the key, red dashed line represents regularity = circularity. **E**: particle area data plotted against aspect ratio of the best fit ellipse as calculated using ImageJ. **F**: Upper - example binarized image post-correction for missing / broken vesicle walls showing vesicle textures for this sample. Lower – original backscattered scanning electron image showing vesicles (black), glass (pale grey) and microlites (darker grey rectangles) in LX regions of 827C_6. Red oval highlights crystal interference with bubble shape.

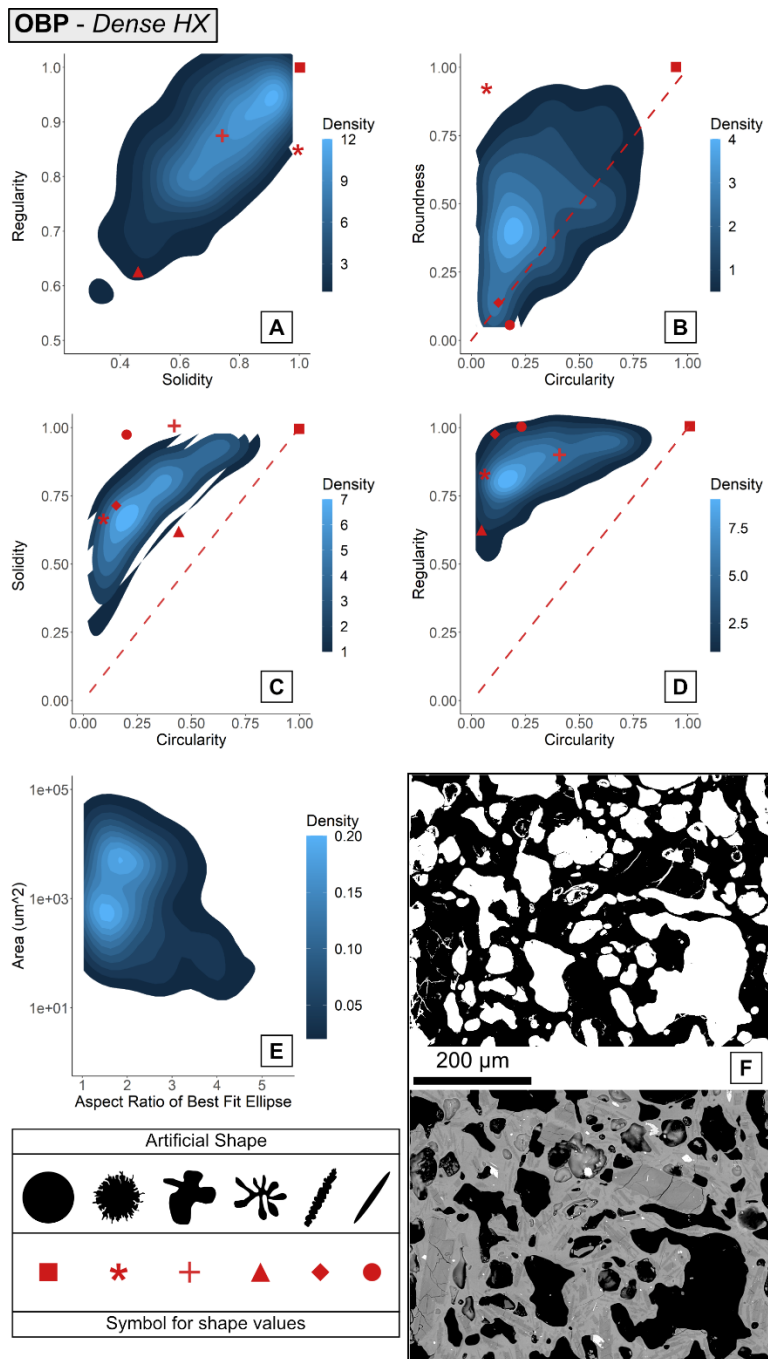


Fig. 3.23– Density plots of shape parameters for vesicles from high microlite content (HX) regions of sample 827C_6, a dense clast from the orange-brown pumice fall (OBP), the post-lava explosive phase of the Echo Canyon deposits. **A**: regularity data plotted against solidity with values plotted (red symbols) for four artificially generated vesicle shapes as displayed in the key. **B**: roundness data plotted against circularity with values plotted (red symbols) for four artificially generated vesicle shapes as displayed in the key, red dashed line represents circularity = roundness. **C**: solidity data plotted against circularity data with values plotted (red symbols) for six artificially generated vesicle shapes as displayed in the key, red dashed line represents solidity = circularity. **D**: regularity data plotted against circularity with values plotted (red symbols) for six artificially generated vesicle shapes as displayed in the key, red dashed line represents regularity = circularity. **E**: particle area data plotted against aspect ratio of the best fit ellipse as calculated using ImageJ. **F**: Upper - example binarized image post-correction for missing / broken vesicle walls showing vesicle textures for this sample. Lower – original backscattered scanning electron image showing vesicles (black), glass (pale grey) and microlites (darker grey rectangles) in HX regions of 827C_6.

Dense HX (827C_6_HX – OBP)

Vesicle shape data for the HX regions of the dense OBP clast (Figs. 3.23A – E and table 3.7) again shows distinct differences between the dense OBP sample and the cone deposit equivalent (844C_10). Differences in vesicle shape between the LX and HX regions of the dense OBP sample are, however, more subtle. As seen for the LX regions, two dominant vesicle populations can be identified in the plot of particle area against aspect ratio (Fig. 3.23E), one at just below 1000 μm^2 and a second at $\sim 10,000 \mu\text{m}^2$. For the HX regions, both populations extend to higher aspect ratios than in the LX regions but again the smaller population contains vesicles with the highest aspect ratios, $\sim 1:5$. The two populations visible in Fig. 3.23E are less easily distinguished using roundness, solidity and regularity vs circularity plots. This reflects more complex shapes overall and a reduction in the importance of elongation in describing the shape of the second population relative to solidity and regularity. The greater complexity of vesicles in HX regions can be seen in Fig. 3.23F, where more elongate vesicles also exhibit morphological and textural roughness. The lower image in Fig. 3.23F shows how the higher microlite abundance in these regions may be responsible for this increased complexity.

Macro-vesicular Equant (827C_3 – OBP)

Finally, in the macro-vesicular equant clast from the OBP, shape data plots (Fig 3.24A – E and table 3.7) reflect a more heterogeneous vesicle population than seen in the macro-vesicular equant sample from Unit 1. Elongation has a stronger control on vesicle shape in the OBP sample and varies substantially with vesicle size. Vesicle areas extend to higher values than in the cone pumice samples (Units 1 – 9) and the highest aspect ratios are concentrated where vesicles have areas of around 100 μm^2 and 10 μm^2 (Fig. 3.24E). A higher proportion of vesicles have aspect ratios greater than 1:2 than the samples from the equant-group samples from the cone units. Vesicle shapes are more complex, reflecting a higher prevalence of particle-scale protrusions (Fig. 3.24C) contributing to imperfect circular cross-sections as can be seen in Fig. 3.24F.

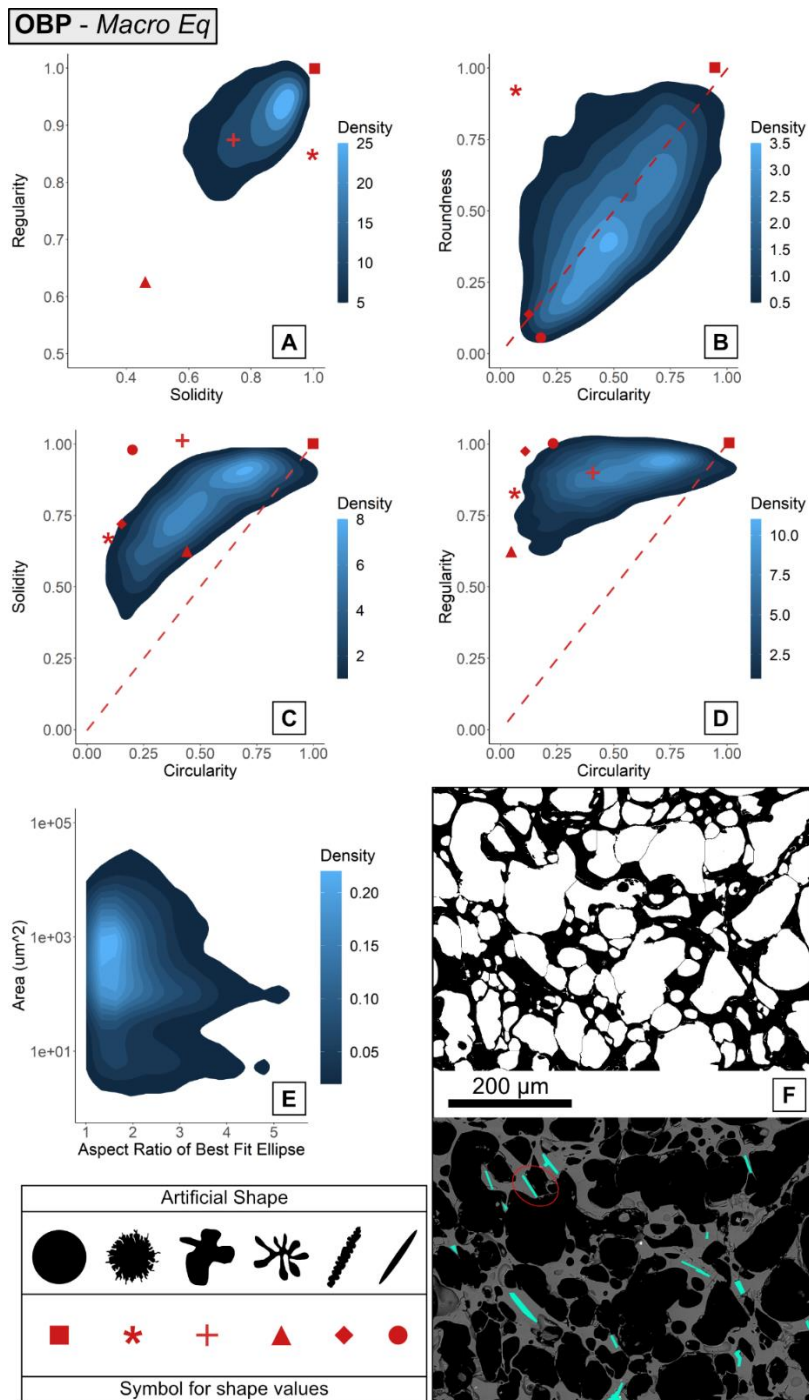


Fig. 3.24 – Density plots of shape parameters for vesicles from sample 827C_3, a macro-vesicular equant clast from the orange-brown pumice fall (OBP), the post-lava explosive phase of the Echo Canyon deposits. **A**: regularity data plotted against solidity with values plotted (red symbols) for four artificially generated vesicle shapes as displayed in the key. **B**: roundness data plotted against circularity with values plotted (red symbols) for four artificially generated vesicle shapes as displayed in the key, red dashed line represents circularity = roundness. **C**: solidity data plotted against circularity data with values plotted (red symbols) for six artificially generated vesicle shapes as displayed in the key, red dashed line represents solidity = circularity. **D**: regularity data plotted against circularity with values plotted (red symbols) for six artificially generated vesicle shapes as displayed in the key, red dashed line represents regularity = circularity. **E**: particle area data plotted against aspect ratio of the best fit ellipse as calculated using ImageJ. **F**: Upper - example binarized image post-correction for missing / broken vesicle walls showing vesicle textures for this sample. Lower - original backscattered scanning electron image showing vesicles (black), glass (pale grey) and microlites (blue rectangles). Red oval highlights crystal interference with bubble shape.

For all samples in the cone deposits regardless of textural group, deviation of vesicle shape from perfect circular cross-sections is best described through elongation. In equant vesicle groups (842A_63 and 843A_4) this remains true despite limited overall elongation (low aspect ratios) demonstrating the general smoothness of vesicle walls - morphological and textural roughness are generally negligible. The vesicle shapes in the micro-vesicular equant cone sample (843A_4) are more heterogeneous than the macro-vesicular equivalent, due to a secondary population of smaller more elongate vesicles. Vesicles in the dense (844C_10) and macro-vesicular elongate (829A_29a) samples extend to higher aspect ratios than equant groups but vesicles with an aspect ratio > 2.5 occur over a wider range of vesicle sizes (particle area) in the elongate sample (829A_29a) than in the dense cone sample (844C_10).

Vesicles in the OBP are more complex than the cone: all three analysed samples/regions exhibit more complex interactions between elongation, solidity (particle scale protrusions) and regularity (small-scale protrusions). In the dense sample (827C_6, HX and LX) vesicle walls are thicker than in cone deposits and microlite crystallinity is at least four times higher in low crystallinity regions, > 30 times higher in HX regions. Elongation has a greater impact on vesicle shape in the low crystallinity regions (relative to solidity and regularity) than in high microlite crystallinity regions and overall vesicles are less elongate – reaching lower aspect ratios and in smaller proportions than for the dense cone sample. Vesicles in the macro-vesicular equant clast from the OBP (827C_3) are more strongly impacted by elongation vs solidity and attain higher aspect ratios than those in the cone sample, have thicker glass walls and their areas span a wider size range. In general, vesicles in the cone deposits are smoother and smaller than those in the OBP.

3.3.5 Shape parameter Ω & Capillary number

If vesicle textures have not undergone post-fragmentation alteration, they represent a time-integrated record of processes of vesiculation, growth, coalescence and shear within the conduit during magma ascent (Moitra *et al.*, 2013). By exploring the relationship between vesicle shape, physical melt properties and changing ambient conditions (e.g., pressure) during ascent we can use vesicle shape to constrain key parameters (e.g., overpressure) to better understand eruption dynamics. Here, the shape parameter (Ω) and

relationships described by Moitra *et al.*, (2013) are applied to clasts from the EC deposits to estimate capillary number, overpressure and fragmentation threshold for different phases of the EC eruption.

The shape parameter Ω as defined by Moitra *et al.*, (2013) (see equation 6) was calculated for vesicles in each EC sample using the semi-long and semi-short axes of the best-fit ellipses (as calculated during VSD analysis in FOAMS, see methods) for vesicles with an area of equivalent circular diameter from 9 – 100 μm . This size range contains the median equivalent circular diameters for all samples analysed while being comparable with the range used by Moitra *et al.*, (2013) (10 – 100 μm). Sample 829A_29a was not included because vesicles are impacted by intense shearing, resulting in a median elongation value of 0.36 - greater than the 0.35 cut-off value used by Moitra *et al.*, (2013). The relationship between vesicle shape and capillary number in sheared samples is not strictly determined by processes of bubble growth during decompression and so cannot be used to explore eruption intensity in this context (Moitra *et al.*, 2013). Cumulative frequency distributions of Ω and $(1 - \Omega)$ are plotted in Fig. 3.25 alongside the Novarupta 1912, Kilauea Iki 1959, Etna 122 BC and the Soufrière Hills Montserrat 1997 eruption data from Moitra *et al.*, (2013) for comparison. You can see from fig. 3.25 that curves from the EC eruption deposits plot closer to the Novarupta and Etna eruptions (Plinian) than the Kilauea Iki eruption (Hawaiian) and that the curve for the macro-vesicular equant sample (842A_63, Unit 1) is the most distinct from the other EC units. The OBP samples have the lowest minimum and median Ω values and the macro-vesicular equant sample has a minimum measured Ω value of 0.2576, close to the minimum value for the Novarupta eruption (0.2660).

Median Ω values from EC samples decrease from 0.9205 in Unit 1 at the base of the cone to 0.8664 in the HX regions of the OBP, reflecting increasing vesicle complexity consistent with changes to other shape parameters in Figs. 3.18 – 3.24. Values for the EC samples are all lower than those quoted for the eruptions studied by Moitra *et al.*, (2013) indicating the bounding surfaces of these vesicles are slightly more complex, and irregular features e.g., records of coalescence or distortion by microlites, are better preserved. However, as all Ω values are greater than 0.8 the degree of vesicle complexity in these samples is still relatively low (see Fig. 2 of Moitra *et al.*, 2013). The lowest Ω value is produced by the HX sample of the OBP and the highest by the macro-vesicular equant sample from Unit 1, consistent with both macro and micro-scale textural observations. In a plot of capillary number vs $1 - \Omega$ (Fig. 3.26) all EC samples have $1 - \Omega$ values closer to those of the vulcanian-

Table 3.8 parameters from images analysed for shape analysis												
Unit	Sample N°	Tex. Group	2D ves. (%)*	Measured 3D ves. (%)	N° vesicles analysed	Analysed area (mm ²)	Med. CD (µm)	Med. Elongation	Min Ω	Max Ω	Med. Ω	Med. 1 - Ω
Unit 1	842A_63	Mac. Eq	78	86	7716	12.52	21.64	0.20	0.2576	0.9992	0.9205	0.0795
Unit 2	843A_4	Mic. Eq	65	76	5788	11.98	12.76	0.22	0.1491	0.9992	0.8833	0.1167
Unit 4	844C_10	Dense	62	69	4960	3.21	9.92	0.31	0.2576	0.9992	0.8791	0.1209
Unit 9	829A_29a	Mac. El	72	79	8296	12.98	14.59	0.36	**	-	-	-
OBP	827C_3	Mac. Eq	57	73	2741	11.66	15.31	0.30	0.1340	0.9992	0.8685	0.1315
OBP	827C_6_LX	Dense	67	65	476	11.62	42.06	0.29	0.1340	0.9994	0.8684	0.1316
OBP	827C_6HX	Dense	59	65	435	12.08	30.84	0.32	0.1340	0.9992	0.8664	0.1336

*measured directly from images used for shape analysis in ImageJ, all non-glass included even vesicles smaller than classified as “resolvable” for shape analysis, aka < 5 pixels. This also includes the edge-touching vesicles because for 2D vesicularity we don’t really need to worry about edge touchers. It’s just to give an idea of the relative differences in vesicularity + confirm roughly the same area of a thin section was covered in each case.
CD = circular diameter
**not analysed because median elongation >0.35 as per Moitra *et al.*, (2013)

-Plinian eruptions with equivalent capillary numbers of 300 – 600 than to Hawaiian and strombolian eruptions ($Ca \ll 1$).

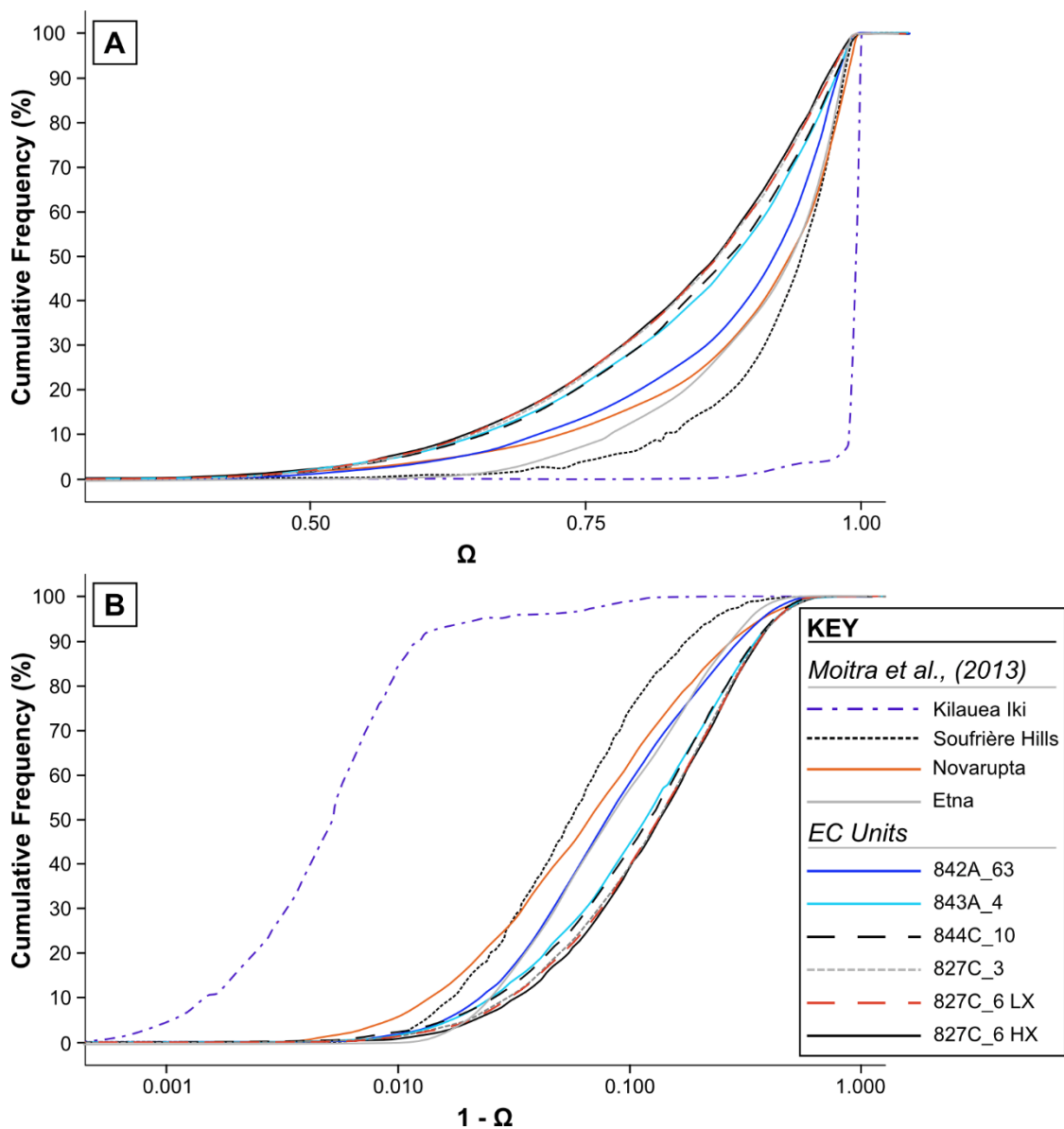


Fig. 3.25 cumulative frequency plots of **A:** Omega and **B:** $1 - \Omega$ for Echo Canyon (EC) units and examples from Moitra *et al.*, (2013) – Kilauea Iki 1959 (Hawaiian), Soufrière Hills Montserrat 1997 (vulcanian), Novarupta 1912 (Plinian) and Etna 122 BC (Plinian).

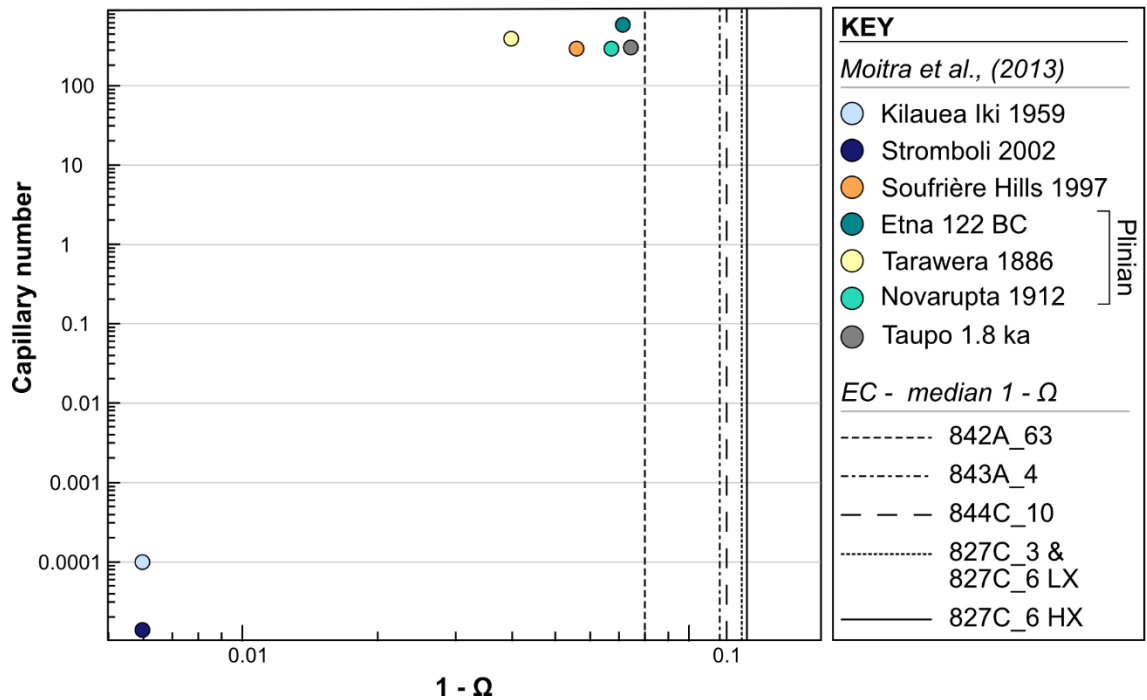


Fig. 3.26 plot of calculated capillary number against $1 - \Omega$ for example eruptions as plotted in fig. 6 of Moitra *et al.*, (2013), with median $1 - \Omega$ values added (solid and dashed lines) for the Echo Canyon (EC) samples. Eruption styles are Kilauea Iki = Hawaiian, Stromboli = strombolian, Soufrière Hills = vulcanian, Etna, Tarawera and Novarupta = Plinian and Taupo = ultra-plinian.

Moitra *et al.*, (2013) calculated capillary numbers for several eruptions by relating bubble growth and magma ascent models for eruptions with well-established eruption and magmatic parameters e.g., conduit radius, plume height, magma discharge rate, total volume erupted and melt temperature and density. For vulcanian – ultra Plinian eruptions calculated capillary numbers ranged from 300 – 600 (rhyolitic – basaltic magmas) associated with bubble overpressures ranging from 2.9 – 7 MPa (rhyolitic – basaltic magmas). Overpressure is calculated using equation 7:

$$\Delta P = \frac{2\sigma}{R} \left(1 + 2\phi^{-2/3}Ca \right) \quad [7]$$

Where ΔP is overpressure, σ is surface tension, R is bubble radius, ϕ is porosity and Ca is capillary number. Moitra *et al.*, (2013) define surface tension (σ) as 0.05 Nm^{-1} and R as $25 \mu\text{m}$. Using these values, capillary numbers of 300 and 600, and measured 3D vesicularities (table 3.8) an upper and lower estimate of bubble overpressure was calculated for each sampled unit of the EC deposits (table 3.9). For Plinian and Hawaiian eruptions Moitra *et al.*, (2013) calculate the fragmentation threshold (ΔP_f) of an ascending magma with a characteristic permeability of $\sim 10^{-12} \text{ m}^2$ using equation 8:

$$\Delta P_f = \frac{2.4}{\phi} \quad [8]$$

Fragmentation thresholds calculated in this way for EC samples are also listed in table 3.9. For all EC samples, overpressures associated with Ca = 300 do not exceed the fragmentation threshold whereas overpressures associated with Ca = 600 easily surpass the fragmentation threshold.

Table 3.9: calculated bubble overpressures for the EC sampled units based on measured Ω values and modelled capillary numbers from Moitra <i>et al.</i> , (2013)				
Unit	Sample	Overpressure (MPa), (Ca = 300)	Overpressure (MPa), (Ca = 600)	Fragmentation threshold (MPa)
Unit 1	842A_63	2.65	5.3	2.79
Unit 2	843A_4	2.88	5.76	3.16
Unit 4	844C_10	3.07	6.1	3.48
OBP	827C_3	2.96	5.92	3.29
OBP	827C_6LX	3.20 (3.13)*	6.4 (6.27)	3.69 (3.58)
OBP	827C_6HX	3.20 (3.41)	6.4 (6.82)	3.69 (4.07)

*In brackets are values calculated using 2D vesicularities for LX (67) and HX (59) regions as these regions are too small for 3D density measurements to be carried out on LX/HX regions of the 827C_6 clast separately.

3.4 Discussion:

Results of qualitative and quantitative textural analyses of the Echo Canyon eruption products provide insights into ascent processes, eruption dynamics and behaviour of trachytic melts during small-volume eruptions. Key findings are:

1. Microlite crystallinity increases by up to 30% between the cone and post-cone units whereas the phenocryst/antecryst cargo stays relatively stable with anorthoclase-feldspar phenocrysts and an antecryst cargo containing plagioclase feldspar and clinopyroxene.
2. Thermometry and hygrometry performed on apparent plagioclase-melt and k-spar-melt equilibrium pairs produced melt temperature estimates of 811 – 1060°C and H₂O contents ranging from 0 – 6.87 wt %.
3. Vesicle volume distributions (Fig. 3.16) show early dominance of a single stage of nucleation and growth gave way to more complex interactions between nucleation, growth, coalescence and collapse – supported by vesicle shapes and size populations identified in Figs. 3.18 – 3.24.
4. Most VSD curves best fit power-law distributions indicating disequilibrium degassing is dominant in the system (Blower *et al.*, 2001) – the exception is 827C_3 which showed a good fit for with both power-law and exponential distributions (Fig. 3.15 and table 3.4).

5. Vesicles tend to be texturally smooth (lacking small-scale surface protrusions), and elongation is typically the main factor contributing to deviations of vesicle shape from spherical, even in dominantly equant samples.
6. Calculated bubble overpressures increase from the lower cone to the post-cone pumice fall deposits (table 3.9). For all samples, the fragmentation threshold is only crossed when using upper estimates of bubble overpressures (at $C_a = 600$ as seen for basaltic Plinian, eruption of Etna 122BC, (Moitra *et al.*, 2013)).

To assess the implications of these results, melt viscosity is reconstructed and its ability to explain developing vesicle textures and eruptive behaviour discussed. The influence of melt composition on feldspar-melt equilibrium tests and calculations of bubble overpressure and fragmentation threshold will be evaluated. This will inform interpretations of vesicle-melt-crystal interactions in trachytic melts and their impact on decompression and ascent rate, and eruptive transitions in the Echo Canyon deposits.

3.4.1 Reconstructing T, H₂O & viscosity – plagioclase-melt vs K-spar-melt pairs

Reconstructing initial and evolving magmatic temperatures and volatile contents is key to understanding ascent and eruption dynamics as they exert a strong control on magma viscosity (Cassidy *et al.*, 2018). Temperature and H₂O content were reconstructed using the plagioclase-melt and k-feldspar-melt thermometers and hygrometers of Putirka (2008), Waters and Lange (2015) and Mollo *et al.*, (2015) (see tables 3.5 and 3.6). These thermometers and hygrometers were chosen because the composition of the Echo Canyon magma falls within the bounds of the compositions against which they were calibrated and tested. This is important as the substitution of ions between crystals and melt is sensitive to changes in melt composition (abundance of K relative to Na and Ca) as well as temperature, water content and pressure (Putirka 2008). All thermometers and hygrometers rely on exchange reactions between equilibrium pairs (either crystal-crystal or crystal-melt) and so identification of equilibrium pairs is paramount (see section 3.3 for description of equilibrium tests).

Equation 23 from Putirka (2008) was able to reproduce measured temperature values ranging from 650 - ~1300°C with an error of $\pm 4.3^\circ\text{C}$ for hydrous melts. For alkali feldspars, equation 24b (Putirka 2008) reproduced temperatures for samples ranging from 600 – 1200°C with an error of $\pm 23^\circ\text{C}$ calibrated against experiments carried out at $<1050^\circ\text{C}$ for hydrous melts. The Echo Canyon magma falls within this compositional range, as do the temperatures obtained using the Putirka (2008) thermometer. Since for both hygrometers,

temperature has a greater impact on the ability of the models to reproduce H₂O concentrations than pressure (Putirka 2005, 2008 and Mollo *et al.*, 2015) and the Putirka temperatures are fed into these hygrometers, ensuring the Echo Canyon compositions fell within the tested range and that pairs satisfy the requirement for equilibrium was vital.

The plagioclase-liquid hygrometer of Waters and Lange (2015) is based on the equilibrium exchange reaction of anorthite and albite components of crystalline plagioclase and the magmatic liquid. The hygrometer assumes the crystal phase is in equilibrium with the melt and so where analysed pairs are not in equilibrium, the ion exchange relationships do not hold, and the hygrometer cannot be applied (hence why disequilibrium pairs are excluded from further discussion). The Waters and Lange (2015) hygrometer was calibrated against metaluminous and alkaline magmas (45 – 80 wt% SiO₂ and 1-10% Na₂O + K₂O), for a temperature range of 250 - 1244°C, and a water content of 0 – 8.3 wt% at pressures from 0 – 350 MPa. The hygrometer yields an error of 0.35 wt%.

The alkali-feldspar – melt hygrometer of Mollo *et al.*, (2015) was calibrated using a dataset with a temperature range of 700 - 950°C, H₂O content of 2 – 9.5 wt %, pressures of 50 – 300 MPa and for a compositional range of SiO₂ = 57.8 – 69 wt% and Ma₂O + K₂O = 10.9 – 16.1 wt%, The model was then tested against trachytic and phonolitic compositions not included in the calibration dataset. The model uses the Si, Ti and Mg content of the liquid to calculate dissolved H₂O as opposed to the Al, Fe, Ca and Na used in plagioclase hygrometers and Si, Fe and Ca compositions for reconstruction of the K-feldspar components of the equilibrium pairs. The pressures used as input for both hygrometers was 250 MPa, within the bounds of other similar eruptions on Ascension Island (Chamberlain *et al.*, 2016; Chamberlain *et al.*, 2019) and within the range over which each hygrometer has been tested.

Rhyolite MELTS v 1.2 (Gualda *et al.*, 2012) was used to assess whether temperatures extracted from apparent plagioclase- and K-spar-melt equilibrium pairs were realistic given the position of the liquidus at reasonable estimates of pressure and redox states as taken from comparable eruptions on Ascension Island. Appropriate temperature and H₂O contents are then used to estimate changing viscosity in the ascending magma during the Echo Canyon eruption.

Several feldspar populations were identified within the Echo Canyon eruption products. The distinctive, up to 8 mm EC crystal population identified in hand specimen in chapter 2 includes euhedral-subhedral anorthoclase phenocrysts (Fig. 3.7 A – F) and plagioclase antecrysts; subhedral (Fig. 3.8), with inclusion rich rims (Fig. 3.9) and sieve textured/resorbed (Fig 3.10). Some plagioclase antecrysts have < 30 µm potassic rims but all lack the distinct zoning commonly associated with plagioclase crystals with a complex magmatic history (Andrews 2021). In the groundmass, 5 – 100 µm albite and anorthoclase microlites (Fig 3.12) and 150 – 300 µm microcrysts (Fig. 3.12C– E) are observed – up to 1% in cone pumices and 31% in the OBP. Microlites are interpreted to have crystallised in the shallow crust during late stages of ascent whereas larger, often euhedral microcrysts likely crystallised deeper in the system. Due to their size, composition, lack of disequilibrium textures and shape, euhedral anorthoclase phenocrysts likely crystallised at depth from the carrier melt. Disequilibrium, indicated by rounded crystal faces, rims and sieve texture suggests plagioclase populations are likely antecrystic, sourced from deep in the sub-surface mush and transported in the carrier melt to the surface.

Feldspar-melt thermometers and hygrometers were applied to crystal – melt pairs from all populations to test for equilibrium, assess whether the textural classification of crystal populations holds, and obtain a range of melt temperatures and H₂O contents for the EC eruptive products. Equilibrium anorthoclase phenocryst-melt pairs yielded temperatures of 811 – 887°C and H₂O concentrations of 5.34 – 6.87wt% at 250 MPa. These temperatures are below the liquidus as modelled by Rhyolite MELTS v.1.2 for this range of H₂O at log *f*O₂ = -2.28 ΔNNO (from Chamberlain *et al.*, 2016). One alkali feldspar microcryst was identified in the OBP but had extremely rounded crystal faces and was not in equilibrium with the host melt. Microlites are euhedral, often fractured and yield temperatures of 835 – 920°C and H₂O concentrations of 2.46 – 6.52wt% but are unlikely to have crystallised under equilibrium conditions (e.g., Brugger and Hammer 2010). As such, the range provided by phenocryst-melt pairs is deemed a more reliable estimate of initial melt temperature and H₂O content.

For plagioclases, an initial temperature was produced for a pressure of 250MPa (Chamberlain *et al.*, 2019) using Eq. 23 of Putirka (2008). The Putirka (2008) temperatures were used as a starting point to iteratively calculate H₂O and T using Eq. 23 of the Waters

and Lange (2015) thermometer/hygrometer, which were typically lower than their Putirka (2008) equivalent. Initial and iterated temperatures are displayed alongside H₂O in table 3.5. In the following sections, quoted plagioclase temperatures are the final best fit iterated temperature obtained from Waters and Lange (2015) where the initial analysis passed the Putirka (2008) equilibrium test. Microlite-melt and microcryst-melt pairs yielded temperatures from 941 – 1044 and 882 – 1044°C and H₂O contents of 0.37 – 2.77 and 0.01 – 3.69 wt% respectively. Plagioclase antecrysts yielded temperatures from 860 – 1039°C and H₂O concentrations of 0 – 4 wt%. For all cone compositions, Rhyolite MELTS v.1.2 modelling at 250 MPa with 1 wt% H₂O and a log *f*O₂ of -2.28 ΔNNO (from Chamberlain *et al.*, 2016), produced a liquidus temperature of ~1037°C, putting the upper bounds of the plagioclase temperatures at or above the liquidus. Increasing the pressure by 100 – 200 MPa increases the liquidus, this could indicate plagioclase antecrysts originate from a genetically related melt composition up to 2 km deeper in the system. A pressure of 250 MPa (consistent with alkali-feldspar Ts and H₂O concentrations) equates to approximately 8.5 km depth (using crustal density of 3300 kg/m³) whereas pressure of 350 MPa equates to approximately 11km depth which would be reasonable given the crustal thickness beneath Ascension is approximately 12km (Klingelhofer *et al.*, 2001). It is unlikely that microlites crystallised under equilibrium conditions (Brugger and Hammer 2010) yet some pairs passed the Putirka (2008) equilibrium test. This may be due to the impact of disequilibrium degassing on effective undercooling and the exchange of Ca and Na ions in plagioclase, which can give a false return of equilibrium and spuriously high temperatures (Humphreys *et al.*, 2016). This may also explain why plagioclase antecrysts displaying textural signs of disequilibrium passed the equilibrium test and yielded temperatures so close to the liquidus.

Disequilibrium textures within the plagioclase “antecryst” population could have been achieved through processes such as reheating, decompression and differential heating in the magma storage region (Huggins *et al.*, 2021) as well as through incorporation of antecrystic material into an ascending magma. Further, many plagioclase-melt pairs passed the equilibrium tests in the applied thermometer/hygrometer. However, the hotter temperatures of these crystals compared to those of the more texturally homogenous alkali-feldspars and the presence of other antecrystic material in some clasts supports the interpretation that these crystals were likely sourced from a slightly deeper part of the magmatic system than the alkali feldspar phenocrysts – though they are described as

“antecrysts” they may be very closely associated to the final extracted melt and its equilibrium crystal population. In addition, U/Th zircon ages from the Echo Canyon units (Scarrow *et al.*, 2023 in prep) record the incorporation of multiple crystal populations of different ages during magma ascent, which further supports inclusion of a mixed crystal population in the ascending melt.

Melt vs Magma viscosity in the cone & post-cone deposits

Crystal-free melt viscosities across the range of temperatures and H₂O values produced for the Echo Canyon eruption products were calculated using Giordano *et al.*, (2008) and are displayed in table 3.10. Temperatures and H₂O contents from alkali-feldspar microlite-melt pairs are included where they passed the equilibrium tests detailed above. Although microlites were likely crystallised under disequilibrium conditions their modelled temperatures and H₂O contents lie within a similar range as the phenocryst phases. As such, microlite-melt pairs provide an upper limit on viscosity for this deposit where other thermometry phases are absent. No equilibrium pairs were found in Units 1 and 2, and temperatures and H₂O contents for Units 3 – 9 were overlapping, so an average whole rock composition was used to calculate viscosities in the cone. Even including variations in temperature and H₂O content between plagioclase antecrysts and alkali-feldspar phenocryst populations, and across the erupted units, the resultant viscosity remains relatively stable at a couple of orders of magnitude below a calc-alkaline melt of a similar SiO₂ content (e.g., Unzen Dacite viscosity calculated in chapter 2, table 2.6). In the **cone**, antecrysts/phenocrysts produce viscosities of approximately $10^{3-3.5}$ Pas and microlites give viscosities of approximately 10^{4-5} Pas. The upper limit of which may be impacted by disequilibrium degassing, raising the calculated temperature and reducing the H₂O content of the melt for plagioclase-melt pairs (Humphreys *et al.*, 2016). No alkali-feldspar-melt equilibrium pairs were found in the dome and lava which may be due to the whole rock composition being used as the melt composition for these pairs. However, the range in viscosities produced from plagioclase temperatures and H₂O concentrations is only slightly higher than the cone, around 10^{4-5} Pas. Microlites in the dome and lava flow also give a viscosity around 10^4 Pas. In the OBP, no macrocryst/phenocryst-melt pairs were found, but plagioclase microcrysts yield viscosities of around 10^{5-6} Pas and microlites – which were slightly more water rich – viscosities of around 10^4 Pas.

Table 3.10: Viscosities calculated from plagioclase and alkali-feldspar crystal-melt equilibrium pairs for the Echo Canyon eruption deposits.

Unit	SiO ₂	Total alkalis	Crystal populations	Derived from plagioclase-melt thermometry / hygrometry			Derived from k-feldspar melt thermometry / hygrometry		
				Plag. T (°C) ¹	Plag. H ₂ O (wt%)	Plag. η (Pas) ³	K-spar T (°C)	K-spar H ₂ O (wt%)	Kspar η (Pas)
Cone	64.48	10.89	Macrocrysts	851 - 1044	1.79 – 4.89	10 ^{3.97 – 3.28}	811 - 887	5.34 – 6.87	10 ^{3.12 – 3.33}
			Microlites	1044	0.37	10 ^{5.29}	835 - 920	2.46 – 5.79	10 ^{4.36 – 3.7}
Dome	62.49	11.11	Macrocrysts & microcrysts	921 - 1039	0.17 – 3.18	10 ^{5.26 – 3.67}	-	-	-
			Microlites	934 - 993	1.14 – 2.77	10 ^{4.05 – 3.86}	-	-	-
Lava Flow	63.66	11.36	Macrocrysts & microcrysts	882 - 1039	0.05 - 4	10 ^{5.66 – 3.36}	-	-	-
OBP	63.76	10.49	Microcrysts	967 - 1044	0.01 – 1.86	10 ^{5.91 – 4.54}	-	-	-
			Microlites	941 - 1016	1.19 – 2.56	10 ^{4.16 – 4.12}	-	-	-

¹Plagioclase temperatures calculated using equation 23 of Putirka (2008), H₂O contents generated via iteration of Putirka (2008) temperatures using Waters and Lange (2015) to achieve a best-fit temperature-H₂O combination.

²K-spar temperatures using equation 24b of Putirka (2008) and H₂O contents using Mollo *et al.*, (2015).

³All viscosities calculated using Giordano *et al.*, (2008)

These variations in viscosity are not large and thus suggest this alone cannot be responsible for changes in eruption character preserved in the EC deposits, irrespective of the uncertainties and variance in T and H₂O described above.

Although melt viscosities between the cone and post-cone deposits are similar, crystallinity increases by more than 20% and thus will have an impact on the effective viscosity of the ascending melt. Viscosity increases in a strongly non-linear manner with crystal content and is further complicated by the presence of bubbles (Pistone *et al.*, 2012 and references therein). The magma must then be considered as a two/three-phase mixture when examining the explosive-effusive-explosive transition in the post-cone phase of the EC eruption. In a two-phase magma (melt + crystals), crystallisation of 20 vol% plagioclase crystals with an aspect ratio of 1:4 would result in an increase in viscosity of approximately 0.5 orders of magnitude. At 30% crystals, viscosity can increase by 2 orders of magnitude, 3 for crystals with an aspect ratio of 1:5 (Laumonier *et al.*, 2014). The dome and lava flow both contain several distinct microlite populations, the smallest, most acicular of which constitutes up to 20 - 30% of the groundmass and may be attributed to post-emplacement crystallisation. Assuming all but the very smallest populations crystallised during ascent, effective viscosity of the lavas could have been increased up to 5-fold. This is almost twice the viscosity change associated with changes in temperature and H₂O between the cone and post-cone deposits (see table 3.10) if you take the minimum viscosity of the cone deposits of 10^{4.47} Pas (at 788°C, the lower temperature limit including -23° error on alkali-feldspar temperatures) and maximum viscosity for the dome of 10^{5.32} Pas (at 1043°C the upper temperature limit including +4.3°C error on plagioclase feldspar temperatures) (see Appendix 2_6 for table). However, the impact of increasing crystallinity on viscosity may have been mitigated by the presence of vesicles in the magma and shear across the conduit. In experiments, Pistone *et al.*, (2012) found that where crystallinities were high e.g., in domes, lower viscosities were maintained via bubble-break up in shear zones, inhibiting outgassing, facilitating flow in shear zones and promoting continued extrusion. Bands of higher and lower vesicularity observed in the lava and dome may provide evidence for this process (Fig. 3.27).

Within the OBP, microlite crystallinity varies from 1.5% to 30%, averaging around 7% - higher than the cone pumices. Unpicking how microlite-bubble-melt interactions influence melt rheology and eruption dynamics in this phase of the eruption is complex and only a few studies attempt this (Bagdassarov *et al.*, (1994); Avar and Whittington (2012); Vona

et al., 2013). Vona *et al.*, (2013) explored the rheology of crystal + bubble bearing trachytic melts from Monte Nuovo. Vona *et al.*, (2013) found that the added presence of bubbles could decrease viscosity by up to 1 order of magnitude relative to a two-phase magma depending on temperature and strain rate. However, the bubble phase simultaneously reduced the strength of the magma promoting localised variations in brittle vs ductile behaviour. In the final explosive phase (OBP) of the EC eruption, microlite crystallisation likely increased magma viscosity and bubble overpressure in the shallow conduit (c.f. Melnik and Sparks 1999), mitigated to some degree by the bubble population.

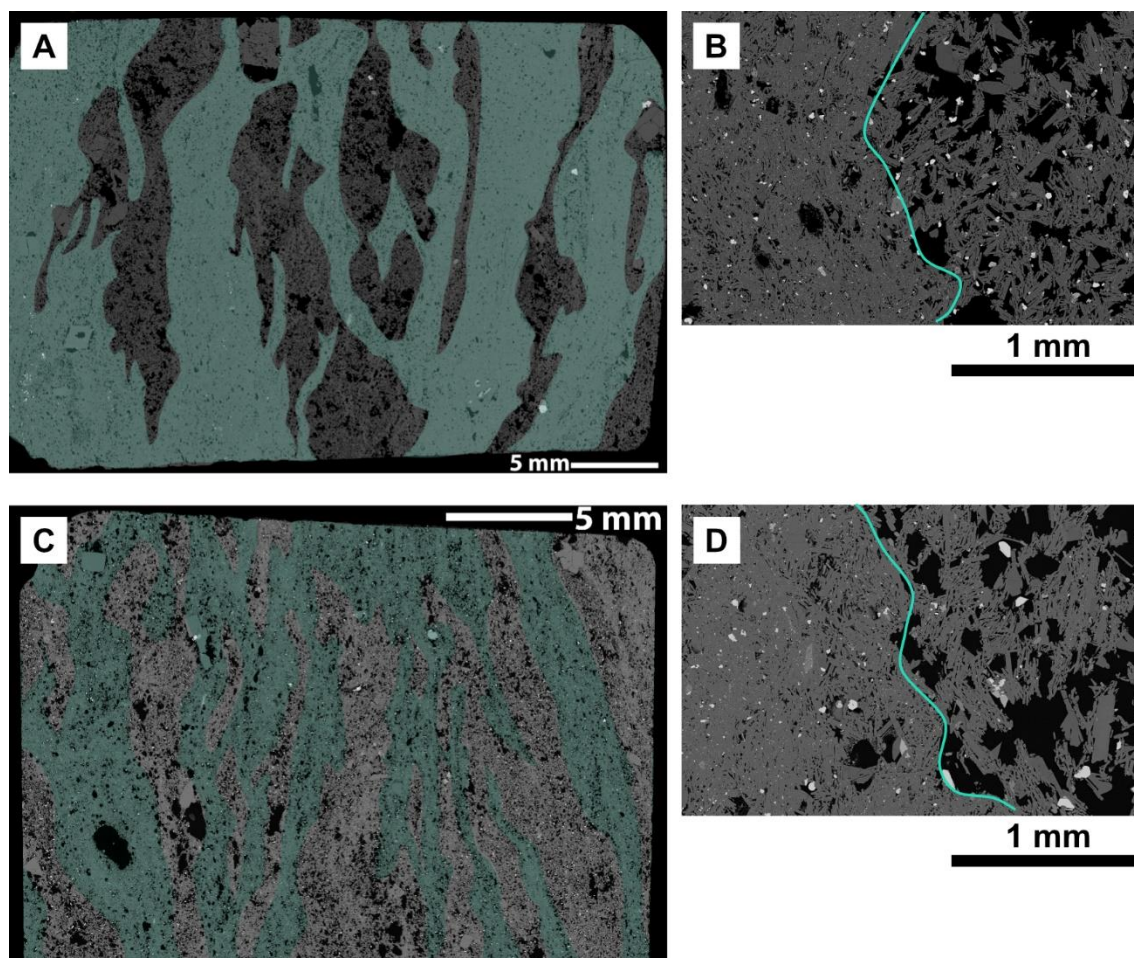


Figure 3.27: Backscattered electron images from the lava (A and B) and dome (C and D). A and C show shear zones with low (highlighted blue) and high vesicularity. B and D show difference in crystal : bubble textures across low (left) and high (right) zones.

Summary

Crystal populations in the Echo Canyon eruption products indicate the ascending melt sampled plagioclase antecrysts sourced from a genetically related, compositionally similar melt crystallising at ~11 km depth. Plagioclase and alkali-feldspars both display textures indicative of a relatively self-contained, self-similar sub-surface mush. There is no textural

or chemical evidence for extensive mixing between compositionally distinct melts or repeated recycling of crystals in a heavily interconnected mush (e.g., heavily zoned crystals or abundant plutonic crystal clots with more mafic mineral phases (e.g., Cashman and Blundy 2013 and Charlier *et al.*, 2008). Phenocrystic alkali-feldspars indicate temperatures ranging from 811 – 920°C, H₂O concentrations of 2.86 – 6.87, and indicate a crystallisation depth of approximately 8.5 km. This is consistent with other trachytic eruptions in the Eastern Felsic Complex (e.g., Chamberlain *et al.*, 2016 and Chamberlain *et al.*, 2019). Whereas melt estimates of viscosity do not change significantly from the initial to final explosive phase, degassing induced crystallisation of microlites could have increased viscosity by 3 – 5 orders of magnitude at the explosive – effusive transition, mitigated in part by preservation of low viscosity regions in shear zones via bubble break-up (Pistone *et al.*, 2012). Prior to the eruption of the OBP, microlite crystallisation in the shallow conduit likely increased bubble overpressure (Melnik and Sparks 1999) pushing the magma towards explosive fragmentation. Magma viscosity likely increased by up to 2 orders of magnitude due to crystallisation, whereas the bubble population likely limited the overall increase by up to 1 order of magnitude while simultaneously reducing the brittle strength of the magma aiding fragmentation (Vona *et al.*, 2013).

3.4.2 Piecing together changing vesiculation & ascent using vesicle size & shape

Quantification of vesicle textures interrogates the rheological imprint of vesiculation processes, analyses degassing and outgassing efficiency during magma ascent and thus can be used to interpret and understand magma ascent dynamics. Vesicle textures from the EC eruption deposits reflect the interplay between vesicle nucleation and growth processes, ascent rates and the relaxation timescale (τ) – strongly controlled by viscosity – in these samples. VVD curves reveal transitions between vesicle populations dominated by nucleation, growth, coalescence, ripening and collapse processes throughout the deposits. Such variations are supported by the changing controls on vesicle shape identified through quantitative analysis. Whilst single clasts were selected for textural quantification and analysis, care was taken to ensure selected clasts represented the range of vesicularities and macro-scale textures observed in the EC deposits (see methods, 2.2.1). Expanding on observations from chapter 2, interpretations of quantified vesicle textures in each sampled group are here coupled with their relative abundance in each unit (Fig. 3.1). Hence,

elucidating dominant (and extreme) vesiculation processes occurring in the melt at each stage of the eruption.

Vesiculation & ascent - Cone deposits

Vesicle volume distributions (VVDs) for the cone deposits (Fig 3.16, 842A_63, 843A_4 and 844C_10) show how different textural groups represent different vesiculation and growth regimes. Macro-vesicular equant clasts (Fig. 3.16, 842A_63) are dominated by a single stage of nucleation with the initiation of coalescence. Micro-vesicular equant clasts (Fig. 6, 843A_4) record multiple stages of nucleation, and dense clasts (Fig. 6, 844C_10) show developing vesicle ripening textures with a distinct larger population which has not yet undergone total vesicle collapse (Shea *et al.*, 2010). Vesicles in the macro-vesicular equant sample lack morphological and textural roughness and deviations from circular cross-sections are mainly controlled by small amounts of elongation. This indicates that where coalescence has occurred, vesicles have had sufficient time to remove small-scale and particle-scale protrusions via relaxation but were unable to return to “spherical” either due to ascent rates exceeding the relaxation timescale or interference between growing vesicles during ascent (Llewellyn and Manga 2005). The micro-vesicular equant sample has the highest bubble number density in the cone and highest overall in the EC eruption deposits (NvCorr in table 3.4). A high bubble number density associated with a regime dominated by multiple stages of nucleation in micro-vesicular equant samples is reflected in the observed vesicle textures where a secondary smaller, more elongate vesicle population is identified (Fig. 3.19 E and F). This smaller population also displays greater evidence of morphological roughness (particle-scale protrusions) indicating these vesicles nucleated in the void spaces between larger vesicles and their shape was partially impacted by the continued growth of the larger population. Vesicles in the dense clast (844C_10) reflect an increased influence of shear as a small proportion achieve best-fit ellipse aspect ratios of 1:5 (Fig. 3.15 E). Textural and morphological roughness continue to have a low impact on vesicle shape relative to elongation (Fig. 3.21B and E). For vesicles coalescing free of shear, this is consistent with timescales for relaxation relative to fragmentation for the macro- and micro-vesicular samples. The NvCorr value for the dense clast is slightly lower than in the macro-vesicular equant clast and a lot lower than the micro-vesicular equant sample. This may reflect initiation of shear-induced coalescence and initiation of collapse as shown by the VVD (Fig.6 844C_10). For intensely sheared vesicles, the same

may be true, but it is also likely that extreme elongation overprints measures of roughness. In the macro-vesicular elongate sample (829a_29a) a higher proportion of vesicles exhibit aspect ratios greater than 1:3 but there is still a significant proportion of low aspect ratio vesicles (Fig. 3.21E), reflecting strain localisation on the micro-scale. Heterogeneous nucleation and/or second boiling is indicated by smaller, more circular vesicles that distort nearby elongate vesicles (Fig. 3.21F) (Piochi *et al.*, 2021). As large phenocryst phases and/or significant microlite populations are largely absent, we favour heterogeneous nucleation.

The shape and mathematical description of VSD curves for non-elongate samples can be compared with experimental data and modelling to reconstruct vesiculation processes in magmas (e.g., Blower *et al.*, 2001). Blower *et al.*, (2001) showed that continuous nucleation in ascending magmas can produce power-law VSDs through Newtonian packing of vesicles, whereby new vesicles nucleate in the volatile rich melt pockets between larger populations. This mechanism can be applied to macro- and micro-vesicular clasts from the cone as both display power-law distributions (Fig. 3.5 and table 3.4). Blower *et al.*, (2001) inferred that continuous nucleation was favoured where conditions preclude efficient degassing e.g., low initial nucleation densities, slow volatile diffusion, or rapid depressurisation. The EC cone deposits have low viscosities (approximately $10^{3-3.5}$ Pas) and H₂O diffusivity in trachytes is high (Shea *et al.*, 2017), meaning rapid depressurisation is the most likely cause of disequilibrium degassing in the cone deposits.

Implications

Macro-vesicular equant clasts are the dominant textural group in units 1 and 2 indicating the initial explosive phase is dominated by magma undergoing a single stage of nucleation followed by extensive growth and continuous coalescence. The consistent presence of micro-vesicular equant clasts in units 1 and 2 suggests some portions of the ascending melt were moving more rapidly (less time for bubble growth) and experiencing multiple nucleation events. Macro-vesicular equant clasts remain the most dominant in units 3 and 4 but their overall abundance drops as sheared and dense clast types become more abundant. The influx of sheared clasts in Unit 3 reflects expansion of shear zones at the conduit margins (chapter 2) and vesicle textures indicate strain localisation which has been invoked as a mechanism for fragmentation of low viscosity magmas (Hughes *et al.*, 2017). The abundance of highly sheared and dense clasts in Unit 9 indicates a greater portion of

the magma is ascending slowly enough for ripening and bubble collapse to initiate, reflecting further expansion of shear zones at the conduit margins.

Vesiculation & ascent – Post-cone deposits

VVDs from the macro-vesicular equant and dense examples from the post-cone explosive unit reflect different processes to the cone deposit equivalents. These differences are also reflected in the vesicle texture analyses. The macro-vesicular equant example (Fig 3.16, 827C_3) has 3 distinct modes reflecting multiple stages of nucleation and is skewed towards higher vesicle diameters, indicating the influence of ripening on the bubble population (Shea *et al.*, 2010). Vesicle textures are also distinct from the cone sample, bubble walls are thicker, the vesicle population is more heterogeneous, elongation varies with particle area and morphological roughness exerts a greater control on vesicle shape than any of the cone samples (Fig. 3.24). The macro-vesicular equant sample (827C_3) also has the lowest NvCorr value of the EC deposits indicating extensive bubble coalescence and collapse or suppressed bubble nucleation. As this clast has a relatively high overall bulk vesicularity (71% measured) we favour high degrees of coalescence and ripening producing a smaller number of large vesicles. VVDs from the dense post-cone sample (Fig 3.16 827C_6 HX and 827C_6 LX) show more complex relationships. The high crystallinity (HX) VVD has two distinct modes and more closely resembles the trace of continuous accelerating vesicle growth overprinted by a coalesced population at the largest vesicle diameters (Shea *et al.*, 2010). The low crystallinity (LX) VVD more closely resembles that of the post-cone macro-vesicular equant sample (827C_3) (Figs. 3.22 and 3.24). This similarity likely reflects the similarity in microlite crystallinities between 827C_3 and LX regions of 827C_6 (see Figs. 3.22F and 3.24F). In both examples, microlites are sparse and only rarely appear to interfere with vesicle shape (see red circles on Figs 3.22F and 3.24F). This contrasts with HX regions of the dense sample (827C_6) where larger crystals often impinge on bubble walls – contributing to the morphological roughness of vesicles in these regions (Fig. 3.23F). Smallest microlites in the HX regions sometimes have long axes oriented to reflect flow around larger vesicles and crystals despite no clear preferred orientation of vesicle long-axes (Fig. 3.23F – lower). In HX regions of the dense sample, smaller, more circular vesicles appear to coincide with regions of high microlite crystallinity (at the smallest crystal size populations) which may be indicative of second boiling due to late stage microlite crystallisation (Piochi *et al.*, 2021).

VSD plots of both HX and LX regions of the dense sample follow a power-law distribution whereas the macro-vesicular equant sample showed a good fit for exponential and power-law distributions. As in the cone deposits, this may be indicative of disequilibrium degassing accompanied by continuous nucleation (Blower *et al.*, 2001). However, low bubble number densities and vesicle textures in the OBP units suggest that in the last explosive phase of the eruption, coalescence and ripening were more dominant processes than nucleation (Shea *et al.*, 2010).

Implications

In the OBP, micro- and macro-vesicular clasts are dominant and in similar proportions to Unit 3 but with a smaller number of pervasively sheared clasts and more dense ones. However, micro-scale examination of vesicle textures indicates that macro-scale textural groupings do not hold between the cone and post-cone deposits. Thicker glass walls and more abundant microlite populations evidence stalling of a relatively degassed melt in the shallow conduit as outlined in chapter 2, supported by the strong signals of coalescence and ripening in the VVDs. Multiple phases of nucleation and crystal growth are evidenced by crystal and bubble sizes, shapes, and interactions. In some cases, bubble-crystal interactions indicate second boiling may have occurred in a closed system (Piochi *et al.*, 2021) which supports the model of a stalled melt beneath a dome/lava cap and may have assisted generation of high overpressures leading to explosive behaviour (Melnik and Sparks 1999).

3.4.3 Relating vesicle shape to capillary number, viscosity & overpressure

Where vesicle populations in pyroclasts capture the state of the melt at the point of fragmentation they provide an integrated record of ascent processes. In un-sheared clasts vesicle shape is dominantly controlled by processes related to decompression e.g., nucleation and growth, and can be used to quantify the balance of internal stresses and constrain bubble overpressures and eruption intensity (Moitra *et al.*, 2013). Bubble-melt-crystal interactions also impact and are impacted by the ascent of the magma in a dynamic way (Vona *et al.*, 2013; Llewellyn and Manga 2005; Melnik and Sparks 1999) On the micro – macro scale textural heterogeneity may contribute to strain localisation during magma ascent – a potential mechanism for inducing fragmentation in low viscosity melts (Hughes *et al.*, 2017). Here I will evaluate the applicability of existing models to trachytic melts, to

assess how variations in vesicle shape across the EC eruption deposits can be used to constrain ascent processes.

Applying models of bubble shape, capillary number & overpressure

Moitra *et al.*, (2013) estimated the capillary number (Ca) for several well-constrained Hawaiian – Ultra-Plinian using diffusive bubble growth and conduit flow modelling. They also calculated the shape factor Ω (defined in Eq. 6) for the erupted vesicle populations to establish a relationship between Ca and Ω . Products of the EC eruption had Ω values < 1 resulting in a likely Ca value close to those of Vulcanian – Plinian examples. From this, overpressure values (ΔP) and fragmentation thresholds (ΔP_f) for each of the studied units were calculated using equations 7 and 8 (table 3.9). Calculated overpressures increased from the base to the top of the EC eruption deposits and only upper estimates of overpressure (associated with Ca = 600) exceeded calculated fragmentation thresholds. This has implications for interpretations of magma ascent and controls on eruption dynamics. To test whether estimates of capillary number - and hence overpressure and fragmentation threshold - for the EC eruption hold, the suitability of the Moitra *et al.*, (2013) relationship to trachytic compositions is assessed.

Whether the relationships between Ω , Ca, ΔP and ΔP_f defined by Moitra *et al.*, (2013) can be applied to the EC eruption depends on whether model inputs and assumptions used to calculate Ca for their example eruptions are reasonable for the Echo Canyon eruption. Moitra *et al.*, (2013) defined Ca in relation to melt viscosity (η), expansion velocity of bubbles (v_e) and the surface tension of the fluid phase (σ) (see Eq. 9).

$$Ca = \frac{\eta v_e}{\sigma} \quad [9]$$

To calculate expansion velocity Moitra *et al.*, (2013) used a model of diffusive bubble growth in which H₂O was the only volatile phase. In trachytic melts, other volatile phases may be present e.g., Cl and F which may also influence bubble growth. However, when Signorelli and Carrol (2002) tested the solubility of Cl in hydrous trachytes at temperatures of 860 – 930°C and pressures of 25 – 250MPa they found Cl concentrations of 0.37 – 0.9 wt% Cl. In cone deposits, H₂O concentrations are up to 5 times greater than potential Cl concentrations and in the OBP H₂O concentrations are 1 – 2 times that of Cl. For the cone in particular, H₂O appears to be the dominant phase and so the assumption holds. This is

less true for the OBP however, incorporation of additional volatile phases (e.g., Cl and F) would promote diffusive bubble growth, increasing the resulting capillary number and associated bubble overpressures. They modelled growth of bubbles from 10 – 25 μm – within the range over which Ω was calculated for the example eruptions in their study. In this scenario diffusive bubble growth operates via the concentration gradient of H_2O between the supersaturated melt phase and the interior of the bubble (Sparks 1978). In rapidly ascending, high viscosity melts where diffusion of volatile phases is slow, decompressive growth is more likely, whereby bubbles expand due to decreasing ambient pressure (Sparks 1978). In the cone deposits, morphological and textural smoothness of vesicles, bubble number densities and low microlite crystallinity indicate rapid ascent which may favour decompressive bubble growth processes. However, calculated melt viscosities are low ($10^3 - 3.5$ Pas) and in trachytes H_2O solubility and diffusivity are high (Shea *et al.*, 2017) meaning that even with rapid ascent, a diffusive bubble growth model may still be applicable. Water solubility in trachytes is higher than in rhyolites at a given pressure, meaning they can reach the shallow crust with a substantial amount of dissolved water (Masotta and Mollo 2019) generating larger concentration gradients at supersaturation over which rapid diffusion can occur. The calculated capillary number also depends on surface tension, Moitra *et al.*, (2013) used a surface tension of 0.05 Nm^{-1} taken from Gardner and Ketcham (2011) for a low viscosity rhyolite. As surface tension is defined by the force applied over a length scale, the suitability of this value can be assessed by considering melt density. Marziano *et al.*, (2007) calculated surface tension in a phonolite melt (equivalent to the 79AD white pumice) with a dry melt density of 2.59 g/cm^3 (using the melt density calculations of Lange and Carmichael (1999) of 0.095 Nm^{-1}). The EC trachyte has a melt density of 2.5 g/cm^3 , almost exactly between the phonolite of Marziano *et al.*, (2007) and the rhyolite of Gardner and Ketcham (2011) - 2.4 g/cm^3 . An estimate of surface tension of 0.075 Nm^{-1} does not change the calculated capillary number or overpressure by more than one order of magnitude compared to the value used in the Moitra *et al.*, (2013) model. Constraints on surface tension also allow calculation of the relaxation timescale to assess whether vesicle textures truly represent the magma at the point of fragmentation. Relaxation timescales for bubbles from 10 – 100 μm using $\tau_r = \eta R / \sigma$ and a viscosity of $\sim 10^{3.5}$ Pas, range from $10^5 - 10^6$ s, this far exceeds the characteristic quench timescale of 100s for ~ 1 cm clasts as defined by Thomas and Sparks (1992). This result confirms that the analysed vesicle textures are likely a true reflection of ascent processes and can be used to elucidate

controls on eruption dynamics. Given consideration of the impact of trachytic melt viscosity, H₂O diffusivity and bubble growth, and surface tension, estimates of capillary number and overpressure for the EC eruption using the Moitra *et al.*, (2013) model are likely reasonable. In chapter 2, bulk vesicularity distributions and deposit characteristics indicated a peak eruption intensity equivalent to a Plinian eruption. Here, the calculated shape parameter Ω puts the EC eruption deposits close to capillary numbers equivalent to silicic and crystalline basaltic Plinian eruptions (Fig. 3.26). Given the evidence for Plinian eruptive behaviour within the EC deposits and the above discussion, Eq. 8 as applied by Moitra *et al.*, (2013) for Plinian, ultra-Plinian and Hawaiian eruptions likely gives a reasonable estimate of fragmentation threshold for this eruption.

Marziano *et al.*, (2007) modelled volatile degassing in phonolites via decompression experiments and found that at high ascent rates (1.7 and 4.8 MPa/s), supersaturation was maintained until rapid exsolution and bubble growth between 150 and 180 MPa. Sitting between a rhyolite and a phonolite, the trachytes of the EC eruption likely behave in an intermediate way, with rapid volatile exsolution and bubble growth at shallow levels likely accelerating ascent and facilitating short-lived highly explosive phases of activity.

Implications for the EC eruption

Accepting that the relationship between Ω and capillary number holds for the EC eruption, upper and lower limits as defined by the Plinian eruptions of the crystal rich basaltic of Etna 1222BC and Novarupta 1912 in Fig. 3.26 generated a range of potential overpressures for each unit. In each case, whether or not bubble overpressure exceeds the fragmentation threshold (at physically reasonable ascent rates) depends on which value of Ca is chosen. For the cone deposits, microlite crystallinity is low and equant vesicle shapes with low textural and morphological roughness dominate. In this case, a capillary number closer to the Novarupta 1912 eruption may be more reasonable (Ca = 300). Conversely, the post-cone explosive phase (the OBP) has crystal rich regions and a morphologically rough vesicle population indicating a capillary number closer to that of the crystal rich basaltic Plinian eruption (Ca = 600) may be more appropriate. This would mean that in the cone, bubble overpressure likely does not exceed the fragmentation threshold and so an alternative fragmentation mechanism is needed. In chapter 2, narrow bulk vesicularity distributions (BVDs) (Fig. 2.20) indicated that, for the lower cone at least, fragmentation likely occurred via bubble interference and rupture. In this instance, fragmentation is achieved through

the impact of expanding bubbles in close-proximity on the volatile content – and hence viscosity – of the interstitial melt pockets. As the melt ascends, adiabatic cooling (to even small degrees) increases the rigidity of the melt, which must be forced through ever-decreasing channels until the supersaturation pressure driving growth is less than the pressure required for further expansion. Larger bubbles burst more easily as the surrounding melt is more easily deformed such that as the magma reaches the disruption surface – across which there is a pressure gradient which promotes fragmentation – a range of bubble sizes will be preserved (Sparks 1978). This is supported by high proportions of micro- and macro-vesicular equant clast types and high bubble number densities (aka closer packing of vesicles) reported in this chapter. In the post-cone deposits, broad BVDs indicated fragmentation due to high bubble overpressures inducing brittle failure of the magma. The presence of additional volatile phases not accounted for in the model of diffusive bubble growth of Moitra *et al.*, (2013) would only serve to increase these overpressures. Crystallisation of microlites in a closed system beneath the dome and lava not only increases effective viscosity (see above) but can also induce second boiling as indicated by vesicle textures (Fig. 3.21F discussed in section 3.4.2) which in turn increases bubble overpressure. As discussed above, brittle strength of the melt is also reduced due to the presence of bubbles in the 3-phase suspension (Vona *et al.*, 2013). Given this, high bubble overpressures, as achieved using a capillary number of 600 provide an appropriate mechanism for fragmentation in the post-cone deposits. These differences in fragmentation mechanism are likely part of a feedback loop with the dynamics of this eruption. In early phases, volatile rich, readily vesiculating magma ascended rapidly with extensive bubble growth and multiple nucleation events promoting rapid growth of bubbles that fed continued and increasingly explosive fragmentation across the disruption surface. As the eruption progressed and the magma degassed, this mechanism of fragmentation could not be sustained, and explosive activity was not reactivated until some other process (microlite crystallisation) induced bubble overpressures sufficient to fragment a much less vesicular, less volatile rich residual melt in a shorter-lived explosive event.

3.4.4 Using bubble number density to reconstruct decompression & ascent rate

As discussed above, vesicle shapes, low microlite abundance and textural characteristics of the crystal cargo indicate rapid ascent rates during the initial stages of the Echo Canyon

eruption. Quantifying ascent rate in crystal poor, unobserved eruptions is challenging. There are no amphibole breakdown rims to measure (e.g., Rutherford *et al.*, 1993) and interrogation of crystal size distribution curves is less useful without constraints on crystal growth timescales (e.g., Preece *et al.*, 2016). Instead, here I apply the bubble number density (Nv) decompression rate meter of Toramaru (2006) to make an initial estimate of decompression rate and place bounds on likely ascent rates for the Echo Canyon eruption.

Toramaru (2006) explored the relationship between Nv , decompression rate and physical melt properties and produced a decompression rate meter based on H_2O concentration (C_w), Nv and SiO_2 (C_{SiO_2}). Their decompression rate meter considers the impact of H_2O diffusivity (D), surface tension (σ), temperature (T) and initial water saturation pressure (P_w) on Nv , the relationships in Eq. 10 simplify to form the decompression meter (Eq. 11).

$$\frac{dP}{dT} = \alpha \cdot D \cdot \sigma^2 \cdot P_w^{-\frac{1}{3}} \cdot T^{-\frac{1}{2}} \cdot Nv^{\frac{2}{3}} \quad [10]$$

$$\frac{dP}{dT} = f(C_w, C_{SiO_2}, Nv) \quad [11]$$

Where α is a constant that allows the decompression rate meter to better fit the experimental data used in Toramaru (2006) while incorporating; difficulty in nucleation, scaled initial saturation pressure and the ratio of the decompression timescale to the diffusion timescale (see formulations of Eqs. 1 and 2 in Toramaru (2006)).

Bubble number densities generated by FOAMS (Shea *et al.*, 2010) and corrected for clast vesicularity of studied clasts from different textural groups of the EC eruption are displayed in table 3.4 as Nv_{Corr} . Figure 6 from Toramaru (2006) was adapted to show Nv_{Corr} values from EC eruption deposits plotted against SiO_2 alongside other eruptions and estimate decompression rate - displayed in Fig. 3.28. High Nv_{Corr} values for the EC eruption deposits place them close to a modelled decompression rate of 10^8 Pas at 4 wt% , close to that of the 1980 Mt St Helens and 1991 Pinatubo eruptions. Toramaru (2006) acknowledge the overall very high decompression rates (up to 10^8 Pas) generated by their decompression meter and explain this through a mechanism of bubble nucleation via a rarefaction shockwave generated by the production of a region of negative pressure – volume in the melt at the point of nucleation. They propose that in a compressible material (aka bubble-

bearing) propagation of this shockwave may increase the rate of decompression above previous estimates at feasible ascent rates.

The decompression meter of Toramaru (2006) considers decompression at a single point within a parcel of magma moving at a uniform rate as described by Eq 12. This relationship shows that as ascent rate increases, so does decompression rate (dP/dt).

$$\left(\frac{dP}{dt}\right) = \left(\frac{\delta P}{\delta z}\right) \cdot \left(\frac{\delta z}{\delta t}\right) \cdot \left(\frac{\delta P}{\delta t}\right) \quad [12]$$

Where $(\delta P/\delta z)$ is the change in pressure with depth, $(\delta z/\delta t)$ is the ascent velocity (change in depth with time) and $(\delta P/\delta t)$ is the change in pressure of a given point with time. All are considered relative to the nucleation depth. This is not the case for the EC deposits, where the presence of different textural groups in varying abundances indicates velocity gradients acting across the conduit that change with time (e.g., expansion of shear zones at conduit margins between units 3 and 9, chapter 2). However, each of the NvCorr values was calculated using an individual clast representing a particular textural group. For each clast analysed, it can be assumed that the package of magma from which it was sourced was moving at a uniform ascent velocity. Variability in the vesicle textures between groups can be linked to the horizontal (see Fig. 3.29) or vertical distribution of the source melt within the conduit. Horizontal gradients are commonly invoked due to friction and cooling at conduit walls (e.g., Sparks *et al.*, 1999 and Shea *et al.*, 2017) but simultaneous development of vertical gradients of gas rich – poor magma has also been suggested as a mechanism driving vulcanian blasts (Cassidy *et al.*, 2015). As periods of high explosivity are interpreted to be short-lived for the Echo Canyon eruption gas-poor and -rich pockets distributed vertically in the conduit may contribute to the observed eruption dynamics whereby early phases are fed by gas-rich pockets and followed by slower ascending gas poor ones. The decompression rates shown on Fig. 3.28 indicate textural groups in the cone deposits likely experienced higher rates of decompression (and hence ascent) than the OBP as they have higher NvCorr values. The exception is the NvCorr value for crystal rich regions of the dense OBP clast which is higher than the other OBP examples. As vesicle and microlite textures indicate a phase of second boiling in these regions due to microlite crystallisation (Piochi *et al.*, 2021) this is not unexpected. The high NvCorr in these regions of the dense clast is likely due to the influence of localised, late-stage bubble nucleation rather than differing decompression rates over 100's of microns in a single clast.

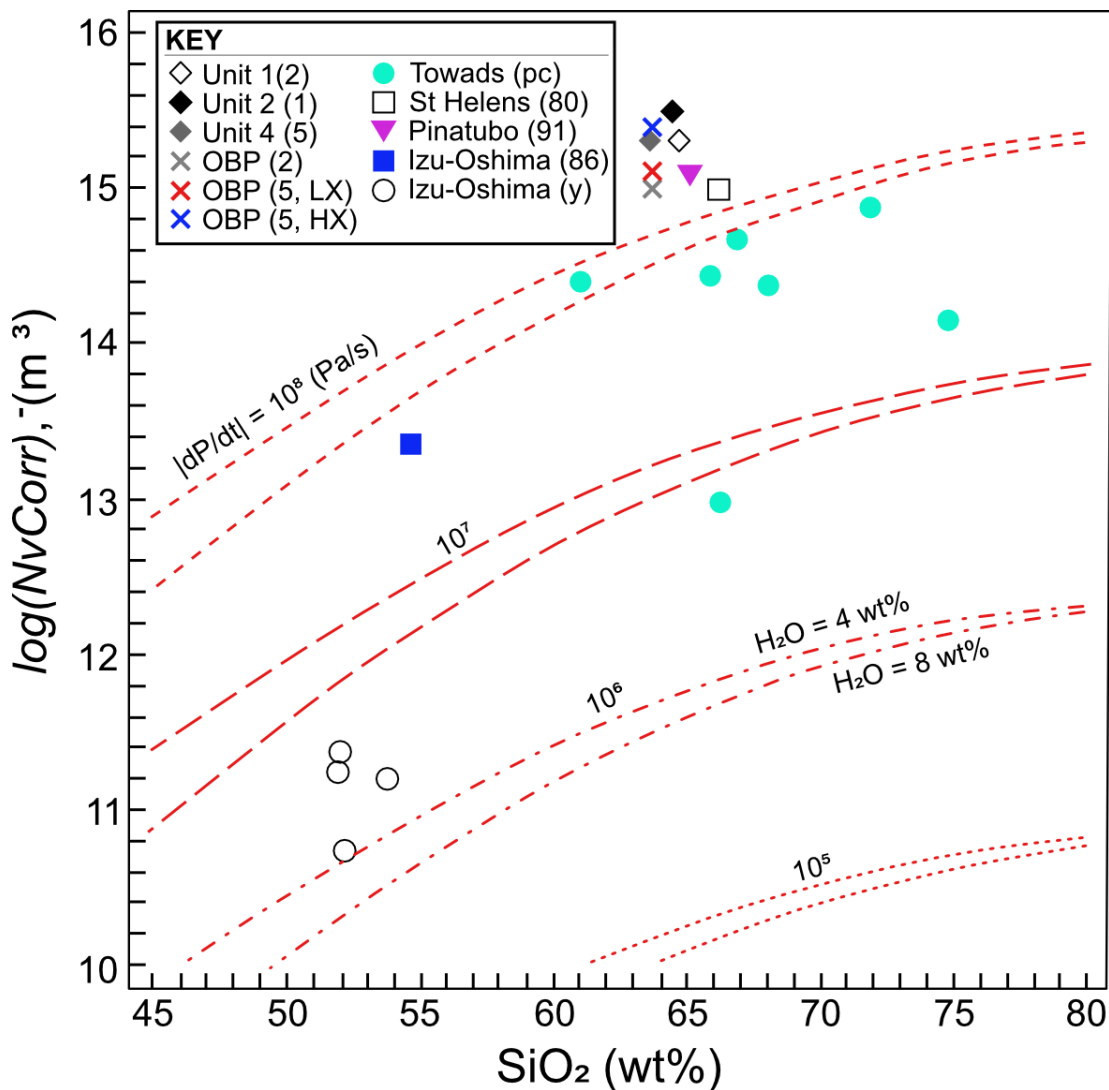


Fig. 3.28 plot of $\log(Nv)$ against SiO_2 for echo canyon eruption deposits and other example eruptions. Adapted from Toramaru (2006). Dashed lines correspond to decompression rates from Toramaru (2006), upper bound represents 4 wt% H_2O , lower bound represents 8 wt % H_2O .

Calculated decompression rates for the EC eruption fall can then be used to place upper and lower limits on reasonable ascent rates for this eruption. Rutherford *et al.*, (1993) derived ascent rates of $6.7 - 29.5 \text{ ms}^{-1}$ from amphibole reaction rims for the 1980 dacitic eruption of Mt St Helens, which plots close to the EC eruptions on Fig. 3.28. Shea *et al.*, (2010b) used the Toramaru (2006) decompression rate meter to model bubble number densities for the more alkali-rich eruption of the 79AD white pumice from Vesuvius. Shea *et al.*, (2010b) found decompression rates of 0.5 – 1 MPa reproduced bubble number densities found in natural samples for a surface tension of 0.035 Nm^{-1} . Increasing the surface tension required higher decompression rates to reproduce the bubble number densities observed in natural samples (Shea *et al.*, 2010b). For the white pumice, ascent rates of 20 – 40 ms^{-1} were required to replicate mass discharge rates calculated by Carey and Sigurdsson (1987) in numerical models (cf. Shea *et al.*, 2010b). With an estimated

surface tension of 0.075, higher decompression rates are thus expected from the Toramaru (2006) decompression rate meter, equivalent to ascent rates within the range of Mt St Helens and the Vesuvius 79AD white pumice.

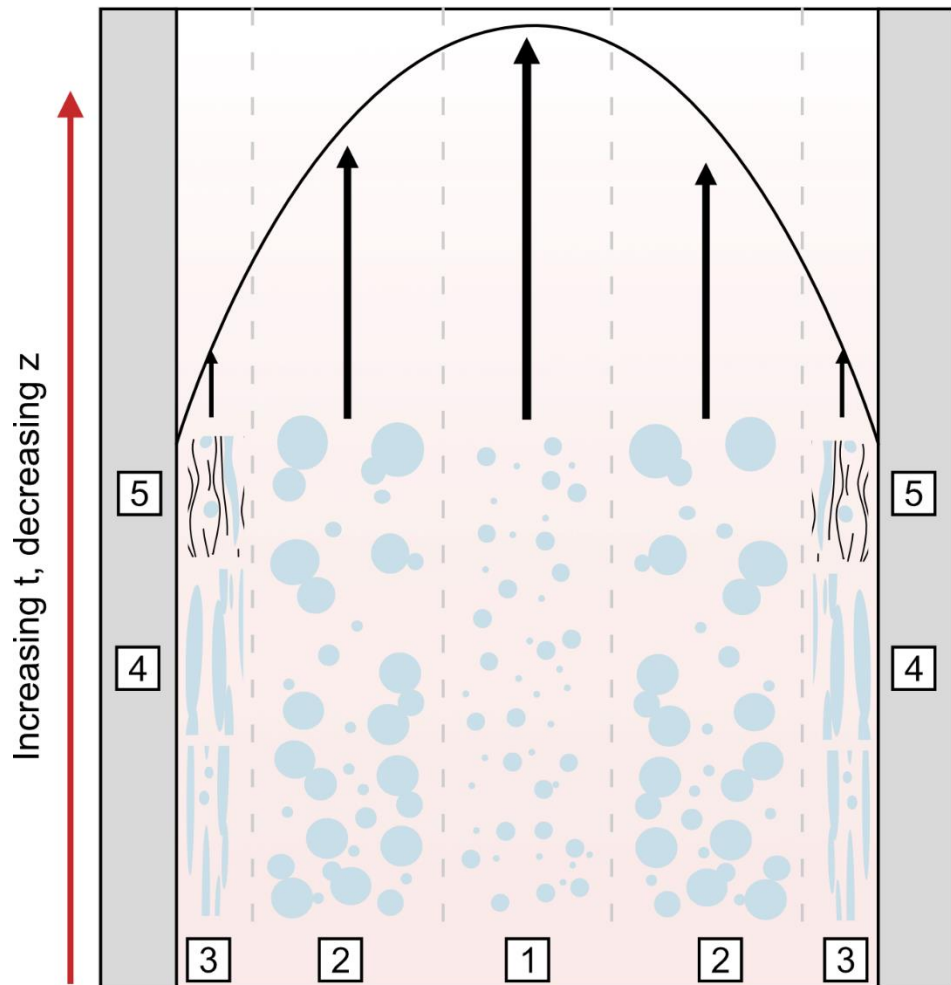


Fig. 3.29: Schematic diagram showing how textural groups represent portions of the melt with different ascent rates due to shear-induced velocity gradients at the conduit margins. Numbers 1 – 5 correspond to textural groups: 1 – micro-vesicular equant, 2 – macro-vesicular equant, 3 – micro-vesicular elongate, 4 – macro-vesicular elongate, 5 – dense.

3.4.5 Reconstructing the ascent of the Echo Canyon magma (summary)

Evidence presented thus far can be used to construct a model of the origin and ascent pathway of magma feeding the Echo Canyon eruption. Here I draw together evidence from the crystal cargo, melt viscosity and vesicle textures with constraints placed on fragmentation mechanism and decompression and ascent rates to summarise the ascent dynamics of the Echo canyon eruption. This is placed in the context of interpretations of field observations and juvenile clast material outlined in chapter 2 to explain the eruptive behaviour of this volcano.

Magma source and crustal interaction:

An initial trachytic melt containing approximately 5 – 6 wt% H₂O ascended rapidly from around 11 km depth (near the base of the crust) through a relatively closed-system, self-similar lower-crustal mush zone entraining plagioclase antecrysts. Evidence for an open-system mush zone is absent in the antecryst population which lacks complex zoning. Crystallisation of anorthoclase phenocrysts likely occurred at approximately 8.5 km depth with a crystallisation temperature of 835 - 920°C. Minimal disequilibrium textures in the antecryst and phenocryst population, coupled with very low microlite content in the cone pumices indicates rapid ascent persisted in the shallow crust. Throughout the eruption deposits the crystal cargo (non-groundmass) remains relatively constant, indicating interaction with other mush zones was minimal.

Early eruptive phase – cone deposits

Rapid ascent through the crust and high H₂O solubility in trachytes meant at shallow levels, exsolution provided strong concentration gradients for diffusive bubble growth. High H₂O diffusivities in trachytes accelerated this process, facilitating rapid bubble nucleation and growth generating high proportions of macro-vesicular equant clasts in early strombolian and vulcanian blasts. Bubble relaxation timescales exceeded rates of ascent in the conduit, preserving some features of coalescence in the vesicle population. Multiple nucleation events occurred generating micro-vesicular equant clasts, increasing the bubble number density. This promoted close packing of rapidly expanding vesicles, and facilitated fragmentation via bubble interference and rupture, as indicated by narrow BVDs (Fig. 3.1) and fact that calculated overpressures do not exceed the fragmentation threshold ($Ca = 300$, table 3.7). Unit thickness and unit bulk vesicularity distributions indicate the eruption reached its peak explosion intensity (Plinian) in Unit 3. At this point, drag at the conduit margins initiated the formation of shear zones leading to an influx of micro- and macro-vesicular elongate clasts. Low melt viscosities ($10^3 - 3.5$ Pas) and the influence of bubble morphology on shear viscosity facilitated rapid evolution of permeable networks in the sheared margins of the conduit. This promoted outgassing leading to melt and column densification eventually leading to column collapse and the explosive – effusive transition.

Effective outgassing through permeable networks, accumulation of melt at the conduit margins and the “kinetic reactivity” of trachytic melts (chapter 2) led to rapid decompression induced microlite crystallisation. Magma viscosity likely increased by up to 4 orders of magnitude while bubble break-up in shear zones impeded outgassing and facilitated lava effusion via low-viscosity zones (e.g., Pistone *et al.*, 2012). Effusion of the dome and lava created a cap, stalling the remaining ascending melt such that decompression (and ascent) rates were low enough to facilitate degassing-induced microlite crystallisation. Bubble overpressures increased due to closed-system volatile exsolution and second boiling in microlite rich regions. Increased viscosity via crystallisation and decreased brittle strength due to the presence of bubbles combined to promote explosive brittle fragmentation of the remaining melt forming the OBP in the final phase of the eruption.

3.5 Conclusions & implications:

In conclusion, careful examination of crystal cargo and vesicle textures has allowed reconstruction of key magmatic properties that underpin the ascent and eruption dynamics of the unobserved EC eruption. The key findings from this chapter are:

- Detailed assessment of textural and compositional evidence for equilibrium in the crystal population allowed phenocryst phases to be distinguished from antecrysts where standard tests for chemical equilibrium fail, avoiding inclusion of spurious temperatures.
- Power-law distributions in VSD curves provided additional evidence for rapid depressurisation, supported by high bubble number densities which correlate to decompression rates of 10^8 Pas as modelled by the Toramaru (2006) decompression rate meter.
- High decompression and ascent rates coupled with high H₂O solubility and diffusivity are likely responsible for the explosive nature of the EC eruption.
- Changing ascent rate, and not variations in viscosity is the dominant factor controlling transitions in eruptive behaviour during the Echo Canyon eruption as variations in ascent rate exert a strong control on developing vesicle textures.

- The dominant vesiculation process transitioned from rapid diffusive growth and coalescence through to ripening and bubble collapse as the eruption progressed, facilitating transitions from explosive – effusive behaviour.
- Calculated capillary numbers, bubble overpressure and fragmentation thresholds for EC eruption deposits support early fragmentation via bubble interference and rupture followed by brittle fragmentation due to bubble overpressure in the post-cone deposits.

The results of this chapter show that magma feeding the Echo Canyon eruption was able to ascend rapidly from depth at comparable ascent rates to eruptions of much larger eruptive volumes (e.g., Mt St Helens 1980 and Vesuvius 79AD). This has significant implications for ongoing hazard assessment at geographically isolated low magma-production rate ocean islands. In such locations, even a small-volume explosive eruption has the potential to cause severe disruption, particularly if there is only a short time between the onset of magma migration (and potential felt signals) and eruption. Here I have shown that careful analysis of vesicle textures and crystal populations can be a powerful tool in reconstructing important eruption controls of unobserved eruptions.

Chapter 4: Textural analysis of the Mingled Fall Deposit in 2D & 3D

4.1 Introduction

Chapters 2 and 3 demonstrated how qualitative and quantitative studies of pyroclast texture can elucidate changing ascent dynamics and processes that underpin eruption styles and transitions. I have shown that placing micro-scale observations of vesicle size and shape into context of the bulk properties of the ascending magma strengthens interpretations by identifying representative and extreme processes in the conduit. In this chapter I build on this framework and use an already stratigraphically and petrologically well characterised deposit to investigate more texturally complex samples in 2D and 3D – the basalt-rhyolite Mingled Fall deposit.

As discussed at length in chapter 3, vesicle textures represent the time-integrated record of processes of bubble nucleation, growth, coalescence, strain, and the development of permeability during ascent (Houghton and Wilson 1989). As such, measurements of vesicle size, shape and connectivity offer insights into the interactions between volatiles, crystals and melt during eruption triggering and ascent (Shea *et al.*, 2010). Volatile exsolution and subsequent bubble nucleation and growth can trigger / accelerate the ascent of a magma. The number of nucleation events identified in a population (e.g., via multiple peaks in a VVD plot) can help elucidate eruptive triggers and phases of syn-ascent crystallisation. For example, a bimodal VVD could record early nucleation at depth due to intrusion of new melt followed by a second stage of bubble nucleation due to a crystallisation event. Blower *et al.*, (2001) used experiments to illustrate how the power- to exponential-law shapes of VSD curves record a process of continuous nucleation where depressurization is rapid and volatile diffusion is slow (aka highly non-equilibrium degassing), which can act to tip systems towards equilibrium as it is a more efficient degassing process (Blower *et al.*, 2001). Preservation/not of coalescence events as surface roughness (i.e., without relaxation back to a spherical shape) can help constrain the relative ascent rates of magmas if the viscosity and relaxation timescale of the melt can be estimated (Castro *et al.*, 2012). Further, quantifying bubble elongation records the influence of shear on the melt. Growth and shear induced coalescence (up until channel collapse e.g., Heap *et al.*, (2015)) can both act to increase permeability and hence outgassing efficiency (Cassidy *et al.*, 2018) which exerts a

control on ash production during fragmentation and/or push an eruption towards effusive activity (Klug and Cashman 1996).

Understanding how these processes interact is important because they impact (and are impacted by) the viscosity of the ascending melt and hence the overpressures it can sustain prior to fragmentation. Ultimately this influences eruption explosivity, column height and stability, ash supply for deposition on infrastructure and the associated hazards.

Studies of vesicle clast texture in 2D are extremely common (e.g., Polacci 2005; Shea *et al.*, 2010b; Houghton *et al.*, 2010; Cross *et al.*, 2012 and Mitchell *et al.*, 2019) and their value recognised amongst the volcanological community. The workflow, and software (FOAMS) developed by Shea *et al.*, (2010) made it easier for vesicle size distribution studies to be carried out consistently between users and volcanic systems. In parallel, efforts to catalogue the many shape descriptors employed in studies of volcanic ash by Liu *et al.*, (2015) have made it easier to choose appropriate and comparable measures of vesicle shape and given a better understanding of how various measures interrelate. Further, work is now underway to produce a standardised workflow for studies of pyroclast texture including sample collection, thin section preparation, imaging technique and choice of analysed parameters (Comida *et al.*, 2021; Ross *et al.*, 2022). Standardising data collection in this way will improve our ability to compare studies and identify patterns in behaviour across a global database. However, studies of pyroclast texture in 2D are inherently limited by their inability to capture vesicle size and shape in 3D. As discussed in chapter 3, most vesicle size distribution studies make use of the stereological conversions of Sahagian and Proussevitch (1998) which assumes a spherical geometry, including the FOAMS software of Shea *et al.*, (2010). Some studies have adapted this conversion to treat samples with more elongate vesicles (e.g., Mitchell *et al.*, 2019) but all conversions are limited by the range of shapes used as input and cannot truly reflect more complex vesicle networks that develop in either highly sheared, or extremely connected samples. Further, a critical step when carrying out textural studies in 2D is the binarization of images. During this process vesicles, glass and crystals are differentiated by their greyscale values in backscattered electron images. However, vesicles may not be fully intersected (poor polishing) and the difference between greyscale values for crystals and glass or thin films and vesicles can be too low to be accurately captured during thresholding. Machine learning can be applied to improve the segmentation of images (see chapter 3 section 3.2.1) but often, some manual correction is still required. Shea *et al.*, (2010) provided a strategy for image processing in

the FOAMS handbook to try and standardise this process however different users may choose to “close bubble throats” of different sizes or reconstruct bubble walls using different methods. While the human eye is very good at identifying features that may be missed by segmentation algorithms, manual correction introduces uncertainty that is difficult to quantify, and the chosen approach is not always specified/justified in published materials. The impact of regularly applied assumptions / manual correction on the interpretations of the output from these studies must be better constrained to better assess when 2D studies add the most value, when they should be applied with caution, or avoided altogether.

One way to avoid the issue of inaccurate 2D – 3D conversion and capture the complexities of sheared or connected bubble populations is to study vesicle textures in 3D via X-ray computed tomography (XCT). During XCT, a rotating sample is bombarded with X-rays which are then imaged with a 2D detector (Baker *et al.*, 2012). As the X-rays pass through the sample, they are attenuated to varying degrees depending on the composition and density of the material (Baker *et al.*, 2012). In this way, a 3D map of the sample is generated, distinguishing between regions of different density e.g., vesicles, glass, crystals, this can then be visualised as 2D slices or by 3D rendering (Baker *et al.*, 2012). XCT is a non-destructive method of capturing textural data in 3D and is becoming more widely applied in volcanological studies (e.g., Gualda and Rivers 2006; Ketcham 2005; Polacci *et al.*, 2006; Hughes *et al.*, 2017 and Gonnerman *et al.*, 2017). The size of the volume that can be scanned depends on the material and the size of the smallest feature to be captured. A higher resolution scan requires a smaller scan volume to minimise noise in the data over reasonable operational timescales (Baker *et al.*, 2012). In addition, the high computational cost of extracting bubble volumes from raw XCT data limits the size of volume that can be processed at any one time (Baker *et al.*, 2012). This means compromises must be made during data collection and processing, and care must be taken to capture features that are representative of larger structures. Once a dataset is acquired, it must be processed to extract phases of interest as binary datasets from the greyscale volume. This requires careful segmentation and interrogation of the greyscale data to distinguish “noise” from real features. In geological samples features of interest are often touching (e.g., crystals side by side) and boundaries between them need to be distinguished to enable accurate measurements of key parameters (long axis, volume etc). Ketcham (2005) developed BLOB3D to allow separation and measurement of irregular features in 3D. Since then, 3D

processing software like Avizo® and Dragonfly® have produced increasingly sophisticated versions that allow users to adapt segmentation and separation workflows depending on the nature of their samples. During processing, choices are made about which voxels represent real structures and where to subdivide touching features etc. and there will be some error associated with the output. Lin *et al.*, (2015) investigated sources of error in XCT data processing and found that systematic errors caused by discrepancies between the true and measured volume can be minimised by choosing appropriate thresholding values when segmenting raw data. Random errors were found to increase with decreasing object volume relative to voxel (3D pixel) size and can be best offset by increasing the number of objects measured in a given size class (Lin *et al.*, 2015). Studies of vesicle texture in 3D have offered insight into the development of permeability in magmas (Kushnir *et al.*, 2017), investigate bubble growth in basalts (Bai *et al.*, 2008), make connections between bubble number density and eruption intensity (Polacci *et al.*, 2006) and explore fragmentation mechanisms in low-viscosity peralkaline rhyolites (Hughes *et al.*, 2017). While these studies have provided critical insights into volcanic systems and ascent dynamics, very few have investigated textures associated with mingling of compositionally distinct endmembers (e.g., Paredes-Marino *et al.*, 2017 and Morgavi *et al.*, 2016). Mingling of melts produces clasts which are extremely texturally heterogeneous in 3-dimensions, such heterogeneities are poorly captured via 2D sectioning even when serial sectioning at different orientations is employed. This study builds on the knowledge developed in past studies to expand the use of XCT-based analysis into texturally complex clasts from the Mingled Fall deposit on Ascension Island.

Chemical mixing of magmas is recognised as being almost ubiquitous in volcanic systems worldwide, feeding into models of open-system crystal mushes as storage regions in most settings (Cashman and Edmonds 2019). Mafic injection is commonly cited as a trigger for explosive silicic eruptions (e.g., Iceland (Rooyackers *et al.*, 2022), Montserrat (Murphy *et al.*, 1998) and Tarawera (Leonard *et al.*, 2002)) and can lead to chemical mixing and or physical mingling. Although the mechanisms through which mafic injection can trigger explosive events has been studied extensively (Sparks *et al.*, 1977 Folch and Martí 1998; Sigmarsson *et al.*, 2011; Paredes-Mariño *et al.*, 2017), the impact of mingling of melts on ascent dynamics is less well understood (e.g., Metrich *et al.*, 1993; Lautze and Houghton 2005). The preservation of physical mingling without chemical mixing is rare, in part because chemical exchange between magmas will inevitably occur once they begin to

physically interact (Morgavi and Perugini 2017). Where preserved, evidence of physical mingling comprises texturally distinct regions in erupted products, e.g., enclaves and banding (Nairn *et al.*, 2004; Morgavi and Perugini 2017; Plail *et al.*, 2018 and Chamberlain *et al.*, 2020). For the Mingled Fall, mafic injection and mingling occurred ~ 24 hours prior to eruption (Chamberlain *et al.*, 2020). The basalt and rhyolite magmas were extensively intermingled down the micron scale, but ascent was so rapid as to preclude compositional mixing (Chamberlain *et al.*, 2020). This deposit offers a rare opportunity to examine how mingling of compositional endmembers impacts vesiculation and ascent.

In the following chapter I will use the example of the basalt-rhyolite Mingled Fall on Ascension Island to:

1. Explore how mingling between compositional endmembers impacts vesiculation processes during ascent.
2. Produce a generalised workflow for extracting textural data from mingled samples in 3D that can be reasonably applied to other samples.
3. Interrogate and assess the limitations of 2D and 3D textural analyses and identify ways to improve 3D analyses.

Doing so will provide new insights into vesiculation processes in physically mingled magmas, and the ways in which we interrogate such deposits.

[4.2 The Mingled Fall deposit](#)

The Mingled Fall (MF) deposit is the record of one of more than 80 explosive felsic eruptions recognised on Ascension (Preece *et al.*, 2021), and contains the only evidence of macro-scale mingling between two compositional endmembers (basalt and rhyolite) identified on the island (Chamberlain *et al.*, 2020). The MF deposit was first characterised by Chamberlain *et al.*, (2020) who mapped its outcrops across the central felsic complex (CFC) on Ascension (see Fig. 4.1). A summary of the stratigraphy presented in Chamberlain *et al.*,

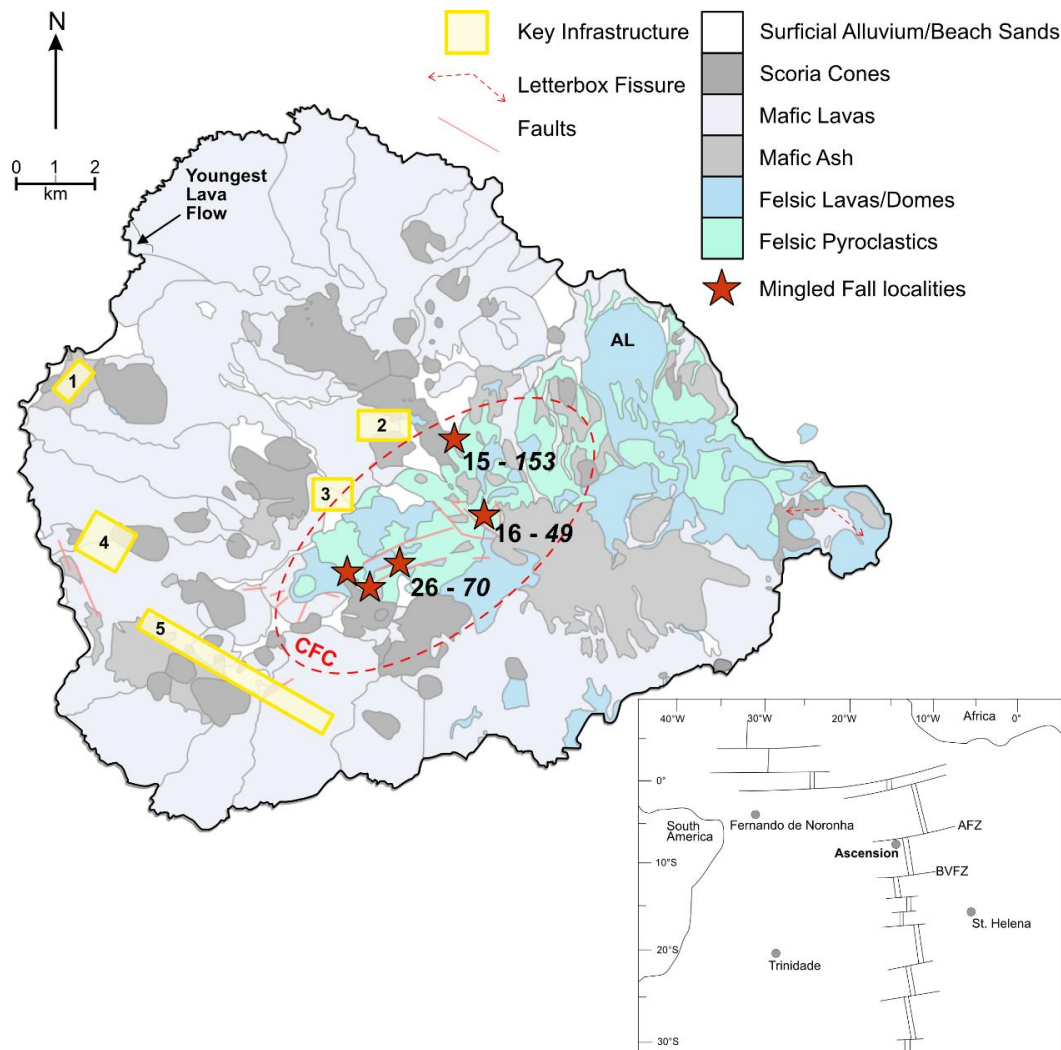


Fig. 4.1: Map showing Mingled Fall localities (stars). Locality numbers where stratigraphic logs were produced, all outcrops reported in Chamberlain *et al.*, (2020) were re-visited and logged for this study shown in **bold**. Total deposit thicknesses are in **bold italics**. Key infrastructure is marked in yellow, numbers 1 – 5 correspond to: 1 – Georgetown (location of government buildings, the hospital and the port), 2 – Two Boats Village (location of the school), 3 – the Royal Airforce Base, 4 – The US Airforce base, 5 – The airport runway. The central felsic complex (CFC) is delineated by the red dashed oval. Inset map shows the location of Ascension Island relative to Africa, South America and the Mid-Atlantic ridge.

(2020) is given here alongside a generalised stratigraphic column supplemented by data collected during this study. The deposit has a maximum thickness (from the base of L1A - where present, to the top of L3) of ~150 cm and its stratigraphy records both a phreatic (sub-units L1A and L1B) and a magmatic phase (sub-units L2A and L2B, and unit 3) (Chamberlain *et al.*, 2020) (Fig. 4.2). Sub-unit L1A comprises a basal fine ash layer with an undulatory upper surface, and a fine layer comprising non-juvenile, dense mafic ash. Sub-unit L1B consists of dense non-juvenile scoria clasts that coarsen upwards from 3 – 10 mm. The magmatic phase is the focus of this study and is sub-divided into three units based on changing proportions of pumiceous, mingled and scoriaceous clasts – L2A, L2B and L3 (see Fig. 4.2). Unit L2 is 13 – 70 cm thick and comprises two sub-units. Sub-unit L2A contains

dense grey scoria, grey pumice, white pumice and 5% lithic clasts – pumice increases in abundance up through the unit. Sub-unit L2B coarsens upwards and is dominated by pumice clasts, with mixed pumice-scoria clasts and 10% lithics. Unit L3 is 36 – 127 cm thick and is dominated by scoria clasts. Pumice clasts and plutonic lithic clasts coated in mafic lava constitute a minor component of the unit (Chamberlain *et al.*, 2020).

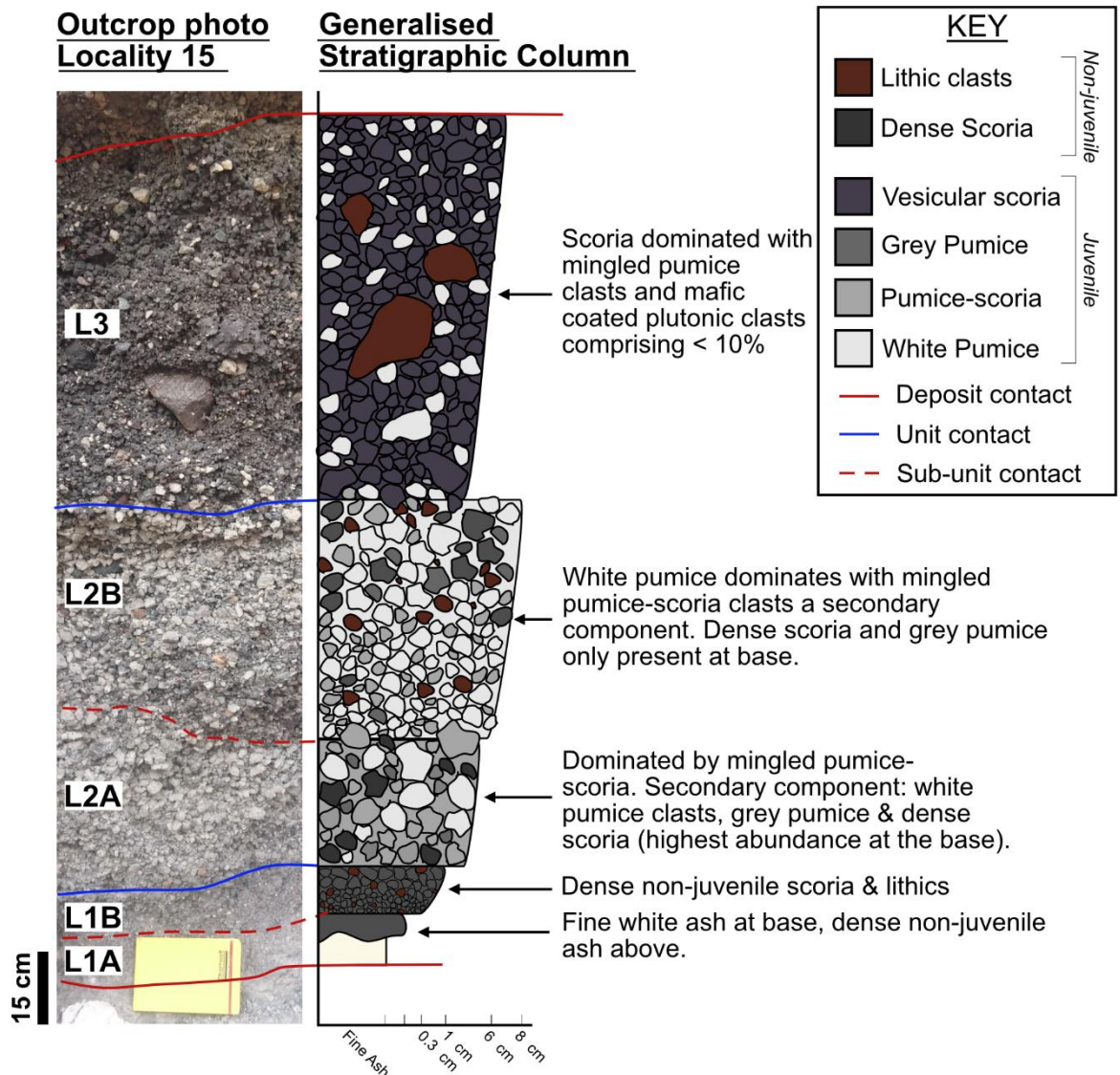


Fig. 4.2: Outcrop photo and generalised stratigraphic log of the Mingled Fall deposit based on Chamberlain *et al.*, (2020) and observations from 2018 – 2020 fieldwork for this study. All units/sub-units are clast supported apart from ash units of L1A. The background colour of each unit indicates the dominant clast type. Secondary components are indicated by coloured clasts. Relative proportions of coloured clasts correspond to abundance of each clast type in the unit. Grain size is plotted as modal clast size.

Chamberlain *et al.*, (2020) found limited equilibrium oxide pairs in clasts from the mingled fall, the only usable pairs were found in the basaltic material and yielded temperatures of 860 – 930°C at fO_2 of -0.75 and +0.2 log units relative to the Nickel-Nickel- Oxide (NNO) buffer using the model of Ghiorso and Evans (2008). As these temperatures and oxygen

fugacities were similar to those calculated for similar compositions in Chamberlain *et al.*, (2019) results of thermometry on similar compositions from that study were adopted to convert melt inclusion volatile concentrations to entrapment pressures - 900°C for basalt, 800°C for rhyolitic melt inclusions by Chamberlain *et al.*, (2020). Whereas it is preferable to use temperatures directly sampled from the analysed magma, the crystal poor nature of many magmas on Ascension often makes it necessary to use proxies from magmas with similar mineral assemblages and crystal/melt compositions (e.g., see Chapters 2 and 3). Chamberlain *et al.*, (2020) calculated that a 50°C discrepancy between the applied and “real” melt temperatures corresponds to a depth uncertainty of 0.5 km. Chamberlain *et al.*, (2020) calculated entrapment pressures (calculated using MagmaSat based on Ghiorso and Gualda (2015)) that yielded storage depths of approximately 11 km, close to the base of the crust on Ascension (Klingehöfer *et al.*, 2001).

Montagna *et al.*, (2015), Perugini *et al.*, (2015) and Perugini *et al.*, (2010) all show how measuring diffusion profiles across mafic-felsic glass contacts can be used to elucidate the timing of mingling. Further, Chamberlain *et al.*, (2014) and Morgan *et al.*, (2004) are just two examples of how the same technique is applied across zoning patterns in crystals to constrain the time between a crystal’s exposure to a compositionally distinct melt and eruption. Chamberlain *et al.*, (2020) interpreted the lack of zoning or overgrowth textures in crystals combined with lack of diffusion profile across the mafic-felsic glass boundaries to indicate short timescales between mingling and eruption. They used the study of Perugini *et al.*, (2010) on a compositionally similar melt to constrain the timeframe between mingling and eruption for the Mingled Fall to ~24 hours. This timescale corresponds to an ascent rate of approximately 0.13 ms^{-1} (Chamberlain *et al.*, 2020). Such rapid ascent from relatively great depths has significant implications for anticipating future eruptions on Ascension as the timeframe between potentially detecting magma movement and the onset of an eruption could be extremely short. Thus, although seemingly rare on Ascension, understanding the impact of magma mingling events on ascent and eruption dynamics is a useful way to anticipate critical precursory signals and suggest useful ways to monitor subsurface changes.

In this chapter, I will use the example of the Mingled Fall deposit eruption products to define a workflow by which complex vesicle textures can be interrogated in 2D and 3D. The workflow is designed to ensure maximum preservation of textural and compositional data

and allow scaling-up of interpretations from the sub-micron to deposit scale. Comparison of the results between the 2D and 3D strategies acts as a demonstration of the value of the additional information about eruptive behaviour yielded by the 3D analysis. The focus of this particular example is the investigation the two mingled melts, and their impact on vesicle textures during ascent.

[4.3 Methods 1 – sampling & clast selection](#)

Careful clast selection is required to ensure interpretations of vesicle textures are representative of the deposit and scalable to larger conduit processes. As such, the methodologies presented in the preceding chapters were here applied to the Mingled Fall deposit prior to further investigations of individual clasts in 2D and 3D.

4.3.1 Stratigraphy & sampling

Chamberlain *et al.*, (2020), identified the MF deposit in several locations across the central felsic complex (CFC), see Fig. 4.1. These locations were re-visited, and stratigraphic logs produced at localities 15, 16 and 26 (Fig. 4.1) using the unit divisions detailed by Chamberlain *et al.*, (2020) (Fig. 4.2). Each Unit was distinguished from its stratigraphic neighbours via componentry and juvenile clast texture. Average maximum clast size was calculated by measuring the 5 largest clasts in outcrop and taking the average long axis. Modal clast size was qualitatively estimated in the field based on careful examination of the wider outcrop. The magmatic phase of the eruption spans units L2A, L2B and L3 as defined by Chamberlain *et al.*, (2020) and these were the focus of sampling. Sampling was carried out at all three localities, but clasts selected for further analysis were from locality 15 (see Fig. 4.1). Bulk samples were collected from each magmatic sub-unit/unit (L2A, L2B and L3) by excavating a region up to 10 cm thick, extending laterally across the unit until at least 100 clasts were collected for each unit (sufficient for bulk density measurements, after Shea *et al.*, (2010)). Grid references for all Mingled Fall localities are listed in table 4.1 along with sample numbers and deposit thicknesses.

Locality N°	Grid Reference (UTM zone 28S)	Deposit thickness (cm)	Sample numbers
AI18_15	-7.93701 -14.357793	153	¹ AI18-848 – 861
AI18_16	-7.947738 -14.352414	49	AI18-882 – 885
AI18_26	-7.955357 -14.365748	70	AI18-863 – 864

¹Samples used for textural analysis

4.3.2 Density measurements & clast selection

In the lab, density measurements were carried out on at least 100 16 – 32 mm clasts from each unit following the methods outlined in chapter 2 after Shea *et al.*, (2010). To calculate clast porosity a value for dry dense rock equivalent (DRE) was calculated using the method of Lange and Carmichael (1987). Whole rock values for pumice / scoria clasts from the mingled fall obtained via XRF by Chamberlain *et al.*, (2020) were used as input (see Appendix 3.1 table 3.1). For clasts dominated by pumice, a DRE value of 2.54 g/cm³ was used, for scoriaceous clasts, 2.85 g/cm³ was used. Measured clasts were then categorised based on macro-scale vesicle / mingling textures observed in hand specimen.

Four textural groups were identified; pumice, mingled (pumice dominated), mingled (scoria dominated) and scoria. To ensure representative sampling of vesicle textures with the limited analytical time available, several clasts from each dominant textural group were selected from within the modal bulk vesicularity of each unit. These clasts were then sent to Dr Matthew Andrew at the Zeiss Microscopy facility in California. A compromise was made between selecting the most appropriate clasts for x-ray computed tomography (XCT) (e.g., size and clast shape), capturing variations in texture, bulk vesicularity and unit source. As a result, three clasts were sampled from L2A (one pumice and two mingled clasts) and one from L3 (scoria) (see stars on Fig. 4.3). The textural characteristics of clasts from L2B broadly matched those from L2A on the macro-scale so the L2A clasts that were more suited to XCT analysis were favoured over ensuring sampling from each unit. Selected clasts are numbered and presented alongside their bulk vesicularities, textural groups, and stratigraphic units in table 4.2.

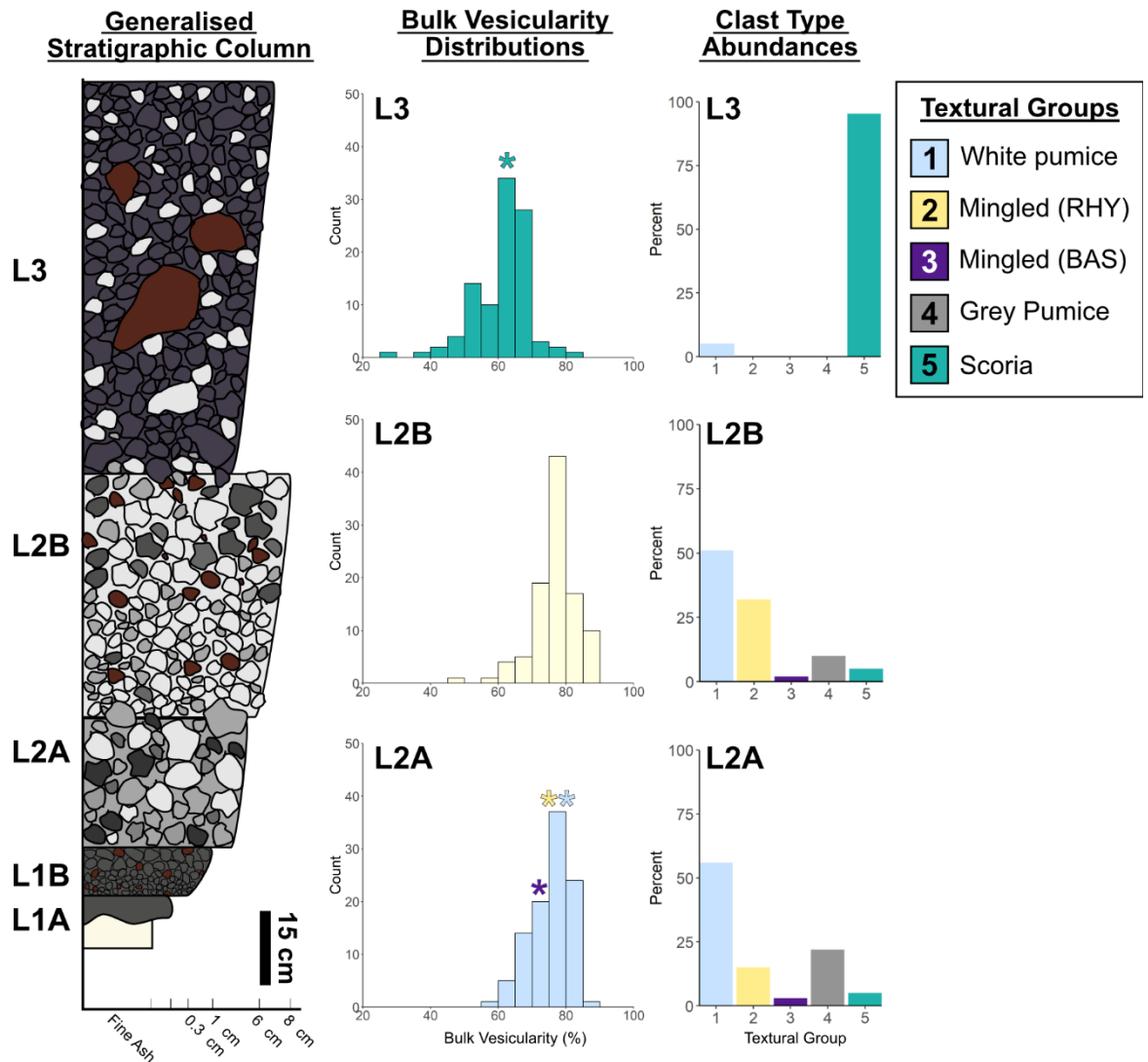


Fig. 4.3: Bulk vesicularity distributions and textural group abundances for sub-units L2A, L2B and unit L3 of the Mingled Fall. **Left:** generalised stratigraphic column as seen in Fig. 4.2. **Middle:** bulk vesicularity distributions from density measurements of at least 100 16 – 32 mm clasts in each unit. **Right:** Abundance of each textural group identified in the deposits: 100 clasts classified from each unit/sub-unit. Asterisks show where clasts were sampled from for further analysis. Blue = white pumice, yellow = pumice-scoria (rhyolite dominated), purple = pumice-scoria (basalt dominated), green = scoria. Grain size is plotted as modal clast size.

Clast N°	Unit	Textural Type	Bulk Vesicularity (%)
4_70	L2A	White Pumice	77
5_102	L2A	Mingled (BAS)	63
6_37	L2A	Mingled (RHY)	77
7_50	L3	Scoria	66

4.4 Methods 2 - 3D data collection & processing

Interpretations of vesicle textures in 3D require careful processing of XCT data to extract a bubble population that most closely reflects the “true” bubble/melt structures of the sample. The main factor to consider is how accurately thin melt films are resolved,

preserved or reconstructed. The impact of each processing step on the resulting bubble population must be considered and understood to allow confident interpretation of the output. In the methods below (and in Appendix 3.1) essential detail is provided on how various algorithms were applied and why, such that another user could re-produce, improve or interrogate my results (raw XCT data for the mingled and scoria clasts can be found in [electronic appendix 3_2]).

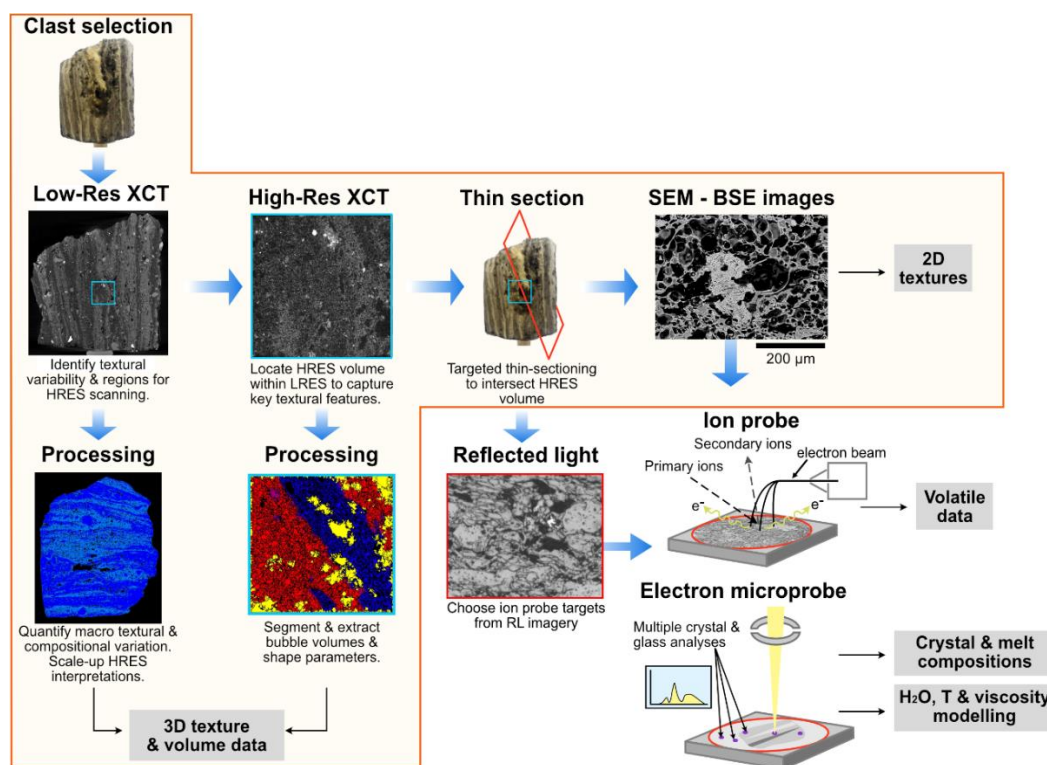


Fig. 4.4: Correlative microscopy workflow showing how data was collected to reduce the impact of destructive sampling techniques. HRES = high-resolution, LRES = low-resolution. BSE images are backscattered electron images. XCT is x-ray computed tomography. Orange outlined region is the part of the workflow used in this study.

Data collection was carried out using a workflow carefully designed to ensure the maximum amount of textural (and to some extent compositional) data was preserved as possible from each clast. Figure 4.4 shows the workflow designed and followed for this study. The workflow was designed such that it can be reapplied to other samples and facilitate texturally constrained and targeted micro-analytical studies. In the below text, all italicised text corresponds to named algorithms or adjustable algorithm parameters available in the academic version of Avizo®.

4.4.1 XCT data collection

To identify key locations for high-resolution (HRES) mapping and preserve a record of macro-scale textures, a low-resolution (LRES) scan of the entirety of each clast was first

collected using a Zeiss Versa 620 X-ray Microscope at the Carl Zeiss X-ray Microscopy facility in Pleasanton, CA. LRES scans comprised isotropic voxels with a pixel size ranging from ~18 – 23 μm , initial scanned volumes were 2000 x 2000 x 2000 voxels (the maximum FOV for the instrument). The pixel size of each scan (HRES and LRES) is listed in table 4.3. The data were examined using Thermo Fisher Avizo® (version 2020.1 or newer) software. The greyscale volumes were trimmed to remove distorted regions at the top and bottom caused by beam cone interference (approximately 150 slices per sample). As clasts were scanned whole, their irregular shape introduced slightly more noise into the data than if they had been trimmed to a regular shape. This is acceptable in order to acquire a full clast scan that enabled the LRES volumes to be used for macro-scale textural identification. In the reconstructed 3D greyscale volumes, high density objects appear brighter, this permits identification of crystals/ lithic clast inclusions and regions of basalt/ rhyolite composition (see Fig, 4.5). These scans were used to select targets for HRES scans. HRES volume locations were chosen based on the following considerations: (a) capturing representative macro-scale textures, (b) capturing interesting micro-scale textures (mingling) and (c) avoiding regions of “signal shadow” and beam hardening artefacts created by large crystals/ lithic inclusions.

Table 4.3: pixel size for high and low-resolution x-ray computed microtomography scans

Sample	Scan type	Pixel size
4_70	LRES	21.8423
	HRES	1.8283
5_102	LRES	18.1850
	HRES	1.6821
6_37	LRES	23.1479
	HRES	1.0022
7_50	LRES	18.1902
	HRES	1.7194

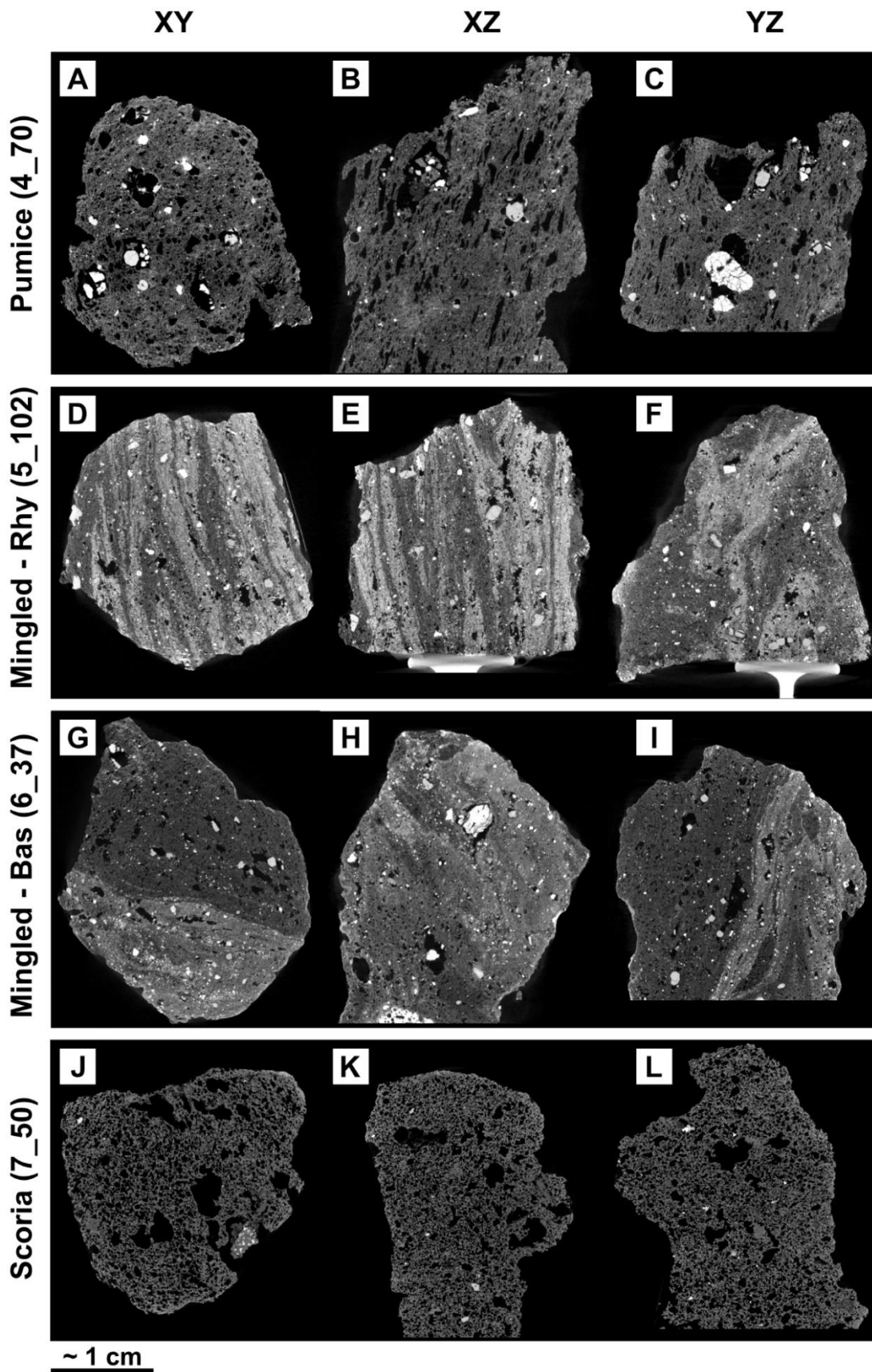


Fig. 4.5: Slices from low resolution (LRES) scans of selected clasts from the Mingled Fall. Bright regions have higher densities. Bright irregular particles are crystals and lithic clast inclusions (e.g., in A – C). Bright interfingered regions (e.g., D – I) are basaltic regions of mingled clasts.

An approximately 2 mm³ region of each clast was scanned at high resolution, voxels were isotropic with a pixel size ranging from ~1 – 1.86 μm (table 4.3). To reduce noise in the scans and enable more reliable reconstruction of thin melt films, some samples were trimmed to give a more circular cross section parallel to the rotation axis. The upper and lower limits of the HRES volumes were again cropped to remove any distortion and then HRES volumes were co-located within the LRES volume by matching distinctive features in each orientation (see Fig. 4.6). The HRES volumes were then processed using Avizo® to extract bubble size and shape information and basalt/rhyolite melt distribution. The locations of the HRES sub-volumes within the LRES datasets were then used to target thin sectioning to capture still higher resolution textural data (including thin melt films and microlite crystallinities) also sampled in 3D (see section 4.5.1).

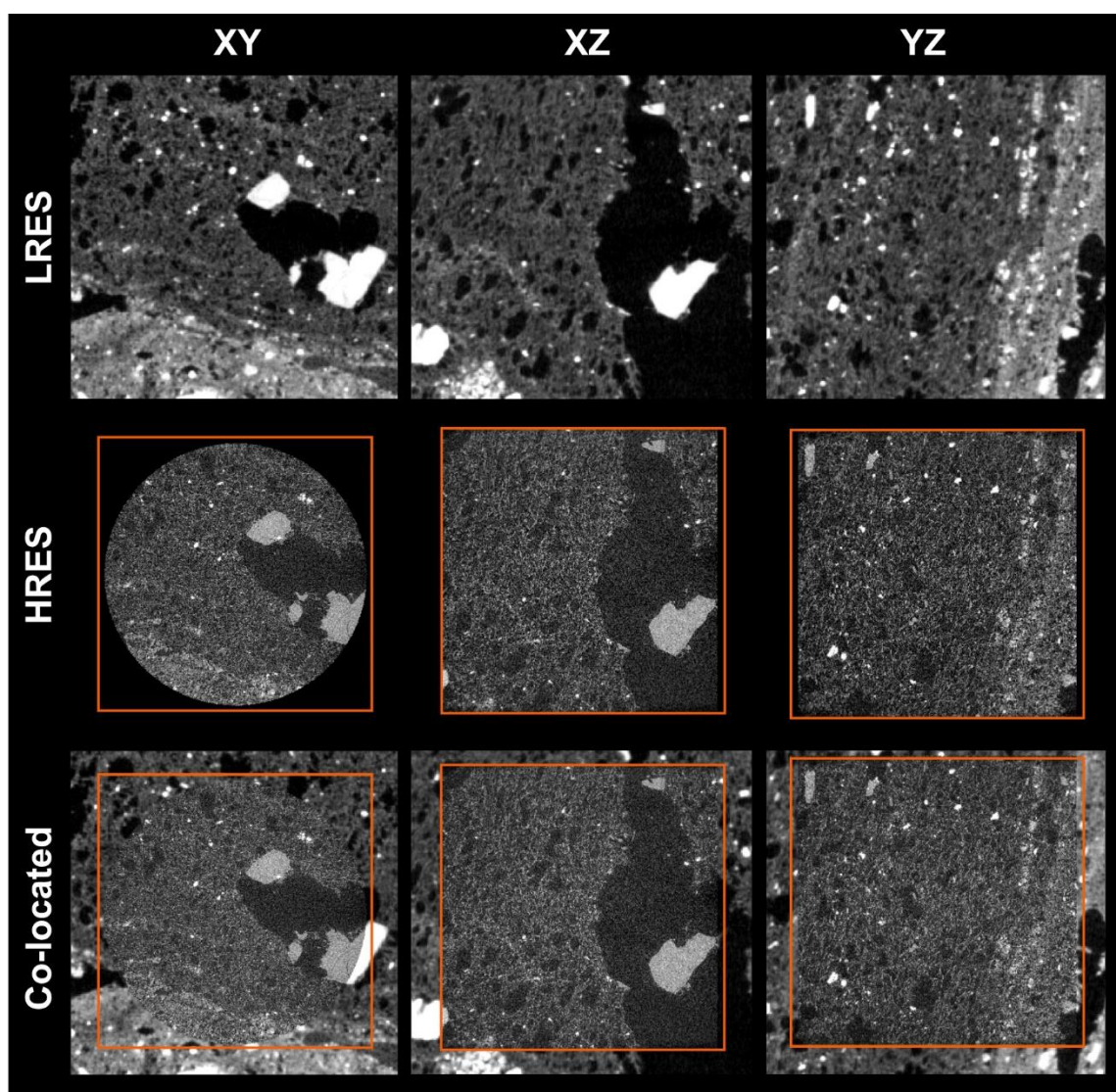


Fig. 4.6 showing how high-resolution (HRES) volumes were located within low-resolution (LRES) ones. Distinctive features were matched up in three orientations. Example from mingled clast 6_37.

4.4.2 Segmentation – HRES

To extract a bubble population from the HRES greyscale volume a labelling, or segmentation must be performed to generate a binary map of bubble/non-bubble – in much the same way as for 2D BSE images. As the size distribution of bubbles is important in interpreting degassing and thus eruptive behaviour it is important that as true a representation as possible of bubble walls (which can become very thin) is made in the final output data. Typically, there is more noise in the 3D data than in 2D, but there are also a greater number of ways to assess whether that “noise” is real (remnants of poorly resolved thin films) or an artefact of data collection. This is in part, due to the fact that collection of XCT data is a non-destructive process that limits the opportunity for fragmentation of the thinnest films. Neighbourhoods can also be interrogated in three dimensions - as opposed to two - to assess whether a voxel (3D pixel) forms part of a cohesive structure. Often, the human eye is better able to identify “real” patterns/features within the noise than image processing algorithms, but it is unfeasible to manually identify each melt film in a 3D dataset (typically 2000x2000x2000 voxels). Here, a method is outlined that balances relatively accurate segmentation with computational restrictions and processing time. The workflow outlined below can be applied to any XCT dataset generated using porous samples, but was particularly focussed toward explosive volcanic products. These types of samples are dominated by large numbers of thin-film bubble walls, complex bubble geometries and bubble volumes that vary over several orders of magnitude. Each sample has a different porosity, melt thickness and microlite crystallinity, all of which impact the segmentation process so while a general workflow can be defined, specific parameters must be varied at each stage and some steps may not be required for all samples. In all instance the workflows change the data as little as possible.

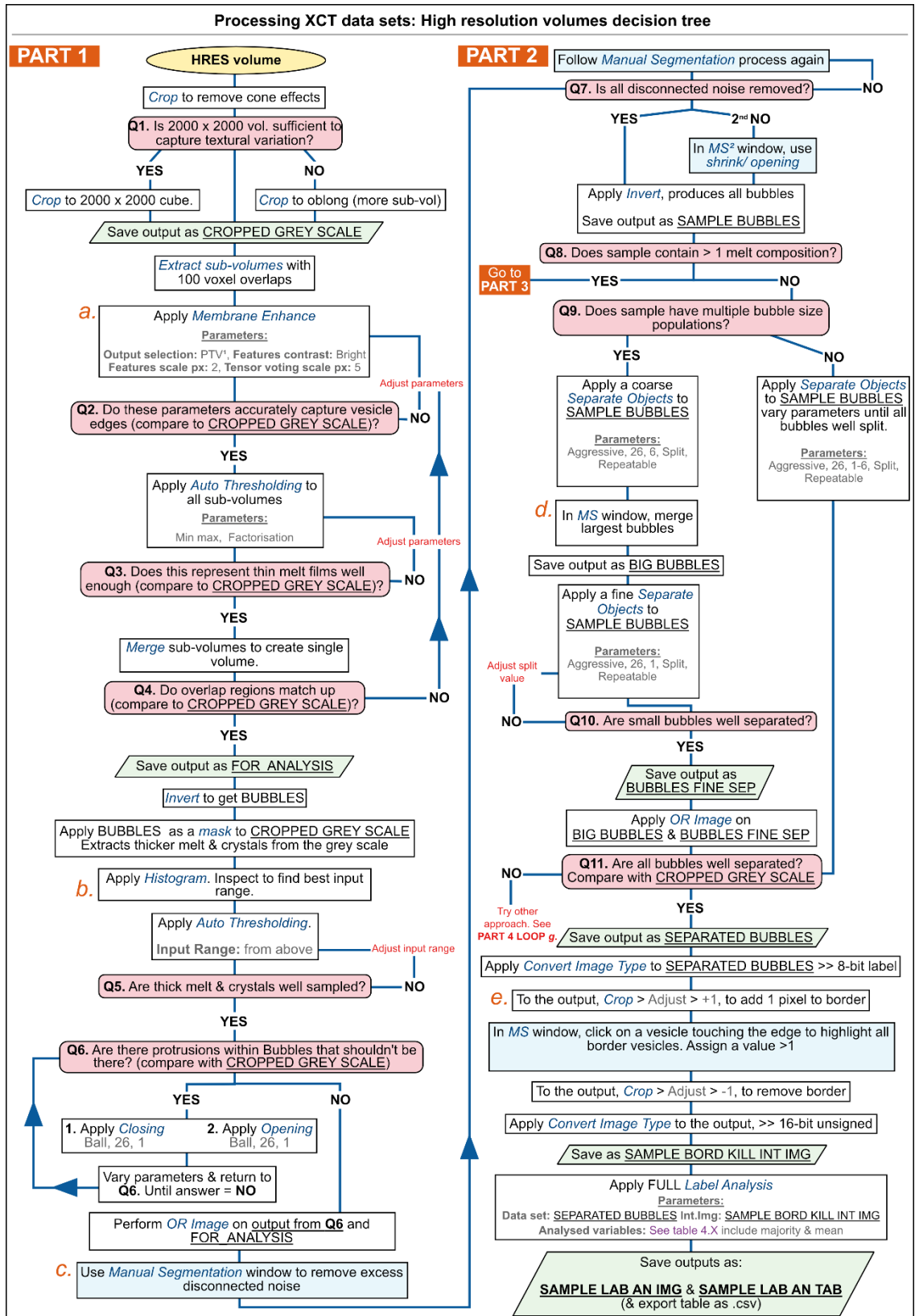


Fig. 4.7 X-ray computed tomography (XCT) data processing workflow for extracting bubble volumes from high resolution data in Avizo. Blue italicised text is used for names of standard algorithms available in Avizo.

4.2.2a Creating a binary melt field:

Each HRES volume was too large to run some of the complex segmentation algorithms in a reasonable time frame, so the data was divided into a series of 8 – 13 overlapping sub-volumes (typically approx. 800 x 800 x 800 voxels) depending on the textural variation of the sample (Fig. 4.7 Q1), with overlap of at least 100 slices to reduce edge effects during re-combination. Standard segmentation techniques are often imprecise with complex thin film structures and could not be applied here. Instead, the “*membrane enhancement*” filter (Avizo® v.2019.1 onwards) was used (Fig. 4.7, box a). This filter assumes a ridge-like membrane profile and uses a tensor voting algorithm to allow voxels in close-proximity on the same structural plane to enhance the structural information of their neighbours. The output is another greyscale volume. Visual inspection following testing showed that “*planeness tensor voting*” produced melt networks of higher quality (although this does increase the computational time) and allowed optimisation of the algorithm parameter for these types of sample microstructures. Varying parameters within the algorithm impacted the quality of melt film extracted. The “*Features scale px*” parameter sets the size of feature the algorithm should enhance, and the “*tensor voting scale*” (*TVS*) value determines the length over which neighbours can be used to strengthen each other’s structural information. A *Feature scale* value of 2 was found to be optimal for capturing the thinner films but missed thicker melt regions. However, these can be captured using less complex algorithms. A *TVS* of 10 px routinely over-estimated the thickness of glass walls, and the most accurate representation of the thin melt films was generated using a *TVS* of 5 and a *feature scale* of 2 for all processed volumes (Fig. 4.8). The thicker melt regions are extracted from the greyscale in a separate processing step.

The greyscale output sub-volumes were then recombined (Fig. 4.9) and the full enhanced data volume segmented using the *Auto threshold* function to produce an 8-bit binary label of the thin films (called “FOR_ANALYSIS”).

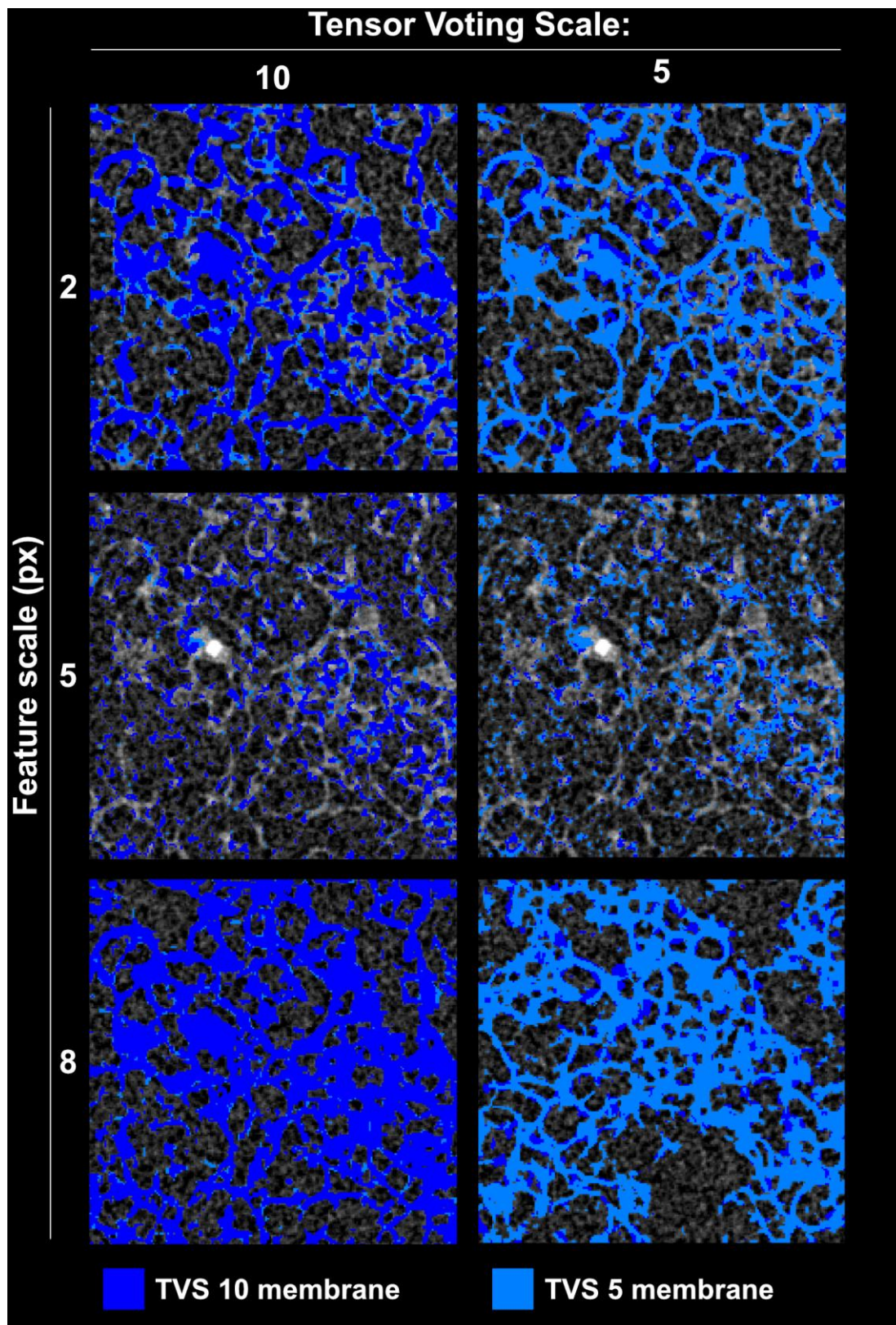


Fig 4.8 showing how varying parameters impacts the quality of thin membrane extraction from greyscale HRES volumes. Dark blue represents results from a tensor voting scale (TVS) of 10 px, pale blue represents results from a TVS of 5 px. Here the output from the membrane enhance algorithm has been thresholded to produce a binary dataset for ease of comparison.

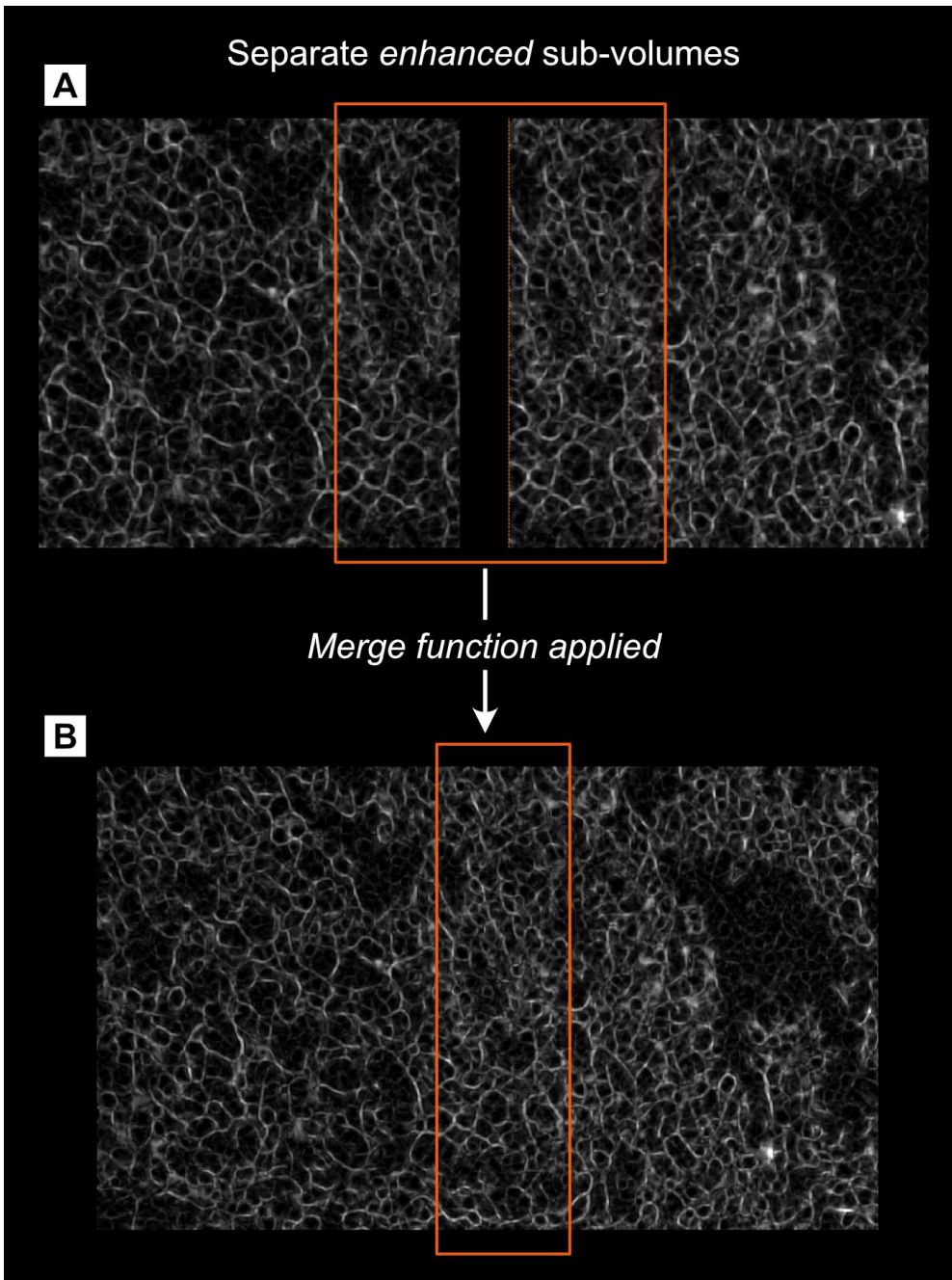


Fig. 4.9: A: side by side greyscale of enhanced membranes with overlap indicated by the orange box. B: the same area after the merge function has been applied.

4.2.2b Add thicker melt films and crystals

Inverting the thin film data produces a binary map of the volume that is NOT thin films. When applied as a *mask* to the original greyscale volume, this yields an image containing only the thicker melt regions and crystals missed by the *membrane enhance* algorithm and the bubbles (Fig. 4.7 b). This can then be segmented using the *Auto Thresholding* algorithm which works well for segmenting datasets where the greyscale histograms of the different phases overlap as is the case for many geological materials. Here we see one peak from the

pores, and one from the thick melt regions + glass. *Auto Thresholding* reduces human biases in setting a single thresholding value and relies only on the analyst providing the limits that define the region of peak overlap in the histogram (Fig. 4.10). The algorithm then defines the threshold value between those limits based on the data structure.

When the limits are broadly correct, the output of the thresholding is a binary dataset that contains the thick melt regions and crystals. The values of these limits vary with the sample and histogram peak shape and may require some minor adjustment (Fig. 4.7 Q5).

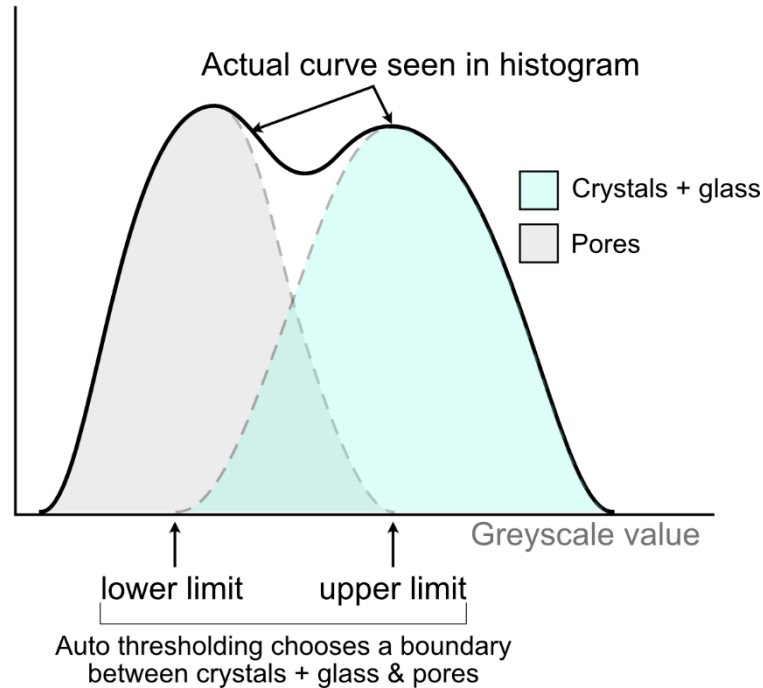


Fig. 4.10: visualisation of a histogram produced from a greyscale volume. The data shows two peaks (thick black line) and the user must extrapolate the peaks of the curves downwards (dashed lines) to identify the start and end point of peak overlap to be used as the lower and upper greyscale limits for auto thresholding.

The thicker melt/crystal regions (output from Fig. 4.7 Q6) are then combined with the thin melt films (FOR_ANALYSIS) using the *Or_Image* function. The output generally contains substantial disconnected noise that was captured by the two segmentation processes (e.g., voxels in pore spaces that are not connected to the melt network). This was removed by selecting the connected melt network (using the picker tool in the *Manual Segmentation* window, Fig. 4.7 c), and deleting the non-selected disconnected features. In datasets where there is still some excess noise on visual inspection of the segmented structure, an *opening* (*erosion* then *dilation*) can be applied (Fig. 4.7 Q7) to remove small features in contact with the melt/crystal network. If needed, a *closing* (*dilation* then *erosion*) is also applied when the user feels real bubble walls are still incompletely connected. The refined melt network

is then inverted producing a binary label dataset of the “bubbles” (here called e.g., 5_102_BUBBLES).

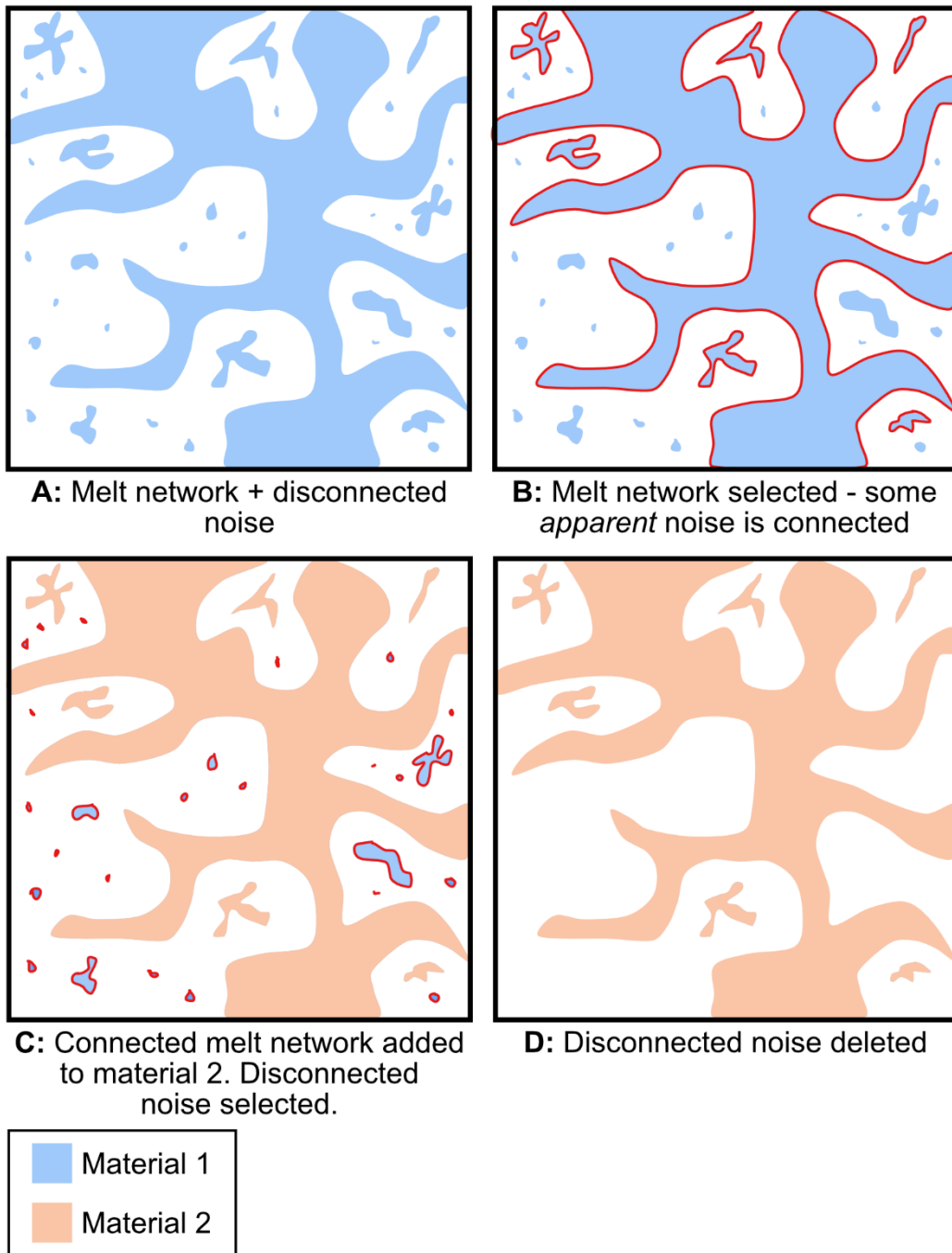


Fig. 4.11 showing how disconnected noise is removed in the manual segmentation window by adding all connected melt + crystals to Material 2 then selecting the remainder of material 1 and deleting it. Red outlines show which material is selected.

4.4.3 Extracting bubbles – single composition

4.4.3a Bubble separation

All imaging methods have a resolution limit, and even with the film enhancements applied above, the finest films are missing or incomplete in the segmented dataset. We can see the existence of films that are 1 – 2 μm thick or less in BSE images, particularly in pumice clasts. In addition, in removing the disconnected noise we may have removed some traces of these poorly resolved films, artificially increasing the size and changing the shape of some bubbles. To address both issues, we apply the *Separate Objects* algorithm to re-impose the most likely missing films.

The separation algorithm uses a distance-based watershed. The local maxima in the distance map define the centres of each pore, and a throat is imposed depending on the magnitude of the local minima between two adjacent maxima (termed the “marker extent”, larger values for the marker extent means less separation of the pores), and the geometry of the required connection. In these samples (particularly the rhyolite regions) melt films can be very thin, and are often correctly segmented where voxels only touch corner to corner. We therefore used a *Neighborhood* of 26 for all separations (Fig. 4.12).

Visual inspection of the data showed that the complex bubble geometries present in these samples meant a single value for the *marker extent* failed to produce a representative separation; either leading to over-separation of large, complex and irregular bubble geometries, or under separation of smaller clustered bubbles (Fig. 4.7 Q9).

To identify the best separation strategy, a coarse and fine separation were applied to each data set using *marker extent* = 6 and *marker extent* = 1. The two results were then compared with the greyscale to determine which was most accurate. While the very largest vesicles were always over-split by *marker extent* = 6, the optimal separation for the intermediate and smaller vesicles varied by sample (Fig. 4.13). Scoria clasts have larger vesicles and fewer thin films, and so the *marker extent* = 6 separation was sufficient with some manual recombination of the largest pores (performed using the *Manual Segmentation window*). The mingled clast (particularly rhyolitic regions) had more abundant thin melt films and so the *marker extent* = 1 separation was more accurate (although some manual recombination of the very largest bubbles was still required) (Fig. 4.7 Q10).

A more complex time intensive sequential separation and filter process to remove the largest (generally well separated) bubbles after applying *marker extent* = 6 and then running the *marker extent* = 1 separation on the remaining smaller bubbles (under separated at *marker extent* = 6) was tested and then discarded as the minor improvement to the overall separation was not worth the computational time cost.

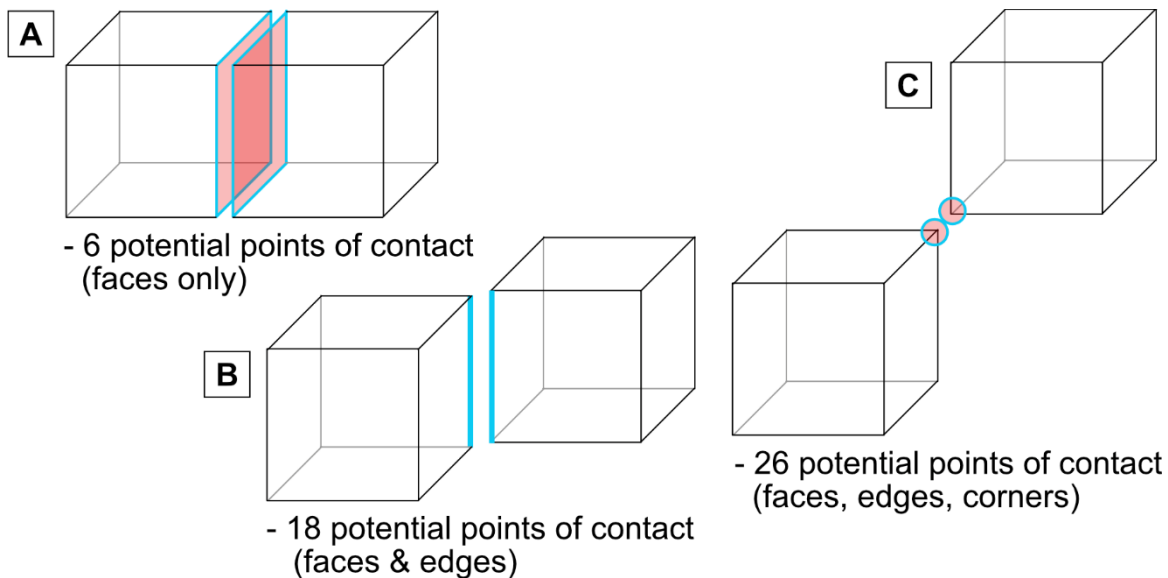


Fig. 4.12: Diagram showing how the Separation algorithm defines what counts as a connected protrusion based on contacts between voxels. **A:** a separation value of 6, only counts voxels as connected if they share a common face. **B:** a separation value of 18 counts voxels as connected if they have either, a common face or a common edge. **C:** a separation value of 26 counts voxels as touching if they share a common face, edge or corner.

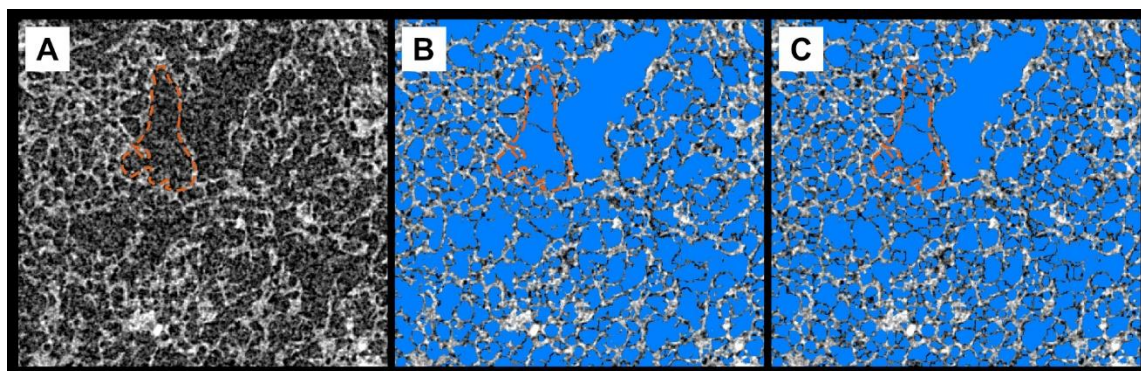


Fig. 4.13 showing the impact of varying the parameters for the *separate_objects* algorithm. **A:** greyscale XCT data showing melt films (bright) and bubbles (black). **B:** Same greyscale region with bubbles generated using a 26_6 separation (overlaid in blue). **C:** Same greyscale region with bubbles generated using a 26_1 separation (overlaid in blue). The 26_6 separation does not split bubbles in as many places, missing some likely thin films as picked out in the “noise” of the greyscale volume. Example highlighted by orange dashed line.

Using the greyscale volume as a reference, the split components of all very large vesicles were selected in all three orientations and added to a new material (Fig. 4.14 a). A new empty label field (aka dataset) was created into which the selected vesicle components

could be added (Fig. 4.14 b). Once imported into the new label field, the components of the very large vesicles were expanded using the “grow” tool to close any gaps generated in the separation process (Fig. 4.14 c). Once gaps were closed the “shrink” tool was used to return the bubble volumes to their original bounds (Fig. 4.14 d & e). This process was repeated as necessary to re-create the very large vesicle population. The output in the new label field was saved as e.g., 7_50_BIG_BUBBLES.

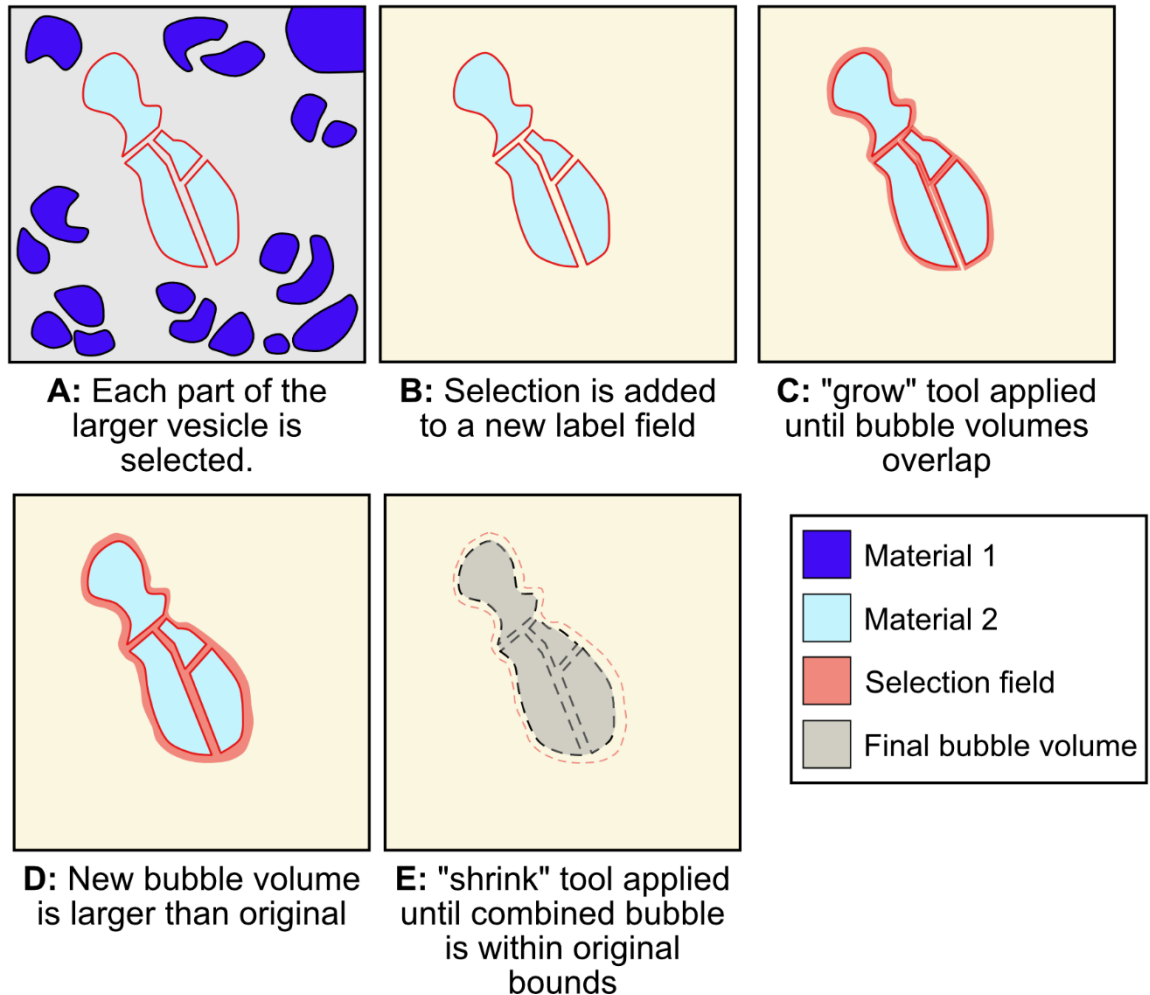


Fig. 4.14: Showing how over-split large bubbles are re-combined using the manual segmentation window. Dark blue bubbles are in Material 1. Pale blue bubbles have been added to material 2. Solid red lines / fields indicate the selection bounds. Black dashed lines in E show outlines of the original bubble segments, red dashed lines in E show extent of “grown” bubble field prior to “shrinking”. Grey bubble is the final re-combined bubble volume.

The two datasets were then added together using *Or_Image*. This generates a full bubbles dataset where the any gaps in the oversplit large bubble population from the FINE_SEP dataset are infilled by voxels from the BIG_BUBBLES dataset. The output is compared with the original greyscale to check bubbles are reasonably well constrained and then saved out as e.g., 7_50_SEPARATED_BUBBLES (Fig. 4.7 Q10).

4.4.3b Removing edge-touching vesicles – single composition

Any bubbles that intersect the edge of the 3D volume are incomplete. Including their volumes in the VSD (or any other quantitative analysis) would thus skew the data to lower size classes, so there needs to be a way to exclude them from the initial analysis. However, it is useful to know what proportion of the total bubble volume intersects the surface and should be removed, and their individual volumes (although only partial bubble volumes) as larger vesicles are more likely to intersect the edges of the volume and therefore their exclusion introduces bias to the VSD.

A *Border Kill* algorithm can remove all features contacting the surface of a 3D image volume, but we wish to retain information about these bubbles so instead sub-divide our total bubble population into two groups. A 1 voxel thick shell (value of all voxels = 1) is temporarily added to the separated bubble binary dataset (Fig. 4.15B). The shell, and all partial bubbles connected to it are then added to a separate material (Fig. 4.15C) before the shell removed (Fig. 4.15D). In this new image, voxels of melt have a value of 0, those in complete pores have a value of 1 and the partial edge touching bubbles a value of 2 (examples from the mingled and scoria clast given in Fig. 4.15 E & F). A *label analysis* can then be performed to extract the volume and geometry data from the full bubble population (output from 4.3.2) while also identifying if the bubble is in the edge or not edge group by reading the mean intensity value of each feature from this modified greyscale image.

The proportion of vesicles that intersects with the edge depends on the connectivity of the bubble population in the sample. For example, the analysed mingled clast (5_102) has far fewer partial bubbles than the scoria clast (7_50) (Fig. 4.15 e and f). The intensity value of each vesicle can be included in the final extracted bubble data when this parameter is included in the label analysis (see section 4.4.5). The cropped 2-value dataset is then converted to a 16-bit unsigned dataset using *Convert Image Type* so that it can be used as the intensity image for the e.g., 7_50_SEPARATED_BUBBLES dataset when performing the *label analysis* (process of measuring and extracting bubble parameters – see section 4.4.5). This is saved out as e.g., 7_50_BORD_KILL_INT_IMG.

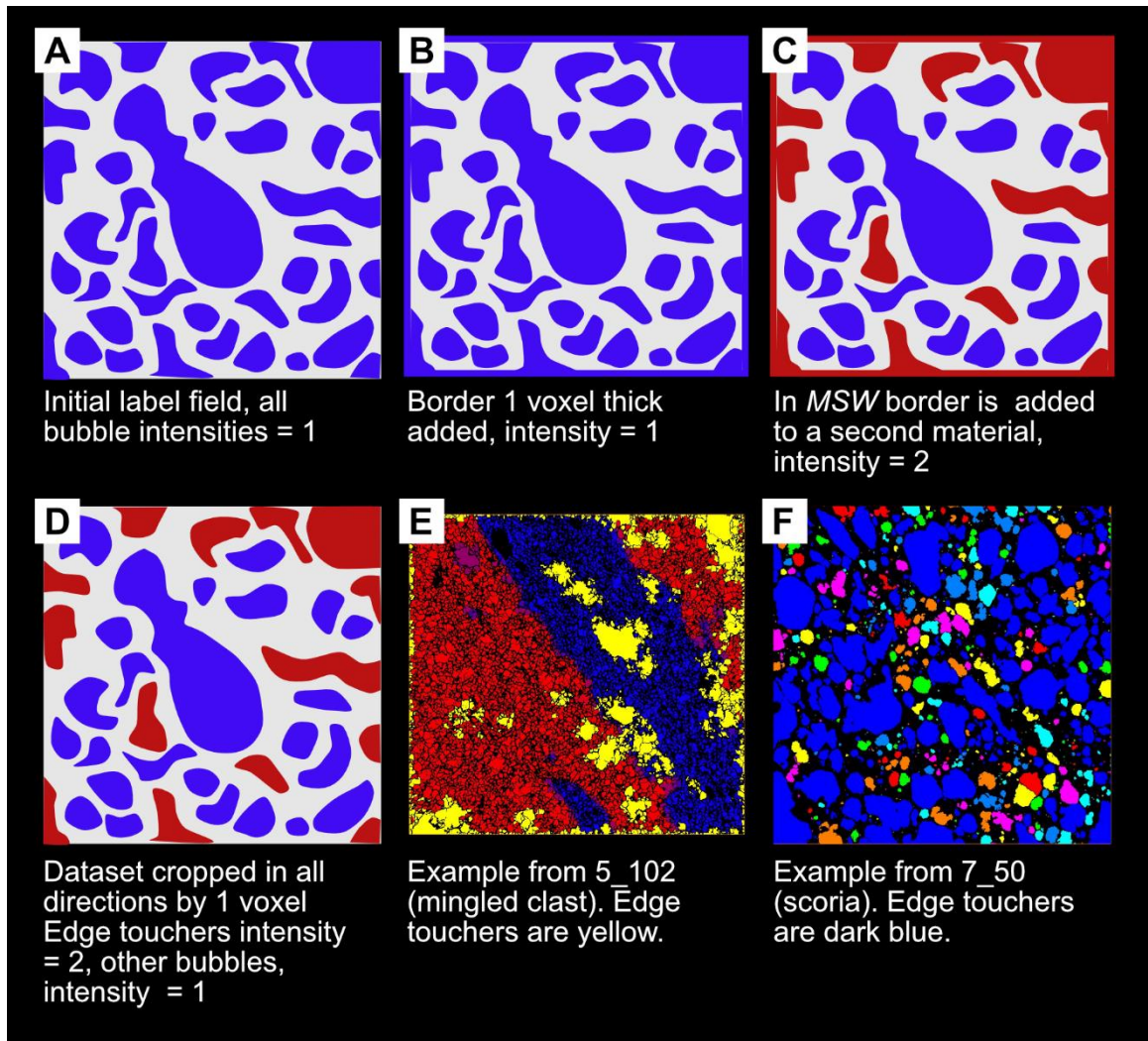


Fig. 4.15: Showing the method to manually remove vesicles that intersect the edge (A – D), an example from the mingled clast (5_102) and from the scoria clast (7_50) showing contrasting connectivity. *MSW* is *Manual Segmentation Window*.

4.4.4 Extracting bubbles - two compositions

For mingled clasts, the *Separate Objects* algorithm needed different marker extent values in the rhyolitic and basaltic regions because of differences in melt film thickness and bubble geometry and volume (e.g., Fig. 4.16). The workflow outlined in Fig. 4.7 (up to Q8) and sections 4.2.2a and b was followed to extract the initial bubble population. From there a modified workflow was used to extract bubble volumes and geometries from basalt and rhyolite regions, detailed below.

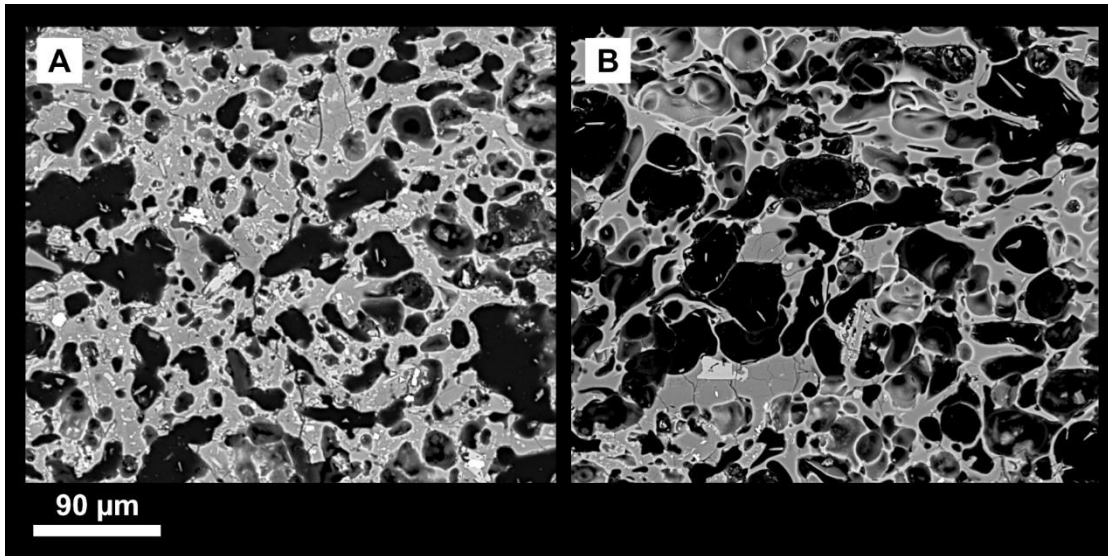


Fig. 4.16: Backscattered electron images from basalt (A) and rhyolite (B) regions of the mingled clast showing different thicknesses of melt walls.

4.4.4a Sub-dividing the volume by composition & applying separation algorithms

The method outlined in section 4.4.3 was modified (detailed workflow shown Fig 4.17) to map the melt composition as 1 = rhyolite and 2 = basalt (Fig. 4.17 a). These regions were defined manually (using *Manual Segmentation* tools) on every 50th or 100th slice (depending on the complexity of the melt distribution and then interpolated through the entire volume.

This simplified map of the melt regions clearly dissects some bubbles, but visual inspection shows that the majority of these bubbles are part of the basalt bubble population. The separate objects marker extent = 6 (correct for basalt) was applied and all bubbles that intersected the basaltic region labelled as “basalt bubbles”. The largest (over-split) bubbles are recombined and added to the dataset using the method outlined above and in Fig. 4.14. The complete dataset was used as a mask to remove all “basalt bubbles” from the segmented bubbles before the separation with marker extent = 1 was run on those on the rhyolite regions (See Fig. 4.17 and Fig. 4.18 (up to a) and Appendix 3.2 for a detailed step-by-step walkthrough of this process). The well separated bubbles in each region are recombined, checked for overlap (Fig. 4.18a), and saved as BAS + RHY_BOUNDARY_SOLVED.

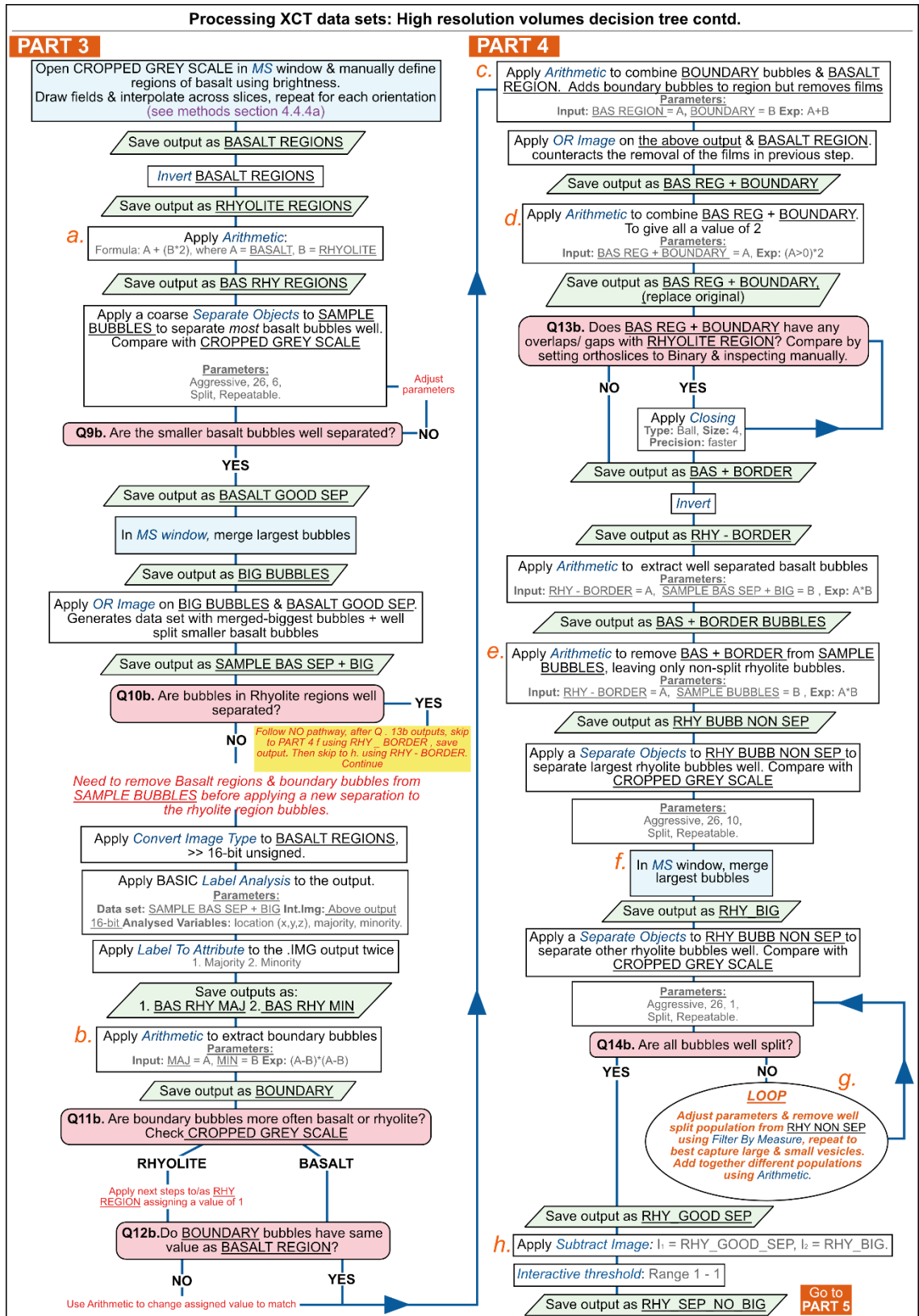


Fig 4. 17 X-ray computed tomography (XCT) data processing workflow for extracting bubble volumes from high resolution data in Avizo for clasts with two melt compositions. Blue italicised text is used for names of standard algorithms available in Avizo.

PART 5

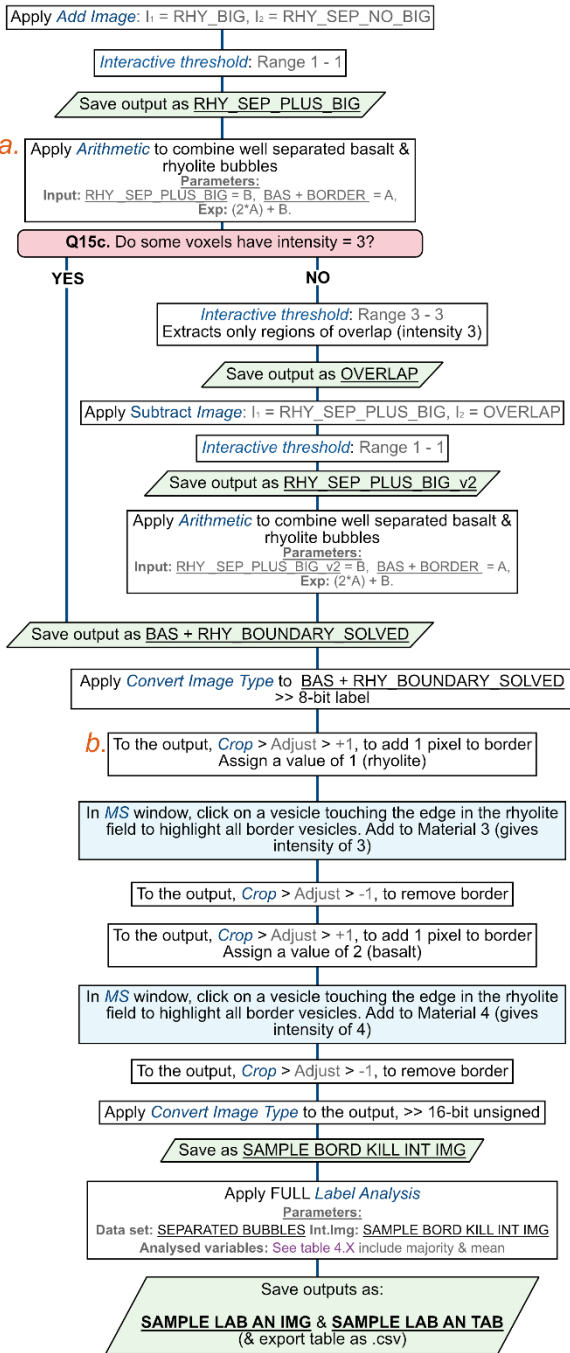


Fig. 4.18 X-ray computed tomography (XCT) data processing workflow for extracting bubble volumes from high resolution data in Avizo for clasts with two melt compositions. Final stages of recombination of basalt and rhyolite regions and removing any noise at the border. Blue italicised text is used for names of standard algorithms available in Avizo.

4.4.4b Removing edge-touching bubbles – two compositions

Edge-touching vesicles in the mingled clast need to be sub-divided by composition so that population densities can be calculated for each set of bubbles (Fig. 4.18 b). To do this, the method detailed in section 4.4.3b is applied twice (Fig. 4.19), first with an added layer with

a value of 1 (same as the rhyolite bubbles, Fig. 4.19 b), then with a value of 2 (same as the basalt bubbles, Fig. 4.19 e). Partial bubbles in the rhyolite region were assigned to “Material 3” and those in the basalt region, to “Material 4” (Fig. 4.19c & d) in the *Manual Segmentation Window*. The final dataset contains 4 bubble populations with different intensity values. This dataset is converted to 16-bit unsigned using *Convert Image Type* and saved as 5_102_BORD_KILL_INT_IMG to be used as the intensity image for the label analysis alongside the binary label field BAS + RHY_BOUNDARY_SOLVED (see section 4.4.5).

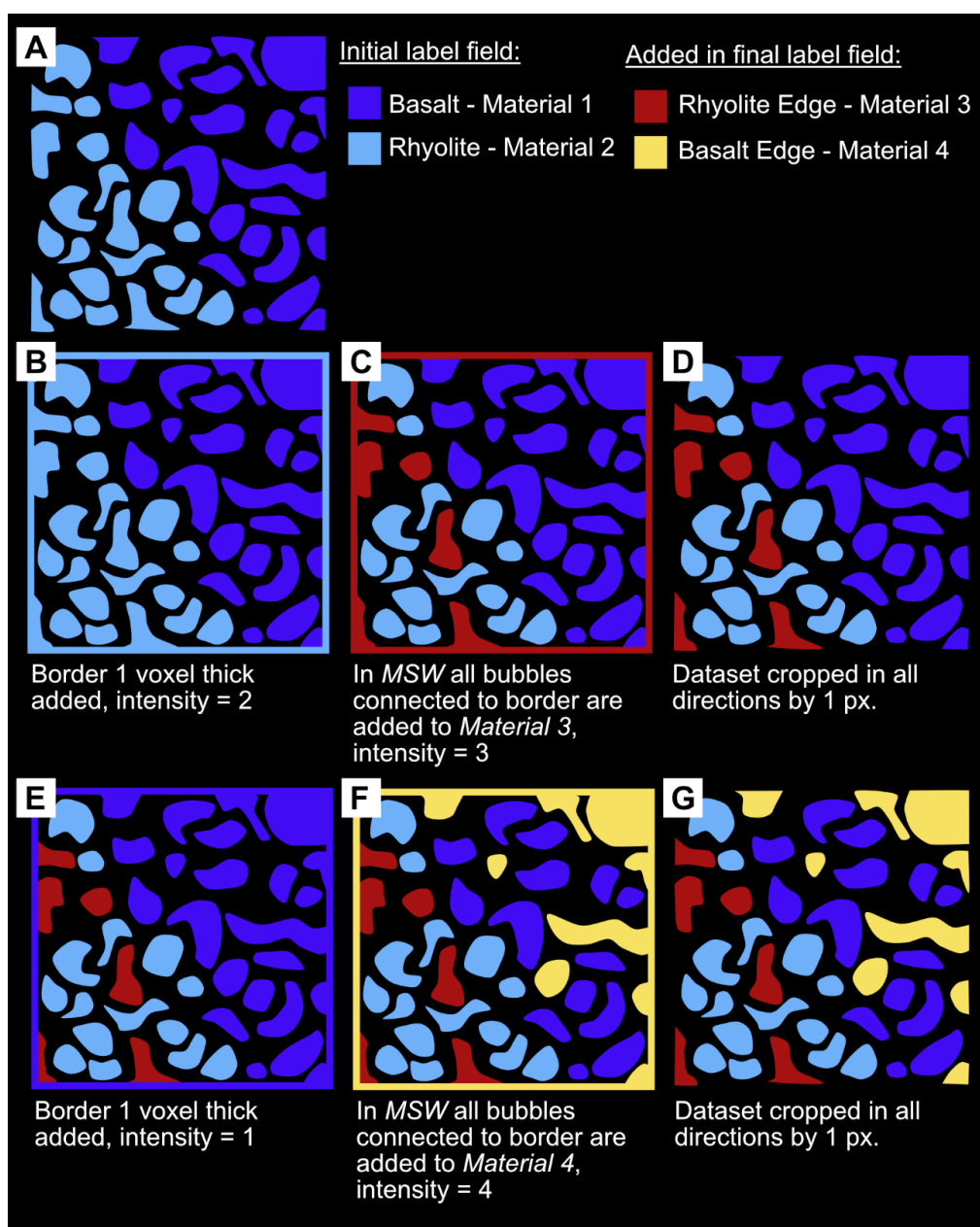


Fig. 4.19 Showing adapted process of identifying partial bubbles for two compositions. A showing initial label field with bubbles of different compositions identified. Black is glass. B – D show how rhyolite edge-touchers are identified, E – G show how basalt edge-touchers are added producing a final dataset with 4 intensity values. Some bubbles don’t intersect the edge in 2D but are connected in 3D.

4.4.5 Quantitative analysis of the bubble populations

Extracting bubble volumes and geometries from raw XCT data is an involved process. However, the advantages of this approach are many; all bubbles in the volume are included (rather than a restricted number of images from a thin section), no 2D – 3D rectification is needed, and complex bubble geometries are better represented. Once satisfied with the bubble separations and partial bubbles are identified (section 4.4.3b and 4.4.4b), the *Label Analysis* was applied to each volume to extract various parameters (see table 4.4 for the parameters and description of what they represent). Key parameters used in further analysis include: *EqDiameter*, *Anisotropy*, *Elongation*, *Volume3d*.

4.4.6 Extracting crystal volumes

To generate VSD curves the percentage of the analysed volume taken-up by melt is needed to generate the bubble number density. As dense objects appear bright in the XCMT greyscale data, extracting crystal volumes can be done via the *Interactive Thresholding* tool. In these samples this extracts larger crystals reasonably well, but the resolution of the 3D data and low contrast between microlites and glass means microlites cannot be captured as accurately as in BSE imagery. In the microlite-rich basaltic regions of the mingled clast (5_102) the impact of this is much more significant. For crystals large enough to resolve in the HRES volume, a *Label Analysis* containing only essential *Location* parameters and *Volume3d* was applied to calculate the total crystal volume, used during generation of 3D VSD curves. 4.4.7 Vesicle Volume & Size Distributions (VVD & VSD)

VVD and VSD curves were generated using R-studio (see [Electronic Appendix 3_1 for code and 3D bubble data files]). The extracted bubble volume and shape data were filtered to remove the partial bubbles. The data from the mingled clast is plotted separately for basalt and rhyolite hosted bubbles. The total analysed volume was acquired by taking the sum of the partial bubble volumes from the total processed HRES cube/cuboid volume (calculated using the HRES volume dimensions) - subdivided by melt composition for the mingled clast. Minimum resolvable object volume was set to 10 voxels following Lin *et al.*, (2015), which yields a less than 10% random error when the number of bubbles analysed is greater than 100. Incorporating these vesicles did not drastically change the shape of the VSD curves so they were removed as they are associated with a high percentage error. Crystal volume %

Table 4.4. Parameters measured for bubbles in the Mingled Fall dataset from x-ray computed tomography data using Avizo.

Parameter name	Type	Description	Equation
BaryCenterX	Location	X coordinate of the centre of gravity using moments of inertia	
BaryCenterY	Location	Y coordinate of the centre of gravity using moments of inertia	
BaryCenterZ	Location	Z coordinate of the centre of gravity using moments of inertia	
Volume3d	Geometry	Volume of the pore. Number of voxels multiplied by the volume of 1 voxel.	
Area3d	Geometry	Area of the pore surface	
EqDiameter	Geometry	Diameter of a sphere with the equivalent volume	$\sqrt[3]{\frac{6 \times Volume}{\pi}}$
Shape_VA3d	Geometry / shape	Shape factor. A perfect sphere has a value of 1, larger values indicate less compact pores.	$\frac{Area3d^3}{36 \times \pi \times Volume3d^2}$
Breadth3d	Geometry / shape	Largest distance between two parallel lines touching the pore without intersecting it, lying in a plane orthogonal to the maximum 3D Feret Diameter	
BreadthOrientPhi	Geometry	Angle of Breadth3D over [0, +90] degrees.	
BreadthOrientTheta	Geometry	Angle of Breadth3D over [-180, +180] degrees.	
Length3d	Geometry / shape	Maximum Feret Diameter*	
LengthOrientPhi	Geometry	Orientation of the maximum Feret diameter in degrees quoted as [0, +90]	
LengthOrientTheta	Geometry	Orientation of the minimum Feret diameter in degrees quoted as [-180, +180]	
Width3d	Geometry / shape	Minimum Feret Diameter*	
WidthOrientPhi	Geometry	Orientation of the minimum Feret diameter in degrees quoted as [0, +90]	

Table 4.4. Contd. Parameters measured for bubbles in the Mingled Fall dataset from x-ray computed tomography data using Avizo.

Parameter name	Type	Description	Equation
WidthORientTheta	Geometry	Orientation of the minimum Feret diameter in degrees quoted as [-180, +180]	
FeretShape3d	Shape	Minimum Feret Diameter* divided by maximum Feret diameter in the orthogonal direction. Feret measures sample a distribution of 31 different directions.	
Anisotropy	Inertia / Shape	Measures the deviation of a pore from a spherical shape (1 is very anisotropic, low sphericity and/ or smoothness)	1 – the ratio of the largest eigenvalue of the covariance matrix
Elongation	Inertia /Shape	Elongated pores with have small values close to zero.	Ratio of medium – largest eigenvalue of the covariance matrix
Flatness	Inertia / Shape	Flat pores will have small values close to zero	Ratio of smallest – medium eigenvalue of the covariance matrix
Neighborhood count	Geometry	Number of pores close to the current pore. Set a cut-off distance and a minimum overlap.	
Intensity	Greyscale Value	Contains the greyscale value for an object using the intensity image from the label analysis input as a mask.	
Majority**	Greyscale Value	Most common pixel intensity value within the pore.	
Minority**	Greyscale Value		
Mean**	Greyscale Value	Mean intensity value for a pore.	
Median**	Greyscale Value	Median intensity value for a pore.	

*Feret diameter is defined as the distribution of the length of bounding boxes oriented along specific directions

**Only used for mingled clasts to differentiate between different compositional regions at boundaries.

was incorporated to calculate bubble number densities and geometric binning was applied after Sahagian and Proussevitch (1998). Textural analysis suggests microlite growth is post bubble nucleation and post / syn-growth. Therefore, microlites have not been treated in this analysis as the current volume occupied by them is assumed to be melt at the time of bubble growth. Equivalent diameter values were used to generate VVD and VSD curves for each analysed sample / sample region. A summary of processed and analysed volumes, minimum resolvable object and crystal abundances for each analysed clast is presented in table 4.5.

Table 4.5: details of processed and analysed volumes used in vesicle analysis.

Sample	Pixel size (μm^2)	HRES cube/region Vol. (mm^3)	Edge-vesicle Vol. (mm^3)	Analysed Vol. (mm^3)	Min Object Vol. (μm^3)	Crystal %
5_102_All	1.8654	16.23	2.26	13.97	18.654	1.58
5_102_BAS	1.8654	8.24	1.71	6.53	18.654	1.58
5_102_RHY	1.8654	7.99	0.55	7.44	18.654	1.58
7_50	1.7194	12.47	7.87	4.6	17.194	0.48

[4.5 Methods 3 - 2D textural analysis](#)

The high magnifications and resolutions that can be attained in backscattered electron images mean they preserve evidence of intact or broken thin melt films, small-scale particle roughness and microlite populations more clearly than in XCT data. Such images can also be used to assess the limitations of 3D data resolution as well as inform decision making around the reconstruction of melt films in 3D. Using the correlative microscopy workflow, thin sectioning was targeted, and images collected to best complement the 3D datasets.

[4.5.1 Thin sectioning & SEM imaging](#)

Targeted thin sectioning of clasts analysed via XCT was carried out at the University of Durham. For each clast, the location of the HRES volume was mapped onto the LRES volume in Avizo® (version 2020.1). Clasts were then photographed, and the location of Zoom volumes marked on clast images in three orientations using distinctive features e.g., crystals, mingling patterns and clast morphology (see Fig. 4.20). For each clast a preferred location and orientation of section was also identified. Preferred location/orientation took into account; presence of large crystals that may be used for later analyses, the orientation of key textural features and intersection with the HRES volume.

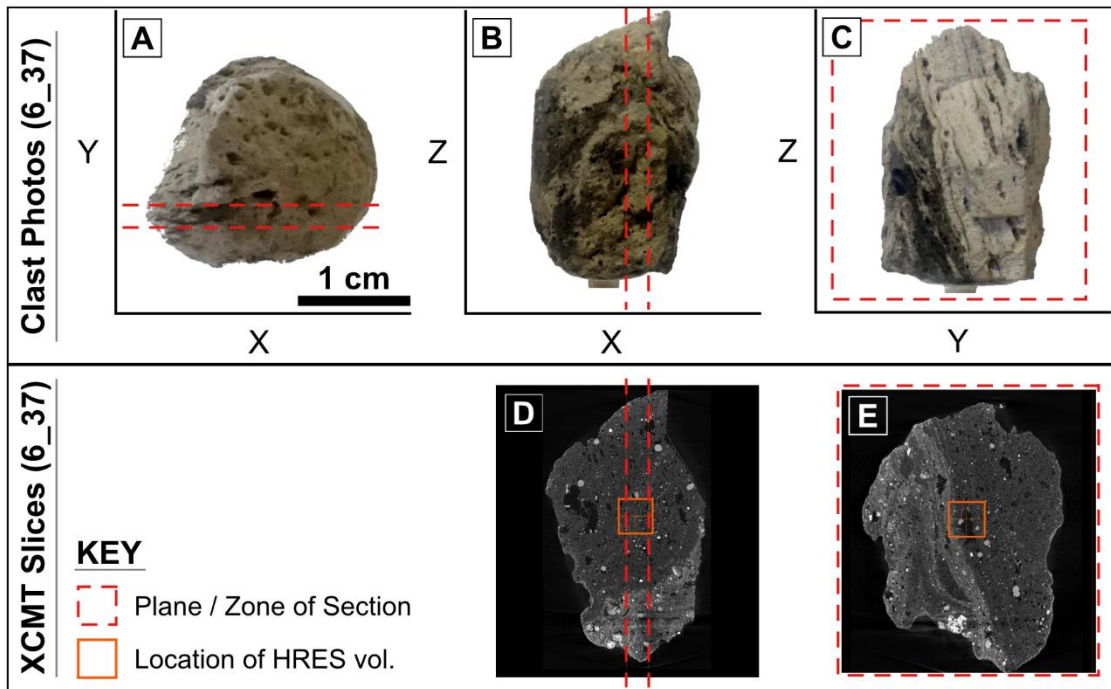


Fig. 4.20: Images showing how targeted sectioning was achieved, example of clast 6_37 from the Mingled Fall. **A – C:** Clast photos in different orientations showing distinctive features with ideal zone/planes of section annotated. **D & E:** Low resolution X-ray computed micro-tomography slices in corresponding orientations showing locations of the high-resolution (HRES) volume scans (orange box). Used to locate desired planes of section.

Back-scattered electron (BSE) images were then collected on a Zeiss Gemini sigma 300 VP at the Zeiss facility in Cambridge, UK. Images were obtained at a range of magnifications for each sample following Shea *et al.*, (2010) to capture the smallest vesicles at sufficient resolution producing a 5% error. For the mingled clast images were acquired for basalt, rhyolite and mingled regions separately to allow comparison of vesicle textures in compositionally distinct regions (as done for basalt vs rhyolite in 3D analysis). Magnifications were selected to capture the smallest vesicles with a 5.1% error as outlined in Shea *et al.*, (2010) and to give sufficient overlap at each successive lower magnification to capture the larger populations. In the scoria sample the smallest resolvable object had an equivalent circular diameter of 1.06 μm , in the mingled clast, 1.04 μm . Images were binarized using the TWS plugin in *ImageJ* (for details of parameters used see [Appendix 2.2]) and image corrections applied as described in the methods of chapter 3 (section 3.2.2). Images from scoriaceous clasts/ regions required less correction than pumiceous clasts / regions due to the relative absence of thin melt films – see Fig. 4.21.

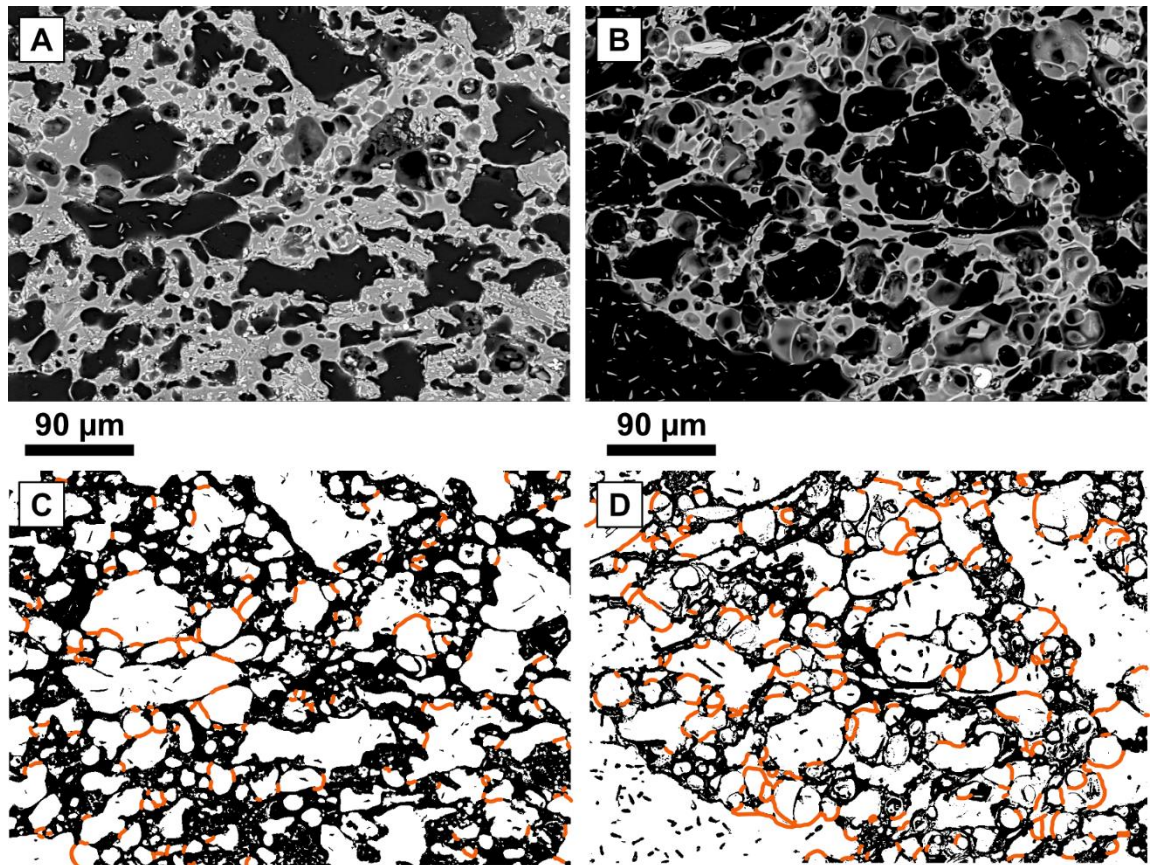


Fig. 4.21 showing difference in segmentation quality between basalt and rhyolite regions of mingled clast 5_102. **A and B:** Backscattered electron images of a basaltic (A) region and a rhyolitic (B) region. **C and D:** Segmented equivalents of A and B, with re-drawn bubble walls highlighted in orange. Walls here are shown at 1.5 px thickness for clarity, in analyses, walls were returned to 1 px thickness.

4.5.2 2D Vesicle shape analysis

Shapes of vesicles in the scoria clast (7_50) and each region of the mingled clast (5_102) were analysed from binary images using the “*Analyze particles*” tool in *ImageJ*. The same shape parameters as used in Chapter 3 were calculated for the Mingled Fall clasts. This included particle area, aspect ratio of the best fit ellipse, roundness (Eq. 1, a form factor after Liu *et al.*, 2015), solidity (Eq. 2, after Liu *et al.*, 2015), equivalent circular diameter of the best fit ellipse (Eq. 3), circularity (Eq. 4) and regularity (Eq. 5, as defined by Mitchell *et al.*, 2019). Where A is particle area, M is major axis of the best fit ellipse, A_c is the area of the convex hull, P is particle perimeter, λ_l and λ_s are the semi-major and semi-minor axes of the best-fit ellipse and D_f is the ferret diameter.

$$Rd = \frac{4A}{\pi \times M^2} \quad [1]$$

$$S = \frac{A}{A_c} \quad [2]$$

$$EqD = 2 \times \sqrt{\frac{A}{\pi}} \quad [3]$$

$$C = 4\pi \frac{A}{P^2} \quad [4]$$

$$Rg = \frac{M}{Df} \quad [5]$$

The shape factors analysed in 2D allow assessment of the various ways in which vesicles deviate from smooth circular cross-sections e.g., elongation and different types of surface roughness (as discussed in chapter 3). In the 3D shape analysis, *Anisotropy* (measuring particle compactness) and *Elongation* were used as comparable 3D equivalents to circularity and roundness.

4.6 Results

The data extracted via 2D, and 3D vesicle analysis provide insight into the development of vesicle textures and connectivity during ascent of the magmas that fed the Mingled Fall deposit. Below, 2D and 3D vesicle size and shape data for one mingled clast (5_102) and one scoria clast (7_50) are presented. Due to time constraints and the complexity of data processing for the mingled samples, results from the other sampled clasts are not presented here and will be the focus of future study. Data extracted in 2D are presented first, as this is the method applied most regularly in studies of clast texture, followed by 3D data. The dominant vesiculation processes implied by the vesicle size and shape data are detailed below. Any conflicts in interpretation of vesicle process between the two datasets will be highlighted and further discussed in section 4.7.4.

4.6.1 2D VSDs

As outlined in Chapter 3, vesicle volume (VVD) and vesicle size (VSD) distributions inform interpretations of dominant processes operating on an ascending package of melt prior to fragmentation. In mingled clasts, vesicle populations may reflect different vesicle nucleation and growth histories, controlled by both the rheology and volatile content of the individual melts, and the impact of physical interactions between the two endmembers. VVD and VSD curves were generated for the scoria clast, as well as regions containing both basalt and rhyolite in close association, and rhyolite dominated regions

Table 4.6: Parameters extracted from 2D vesicle size distributions and shape analysis											
Sample / region	Whole clast Ves. (%)	2D Ves.	Nv derived 3D Ves.	NvCorr (mm⁻⁴)	N° analysed	Min EqD (µm)	Median EqD (µm)	Max EqD (µm)	Median elongation	D-type*	R²
5_102 / Rhyolite	63	51	49.37	3.87x10 ⁶	962	1.75	20.79	214	0.27	<i>p</i> (1.08)	0.9836
5_102 / Basalt		51	-	-	684	1.75	16.5	104	0.23	-	-
5_102 / Mingled		58	57	4.19x10 ⁷	4855	1.69	5.98	455	0.27	<i>p</i> (3.06)	0.9835
7_50/ Scoria	66	56.9	14.7	3.63x10 ⁶	808	1.08	5.07	358	0.17	<i>p</i> (2.74)	0.992

* Type of distribution: *p* = power law distribution of the form $Nv(>L) \sim f(L^{-d})$ with exponent *d* in parentheses. Power law exponents were calculated using a plot of $\log(Nv>L)$ vs $\log(L)$, exponential fit exponents were calculated using a semi-log plot of $\log(Nv>L)$ vs L – when tested against exponential laws all samples returned R^2 values < 0.65 so all were classified as power law.

within the mingled clast. Regions of different composition were identified by their greyscale value, presence / absence of microlites and the character of the bubble populations. Images classified as “rhyolite dominated” contained < 5% basalt material as estimated via visual inspection of images. Typically, basalt regions in “rhyolite dominated” images were constrained to the margins or a few μm s width tips of melt interfingering features. Table 4.6 reports the measured clast vesicularity (from 2D images), calculated vesicularity (from FOAMS), and other calculated output values for each measured clast/region. The magnifications used to collect BSE images allowed analysis of vesicles with an equivalent circular diameter ranging from $\sim 1 - 455 \mu\text{m}$.

Plots of vesicle size and volume data for the rhyolitic regions are all consistent with the same dominating vesiculation scenario. The VVD of the rhyolitic portions of the mingled clast displays distinct characteristics representative of continuous, accelerating bubble growth (c.f. Shea *et al.*, 2010). The distribution has a primary mode at 0.029 mm, a secondary one at 0.072 mm, and a distinct tail towards smaller equivalent diameters (Fig. 4.22A). The same process is reflected in the plot of $\ln(n)$ (n is population density) vs equivalent diameter (Fig. 4.23A) where the curve is concave upwards, and in the plot of $\log(Nv > L)$ against $\log(\text{equivalent diameter})$ (Fig. 4.23B) where the curve best fits a power-law distribution (see table 4.6). Despite containing several kinks around $\log(L) = -1$, the plot of cumulative volume fraction (Fig. 4.23C) shows a strong resemblance to curves typical of continuous, accelerating growth (Shea *et al.*, 2010) Data from regions that contain both rhyolitic and basaltic material in close association (e.g., Fig. 4.24C) are dominated by the same process, with smoother VSD curves (Fig. 4.23 A– C). The corresponding VVD plot (Fig. 4.22B), however, shows a more distinct second distribution about a peak of 0.072 mm than the rhyolitic regions, indicating that here the impact of coalescence is stronger – likely due to the presence of the basaltic bubble population. The minor influence of coalescence in rhyolitic regions is indicated by the secondary mode at 0.072 in the VVD, though less distinct than in the combined basalt + rhyolite images.

The vesicle size distribution analysis of the scoriaceous clast in 2D was less successful, as indicated by the irregular and incomplete cumulative volume fraction curve (Fig. 4.23C). Other outputs from FOAMS – Fig. 4.23A and B and Fig. 4.22 – imply conflicting vesiculation processes operated within the bubble population. The slope of the curve in Fig. 4.23B, and good fit with a power-law distribution ($R^2 > 0.95$ – table 4.6) implies dominance of

continuous accelerating growth (Shea *et al.*, 2010). In contrast, the multiple modes in the VVD plot (Fig. 4.22C) are more representative of multiple stages of nucleation and growth. Finally, coalescence is indicated by the shallowing of the curve between equivalent diameters of 0.04 and 0.1 mm in Fig. 4.23A, and the skew of the data in the VVD curve to higher equivalent diameters (Fig. 4.22C).

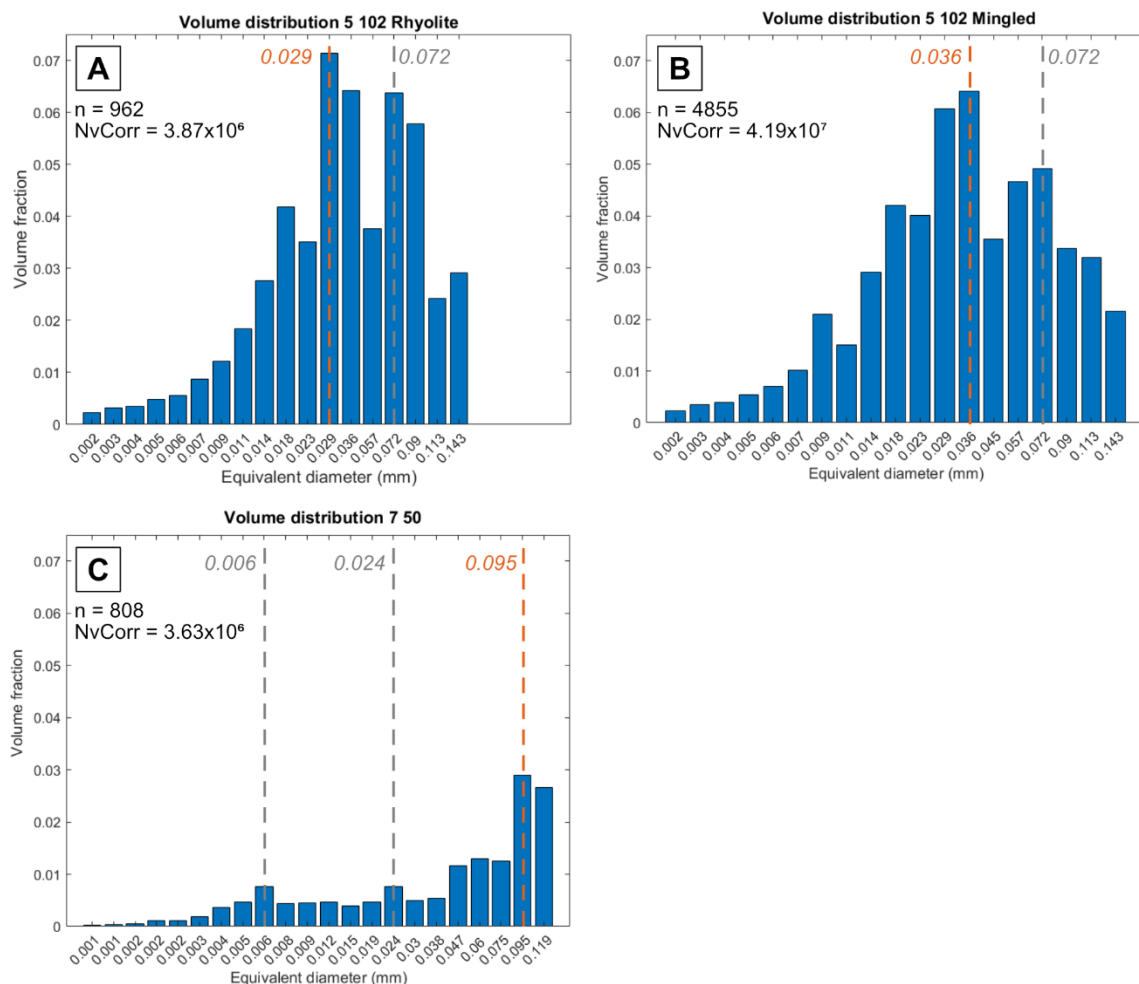


Fig. 4.22: vesicle volume distributions (VVDs) for regions / clasts from the Mingled Fall. A – from rhyolite regions of the mingled clast (5_102). B: from mingled regions of the mingled clast (5_102). C: from the scoriaceous clast (7_50).

The lack of agreement between various VVD and VSD plots may be a function of poor vesicle volume reconstruction in FOAMS, as implied by the cumulative volume fraction curve and incredibly low 3D vesicularity of 14% calculated by FOAMS. The calculated vesicularity of 14% does not agree with either the direct measurement of whole clast vesicularity (66%) or the 2D vesicularity measured directly from binary images (56.9% - inclusive of partial vesicles).

There are several potential sources of this error:

1. *High degrees of connectivity*

During FOAMS analysis, any vesicles that intersect the edge of the image (partial bubbles) are excluded from the analysis as they would provide only a minimum estimate of bubble volume after stereological conversion. High degrees of connectivity in each individual image - facilitated by narrow pipes / fractures connecting multiple bubbles – cumulatively reduces the overall porosity by a large amount.

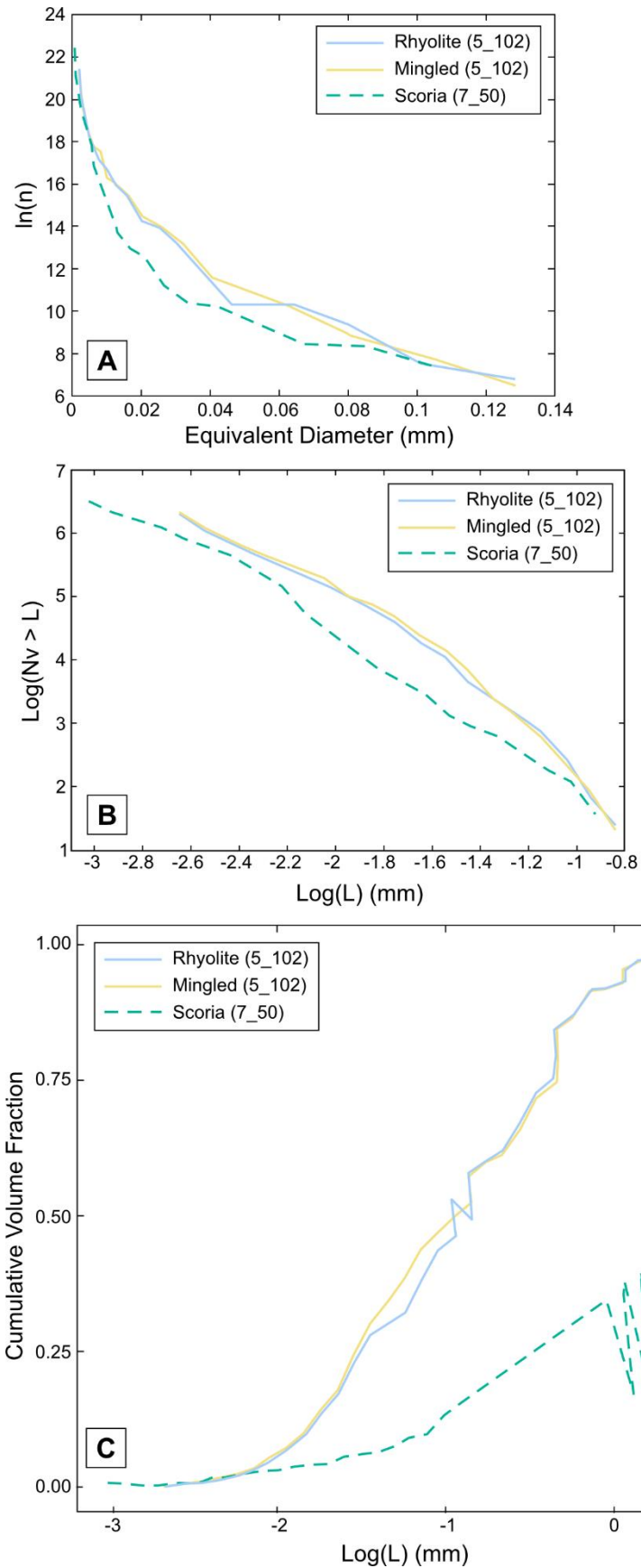


Fig. 4.23 2D vesicle size distribution (VSD) curves from samples from the mingled fall. Rhyolite data was collected from images that only contained rhyolite in the mingled clast (5_102). Mingled data was collected from regions containing both rhyolite and basalt in the mingled clast (5_102). Scoria data was collected from the scoriaceous clast 7_50.

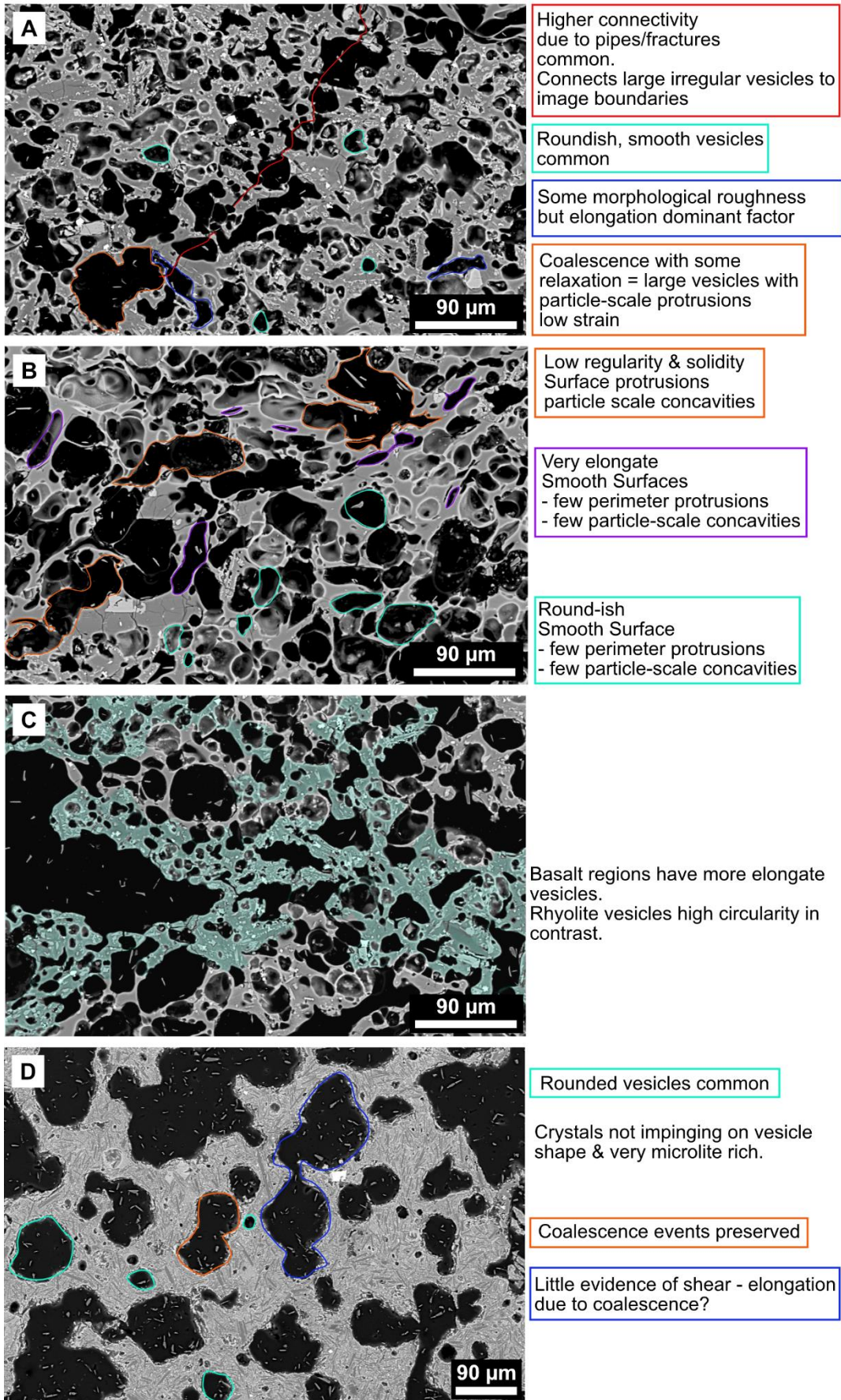


Fig. 4.24: backscattered electron images of typical vesicle textures from different regions / clasts of the Mingled Fall. A: from basaltic regions, B from rhyolitic regions, C from basalt and rhyolite mixed regions and D from the scoria clast. Coloured outlines of vesicles correspond to descriptive text in coloured boxes to the right.

2. *The 2D – 3D stereological conversion assumes spherical bubble geometry.*

In scoriaceous clasts, bubble shapes typically reflect greater coalescence, are more complex and can have a much higher connectivity. This means 2D – 3D stereological conversions are less reliable as cross-sections are less representative of the total bubble volume. Much as is seen for clasts containing intensely sheared vesicles, which Shea *et al.*, (2010) state should be excluded from analysis in FOAMS.

3. *Impact of minimal “manual de-coalescence”*

In other VSD studies using FOAMS, a process of “bubble de-coalescence” is often applied to segmented images (e.g., Mitchell *et al.*, 2019). In this process, bubble walls are re-drawn to reconstruct pre-coalescence vesicle shapes and sizes. However, in this study, bubble walls were *only* added or repaired where evidence of thin melt films was preserved in the original BSE image. For the scoriaceous clast this represented only a few individuals as most vesicles appeared sufficiently relaxed that the lack of thin melt films likely reflected the extent of the true coalescence process rather than an effect of sample preparation or image segmentation. If de-coalescence had been applied more aggressively, connectivity would have been lower, fewer individuals excluded, and FOAMS may have produced a more complete output. As such, 2D VSD and VVD data from the scoriaceous clast should be interpreted with caution.

Higher bubble number densities are associated with rapid ascent and dominance of bubble nucleation relative to growth/coalescence. In table 4.6, N_v values for regions where mingling is the dominant textural feature are higher than in either the rhyolite regions or the scoria clast, indicating mingling may facilitate bubble nucleation / suppress coalescence, or both.

4.6.2 2D shape parameters

Quantification of vesicle shapes in thin section allows a more robust comparison of dominant (and outlying) controls on vesicle shape than qualitative observations. Collected data provide evidence of bubble nucleation, growth, interference, coalescence and shear and allow comparisons between different regions / clasts. The shape parameters assessed in 2D can be broadly compared with shape parameters measured in 3D (see section 4.6.4). Density plots of roundness vs circularity, regularity vs solidity, and area vs aspect ratio are plotted for each region of the mingled clast (rhyolite, mingled, basalt – 5_102) and the

Density plots of 2-Dimensional vesicle shape data from the Mingled Fall Deposit: 2D kernel with 95% cut off

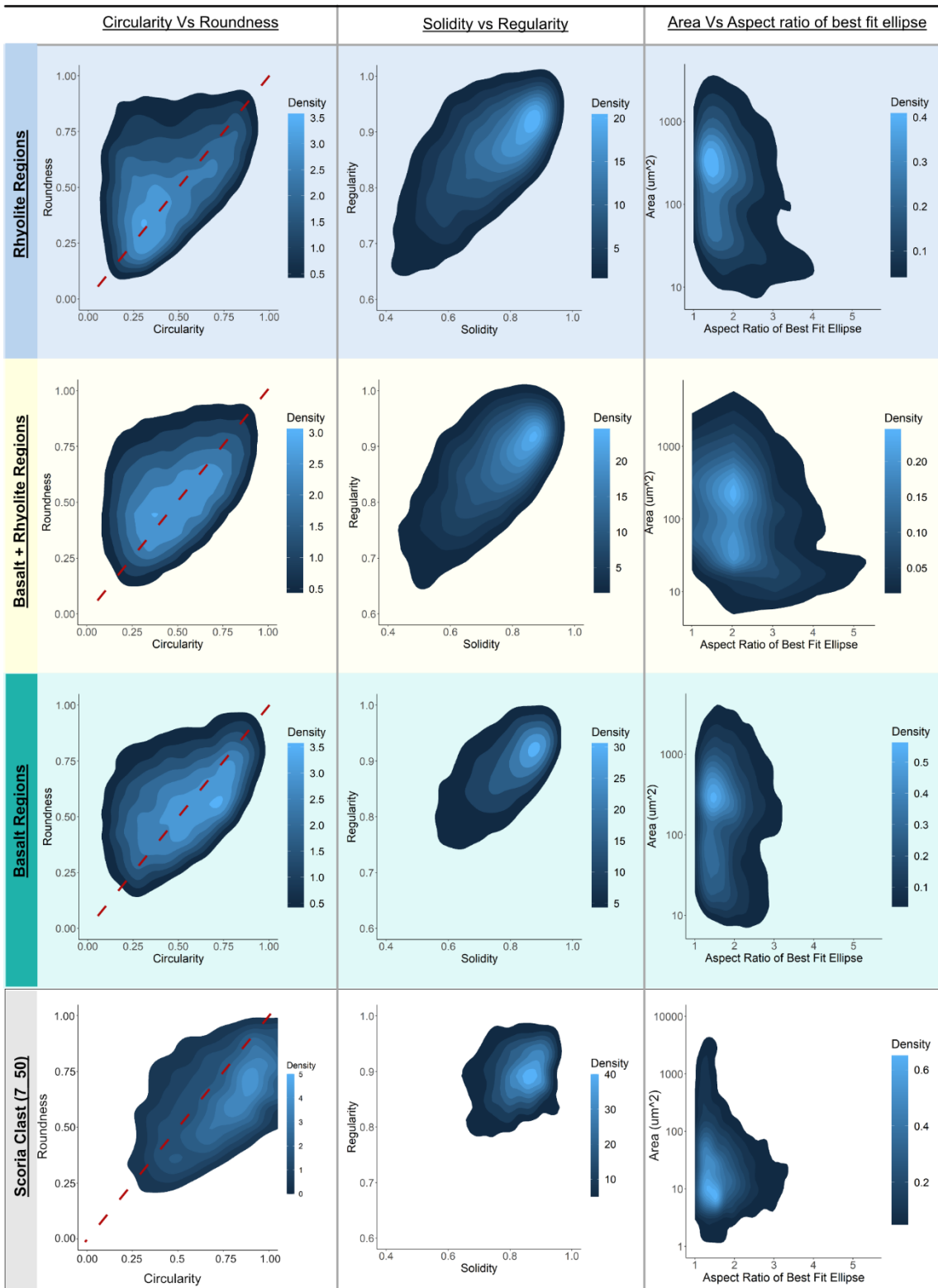


Fig. 4.25: Plots of shape parameters from 2D data for regions / clasts from the Mingled Fall. Red dashed lines correspond to roundness = circularity.

Table 4.7: 2D shape parameters from the mingled fall				
Sample/ clast type/region	Roundness vs Circularity	Regularity vs Solidity	Area Vs Aspect Ratio	Major / minor controls on vesicle shape.
5_102/ mingled / rhyolite	<ul style="list-style-type: none"> • Low circularity ≈ low roundness in some vesicles • Highest density at low circularity 	<ul style="list-style-type: none"> • Densest at high values of solidity and regularity • Extends to relatively low values compared to basalt regions. 	<ul style="list-style-type: none"> • Max AR 1 : 4, in smallest population. • Densest at low AR and Area = 100 – 100 μm² 	<ul style="list-style-type: none"> • Some vesicles controlled by elongation (Ro/C) • Small proportion have more complex vesicle shapes (Re/S) • Smallest population = most sheared (A/AR)
5_102/ mingled/ mixed	<ul style="list-style-type: none"> • Low circularity ≈ low roundness • Densest values around moderate circularity 	<ul style="list-style-type: none"> • Densest at high values of regularity and solidity • Extends to similar range as in rhyolite. 	<ul style="list-style-type: none"> • Highest aspect ratios of all regions / samples • Max AR of 1 : 5 in smallest vesicle population ~ 10's μm² 	<ul style="list-style-type: none"> • Some vesicles controlled by elongation, but less than in rhyolite (Ro/C) • More extensive and more pervasive shear in mixed regions than elsewhere (A/AR)
5_102/ mingled / basalt	<ul style="list-style-type: none"> • Densest towards higher circularities • Some at low circularity ≈ roundness 	<ul style="list-style-type: none"> • Densest at high regularity and solidity. • More constrained data range than in mixed or rhyolite 	<ul style="list-style-type: none"> • Densest at low AR, around 500 μm². • Little variation in AR with area. • Max AR = 1 : 3 	<ul style="list-style-type: none"> • Higher circularity values fewer controlled by elongation than in rhyolite / mixed (Ro/C). • More homogenous vesicle population, most vesicles = smooth (Re/S) • Minor population with higher AR, shear relatively homogenous across vesicle populations (A/AR).
7_50/ scoria	<ul style="list-style-type: none"> • Densest at higher circularities • Doesn't extend to very low circularities • Circularity ≠ roundness, offset towards higher circularity 	<ul style="list-style-type: none"> • High values of regularity and solidity • Small spread in data 	<ul style="list-style-type: none"> • Densest at low aspect ratio • Minor population at 10 – 100 μm² with AR up to 1 : 3 • Largest vesicles have low AR. 	<ul style="list-style-type: none"> • Elongation not controlling vesicle shape (Ro/C) • More circular vesicles than in mingled clast – less shear (Ro/C) • More homogenous vesicle population, mostly relatively smooth vesicles (Re/S) • Minor population of more intensely sheared vesicles. Larger vesicles closer to circular (A/AR)

scoria clast (7_50), displayed in Fig. 4.25 and summarised in table 4.7. Some key features are listed below:

1. Bubbles in rhyolitic regions of the mingled clast typically do not preserve evidence of extensive shear, also reflected in BSE images (Fig. 4.24B). A population of small vesicles (area = 10 – 100 μm^2) has aspect ratios of up to 1:4 but these are a minority amongst the total population (Fig. 4.25, top right) and their shape appears to be linked to interactions with larger vesicles (Fig. 4.24B).
2. In mixed regions, shearing is more significant across all vesicle size populations, reaching aspect ratios up to 1:5 – higher than in any either individual compositional region, or the scoria clast.
3. In contrast, basaltic regions of the mingled clast only rarely reach aspect ratios of 1:3, and then constrained to vesicles around 100 μm^2 . Most vesicles have an aspect ratio < 1:2 and the majority of vesicles are between 100 and 1000 μm^2 .
4. Values of regularity and solidity are much higher in the basaltic regions, and the spread of data more constrained than the rhyolite or mixed regions.

This contrasts with observations made in BSE images of basaltic regions, which often show irregular vesicle shapes exhibiting morphological roughness (particle scale protrusions) (Fig. 4.24A). An explanation for this may be the prevalence of narrow connective networks between vesicles in the basaltic regions (Fig. 4.24A). These features increase the likelihood of complex vesicles being connected to the edge of the image, and therefore discarded during data collection.

5. The scoriaceous clast (7_50) has a high proportion of vesicles with high values of circularity and roundness and a high proportion of vesicles with high regularity and solidity indicating a population that dominantly lacks intense shear and is less morphologically complex than in the mingled clast.
6. The area vs aspect ratio plot shows that most vesicles have aspect ratios of < 1:2.5 but there is a minor population with aspect ratios up to 1:3 at approximately 10 μm^2 .

These observations point to rhyolitic and basaltic regions of the mingled clast that were able to vesiculate in the absence of significant shear, despite the micro-scale interfingering of the two melts. In 2D, basaltic regions and the scoriaceous clast appear to contain a high proportion of vesicles with close to circular cross-sections. However, this may not be representative of 3D structures and some of the more complex networks preserved in 2D are under-sampled due to edge-effects in images. Preservation of more complex shapes

amongst a small proportion of vesicles in rhyolitic regions (extension of data to lower values of solidity and regularity) indicates the time between coalescence events, fragmentation and quenching was less than the relaxation timescale of the melt.

4.6.3 3D VVDs & VSDs

Vesicle volume, size and shape studies in 2D indicated a range of vesiculation processes operating within the mingled and scoriaceous clasts. However, one of the main limitations of most VVD/VSD studies is that 2D intersections from BSE images must be converted to 3D bubble volumes using stereological conversion (e.g., Shea *et al.*, 2010). Such conversion methods become less reliable where melts are extensively sheared (Sahagian and Proussevitch 1998 and Shea *et al.*, 2010), and/or contain well-connected vesicle networks with complex 3D geometries. As shear does not appear to have had a significant impact on vesicles in either analysed clast, the most likely source of error is the complexity of vesicle networks in each analysed region/ clast – this can be tested by examining differences between 2D and 3D studies and will be discussed in section 4.7.4.

Below, 3D vesicle volume (VVD) and vesicle size (VSD) distributions for (a) basalt regions of the mingled clast, (b) rhyolite regions of the mingled clast and (c) the scoria clast are described. For comparison, the VVD and VSD plots for the mingled clast as a whole (basalt + rhyolite regions) are presented in Figs. 4.26C – 4.29. Results from the combined dataset show how analysing the whole clast masks the dominant processes in each region. Vesicularities, population densities, number of vesicles analysed and other calculated parameters from VVD/VSDs are presented in table 4.8. These results offer insights into the impact of basalt-rhyolite mingling on vesiculation processes in three dimensions that may have been missed or mis-represented in 2D analyses. The resolution and total analysed volume of XCT data processed allowed analysis of vesicles with an equivalent spherical diameter ranging from 3.33 μm – 2402 μm .

Vesicle volume distributions for the analysed compositional regions/clasts are shown in Fig. 4.26. Geometric binning was applied as outlined in Sahagian and Proussevitch (1998) and EqD is the diameter of a sphere with the same volume as the analysed particle.

Most VVD and VSD curves for the rhyolitic regions reflect a different dominant vesiculation process to the 2D data. The VVD curve for the rhyolite regions of the mingled clast (Fig. 4.26 A) has a close to normal distribution with a mode at $\log(\text{EqD}) \sim 1.5$ and a poorly

Table 4.8: Parameters from 3D studies of vesicle texture.

Sample/clast type/region	3D vesicularity	Nv (mm ⁻⁴)	N° Analysed	Min EqD (μm)	Median EqD (μm)	Max EqD (μm)	D. type*	R ²
5_102/ mingled/ basalt	57.4	24835	162175	3.33	5.29	1261	<i>p</i> (1.96)	0.814
5_102/ mingled/ rhyolite	42.2	45223	336463	3.33	18.76	270	<i>e</i> (0.0409)	0.873
5_102/ mingled/ All	49.3	35693	498638	3.33	16.53	1261	<i>p</i> (2.31)	0.821
7_50/ scoria	59.5	45962	211429	3.34	4.21	2402	<i>p</i> (3.95)	0.903

*Type of distribution: *p* = power law distribution of the form $Nv(>L) \sim f(L^{-d})$ with exponent *d* in parentheses, *e* = exponential of the form $Nv \sim f(e^{-aL})$ with corresponding exponents *a* in parenthesis. Power law exponents were calculated using a plot of $\log(Nv>L)$ vs $\log(L)$, exponential fit exponents were calculated using a semi-log plot of $\log(Nv>L)$ vs *L*.

developed secondary population at $\log(\text{EqD}) > 2.08$. These characteristics are indicative of a bubble population dominated by a single stage of nucleation and growth (dominant peak) with a secondary influence of coalescence (minor secondary population) generating a few bubbles at larger size classes (Shea *et al.*, 2010). The cumulative volume fraction curve (Fig. 4.27) supports this interpretation as it shows a smooth curve with a steep increase in volume fraction at intermediate bubble diameters (Shea *et al.*, 2010). In contrast, the plot of $\ln(n)$ vs equivalent diameter (Fig. 4.28) reflects conflicting processes. An initial peak at low bubble diameters followed by a relatively linear decrease is usually indicative of ripening (Shea *et al.*, 2010). However, this peak is in part a function of a sharp downward trend in population density for bubbles at diameters $< 10 \mu\text{m}$. This “hockey stick” trend is often seen in VSD plots from XCT data and is currently poorly understood (Pers. Comm. Kate Dobson 2022). The pattern is seen in plots of combined basalt + rhyolite regions and the basaltic region, but not the scoriaceous clast. Possible explanations for this effect are discussed in section 4.7.3. The remainder of the curve is concave upwards with a small hump at bubble diameters around $200 \mu\text{m}$. This most closely resembles a signal of continuous accelerating growth – as observed in the 2D data –, though is altered by the secondary bubble population at larger diameters, most likely due to coalescence. When the “hockey stick” region of the $\log(N_v > L)$ vs $\log(N_v)$ plot (Fig. 4.29) is discounted, the remainder of the curve is very similar to those produced by a single stage of nucleation and growth (Shea *et al.*, 2010).

For basaltic regions, VVD and VSD plots are all relatively consistent with a strong influence of coalescence. The VVD plot (Fig. 4.26B) has two distinct modes – at $\log(\text{Eqd}) \sim 1.7$ and 3.1 – and is shifted to larger bubble diameters than the rhyolitic regions. The peak at $\log(\text{Eqd}) = 3.1$ is produced by a single individual, highlighting the extent of coalescence in basaltic regions. Although bins with very low numbers of individuals are not statistically robust, they are important to include on VVD plots as they reveal important characteristics of scoriaceous regions / clasts (Shea *et al.*, 2010). The plot of cumulative volume fraction for the basaltic regions has a shallower slope than the rhyolite, a distinct hump at intermediate bubble sizes and extends to higher bubble diameters. This is a clear indication of coalescence within the bubble population and is supported by the shape of the $\ln(n)$ vs equivalent diameter which shallows out distinctly at bubble diameters around $200 \mu\text{m}$ (Fig. 4.28). The influence of coalescence is also reasonably clear in the plot of $\log(N_v > L)$ vs $\log(L)$

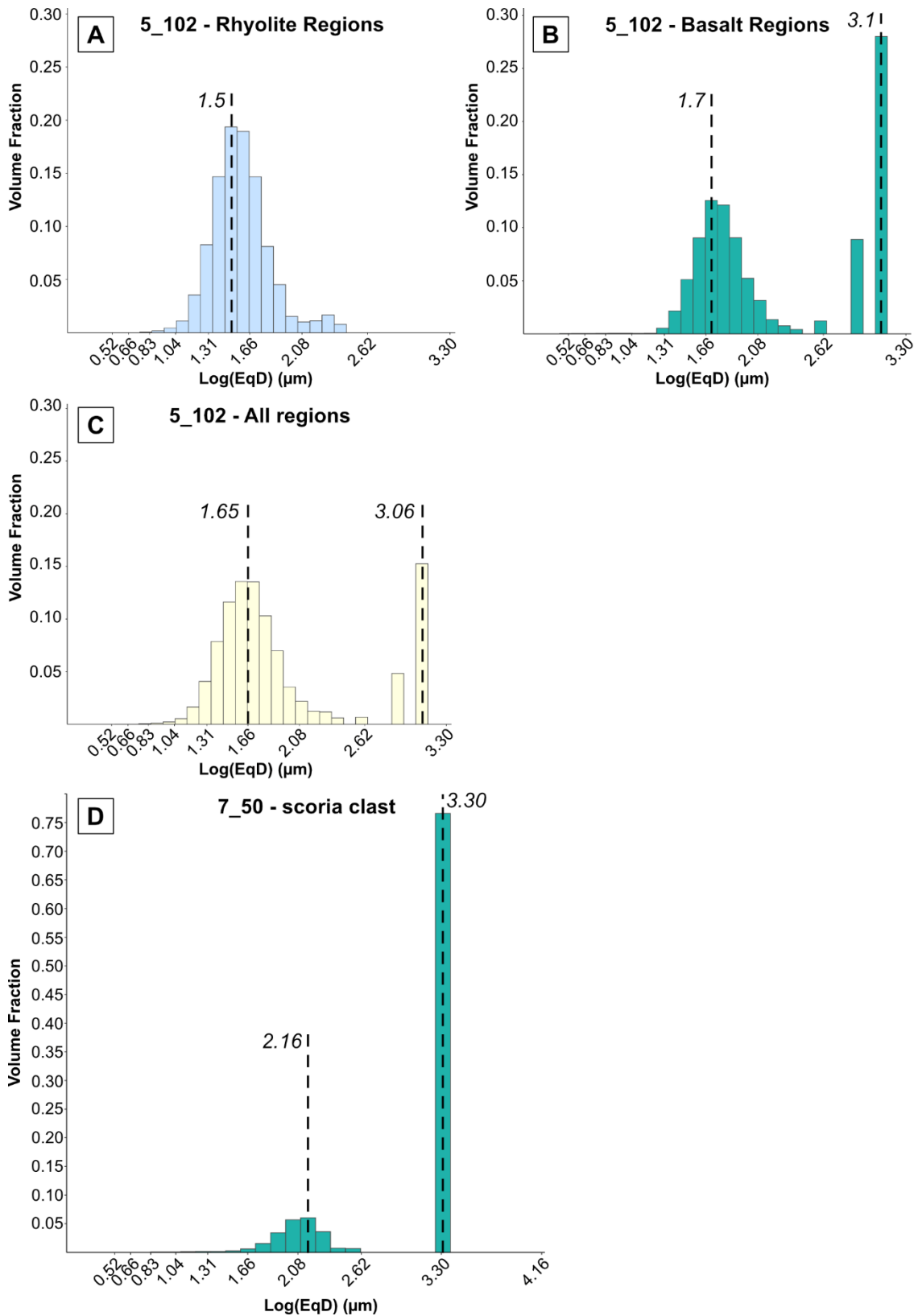


Fig. 4.26: vesicle volume distributions (VVDs) for regions / clasts from the mingled fall deposit from 3D data. Black dashed lines and italicised numbers identify modes for $\log(\text{EqD})$ where EqD is the equivalent diameter of a sphere with the same volume as the analysed vesicle.

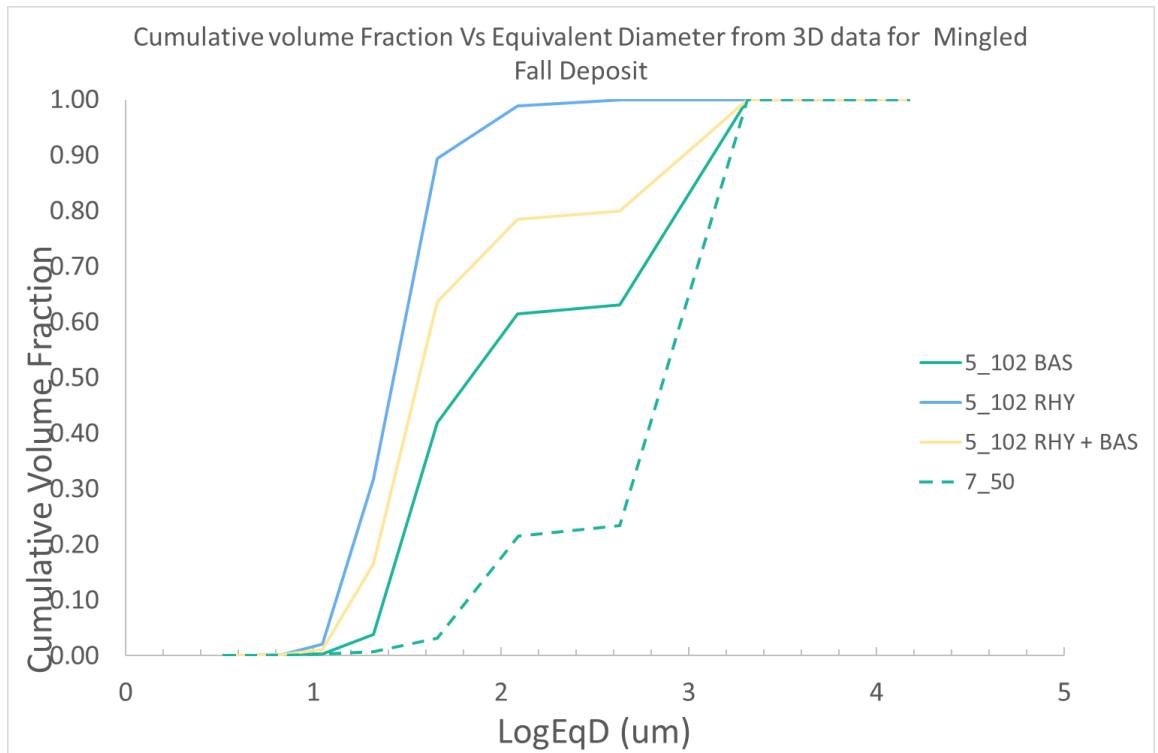


Fig. 4.27: Plots of cumulative volume fraction vs log(EqD) for basalt regions (5_102 BAS), rhyolite regions (5_102 RHY) of the mingled clast, the whole dataset for the mingled clast (5_102 RHY + BAS) and the scoria clast (7_50). EqD is the equivalent diameter of the spherical bubble with the same volume as the analysed bubble.

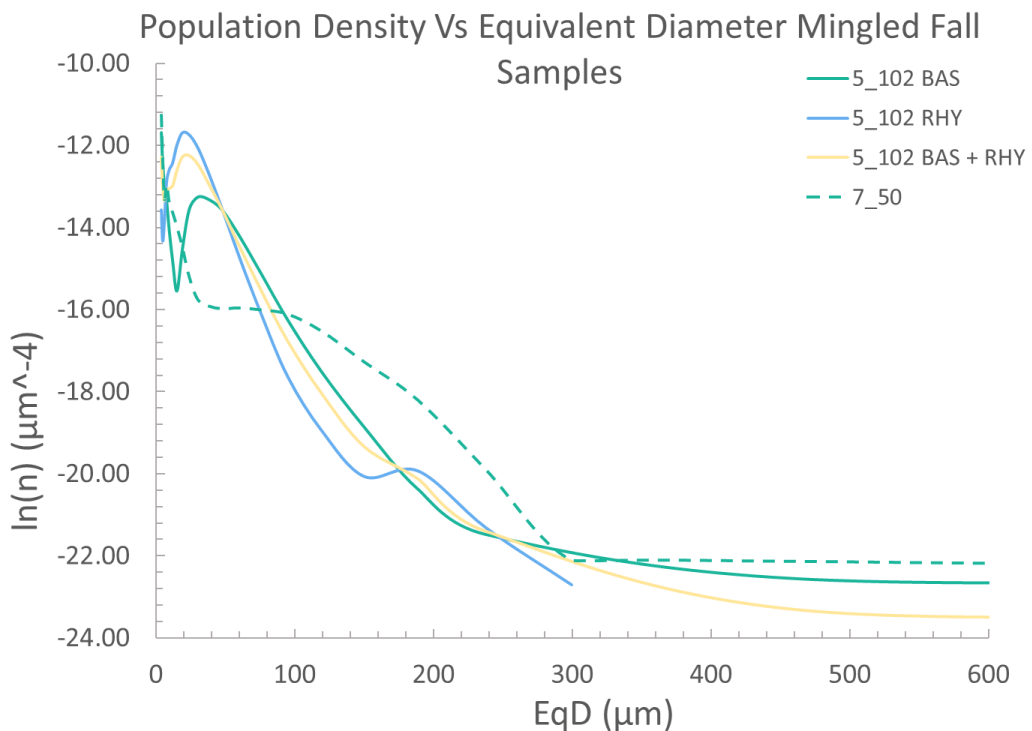


Fig. 4.28: Plots of $\ln(n)$ vs EqD for basalt regions (5_102 BAS), rhyolite regions (5_102 RHY) of the mingled clast, the whole dataset for the mingled clast (5_102 RHY + BAS) and the scoria clast (7_50). Where n is population density and EqD is the equivalent diameter of the spherical bubble with the same volume as the analysed bubble. Partial bubbles that intersected the edge of the analysed volume are not included.

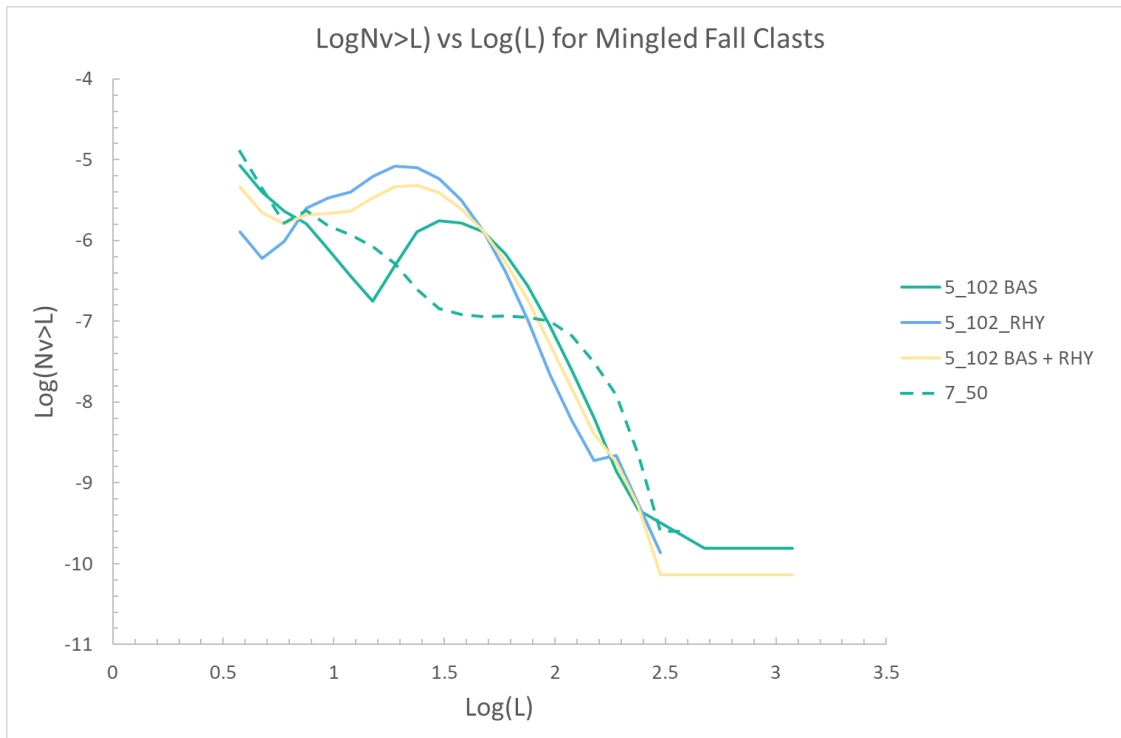


Fig. 4.29: Plots of $\log(N_{v>L})$ vs $\log(L)$ for basalt regions (5_102 BAS), rhyolite regions (5_102 RHY) of the mingled clast, the whole dataset for the mingled clast (5_102 RHY + BAS) and the scoria clast (7_50). Where N_v is population density and L is the equivalent diameter of the spherical bubble with the same volume as the analysed bubble. Partial bubbles that intersected the edge of the analysed volume are not included.

with the shallowing of the curve at higher bubble diameters (Fig. 4.29). As a whole, the curve showed a better fit for a power law distribution than an exponential one, though both returned R^2 values < 0.975 (table 4.8). As coalescence is typically represented by a transition from power-law to exponential, the poor fit to each distribution type individually is expected.

In the scoriaceous clast, coalescence has had an even greater impact on the bubble population, reflected in the VVD and VSD curves (Figs. 4.26D, 4.27, 4.28 and 4.29). The vesicle volume distribution (Fig. 4.26D) is offset to higher bubble diameters than either region of the mingled clast, with modes at 2.16 and 3.30 reflecting the coarser bubble population. The second mode at $\log(\text{EqD}) = 3.30$ is produced by a single individual that constitutes $\sim 75\%$ of the total vesicle population volume highlighting the development of extensive, complex vesicle networks in the scoria clast (Fig. 4.26D). The low number of large vesicles captured is controlled by the size of the HRES cube used in the analysis - for a larger volume, more larger vesicles would be captured. In addition, large vesicles are more likely to intersect the edge of the volume and so the process of removing partial vesicles reduces the number of individuals captured in these size ranges (see section 4.7.2 for full

discussion). The shape of the cumulative volume fraction curve also indicates the strong influence of coalescence on the vesicle population, with a hump in the curve at the same bubble diameters as in the basaltic clast (Fig. 4.27). The hump in the scoria data constitutes a smaller volume fraction due to the high volume fraction contributed by the single largest bubble. The shape of the $\ln(n)$ vs equivalent diameter curve is also representative of coalescence amongst the vesicle population, shallowing out at bubble diameters of 300 μm (Fig. 4.28). However, the multiple distinct changes in slope of this curve also imply there may have been multiple stages of bubble nucleation and growth amongst this population. This is carried through to the plot of $\log(Nv > L)$ vs $\log(L)$ where the same changes can be observed (Fig. 4.29).

Population density is used to infer the relative dominance of bubble nucleation vs growth in a bubble population. Population densities for the mingled regions and scoria clast are presented in table 4.8. All the population densities recorded for 3D data are lower than those in the 2D equivalent, reasons for this will be discussed in detail in section 4.7.3. However, useful comparisons can be made between the different regions / clasts using the 3D data alone. All population densities are of the same order of magnitude but the basaltic regions of the mingled clast have the lowest population density. A low population density can indicate low overall vesicularity, or a higher proportion of large vesicles. Vesicularity in the basaltic regions is higher than the rhyolite ones so it is likely the low population density is related to higher degrees of coalescence than in the rhyolite. As there is evidence for multiple phases of bubble nucleation and growth within the scoria, a higher bubble number density may be achieved through additional nucleation events during the ascent of the scoria.

4.6.4 3D shape parameters

Although shape parameters in 2D provide useful insights into controls on vesicle shape and bubble-melt interactions, the true 3D vesicle geometry and more complex textures can't be captured. The formation of such networks, development of permeability and subsequent impact on bubble overpressures exerts a strong control on eruptive style (Cassidy *et al.*, 2018). Bubble geometries were evaluated in 3D using two standard shape parameters defined in Avizo® – *anisotropy* and *elongation*. In doing so, interactions between bubble growth, coalescence, relaxation and shearing across the different regions / clasts can be explored without additional computational steps. Results from 3D analyses

are compared with 2D datasets to assess whether resulting interpretations are consistent across the two methods.

Fully quantified permeability models can be constructed using XCT data to explore these relationships in more detail (e.g., Wadsworth *et al.*, 2020), but this is computationally expensive, only feasibly on relatively small XCT volumes (typically limited to a 500x500x500 voxel volume) and are beyond the scope of this study.

Of the many 3D geometry measures that can be extracted from the 3D data (see section 4.4.5 and table 4.4), the shape parameters with the closest equivalency to those studied in 2D are *anisotropy* and *elongation*. *Anisotropy* measures the deviation of a pore from a spherical shape - the 3D equivalent to the 2D measure of circularity - and values close to zero are closer to perfect smooth spheres. As with 2D circularity, anisotropy can be impacted by both elongation of particles and high degrees of surface roughness. *Elongation* is a direct 3D equivalent of 2D elongation, but more elongate vesicles will have values close to zero. *Anisotropy* and *elongation* are plotted against each other, and against *Volume3d* using density plots to examine the influence of shear and other processes on the bubble population. The high proportion of smaller vesicles relative to large ones skewed the density scale such that it masked the range in values for higher vesicle volumes. As such, to give the best visual representation of the range of values each dataset was sub-divided by volume. Two plots of each set of parameters were produced above and below a cut-off value of 500 μm^3 for the mingled clast and 1000 μm^3 for the scoria clast. These cut-offs were chosen as they produced the clearest overall visual representation of variations in vesicle shape. *Elongation* is plotted against *anisotropy* in Fig. 4.30, *volume3d* against *anisotropy* in Fig. 4.31 and *volume3d* against *elongation* in Fig. 4.32.

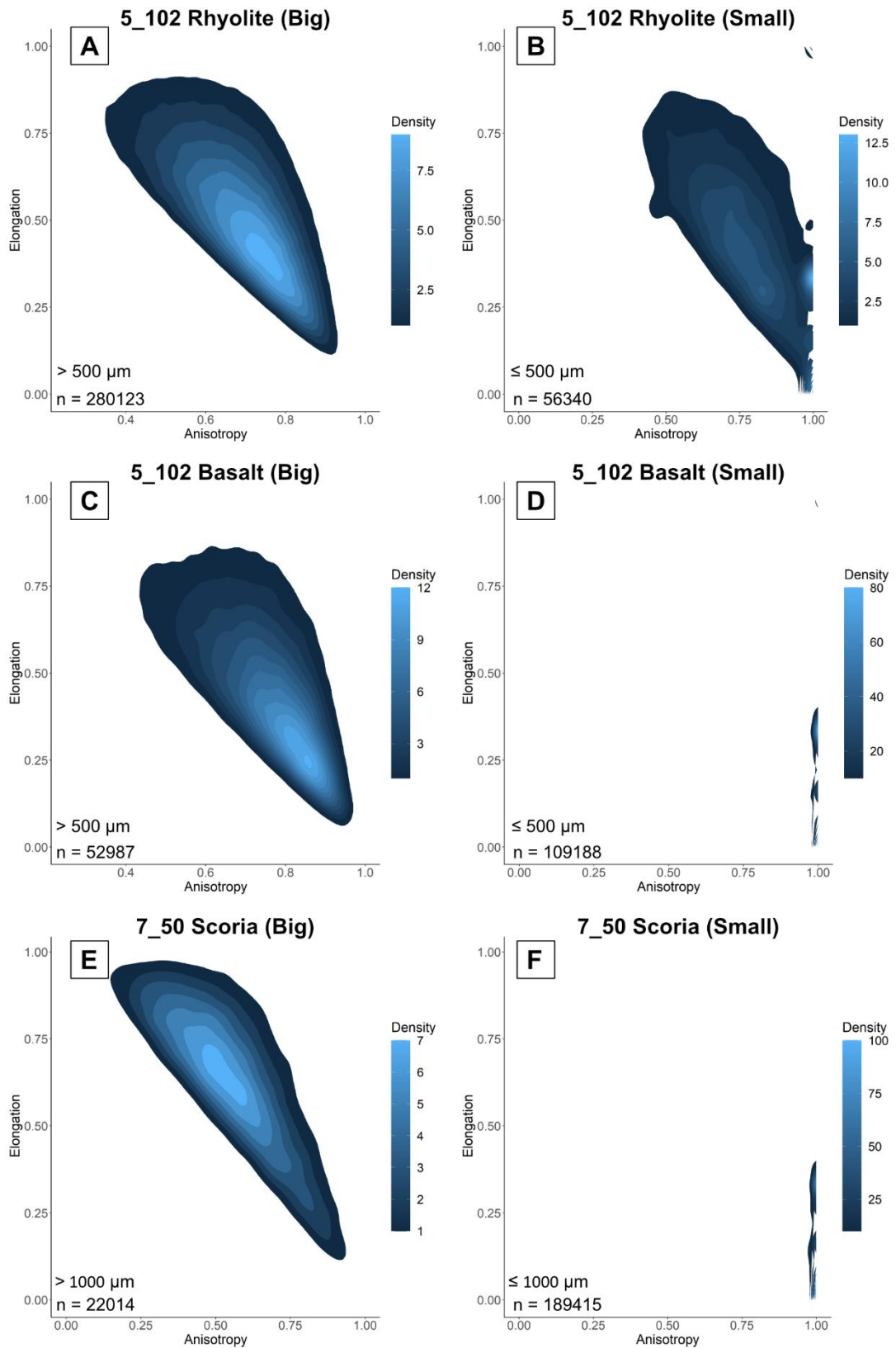


Fig. 4.30: Plots of elongation vs anisotropy for rhyolite and basalt regions of the mingled clast (5_102), and the scoria clast (7_50) from the Mingled Fall. Brighter colours represent regions with a higher density of data points.

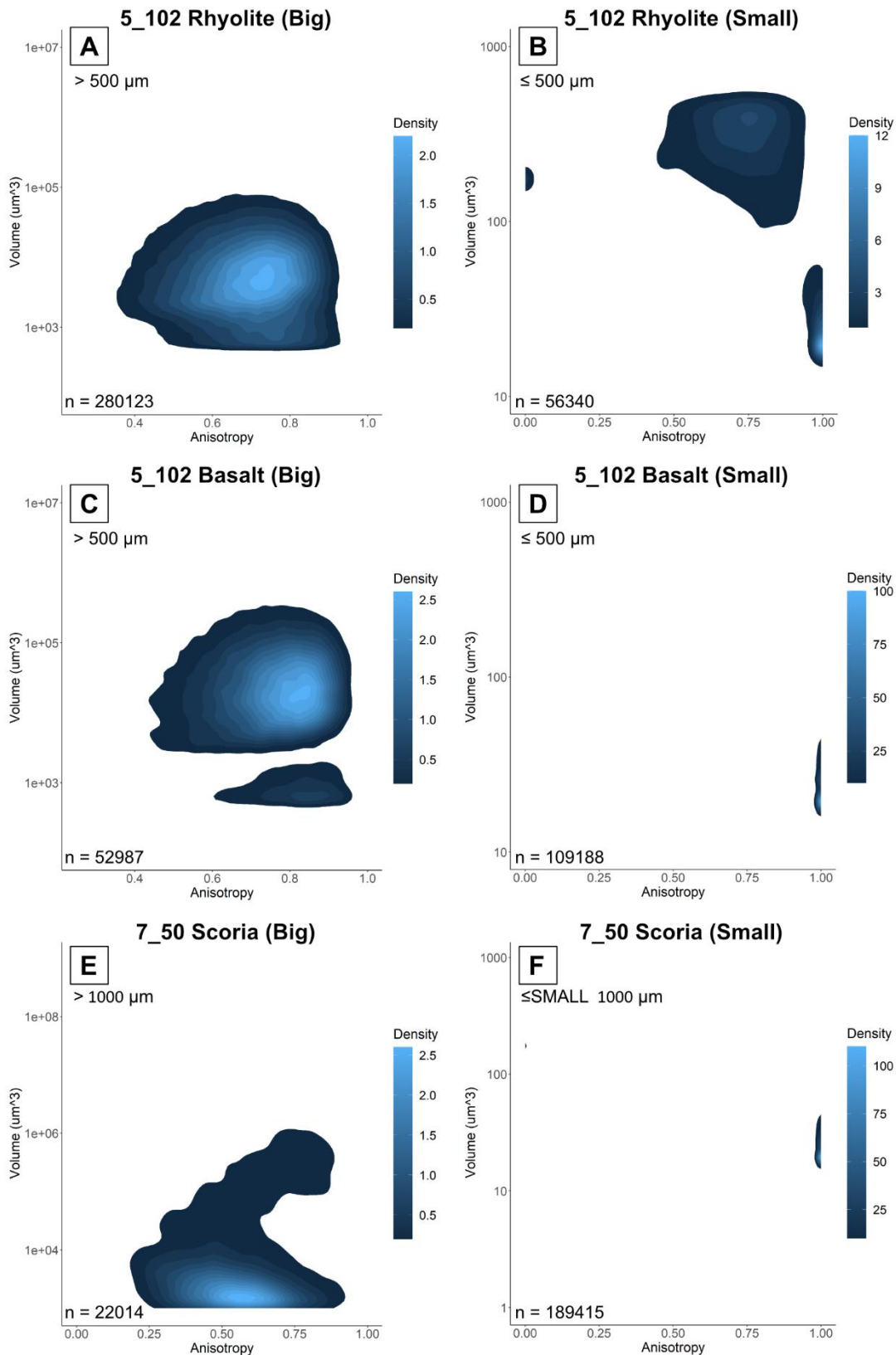


Fig. 3.31 Plots of Volume3d vs Anisotropy for rhyolite and basalt regions of the mingled clast (5_102), and the scoria clast (7_50) from the Mingled Fall. Brighter colours represent regions with a higher density of data points.

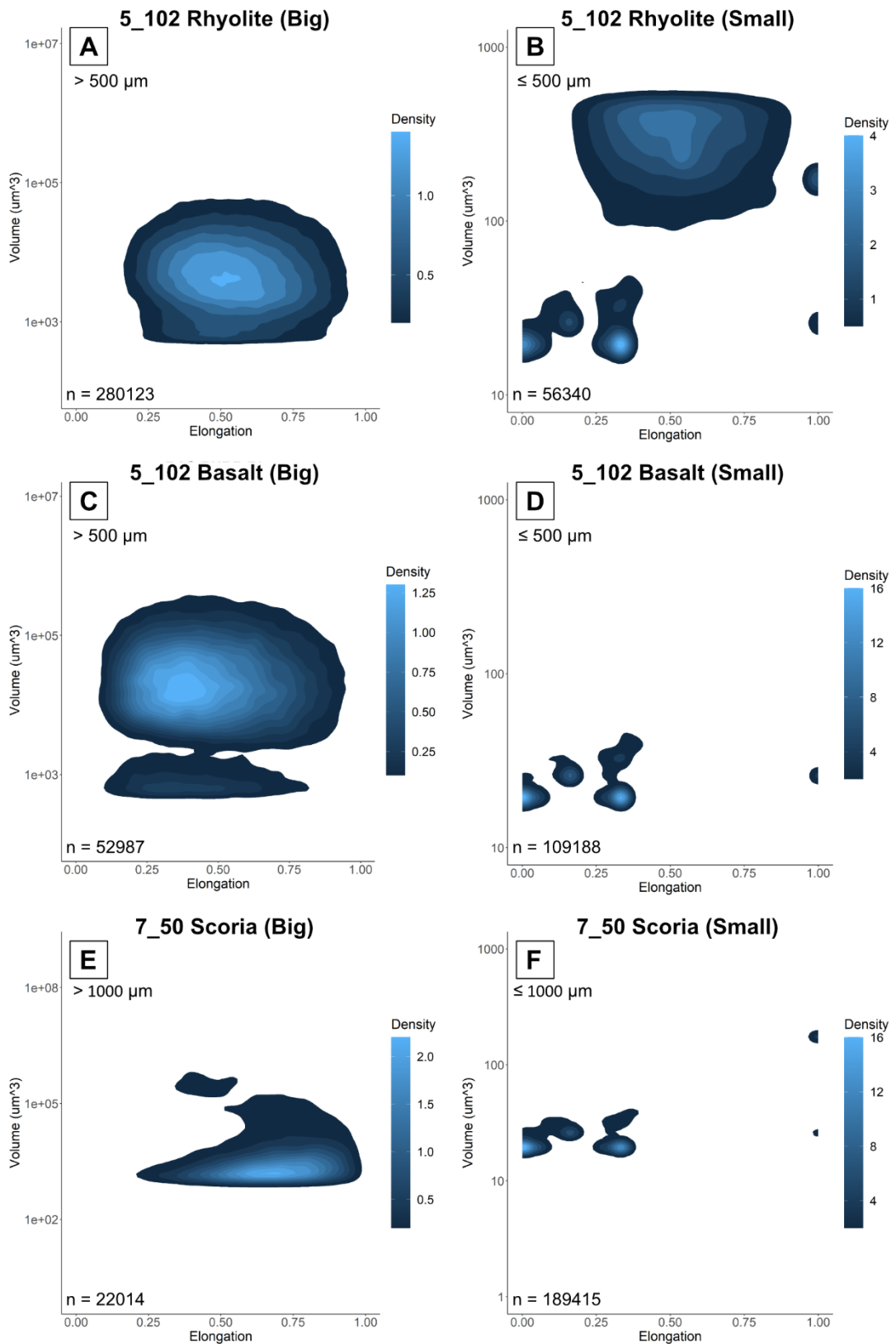


Fig. 3.32 Plots of Volume3d vs elongation for rhyolite and basalt regions of the mingled clast (5_102), and the scoria clast (7_50) from the Mingled Fall. Brighter colours represent regions with a higher density of data points.

4.6.4a Larger bubble populations 3D trends

Variations in shape parameters and vesicle volume of the larger bubble populations, as displayed in Figs. 4.30 – 4.32 are described in table 4.9. In rhyolite regions, extremes in elongation are rare and do not correlate with extremes in anisotropy (Figs. 4.30A and 4.32A). This indicates elongation (via shear) is not the dominant factor controlling deviation of vesicles from spherical. Application of the separation algorithm should have split any bubbles where there were significant small-scale protrusions (aka partial bubble walls – textural roughness), but larger features were not included. Thus, for bubbles with high values of anisotropy in the $> 500 \mu\text{m}^3$ population, particle-scale protrusions/concavities may be the dominant contributor over elongation or textural roughness. This highlights how 3D measurements can better capture some of the complexities of bubble shapes where networks are not as extensive as in basaltic materials and 2D cross-sections indicate relatively simple bubble textures.

Basaltic regions of the mingled clast (Figs. 4.30C, 4.31C and 4.32C) are overall more elongate than in the rhyolite and *elongation* is generally the dominant factor influencing deviations from perfect spherical vesicles. However, again, there is a wide range in elongation amongst the population and very few vesicles approach high extremes of elongation – extreme shear is not pervasive in the mingled clast.

In the scoria clast, vesicles are much less elongate and anisotropic than in the mingled clast (Figs. 4.30C, 4.31C and 4.32C), but highly anisotropic vesicles do tend to be more elongate. This indicates that at extremes in anisotropy, elongation, not surface roughness is the dominant factor impacting deviations from spherical. Only a few individuals have high anisotropy and are very elongate, these are the larger volume individuals forming extensive networks in the analysed cube.

These results indicate that within the rhyolitic regions of the mingled clast, relaxation timescales were longer than the timescale between coalescence and quenching upon fragmentation, preserving irregular vesicle shapes. The differences between the scoriaceous and mingled clasts support the interpretation of more extensive coalescence in the scoria clast, increasing connectivity. Even within the scoria however, relaxation has not progressed sufficiently to entirely remove the impact of coalescence events on the shapes of the bubble population.

Table 4.9: description of variations in shape parameters in 3D, larger* vesicle populations from the Mingled Fall				
Sample/ region	Anisotropy vs Elongation	Anisotropy vs Volume	Elongation vs Volume	Major/ Minor controls
5_102 / Rhyolite	<ul style="list-style-type: none"> • Densest at highly anisotropic, relatively elongate. • At high anisotropy, Δ elongation \neq Δ anisotropy 	<ul style="list-style-type: none"> • Densest around 0.7 anisotropy and $10^4 \mu\text{m}^3$ • No strong control of volume on anisotropy on large population 	<ul style="list-style-type: none"> • Densest around moderate elongation • No strong control of volume on elongation in larger population 	<ul style="list-style-type: none"> • Elongation not dominating factor controlling deviation from spherical • Surface roughness may play a larger role in high anisotropy.
5_102 / Basalt	<ul style="list-style-type: none"> • Denser at more elongate and more anisotropic vesicles than in the rhyolite. • At high anisotropy Δ elongation closer to Δ anisotropy than rhyolite 	<ul style="list-style-type: none"> • Slightly larger bubbles than rhyolite • Densest shifted to higher anisotropy than rhyolite • Secondary population at lower bubble volumes, also high anisotropy. 	<ul style="list-style-type: none"> • Shifted towards more elongate vesicles than rhyolite • No strong control of volume on elongation 	<ul style="list-style-type: none"> • Elongation a stronger influence on deviation from spherical than in rhyolite. • Not all vesicles are elongate, some influence of surface roughness.
7_50 / Scoria	<ul style="list-style-type: none"> • Densest at lowest anisotropy and elongation compared to basalt and rhyolite. • At low anisotropy Δ elongation \approx Δ anisotropy 	<ul style="list-style-type: none"> • Densest at moderate anisotropy and vesicles $100 - 1000 \mu\text{m}^3$. • Very few larger vesicles, have high anisotropy. But no distinct control of size on anisotropy. 	<ul style="list-style-type: none"> • Much less elongate overall than basalt or rhyolite. • Some large individuals are very elongate. • No real control of volume on elongation. 	<ul style="list-style-type: none"> • Elongation an important factor but overall elongation of vesicles is low. • A few individuals at high anisotropy and elongation from complex vesicle networks

*5_102 plots contain bubbles $> 500 \mu\text{m}^3$, 7_50 plots contain bubbles $> 1000 \mu\text{m}^3$

4.6.4b Smaller bubble populations

Plots of anisotropy and elongation in the smaller bubble populations ($< 500 \mu\text{m}^3$ in the basalt and rhyolite regions, $< 1000 \mu\text{m}^3$ in the scoria clast) are more difficult to reconcile with vesicle shapes observed in SEM images and visualisations of the 3D dataset. For the basalt regions and the scoria clast, almost all vesicles in the “small bubbles” plots have *anisotropy* values of ~ 1 (Fig. 4.30D & F and Fig. 4.31 & F). Such extreme values of *anisotropy* are unexpected as typically the smaller vesicles in SEM images are the smoothest and closest to spherical - they haven't undergone extensive bubble growth or phases of coalescence. The same populations also appear to be quite *elongate* in the 3D data compared to their larger counterparts. If the values are taken to reflect the true vesicle population, they could represent small populations of intensely sheared vesicles, or small vesicles that have been distorted by growth of other larger vesicles. Considering such a large proportion of the vesicles analysed occupy this space on density plots we would expect to see these shapes heavily represented in 2D analyses. However, such populations do not appear to be particularly prevalent in SEM images (Fig. 4.24A, & D) and are not seen in shape parameter plots in 2D (Figs. 4.25). Another explanation could be that at low bubble volumes, voxel size has a greater impact on the calculated values of shape parameters. Since *anisotropy* is calculated as a ratio (table 4.4), the impact of small changes in vesicle shape in small vesicles will be much larger than the impact of small changes in large vesicles. In addition, as the resolution limit of the data is approached, bubble surfaces become more vulnerable to pixilation – generating deviations on the particle surface that may not be significant enough to require a bubble separation but may have an impact on *anisotropy*. For bubbles above approximately $100 \mu\text{m}^3$ the impact of this effect seems to lessen producing plots that show a range of anisotropy values for vesicles of $100 - 1000 \mu\text{m}^3$ in the rhyolite regions of the mingled clast (Fig. 4.31B).

More work needs to be done to identify how voxel size impacts the Avizo® measure of *anisotropy* and *elongation* at low bubble volumes. Other shape parameters measured in this study should also be explored to better distinguish between morphological and textural roughness (particle scale concavities vs small protrusions) in 3D analyses.

[4.7 Discussion](#)

Previous sections have outlined a workflow that can be applied to texturally complex volcanic eruption products containing one or two melt compositions. Using this method, key vesicle size and shape data can be extracted across different length scales and in 2D and 3D while identifying and preserving targets for later compositional analyses. Vesicle size and shape data for the Mingled Fall are used to assess how mingling impacted vesiculation during ascent. The influence of various aspects of data collection and processing on these interpretations will be discussed, and the value of 2D vs 3D textural studies reflected upon.

[4.7.1 Initial interpretations for ascent dynamics of the Mingled Fall](#)

The previous study by Chamberlain *et al.*, (2020) inferred storage of the basaltic and rhyolitic endmembers at approximately 11 km depth and that mingling triggered rapid ascent leading to eruption within ~24 hours. Interrogation of vesicle size and shapes between the two compositions helps elucidate how the mingling event influenced the vesiculation history of this magma during ascent. The shapes of 2D and 3D VVD and VSD plots presented above present evidence of conflicting vesiculation histories for the same sampled region / clast. Given the limitations of vesicle analyses in 2D interpretations of ascent dynamics for the mingled fall primarily make use of the vesicle volume data presented in Figs. 4.26 – 4.29 and shape data from Figs. 4.30 – 4.32. A full discussion of possible sources of conflict between interpretations of the two datasets is presented in section 4.7.4.

When the “hockey stick” region is discounted, data in the VVD plot, the plot of $\log(N_v > L)$ vs $\log(L)$ and the cumulative volume fraction curve (Figs. 4.26A, 4.27 and 4.29) all support dominance of a single stage of nucleation and growth, with a small influence of coalescence for the rhyolitic regions of the mingled clasts. The plot of $\ln(n)$ vs equivalent diameter more strongly supports continuous acceleration and growth (Fig. 4.28), as seen for plots of 2D data. However, the shape of the curve may be being pushed towards this trend by the presence of only a minor signal of coalescence at larger bubble diameters. In the basalt regions of the mingled clast, all the plots support a stronger influence of coalescence on the bubble population (Figs. 4.26B, 4.27, 4.28 and 4.29). In the scoria clast, the VVD curve, and cumulative volume fraction curves indicate the influence of coalescence on the bubble

population is strong, and more extensive than in the basaltic regions of the scoria (Figs. 4.26C, 4.27). The changes in slope of the $\ln(n)$ vs equivalent diameter and $\log(Nv > L)$ vs $\log(L)$, provide evidence of multiple nucleation and growth events (Figs. 4.28 and 4.29).

Shape data for rhyolitic regions indicate that shear is not a significant factor impacting the bubble population. In the basaltic regions, elongation has a greater influence than in the rhyolite, but this is likely associated with the development of larger, more complex vesicle networks than a high degree of shear. This indicates that the process of mingling did not induce significant shear across the contacts of the two melts – supported by textures observed in SEM images (Fig. 4.24). Vesicle shape data in the scoria clast is very similar to the basaltic regions of the mingled clast but with higher degrees of anisotropy and elongation in the largest bubble population – again, likely associated with the formation of very large, complex bubble networks.

Together, the vesicle size and shape data from the mingled and scoria clasts elucidate the vesiculation histories of the melts during triggering and ascent. A volatile rich (~6 wt% H₂O) rhyolitic melt, stored at ~11km depth at a temperature of 800°C was intruded by the hotter (~900°C), also relatively volatile rich (2.5 wt% H₂O) basalt (Chamberlain *et al.*, 2020). Heating of rhyolitic magmas via mafic injection can trigger volatile exsolution and bubble nucleation (Paredes-Mariño *et al.*, 2017), mobilising material in the storage region and is interpreted by Chamberlain *et al.*, (2020) to represent the trigger for this eruption. The vesicle studies presented in this chapter do not preclude this explanation, though it is difficult to determine at what depth nucleation occurred with the available data. The 3D VVD's for the rhyolite and basalt mingled clast do not reflect multiple distinct nucleation events. The dominant nucleation event may therefore, have occurred due to the intrusion of the hotter mafic melt, facilitating rapid ascent and bubble growth. Due to the short timescales between mafic injection and eruption, mingling between the two melts was incomplete and did not progress to geochemical mixing (Chamberlain *et al.*, 2020). Given the temperatures and volatile contents of the two melts, their viscosities were approximately only one order of magnitude different (basalt = $10^{3.42}$ at 900°C and 2.5 wt% H₂O, rhyolite = $10^{4.02}$ at 800°C and 6 wt% H₂O using the model of Giordano *et al.*, 2008 and data from Chamberlain *et al.*, 2020 – see appendix 3.1) facilitating mingling with little – no shear at the contacts. Rapid volatile exsolution in the two magmas likely facilitated high ascent rates as the two magmas vesiculated freely with little – no impact on each other. Bubble-microlite-mingling contact geometries in the basalt regions suggest microlite

crystallisation occurred syn-eruptively, after / alongside significant vesiculation. Once the rhyolitic and mingled magma was exhausted, non-mingled, basaltic scoria was erupted containing a more connected bubble population reflecting more extensive bubble growth and coalescence. Late stage, extensive microlite crystallisation has been inferred to promote high explosivity in basalts through increased magma viscosity and viscoelastic deformation, promoting brittle failure (Moitra *et al.*, 2018). Extensive crystallisation can also help bubble networks retain their shape post-fragmentation due to rheological stiffening and high yield stress at bubble walls, reducing the impact of post-fragmentation relaxation on interpretations of bubble textures (Moitra *et al.*, 2018). In the scoria clast, partial bubbles comprised more than 50% of the total volume. In contrast, in the basaltic region of the mingled clast partial bubbles comprised only ~20%. This indicates vesicle growth and development of connectivity in basaltic regions of the mingled magmas was inhibited relative to the ascending entirely basaltic melt – supported by bubble size data. The lower connectivity of basaltic regions may be caused by faster ascent of mingled magmas than the later erupting basalt, driven by excess buoyancy due to the high volatile content of the rhyolite. Each endmember composition in the mingled regions followed relatively “normal” vesiculation pathway for their composition. However, the mingling process clearly impacted the development of permeability in the basaltic regions. Further work to quantify the permeabilities of each region, and permeability across the boundaries would be useful to constrain how volatiles migrate and outgas in mingled events and place constraints on the development of bubble overpressures during mingling events.

4.7.2 Impact of excluding partial bubbles from VVD and VSD analysis

Volume data for bubbles that intersect the edge of the analysed volume are incomplete. Inclusion of partial bubbles in the VVD and VSD curve would therefore skew some of the data to smaller bubble volumes. However, as larger bubbles are more likely to intersect the edges, not including partial bubbles can mean larger bubble classes are not sampled at all which could dramatically alter interpretations of vesiculation processes. To account for this bias, all the same vesicle parameters were collected for partial bubbles and interrogated. Plots in Fig. 4.33 show how including partial bubbles impacts the shape of the VVD plots. Including the partial bubbles does not drastically alter the interpretation of these plots. For the rhyolite curve, including partial bubbles does extend the maximum vesicle diameter but these bubbles do not constitute a significant portion of the total volume (Fig. 4.33A).

The presence of the smaller second population in the rhyolite curve without partial bubbles included was sufficient to yield an interpretation that coalescence had started to occur in these regions. A similar effect is seen in the basaltic regions and scoria clast. While partial bubbles fill in some of the gaps at intermediate size classes, they don't dramatically alter the interpretation compared to the plot with no partial bubbles. The original plot (Fig. 4.26B) contained sufficient bubbles at larger size classes to yield an interpretation of more significant coalescence than in the rhyolite regions. The same is seen in the scoria clast (Figs. 4.26D and 4.33D).

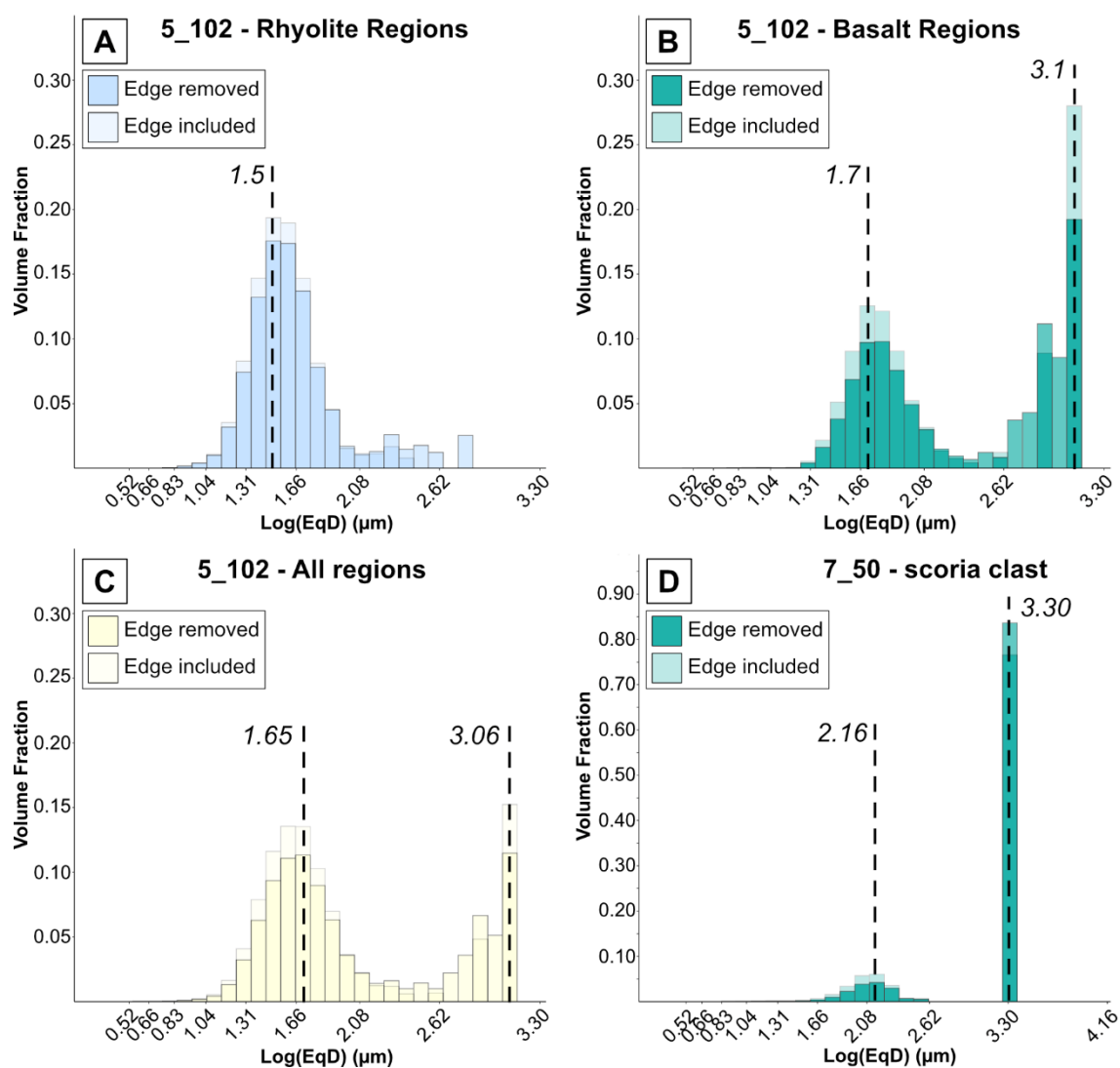


Fig. 4.33: vesicle volume distributions from 3D data for regions / clasts of the Mingled fall shown without (darker shades) and with (lighter shades) partial bubbles (that intersected the edge of the analysed cube) included. Modes are indicated by black dashed lines.

Incorporating partial bubbles in the VSD curves helps increase the number of individuals at equivalent diameters above 350 μm (5 individuals > 350 for scoria, 16 for all, 5 for rhyolite, 10 for basalt) but does not change their general trends (see the example of Fig. 4.34). The

main difference is the addition of a third peak around 370 μm in the rhyolitic curve. As all partial bubbles are minimum volume estimates the true curves may extend to greater equivalent diameters, altering the slope such that the signal of coalescence is more obvious.

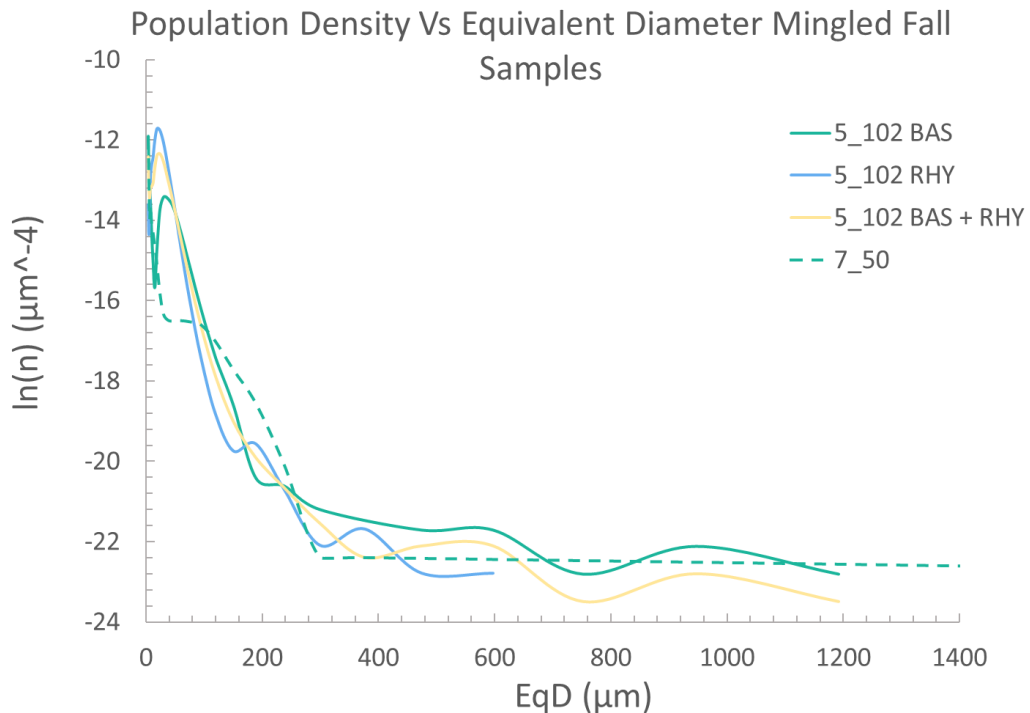


Fig. 4.34: Plots of $\ln(n)$ vs EqD for basalt regions (5_102 BAS), rhyolite regions (5_102 RHY) of the mingled clast, the whole dataset for the mingled clast (5_102 RHY + BAS) and the scoria clast (7_50). Where n is population density and EqD is the equivalent diameter of the spherical bubble with the same volume as the analysed bubble. Partial bubbles that intersected the edge of the analysed volume are included.

Although inclusion of partial bubbles did not dramatically impact the interpretation of VVD and VSD data in this case, it is recommended that this data is always collected so that this can be tested.

4.7.3 Considerations from XCT data processing

The main concern with any technique used to collect data on bubble shape and size is the ability to preserve the thinnest melt films and accurately represent smooth rounded features (bubbles) using square pixels (or voxels in 3D). Both issues can be resolved to some extent by collecting data at an appropriate resolution for the dimensions of the features in question. Recent advances in XCT technologies mean that scan resolutions of down to 50 nm can be achieved but can only be applied to volumes up to $50 \mu\text{m}^3$. Reducing the size of

the sampled volume limits your ability to capture textural variations and larger features, making it harder to justify the scaling-up of interpreted processes to the clast, unit, and deposit scale of an eruption (the same applies to 2D studies). As such, compromises must be made between total analysed volume and data resolution. These choices must be justified, and any steps taken to reduce the impact of a lower resolution applied consistently to ensure human biases are not introduced to the data. Below, some key decisions are briefly discussed, choices rationalised, and suggestions made for improving future data collection / interpretation.

Limitations of resolution – error on bubble volumes & preservation of thin films

High resolution volumes from the mingled (5_102) and scoria clasts (7_50) from the MF had voxel sizes of $1.68 \mu\text{m}^3$ and $1.71 \mu\text{m}^3$ respectively. This meant vesicles with a volume below $1 \mu\text{m}^3$ and melt films with an equivalent thickness could not be well captured. Inspection of SEM images shows there are vesicles with diameters of as small as $1.99 \mu\text{m}$ and melt films $< 0.5 \mu\text{m}$ thick in the mingled clast (5_102). In the scoria clast, melt films are rarely $< 3 \mu\text{m}$ and the smallest bubble has an equivalent diameter of $\sim 2.5 \mu\text{m}$. Bubbles below the voxel size range are not easily resolved in the XCT data and extraction of any of these features was not attempted. For small bubbles (volume < 125 voxels) the % error in the volume measurement increases with decreasing volume mainly because of the systematic and random errors introduced by the partial volume effect (voxels partially film and partially bubble) and how these are treated in the segmentation process. This means that while for any single small bubble, the error in measured volume will be high (5% at volumes of ~ 125 voxels, rising to $\sim 200\%$ for volumes of 1 voxel), for a bubble population (and hence the VSD analysis) the uncertainty is much lower provided the frequency in each size bin is high ($< 5\%$ for the smallest size fraction (1 - 10 voxels) when $n > 1000$) Lin *et al.*, 2015). To ensure all uncertainties associated with bubble volumes in all parts of all volumes, VVD and VSD curves are $\ll 1\%$, bubbles with volumes < 10 voxels were removed from all analysed regions / clasts. In most parts of most clasts the number of these smallest bubbles (< 10 voxels) would mean $< 1\%$ error in volume for the bin, but for consistency these are all removed. For bubbles > 10 voxels, the number of bubbles analysed was > 10000 .

There are numerical methods to enhance and rectify the thin melt films that are not captured well because of the resolution limitations. Typically, films thicken towards the point at which they anchor to the melt network and so are usually at least partially

preserved as protrusions from the bubble wall. Where appropriate (geological understanding and prior knowledge e.g., from SEM images) these partial films can be used to drive feature separation algorithms (sections 4.4.3a and 4.4.4b). There are several other network-forming and skeletonization algorithms available in Avizo which could have been used in various combinations to tailor the reconstruction of melt films more flexibly across the different regions / clasts. However, the strategy adopted here was to change the raw data as little as possible to get a geologically sensible answer. Processing of XCT data from geological samples is not a standardised process as the required algorithms vary with clast texture and data resolution. Systematically applying a few algorithms to all regions/ clasts ensured all the data was treated in a numerically consistent way. All variations in parameter settings were tested to find the “best” solution based on prior geological understanding of samples. In this way, a workflow has been produced that can reasonably be followed and adapted to assess other texturally complex samples.

The sharp decrease in population density around bubble diameters of approximately 10 μm referred to as the “hockey stick” region, is often observed in VSD curves produced using XCT data. However, the underlying causes of this trend are not well understood (Pers. Comm. Kate Dobson 2022). An equivalent diameter of <10 μm should be within the range at which bubbles can be accurately captured in XCT data of the resolution used in this study – resolution limits cannot explain this trend. The VSD curves for the scoriaceous clast lack the “hockey stick” region indicating the observed trend may be due to the handling of thin melt films during the segmentation process. The separation applied to the XCT data from the scoria clast was coarser (object pixel size of 6) than that applied to the rhyolite (object pixel size of 1). It may be that a combination of the separation value used, the resolution of the data relative to bubble size and some feature of bubble morphology may be contributing to this observed trend. Some way to further investigate the cause of the “hockey stick” trend in VSD curves include:

1. Apply a wider range of separation parameters to the same dataset and see if this changes the VSD curve at this size range.
2. Examine other datasets that produce the same effect and the data processing algorithms used.
3. Investigate other parameters e.g., vesicle shape and surface roughness and see whether particular groups intersect with the impacted range in vesicle diameters.

It is important to understand what causes this irregularity in VSD curves from 3D data to ensure accurate and consistent interpretation of these textures.

The data presented in this study has shown the impact of physical mingling between two distinct compositional endmembers on vesiculation during ascent in comparison to the ascent of the same basalt in isolation. Further valuable insights would have been gained via inclusion of a wholly pumaceous clast. Doing so would enable evaluation of how mingling impacts the vesiculation of rhyolitic portions of the ascending magma and was initially a target for this study. However, segmentation and extraction of bubble data for a clast with two distinct compositions and associated vesicle textures was both intellectually and computationally challenging. The processes outlined in sections 4.4.2 – 4.4.6 took longer than expected for several reasons:

(a) Algorithms and mathematical functions in Avizo® were not designed to deal effectively with a dataset comprising two compositions with such complex fine-scale textures. The workflow thus had to be developed from scratch, requiring extensive testing and adjustment at each stage.

(b) The HRES datasets were large (to capture all key textural features) and so processing timescales were long and would sometimes fail mid-way through (one key algorithm ceased functioning altogether on the pumice sample (4_70) which could not be explained even after > 6 months of investigation by Avizo® engineers).

(c) Onset of the COVID-19 pandemic meant > 70% of the processing had to be carried out remotely. Remote working led to several issues including corruption of datasets during file transfer (each HRES dataset could be > 15GB), no in-person access to computer labs meant several software updates and power outages occurred mid-way through processing steps, and the need for virtual meetings made troubleshooting the workflow more complex.

Despite these constraints, this study still provides valuable insights into vesiculation processes in mingled melts and the importance of careful consideration of how data processing impacts interpretation of 3D textural data.

4.7.4 Comparing 2D and 3D textural studies

As is evident from the extensive data processing workflow presented in section 4.4, undertaking textural studies in 3D is complex and time-consuming, particularly for samples containing multiple compositions / distinct textural regions. In contrast, since the

development of the FOAMS software by Shea *et al.*, (2010) and the collation and interrogation of various shape factors by Liu *et al.*, (2015), quantification of vesicle textures using 2D inputs is now relatively simple given access to adequate sample prep and imaging facilities. However, as previously stated, 2D investigations likely miss key bubble-melt network characteristics that exert a strong control on ascent dynamics and eruptive behaviour. Thus, it is important to compare studies in 2D and 3D, identify differences and try to understand their underlying causes. Here, the 2D and 3D results from the rhyolite regions of the mingled clast, and the scoria clast are compared, and efforts made to explain similarities / differences. The 2D data from the mingled regions is not compared to the whole clast data for the mingled clast in 3D as they do not represent the same textures. Data collected in the mingled regions focusses specifically on boundaries between basaltic and rhyolitic melt, this cannot be directly compared with data collected across the whole HRES volume in 3D as the latter is an average of the individual basalt and rhyolite regions, extending much further away from contacts between the two. For basaltic regions of the mingled clast, a comparison between 2D and 3D VSD and VVD data is not possible as insufficient BSE images were collected at each magnification within these regions to perform a robust analysis. However, vesicle shape data can be compared in 2D and 3D. Comparing the 2D rhyolite regions and scoria clast data with their 3D counterparts will improve our ability to interpret 2D studies where 3D data collection is not possible (e.g., due to time constraints), highlight the added value 2D studies can bring and identify key areas of uncertainty that should be the target of future studies.

VVD and VSD

Vesicle size distribution studies in 2D depend on the assumption that the 2D – 3D stereological conversions of Sahagian and Proussevitch (1998) appropriately reconstruct bubble volumes. As the conversion of Sahagian and Proussevitch (1998) assumes spherical bubbles, the 2D – 3D conversion breaks down in samples with high connectivity, extremely sheared vesicles, or both (Shea *et al.*, 2010; Mitchell *et al.*, 2019). As melt viscosity, volatile content and ascent rate all influence the development of bubble textures (Cassidy *et al.*, 2018), the accuracy of 2D – 3D conversions will vary between clasts and even across different regions of the same sample.

Rhyolite Regions:

For the rhyolite regions of the mingled clast, the range of equivalent diameters (calculated post-2D – 3D conversion) in the 2D dataset encompasses the entire range of equivalent diameters captured in analysis of the 3D data. Bubble number densities in the 2D data (3.87×10^6) are two orders of magnitude higher than the 3D data (3.56×10^4), even when bubbles below 10 voxels are added back into the 3D dataset (5.39×10^4). In 2D data, 2.5% of bubbles have equivalent diameters $< 1.68 \mu\text{m}$ – below the resolution of the XCT data. Increasing the number of bubbles in the 3D volume by 2.5% increases the bubble number density by 1 order of magnitude (both with and without bubbles < 10 voxels), which goes some way to explaining the discrepancy between the 2D and 3D datasets, but not all. Another contributing factor could be that in 2D images, a single bubble is intersected more than once in a thin section image. This would increase the number of intermediate size bubbles increasing bubble number densities in these portions of the VSD, and overall (in Fig. 4.35). The median bubble volume in the 2D data (based on a spherical bubble with an equivalent diameter of $14 \mu\text{m}$) is $1436 \mu\text{m}^3$ whereas the median bubble volume from the 3D dataset is $3466 \mu\text{m}^3$ - almost 2.5 times greater - which could indicate some bubbles are being sampled twice in the 2D dataset.

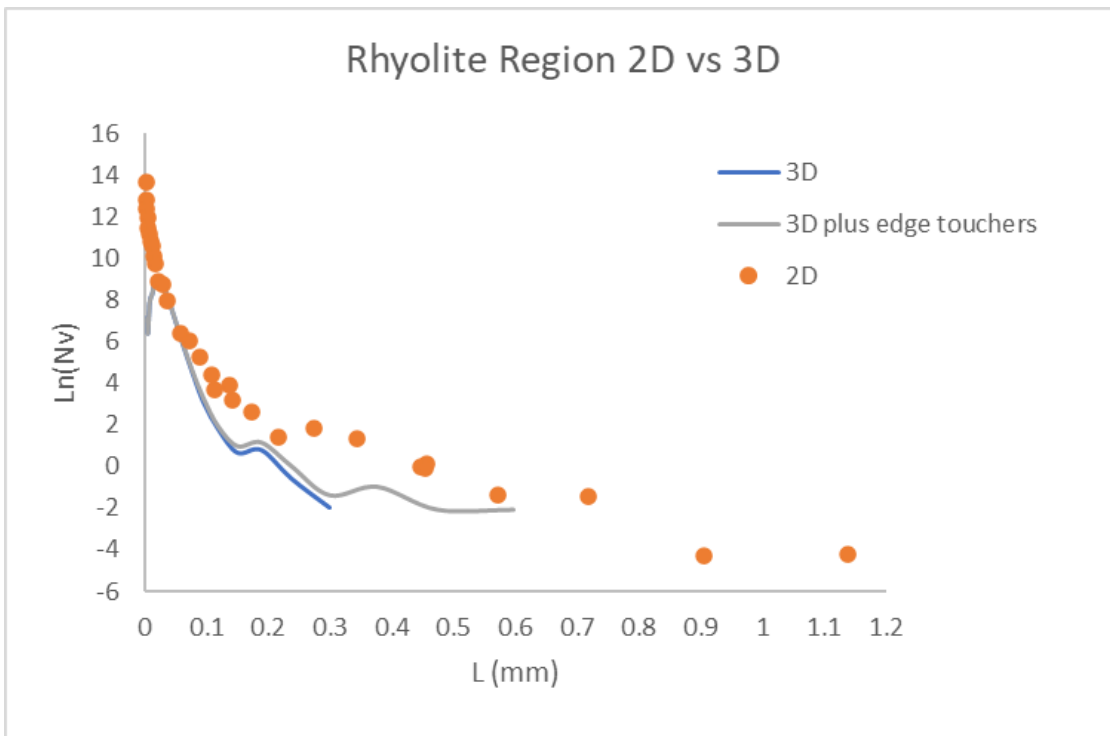


Figure 4.35: Plots of $\text{Ln}(Nv)$ vs L for the rhyolite regions from 2D and 3D data. Nv is population density and L is the diameter of a sphere of equivalent volume.

As highlighted previously, the 3D VSD curves for the mingled clast have a “hockey stick” shape caused by a drop in bubble number density at diameters between 10 and 20 μm . Even when excluding the “hockey stick” region of the 3D VSD curves, the VSDs are slightly different. The slopes of the curves are steeper at bubble diameters $< 200 \mu\text{m}$ due to the variations in bubble number densities discussed above, and the 2D curve extends to larger bubble diameters. The difference between the 2D and 3D dataset is most obvious in the VVD plots (Fig. 4.22A and Fig. 4.26A). The trend of the 2D VVD indicates a strong influence of continuous and accelerating growth, whereas the 3D VVD more closely resembles that associated with a single stage of nucleation and growth and the onset of coalescence (Shea *et al.*, 2010). The cumulative volume fraction vs EqD curves (Fig. 4.23C and Fig. 4.27) show the same trends. The most likely sources of this discrepancy are (a) differences in bubble number density at different size populations due to XCT resolution and bubble intersections in 2D (b) low numbers of individuals included at high bubble diameters, and (c) the assumption of spherical geometry during 2D – 3D conversion in FOAMS.

Scoria clast:

For the scoria clast (7_50), the range of equivalent diameters (calculated post 2D – 3D conversion) in the 2D dataset also encompasses the entire range captured in the 3D data. The bubble number density of the 2D data (3.63×10^6) is also two orders of magnitude greater in the 2D data than the 3D (4.59×10^4), when bubbles below 10 voxels are added back into the 3D dataset this increases to 1.67×10^5 . In the 2D data, 3.2% of bubbles have equivalent diameters $< 1.71 \mu\text{m}$ – below the resolution of the XCT data. Increasing the number of bubbles in the 3D volume does not change the bubble number density by an order of magnitude in the > 10 voxel dataset (4.75×10^4) or in the full dataset (1.73×10^5) so XCT resolution is not a significant contributing factor to the lower bubble number density of the 3D data. It is possible that larger, more complex vesicle networks are being repeatedly sampled in the 2D images (as suggested for the rhyolite regions of the mingled clast) but we don’t see a significant difference between the VSD curves of the 2D and 3D scoria datasets (Fig. 4.36). However, as noted in section 4.6.1, the plot of cumulative volume fraction (Fig. 4.23) suggests the 2D reconstruction of bubble volumes was not particularly reliable. As such, the 2D VSD and VVD curves and associated bubble number density must be interpreted with caution. The trends seen in the 3D dataset are therefore deemed more representative of true clast texture (see section 4.7.3). Interrogation of the

objects included by FOAMS during analysis of each input image would help to test whether high levels of connectivity (and intersection with image boundaries) are the source of this error and should be the focus of future work.

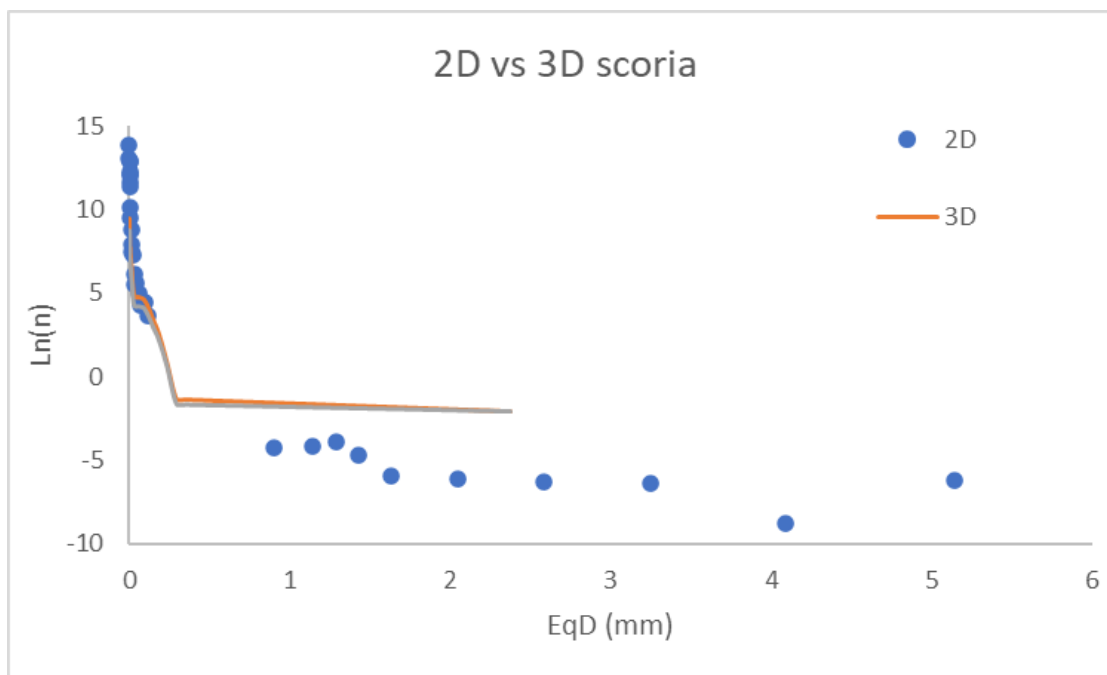


Figure 4.36: Plots of $\ln(N_v)$ vs L for the scoria clast (7_50) from 2D and 3D data. N_v is population density and L is the diameter of a sphere of equivalent volume.

Shape parameters

Although the shape parameters measured in 2D and 3D do not measure the exact same features, they are broadly equivalent and can be compared to assess how well vesicle shapes are described in 2D. Main controlling factors of bubble shape in 2D – identified through interrogation of circularity, regularity and elongation – are compared with those observed in 3D data, as described by the 3D parameters *anisotropy* and *elongation* available in Avizo®. Vesicle data in 2D and 3D is compared for the rhyolite regions, basalt regions and the scoria clast and similarities and differences discussed.

Rhyolite regions:

Two-dimensional and 3D bubble shape data from the rhyolite regions agree quite well. In both datasets, a smaller, more elongate bubble population is identified and values for circularity, regularity and anisotropy all indicate bubble shapes are more complex than in basaltic regions. In both datasets, larger bubbles are less influenced by elongation. The closer to spherical bubbles are, the closer the description of the 2D intersection will be to

the 3D shape. This may be why 2D shape descriptors capture the key features of these populations reasonably well when compared to the 3D volumes.

Basalt regions:

The higher relative smoothness of vesicles in basalt regions compared to rhyolitic ones is captured by both 2D and 3D shape analyses. However, elongation is a much more important factor in vesicles in the 3D data than in 2D. The basaltic regions contain some larger, more complex vesicle networks than those observed in the rhyolitic regions. Thus, the 2D intersection of each bubble is less likely to reflect the true 3D shape and so measures of elongation are less reliable in 2D.

Scoria clast:

Similar contrasts are seen in the scoria bubble shape data, as elongation also appears less important in the 2D data than the 3D. In addition, the 2D data indicates that larger vesicles are closer to circular cross-sections whereas in the 3D data vesicle shape does not correlate with bubble volume. As vesicles coalesce, networks become more complex and connectivity increases, 2D descriptions of bubble shapes become less reliable – all of which occurs more freely in low viscosity basaltic melts than in more silicic endmembers.

Studies of 2D and 3D vesicle texture have different advantages. In this example, the 3D dataset did not capture a wider range of vesicle sizes than the 2D study. However, using a larger scan volume at a lower resolution would capture larger vesicles and could be coupled with high magnification 2D studies to capture the full range in vesicle sizes. This would work best for samples where the smaller populations are close to spherical. The main benefit of the 3D study is that true bubble volumes are recorded (accepting the separation process has been applied correctly). This means interpretations of VVD and VSD curves are more likely to reflect true vesiculation processes. Although 2D VVD and VSD studies are less reliable for complex vesicle textures the high resolution of BSE images allows greater detail to be captured RE fine-scale vesicle shape variations. In addition, the extensive interrogation of 2D shape parameters (e.g., Liu *et al.*, 2015) in the volcanological community means we understand how elongation, morphological roughness and textural roughness interact and impact measures of vesicle shape much better than those used in 3D studies. Studies of vesicle shape in 2D are also very common, meaning they are useful

for inter-eruption comparisons of qualitative differences even where we acknowledge that some vesicle networks are poorly constrained in 2D.

4.7.5 Future work

More detailed analysis of the 3D data sets to define “standard” shape parameters for separation (and assessment of separation accuracy/consistency) would have been a key target for additional work in the method development aspect of this study. This would have included correlation of 2D and 3D datasets through the same bubbles, and more in-depth analysis of the geometric analysis possible in 3D. The samples in this study have the potential to allow definition of a standard protocol (akin to that developed in Shea *et al.*, 2010) but further work to this end was not possible in the timeframe of the project (and its completion during the COVID-19 pandemic). Further interrogation of the impact of various separation algorithms on bubble populations close to data resolution and the generation of the “hockey stick” trend in 3D VSDs is needed to establish whether this trend represents a real bubble population that is not captured in 2D or is an artefact of data processing. Expansion of the analysed sample set to include the pumaceous clast (4_70) and clasts from each unit in the Mingled Fall would allow interrogation of how mingling impacts rhyolitic melts. This would also permit extrapolation of dominant vesiculation processes and their impact on ascent dynamics based on clast type abundance in each unit – as done for the Echo Canyon deposits in chapter 2.

4.8 Conclusions & implications

Vesicle textures from the Mingled Fall deposit have been examined in detail in 2D and 3D through a correlative microscopy workflow that can be reapplied to other samples and facilitate texturally constrained and targeted micro-analytical studies. Outcomes from this work include deposit-specific insights into vesiculation and ascent, and broader implications for the way in which we approach textural studies in 2D and 3D.

The conclusions from this study can be sub-divided into three main categories:

Vesiculation in the Mingled Fall:

1. Basaltic and rhyolitic melts were physically mingled with little – no significant shear, even on the micro-scale at melt contacts.
2. Vesiculation in basaltic regions of the mingled clast was dominated by growth and coalescence. Generating larger, more well-connected vesicle networks.

3. Vesiculation in rhyolitic regions was dominated by a single stage of nucleation and growth, with minor coalescence generating a small population of larger vesicles.
4. Vesiculation in the two ascending melts occurred relatively independently to each other, with mingling only slightly inhibiting bubble growth and coalescence in the basaltic regions relative to scoriaceous samples which progressed to larger, more connected vesicle networks.

2D vs 3D studies:

1. VVD and VSD studies of texturally complex samples in 2D and 3D can lead to significantly different interpretations of process for the same samples.
2. Interpretations of vesiculation processes from studies in 3D can be made with greater confidence as true bubble volumes are measured.
3. Small-scale variations in vesicle shape are better constrained via studies in 2D and allow comparison with other eruptions.

XCT processing

1. It is possible to extract bubble volume and geometry data for texturally complex samples e.g., mingled clasts but compositionally distinct regions require different processing parameters.
2. Choices made during data processing (in 2D and 3D) impact interpretations of process and must be made in the context of existing geological knowledge for the analysed sample (e.g., from SEM images).
3. Some aspects of 3D VSD outputs are still poorly understood and must be investigated to establish whether these reflect “real” bubble geometries or are artefacts of data processing techniques.

This study has used the example of the Mingled Fall deposit from Ascension Island to develop workflows for textural studies in 2D and 3D that can be applied to other texturally complex samples. The value of different techniques has been demonstrated and several key areas for improvement identified. To interpret studies of vesicle texture with confidence, the impact of various data processing techniques (e.g., manual image correction or separation algorithms) on the output must be understood. Only in doing so can we ensure artefacts of data processing do not get mis-interpreted as indicators of process. This study has highlighted the importance of interrogating the methods we use to generate bubble size and shape data and constitutes a key contribution to ensuring the effective interpretation of future textural studies.

Chapter 5: Synthesis

5.1 Introduction

Understanding what controls transitions in eruptive behaviour is one of the grand challenges of volcanology (Cassidy *et al.*, 2018). At a single volcanic centre, such transitions are controlled by processes acting across timescales ranging from > 1000's of years, to minutes (Siebert *et al.*, 2011). Our ability to anticipate these changes depends on our understanding of how the sub-volcanic system evolves and the correct interpretation of monitored or felt signals during periods of unrest or eruptive activity (Caricchi *et al.*, 2021). Crucially, in the context of volcanic hazard management, our understanding of processes, and the data we collect in order to gain it, needs to elucidate these processes and changes consistent with the timescales over which decisions must be made (e.g., Joseph *et al.*, 2022). Long-term planning requires the reconstruction of volcanic histories that comes from large-scale field mapping that traces the extent of ancient deposits and records the range of styles that occur (e.g., Ablay & Marti 2000; Carrecedo *et al.*, 2001). Geochemical and petrographic mapping can be used to establish models of magma generation and storage (e.g., Chamberlain *et al.*, 2019), and identify patterns in eruptive behaviour that can provide vital insights into the interpretation of geophysical monitoring on the timescale of individual episodes of eruption or unrest (e.g., Pankhurst *et al.*, 2018). In concert these types of study allow for planning and hazard mitigation. In the first instance the recognition of an active volcanic system provides justification for further monitoring and mitigation. Full knowledge of the likely storage regions and timescales of perturbation are crucial in interpreting any felt or monitored signals when the system re-activates (Sparks & Kashman 2017). However, justifying monitoring and hazard mitigation strategies remains a particular challenge in locations where there has been no volcanic activity in living memory (e.g., Ascension Island).

Reconstructing the progression of unobserved eruptions is particularly challenging as we have no primary data through which to constrain timescales of activity or measure eruption intensity. Instead, we rely on information preserved in the erupted materials (Houghton and Wilson 1989; Cas and Wright 1996; Pyle 2015). Unfortunately, volcanic deposits (particularly for small volume events) are often an incomplete record of activity, and the resolution of most dating methods too coarse to preserve information relevant to changes

in behaviour during a single event (Dosetto *et al.*, 2011). Recent advances in the use of diffusion profiles in minerals and across mingling features have begun address this problem, revealing rapid assembly and ascent of magmas beneath Iceland (Mutch *et al.*, 2019) and on Ascension Island (Chamberlain *et al.*, 2020). However, mineral phases for which we can reliably model diffusion are few (Chakraborty and Dohmen 2022), and not always present. Even when the desired phases are present, there is no guarantee an individual crystal will contain a measurable profile. This is a particular problem in locations with a relatively closed system, compositionally homogenous mush zones or where erupted materials are crystal poor, like Ascension Island.

In the preceding chapters I have addressed the challenge of reconstructing unobserved eruptions by:

1. Using forensic analysis of field deposits and pyroclast textures to reconstruct the dynamics of an exceptionally well exposed example of a small-volume, trachytic eruption (the Echo Canyon eruption).
2. Placing constraints on important physical melt properties via careful characterisation of crystal populations and calculation of intensive parameters.
3. Using these constraints to interpret quantitative analyses of vesicle textures from representative clasts to identify the processes that underpin transitions in eruptive behaviour.
4. Assessed the broader insights that can be gained by applying 2D and 3D textural studies to texturally complex products of intermingled basalt-rhyolite magmas.

The following discussion will draw together and reflect upon insights from these chapters to highlight the main contributions this work has made to addressing some key challenges in volcanology. I will also show how the strategies used to study the Ascension Island deposits were successfully employed to provide critical insights into the evolution of the 2020-21 eruption of La Soufrière St Vincent, during and after the volcanic crisis. Further, I will identify some key priorities for future work that will help us better understand and anticipate changes in the eruptive behaviour of trachytic magmas on timescales relevant to decision-making during volcanic crises. I will conclude by summarising the main findings of this thesis.

[5.2 Value of forensic volcanology and petrology](#)

Stratigraphic studies have always underpinned reconstructions of past eruptions, particularly those that are unobserved (e.g., Daly 1925; Houghton & Wilson 1985; Martí *et al.*, 2018; Preece *et al.*, 2021). Grain size studies and mapping of deposits can constrain the

VEI of an eruption (Biass *et al.*, 2019). VEI is often used to place constraints on eruption intensity and provide a useful visualisation of the likely and maximum expected behaviour of a given volcanic centre. Although the VEI has value, particularly for centres capable of larger steady-state eruptions with well-preserved deposits (e.g., Mastrolorenzo *et al.*, 2017, Campi Flegrei), it is a time-averaged measure that fails to capture the explosive potential and transient nature of smaller eruptions and falls down entirely where deposit preservation is low. During a volcanic crisis, understanding how explosive activity will change over time is just as vital as anticipating the onset and termination of an explosive phase. A collapsing column presents a very different hazard to persistent ash and pumice, or scoria fall from a buoyant plume.

The preceding chapters have illustrated how detailed stratigraphic observations facilitate high-resolution reconstruction of changes in eruptive style and intensity. Stratigraphic characterisation of deposits must go beyond the quantification of juvenile vs non-juvenile clasts and changes in grain size. They must also include information on the bulk characteristics of juvenile material (e.g., density) and macro-scale textural variations. Doing so allows assessment of the changing bulk character of the magma as the eruption progresses, providing a framework in which to interpret micro-scale vesicle and crystal textures. Without this context, interpretations of micro-scale textures from a few clasts cannot be assumed to be representative of conduit-scale processes: at a given height in the conduit, processes controlling vesicle texture can vary laterally resulting in a diverse juvenile clast population upon fragmentation (Polacci *et al.*, 2003; Shea *et al.*, 2012; Cassidy *et al.*, 2018). When the relative abundances of different textural groups are known, so too is the relative importance of the processes controlling the formation of micro-scale textures. This means detailed, quantitative textural studies (e.g., VSD) can be carried out on a feasible number of clasts to elucidate how bubble nucleation, growth, relaxation, and shear impacted the magma. This high-resolution data can then be confidently scaled-up to assess variations in permeability, overpressure, and fragmentation mechanism at each stage of an eruption. Ultimately this approach provides crucial insights into the processes that control transitions in eruptive behaviour at a resolution relevant for decision-making processes during volcanic crises.

Placing constraints on melt temperature and volatile content is vital for effective interpretation of vesicle textures as they are strongly controlled by melt rheology and the supply of volatiles (Cassidy *et al.*, 2018). Doing so is particularly challenging in alkali-rich

crystal poor magmas where equilibrium pairs are scarce and there are fewer models that have been tested in the correct compositional space (e.g., Putirka 2008; Lange *et al.*, 2009; Waters and Lange 2015 and Mollo *et al.*, 2015). Typically, such studies make use of the increasing availability (and reducing cost) of electron microprobe (EPMA), secondary ion mass spectrometry (SIMS) and Fourier Transform Infrared spectroscopy (FTIR) to collect a high number of datapoints (e.g., Mangler *et al.*, 2020, Chamberlain *et al.*, 2019, Weber *et al.*, 2023). These studies are comprehensive and allow quantification of the uncertainties associated with calculated volatile concentrations and storage depths and temperatures. However, averaging such large datasets can mask true variations in crystal storage conditions and important outliers can be neglected in interpretations, if not combined with careful petrographic examination. Further, where magmas have ascended through relatively closed-system, self-similar crustal mush systems (as seen on Ascension Island) crystal compositions can falsely pass equilibrium tests and return unrealistic magmatic temperatures / depths. Detailed examination of crystal textures in the Echo Canyon eruption products meant that true phenocrysts could be distinguished from antecrysts despite the narrow compositional range occupied by most large crystals. From this, reconstructions of temperature and volatile content allowed constraints to be placed on melt viscosity throughout the eruption. Crucially, it was found that variations in melt viscosity and volatile content alone could not be responsible for the changing dynamics of the eruption. A small number of analyses can prove just as valuable as a more substantial geochemical study, provided the textural context of each individual is first ascertained.

[5.3 Importance of small-volume trachytic eruptions](#)

As shown in Chapter 2 (table 2.1), small volume trachytic eruptions are relatively common across a range of settings and exhibit a wide range in eruptive behaviour (e.g., Hernando *et al.*, 2019; Rappich *et al.*, 2016; Ablay and Martí 2000). Despite this, detailed studies of intra-eruption variability of ascent and eruption dynamics have been limited (e.g., Shea *et al.*, 2017; Houghton and Wilson 1985). Small-eruptive volumes and their tendency to occur in ocean island settings means the products of these eruptions are often poorly preserved (e.g., Preece *et al.*, 2021) or lacking adequate exposure (e.g., Hernando *et al.*, 2019) making detailed phase-by-phase stratigraphic and textural investigations challenging. Further, recent advances in our understanding of trachytic melts have shown them to be “kinetically reactive” with low viscosities, high H₂O diffusivity and the ability to rapidly degas and

crystallise in response to perturbations (Giordano *et al.*, 2004; Arzilli and Carroll 2013; Fanara *et al.*, 2013; Shea *et al.*, 2017; Deniel *et al.*, 2020).

The Echo Canyon eruption on Ascension Island is an exceptionally well-preserved and exposed example of a small-volume trachytic eruption. High-resolution investigations of eruptive behaviour (stratigraphy), bulk magma properties (density measurements and qualitative clast texture), and vesiculation processes (quantitative texture) have highlighted several key features of these eruptions.

1. Trachytic eruptions are capable of multiple, rapid transitions in eruptive style during eruption of relatively small volumes of magma.
2. Explosive phases can reach a short-lived, peak intensities equivalent to that of a VEI6 eruption.
3. Ascent is rapid, indicated by decompression rates as high as 10^8 Pas
4. Interaction with the sub-surface crystal mush during ascent is limited indicated by low % crystallinity magmas.
5. Rapid vesiculation during late-stage degassing can lead to high overpressures contributing to these high explosivities but bubble networks evolve rapidly facilitating rapid transitions towards effusive behaviour.
6. Conduit interactions and rapid crystallisation accelerate the explosive-effusive transition.
7. Changes in ascent rate (and its impact on vesiculation and crystallisation processes) and not variations in viscosity control transitions in eruptive behaviour.

Crucially, small-volume trachytic eruptions are capable of ascent rates and explosivities comparable to much larger, often more well-studied eruptions (e.g., Mt St Helens 1980 and Vesuvius 79AD). Even if short-lived, high intensity eruption phases can have devastating impacts particularly in small, isolated ocean-island settings. Rapid ascent of magmas with little interaction with the surrounding crust may provide little advance warning of an eruption. It is critical therefore, that we focus on constraining how processes identified in the preceding chapters can be identified through subtle changes to potentially monitored signals.

5.4 Insights from 2D and 3D textural studies

Studies of vesicle textures in 2D have long been applied to infer the changing dynamics of ascending melts (e.g., e.g., Houghton and Wilson 1989; Polacci *et al.*, 2003, Houghton *et al.*, 2010; Shea *et al.*, 2010b; Alfano *et al.*, 2012 and Mitchell *et al.*, 2019). The limitations of such studies are associated with (a) poor preservation of thin melt films during sample preparation, (b) image resolution relative to feature size and (c) reconstructing irregular 3D features from random 2D intersections. Vacuum impregnation of vesicular samples with resin and carefully applied thin sectioning techniques improve bubble wall preservation (Ross *et al.*, 2022) and advances in microscopy mean nano-scale features can now be reliably resolved. However, the issue of translating 2D information to 3D bubble volumes is more difficult to solve. Many vesicle size distribution studies make use of the FOAMS software developed by Shea *et al.*, (2010) which uses the stereological conversion of Sahagian and Proussevitch (1998) to reconstruct bubble volumes from binary images. While this conversion yields reasonable results for samples with low connectivity and relatively spherical bubbles, it is less reliable for intensely sheared clasts (Shea *et al.*, 2010). Mitchell *et al.*, (2019) adapted the stereological conversions of Sahagian and Proussevitch (1998) to better reconstruct elongate vesicles in tube pumices but the applicability of all such adaptations is restricted to textures that fall within the bounds of pre-defined, simple bubble shapes. Advances in x-ray computed tomography in the last 15 years have made studying volcanic textures in 3D more useful (Cid *et al.*, 2017) as scan resolutions of as little as 50 nm are now possible – albeit only on very small sample volumes. Textural studies in 3D allow the preservation and interrogation of complex bubble networks in 3D, giving a better understanding of how permeability develops in ascending magmas.

In chapter 4 the impact of mingling between basaltic and rhyolitic melts on vesicle textures was investigated in 2D and 3D to (a) elucidate the dominant vesiculation processes occurring in ascending melts and (b) test the limits of both approaches when considering texturally complex samples.

Independent assessment of bubble textures in basaltic and rhyolitic regions of mingled clasts, and the scoriaceous endmember highlighted key differences in vesiculation histories. Although vesicles in basaltic regions were larger and had undergone more extensive coalescence than their rhyolitic counterparts, coalescence and connectivity in the scoriaceous endmember was more extensive. Mingling between rhyolitic and basaltic

melts inhibited the development of permeable networks in the basaltic regions relative to a non-mixed melt package and may have increased the explosivity of these eruptive phases.

Comparison of VSDs in 2D and 3D confirmed that 2D studies are less reliable for regions / samples with more complex vesicle networks, even in samples lacking extensive shear. Crucially, in hand specimen and in BSE images, vesicles within the mingled clast did not appear significantly sheared. Such samples would not traditionally be excluded from 2D VSD analyses, but generated VVD curves that contradicted those acquired from “true” bubble volumes in 3D. This implies that the range of textures for which 2D VSD studies produce reliable results may be smaller than previously thought. As expected, VVD and VSDs in the scoriaceous sample were even more poorly constrained using 2D analyses, likely due to the high connectivity and complex shapes of vesicles.

Measures of vesicle shape across different regions of the mingled clast were more consistent between the 2D and 3D datasets, with the two methods indicating the same dominant controls on vesicle shape. Again, in the scoriaceous clast, vesicle shape data in 2D did not match that acquired from the 3D dataset although the mismatch was less significant than for VSD/VVD curves.

Studies of vesicle texture in 3D clearly have advantages over studies in 2D, however some features of the outputs from 3D data are still unexplained. In both the mingled and scoriaceous clast, the smallest bubble populations returned spuriously high values of anisotropy that were not consistent with observations made in the 3D dataset, or in BSE images. In VSD curves for the mingled clast, a drop in bubble number density at bubble diameters around 10 μm creates a “hockey stick” effect not observed in 2D data or in the scoria clast despite being well within the resolution of the dataset. This is a common occurrence in VSDs produced by XCT data and is as yet unexplained (Pers. Comm. Kate Dobson, 2022).

To effectively apply 3D studies we need a better understanding of (a) how separation algorithms impact bubble populations and (b) how resolution impacts shape parameters for small bubble volumes. Extracting reliable bubble volumes from complex, high porosity volcanic samples is an intensive process. However, the resulting datasets can be powerful tools through which to understand the behaviour of more complex magmas, but only when analysed clasts can be carefully placed into the wider context of their eruptive sequence.

5.5 Application of principles to the 2020 – 21 volcanic crisis at La Soufrière St Vincent

Most of the work presented in this thesis has focussed on how vesicle textures offer insight into the evolving dynamics of eruptions using examples from the low magma-flux intra-plate volcano, Ascension Island. This, in part was due to the crystal-poor nature of most of the eruption products, a function of their rapid ascent and relatively closed-system magma storage region.

As shown in Chapter 3, interrogation of even limited crystal populations provides vital information on magma storage and transport and can be used to reconstruct ascent dynamics. Forensic petrographic analyses were performed on the products of the 2020-21 eruption of La Soufrière which, as in previous events (Cole *et al.*, 2019), contained abundant microlites, microphenocrysts, phenocrysts/antecrysts and plutonic enclaves. While the crystal and vesicle textures of the La Soufrière eruption are distinctly different to the Echo Canyon eruption, the principles applied in previous chapters and knowledge gained throughout this PhD heavily informed the choices made during analysis of the La Soufrière rocks and subsequent field campaigns and analyses.

Learning from Chapters 2 – 4 impacted decision-making and workflows in several key ways:

1. *Carrying out analyses with limited resources and time:* Much of the data collection for Chapters 3 and 4 was carried out during the COVID-19 pandemic. This heavily restricted lab access, forcing me to make the most of the machines at my disposal within my own institution (scanning electron microscope). My expertise with the SEM at UEA meant I was able to optimise BASE imagery and eds/wds analyses to get the most reliable results, quickly, when presented with samples from the St Vincent lava dome in early 2021.
2. *Forensic analysis of crystal textures:* I spent a significant amount of time exploring the textures and compositions of crystals in the Echo Canyon samples via BSE imagery and eds/wds analyses at UEA to identify key targets prior to undertaking expensive e-probe analyses elsewhere. As such, when assessing the St Vincent dome samples, I chose to focus on identifying key crystal populations using textural characteristics (in tandem with rapid eds/wds spots) first and feed this back to the monitoring team. The crystal populations identified gave the monitoring team (and wider team of the urgency grant) an initial idea of the likely source of the erupting magma, as well as some of its ascent history.

3. *Interrogation of dome vesicle textures:* The dome rocks contained extensive vesicle networks and evidence of volatile migration through a variety of mechanisms. As the presence and build-up of gases was a key concern for the monitoring team making vesicle studies an obvious target for analysis. However, my experience with the complexities of undertaking quantitative vesicle studies meant I chose not to immediately begin the time-consuming process of acquiring and processing BSE images for a full VSD analysis. The dome rock samples had a high connectivity due to the presence of both brittle fractures and connected bubble throats. Further, bubble shapes indicated they formed complex networks in 3D which would reduce the effectiveness of 2D VSD studies. A 3D study was also rejected due to instrumentation availability and the extensive processing time required for 3D bubble data. Instead, qualitative analysis of vesicle textures and how they related to the crystal and groundmass textures observed was chosen to give key insights into the nature of volatile migration through the dome rocks.
4. *Forensic fieldwork and sample collection for future analyses:* After the explosions stopped on the 22nd April, field campaigns were carried out to describe and sample the eruptive stratigraphy before heavy rains removed much of the deposits. Prior to these campaigns I discussed the value of systematically and consistently sampling sufficient clasts from each layer of the sequence to carry out density measurements as described in Chapter 2, such that we could be confident that any future VSD or CSD analyses were representative of the bulk properties of the magma as highlighted in my work in Chapters 2 and 3. This systematic approach has formed the basis of work by members of the wider research team both in the UK and the US, to constrain the ascent and eruption dynamics of the explosive phase of the eruption (Christopher *et al.*, in review 2023; Frey *et al.*, 2023).

Textural and petrographic analysis of the 2020-21 La Soufrière eruption products is an ongoing collaboration between researchers from the University of East Anglia, the University of Oxford, the University of Plymouth, Union College in the United States and UWI SRC. This work forms part of a contribution to several papers that will form a Geological Society special volume on the 2020-21 St Vincent eruption. As such, the following discussion will focus on some key reflections on how work detailed in the preceding chapters informed the use of petrographic and textural studies during and after of the 2020-21 volcanic crisis.

5.5.1 Background to La Soufrière St Vincent and the 2020-21 eruption

The island of St Vincent's active volcanic centre - La Soufrière - is the most active subaerial volcano in the East Caribbean Arc. The 29 km by 17 km (widest point) island is the product of subduction between the American/N-American and Caribbean plates (Macdonald *et al.*, 2000). La Soufrière has had 7 periods of eruptive activity in the last 300 years and the system has been investigated through analysis of historical accounts (e.g., Pyle *et al.*, 2018; Scarlett 2020), mapping and characterisation of eruption deposits (e.g., Cole *et al.*, 2019) and interrogation of cumulate xenoliths (e.g., Tollan *et al.*, 2012). Eruptive activity includes dome formation, Vulcanian – Plinian explosions and the production of pyroclastic density currents and lahars (Cole *et al.*, 2019). In 1971 a lava dome grew beneath the crater lake of La Soufrière and was subsequently disrupted by the sudden onset of an explosive eruption in 1979, this eruption ended with the effusion of another dome, now into a dry crater (Cole *et al.*, 2019). These events are well remembered by the population, many of whom frequented the crater to see the 1979 dome regularly until the eruption in 2020 (Pers. Comm. Richard Robertson 2018 and Croweller 2009).

The 2020 – 21 eruption of La Soufrière St Vincent began with the effusion of a basaltic andesite dome - first identified on the 27th December 2020 - after a period of increased seismic activity from the 1st November (Joseph *et al.*, 2022). Dome growth continued over three months, reaching 912 m long, 243 m wide and 105 m high by the 19th of March 2021. Growth accelerated in early April 2021 before several explosive events produced 0.12 km³ ash and scoria between the 9th and 22nd April 2021, with significant ash fall reaching Barbados within hours of the first explosion (Cole *et al.*, in prep). An increase in magnitude of banded tremor on the 8th of April prompted an evacuation order to be issued to residents in the high hazard zones of the island. Some 20,000 people were evacuated, the majority of whom had left the high hazard zone before the first explosion occurred (Joseph *et al.*, 2022). Most eruptive activity, monitoring efforts and hazard management decisions took place during the height of the COVID-19 pandemic, all in a resource constrained setting. That there were no fatalities or serious injuries associated with the onset of explosive activity is a testament to the efforts of the monitoring team from the University of the West Indies Seismic Research Centre (UWI-SRC), the National Emergency Management Organisation (NEMO) and their strong collaborations with government officials and the general public on St Vincent.

5.5.2 Time & resource constrained characterisation of complex crystal populations

In recent years, the value of real-time petrographic analyses of eruption products during volcanic crises has been increasingly recognised (Re *et al.*, 2021). Most recently at La Palma, where analyses of textures and compositions of erupted products were fed directly back to the monitoring team within weeks of their eruption (Pankhurst *et al.*, 2022). Such observations can help elucidate the magma source and provide constraints on the evolution of the magmatic system and rheology (e.g., Gansecki *et al.*, 2019) – strengthening interpretations of seismic data to better anticipate transitions in eruptive behaviour. Characterisation of the 2020-21 La Soufrière dome was thus identified as a key priority at the onset of the eruption. Samples were collected from an active lobe on the 16th of January 2021 by members of the UWI SRC monitoring team and were sent to the University of East Anglia for petrographic analysis by myself and Jenni Barclay. Thin sections were prepared by late February 2021. Backscattered electron images (BSE) were acquired using the Zeiss Gemini 300 scanning electron microscope and mineral and glass compositions were acquired via electron-dispersive spectroscopy (eds) using an Oxford Instruments Ultim Max 170 system.

The priority at this stage was to provide petrographic descriptions of the dome samples to members of the monitoring team in a timely manner to help answer the following questions:

1. Is the dome a new magma batch? Or remnants of the 1979 eruption?
2. What is mobilising the magma?
3. Is an explosive eruption likely?

In contrast to the Ascension Island samples, the dome rocks contained multiple, texturally heterogeneous crystal populations. While the full characterisation of each population via a comprehensive electron microprobe study (comprising hundreds of data points) would be carried out by Gregor Weber and John Blundy at the University of Oxford (Weber *et al.*, , 2023), the timescale of such a study was outwith that on which UWI SRC needed information.

Careful characterisation of the crystal populations was carried out via BSE imaging and eds analyses and a report compiled and distributed to UWI SRC and the wider research team during March 2021 (See [Appendix 5_1]). Fewer than 100 eds spot analyses were rapidly

collected over several days to characterise crystal populations, identify alteration products and breakdown textures, and check for the presence of potentially hazardous cristobalite in the dome samples (Horwell *et al.*, 2021). Full thin section BSE images were generated by stitching together high-resolution SEM images to capture large-scale textures of the dome rocks and identify patterns of alteration. Some key features identified are presented in Fig. 5.1.

SEM images from the 1902, 1971 and 1979 eruptions of La Soufrière were acquired and examined by myself, Jenni Barclay and Paul Cole, which confirmed that at least some of the crystal cargo of the 2020-21 eruption had a shared history with previous eruptions. Large, euhedral plagioclase feldspars with complex zoning patterns and oscillatory zoned rims from 200 – 400 μm thick were observed in each of the eruptions (see 1971, 1979 and 2020-21 in Fig. 5.1A - D., 1902 rims were observed by Paul Cole). Careful examination of crystal textures identified evidence of brittle fracture occurring in the presence of liquid melt in

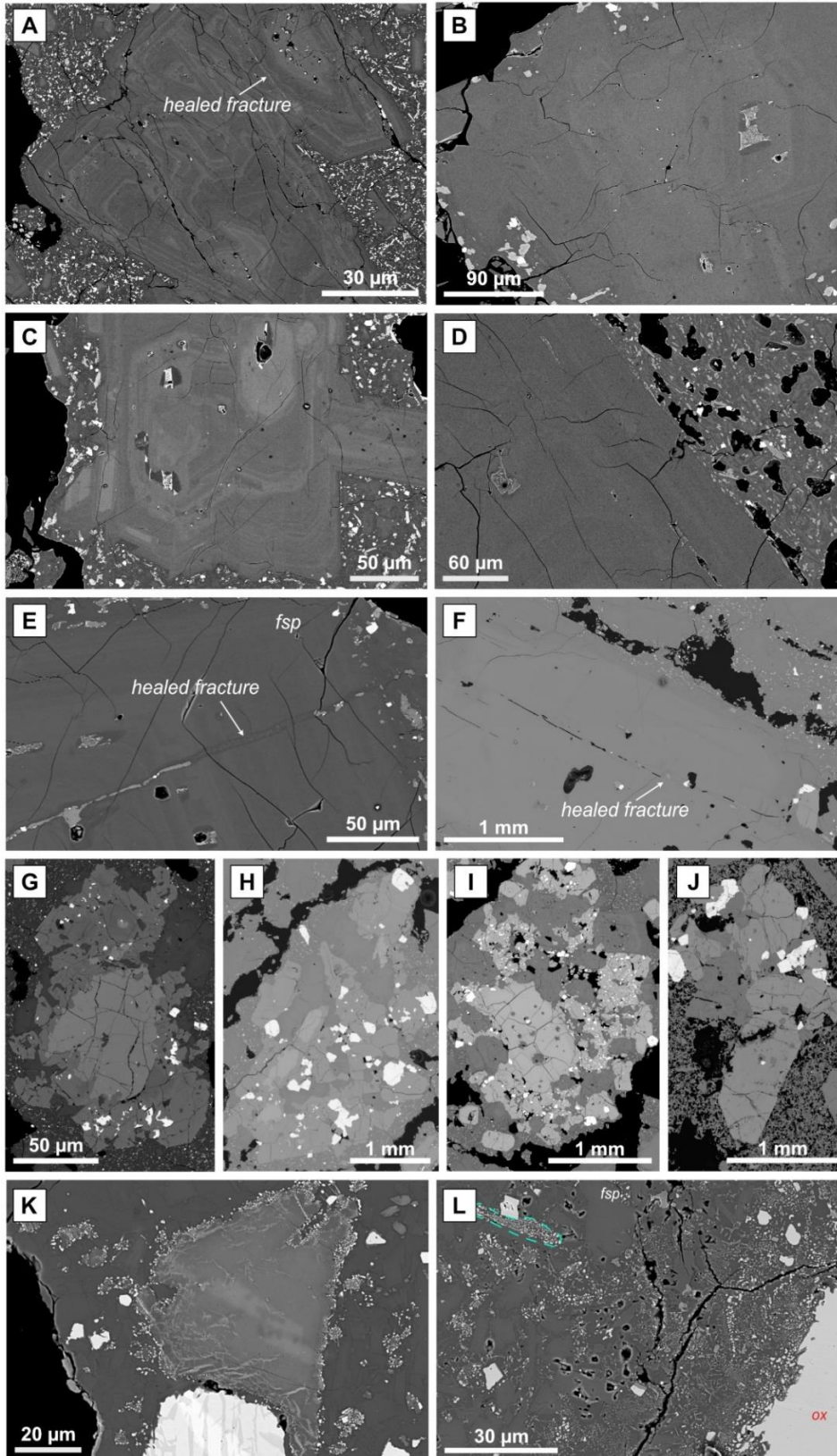


Fig. 5.1: Crystal populations in eruption products from the 1979 – 2021 eruptions of La Soufrière. Complexly zoned feldspar crystals from the 1971 dome (A), 1979 dome (B), 2020-21 dome (C) and 2021 scoria (D). Healed fractures show evidence of brittle fracturing in the presence of melt in the 1979 dome (A), 2020-21 dome (E) and 1979 dome (F). Plutonic enclaves with similar mineral assemblages and crystal morphologies from the 1971 (G) and 1979 domes (H) and 2020-21 dome (I) and 2021 scoria (J). Breakdown textures in clinopyroxene and Fe-Ti oxides in the 2020-21 dome (K and L). Teal dashed line shows relict structure of a broken-down orthopyroxene microlite. Ox = Fe-Ti oxide, Fsp = feldspar.

the sub-surface within eruption products from 1971, 1979 and 2020-21 (Fig. 5.1A, E & F). In addition, fragments of plutonic enclaves across all three eruptions had shared mineral assemblages and crystal morphologies (Fig. 5.1G - J). Identification of commonalities between crystal populations of the most recent eruption products provided strong evidence that the first erupted magma in 2020-21 was likely sourced from residual material from previous events. Question 1 was thus addressed in a timely manner using readily accessible analytical equipment.

One of the most significant features of the 2020-21 dome rocks was the location, prevalence and extent of degradation / alteration textures across the different crystal populations. Large clinopyroxene crystals often exhibited breakdown textures at their rims, comprising Fe and Mg-rich oxides (Fig. 5.1K). The same texture was observed (to a greater extent) in Fe-Ti oxides > approximately 200 μm in diameter (Fig. 5.1L) Orthopyroxene microlites in close proximity to these larger crystals often displayed the same breakdown texture, the effect lessening with distance from the larger feature (Fig. 5.1L). These textures became more extreme in the regions confined between multiple larger mafic crystals and in close association with large vesicles or fracture pathways. The presence of these features in the 2020-21 dome suggested significant interaction between the erupted material and reactive fluids / volatile phases. This contrasted with the available 1971 and 1979 dome samples which contained very little evidence of such interactions. This was significant, as both earlier domes were extruded either without explosive activity (1971), or after explosive activity ceased (1979). This indicated that the 2020-21 dome effusion was likely extruding under different (more volatile rich?) conditions than its predecessors – perhaps via heating from below by a new pulse of magma (Question 2). Although initial interpretations were made with caution due to the limited range of samples collected, when coupled with other observations at La Soufrière the identified textures suggested a transition to explosive activity could be likely (Question 3).

In the Echo Canyon eruption deposits, careful textural interrogation of the crystal population and a small number of analyses was dictated by the limited number of individuals. For the St Vincent samples, similar limitations were enforced but for different reasons e.g., short operational timescales and availability of instrumentation. In both cases, detailed textural descriptions and targeted analyses produced valuable information critical to understanding transitions in eruptive style. In the case of St Vincent, this knowledge was generated over timescales useful for decision-making processes during the volcanic crisis.

My early analyses of the dome samples (in collaboration with Jenni Barclay) facilitated critical discussions between the monitoring team and wider research group centred around the presence of volatile phases in the magmatic system at a time when gas measurements at the surface were challenging and could not provide a definitive answer. Timely provision of a thorough petrographic description of the samples, identification of textures associated with volatile migration and the presence of sulphides in melt inclusions helped confirm the likelihood of a transition to explosive activity through the interpretation that a deeper, more volatile-rich magma was likely acting as the driving force for the extrusion of the dome.

5.5.2 Forensic fieldwork producing insights for specific eruption phases & textures informing geochemical studies

Where eruptions are observed, particularly those that have occurred since the advent of satellite observations, prevalence of camera phones and expansion of monitoring networks, the dynamic behaviours and changing intensities of eruptions can be directly recorded. In these contexts, careful characterisation of deposit stratigraphy offers an opportunity to explore how textures preserved in individual (and populations of) pyroclasts relate to specific known phases of activity, strengthening our interpretations for unobserved eruptions. In the weeks after explosions on St Vincent ceased, a field campaign was undertaken to preserve a record of the eruption stratigraphy before significant erosion took place at the onset of the rainy season. Paul Cole and Jenni Barclay coupled their deposit descriptions with satellite data and observations of UWI-SRC monitoring staff to link stratigraphic horizons to explosive phases (Cole *et al.*, 2023) and sampled clasts from each unit for further analysis. Care was taken to ensure sufficient clasts were collected to perform density analyses on each unit of interest to allow representative clasts to be selected for further analysis – following the strategies applied in this thesis.

Five main eruption units were identified (U1 – 5) and tied to explosions traced through observational data. U1 represents the first phase of explosive activity, overnight from the 9th – 10th April, in which time most of the 2020-21 dome was excavated and the conduit cleared (Cole *et al.*, 2023). The base of the U2 layer is correlated with a large explosion at 09:50 UTC on the 10th of April, the unit is associated with 7 discrete explosions in total, each lasting up to 30 minutes. The U5 layer records the final bigger explosion that marked the beginning of the end of explosive activity, starting overnight between the 10th and 11th of

April (Cole *et al.*, 2023). Representative scoria clasts from U1, U2 and U5 were selected for textural analysis and crystal size distributions (CSDs) alongside the 1979 dome, 1979 scoria, 2020-21 dome. CSDs focussed on the smallest crystal population (long-axis less than 150 μm) due to the heterogeneous nature of the crystal cargo and to capture information about the final stages of ascent in each case. The process of constructing CSD curves for each sampled eruption phase highlighted several things:

1. A common crystal population between the 1979 and 2020-21 domes (tabular plagioclase crystals with anorthite-rich cores – Fig. 5.2B and C)
2. Distinctly different microlite population between the 2021 dome and U1 scoria (Fig. 5.2C and D)
3. A progressive decrease in microlite abundance from U1 – U5 (Fig. 5.2 D – F)
4. The decreasing microlite abundance between U1 and U5 correlates with higher proportions of tabular crystals (U2 – U5) (Fig. 5.2 D – F).

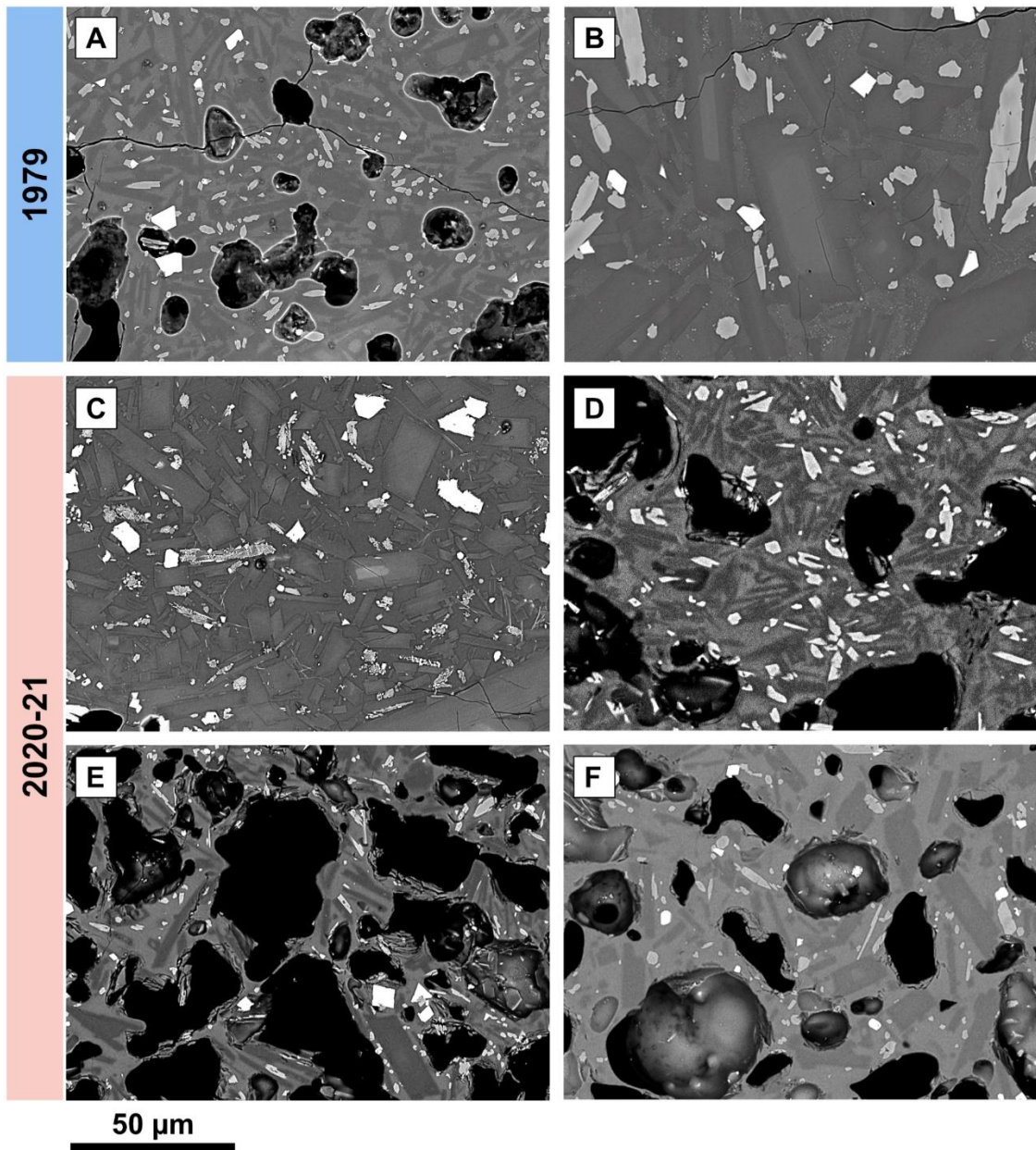


Figure 5.2 backscattered electron images of crystal populations in the 1979 products (scoria – A and dome – B) and 2020-21 products (dome – C, unit 1 scoria – D, unit 2 scoria – E, unit 5 scoria – F). All images are the same scale. Black features are bubbles and brighter phases are more dense. From brightest to darkest: oxides, pyroxene, matrix glass and plagioclase feldspars.

CSD curves for the 1979 and 2020-21 eruption products are shown in Fig. 5.3. The CSD curve for the first 2021 explosion (U1) is much steeper than that of the 2020-21 dome (Fig. 5.3 A), as expected from crystal populations in the BSE images. Volcano-tectonic swarms detected beneath La Soufrière indicated ascent of magma from approximately 10 km depth between the 5th and 6th April (Joseph *et al.*, 2022). This relatively rapid ascent of magma prior to the first explosion is borne out in the acicular shapes and high crystal number densities in the U1 scoria (Fig. 5.3 D). In later stages, overall microlite crystallinity is lower, and crystals are more tabular (Fig. 5.3 E and F). A reduction in ascent rate would shift crystallisation to growth dominated, producing more tabular crystals (as observed) but

should not decrease the overall crystallinity of the sample. However, exceptionally high ascent rates could inhibit nucleation in the final stages of ascent, leaving only the tabular crystals that grew at greater depths (e.g., Preece *et al.*, 2016). An increase in ascent rate between U1 and U2 is also supported by seismic data and modelling of magma storage depths (Joseph *et al.*, 2022; Weber *et al.*, 2023). When we contrast the 1979 scoria with the 2020-21 samples, we see that the CSD curve is more similar to the 2020-21 dome than the explosive products (Fig. 5.3 A & B). The 1979 scoria sample was taken on the 17th of April after a series of discrete explosions which ended on the 16th (Shepherd *et al.*, 1979). By this time, the vent had been enlarged such that the 1971 dome had been breached and the vent flooded by the crater lake (Graham and Thirlwall 1981; Fiske and Sigurdsson 1982). The shallower slope of the CSD curve, and high groundmass crystallinity (39%) accompanied by tabular crystal shapes of the 1979 scoria, are indicative of slower ascent as would be expected in the later explosive stages as the eruption transitioned towards effusive behaviour (Shepherd *et al.*, 1979).

Careful analysis of crystal textures placed in the context of high-resolution stratigraphy and real-time observations are providing insights into:

1. The source of the initial effusive dome material
2. The driving force for effusion of the dome
3. Step-changes in ascent rate between effusive and explosive phases
4. Dominance of a new magma batch in explosive phases
5. Variations in ascent rate linked to changing explosion intensities

Further, the recognition of texturally distinct crystal populations between microlites in the domes and scoria clasts directed collection of electron microprobe data in previously overlooked size classes. This data provides additional evidence of a compositionally distinct magma as the driving force for effusive activity and the source of the explosive phases (Frey *et al.*, 2023). Initial results from the St Vincent study show the power of simple observations to improve our understanding of eruption dynamics when coupled with careful characterisation of deposit stratigraphy.

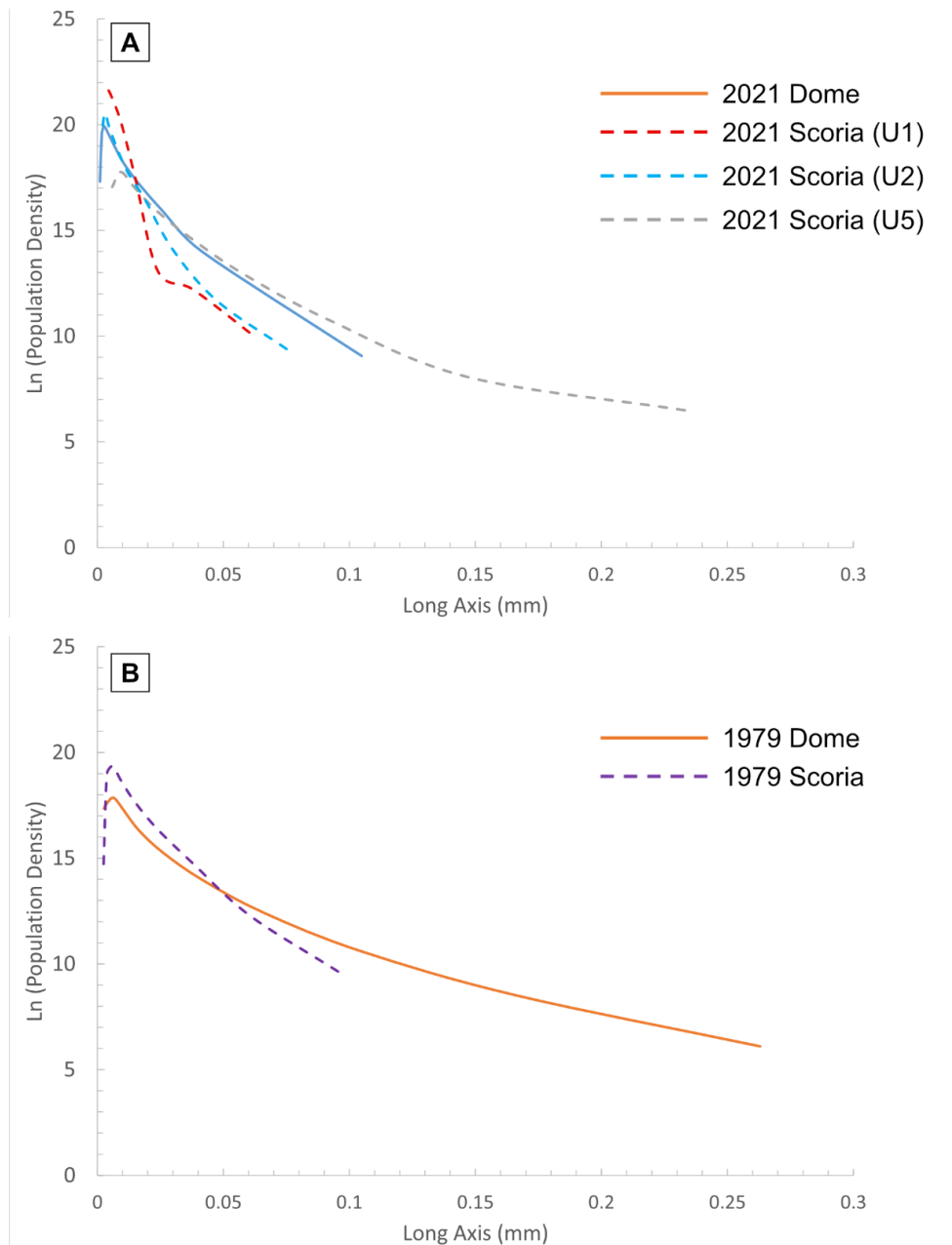


Fig. 5.3: Crystal size distributions for the explosive and effusive products of the 2020-21 (A) and 1979 (B) eruptions of La Soufrière St Vincent.

The reconstruction of the Echo Canyon eruption identified periods of high intensity explosive eruptions and rapid transitions in behaviour for an event that would have only been classified as a VEI 2 using volume alone (estimated volume 0.01 – 0.3 km³). By volume, the 2020-21 eruption of La Soufrière St Vincent is relatively comparable (0.12 km³). This eruption also produced a series of high intensity explosions, exhibited several transitions in behaviour (effusive – explosive – PDC formation – scoria/ash fall) and occurred on a relatively small island, with much of the erupted volume falling offshore. In contrast to Ascension, St Vincent is a calc-alkaline volcano where magma supply rate is higher and ascending melts have much more interaction with the sub-surface crystal mush (evidenced

by the crystal cargo Fig. 5.1). Despite these differences, the eruption at St Vincent (and several others in recent years e.g., La Palma 2021 and Whakaari 2019) provides a pertinent reminder of the importance of understanding the behaviour of eruptions that form a relatively small part of the rock record. Incorporating this study here demonstrates that applying the same forensic approach to the characterisation of the eruption stratigraphy and interrogation of clast textures to both ancient and modern deposits has the power to elucidate key processes influencing the hazards these volcanoes present.

5.5.3 Reflections and learning from 2020-21 workflows:

In the preceding sections, I have already highlighted the ways in which the knowledge I acquired through completing work for chapters 2 – 4 guided the petrographic approach to monitoring during the 2020-21 eruption of La Soufrière. Here I will reflect my experience as a PhD researcher contributing to this effort, highlight reasons for any successes and identify areas where the workflow / approach could have been improved to be more useful for the monitoring team on the ground in St Vincent.

As a PhD researcher whose focus was Ascension Island, which has not seen an eruption since before the island was inhabited, I had not previously had any experience with monitoring, or analysing samples from an actively erupting volcano. Contributing to the monitoring effort for La Soufrière through the NERC urgency grant funded collaboration between the University of East Anglia, University of Oxford, University of Plymouth and the University of the West Indies Seismic Research Centre certainly gave me new insights into the ways volcanological and petrological data are applied in a volcanic crisis. It became evident very quickly that the most important datasets were those that would contribute to an assessment of the supply and escape of volatiles in the system and the possible sources for the erupted material forming the dome. Volcanologists monitoring the volcano needed insight that would help them determine whether it was safe for them to access the crater rim to take critical gas measurements and attempt further sampling as well as feed into plans for potential evacuations. These needs/questions dictated our focus from a petrologic standpoint and helped streamline the information we provided to them in our reports and meetings. Open, frank, and frequent communication between the *many* collaborators involved in the monitoring effort and urgency grant helped facilitate this. Meetings attended by all involved were supplemented by smaller sub-groups whose focus was on a particular aspect e.g., petrology, gas measurements etc. While the eruption was

ongoing, these sub-group meetings always contained at least one member of the team from UWI-SRC to ensure they were receiving all the vital information and could feed in interpretations from the other data streams (and observations on the ground) that may impact interpretations of each sub-group. As soon as thin sections were available there was a sense of urgency to get images and descriptions to the team as soon as possible, which meant the ability to prioritise (researcher and instrument) time to this task was invaluable. The biggest thing I drew from my time working on the urgency grant was how vital the communication between different groups and management of those interactions and resulting data and interpretations was to ensure efforts were effective and useful.

From my perspective, several aspects of the approach applied in this crisis helped it to be successful:

1. Clear communication of the key questions of the monitoring team from the outset gave the rest of the research group real focus and unity in intent (most of the time)
2. Ability to dedicate researcher and instrument time to key tasks ensured timely delivery of information to UWI-SRC and the wider group for interpretation.
3. Periodic “coming together” of full research & monitoring groups to consolidate interpretations / findings from smaller sub-groups ensured time was used efficiently while UWI-SRC team members retained a detailed oversight and acted as a bridge between groups.

There were however, some aspects that delayed progress and could be improved for future crises:

- 1. Speed at which thin sections were available once samples were acquired.*

The team from UWI-SRC collected samples of the dome rock in mid-January 2021. These arrived in the UK by the end of that month. However, thin sections were not available for analysis until late February 2021. Though 4 weeks is a relatively quick turnaround for normal thin sectioning services, this delay undoubtedly hindered progress. Partly due to the ongoing COVID-19 pandemic, samples were sent to the University of Granada for sectioning thanks to the offer of services by a colleague to speed up the process. The ability to rapidly section and analyse erupted materials is crucial for effective use of “real-time” petrology as applied at La Palma in 2021 (Pers. Comm., Scarrow 2023). Identifying mechanisms for thin section production (and analysis) and formalising such agreements

amongst partnerships would make this process more efficient allowing data to get into the hands of the monitoring team more rapidly.

2. The ability to locate and access / analyse products from historical eruptions in a timely manner.

Previous eruptions in St Vincent had comprised both dome forming and explosive activity in different sequences, and the 1979 eruption ended with extrusion of a dome. As such, comparison between the newly erupting dome and those present both before (1971) and after (1979) explosive eruptions of La Soufrière was identified as a priority. Similarities / differences in groundmass textures, crystal populations and vesicles offered insight into the likely conditions under which the 2020-21 dome was erupting, its likely source and the potential driver of the effusive activity. Despite both the 1971 and 1979 eruptions feeding a wealth of research, and those involved being known still to the group working on the Urgency grant, tracking down still existing samples and images of the dome rocks proved difficult. Only two thin sections of the 1979 effusive and explosive materials (from early in the eruption - held at Oxford) and a small selection of images from the 1971-72 dome were found. A better system for curating collections from eruptions is vital to ensure those that need access to them (namely those actively monitoring the source volcanoes of these samples) can do so without relying on the good will and record-keeping of multiple researchers across different institutions and continents.

During the 2020-21 eruption, travel was greatly restricted due to the COVID-19 pandemic. This meant sampling opportunities were fewer which had both positives and negatives for UWI-SRC. On one hand, it was easier to keep track of who was on island sampling and for what purpose. However, it also meant that UWI-SRC had to sub-divide many samples they acquired to send for analysis in many different institutions. The initial sample set is now very widely dispersed and easy to lose track of. To counter this, at the request of UWI-SRC, I am currently attempting to engage members of the wider research community in contributing to a database of the samples from this event, what they have been used for and what is available for future use. This has however, proven quite challenging. The volcanological community must be better at ensuring researchers and monitoring organisations based in volcanically active regions have and feel greater ownership over the rock record.

[5.6 Future work](#)

The work in this thesis has established the importance of understanding small-volume trachytic eruptions and the hazards they pose in many locations worldwide and outlined a strategy for reconstructing the drivers of transitions in eruptive behaviour using high-resolution stratigraphic and textural studies. However, several aspects vital to our understanding of the behaviour of these magmas, and the techniques we use to explore them need further consideration.

1. Vesicle textures in trachytes evolve rapidly, transiently generating large overpressures before promoting high connectivity and outgassing leading to transitions in eruptive behaviour. Though our understanding of the physical properties of trachytes has greatly improved (Giordano *et al.*, 2004; Arzilli and Carroll 2013; Fanara *et al.*, 2013; Shea *et al.*, 2017) more work is needed (experimental and computational) to better constrain the impact of volatile and alkali content on surface tension, bubble relaxation timescales and fragmentation in these melts. This will allow more effective interpretation of vesicle textures, and place further constraints on ascent dynamics.
2. Vesicle textures, crystal cargo, and basalt-rhyolite contacts (Chamberlain *et al.*, 2020) indicate extremely rapid ascent and low levels of crustal interaction for trachytes on Ascension Island. We need to better understand how trachytic melts migrate through relatively closed-system crystal mushes where magma supply rates are low. How do conduits form in these environments and how is this expressed through monitored signals?
3. XCT studies of vesicle textures can provide key insights into ascent dynamics when analysed volumes are representative and can be scaled-up to reflect bulk properties of the magma. However, to apply these more effectively we need to better understand the impact of specific segmentation and bubble separation workflows on bubble populations, and how 3D shape parameters are impacted in bubbles close to the limit of data resolution. This could be done by performing VSD studies on 2D slices from XCT datasets and comparing them with the true measured 3D volumes from intersecting bubbles.

[5.7 Conclusions](#)

This thesis has combined detailed stratigraphic observations and characterisation of bulk magma properties with detailed textural and petrographic studies in 2D and 3D to gain a better understanding of the ascent and eruption dynamics of unobserved small-volume trachytic eruptions on Ascension Island. In doing so, I have highlighted the value of this approach and the advantages and limitations of both well-established, and cutting-edge methods of textural analysis.

The main conclusions from this thesis fall into three main themes:

[Trachytic eruption styles and the Echo Canyon eruption](#)

1. The Echo Canyon eruption had multiple transitions in eruptive style controlled by rapid ascent and depressurisation, vesiculation and development of shear zones at conduit margins.
2. Early phases of the Echo Canyon eruption were dominated by rapid diffusive growth and coalescence with fragmentation via bubble interference and rupture. In the post cone explosive deposits, fragmentation was caused by high bubble overpressures facilitated in part by high microlite crystallinity.
3. Magmas of trachytic composition are capable of transient highly explosive phases with intensities (intensity = 12) equivalent to those seen at the peak of VEI 6 eruptions.
4. High decompression rates and H₂O solubility in trachytic melts contributed to the high explosivity of the Echo Canyon eruption
5. Rapid transitions in eruptive style could be characteristic of low-volume trachytic magmas found worldwide with significant implications for our understanding of volcanic hazard in remote ocean island settings.

[Strategies for reconstructing past eruptions:](#)

1. Forensic interrogation of stratigraphy and bulk vesicularity and clast texture are powerful tools in reconstructing the progression of unobserved eruptions.
2. Coupling the above with careful petrographic analysis and quantitative textural studies provides critical insight into processes that control ascent dynamics.

3. Small-volume eruptions have the potential to have a serious impact on nearby communities (as evidence at St Vincent). Smaller, modern eruptions should be investigated in the same forensic way as ancient eruptions to provide key insights into the behaviour and likely impacts of similar events in regions without recent volcanic activity.

2D vs 3D textural studies and the Mingled Fall:

1. Mingling of basalt and rhyolite had very little impact on the vesiculation process of each region during ascent, which occurred largely in the absence of shear.
2. Coalescence of vesicles in basaltic regions of mingled clasts was only slightly inhibited relative to that in ascending non-mingled basalt.
3. VVD and VSD studies of texturally complex samples in 2D and 3D can lead to significantly different interpretations of process.
4. Interpretations of vesicle size distributions in 3D are more robust as true bubble volumes are measured but 2D shape descriptors are better constrained and more comparable between eruptions.
5. Data processing in 2D and 3D can have profound impacts on interpretations of process and must be carefully considered against existing geological knowledge of the sample. Some aspects of 3D studies are still poorly understood and need further investigation to improve confidence in interpretations.

The work presented here has made a new contribution to our understanding of these types of eruption and highlights the need for further, detailed interrogation of not only their deposits, but the methods we use to interpret them. Incorporating the findings of this thesis into future studies will enable more confident interpretation of the processes governing these systems, improving our ability to forecast transitions in eruptive style in isolated ocean island settings.

Moving forward, we must give small-volume alkali-rich eruptions the same attention that has historically been paid to larger, more well-preserved calc-alkaline examples. Focus should be given to reconstructing the bulk properties of these “kinetically reactive” melts during ascent through careful characterisation of clast texture and an improved understanding of their bubble-crystal-melt interactions. In isolated ocean island settings, the impact of a short-lived, high intensity eruption with little warning would be profound. As such, it is vital that we move towards identifying monitored signals that could give early

warning of these events. In this way, we can improve our ability to effectively monitor these volcanoes and safeguard at-risk populations worldwide.

Appendices:

Appendix1 – Echo Canyon eruption deposits

1.1 – Echo Canyon localities

Table 1.1 Part 1: All Echo Canyon Deposit localities and sample sites from 2018 - 2020

Locality N°	Sample number	Sample Description	Locality Description	UTM (28S)	
				Lat	Long
AI18-04	AI18-842 – 847 AI19-060	EC Cone Pumice	At base of E cliff face in Echo Canyon, first sight of full section exposed in valley, below toe of lava flow.	-7.9307	-14.3285
AI18-19	AI18-827	OBP Pumice	Contact between orange-brown pumice and brecciated EC lava	-7.93025	-14.3268
AI18-20	AI18-828	EC Lava	Brecciated EC lava cliff face	-7.93023	-14.3278
AI18-22	AI18-829	EC middle-cone pumice	Echo Canyon bedded units, part way up canyon in cliff face	-7.93171	-14.3282
AI18-33	AI18-871	EC Dome	Dome outcropping at head of rainbow Canyon	-7.93327	-14.3233
AI18-57			At the Dead of Rainbow Canyon E-face, viewing dome (354 m N of 33)	-7.93	-14.322
AI18-73	AI19-014,105	EC pumice and obsidian	Spire Beach Letterbox cairn looking N.	-7.93841	-14.3207
AI18-84			Echo Canyon Letterbox, W - face of Echo Canyon Cliff, looking East into Canyon	-7.93064	-14.3295
AI19-EC1			Top of Rainbow Canyon E-face in cliff EC PDC deposits	-7.93058	-14.3223
AI19-EC2	AI19-05,6	EC Pumice and PDC Obsidian	W face Rainbow Canyon cliff face EC PDC deposits	-7.93021	-14.3239
AI19-EC3			Walking back along route from RC to NE Coast logging EC deposit exposures	-7.92903	-14.324
AI19-EC4			As Above	-7.92844	-14.3245
AI19-EC5			As Above	-7.92606	-14.3245
AI19-EC6			As Above	-7.9252	-14.324
AI19-EC7			As Above	-7.92113	-14.3255
AI19-EC8			As Above	-7.92089	-14.3255
AI19-EC9			As Above	-7.92097	-14.3265

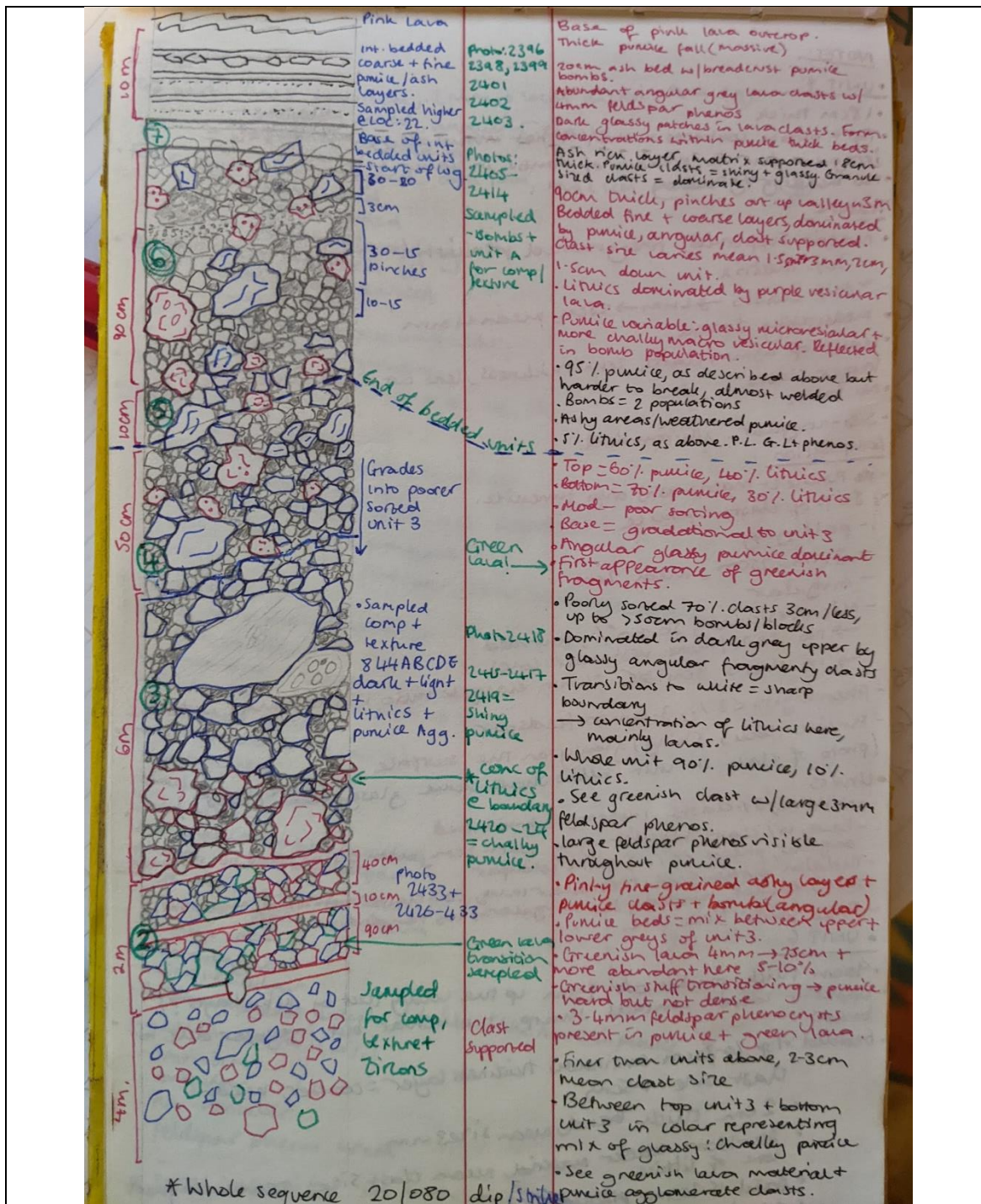
Locality Number	Sample number	Sample Description	Locality Description	UTM (28S)	
				Lat	Long
AI19-EC10			Under the Ariane Lava flow first break point in lava underlying the CZF and EC. Contact between CZF and EC.	-7.92613	-14.3274
AI19-EC11			EC PDC deposit markers along NE Bay	-7.91801	-14.3278
AI19-EC12			EC PDC deposit markers along NE Bay Cliff near Ariane Car Park, at path round to NE Bay.	-7.91711	-14.3311
AI19-EC13			EC Deposits exposed in quarry near Ariane Site.	-7.91626	-14.3344
AI19-BD1			View from Letterbox Hillside towards Spire Beach Valley sketch to help cross-sections of EC deposits	-7.94143	-14.3099
AI19-EC21			Walked to Devil's Cauldron then carried on round the crater rim before dropping N down into the EC OBP.	-7.93408	-14.3269
AI19-EC22			Following EC Units round towards Rainbow Canyon	-7.93416	-14.3268
AI19-EC23			Following EC Units round towards Rainbow Canyon	-7.93316	-14.3248
AI19-EC24			EC Units, at head of Rainbow Canyon	-7.93293	-14.3243
AI19-EC25			Walking into EC dome exposure around top of RC.	-7.93316	-14.3232
AI19-EC29			In Echo Canyon, W cliff face beneath Ariane, EC CZF exposures.	-7.92497	-14.3271
AI19-EC30			Contact between NE-Bay Lava, CZF and EC, Ariane overlies.	-7.92625	-14.3273
AI19-EC31	AI19-055 - 058	Rubbly EC unit head EC	Head of Echo Canyon, beneath OBP contact.	-7.93364	-14.3274

Table 1.1 Part 3. All Echo Canyon Deposit localities and sample sites from 2018 - 2020					
Locality Number	Sample number	Sample Description	Locality Description	UTM (28S)	
				Long	Lat
AI19-EC32			Head of Echo Canyon, beneath OBP contact.	-7.93377	-14.3272
AI19-EC33	AI19-059	White pumice / lava	Head of Echo Canyon, beneath OBP contact, N of 32.	-7.93365	-14.3273
AI19-EC34			Across into cliff face to get dip of EC PDCs beneath OBP	-7.93336	-14.3277
AI19-EC35			As above	-7.93111	-14.3283
AI19-EC36			Contact between units 3 and 4 up EC in E cliff face.	-7.93308	-14.3275
AI19-EC37			Base exposure of middle cone units EC	-7.93174	-14.3282
AI19-EC38			Top exposure of middle cone units EC	-7.9317	-14.3279
AI19-EC39			Base of gulley where sampled (AI18-22) in 2018. After scouting up gulley all the way to PDC - Lava contact	-7.93184	-14.3281
AI19-EC40			Gulley W-face of EC beneath Ariane flow, EC-CZF contact	-7.92777	-14.3285
AI19-EC41			Highest explored in W face gulley EC units beneath Ariane flow.	-7.92773	-14.3287
AI19-EC42			NE Bay coastal exposures of EC-CZF contacts	-7.92112	-14.3247
AI19-EC43			As Above	-7.92043	-14.3249
AI19-EC44			As Above	-7.92039	-14.3253
AI19-EC45			As Above	-7.91989	-14.3253
AI19-EC46	AI19-061 - 63		Logged EC distal PDC-CZF contact in coastal exposure	-7.92006	-14.3259
AI19-EC47			Coastal exposures of distal PDC CZF	-7.91801	-14.3278
AI19-EC49			Off NE Bay Road distal PDCs	-7.92603	-14.3422
AI19-EC50			NE-bay Road after fork, road cut.	-7.91894	-14.3372
AI19-EC51			NE-Bay road W of Quarry.	-7.91647	-14.335

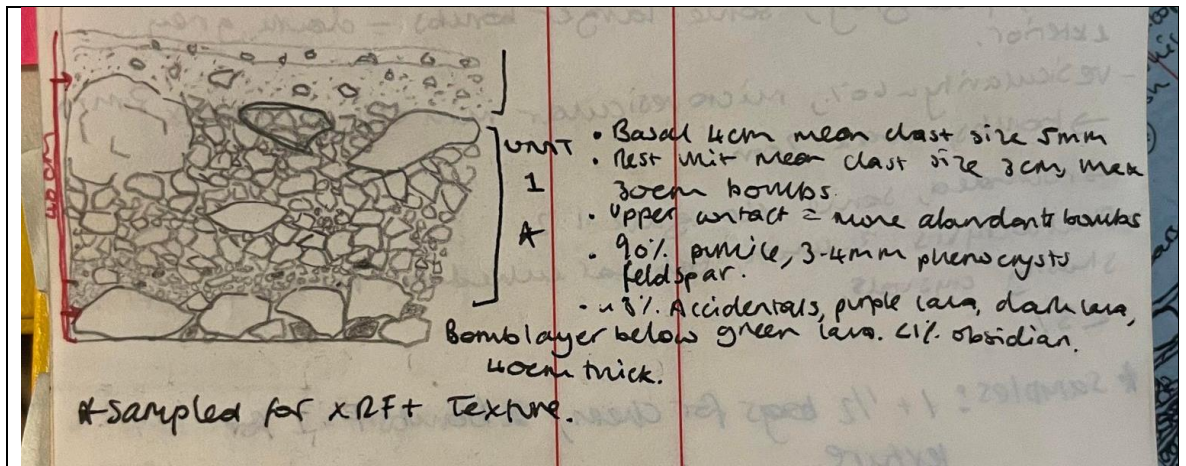
Table 1.1 Part 4. All Echo Canyon Deposit localities and sample sites from 2018 - 2020					
Locality Number	Sample number	Sample Description	Locality Description	UTM (28S)	
				Lat	Long
AI19-EC52	AI19-135 - 38	PDC Pumice banded pumice/obsidian	PDC units in top of RC, logged	-7.93081	-14.3224
AI19-EC53			EC PDC units - CZF outcrop along path from RC towards NE bay. Logged	-7.92453	-14.3227
AI19-EC54			Outcrop EC PDC just below breached scoria cone NE-Bay path, logged	-7.92102	-14.3265
AI19-EC55			Below Ariane flow. EC PDC altered	-7.92453	-14.3271
AI19-EC56	AI19-139	EC pumice from under Ariane	In mouth of Echo Canyon, Ariane - CZF - EC contacts	-7.92517	-14.3271
AI19-EC57			In mouth of Echo Canyon, Ariane - CZF - EC contacts	-7.92538	-14.3273
AI19-EC59			NE-bay Road	-7.91453	-14.3363

1.2 – Original logs and sketches

1.21 – Logs from Echo Canyon units 1 – 10.



Original stratigraphic log from AI18-04 units 1 – 10 logged.



Original log from AI18-022 units 7 – 10.

LOG A LOC 22: GR? 0574044
9123192

UNIT 1: ~ 40cm thick

- 40cm thick
- Continuous, can track round to other side of same slope
- Base contact sharp but irregular surface
 - unit below = coarse pumice bombs + blocks ~ 20cm diameter
 - UNIT 1 = finer = fills gaps, undulating over clasts below.
- Upper contact also sharp
 - overlying unit defined by even finer material
 - Again contact undulates over irregular surface of the underlying pumice blocks + bombs.
- Bottom 4cm, near clast side ~ 5mm, min 1mm, 1.5-2cm max.
 - Well sorted.
 - clast supported
- Overlying ~ 30cm = coarser
 - mean 3cm, min 3mm, max 10cm.
- Top 6cm
 - mean ~ 6cm, min 3cm, max 33cm (bombs).
- Angular clasts.

Composition

Accidentals

- Purple-red lava ~ 2-3%.
 - fine-grained crystalline
 - sub-rounded-sub-angular
 - 0.2cm - 2cm, mean ~ 4mm in base 4cm, ~ 1.5cm elsewhere.
 - vesicularity < 3%, rounded 1-2mm.
- phenocrysts: < 2%, white feldspar? 1mm.
- Black vesicular pheno lava. ~ 1%.
 - angular, 0.4 - 0.6cm, mean base 4cm = ~ 4mm, rest with same.
 - vesicularity ~ 45%, rounded microvesicular < 1mm → 1mm.
 - phenocrysts < 3%, 1-2mm feldspar.

clast supported

- Greenish lava - 3%
- Angular,
- Min ϕ : 4cm, max 3.5cm mean main unit = 3cm, lower unit =
- fine-grained crystalline
- not vesicular
- Phenocrysts up to 2mm, 3% feldspar.

• Have obsidian chunks < 3mm mean: < 1%
 Accidentals = 8%

Juvenile:

- Pumice: ~ 90%
- Bottom 4cm: min 1mm, max 2-3cm, mean = 0.4cm
- Rest unit: min 3mm, max = 3.5cm, mean 1cm.
- Angular
- Color, pale grey, some larger bombs = dark grey exterior.
- vesicularity = 60%, microvesicular min 1mm, max 3mm
 → bombs, max 2cm
 → rounded, some elongate 1:2
- Phenocrysts 3-4mm, tabular euhedral feldspar + stubby crystals.
 < 3%

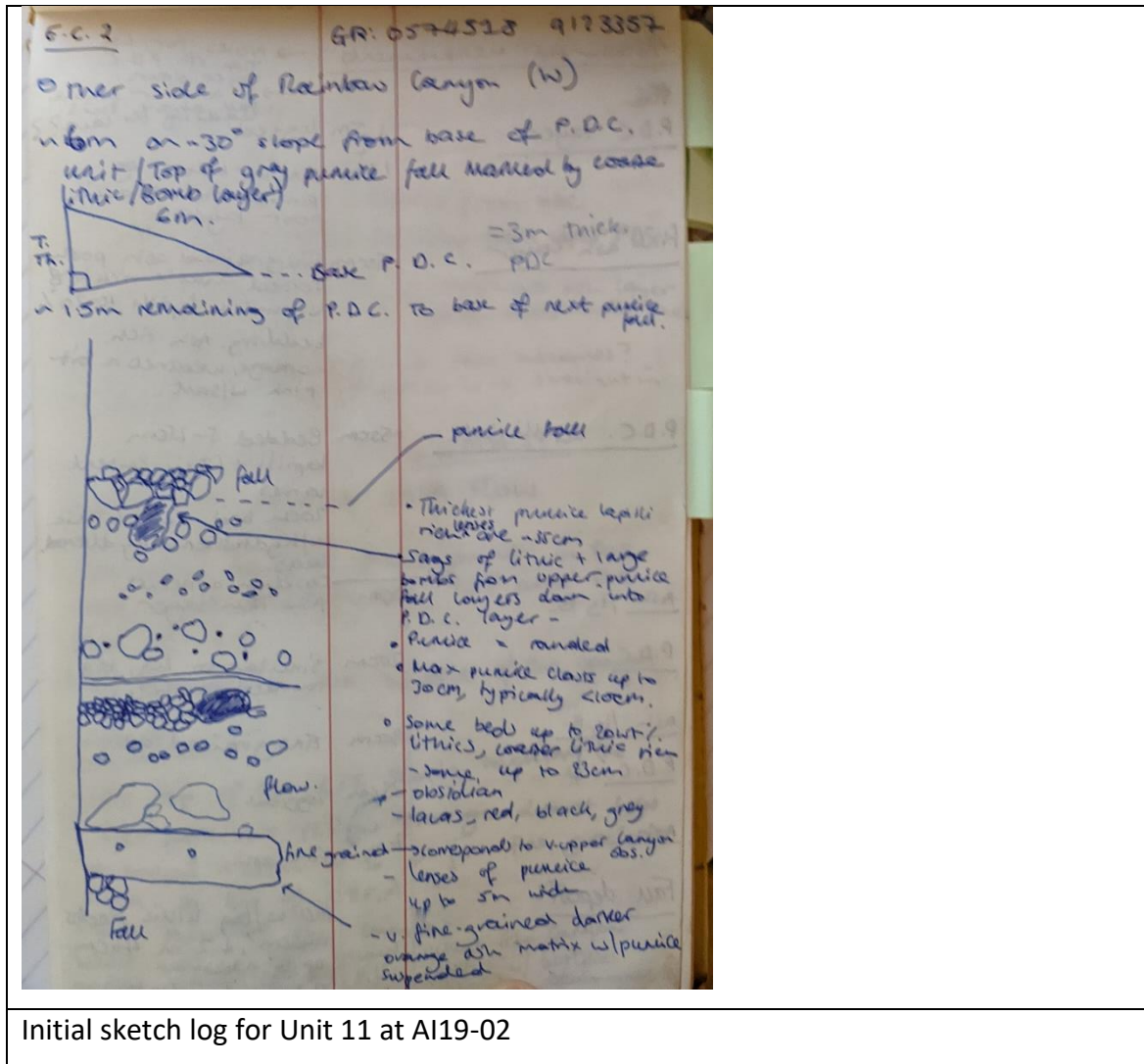
* Samples: 1 + 1/2 bags for chem, 2 bombs + 1 for texture.
 # A118-029, A, B1, B2, C1, C2.

UNIT 2:

- orange-brown color.
- Base 3cm = fine-grained mean 2mm.
- Interbedded resistant ash spotted layer containing pumice clasts + lithics from unit below.
 → clasts = sub-rounded - sub-angular
- layers fine ash + sand-grade clayer w. rounded clasts in bedded w/ sub-angular mean 4cm pumice clast rich layers.
 → more transport? lit. B. layer? 4.5cm thick

Original descriptions used to generate log at A118-022.

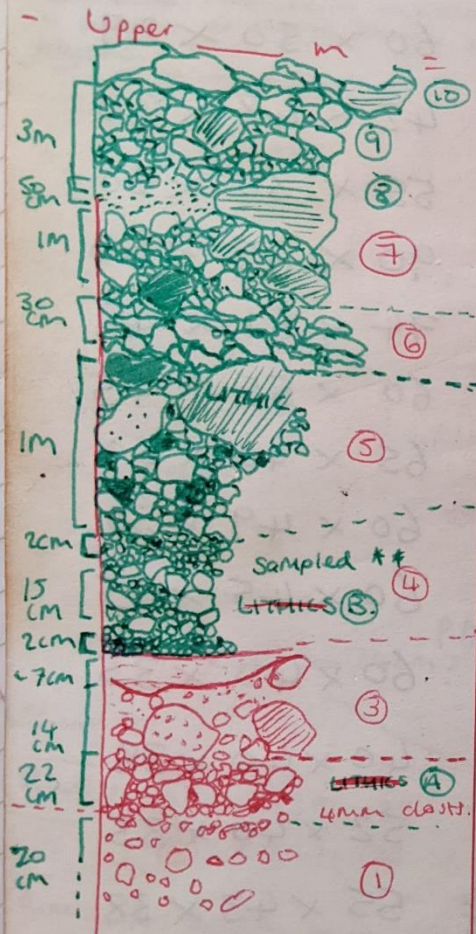
1.22 – logs and sketches from Unit 11



Initial sketch log for Unit 11 at AI19-02

Elevation 230m. 7125290.

- In PDC units @ top Rainbow Canyon.
- Approx 4m of pumice fall deposit @ base
- ~6m of PDC units = yellow.



obsidian rich

largest juvenile clasts = yellow dense type
 Much coarser max clast ~60cm
 Dense type yellow blocks + lithic
 clasts + obsidian breccia + fragments
 of pumice bombs + rounded pumice
 4mm - 10cm. ex. bombs

Upper = coarser but overlain by 2cm
 band of fine within modal.
 Bombs up to 12cm clast supported
 obsidian breccia ~6cm clasts
 3mm - 4cm modal ~3cm 10%
 pumice = dense.

Base = 1-4mm clast supported rounded
 2mm obsidian 10%
 pumice = type 4, dense / elongate w/
 5cm surfaces. larger clasts >3cm
 softer macro-vesicular - bomb fragments?

Upper 5-9cm = undulating
 ash medw <5% clasts seems to
 be in a unit above.

Bomb rich layer matrix
 supported w/ 18.5cm pumice bombs +
 2cm obsidian blocks. Pumice =
 broad crust bombs. Rounded
 pumice clasts 0.4cm - 5cm. Modal
 ~10% of unit. Ashy matrix supported.

Some small lithics on outside of
 pumice clasts. 3mm - 6cm modal
 lithics ~6%. 2cm obsidia = V small fragments.
 vesicles often elongate.

Pumice 4mm - 10cm modal rich
 coarsens upwards

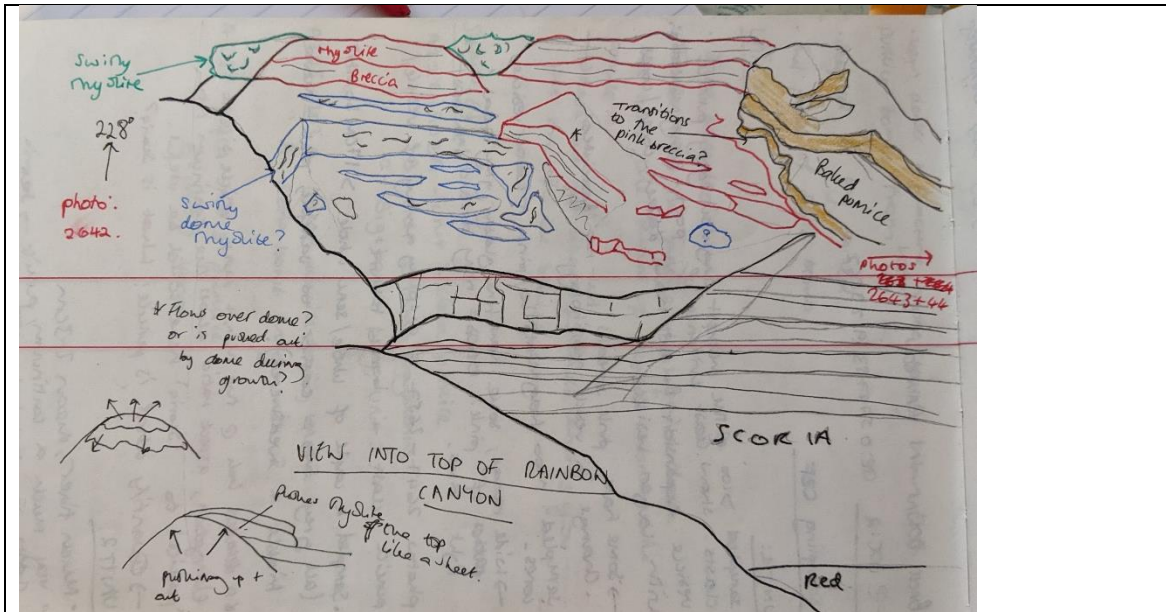
clast supported rounded pumice
 microvesicular glassy surfaces
 some pink alteration inside

More clast rich 2 top grades
 into unit above.
 Rounded pumice 3mm - 5cm
 modal 2cm ~10% of unit
 Ashy matrix supported
 welded

~3cm bands of ash w/clast
 rich layers.
 <5% lithics 3mm - 1cm
 obsidian, purple lang, red lam.

↓ P.D.C. units continue down
 for ~6m, then underneath =
 pumice fall. This log overlaps
 w/ log from other side of R.C.
 → extends above the first log
 baked pumice.

Follow up sketch log of Unit 11 at more easily accessible A119-52



Sketch view of stratigraphy in the top of Rainbow Canyon from near A19-52

- Pumice = sub-angular - sub-rounded
0.5cm - 35cm.
- Lava = red + black banded as above
- variably vesicular <1% → 30%.
- Unit = clast supported but highly altered pumice
clasts merge w/ <10% ash matrix
lava banded w/ dense + more vesicular
material.
- This lower unit (especially @ contact w/ upper)
has smaller clasts modal ~3cm @ contact
(graded, bigger @ base)
- modal 4-5 m below contact
- Beds / layers of coarse lavas + bombs
every ~1.5m down the outcrop

Sketch log:

6m to top

4m

Upper lava dominated.

2-3cm pumice dominant.

4-5cm w/ bombs > 20cm

Coarse unit blocks > 35cm w/ finer clasts @ top.

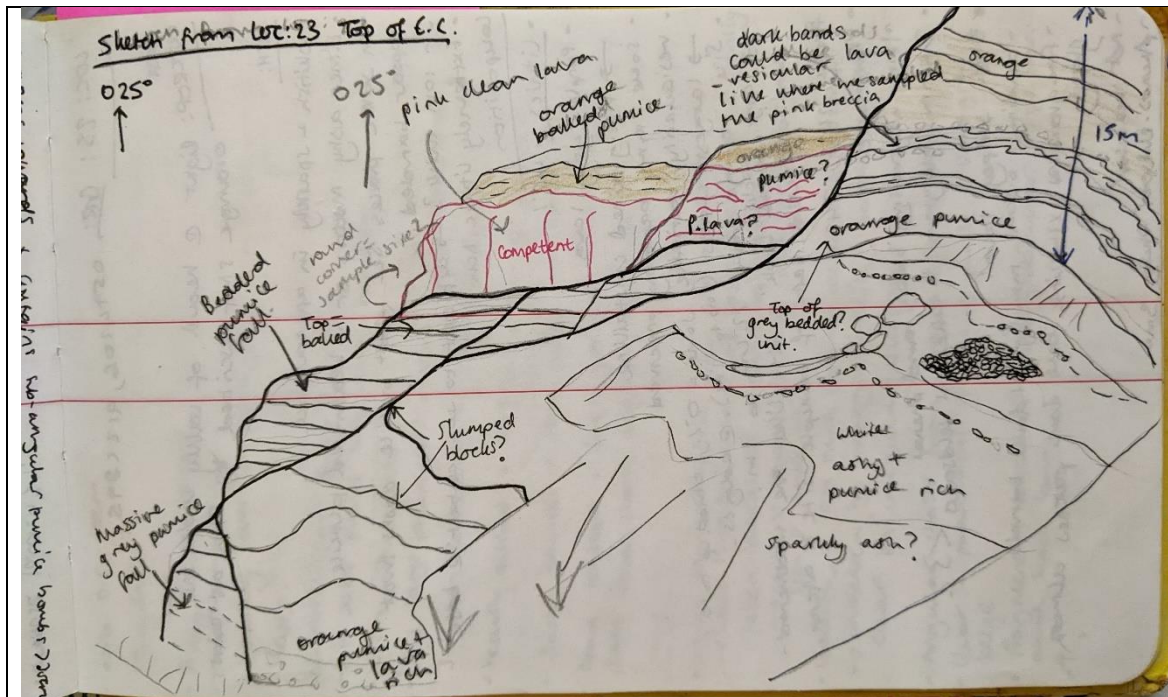
Coarse blocky unit

4-5cm clasts

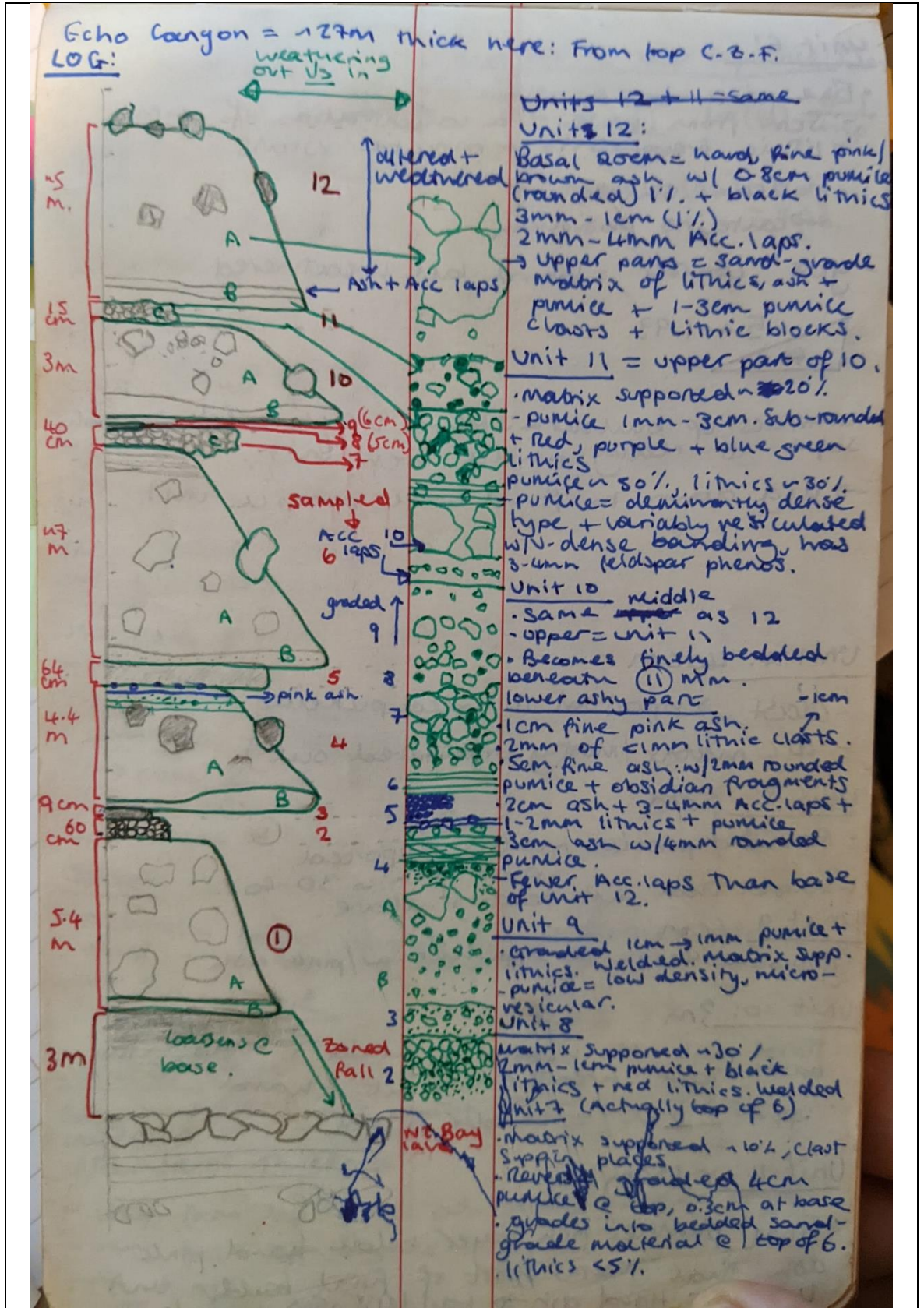
blocky unit

lower, pumice dominated

Sketch log produced at poorly accessible outcrop of unit 12 at the top of Echo Canyon.

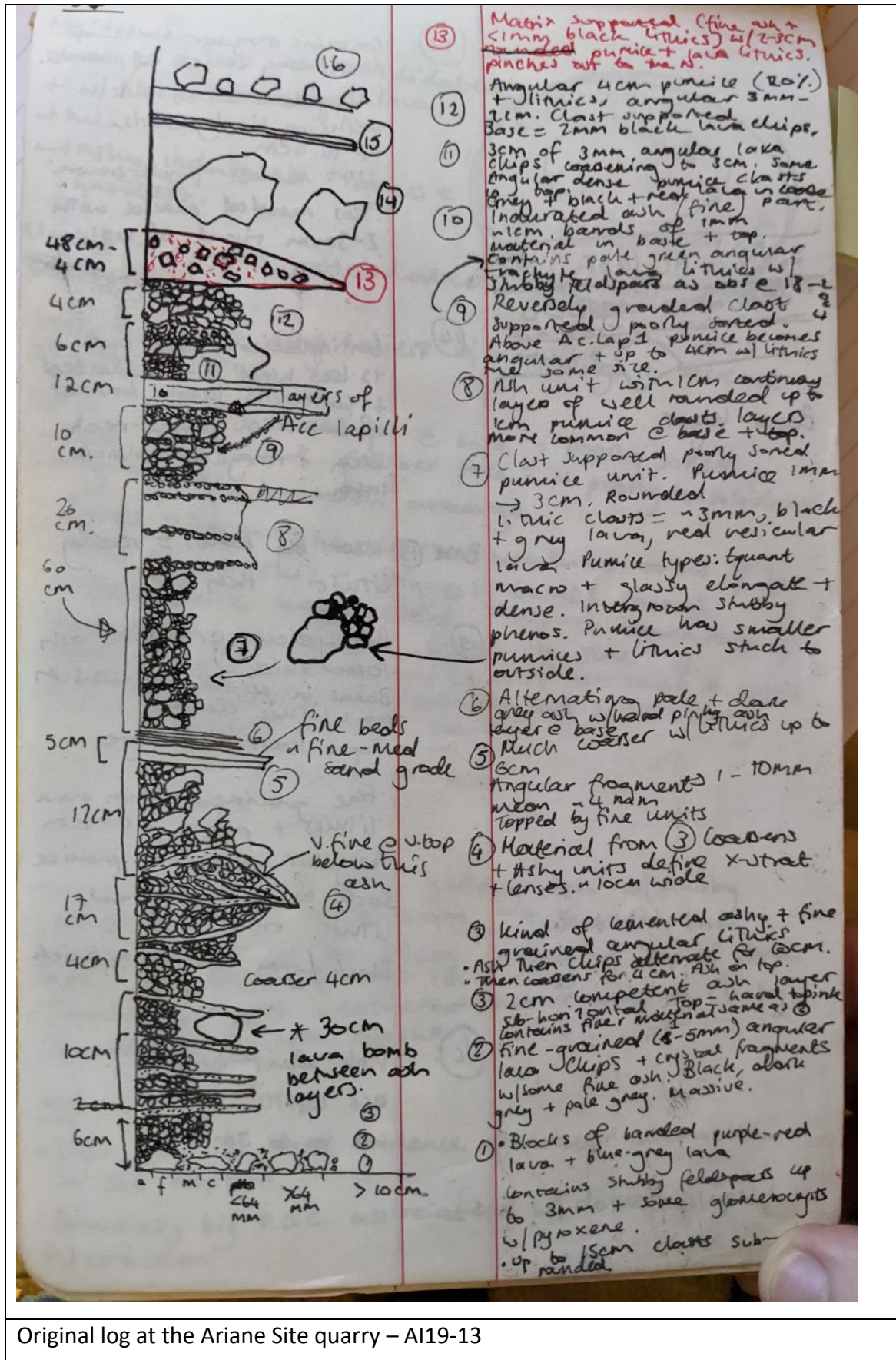


Sketch showing unit relationships from top of Echo Canyon.



Log through distal PDC deposits at NE-Bay coastal locality. A19-46

1.25 – logs of distal PDC deposits in and around the Ariane Site Quarry and NE Bay



Original log at the Ariane Site quarry – A19-13

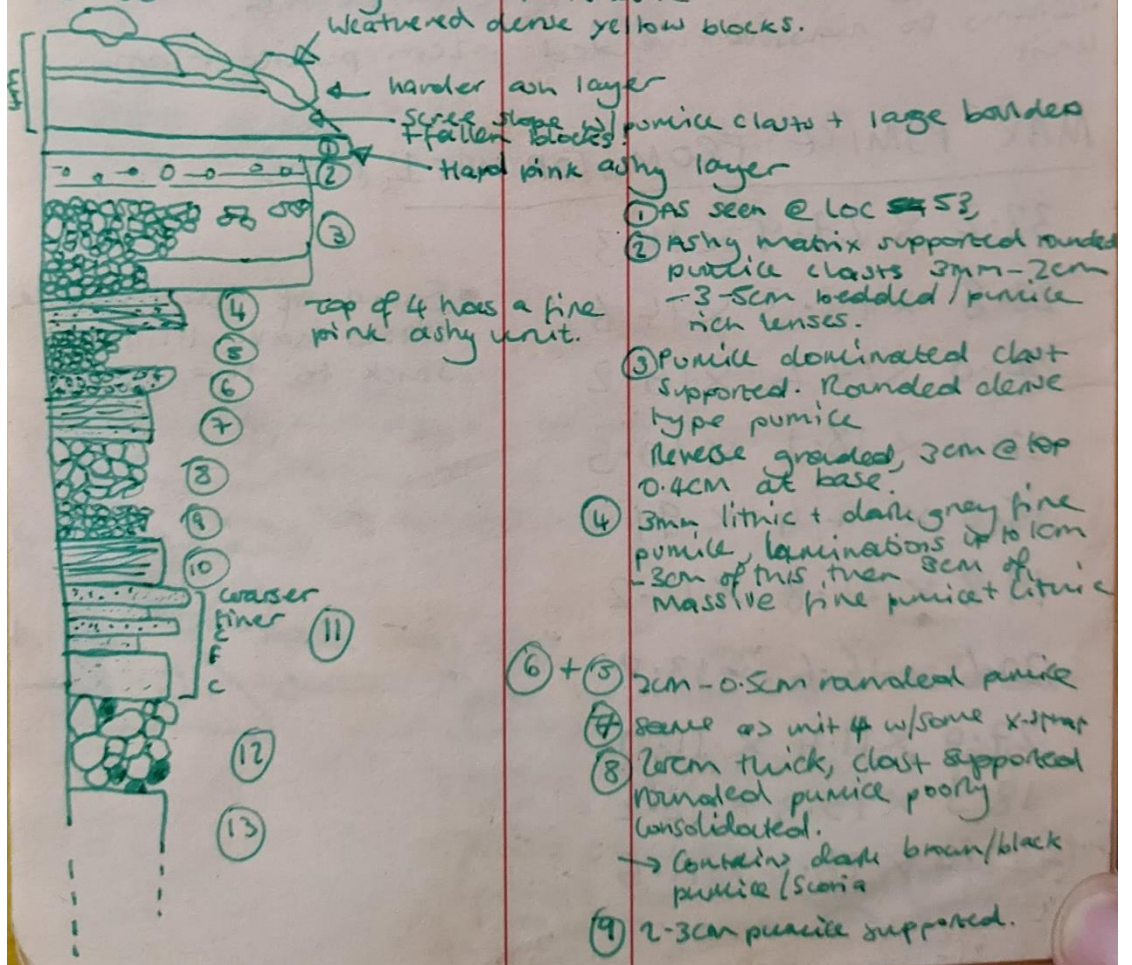
GR: 0574239 9124374

Elevation 41m a.s.l.

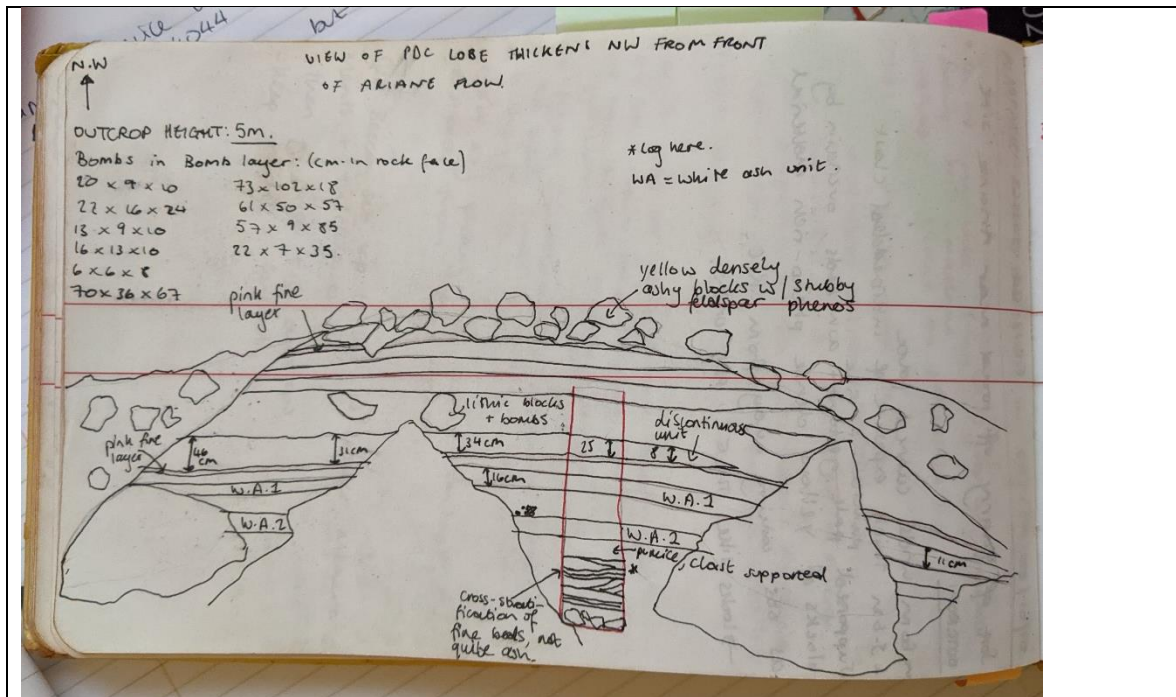
Outcrop is 7m high from base mound to contact w/overlying scoria.

3m up = hard pink ash with dips = S. 06/180°
→ Above first ash bed = another that tapers + lenses down into it. cutting a bit steeper.

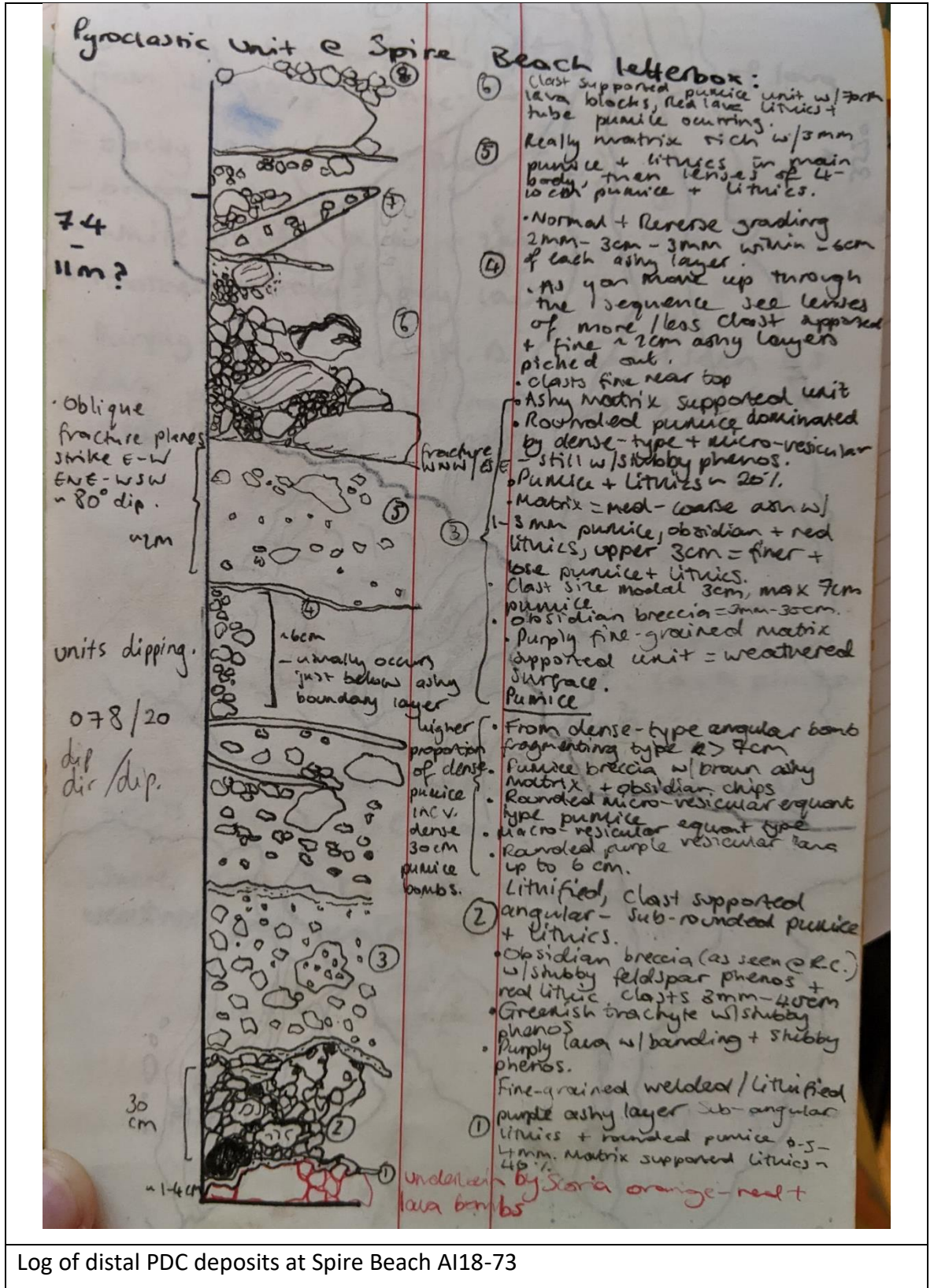
- Outcrop thickens towards the south to ~10m and thins to ~2m ~ 100m to the N → but continues down into coastal cliffs (see other localities - E.C.46)
- Outcropping below hard pink ash layer looks similar to Quarry near Ariane site.



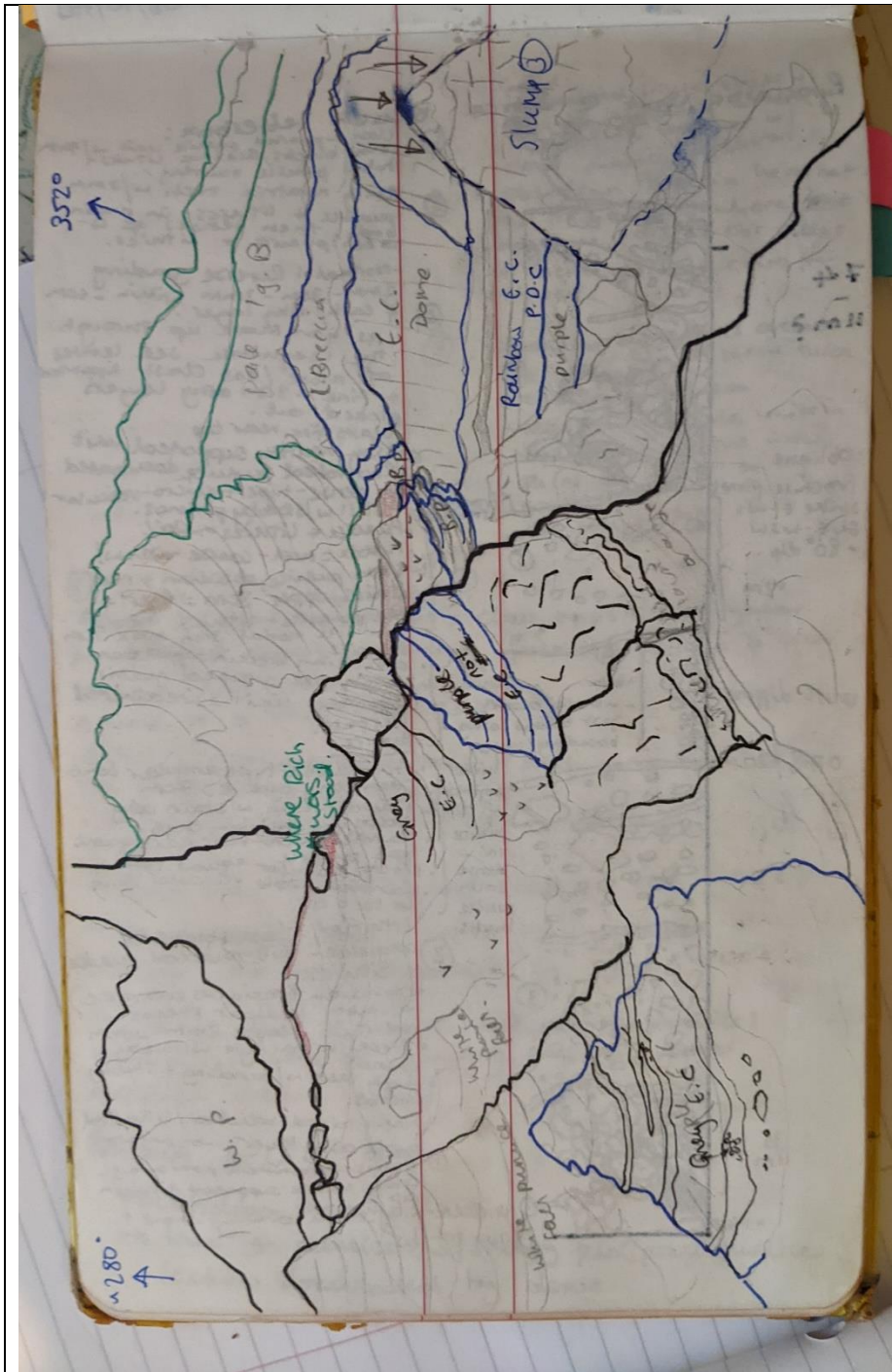
Log of distal PDC deposits with same character as Ariane Site Quarry deposits - A19-054



Sketch of distal PDC deposits at Ariane Site Quarry – AI19-13



Log of distal PDC deposits at Spire Beach A18-73



View showing EC deposit relationships from Spire Beach locality A118-73

1.3 – XRF standards data

Standard	Date	SiO ₂ (%)	TiO ₂ (%)	Al ₂ O ₃ (%)	MnO (%)	MgO (%)	Fe ₂ O ₃ (%)	CaO (%)	P ₂ O ₅ (%)	K ₂ O (%)	Na ₂ O (%)
SDO-1	Certified values	49.28	0.71	12.27	0.04	1.54	9.34	1.05	0.11	3.35	0.38
SDO-1	13/12/18	48.86	0.71	12.19	0.04	1.46	9.31	1.01	0.11	3.31	0.41
SDO-1	28/01/19	48.41	0.71	12.13	0.04	1.47	9.26	1.01	0.11	3.32	0.42
SDO-1	07/03/19	48.29	0.7	12.13	0.04	1.48	9.27	1.01	0.11	3.32	0.45
GSP-2	certified values	66.6	0.66	14.9	0.032	0.96	4.9	2.1	0.29	5.38	2.78
GSP-2	13/12/18	67.11	0.67	15.15	0.04	0.96	4.82	1.95	0.29	5.4	2.88
GSP-2	28/01/19	66.63	0.66	15.09	0.04	0.96	4.79	1.95	0.28	5.43	2.89
GSP-2	07/03/19	66.5	0.66	15.18	0.04	0.96	4.8	1.94	0.28	5.4	2.93
W2a	certified values	52.68	1.06	15.45	0.167	6.37	10.83	10.86	0.14	0.626	2.2
W2a	13/12/18	52.45	1.05	15.39	0.16	6.3	10.47	10.25	0.13	0.63	2.31
W2a	28/01/19	52.2	1.05	15.35	0.16	6.32	10.44	10.25	0.13	0.63	2.34
W2a	07/03/19	52.15	1.05	15.38	0.17	6.34	10.45	10.25	0.13	0.63	2.38
AC-E	certified values	70.35	0.11	14.7	0.058	0.03	2.53	0.34	0.014	4.49	6.54
AC-E	13/12/18	70	0.1	14.91	0.06	0	2.49	0.34	0.02	4.46	6.85
AC-E	28/01/19	69.6	0.1	14.87	0.06	0.01	2.47	0.35	0.02	4.48	6.89
AC-E	07/03/19	69.53	0.1	14.93	0.06	0.02	2.48	0.35	0.02	4.47	6.96
AGV-2	certified values	59.3	1.05	16.91	0.099	1.53	6.69	5.2	0.5	2.88	4.19
AGV-2	13/12/18	59.9	1.04	17.08	0.1	1.76	6.58	4.87	0.45	2.88	4.42
AGV-2	28/01/19	59.72	1.04	17.08	0.1	1.78	6.56	4.87	0.45	2.89	4.43
AGV-2	07/03/19	59.61	1.04	17.04	0.1	1.78	6.57	4.87	0.45	2.89	4.47

Standard	Date	Zr (ppm)
SDO-1	certified	165
SDO-1	14/12/2018	162
SDO-1	25/01/2019	162
SDO-1	11/03/2019	164
MESS-2	certified	NA
MESS-2	14/12/2018	141
MESS-2	25/01/2019	142
MESS-2	11/03/2019	142
STSD-2	certified	185
STSD-2	14/12/2018	184
STSD-2	25/01/2019	186
STSD-2	11/03/2019	187
W2a	certified	100
W2a	14/12/2018	92
W2a	25/01/2019	94
W2a	11/03/2019	94

1.4 – Stratigraphic data used for Fig. 2.9

Table 1.4: Echo Canyon stratigraphic data used to produce Fig. 2.9.

Unit	Sample number / sub-unit*	Height in outcrop (m from base)	Modal lithic (cm)	max lithic (cm)	Percentage lithic	Modal Pumice (cm)**	Max pumice (cm)**
1	AI18-842A	1	3	20	20	2	3
2	AI18-843A	5	2	30	20	3	25
3	AI18-844A	7	3	30	10	4	50
4	AI18-844C	11	3	30	10	4	50
5	N/A	12	1.5	4	35	2	25
6	N/A	12.15	0.5	12	5	0.5	25
7	Sub-unit a	12.3	2.5	28	10	1.5	20
7	Sub-unit b	12.55	2.5	28	30	2	20
7	Sub-unit c	12.66	2.5	28	50	0.3	20
7	Sub-unit d	12.77	2.5	28	5	1.5	20
8	N/A	13	0.3	0.5	15	2	25
9	AI18-829A-C	13.4	0.2	3.5	10	3	10
9	AI18-829A-C	13.5	0.2	3	2	0.2	33
10+	Obsidian rich units	14		28	high		30
11	AI19-137	NA	3	25	10	6	50
12	Rubbly units head of canyon	17	12	50	45	12	-
OBP	AI18-827C	37	10	45	5	10	

*sub-units and layers marked N/A not sampled. **Maximum and modal pumice calculated by measuring longest axis of the five largest clasts (maximum) and measuring a range of clasts from across the outcrop. Modal pumice clast size is a qualitative estimate for each unit.

1.5 – Clast Bulk Vesicularity Data

Table 1.5: Vesicularity of clasts from Unit 1 of the Echo Canyon deposits used to generate Figs. 2.9 and 2.20

Sample	Clast N°	Vesicularity (%)	Clast N°	Vesicularity (%)	Clast N°	Vesicularity (%)
AI18-842A	1	80	35	74	69	75
	2	80	36	67	70	81
	3	85	37	78	71	82
	4	92	38	77	72	79
	5	76	39	80	73	84
	6	77	40	88	74	72
	7	72	41	87	75	82
	8	67	42	75	76	78
	9	84	43	81	77	83
	10	77	44	77	78	81
	11	75	45	73	79	78
	12	78	46	78	80	84
	13	77	47	83	81	79
	14	68	48	81	82	78
	15	75	49	78	83	72
	16	69	50	82	84	84
	17	80	51	73	85	82
	18	78	52	82	86	82
	19	74	53	85	87	81
	20	20	54	78	88	76
	21	79	55	71	89	77
	22	83	56	78	90	80
	23	75	57	78	91	70
	24	79	58	73	92	83
	25	85	59	82	93	81
	26	73	60	80	94	79
	27	82	61	82	95	76
	28	71	62	84	96	74
	29	80	63	86	97	57
	30	71	64	66	98	79
	31	84	65	79	99	81
	32	78	66	81	100	82
	33	81	67	78		
	34	80	68	79		

Table 1.6: Vesicularity of clasts from Unit 2 of the Echo Canyon deposits used to generate Figs. 2.9 and 2.20

Sample	Clast N°	Vesicularity (%)	Clast N°	Vesicularity (%)	Clast N°	Vesicularity (%)
AI18-843A	1	73	35	82	69	76
	2	78	36	77	70	81
	3	84	37	85	71	76
	4	75	38	78	72	78
	5	77	39	77	73	78
	6	81	40	77	74	79
	7	82	41	77	75	76
	8	81	42	79	76	82
	9	74	43	83	77	82
	10	78	44	82	78	80
	11	78	45	83	79	80
	12	86	46	84	80	83
	13	81	47	84	81	77
	14	73	48	77	82	77
	15	84	49	82	83	79
	16	86	50	83	84	82
	17	78	51	81	85	75
	18	73	52	78	86	81
	19	77	53	78	87	80
	20	74	54	79	88	83
	21	86	55	80	89	72
	22	77	56	73	90	64
	23	82	57	74	91	81
	24	74	58	79	92	73
	25	77	59	82	93	86
	26	81	60	84	94	78
	27	78	61	73	95	84
	28	74	62	77	96	75
	29	76	63	83	97	71
	30	75	64	73	98	79
	31	72	65	76	99	85
	32	80	66	84	100	77
	33	81	67	82		
	34	77	68	79		

Table 1.7: Vesicularity of clasts from Unit 3 of the Echo Canyon deposits used to generate Figs. 2.9 and 2.20

Sample	Clast N°	Vesicularity (%)	Clast N°	Vesicularity (%)	Clast N°	Vesicularity (%)
AI18-844A	1	74	35	78	69	76
	2	83	36	83	70	78
	3	79	37	80	71	82
	4	78	38	79	72	84
	5	73	39	82	73	82
	6	79	40	69	74	86
	7	82	41	85	75	85
	8	80	42	77	76	81
	9	84	43	77	77	84
	10	81	44	80	78	79
	11	78	45	82	79	66
	12	81	46	76	80	76
	13	78	47	84	81	81
	14	83	48	84	82	81
	15	74	49	79	83	77
	16	77	50	78	84	79
	17	83	51	78	85	80
	18	77	52	83	86	78
	19	76	53	82	87	80
	20	78	54	76	88	82
	21	82	55	76	89	82
	22	77	56	74	90	79
	23	83	57	76	91	82
	24	76	58	80	92	75
	25	80	59	83	93	78
	26	78	60	78	94	81
	27	79	61	82	95	77
	28	78	62	78	96	82
	29	81	63	80	97	77
	30	83	64	84	98	77
	31	83	65	79	99	76
	32	83	66	77	100	79
	33	81	67	80		
	34	85	68	81		

Table 1.8: Vesicularity of clasts from Unit 4 of the Echo Canyon deposits used to generate Figs. 2.9 and 2.20

Sample	Clast N°	Vesicularit y (%)	Clast N°	Vesicularit y (%)	Clast N°	Vesicularity (%)
Al18-844C	1	73	35	71	69	69
	2	72	36	83	70	74
	3	73	37	73	71	74
	4	83	38	76	72	75
	5	68	39	73	73	66
	6	70	40	68	74	68
	7	68	41	66	75	70
	8	71	42	65	76	79
	9	81	43	61	77	70
	10	69	44	77	78	70
	11	62	45	73	79	76
	12	79	46	72	80	68
	13	74	47	85	81	74
	14	71	48	63	82	80
	15	78	49	72	83	74
	16	60	50	78	84	68
	17	78	51	77	85	71
	18	81	52	72	86	56
	19	73	53	68	87	78
	20	69	54	76	88	66
	21	72	55	71	89	65
	22	73	56	72	90	60
	23	71	57	79	91	62
	24	83	58	77	92	80
	25	77	59	79	93	67
	26	75	60	70	94	79
	27	70	61	68	95	77
	28	65	62	73	96	69
	29	62	63	70	97	74
	30	79	64	77	98	56
	31	82	65	69	99	76
	32	68	66	75	100	62
	33	81	67	68		
	34	66	68	77		

Table 1.9: Vesicularity of clasts from Unit 9 of the Echo Canyon deposits used to generate Figs. 2.9 and 2.20

Sample	Clast N°	Vesicularity (%)	Clast N°	Vesicularity (%)	Clast N°	Vesicularity (%)
Al18-829A	1	80	35	53	69	76
	2	69	36	79	70	67
	3	71	37	65	71	74
	4	63	38	59	72	73
	5	75	39	57	73	65
	6	65	40	77	74	62
	7	67	41	63	75	59
	8	76	42	57	76	69
	9	70	43	76	77	66
	10	74	44	79	78	54
	11	55	45	69	79	64
	12	74	46	80	80	78
	13	59	47	74	81	79
	14	71	48	67	82	73
	15	67	49	60	83	75
	16	60	50	76	84	74
	17	72	51	80	85	74
	18	86	52	64	86	73
	19	74	53	60	87	76
	20	65	54	63	88	79
	21	77	55	58	89	82
	22	58	56	51	90	73
	23	66	57	57	91	65
	24	67	58	73	92	62
	25	72	59	70	93	73
	26	58	60	57	94	71
	27	73	61	69	95	74
	28	63	62	74	96	71
	29	79	63	77	97	69
	30	79	64	61	98	58
	31	60	65	65	99	69
	32	69	66	67	100	80
	33	57	67	62		
	34	71	68	71		

Table 1.10: Vesicularity of clasts from Unit 11 of the Echo Canyon deposits used to generate Figs. 2.9 and 2.20

Sample	Clast N°	Vesicularity (%)	Clast N°	Vesicularity (%)	Clast N°	Vesicularity (%)
Al19-137	1	78	35	70	69	66
	2	75	36	73	70	72
	3	73	37	81	71	66
	4	75	38	71	72	78
	5	70	39	57	73	77
	6	80	40	76	74	67
	7	75	41	74	75	69
	8	76	42	65	76	76
	9	75	43	72	77	75
	10	81	44	78	78	73
	11	83	45	83	79	75
	12	74	46	77	80	80
	13	81	47	77	81	71
	14	79	48	57	82	74
	15	79	49	75	83	75
	16	78	50	71	84	74
	17	71	51	78	85	68
	18	74	52	83	86	85
	19	70	53	72	87	67
	20	71	54	78	88	74
	21	66	55	82	89	72
	22	78	56	71	90	76
	23	77	57	78	91	73
	24	73	58	79	92	76
	25	69	59	79	93	67
	26	64	60	76	94	70
	27	71	61	75	95	72
	28	65	62	70	96	80
	29	73	63	73	97	80
	30	81	64	74	98	74
	31	75	65	67	99	57
	32	80	66	80	100	71
	33	66	67	78		
	34	59	68	78		

Table 1.11: Vesicularity of clasts from the Orange-Brown Pumice (OBP) of the Echo Canyon deposits used to generate Figs. 2.9 and 2.20

Sample	Clast N°	Vesicularity (%)
AI18-827C	1	72
	2	70
	3	71
	4	70
	5	76
	6	63
	7	57
	8	74
	9	76
	10	66
	11	76
	12	75
	13	78
	14	80
	15	71
	16	75
	17	69
	18	56
	19	64
	20	79
	21	78
	22	80
	23	73
	24	70
	25	78
	26	76
	27	73
	28	78
	29	71
	30	71
	31	68
	32	76
	33	56

1.6 Textural group abundance data used in Fig. 2.9

Table 1.12: Abundance of textural groups in the Echo Canyon Eruption Deposits. Used to generate Fig. 2.9

Unit	% Clasts in each textural group				
	1	2	3	4	5
Unit 1	26	58	4		12
Unit 2	28	62	2	4	4
Unit 3	31	37	16	15	1
Unit 4	17	44	10	4	25
Unit 9	29	17	7	11	36
Unit 11	30	13	27	16	14
OBP	33	36	9	3	18

*OBP = Orange-Brown pumice. Group 1 = micro-vesicular equant, group 2 = macro-vesicular equant, group 3 = micro-vesicular elongate, Group 4 = macro-vesicular elongate, group 5 = dense as described in Chapter 2.

Appendix 2 – quantification of vesicle textures

2.1: microlite crystallinities

Microlite crystallinity calculations for high (HX) and low (LX) crystallinity regions of clast 827C_6 from the OBP.

Table 2.1: Crystal data for high and low crystallinity regions in sample 827C_6

Sample region	N° Analysed	Microlite area (mm ²)	Image Area (mm ²)	Ves.%	Areal N° Density (mm ²)	Vesicle free Fsp %
LX	654	0.38	29	59	55	1.3
HX	1229	0.11	1	52	3380	31

2.2: Machine learning image segmentation

Parameters selected during image segmentation process using the *Trainable Weka Segmentation* plugin in ImageJ.

- Gaussian blur
- Hessian
- Membrane Projections
- Sobel Filter
- Difference of Gaussians
- Entropy

Membrane thickness: 1

Membrane Patch size: 19

Minimum sigma: 1

Maximum sigma: 16

Class 1: Vesicles

Class 2: Infilled vesicles

Class 3: glass

Class 4: crystals

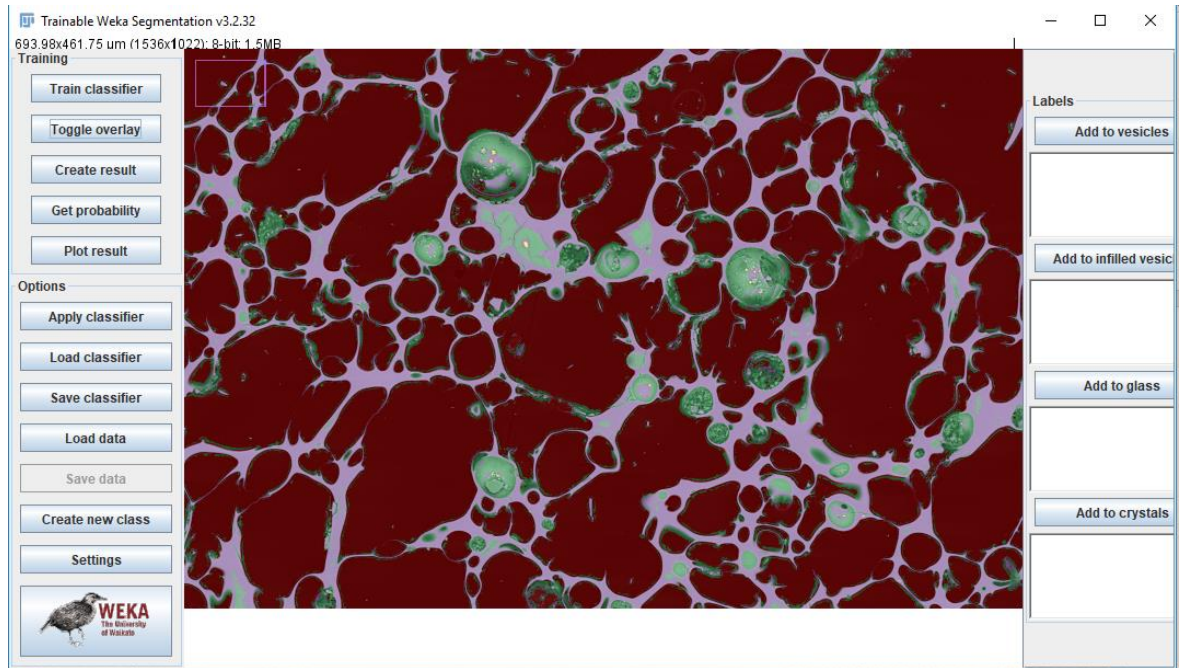
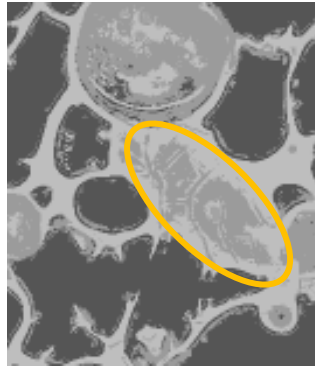
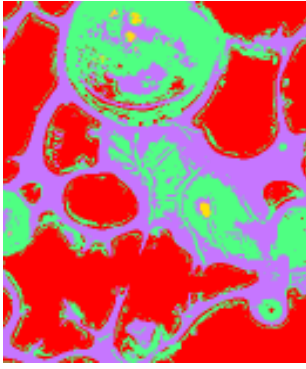


Fig. 2.1: Screenshot of Trainable Weka Segmentation plugin window showing segmentation algorithm applied to an image after training. Purple regions are correctly identified as glass, green regions are identified as “infilled vesicles”, red regions are vesicles, and spots of yellow represent crystals identified by the TWS algorithm.



A: Original classified image

B: Greyscale image. Highlighted classification error yellow circle. Feldspar incorrectly classified as infilled vesicle.

C: Error corrected by hand using brush or fill tool.

Figure 2.2 A – C: Three images showing the process of correcting poorly segmented regions after Trainable Weka Segmentation has been applied.

2.3: Regularity and Solidity descriptors

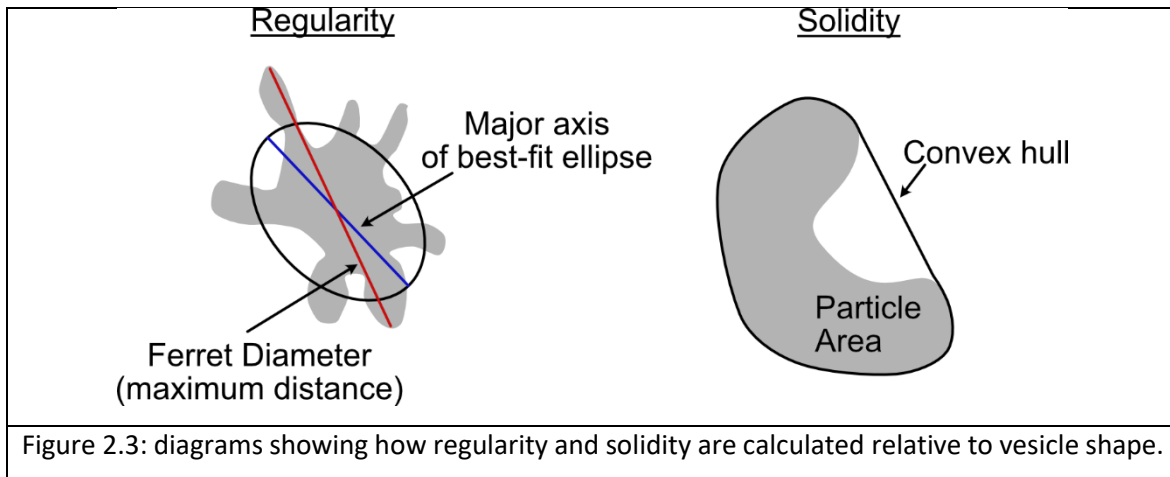


Figure 2.3: diagrams showing how regularity and solidity are calculated relative to vesicle shape.

2.4: Additional vesicle shape plots

Density plots of vesicle shape data from the EC eruption deposits. The shape parameter results for each unit are plotted side by side (Figs. 2.3 – 2.7) to allow comparison between the units for each plot of interacting shape factors.

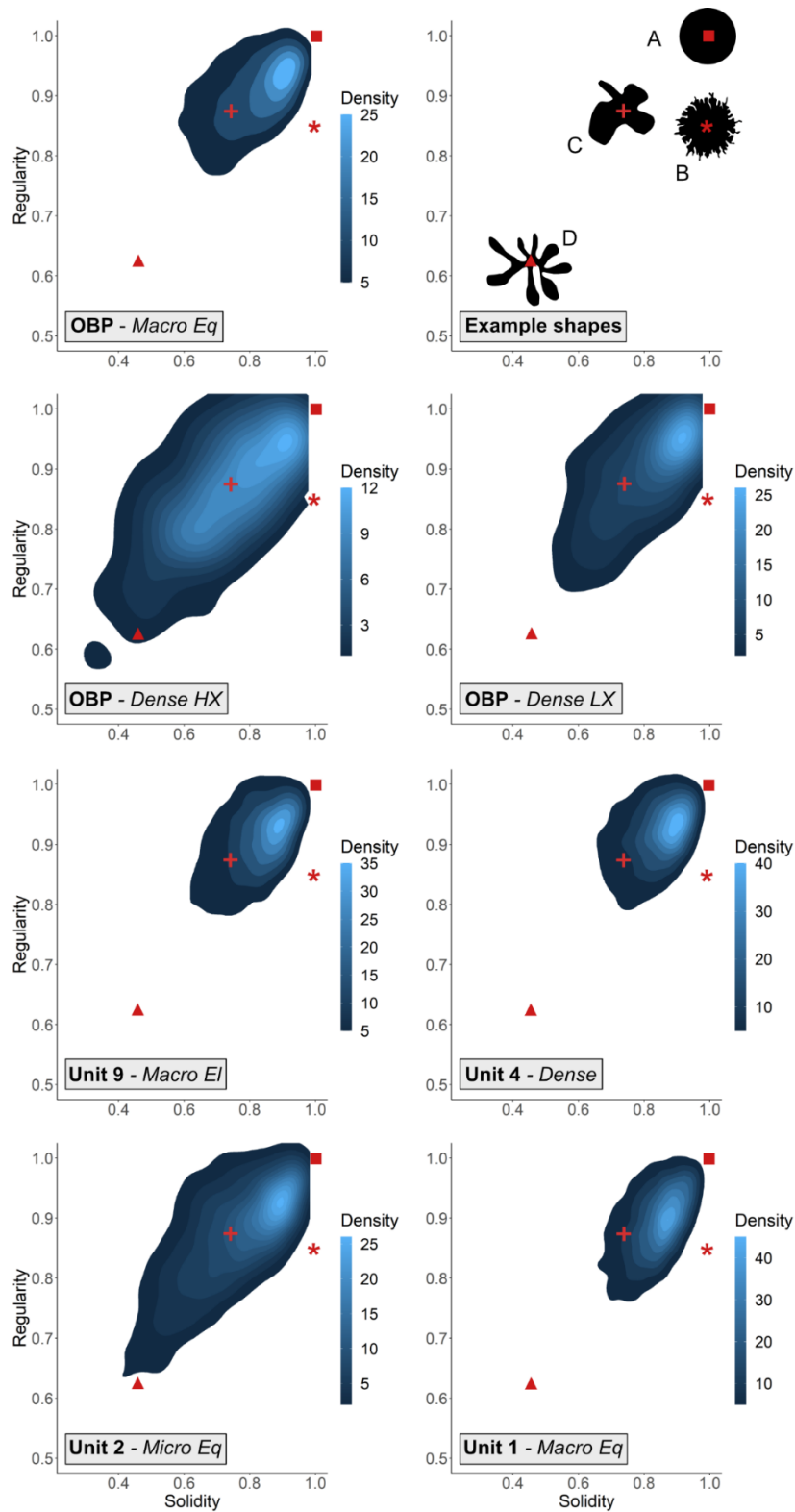


Fig. 2.4 Density plots of regularity vs solidity for samples from units 1,2,4,9, and the Orange-brown pumice (OBP), both high (HX) and low (LX) microlite concentration regions are plotted. Artificial vesicle shapes A-D were generated manually and are shown plotted on the upper right plot in black with red points corresponding to their regularity / solidity values which are overlain on the density plots for reference. Squares correspond to shape A, asterisks to shape B, crosses to shape C and triangles to shape D. Density plots are generated using geom_stat_2d in R-studio with a 2d kernel and 95% cut off, density scales are absolute rather than scaled to max-min density. Micro Eq = micro-vesicular equant, Macro Eq = macro-vesicular equant, Macro El = macro-vesicular elongate. Red dashed line represents regularity = solidity.

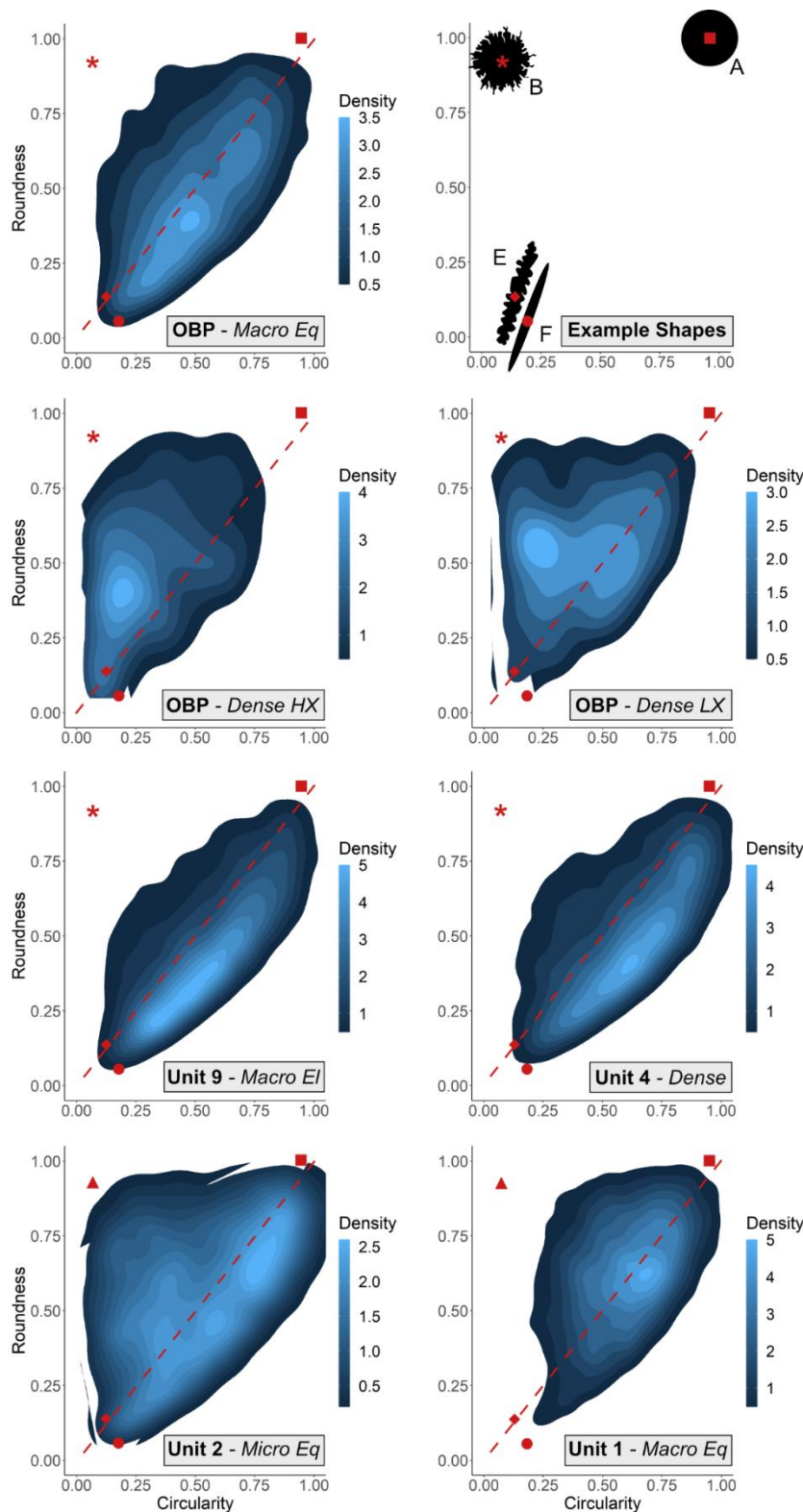


Figure 2.5 – Density plots of roundness vs circularity for samples from units 1,2,4,9 and the Orange-brown pumice (OBP), both high (HX) and low (LX) microlite concentration regions are plotted. Artificial vesicle shapes A, B, E and F were generated manually and are shown plotted on the upper right plot in black with red points corresponding to their roundness / circularity values which are overlain on the density plots for reference. Squares correspond to shape A, asterisks to shape B, diamonds to shape E and circles to shape F. Density plots are generated using `geom_stat_2d` in R-studio with a 2d kernel and 95% cut off, density scales are absolute rather than scaled to max-min density. Micro Eq = micro-vesicular equant, Macro Eq = macro-vesicular equant, Macro El = macro-vesicular elongate. Red dashed line represents roundness = circularity.

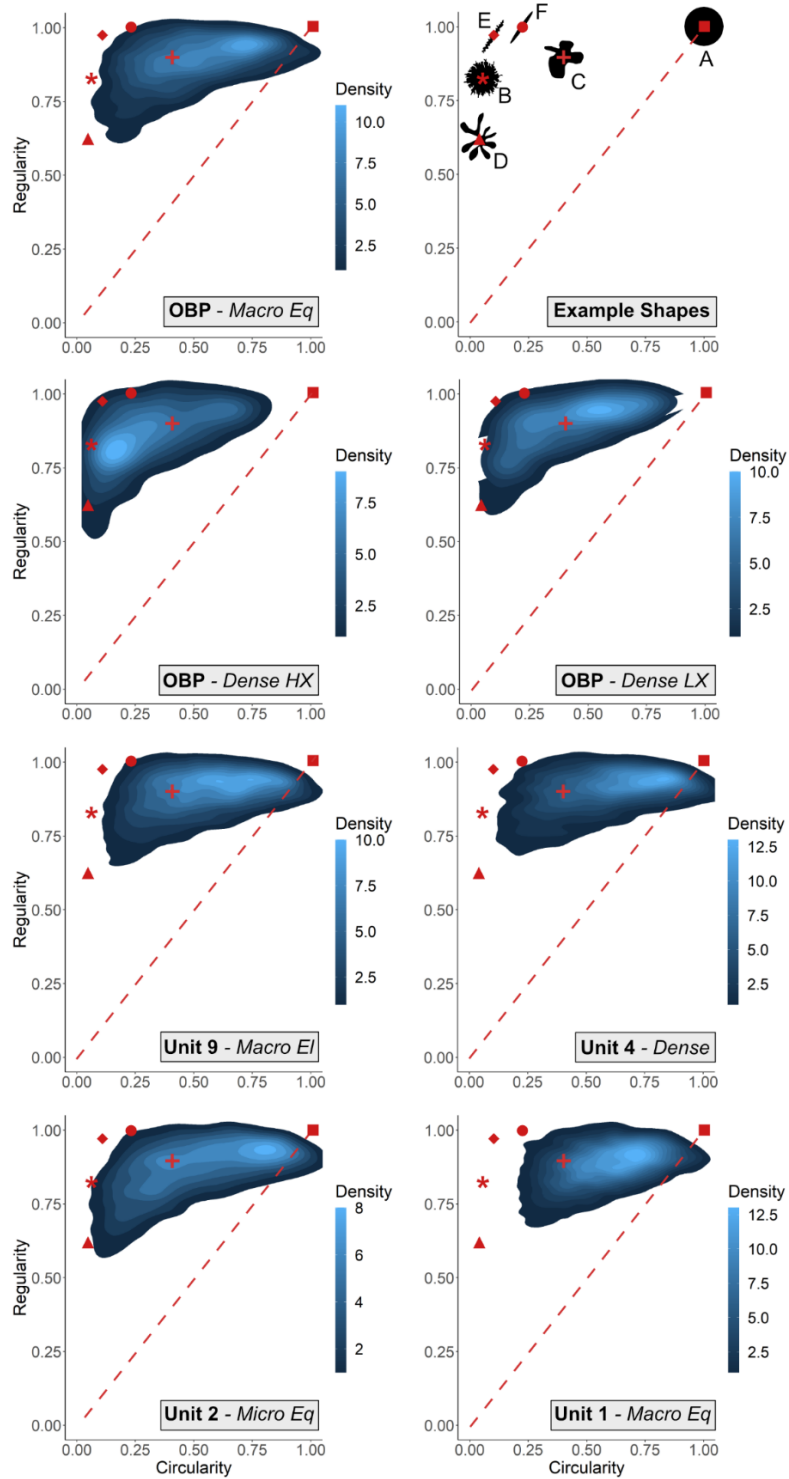


Figure 2.6 - Density plots of regularity vs circularity for samples from units 1,2,4,9 and the Orange-brown pumice (OBP), both high (HX) and low (LX) microlite concentration regions are plotted. Artificial vesicle shapes A, B, C, D, E and F were generated manually and are shown plotted on the upper right plot in black with red points corresponding to their roundness / circularity values which are overlain on the density plots for reference Squares correspond to shape A, asterisks to shape B, crosses to shape C, triangles to shape D, diamonds to shape E and circles to shape F. Density plots are generated using geom_stat_2d in R-studio with a 2d kernel and 95% cut off, density scales are absolute rather than scaled to max-min density. Micro Eq = micro-vesicular equant, Macro Eq = macro-vesicular equant, Macro El = macro-vesicular elongate. Red dashed line represents regularity = circularity.

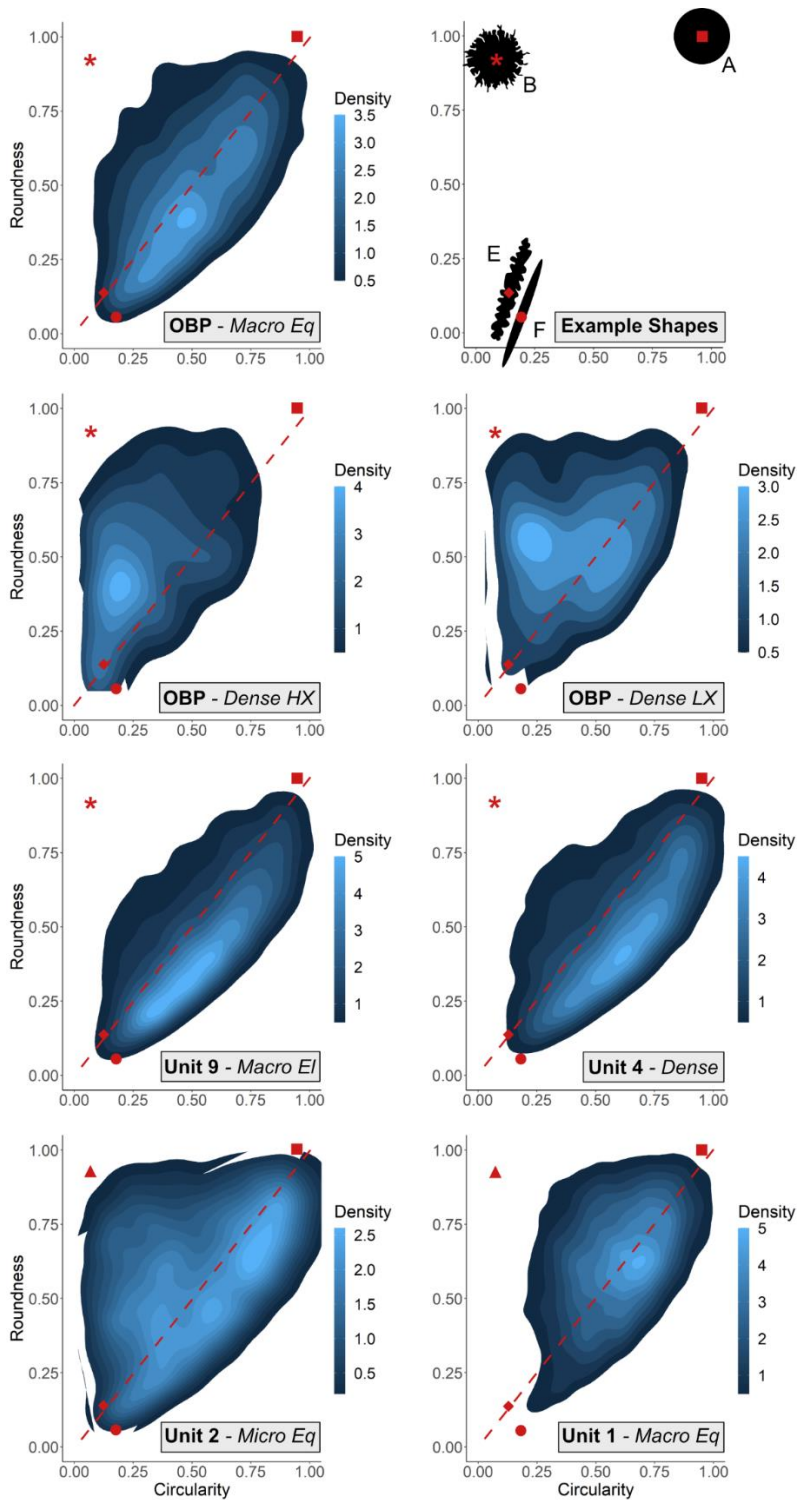


Fig. 2.7 - Density plots of roundness vs circularity for samples from units 1,2,4,9 and the Orange-brown pumice (OBP), both high (HX) and low (LX) microlite concentration regions are plotted. Artificial vesicle shapes A, B, C, D, E and F were generated manually and are shown plotted on the upper right plot in black with red points corresponding to their roundness / circularity values which are overlain on the density plots for reference. Squares correspond to shape A, asterisks to shape B, crosses to shape C, triangles to shape D, diamonds to shape E and circles to shape F. Density plots are generated using `geom_stat_2d` in R-studio with a 2d kernel and 95% cut off, density scales are absolute rather than scaled to max-min density. Micro Eq = micro-vesicular equant, Macro Eq = macro-vesicular equant, Macro El = macro-vesicular elongate. Red dashed line represents solidity = circularity.

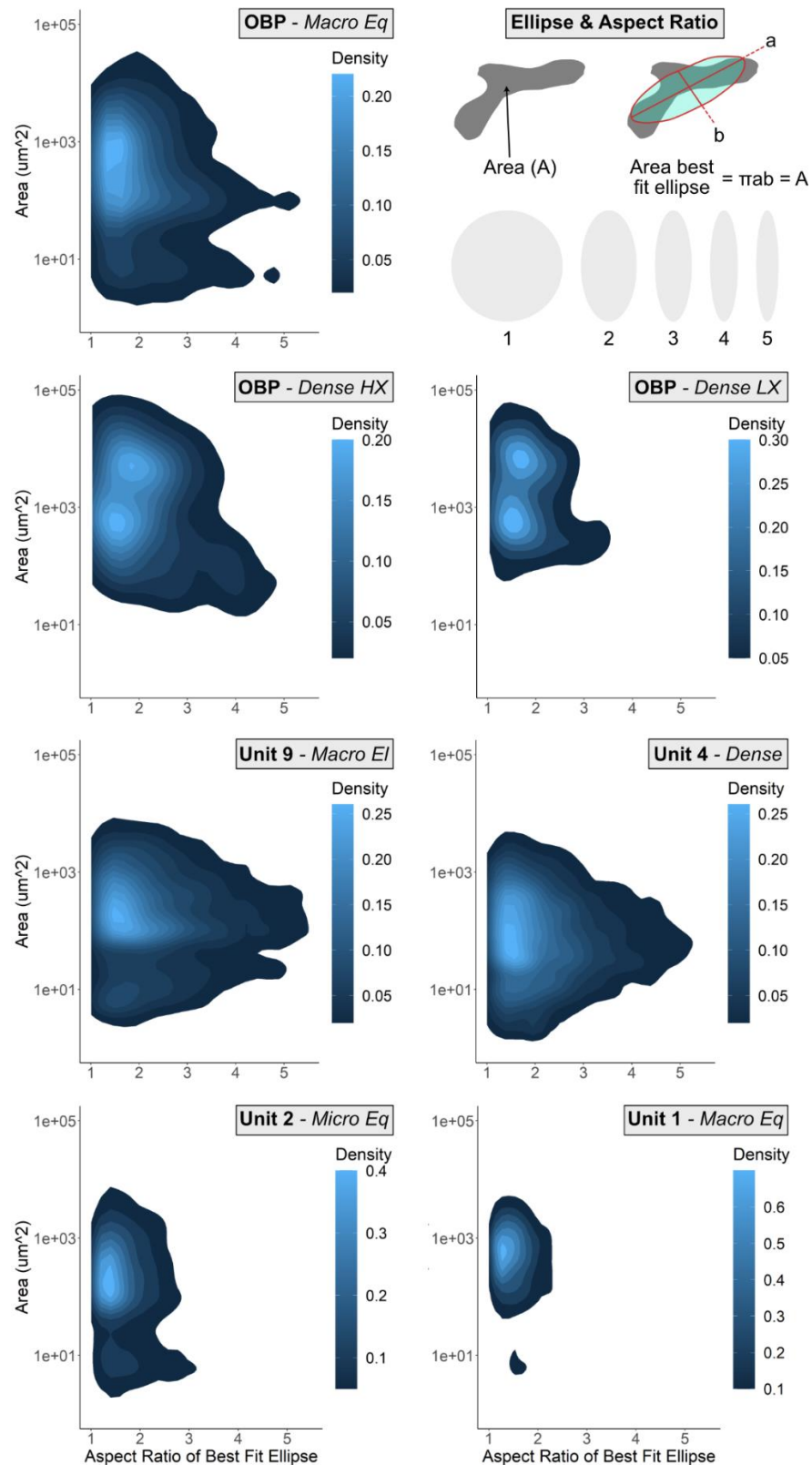


Fig. 2.8 – Density plots of particle area vs aspect ratio of best fit ellipse for samples from units 1,2,4,9 and the Orange-brown pumice (OBP), both high (HX) and low (LX) microlite concentration regions are plotted. Density plots are generated using geom_stat_2d in R-studio with a 2d kernel and 95% cut off, density scales are absolute rather than scaled to max-min density. Micro Eq = micro-vesicular equant, Macro Eq = macro-vesicular equant, Macro El = macro-vesicular elongate. Upper right shows how particle area and area of the best fit ellipse correspond and examples of ellipses corresponding to aspect ratios from 1:1 to 1:5.

[Appendix 3: 2D and 3D studies of the Mingled Fall](#)

Appendix 3.1: XRF data for the Mingled Fall used to calculate DRE from Chamberlain *et al.*, (2020)

Table 3.1: Whole rock data for the Mingled fall from Chamberlain *et al.*, (2020) used to calculate dense rock equivalent density.

Sample	SiO ₂ (%)	TiO ₂ (%)	Al ₂ O ₃ (%)	MnO (%)	MgO (%)	Fe ₂ O ₃ (%)	CaO (%)	P ₂ O ₅ (%)	K ₂ O (%)	Na ₂ O (%)	Total - LOI	Total (%)	Fe Ratio	Density *
615B Ming. L2 Pumice	67.95	0.96	13.69	0.12	1.05	5.88	2.28	0.65	4.39	3.04	93.95	100	0.5	2.54
615A Ming. L2 scoria	52.25	2.89	15.34	0.20	3.59	12.08	6.81	1.15	1.71	3.99	96.94	100	0.35	2.84
607B pumice L3	67.95	0.97	13.26	0.13	1.39	5.58	2.23	0.35	4.24	3.65	95.26	100	0.5	2.54
607C Ming. scoria L3	52.46	2.94	15.14	0.20	3.96	12.43	6.75	0.96	1.67	3.49	96.49	100	0.35	2.85

*Calculated using the method of Lange and Carmichael (1987)

Appendix 3.2: Detail on separation algorithms between basalt and rhyolite regions.

When applying different separation algorithms to each region complexity is added by the presence of bubbles at the boundary between rhyolite and basalt regions, these bubbles must be lumped either into the basalt, or the rhyolite subset. Boundary bubbles are identified within the dataset by applying a basic *Label Analysis* to the BAS_SEP + BIG dataset using a 16-bit unsigned version of BASALT_REGIONS as the intensity image (measuring *Majority* and *Minority*). The output can be sub-divided using *Label to Attribute*, once by the *Majority* intensity value, and once by the *Minority* intensity value. The two are combined using *Arithmetic* to extract only boundary vesicles (those where the intensity value is < 1) using the expression in Fig. 3.1 b.

Because basaltic regions are easier to define due to their thicker melt networks, when the BAS_REGION dataset was examined alongside the greyscale volume it was clear that most vesicles at the boundary were likely more closely associated with the basaltic melt (Fig. 3.1 Q11b). All boundary bubbles were thus classified as lying within basalt regions. Another way to deal with the boundary bubbles would be to capture what proportion of each bubble volume overlaps with the basalt/rhyolite field (using a *Label Analysis*) and assign them to their dominant field. This approach was attempted but led to doubling-up of bubble populations at the boundary and introduced artefacts into the data that were not easily explained / removed. Lumping all boundary bubbles into one material is relatively arbitrary but saves time and reduces complication in onward processing steps. The boundary bubbles are added to the basalt field (the manually drawn field, not the bubble dataset) using *Arithmetic* and the expression in Fig. 3.1 c. This incorrectly removes melt films from the basalt field due to the gaps between bubbles in the boundary dataset. Melt films are added back in using *Or_Image* (Fig. 3.1 d) and the dataset saved as BAS_REG + BOUNDARY. The dataset is manually checked for any other gaps / artefacts caused by the addition of the boundary bubbles and rectified using the loop at Fig. 3.1 Q. 13b. Once happy, the output is saved as BAS + BORDER, and inverted to give the rhyolite region minus border bubbles (saved as RHY – BORDER).

Un-separated bubbles in the rhyolite region are isolated using *Arithmetic* and the equation used in Fig. 3.1 e (saved as RHY_BUBB_NON_SEP). A coarse separation is applied to the rhyolite bubbles and the largest population manually re-combined using the method described in section 4.4.3a. The large rhyolite bubbles are saved out as RHY_BIG. *Separate*

Objects is applied again to RHY_BUBB_NON_SEP to effectively split the remaining rhyolite bubble populations using the loop at Fig. 3.1 Q.14b (save as RHY_GOOD_SEP). To combine the large bubbles with the well separated rhyolite bubbles *Subtract Image* is applied. This removes any voxels that occur in BIG_RHY from RHY_GOOD_SEP so that there is no overlap when the BIG_RHY dataset is added later. This step differs from the standard procedure because we used a different separation between the BIG_RHY and the RHY_GOOD_SEP bubbles. This was because applying a finer separation (e.g., 26_1) splits the largest bubbles to a greater degree and makes the manual re-combination process more time consuming. *Subtract Image* generates a greyscale dataset so an interactive threshold is applied with a range of 1 – 1 to convert it to binary. This output is saved as RHY_SEP_NO_BIG. To combine RHY_BIG and RHY_SEP_NO_BIG (Fig. 3.2), *Add Image* is applied, and the histogram of the output examined to make sure the greyscale range is from 0 – 1 (aka there is no overlap). *Interactive thresholding* is applied to binarize the output with an intensity of 1. The output is saved as RHY_SEP_PLUS_BIG.

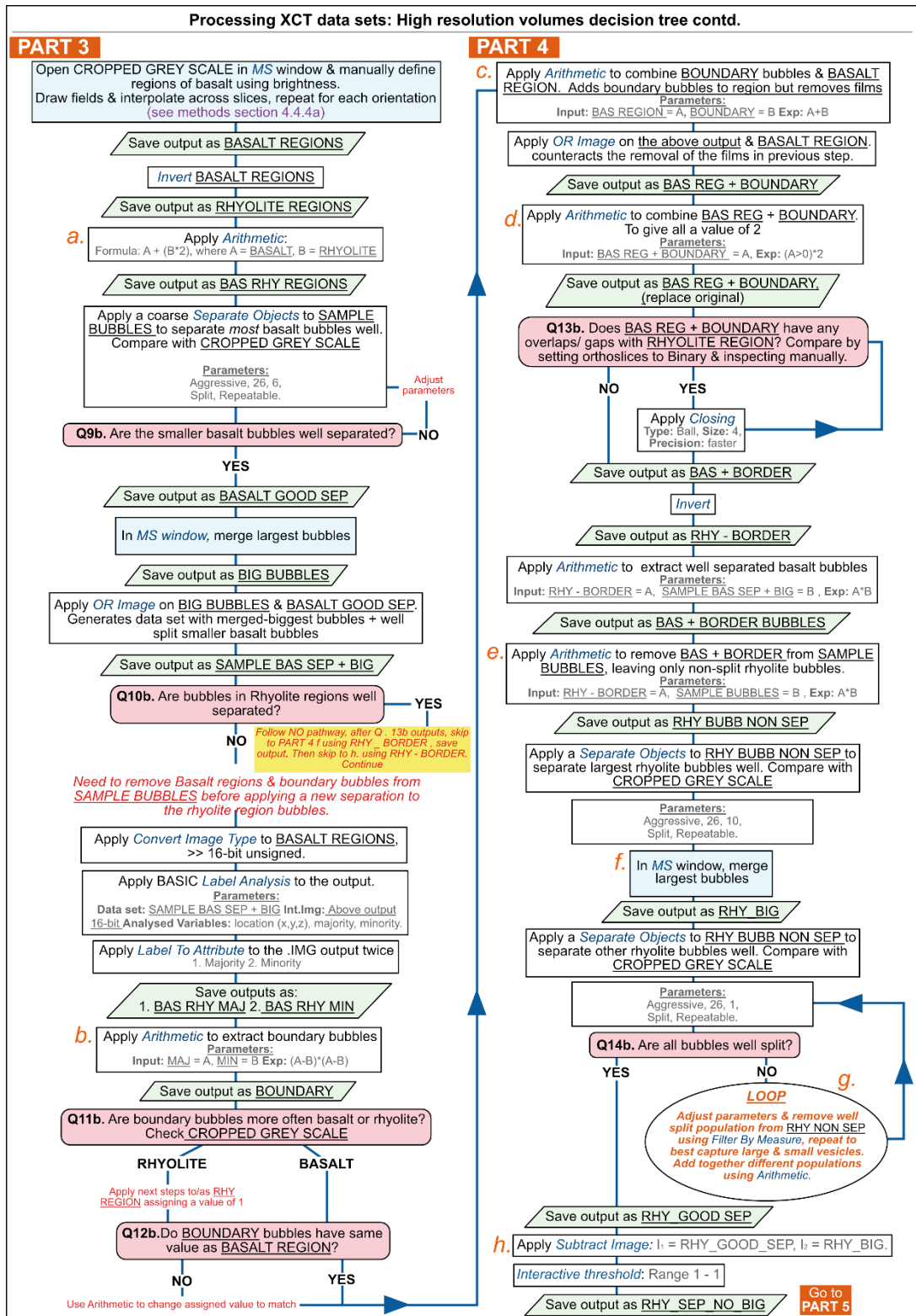


Fig 3.1 X-ray computed tomography (XCT) data processing workflow for extracting bubble volumes from high resolution data in Avizo for clasts with two melt compositions. Blue italicised text is used for names of standard algorithms available in Avizo.

The correctly separated rhyolite and basalt bubbles are combined using *Arithmetic* and the equation in Fig. 3.2 a. This gives the rhyolite an intensity value of 1 and the basalt an intensity value of 2. Applying different separation algorithms across the two adjacent

regions (basalt and rhyolite) can lead to the generation of overlapping voxels on re-combination. If there is any overlap, it will be identified in the output of this *Arithmetic* as a population with an intensity value of 3 (Fig. 3.3 A). *Interactive thresholding* (from 3 – 3) is applied to filter out any overlap at the boundary (see Fig. 3.3 B) – saved as OVERLAP. As the boundary bubbles were grouped with the basalt the overlapping voxels are also assigned to basalt rather than rhyolite. Voxels in the OVERLAP dataset therefore need to be removed from the rhyolite bubbles dataset. The overlap is removed from RHY_SEP_PLUS_BIG using *Subtract Image*, with OVERLAP as the second input dataset. The greyscale output is binarized using *Interactive Thresholding* and the *Arithmetic* from Fig. 3.2 a reapplied on the new dataset. The output now contains only voxels with values 1 – 2 as all overlap has been removed (Fig. 3.3 C). This output is saved as BAS + RHY_BOUNDARY_SOLVED.

PART 5

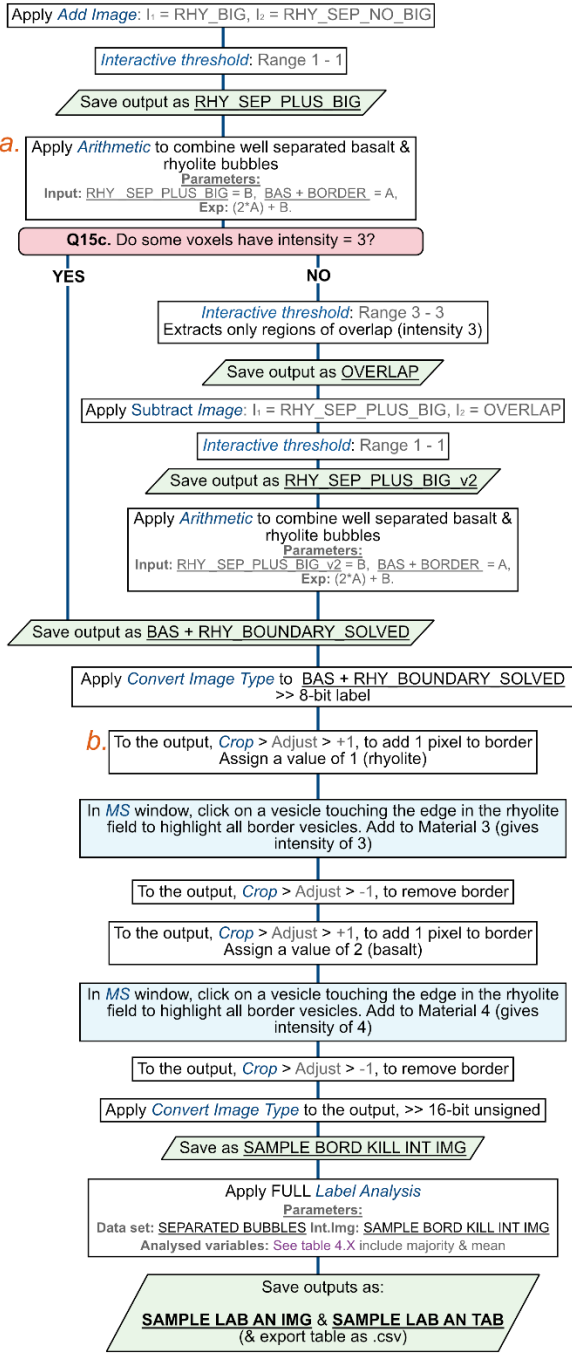


Fig.3.2 X-ray computed tomography (XCT) data processing workflow for extracting bubble volumes from high resolution data in Avizo for clasts with two melt compositions. Final stages of recombination of basalt and rhyolite regions and removing any noise at the border. Blue italicised text is used for names of standard algorithms available in Avizo®.

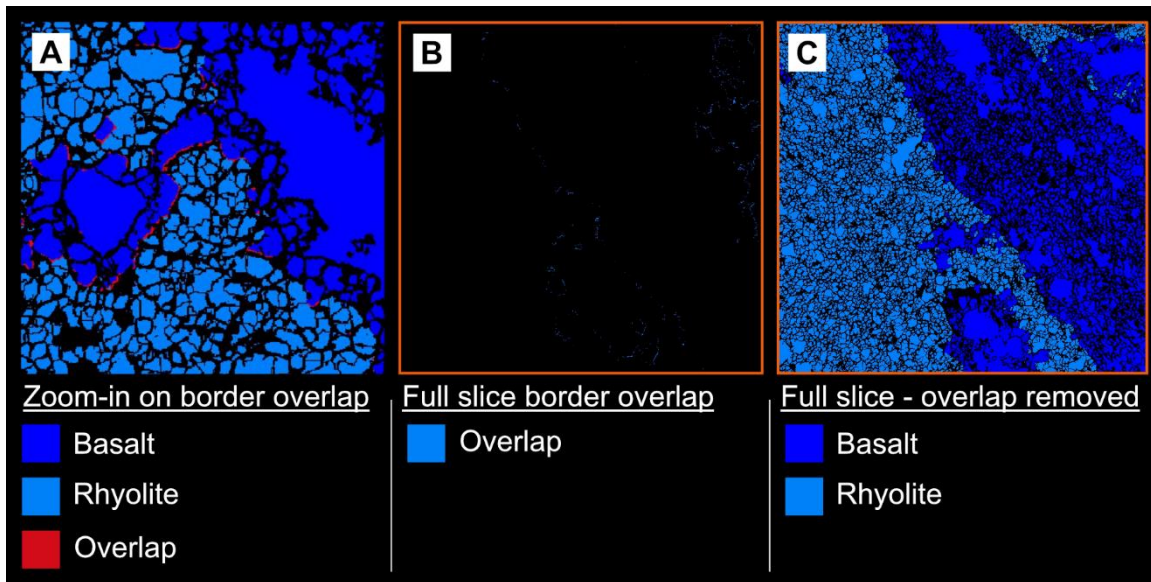


Fig. 3.3 showing regions of bubble overlap at the border between basalt and rhyolite. **A:** zoomed in view showing overlap with an intensity value of 3 (red). **B:** showing a full slice view of small regions of overlap once extracted using thresholding (blue). **C:** full slice view once overlap removed showing only basalt and rhyolite.

[Appendix 4 – Initial Petrography of the 2020-21 La Soufrière Dome rocks](#)

The following report is presented exactly as it was distributed to members of the UWI SRC and broader research group on the 19th April 2020. Much of the information collated here was presented informally during March and early April 2020 during meetings with UWI SRC and collaborators from Oxford, Plymouth and UEA. Figure numbers were added during compilation of the thesis but are not referenced in the main text.

St Vincent 2021 Dome Crystal Populations:

Degraded textures:

Are most prevalent:

- Near to macro Fe-Ti oxides, both in crystal clots and those free in the groundmass
- Near to vesicles
- Near to fractures (only some fractures, others are clearly post cooling)
- Within crystal clots only along boundaries that may be connected to the exterior
- This includes degree of degradation of opx microlites. More degraded near the above features.

Large crystal clots - heavily degraded: approx. 15% of rock (vesicle free)

Clinopyroxene dominated with zoned Ca-rich feldspar and Fe-Ti oxides

Exterior edges of Cpx crystals in clots have rims of Mg-rich opx and Mg oxides in a breakdown/reaction texture. More pronounced where sharing a contact with Fe-Ti Oxide, but present on all Cpx crystal faces exposed to the groundmass texture. (SVG-16-2-51) Degradation reaction goes Cpx-Opx + Fe-Mg Oxides-Silica. Silica only occurs at most extreme version of this alteration texture. (SVG-2021-16-4-11)

Where Cpx makes contact with irregular shaped (melt inclusions?) Ca-rich Feldspar, sometimes see a minor version of the breakdown texture propagating into the cpx: feathery degraded texture also present at edges not in contact with Fe-oxides. (SVG-2021-16-4-01) Reaction with melt? Contact with exterior environment via crystal boundaries?

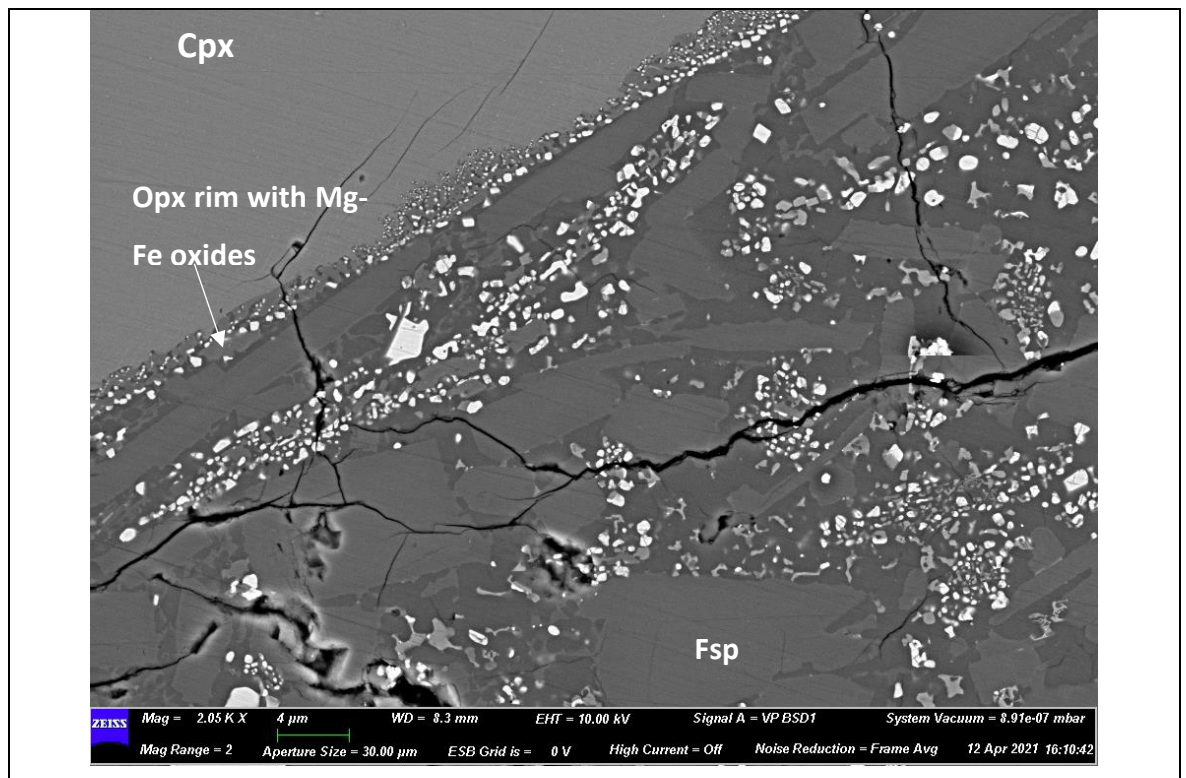


Fig. 4.1: Showing degraded rim on Cpx macro-phenocryst containing Opx and Mg-Fe oxides. Feldspar microlites are present with some devitrification of glass. In Far right, clumps of oxides and opx are remnants of degraded Opx microlites.

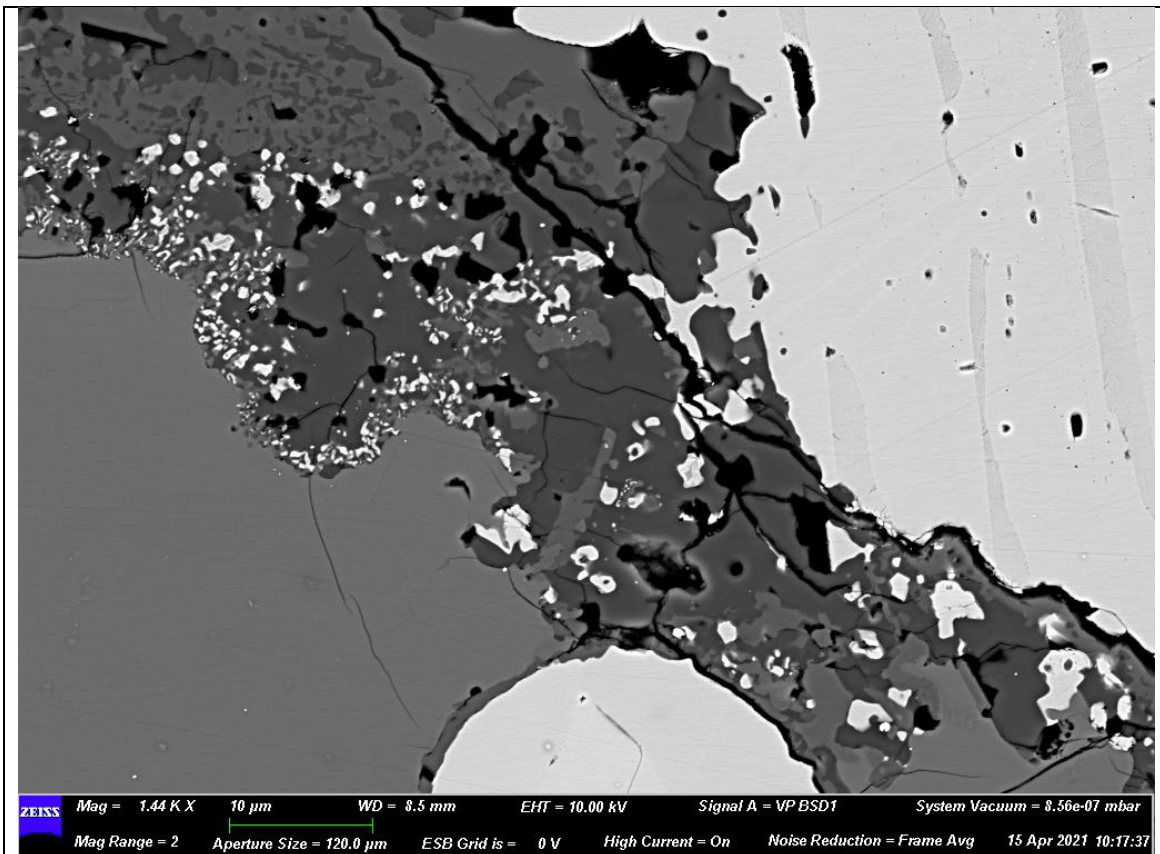


Fig. 4.2: Close up of extreme degraded region between Cpx and Fe-Ti oxide with silica (darkest grey) Opx and Oxides at Cpx breakdown rim.

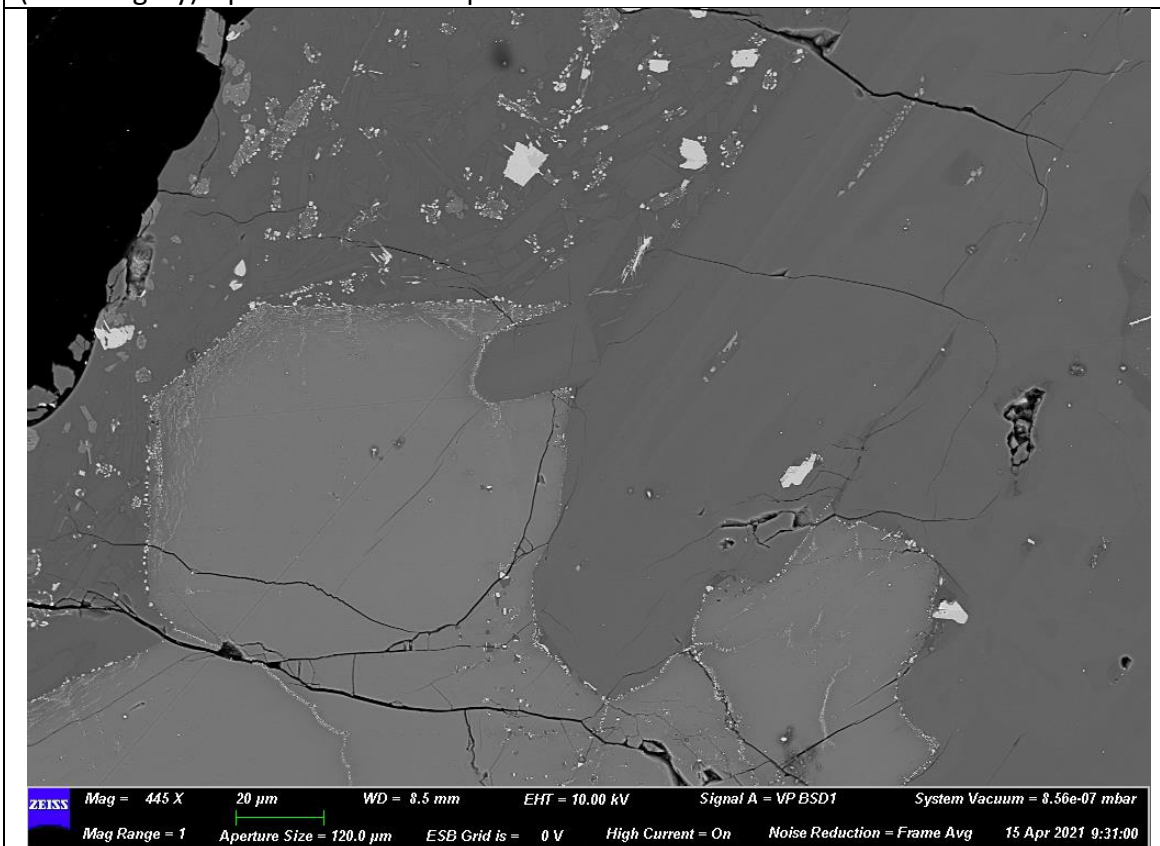


Fig. 4.3: Less extreme version of Cpx degradation “feathery” texture at rim picked out by bright oxides. No large oxide in close proximity.

Fe-oxides have almost vesicular appearance at exterior edges with irregular crystal boundaries, Fe-oxides can have vesicular irregular crystal margins internally to the clots if the Fe-Ti oxide makes contact with the exterior of the clot either protruding or via cracks, particularly dramatic textures where in contact with Cpx as opposed to Ca-feldspar. (SVG-16-2-49). **Approx. 3% of rock (vesicle free), from 20 – 600 μm**

Smaller, fully entrapped Fe-Ti oxides within larger cpx/feldspar lack this texture.

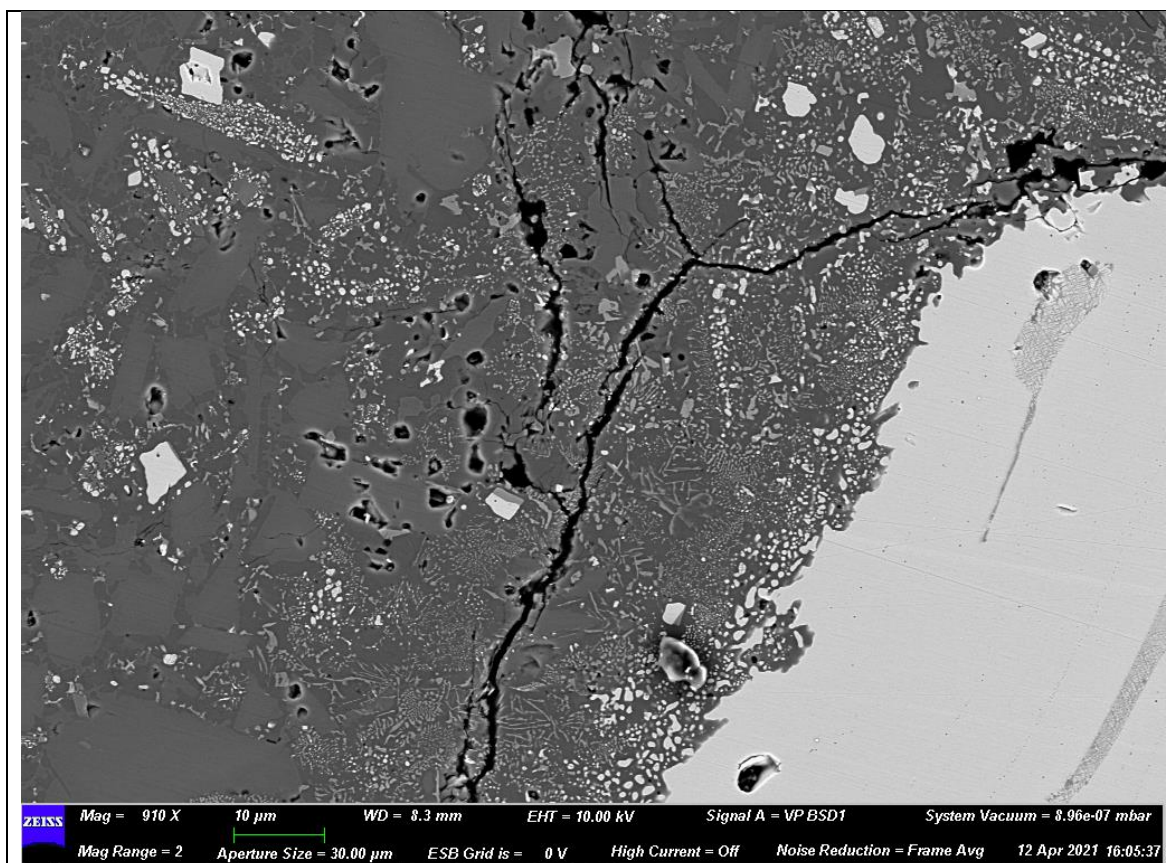


Fig. 4.4: Fe-Ti oxide macro-phenocryst with very irregular degraded exterior, regions closest to degrading Oxides have high proportions of broken down Opx microlites and almost symplectitic Opx. Smaller oxides are less affected and feldspar microlites are also unaffected.

Large zoned Ca-rich feldspars lack altered rims but have melt inclusions often containing immiscibility textures containing Cpx and Mg-rich oxides. Sometimes containing apatite, Cu-sulphides or Cu-oxide. (SVG-2021-16-4-04) **20% of total rock (vesicle free)**

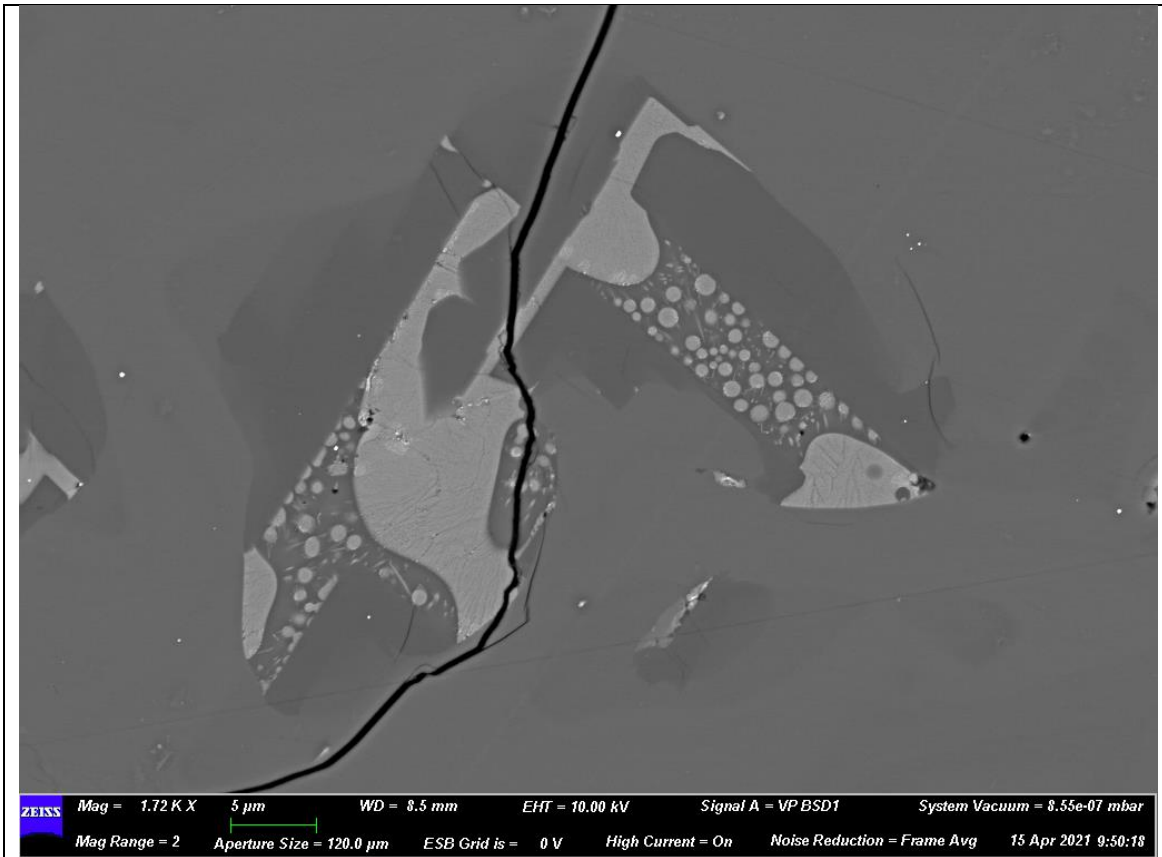


Fig. 4.5: Immiscibility textures in melt inclusion in large zoned feldspar phenocryst. Rounded features are Mg-rich oxides.

Large crystal clots – less degraded: Included in the large Ca-zoned feldspars make up to 20% of the rock (vesicle free).

Dominated by Ca-rich zoned feldspar, as above but with less cpx and fewer oxides = less opportunity for weird reaction textures. Even in seemingly fully entrapped melt inclusions, get immiscible textures.

Feldspars can contain cracks which have subsequently been infiltrated by new melt + microlites (feldspar, Fe-oxides, cpx). New melt forms Na-rich layer filled by inner channel containing very tiny oxides (assumed from greyscale) and this is what hosts the microlites. (SVG-2021-16-5-51)

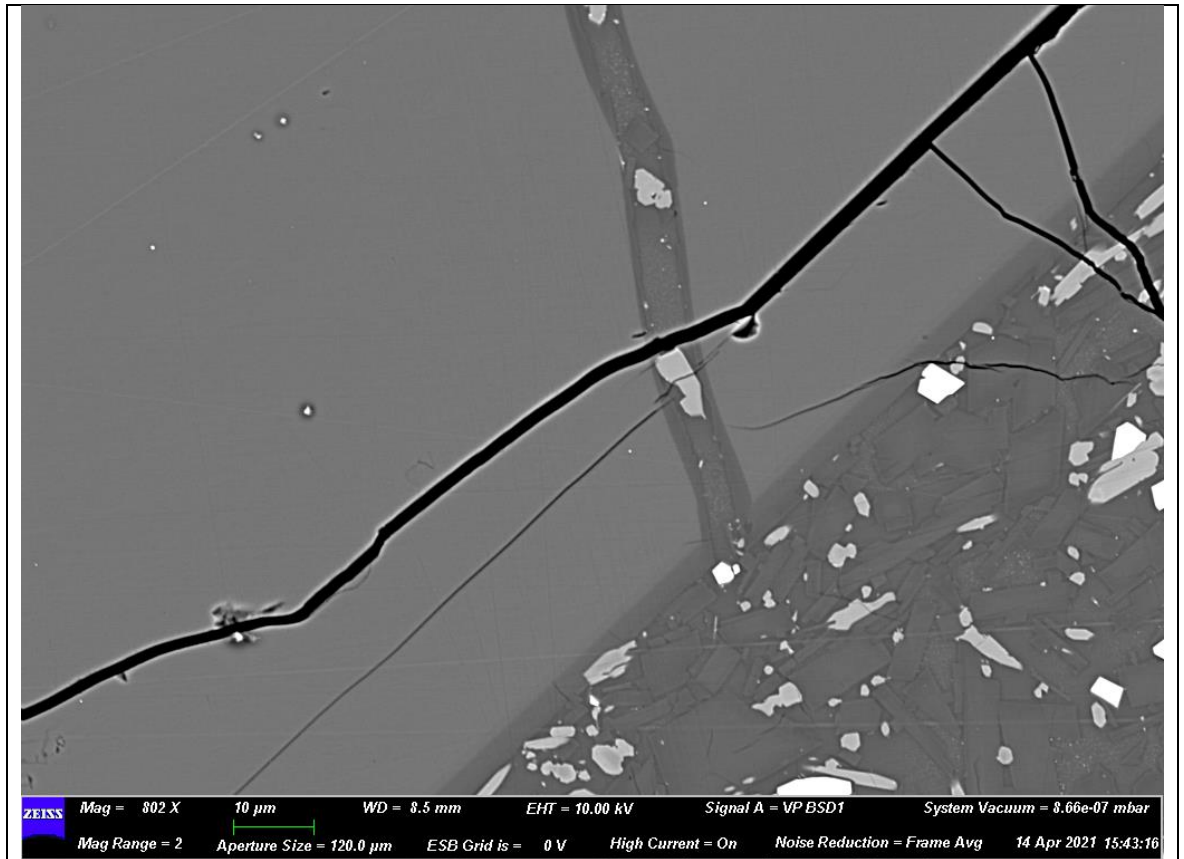


Fig. 4.6: Healed fracture in feldspar, infilled by melt and microlites.

Individual / paired phenocrysts

Cpx with feathery Mg-oxide breakdown texture at rims. Mg-rich Opx forms very fine layer at edges of crystals / around Mg-oxides. Larger Mg-oxides at exterior edges of crystals but also found as tiny inclusions along cleavage(?) and internally in irregular wavy patterns giving the feathery texture. Not associated with cracks that are often seen in Cpx phenocrysts (cracks must be post-cooling). (SVG-2021-16-5-41). **Included with clots up to 15% of rock (vesicle free)**

Can contain melt inclusions with Cu-sulphides and apatite. (SVG-2-21-16-4-28)

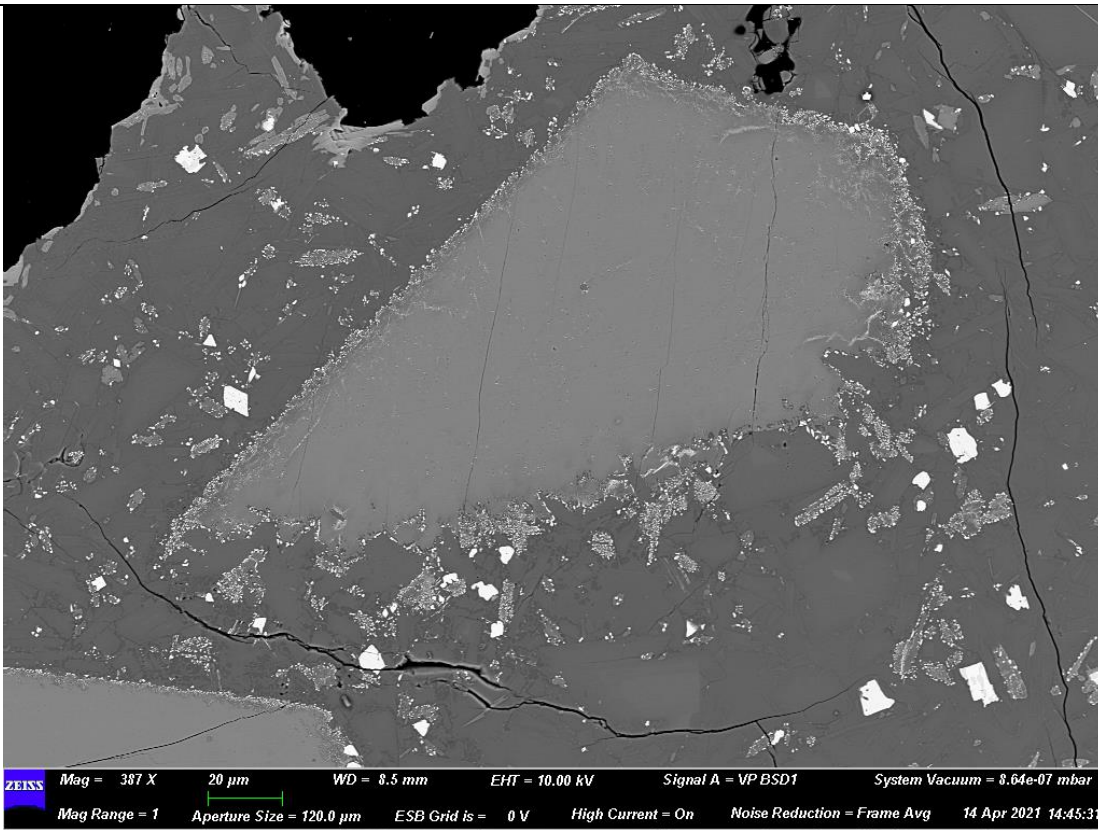


Fig. 4.7: Cpx macro-phenocryst (fragment) with degraded rims showing “feathery” texture, darker rim just visible is Mg-rich Opx. Upper left = vesicle with Cpx growing at the edge.

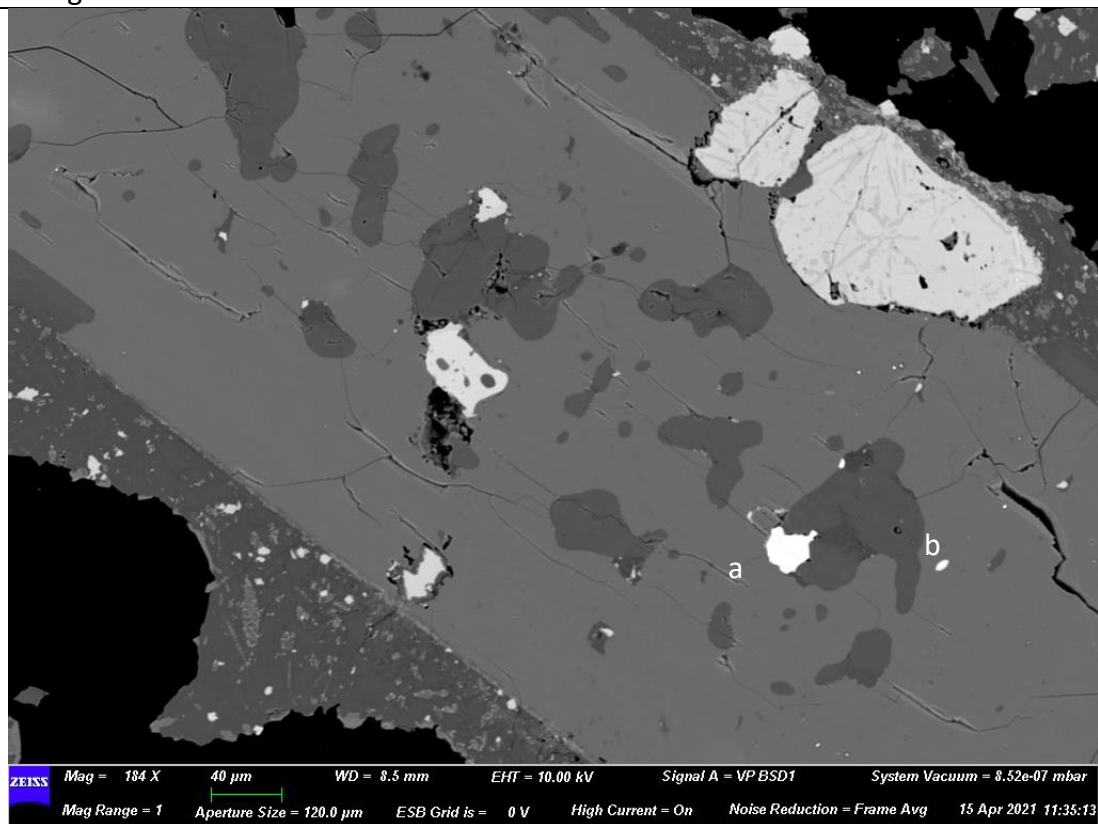


Fig. 4.8: Cpx with melt inclusions, Copper sulphide (a) and Fe sulphide (b) Degraded rim just visible in lower left, Fe-oxide vesicular degradation just visible upper right.

Symplectic Forsterite. Symplectites are extremely Mg-rich and form within and at edges of crystals. Also see a forsterite (could be really Mg-rich opx) rim with smaller more equant Mg-oxides at the external crystal face. Symplectites become thicker oxide zones where in close proximity to a potential fluid pathway e.g. near cracks. (SVG-16-7-10) rare. **Less than 2% of the rock.**

Potential Olivine with feathery oxide breakdown textures. Rounded crystals with no obvious cleavage, exhibit same breakdown texture as Cpx crystals, smaller than symplectic forsterite (SVG-2021-16-4-30).

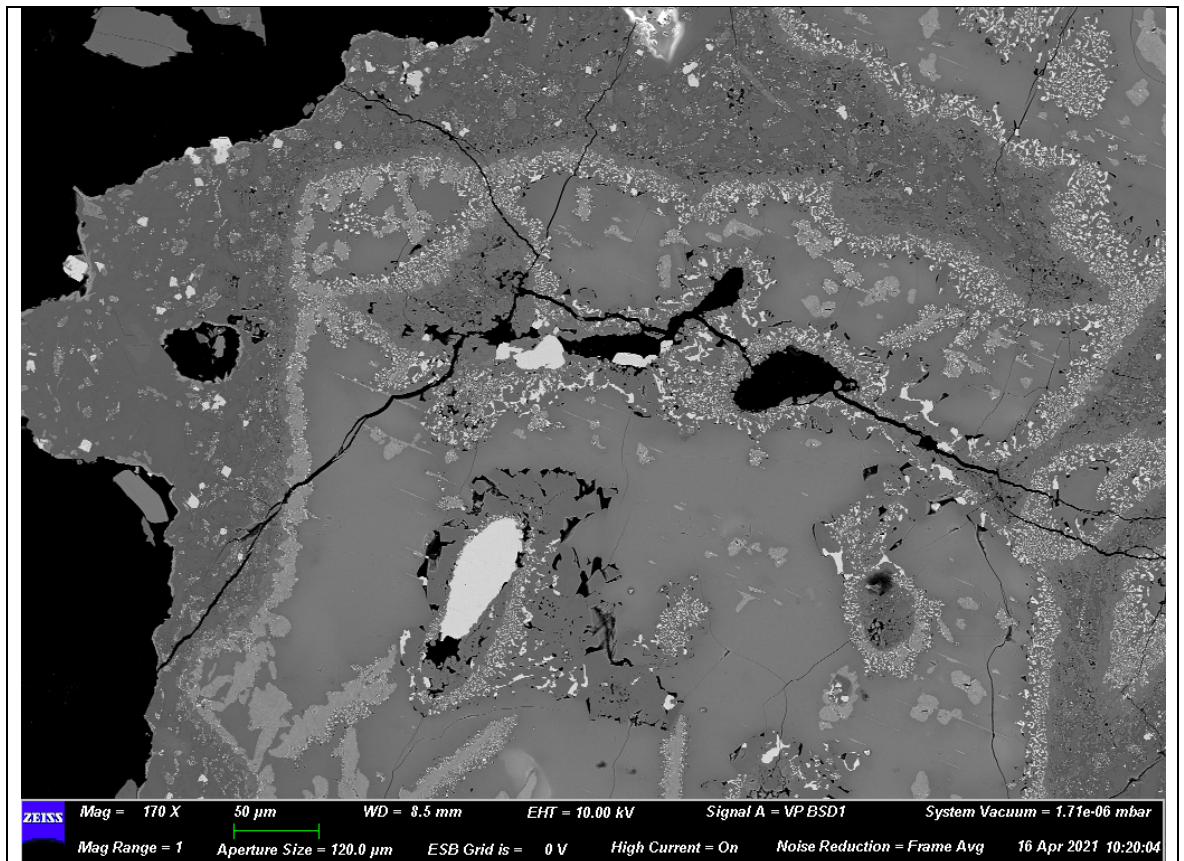


Fig. 4.9: Symplectic forsterite with internal vesicles/void space. Oxide symplectites are thicker/more cohesive at margins with void space.

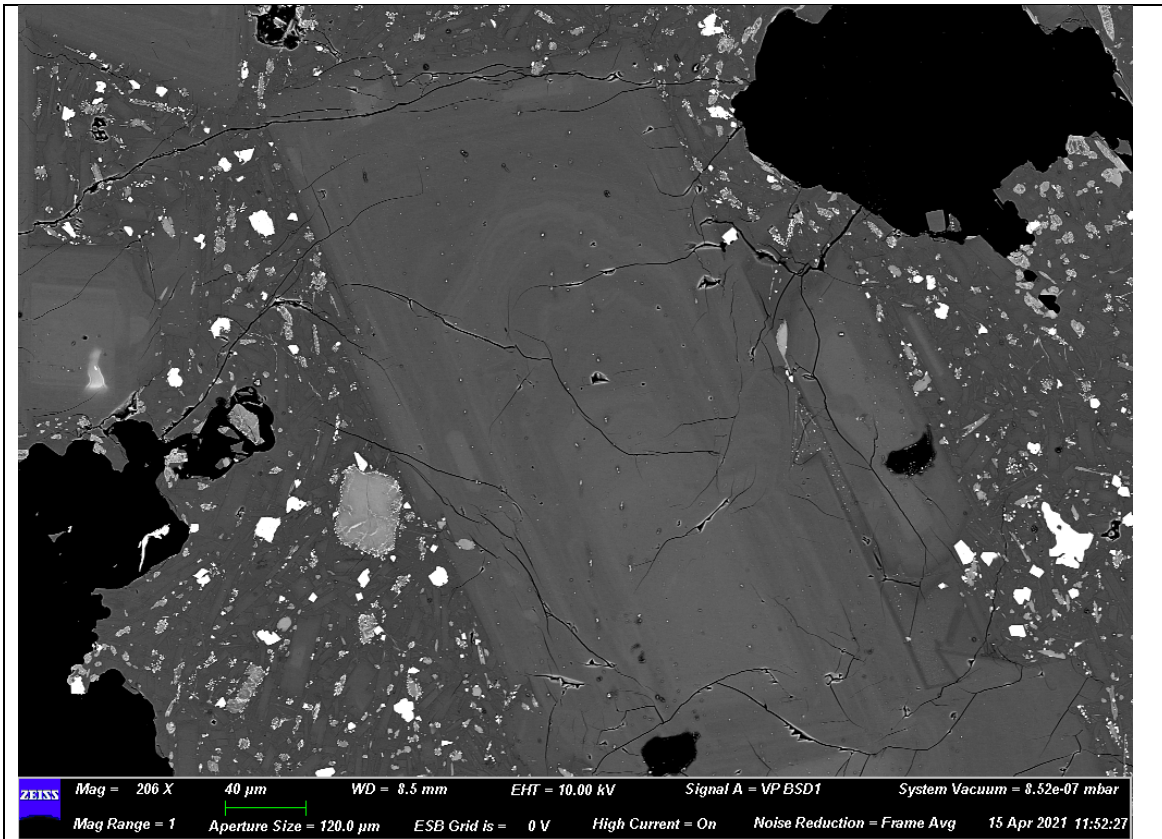


Fig. 4.10: Zoned feldspar macro-phenocryst with smaller potential olivine micro-phenocryst to the left, pale grey with feathery degradation texture at rim.

Fe-Ti oxides. Have irregular crystal surfaces and are surrounded by the vesicular-ish texture described above for crystal clots. All oxides of this size loose in groundmass exhibit this degraded texture. (SVG-2021-16-7-19)

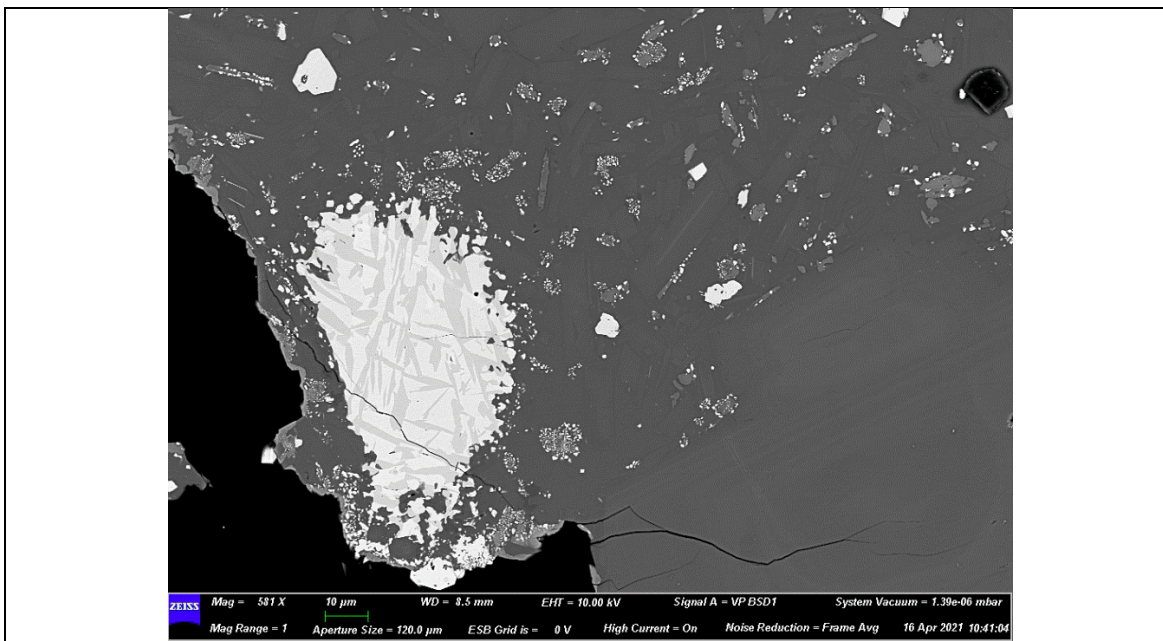


Fig. 4.11: Fe-Ti oxide showing extreme degradation at rim within groundmass. Opx microlites nearby are all degraded to some extent, closest are most degraded.

Groundmass: Approx. 62% of solid rock

Larger Ca-core zoned feldspars have a tabular shape and lack complex zoning of larger feldspars. Ca-rich cores range from tabular with rounded corners, to irregular polygons. 20 x 50 μm (SVG-2021-16-2-16) **approx. 5% of groundmass**

Smaller Na-rich feldspars. More often needle-like than larger population but range from elongate to tabular and sometimes equant shapes. Potentially have a paler outer zone but this may just be an edge effect. Less than 20 μm (SVG-16-2-53) **Tabular larger population of feldspars approx. 30-35% of groundmass. Smallest, equant – acicular feldspars 5% of groundmass.**

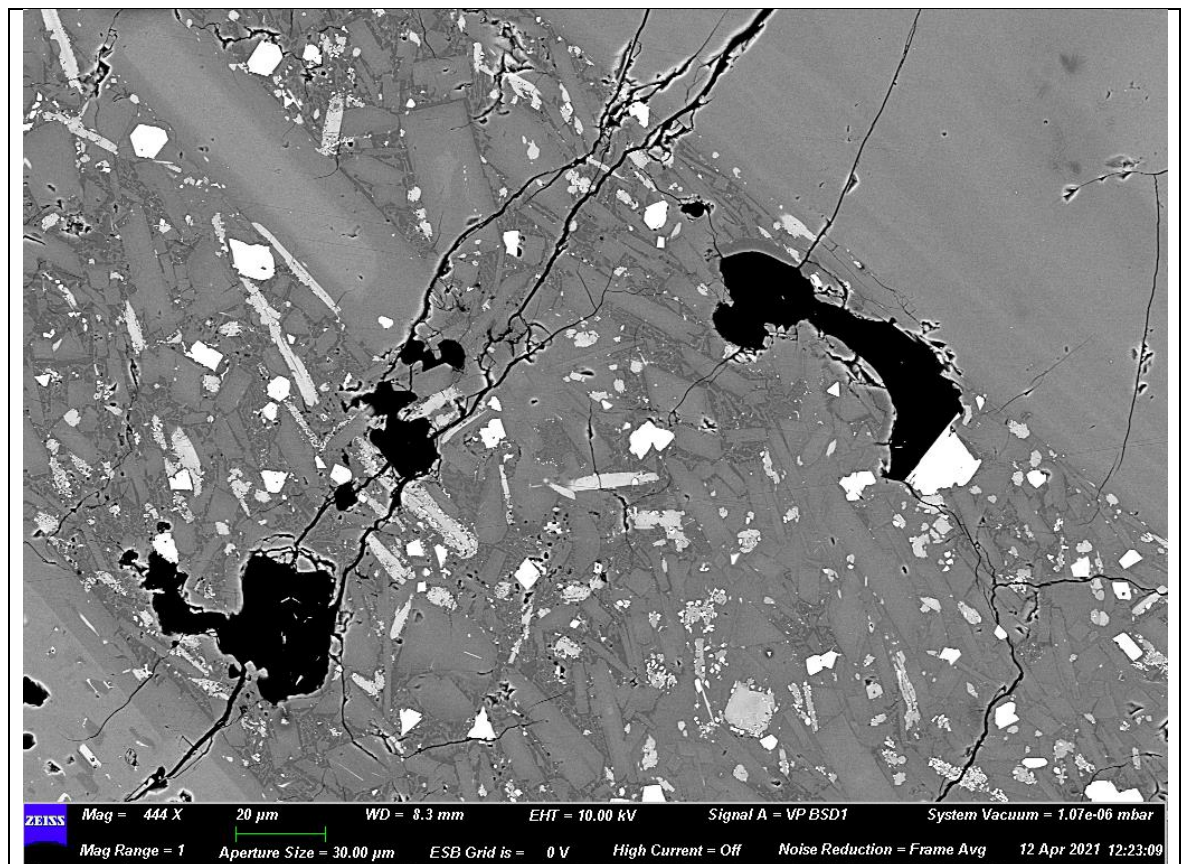


Fig. 4.12: Feldspar microlites in groundmass, larger crystals show tabular form and contain Ca-rich cores. Some patches of devitrification visible. Upper right is edge of large complex zoned feldspar.

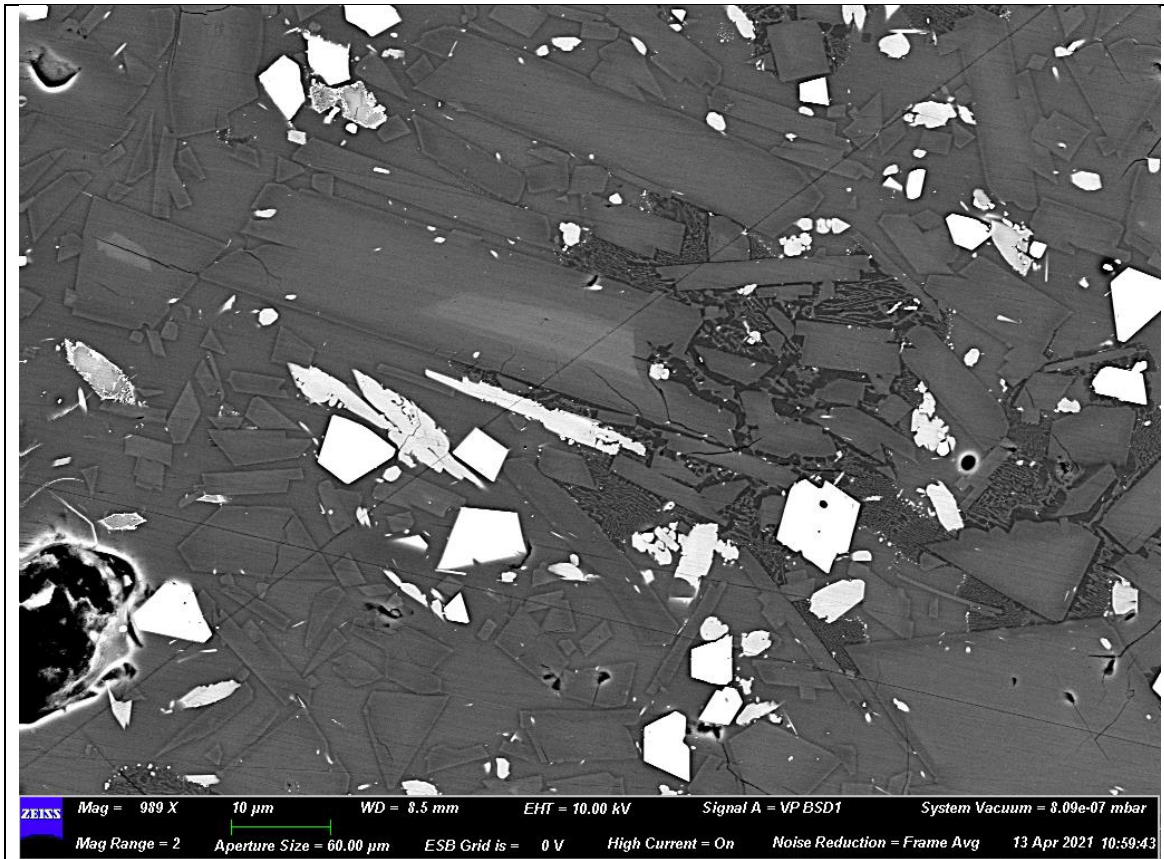


Fig. 4.13: Examples of zoned feldspar microlites with Ca-rich cores of varying shapes and potential edge-effect / zoning on smallest feldspar microlites just visible. Devitrifying glass visible as darkest patches with irregular feldspar grids/irregular patterns.

Equant oxides: Fe-Ti (some variation on Mg content) oxides often more equant shapes, some hexagonal. Lots of touching pairs of ilmenite and magnetite. (SVG-2021-16-4-15) **10 % of groundmass.**

Needle-like oxides. Fe-rich, some Mg. Form acicular / needle-like oxides, very fine, can form as clusters between other groundmass crystals. Maybe max 10 µm long, less than 1 µm wide. (SVG-2021-16-4-12) **<1% of groundmass.**

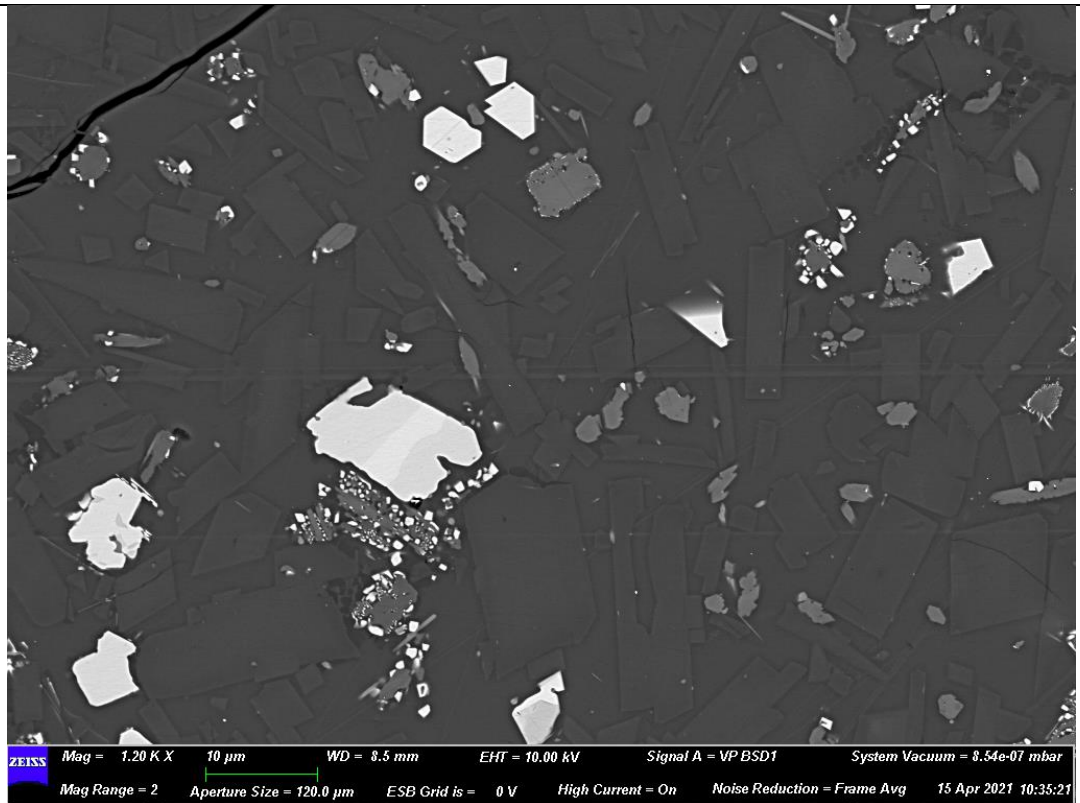


Fig. 4.14: Oxides from groundmass population lack degraded texture of larger equivalents and often show ilmenite-magnetite shared boundaries. Typically have more equant shapes.

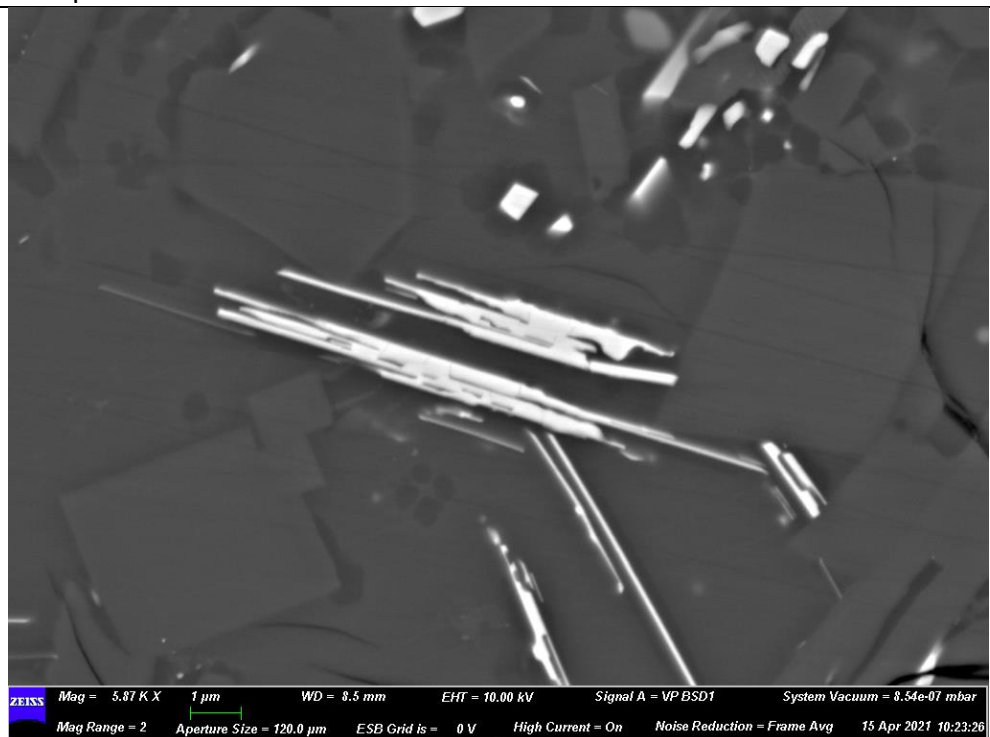


Fig. 4.15: Fe-Ti oxide needles. Rarer than equant oxides in groundmass and mostly found close to degraded textures. Can also see dark patches of potentially devitrifying glass around oxides.

Opx – not breaking down: Mg-Rich Opx. Elongate crystals common but most are sub-anhedral. Also often get rounded more equant sections. **5% of groundmass total, but more common further away from “fizzy” oxides & cpx macrocrysts.**

Breaking down Opx – Mg-rich but also can contain Ca, Na and Al – no potassium). Oxides forming the feathery texture in less broken-down examples seen in larger Cpx, sometimes following cleavage (SVG-16-2-59). Some are completely disaggregated to clumps of oxides and Opx. (SVG-16-4-05) total breakdown. **15% of groundmass, but up to 20% in regions close to “fizzy” oxides & cpx macrocrysts (which lack non-degraded opx).**

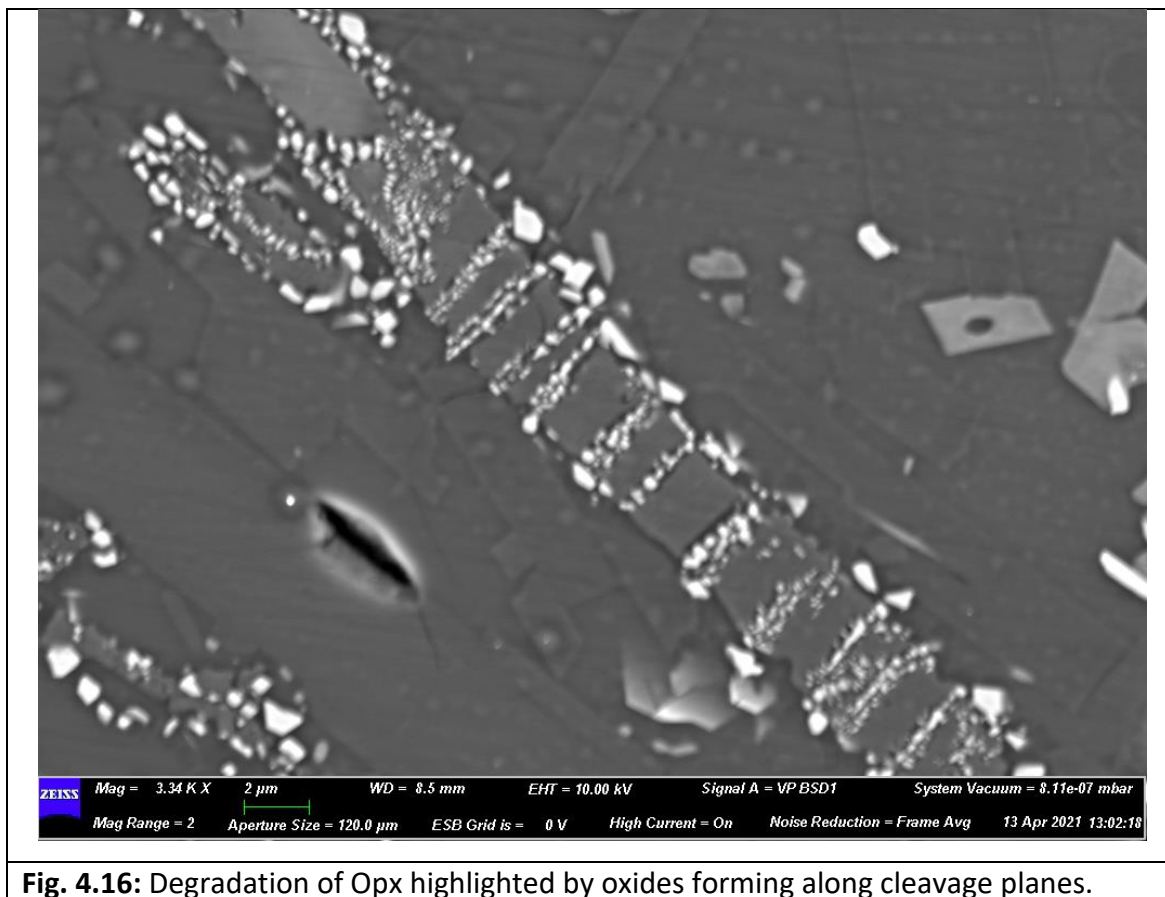


Fig. 4.16: Degradation of Opx highlighted by oxides forming along cleavage planes.

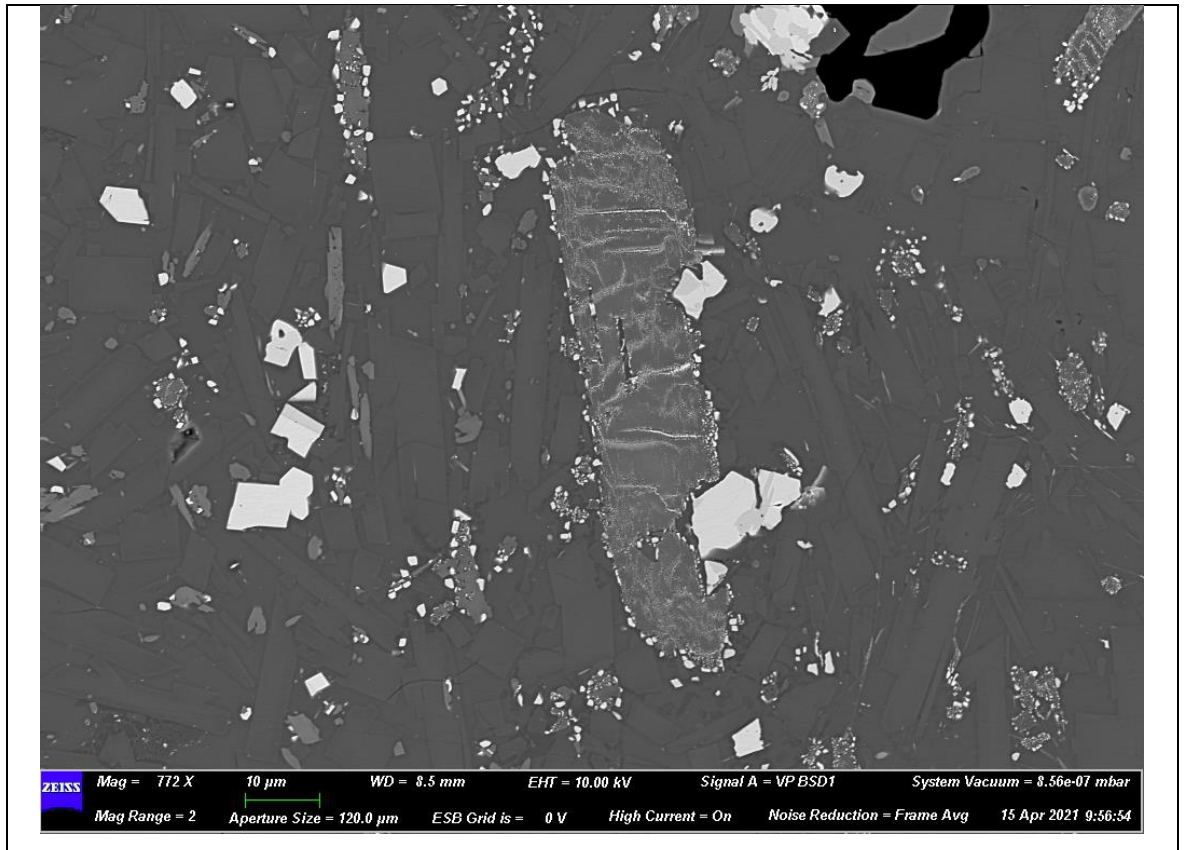


Fig. 4.17: Different degrees of Opx degradation. Smaller ones with little evidence of degradation on the left. Central is a larger Opx showing feathery degradation texture and in lower right, almost totally degraded example appears as clump of oxides and Opx.

Groundmass textures / features

Patches of devitrification of glass to needle-like/grid pattern Na feldspar. (SVG-16-2-53 – also shows zoning in feldspar micro-phenocrysts and feldspar microlites) < 5% of rock, <2% = cristobalite phase.

Cpx crystallising on edges of vesicles, breaking down to Opx and oxides as you penetrate into the groundmass. (SVG-2021-16-5-34)

Tiny equant patches of glass between oxides and smallest feldspar microlites. Al-rich.

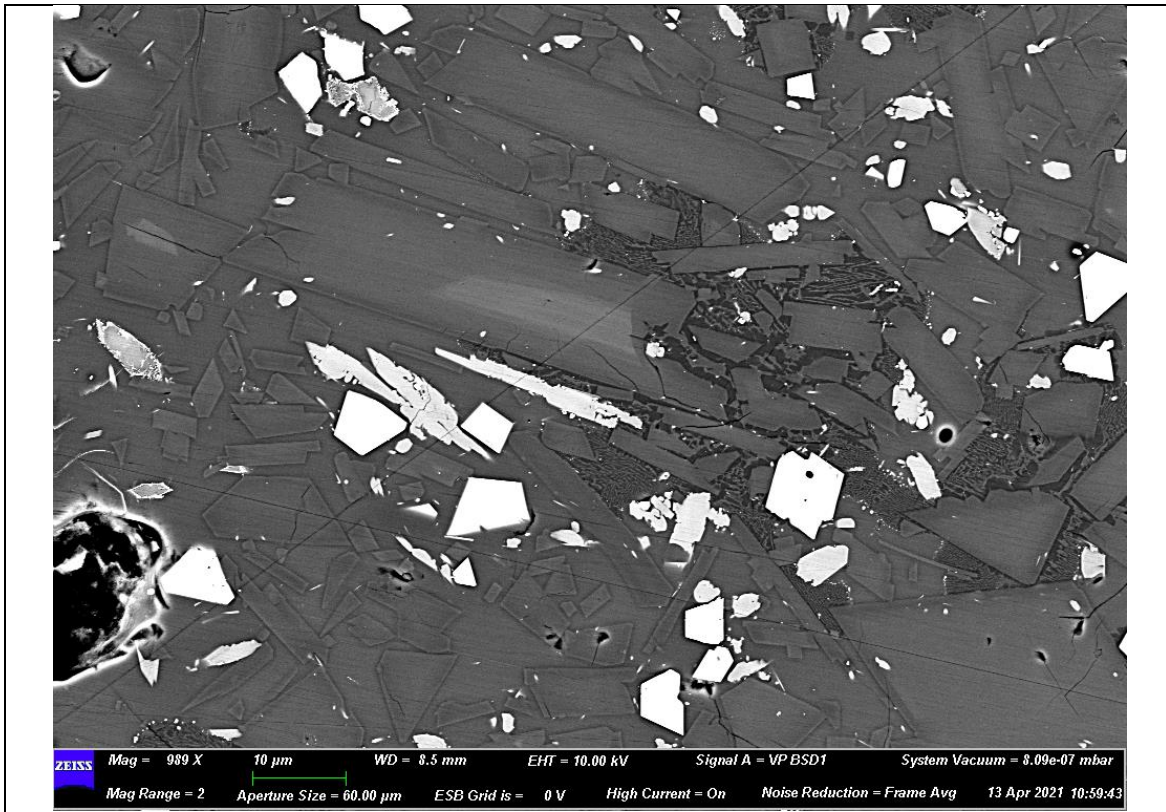


Fig. 4.18: Devitrification of glass

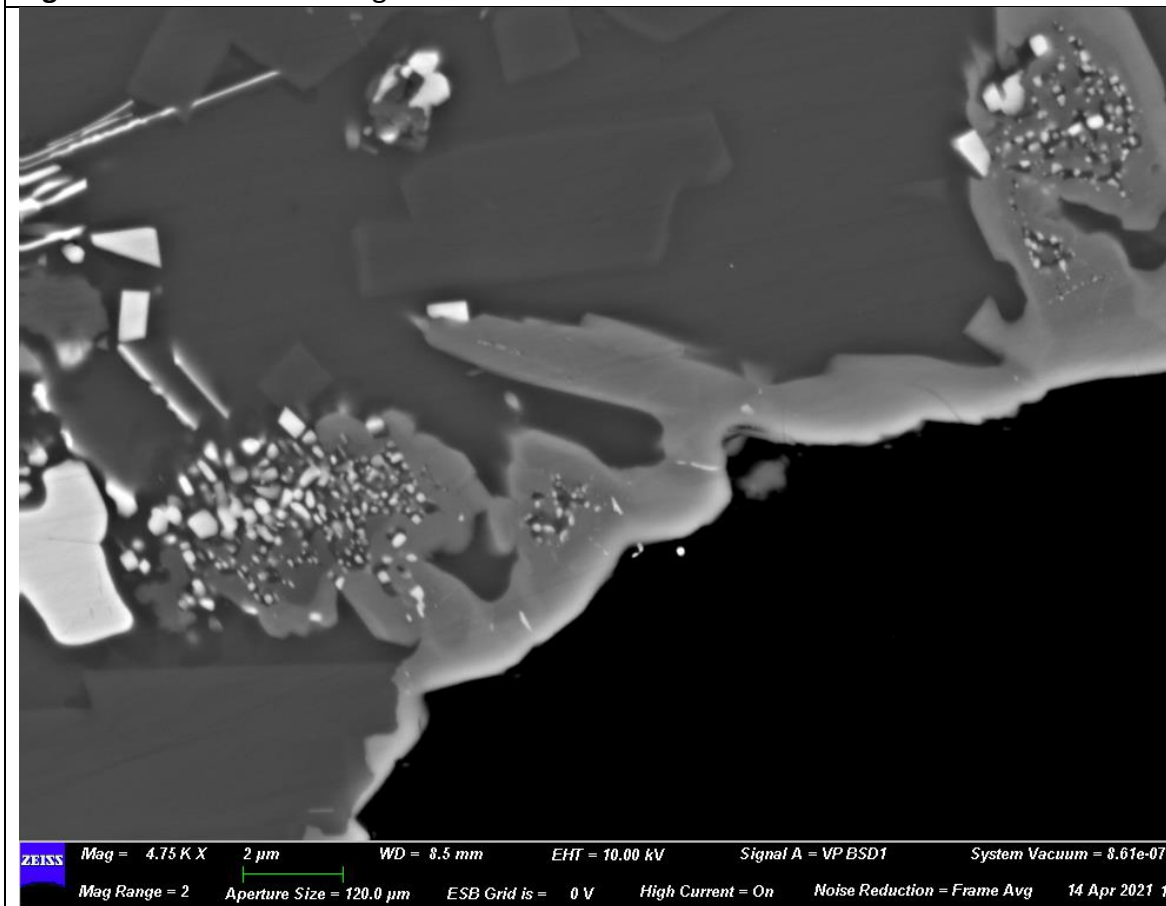


Fig. 4.19: Growth of Cpx on vesicle edges degrading to Opx and oxides.

Summary of phase percentages:

Vesicularity: approx. 36%

Crystal percentages are vesicle free

Large zoned feldspars, lone or in clots without pyroxene – 20%

Cpx + oxide + feldspar clots / cpx + oxide clots - 15%

Large oxides with vesicular edge textures – 3%

Groundmass – 62%

- 70 – 80% crystalline
 - Zoned feldspar tablets – 5%
 - Smallest needle-like elongate and equant sections – <5%
 - Equant oxides – 10%
 - Orthopyroxene microlites – 20%
 - 15% degraded
 - 5% not degraded (proportions vary depending on proximity to larger oxides)
 - Tabular/ twinned feldspar microlites – 30 – 35%

Textures:

De-vitrification of glass to cristobalite and feldspar - <5% of the rock (vesicle free)

Total cristobalite - <2% (due to high crystallinity of groundmass and low incidence of this texture)

List of References:

Ablay, G.J. and Martí, J. (2000) Stratigraphy, structure, and volcanic evolution of the Pico Teide–Pico Viejo formation, Tenerife, Canary Islands. *JVGR* 103(1-4):75-208.

[https://doi.org/10.1016/S0377-0273\(00\)00224-9](https://doi.org/10.1016/S0377-0273(00)00224-9)

Adams, N.K., Houghton, B.F., Fagents, S.A. and Hildreth, W., 2006. The transition from explosive to effusive eruptive regime: the example of the 1912 Novarupta eruption, Alaska. *Geological Society of America Bulletin*, 118(5-6), pp.620-634.

Alfano, F. Bonadonna, C. Gurioli, L. (2012) Insights into eruption dynamics from textural analysis: The case of the May, 2008, Chaitén eruption. *Bull. Volc.* 74(9):2095–2108.

<https://10.1007/s00445-012-0648-3>

Andrews, B.J. Dufek, J. Ponomareva, V. (2018) Eruption dynamics and explosive-effusive transitions during the 1400 cal BP eruption of Opala volcano, Kamchatka, Russia. *JVGR*, 356: 316-330. <https://doi.org/10.1016/j.jvolgeores.2018.02.019>.

Andrews, B.J. (2021) Plagioclase population dynamics and zoning in response to changes in temperature and pressure. *American Mineralogist: Journal of Earth and Planetary Materials*, 106(9), pp.1438-1452.

Arzilli, F. Carroll, M.R. (2013) Crystallization kinetics of alkali feldspars in cooling and decompression-induced crystallization experiments in trachytic melt. *Contributions to Mineralogy and Petrology*, 166(4):1011-1027. [https://doi.org/10.1007/s00410-013-0906-](https://doi.org/10.1007/s00410-013-0906-1)

[1](#)

Arzilli, F. Piochi, M. Mormone, A. Agostini, C. and Carroll, M.R. (2016) Constraining pre-eruptive magma conditions and unrest timescales during the Monte Nuovo eruption

(1538 AD; Campi Flegrei, Southern Italy): integrating textural and CSD results from experimental and natural trachy-phonolites. *Bulletin of Volcanology*, 78(10), pp.1-20.

Avard, G. and Whittington, A.G. (2012) Rheology of arc dacite lavas: experimental determination at low strain rates. *Bulletin of Volcanology*, 74(5), pp.1039-1056.

Bagdassarov, N.S. Dingwell, D.B. and Webb, S.L. (1994) Viscoelasticity of crystal-and bubble-bearing rhyolite melts. *Physics of the earth and planetary interiors*, 83(2), pp.83-99.

Bai, L. Baker, D.R. and Rivers, M. (2008) Experimental study of bubble growth in Stromboli basalt melts at 1 atm. *Earth and Planetary Science Letters*, 267(3-4), pp.533-547.

Baker, D.R. Mancini, L. Polacci, M. Higgins, M.D. Gualda, G.A.R. Hill, R.J. and Rivers, M.L. (2012) An introduction to the application of X-ray microtomography to the three-dimensional study of igneous rocks. *Lithos*, 148, pp.262-276.

Barclay, J., Carroll, M.R., Houghton, B.F. and Wilson, C.J.N., 1996. Pre-eruptive volatile content and degassing history of an evolving peralkaline volcano. *Journal of Volcanology and Geothermal Research*, 74(1-2), pp.75-87.

Barth, T.W. (1951) The feldspar geologic thermometers. *Neues Jahrbuch für Mineralogie*, 82, pp.143-154.

Barth T.W. (1962) The feldspar geologic thermometers. *Norsk Geol Tidsskr* 42:330-339

Barth T.W. (1968) Additional data for the two-feldspar geothermometer. *Lithos*1:21-22

Biass, S. Bonadonna, C. and Houghton, B.F. (2019) A step-by-step evaluation of empirical methods to quantify eruption source via parameters from tephra-fall deposits. *Journal of Applied Volcanology*, 8(1), pp.1-16.

Blong, R. (1994) The Rabaul eruption, 1994. *The Australian Geographer* 25(2):186-190.

<https://doi.org/10.1080/00049189408703118>

Blower, J.D. Keating, J.P. Mader, H.M. and Phillips, J.C. (2001) Inferring volcanic degassing processes from vesicle size distributions. *Geophysical research letters*, 28(2), pp.347-350.

Blundy, J. and Cashman, K. (2008) Petrologic reconstruction of magmatic system variables and processes. *Reviews in Mineralogy and Geochemistry*, 69(1), pp.179-239.

Branney, M.J., Kokelaar, P. and Kokelaar, B.P., 2002. Pyroclastic density currents and the sedimentation of ignimbrites. Geological Society of London.

Brugger, C.R. and Hammer, J.E. (2010) Crystallization kinetics in continuous decompression experiments: implications for interpreting natural magma ascent processes. *Journal of Petrology*, 51(9), pp.1941-1965.

Buck, M.D. Briggs, R.M. Nelson, C.S. (1981) Pyroclastic deposits and volcanic history of Mayor Island. *New Zealand Journal of Geology and Geophysics* 24(4):449-467.

Capaldi, G. Civetta, L. and Gasparini, P. (1976) Volcanic history of the island of Ischia (South Italy). *Bulletin Volcanologique*, 40(1), pp.11-22.

Carey, S. and Sigurdsson, H. (1987) Temporal variations in column height and magma discharge rate during the 79 AD eruption of Vesuvius. *Geological Society of America Bulletin*, 99(2), pp.303-314.

Carey, S., Sigurdsson, H., Gardner, J.E. and Criswell, W., 1990. Variations in column height and magma discharge during the May 18, 1980 eruption of Mount St. Helens. *Journal of Volcanology and Geothermal Research*, 43(1-4), pp.99-112.

Carr, B.B., Clarke, A.B. and Vitturi, M.D.M., 2020. Volcanic conduit controls on effusive-explosive transitions and the 2010 eruption of Merapi Volcano (Indonesia). *Journal of Volcanology and Geothermal Research*, 392, p.106767.

Carracedo, J.C., Badiola, E.R., Guillou, H., de La Nuez, J. and Torrado, F.P., 2001. Geology and volcanology of la Palma and el Hierro, western Canaries. *Estudios Geológicos-Madrid*, 57, pp.175-273.

Cas, R.A.F. Wright, J.V. (1996) (eds) Three types of pyroclastic deposits and their eruptions: an introduction. In: *Volcanic Successions Modern and Ancient: A geological approach to processes, products and successions*. 5th edn. *Chapman & Hall*, London, pp94–126.

Castro, J.M. Bindeman, I.N. Tuffen, H. Schipper, I. (2014) Explosive origin of silicic lava: Textural and $\delta D-H_2O$ evidence for pyroclastic degassing during rhyolite effusion. *Earth and Planetary Science Letters* 405:52–61. <https://doi.org/10.1016/j.epsl.2014.08.012>

Cashman, K.V. Mangan, M.T. (1994) PHYSICAL ASPECTS OF MAGMATIC DEGASSING II. Constraints on vesiculation processes from textural studies of eruptive products. In: Carroll MR, Holloway JR (ed.) *A practical two-feldspar geothermometer*. *Mineralogical Society of America*, Washington DC, pp 447–478.

<https://doi.org/10.1515/9781501509674-018>

Cashman, K.V. and Blundy, J. (2013) Petrological cannibalism: the chemical and textural consequences of incremental magma body growth. *Contributions to Mineralogy and Petrology*, 166(3), pp.703-729.

Cashman, K.V. and Edmonds, M. (2019) Mafic glass compositions: a record of magma storage conditions, mixing and ascent. *Philosophical Transactions of the Royal Society A*, 377(2139), p.20180004.

Cassidy, M., Cole, P.D., Hicks, K.E., Varley, N.R., Peters, N. and Lerner, A.H., 2015. Rapid and slow: Varying magma ascent rates as a mechanism for Vulcanian explosions. *Earth and Planetary Science Letters*, 420, pp.73-84.

Cassidy, M. Manga, M. Cashman, K. Bachmann, O. (2018) Controls on explosive-effusive volcanic eruption styles. *Nature Communications*. 9(2839).

<https://doi.org/10.1038/s41467-018-05293-3>

Castro, J.M., Burgisser, A., Schipper, C.I. and Mancini, S., 2012. Mechanisms of bubble coalescence in silicic magmas. *Bulletin of Volcanology*, 74, pp.2339-2352.

Chakraborty, S. and Dohmen, R. (2022) Diffusion chronometry of volcanic rocks: looking backward and forward. *Bulletin of Volcanology*, 84(6), pp.1-9.

Chamberlain, K.J., Barclay, J., Preece, K., Brown, R. and McIntosh, I., 2020. Deep and disturbed: conditions for formation and eruption of a mingled rhyolite at Ascension Island, South Atlantic. *Volcanica*, 3(1), pp.139-153.

Chamberlain, K.J. Barclay, J. Preece, K.J. Brown, R.J. Davidson, J.P. (2019) Lower Crustal Heterogeneity and Fractional Crystallization Control Evolution of Small-volume Magma Batches at Ocean Island Volcanoes (Ascension Island, South Atlantic). *Journal of Petrology*. 60(8): 1489–1522. <https://doi.org/10.1093/petrology/egz037>

Chamberlain, K.J. Barclay, J. Preece, K. Brown, R.J. Davidson, J.P. EIMF (2016) Origin and evolution of silicic magmas at ocean islands: Perspectives from a zoned fall deposit on Ascension Island, South Atlantic. *Journal of Volcanology and Geothermal Research*. 327:349–360. <https://doi.org/10.1016/j.jvolgeores.2016.08.014>

Chamberlain, K.J., Morgan, D.J. and Wilson, C.J., 2014. Timescales of mixing and mobilisation in the Bishop Tuff magma body: perspectives from diffusion chronometry. *Contributions to Mineralogy and Petrology*, 168, pp.1-24.

Charlier, B.L. Wilson, C.J. and Davidson, J.P. (2008) Rapid open-system assembly of a large silicic magma body: time-resolved evidence from cored plagioclase crystals in the Oruanui eruption deposits, New Zealand. *Contributions to Mineralogy and Petrology*, 156(6), pp.799-813.

Christopher T.E, Frey, H.M, Mourne, S, Davies, B.V, Manon, M.R, Contreras, R, Barclay, J, Joseph, E.P, Robertson, R.E, Henry, L, Howe, T. The role of volatiles in the (2020-2021) La Soufrière eruption St Vincent, revealed from vesicle size distribution and degassing studies. *Submitted to the Geological Society special volume, in review 2023.*

Cid, H.E. Carrasco-Núñez, G. and Manea, V.C. (2017) Improved method for effective rock microporosity estimation using X-ray microtomography. *Micron*, 97, pp.11-21.

Cioni, R. Pistolesi, M. Rosi, M. (2015) Plinian and Subplinian Eruptions. In: Sigurdsson H (ed) The Encyclopedia of Volcanoes 2nd edn, *Academic Press*, pp 519–535.

<https://doi.org/10.1016/b978-0-12-385938-9.00029-8>

Cioni, R. Bertagnini, A. Santacroce, R. Andronico, D. (2008) Explosive activity and eruption scenarios at Somma-Vesuvius (Italy): Towards a new classification scheme. *Journal of Volcanology and Geothermal Research* 178(3): 331–346.

<https://doi.org/10.1016/j.jvolgeores.2008.04.024>.

Clarke, B. Calder, E.S. Dessalegn, F. Fontijn, K. Cortés, J.A. Naylor, M. Butler, I. Hutchison, W. and Yirgu, G. (2019) Fluidal pyroclasts reveal the intensity of peralkaline rhyolite pumice cone eruptions. *Nature communications*, 10(1), pp.1-10.

Clarke, B. (2020) Post-caldera eruptions and pyroclastic density current hazard in the Main Ethiopian Rift. (Doctoral dissertation, *University of Edinburgh*).

<http://dx.doi.org/10.7488/era/153>

Clyne, M.A. (1999) A complex magma mixing origin for rocks erupted in 1915, Lassen Peak, California. *Journal of Petrology*, 40(1), pp.105-132.

Cole, P.D. Queiroz, G. Wallenstein, N. Gaspar, J.L. Duncan, A.M. Guest, J.E. (1995) An historic subplinian/phreatomagmatic eruption: the 1630 AD eruption of Furnas volcano, Saõ Miguel, Azores. *Journal of volcanology and geothermal research*, 69(1-2):117-135.

[https://doi.org/10.1016/0377-0273\(95\)00033-X](https://doi.org/10.1016/0377-0273(95)00033-X)

Cole, P.D. Guest, J.E. Queiroz, G. Wallenstein, N. Pacheco, J.M. Gaspar, J.L. Ferreira, T. Duncan, A.M. (1999) Styles of volcanism and volcanic hazards on Furnas volcano; Sao Miguel, Azores, *Journal of Volcanology and Geothermal Research*, 92(1–2): 39–53.

[https://doi.org/10.1016/S0377-0273\(99\)00066-9](https://doi.org/10.1016/S0377-0273(99)00066-9)

Cole, P.D. Robertson, R.E.A. Fedele, L. and Scarpati, C. (2019) Explosive activity of the last 1000 years at La Soufrière, St Vincent, Lesser Antilles. *Journal of Volcanology and Geothermal Research*, 371, pp.86-100.

Cole, P.D., Barclay, J., Robertson, R.E., Mitchell, S., Davies, B.V., Constantinescu, R., Sparks, R.S.J., Aspinall, W. and Stinton, A., 2023. Explosive sequence of La Soufrière St Vincent April 2021: insights into drivers and consequences via eruptive products. *Geological Society, London, Special Publications*, 539(1), pp.SP539-2022.

Colombier, M. Scheu, B. Wadsworth, F.B. Cronin, S., Vasseur, J. Dobson, K.J. Hess, K.U. Tost, M. Yilmaz, T.I. Cimarelli, C. and Brenna, M. (2018) Vesiculation and Quenching During Surtseyan Eruptions at Hunga Tonga-Hunga Ha'apai Volcano, Tonga. *Journal of*

Geophysical Research: Solid Earth, 123(5), pp.3762-3779.

Colucci, S., Vitturi, M.D.M., Neri, A. and Palladino, D.M., 2014. An integrated model of magma chamber, conduit and column for the analysis of sustained explosive eruptions. *Earth and Planetary Science Letters*, 404, pp.98-110.

Comida, P.P. Ross, P.S. Dürig, T. White, J.D. and Lefebvre, N. (2022) Standardized analysis of juvenile pyroclasts in comparative studies of primary magma fragmentation: 2. Choice of size fraction and method optimization for particle cross-sections. *Bulletin of Volcanology*, 84(1), pp.1-24.

Costa, S. Masotta, M. Gioncada, A. Pistolesi, M. Bosch, D. and Scarlato, P. (2020) Magma evolution at La Fossa volcano (Vulcano Island, Italy) in the last 1000 years: evidence from eruptive products and temperature gradient experiments. *Contributions to Mineralogy and Petrology*, 175(4), pp.1-22.

Croasdale, R. Walker, G.P.L. Booth, B. (1978) A quantitative study of five thousand years of volcanism on Sao Miguel, Azores. *Philosophical Transactions of the Royal Society of London. Series A, Mathematical and Physical Sciences* 288(1352):271-319.

<https://doi.org/10.1098/rsta.1978.0018>

Cross, J.K. Roberge, J. and Jerram, D.A. (2012) Constraining the degassing processes of Popocatepetl Volcano, Mexico: A vesicle size distribution and glass geochemistry study. *Journal of volcanology and geothermal research*, 225, pp.81-95.

Croweller, H.S. (2009) An analysis of factors influencing volcanic risk communication on two islands in the Lesser Antilles (Doctoral dissertation, *University of East Anglia*).

Daly, R.A. (1925). The geology of Ascension island. In *Proceedings of the American Academy of Arts and Sciences* (Vol. 60, No. 1, pp. 3-80). American Academy of Arts & Sciences.

Davì, M. De Rosa, R. Donato, P. Sulpizio, R. (2011) The Lami pyroclastic succession (Lipari, Aeolian Islands): A clue for unravelling the eruptive dynamics of the Monte Pilato rhyolitic pumice cone. *Journal of Volcanology and Geothermal Research*, 201:285-300.

<https://doi.org/10.1016/j.jvolgeores.2010.09.010>

Davies, B.V. Brown, R.J. Barclay, J. Scarrow, J.H. and Herd, R.A. (2021) Rapid eruptive transitions from low to high intensity explosions and effusive activity: insights from textural analysis of a small-volume trachytic eruption, Ascension Island, South Atlantic. *Bulletin of Volcanology*, 83(9), pp.1-40.

Degruyter, W., Bachmann, O., Burgisser, A. and Manga, M., 2012. The effects of outgassing on the transition between effusive and explosive silicic eruptions. *Earth and Planetary Science Letters*, 349, pp.161-170.

Dellino, P. and La Volpe, L. (1995). Fragmentation versus transportation mechanisms in the pyroclastic sequence of Monte Pilato-Rocche Rosse (Lipari, Italy). *Journal of Volcanology and Geothermal Research* 64(3-4):211-231. [https://doi.org/10.1016/0377-0273\(94\)00084-T](https://doi.org/10.1016/0377-0273(94)00084-T)

Deniel, C. Boivin, P. Miallier, D. Gerbe, M.C. (2020) Multi-stage growth of the trachytic lava dome of the Puy de Dôme (Chaîne des Puys, France). Field, geomorphological and petro-geochemical evidence. *Journal of Volcanology and Geothermal Research* 396:106749. <https://doi.org/10.1016/j.jvolgeores.2019.106749>

Di Genova, D. Romano, C. Hess, K-U. Vona, A. Poe, B.T. Giordano, D. Dingwell, D.B.

Behrens, H. (2013) The rheology of peralkaline rhyolites from Pantelleria Island. *Journal of*

Volcanology and Geothermal Research 249:201–216.

<https://doi.org/10.1016/j.jvolgeores.2012.10.017>

Dowey, N. and Williams, R., 2022. Simultaneous fall and flow during pyroclastic eruptions:

A novel proximal hybrid facies. *Geology*, 50(10), pp.1187-1191.

<https://doi.org/10.1130/G50169.1>

Dosseto, A. Turner, S.P. and Van-Orman, J.A. eds., (2011) Timescales of magmatic processes: from core to atmosphere. *John Wiley & Sons*.

<https://doi.org/10.1002/9781444328509>

Edmonds, M., Pyle, D. and Oppenheimer, C., 2001. A model for degassing at the Soufriere Hills Volcano, Montserrat, West Indies, based on geochemical data. *Earth and Planetary Science Letters*, 186(2), pp.159-173.

Evangelidis, C.P. Minshull, T.A. and Henstock, T.J. (2004) Three-dimensional crustal structure of Ascension Island from active source seismic tomography. *Geophysical Journal International*, 159(1), pp.311-325.

Fanara, S. Behrens, H. Zhang, Y. (2013) Water diffusion in potassium-rich phonolitic and trachytic melts. *Chemical Geology* 346:49-161.

<https://doi.org/10.1016/j.chemgeo.2012.09.030>

Fiske, R.S. and Sigurdsson, H. (1982) Soufriere Volcano, St. Vincent: Observations of its 1979 eruption from the ground, aircraft, and satellites. *Science*, 216(4550), pp.1105-1106.

Folch, A. and Martí, J. (1998) The generation of overpressure in felsic magma chambers by replenishment. *Earth and Planetary Science Letters*, 163(1-4), pp.301-314.

Fowler, A.C. Scheu, B. Lee, W.T. McGuinness, M.J. (2010) A theoretical model of the explosive fragmentation of vesicular magma. *Proceedings of the Royal Society A: Mathematical, Physical and Engineering Sciences* 466(2115):731–752.

<https://doi.org/10.1098/rspa.2009.0382>

Frey H. M, Manon M. R., Barclay J, Davies B. V, Walters S. A, Cole P. D. Christopher T. E & Joseph E. P.. Petrology of the explosive deposits from the April 2021 eruption of La Soufrière volcano, St Vincent: a time-series analysis of microlites. Geological Society, London, Special Publications, 539(1), SP539 – 2022 – 291. DOI:

<https://doi.org/10.1144/SP539-2022-291>**Gansecki**, C. Lee, R.L. Shea, T. Lundblad, S.P. Hon, K. and Parcheta, C. (2019) The tangled tale of Kīlauea’s 2018 eruption as told by geochemical monitoring. *Science*, 366(6470), p.eaaz0147.

Gardner, J.E. Llewelin, E.W. Watkins, J.M. Befus, K.S. (2017) Formation of obsidian pyroclasts by sintering of ash particles in the volcanic conduit. *Earth and Planetary Science Letters*. 459:252–263. <https://doi.org/10.1016/j.epsl.2016.11.037>

Gardner, J.E. and Ketcham, R.A. (2011) Bubble nucleation in rhyolite and dacite melts: temperature dependence of surface tension. *Contributions to Mineralogy and Petrology*, 162(5), pp.929-943.

Giachetti, T. Burgisser, A. Arbaret, L. Druitt, T.H. Kelfoun, K. (2011) Quantitative textural analysis of Vulcanian pyroclasts (Montserrat) using multi-scale X-ray computed microtomography: comparison with results from 2D image analysis. *Bulletin of Volcanology* 73: 1295 – 1309. <https://doi.org/10.1007/s00445-011-0472-1>

Giordano, D. Romano, C. Papale, P. Dingwell, D.B. (2004) The viscosity of trachytes, and comparison with basalts, phonolites, and rhyolites. *Chemical Geology* 213(1–3):49–61. <https://doi.org/10.1016/j.chemgeo.2004.08.032>

Giordano, D. Nichols, A.R.L. Dingwell, D.B. (2005) Glass transition temperatures of natural hydrous melts: a relationship with shear viscosity and implications for the welding

process. *Journal of Volcanology and Geothermal Research* 142(1-2):105-118.

<https://doi.org/10.1016/j.jvolgeores.2004.10.015>.

Giordano, D. Russell, J.K. Dingwell, D.B. (2008) Viscosity of magmatic liquids: A model.

Earth and Planetary Science Letters 271(1–4):123–134.

<https://doi.org/10.1016/j.epsl.2008.03.038>

Global Volcanism Program, 2023. Ascension (385050), in [Database] Volcanoes of the World (v. 5.0.2; 2023 23 Jan 2023). Distributed by Smithsonian Institution, compiled by Venzke, E. <https://doi.org/10.5479/si.GVP.VOTW5-2022.5.0>

Gonnermann, H.M. Giachetti, T. Fliedner, C. Nguyen, C.T. Houghton, B.F. Crozier, J.A. and Carey, R.J. (2017) Permeability during magma expansion and compaction. *Journal of Geophysical Research: Solid Earth*, 122(12), pp.9825-9848.

Gonnerman, E.C. Neave, D.A. Dobson, K.J. Withers, P.J. Edmonds, M. (2017) How to fragment peralkaline rhyolites: Observations on pumice using combined multi-scale 2D and 3D imaging. *Journal of Volcanology and Geothermal Research* 336:179–191.

<https://doi.org/10.1016/j.jvolgeores.2017.02.020>.

Google Earth V7.3.3.7721. (24/01/2006). Ascension Island, South Atlantic. 7°55'44.74"S 14°19'26.42" W, Eye alt 4.72 km. Maxar Technologies 2020.

<http://www.earth.google.com> (18/11/2020)

Google Earth V7.3.3.7721. (12/03/2016). Rabaul, Papua New Guinea. 4 14 58.14 S 152 11 17.37 E, Eye alt 11.4 km. Maxar Technologies 2020. <http://www.earth.google.com>

<http://www.earth.google.com> (11/08/2020)

Gottsmann, J. and Dingwell, D.B., 2002. The thermal history of a spatter-fed lava flow: the 8-ka pantellerite flow of Mayor Island, New Zealand. *Bulletin of Volcanology*, 64, pp.410-422.

Graham, A.M. and Thirlwall, M.F. (1981) Petrology of the 1979 eruption of Soufriere Volcano, St. Vincent, Lesser Antilles. *Contributions to Mineralogy and Petrology*, 76(3), pp.336-342.

Gualda, G.A.R. Ghiorso, M.S. Lemons, R.V. Carley, T.L. (2012) Rhyolite-MELTS: A modified calibration of MELTS optimized for silica-rich, fluid-bearing magmatic systems. *Journal of Petrology*, 53, 875-890.

Gualda, G.A. and Rivers, M. (2006) Quantitative 3D petrography using X-ray tomography: Application to Bishop Tuff pumice clasts. *Journal of Volcanology and Geothermal Research*, 154(1-2), pp.48-62.

Harford, C.L., Sparks, R.S.J. and Fallick, A.E., 2003. Degassing at the Soufrière Hills Volcano, Montserrat, recorded in matrix glass compositions. *Journal of Petrology*, 44(8), pp.1503-1523.

Heap, M.J. Tuffen, H. Wadsworth, F.B. Reuschlé, T. Castro, J.M. Schipper, C.I. (2019) The Permeability Evolution of Tuffisites and Implications for Outgassing Through Dense Rhyolitic Magma. *Journal of Geophysical Research: Solid Earth* 124(8):8281–8299.

<https://doi.org/10.1029/2018JB017035>

Heap, M.J., Farquharson, J.I., Wadsworth, F.B., Kolzenburg, S. and Russell, J.K., 2015. Timescales for permeability reduction and strength recovery in densifying magma. *Earth and Planetary Science Letters*, 429, pp.223-233.

Heilbronner, R. and Barrett, S. (2014) Shape descriptors. In *Image Analysis in Earth*

Sciences (pp. 323-347). Springer, Berlin, Heidelberg.

Hernando, L.R. Petrinovic, I.A. D'Elia, L. Guzmán, S. Páez, G.N. (2019) Post-caldera pumice cones of the Payún Matrú caldera, Payenia, Argentina: Morphology and deposits characteristics. *Journal of South American Earth Sciences* 90:453-462.

<https://doi.org/10.1016/j.jsames.2018.12.017>

Hoblitt, R.P., 1986. Observations of the eruptions of July 22 and August 7, 1980, at Mount St. Helens, Washington (Vol. 1335). US Government Printing Office.

Horwell, C.J. Davies, B.V. Mangler, M. Barclay, J. (2021) Version 1.3. Last Updated 10 May 2021. Report on the presence of crystalline silica in La Soufrière, St Vincent dome rock.

International Volcanic Health Hazard Network.

Houghton, B.F. Wilson, C.J.N. Weaver, S.D. (1985) Strombolian deposits at Mayor Island: "Basaltic" eruption styles displayed by a peralkaline volcano. *New Zealand Geological Survey Record* 8:45–51.

Houghton, B.F. Wilson, C.J.N. (1989). A vesicularity index for pyroclastic deposits. *Bulletin of volcanology*, 51(6):451-462. <https://doi.org/10.1007/BF01078811>

Houghton, B.F. Weaver, S.D. Wilson, C.J. and Lanphere, M.A. (1992) Evolution of a quaternary peralkaline volcano: Mayor Island, New Zealand. *Journal of Volcanology and Geothermal Research*, 51(3), pp.217-236.

Houghton, B.F. Wilson, C.J.N. Fierstein, J. Hildreth, W. (2004) Complex proximal deposition during the Plinian eruptions of 1912 at Novarupta, Alaska. *Bulletin of Volcanology* 66:95-133. <https://doi.org/10.1007/s00445-003-0297-7>

Houghton, B.F. Carey, R.J. Cashman, K.V. Wilson, C.J.N. Hobden, B.J. Hammer, J.E. (2010) Diverse patterns of ascent, degassing, and eruption of rhyolite magma during the 1.8ka

Taupo eruption, New Zealand: Evidence from clast vesicularity. *JVGR* 195(1): 31-47.

<https://doi.org/10.1016/j.jvolgeores.2010.06.002>

Houghton, B.F. Swanson, D.A. Rausch, J. Carey, R.J. Fagents, S.A. Orr, T.R. (2013) Pushing the Volcanic Explosivity Index to its limit and beyond: Constraints from exceptionally weak explosive eruptions at Kīlauea in 2008. *Geology* 416.

<https://doi.org/10.1016/j.jvolgeores.2021.107284>

Humphreys, M.C., Kearns, S.L. and Blundy, J.D., 2006. SIMS investigation of electron-beam damage to hydrous, rhyolitic glasses: Implications for melt inclusion analysis. *American Mineralogist*, 91(4), pp.667-679.

Huggins, E.G., Ruprecht, P. and Ghiorso, M.S., 2021. Using chemical affinities to understand disequilibrium textures of plagioclase preserved in magmatic systems. *Geophysical Research Letters*, 48(10), p.e2021GL092884.

Humphreys, M.C. Edmonds, M. and Klöcking, M.S. (2016) The validity of plagioclase-melt geothermometry for degassing-driven magma crystallization. *American Mineralogist*, 101(4), pp.769-779.

Huppert, H.E. Sparks, R.S.J. and Turner, J.S. (1982) Effects of volatiles on mixing in calc-alkaline magma systems. *Nature*, 297(5867), pp.554-557.

Hutchison, W. Pyle, D.M. Mather, T.A. Yirgu, G. Biggs, J. Cohen, B.E. Barfod, D.N. Lewi, E. (2016) The eruptive history and magmatic evolution of Aluto volcano: new insights into silicic peralkaline volcanism in the Ethiopian rift. *Journal of Volcanology and Geothermal Research* 328:9-33. <https://doi.org/10.1016/j.jvolgeores.2016.09.010>

Janebo, M.H. Thordarson, T. Houghton, B.F. Bonadonna, C. Larsen, G. and Carey, R.J. (2016) Dispersal of key subplinian–Plinian tephras from Hekla volcano, Iceland:

implications for eruption source parameters. *Bulletin of Volcanology*, 78(10), pp.1-16.

Jeffery, A.J. Gertisser, R. O'Driscoll, B. Pacheco, J.M. Whitley, S. Pimentel, A. Self, S. (2016)

Temporal evolution of a post-caldera, mildly peralkaline magmatic system: Furnas volcano, São Miguel, Azores. *Contributions to Mineralogy and Petrology* 171(5):42.

<https://doi.org/10.1016/j.jvolgeores.2016.09.010>

Jeffery, A.J. and Gertisser, R. (2018) Peralkaline felsic magmatism of the Atlantic Islands. *Frontiers in Earth Science*, 6, p.145.

Jicha, B.R. Singer, B.S. Valentine. M.J. (2013) $^{40}\text{Ar}/^{39}\text{Ar}$ geochronology of subaerial Ascension Island and a re-evaluation of the temporal progression of basaltic to rhyolitic volcanism. *Journal of Petrology*, 54(12):2581-2596.

<https://doi.org/10.1093/petrology/egt058>

Joseph, E.P. Camejo-Harry, M. Christopher, T. Contreras-Arratia, R. Edwards, S. Graham, O. Johnson, M. Juman, A. Latchman, J.L. Lynch, L. and Miller, V.L. (2022) Responding to eruptive transitions during the 2020–2021 eruption of La Soufrière volcano, St. Vincent. *Nature Communications*, 13(1), pp.1-15.

Kar, A. Weaver, B. Davidson, J. Colucci, M. (1998) Origin of differentiated volcanic and plutonic rocks from Ascension Island, South Atlantic Ocean. *Journal of Petrology* 39(5):1009–1024. <https://doi.org/10.1093/petroj/39.5.1009>

Katsui, Y. and Katz, H.R. (1967) Lateral fissure eruptions in the southern Andes of Chile. *Journal of the Faculty of Science, Hokkaido University. Series 4, Geology and mineralogy* 13(4):433-448. <http://hdl.handle.net/2115/35970>

Ketcham, R.A. (2005) Computational methods for quantitative analysis of three-dimensional features in geological specimens. *Geosphere*, 1(1), pp.32-41.

Klingelhöfer, F. Minshull, T.A. Blackman, D.K. Harben, P. and Childers, V. (2001) Crustal structure of Ascension Island from wide-angle seismic data: implications for the formation of near-ridge volcanic islands. *Earth and Planetary Science Letters*, 190(1-2), pp.41-56.

Klug, C. and Cashman, K.V. (1996) Permeability development in vesiculating magmas: implications for fragmentation. *Bulletin of Volcanology* 58(2–3) 87–100.

<https://doi.org/10.1007/s004450050128>

Kushnir, A.R. Martel, C. Champallier, R. and Arbaret, L. (2017) In situ confirmation of permeability development in shearing bubble-bearing melts and implications for volcanic outgassing. *Earth and Planetary Science Letters*, 458, pp.315-326.

Lange, R.A. and Carmichael, I.S. (1987) Densities of Na₂O-K₂O-CaO-MgO-FeO-Fe₂O₃-Al₂O₃-TiO₂-SiO₂ liquids: new measurements and derived partial molar properties.

Geochimica et Cosmochimica Acta 51(11):2931-2946. [https://doi.org/10.1016/0016-7037\(87\)90368-1](https://doi.org/10.1016/0016-7037(87)90368-1)

Lange, R.A. Frey, H.M. and Hector, J. (2009) A thermodynamic model for the plagioclase-liquid hygrometer/thermometer. *American Mineralogist*, 94(4), pp.494-506.

Larsen, J.F. and Gardner, J.E. (2004) Experimental study of water degassing from phonolite melts: implications for volatile oversaturation during magmatic ascent. *Journal of Volcanology and Geothermal Research*, 134(1-2), pp.109-124.

Laumonier, M. Scaillet, B. Pichavant, M. Champallier, R. Andujar, J. and Arbaret, L. (2014) On the conditions of magma mixing and its bearing on andesite production in the crust. *Nature communications*, 5(1), pp.1-12.

Lautze, N.C. and Houghton, B.F. (2005) Physical mingling of magma and complex eruption dynamics in the shallow conduit at Stromboli volcano, Italy. *Geology*, 33(5), pp.425-428.

- Le Maitre, R.W.** (1976) The chemical variability of some common igneous rocks. *Journal of Petrology* 17(4):589–598. <https://doi.org/10.1093/petrology/17.4.589>.
- Leonard, G.S. Cole, J.W. Nairn, I.A. and Self, S.** (2002) Basalt triggering of the c. AD 1305 Kaharoa rhyolite eruption, Tarawera volcanic complex, New Zealand. *Journal of Volcanology and Geothermal Research*, 115(3-4), pp.461-486.
- Lin, Q. Neethling, S.J. Dobson, K.J. Courtois, L. and Lee, P.D.** (2015) Quantifying and minimising systematic and random errors in X-ray micro-tomography based volume measurements. *Computers & Geosciences*, 77, pp.1-7.
- Liu, E.J. Cashman, K.V. and Rust, A.C.** (2015) Optimising shape analysis to quantify volcanic ash morphology. *GeoResJ*, 8, pp.14-30.
- Macdonald, R. Hawkesworth, C.J. and Heath, E.** (2000) The Lesser Antilles volcanic chain: a study in arc magmatism. *Earth-Science Reviews*, 49(1-4), pp.1-76.
- Mader, H.M., Llewelin, E.W. and Mueller, S.P.,** 2013. The rheology of two-phase magmas: A review and analysis. *Journal of Volcanology and geothermal Research*, 257, pp.135-158.
- Mahood, G.A. Hildreth, W.** (1986) Geology of the peralkaline volcano at Pantelleria, Strait of Sicily. *Bulletin of Volcanology* 48(2-3):143-172. <https://doi.org/10.1007/BF01046548>
- Mangler, M.F. Petrone, C.M. Hill, S. Delgado-Granados, H. and Prytulak, J.** (2020) A pyroxenic view on magma hybridization and crystallization at Popocatepetl Volcano, Mexico. *Frontiers in earth Science*, 8, p.362.
- Martí, J. Gropelli, G. and da Silveira, A.B.** (2018) Volcanic stratigraphy: A review. *Journal of Volcanology and Geothermal Research*, 357, pp.68-91.

Marziano, G.I. Schmidt, B.C. and Dolfi, D. (2007) Equilibrium and disequilibrium degassing of a phonolitic melt (Vesuvius AD 79 “white pumice”) simulated by decompression experiments. *Journal of Volcanology and Geothermal Research*, 161(3), pp.151-164.

Masotta, M. and Mollo, S. (2019) A new plagioclase-liquid hygrometer specific to trachytic systems. *Minerals*, 9(6), p.375.

Mastrolorenzo, G. Palladino, D.M. Pappalardo, L. Rossano, S. (2017) Probabilistic-numerical assessment of pyroclastic current hazard at Campi Flegrei and Naples city: Multi-VEI scenarios as a tool for “full-scale” risk management. *PloS one* 12(10): e0185756.
<https://doi.org/10.1371/journal.pone.0185756>

Mathworks™, (2022a) regionprops – measure properties of image regions (documentation). Available at:

<https://uk.mathworks.com/help/images/ref/regionprops.html>. (Accessed 29th March 2022)

McDonough, W.F. Sun, S-s. (1995) The composition of the Earth, *Chemical Geology* 120(3–4):223-253. [https://doi.org/10.1016/0009-2541\(94\)00140-4](https://doi.org/10.1016/0009-2541(94)00140-4)

McKee, C.O. Johnson, R.W. Lowenstein, P.L. Riley, S.J. Blong, R.J. De Saint Ours, P. Talai, B. (1985) Rabaul caldera, Papua New Guinea: volcanic hazards, surveillance, and eruption contingency planning. *Journal of Volcanology and Geothermal Research* 23(3-4):195-237.
[https://doi.org/10.1016/0377-0273\(85\)90035-6](https://doi.org/10.1016/0377-0273(85)90035-6)

McKee, C.O. Duncan, R.A. (2016). Early volcanic history of the Rabaul area. *Bulletin of Volcanology* 78(4):24. <https://doi.org/10.1007/s00445-016-1018-3>

Melnik, O. and Sparks, R.S.J. (1999) Nonlinear dynamics of lava dome extrusion. *Nature*, 402(6757), pp.37-41.

Metrich, N. Clocchiatti, R. Mosbah, M. and Chaussidon, M. (1993) The 1989–1990 activity of Etna magma mingling and ascent of H₂O-Cl-S-rich basaltic magma. Evidence from melt inclusions. *Journal of Volcanology and Geothermal Research*, 59(1-2), pp.131-144.

Mitchell, S.J. Houghton, B.F. Carey, R.J. Manga, M. Fauria, K.E. Jones, M.R. Coule, A.S. Conway, C.H. Wei, Z. Giachetti, T. (2019) Submarine giant pumice: a window into the shallow conduit dynamics of a recent silicic eruption. *Bulletin of Volcanology* 81:42.
<https://doi.org/10.1007/s00445-019-1298-5>

Miyabuchi, Y. (2011) Post-caldera explosive activity inferred from improved 67–30 ka tephrostratigraphy at Aso Volcano, Japan. *Journal of volcanology and geothermal research*, 205(3-4):94-113. <https://doi.org/10.1016/j.jvolgeores.2011.05.004>

Moitra, P. Gonnermann, H.M. Houghton, B.F. Giachetti, T. (2013) Relating vesicle shapes in pyroclasts to eruption styles. *Bulletin of Volcanology*, 75(2):1–14.
<https://doi.org/10.1007/s00445-013-0691-8>.

Moitra, P. Gonnermann, H.M. Houghton, B.F. and Tiwary, C.S. (2018) Fragmentation and Plinian eruption of crystallizing basaltic magma. *Earth and Planetary Science Letters*, 500, pp.97-104.

Mollo, S. Masotta, M. Forni, F. Bachmann, O. De Astis, G. Moore, G. and Scarlato, P. (2015) A K-feldspar–liquid hygrometer specific to alkaline differentiated magmas. *Chemical Geology*, 392, pp.1-8.

Mongrain, J. Larsen, J.F. and King, P.L. (2008) Rapid water exsolution, degassing, and bubble collapse observed experimentally in K-phonolite melts. *Journal of Volcanology and Geothermal Research*, 173(3-4), pp.178-184.

Montagna, C. P., P. Papale, and A. Longo (2015). “Timescales of mingling in shallow magmatic reservoirs”. *Geological Society, London, Special Publications* 422.1, pp. 131–140. doi:10.1144/sp422.6.

Montelli, R. Nolet, G Dahlen, F.A. and Masters, G. (2006) A catalogue of deep mantle plumes: New results from finite-frequency tomography. *Geochemistry, Geophysics, Geosystems*, 7(11).

Moore, R.B. (1991) *Geologic map of São Miguel, Azores* (No. 2007).

Morgan, D., S. Blake, N. Rogers, B. DeVivo, G. Rolandi, R. Macdonald, and C. Hawkesworth (2004). “Timescales of crystal residence and magma chamber volume from modelling of diffusion profiles in phenocrysts: Vesuvius 1944”. *Earth and Planetary Science Letters* 222.3-4, pp. 933–946. doi: 10.1016/j.epsl. 2004.03.030.

Morgavi, D. Arzilli, F. Pritchard, C. Perugini, D. Mancini, L. Larson, P. and Dingwell, D.B. (2016) The Grizzly Lake complex (Yellowstone Volcano, USA): Mixing between basalt and rhyolite unraveled by microanalysis and X-ray microtomography. *Lithos*, 260, pp.457-474.

Mueller, S. Scheu, B. Kueppers, U. Spieler, O. Richard, D. Dingwell, D.B. (2011) The porosity of pyroclasts as an indicator of volcanic explosivity, *Journal of Volcanology and Geothermal Research* (3–4):168–174. <https://doi.org/10.1016/j.jvolgeores.2011.04.006>.

Mutch, E.J. Maclennan, J. Shorttle, O. Edmonds, M. and Rudge, J.F. (2019) Rapid transcrustal magma movement under Iceland. *Nature Geoscience*, 12(7), pp.569-574.

Nairn, I.A. Shane, P.R. Cole, J.W. Leonard, G.J Self, S. and Pearson, N., (2004) Rhyolite magma processes of the ~ AD 1315 Kaharoa eruption episode, Tarawera volcano, New Zealand. *Journal of Volcanology and Geothermal Research*, 131(3-4), pp.265-294.

- Neave**, D.A. Fabbro, G. Herd, R.A. Petrone, C.M. Edmonds, M. (2012) Melting, differentiation and degassing at the Pantelleria volcano, Italy. *Journal of Petrology* 53(3):637-663. <https://doi.org/10.1093/petrology/egr074>
- Newhall**, C.G. Self, S. (1982) The volcanic explosivity index (VEI): an estimate of explosive magnitude for historical volcanism. *Journal of Geophysical Research*, 87(C2):1231–1238. <https://doi.org/10.1029/jc087ic02p01231>.
- Nielson**, D.L. Sibbett, B.S. (1996) Geology of Ascension Island, South Atlantic Ocean. *Geothermics* 25(4-5):427-448. [https://doi.org/10.1016/0375-6505\(96\)00018-1](https://doi.org/10.1016/0375-6505(96)00018-1)
- Orsi**, G. Ruvo, L. Scarpati, C. (1989) The Serra della Fastuca Tephra at Pantelleria: physical parameters for an explosive eruption of peralkaline magma. *Journal of volcanology and geothermal research* 39(1):55-60. [https://doi.org/10.1016/0377-0273\(89\)90020-6](https://doi.org/10.1016/0377-0273(89)90020-6)
- Orsi**, G. Ruvo, L. Scarpati, C. (1991) The recent explosive volcanism at Pantelleria. *Geologische Rundschau*, 80(1):187-200. <https://doi.org/10.1007/BF01828776>
- Pankhurst, M.J.**, Morgan, D.J., Thordarson, T. and Loughlin, S.C., 2018. Magmatic crystal records in time, space, and process, causatively linked with volcanic unrest. *Earth and Planetary Science Letters*, 493, pp.231-241.
- Pankhurst**, M.J. Scarrow, J.H. Barbee, O.A. Hickey, J. Coldwell, B.C. Rollinson, G.K. Rodríguez-Losada, J.A. Lorenzo, A.M. Rodríguez, F. Hernández, W. and Fernández, D.C. (2022) Rapid response petrology for the opening eruptive phase of the 2021 Cumbre Vieja eruption, La Palma, Canary Islands. *Volcanica*, 5(1), pp.1-10.
- Pappalardo**, L. Buono, G. Fanara, S. and Petrosino, P. (2018) Combining textural and geochemical investigations to explore the dynamics of magma ascent during Plinian eruptions: a Somma–Vesuvius volcano (Italy) case study. *Contributions to Mineralogy and Petrology*, 173(7), pp.1-20.

- Parcheta, C.E.** Houghton, B.F. and Swanson, D.A. (2013) Contrasting patterns of vesiculation in low, intermediate, and high Hawaiian fountains: a case study of the 1969 Mauna Ulu eruption. *Journal of Volcanology and Geothermal Research*, 255, pp.79-89.
- Paulick, H.** Münker, C. and Schuth, S. (2010) The influence of small-scale mantle heterogeneities on Mid-Ocean Ridge volcanism: evidence from the southern Mid-Atlantic Ridge (7° 30' S to 11° 30' S) and Ascension Island. *Earth and Planetary Science Letters*, 296(3-4), pp.299-310.
- Perugini, D.,** De Campos, C.P., Petrelli, M. and Dingwell, D.B., 2015. Concentration variance decay during magma mixing: a volcanic chronometer. *Scientific reports*, 5(1), p.14225.
- Perugini, D.,** Poli, G., Petrelli, M., De Campos, C.P. and Dingwell, D.B., 2010. Time-scales of recent Phlegrean Fields eruptions inferred from the application of a 'diffusive fractionation' model of trace elements. *Bulletin of Volcanology*, 72, pp.431-447.
- Pinkerton, H.,** Wilson, L. and MacDonald, R., 2002. The transport and eruption of magma from volcanoes: a review. *Contemporary Physics*, 43(3), pp.197-210.
- Piochi, M.** Polacci, M. Arzilli, F. and Ventura, G. (2021) Microscale textural heterogeneity and tip-streaming instability in alkaline magmas: Evidence in tube pumices from Campi Flegrei, Italy. *Journal of Volcanology and Geothermal Research*, 413, p.107200.
- Pistolesi, M.** Cioni, R. Bonadonna, C. Elissondo, M. Baumann, V. Bertagnini, A. Chiarai, L. Gonzales, R. Rossi, M. Francalanci, L. (2015) Complex dynamics of small-moderate volcanic events: the example of the 2011 rhyolitic Cordón Caulle eruption, Chile. *Bulletin of Volcanology* 77(1). <https://doi.org/10.1007/s00445-014-0898-3>
- Pistone, M.** Caricchi, L. Ulmer, P. Burlini, L. Ardia, P. Reusser, E. Marone, F. and Arbaret, L. (2012) Deformation experiments of bubble-and crystal-bearing magmas: Rheological and microstructural analysis. *Journal of Geophysical Research: Solid Earth*, 117(B5).

Plail, M. Edmonds, M. Woods, A.W. Barclay, J. Humphreys, M.C. Herd, R.A. and Christopher, T. (2018) Mafic enclaves record syn-eruptive basalt intrusion and mixing. *Earth and Planetary Science Letters*, 484, pp.30-40.

Polacci, M. Papale, P. and Rosi, M. (2001) Textural heterogeneities in pumices from the climactic eruption of Mount Pinatubo, 15 June 1991, and implications for magma ascent dynamics. *Bulletin of Volcanology*, 63(2), pp.83-97.

Polacci, M. Pioli, L. Rosi, M. (2003) The Plinian phase of the Campanian Ignimbrite eruption (phlegrean fields, Italy): Evidence from density measurements and textural characterization of pumice. *Bulletin of Volcanology* 65(6):418–432.

<https://doi.org/10.1007/s00445-002-0268-4>.

Polacci, M., Papale, P., Del Seppia, D., Giordano, D. and Romano, C., 2004. Dynamics of magma ascent and fragmentation in trachytic versus rhyolitic eruptions. *Journal of volcanology and geothermal research*, 131(1-2), pp.93-108.

Polacci, M. (2005) Constraining the dynamics of volcanic eruptions by characterization of pumice textures. *Annals of Geophysics* 48(4):731-738. <http://hdl.handle.net/2122/934>

Preece, K. Gertisser, R. Barclay, J. Berlo, K. Herd, R.A. (2014) Pre-and syn-eruptive degassing and crystallisation processes of the 2010 and 2006 eruptions of Merapi volcano, Indonesia. *Contributions to Mineralogy and Petrology* 168(4):1061.

<https://doi.org/10.1007/s00410-014-1061-z>

Preece, K. Mark, D.F. Barclay, J. Cohen, B.E. Chamberlain, K.J. Jowitt, C. Vye-Brown, C.

Brown, R.J. Hamilton, S. (2018) Bridging the gap: $^{40}\text{Ar}/^{39}\text{Ar}$ dating of volcanic eruptions from the 'Age of Discovery'. *Geology* 46(12):1035-1038.

<https://doi.org/10.1130/g45415.1>

Preece, K.J. Barclay, J. Brown, R.J. Chamberlain, K.J. Mark, D.F. (2021) Explosive felsic eruptions on ocean islands: a case study from Ascension Island (South Atlantic). *Journal of Volcanology and Geothermal Research* 416.

<https://doi.org/10.1016/j.jvolgeores.2021.107284>.

Preece, K. Gertisser, R. Barclay, J. Charbonnier, S.J Komorowski, J.C. and Herd, R.A. (2016) Transitions between explosive and effusive phases during the cataclysmic 2010 eruption of Merapi volcano, Java, Indonesia. *Bulletin of Volcanology*, 78(8), pp.1-16.

Putirka, K.D. (2008) Thermometers and barometers for volcanic systems. *Reviews in mineralogy and geochemistry*, 69(1), pp.61-120.

Pyle, D.M. (2015) 'Sizes of Volcanic Eruptions', In: Sigurdsson H (ed) The Encyclopedia of Volcanoes 2nd edn, *Academic Press*, pp 257–264. <https://doi.org/10.1016/B978-0-12-385938-9.00013-4>.

Pyle, D.M. Barclay, J. and Armijos, M.T. (2018) The 1902–3 eruptions of the Soufrière, St Vincent: Impacts, relief and response. *Journal of Volcanology and Geothermal Research*, 356, pp.183-199.

Queiroz, G. Pacheco, J.M. Gaspar, J.L. Aspinall, W.P. Guest, J.E. and Ferreira, T. (2008) The last 5000 years of activity at Sete Cidades volcano (São Miguel Island, Azores): implications for hazard assessment. *Journal of Volcanology and Geothermal Research*, 178(3), pp.562-573.

Rapprich, V. Žáček, V. Verner, K. Erban, V. Goslar, T. Bekele, Y. Legesa, F. Hroch, T.

Hejtmánková, P. (2016) Wendo Koshe Pumice: The latest Holocene silicic explosive eruption product of the Corbetti Volcanic System (Southern Ethiopia). *Journal of*

Volcanology and Geothermal Research 310: 159-171.

<https://doi.org/10.1016/j.jvolgeores.2015.12.008>.

Re, G. Corsaro, R.A. D'Orlando, C. and Pompilio, M. (2021) Petrological monitoring of active volcanoes: A review of existing procedures to achieve best practices and operative protocols during eruptions. *Journal of Volcanology and Geothermal Research*, 419, p.107365.

Robert, G. Whittington, A.G. Stechern, A. and Behrens, H. (2013) The effect of water on the viscosity of a synthetic calc-alkaline basaltic andesite. *Chemical Geology*, 346, pp.135-148.

Ross, P.S. Dürig, T. Comida, P.P. Lefebvre, N. White, J.D. Andronico, D. Thivet, S. Eycheenne, J. and Gurioli, L. (2022) Standardized analysis of juvenile pyroclasts in comparative studies of primary magma fragmentation; 1. Overview and workflow. *Bulletin of Volcanology*, 84(1), pp.1-29.

Rooyakkers, S.M. Stix, J. Berlo, K. Morgavi, D. Petrelli, M. Rusiecka, M.K. Barker, S.J. Charlier, B.L. Neave, D.A. Vetere, F.P. and Perugini, D. (2022) Rifting and recharge as triggers of the mixed basalt–rhyolite Halarauður ignimbrite eruption (Krafla, Iceland). *Contributions to Mineralogy and Petrology*, 177(3), pp.1-24.

Rotella, M.D. Wilson, C.J. Barker, S.J. Cashman, K.V. Houghton, B.F. and Wright, I.C. (2014) Bubble development in explosive silicic eruptions: insights from pyroclast vesicularity textures from Raoul volcano (Kermadec arc). *Bulletin of Volcanology*, 76(8), pp.1-24.

Rotolo, S.G. La Felice, S. Mangalaviti, A. Landi, P. (2007) Geology and petrochemistry of the recent (< 25 ka) silicic volcanism at Pantelleria Island. *Bollettino-Societa Geologica Italiana*, 126(2):191.

Rust, A.C. Cashman, K.V. Wallace, P.J. (2004) Magma degassing buffered by vapor flow through brecciated conduit margins. *Geology* 32(4): 349–352.

<https://doi.org/10.1130/G20388.2>.

Rutherford, M.J. and Hill, P.M. (1993) Magma ascent rates from amphibole breakdown: an experimental study applied to the 1980–1986 Mount St. Helens eruptions. *Journal of Geophysical Research: Solid Earth*, 98(B11), pp.19667-19685.

Sable, J.E., Houghton, B.F., Wilson, C.J.N. and Carey, R.J., 2009. Eruption mechanisms during the climax of the Tarawera 1886 basaltic Plinian eruption inferred from microtextural characteristics of the deposits.

Sahagian, D.L. and Proussevitch, A.A. (1998) 3D particle size distributions from 2D observations: stereology for natural applications. *Journal of Volcanology and Geothermal Research*, 84(3-4), pp.173-196.

Saubin, E. Tuffen, H. Gurioli, L. Owen, J. Castro, J.M. Berlo, K. McGowan, E.M. Schipper, I.C. Wehbe, K. (2016) Conduit dynamics in transitional rhyolitic activity recorded by tuffisite vein textures from the 2008–2009 chaitén eruption. *Frontiers in Earth Science*, 4(May). <https://doi.org/10.3389/feart.2016.00059>

Sbrana, A. Marianelli, P. Pasquini, G. (2018) Volcanology of Ischia (Italy). *Journal of Maps*, 14(2):494-503. <https://doi.org/10.1080/17445647.2018.1498811>

Scarlett J.P. (2020) Coexisting With Volcanoes: The Relationships Between La Soufrière and the Society of St. Vincent, Lesser Antilles. Hull: The University of Hull. Available at: <https://hydra.hull.ac.uk/resources/hull:18230>

Schipper, C.I. Castro, J.M. Tuffen, H. James, M.R. How, P. (2013) Shallow vent architecture during hybrid explosive–effusive activity at Cordón Caulle (Chile, 2011–12): evidence from direct observations and pyroclast textures. *Journal of Volcanology and Geothermal Research* 262:25-37. <https://doi.org/10.1016/j.jvolgeores.2013.06.005>

Schmith, J. Höskuldsson, Á. Holm, P.M. and Larsen, G. (2018) Large explosive basaltic eruptions at Katla volcano, Iceland: Fragmentation, grain size and eruption dynamics. *Journal of Volcanology and Geothermal Research*, 354, pp.140-152.

Scott, W.E. Hoblitt, R.P. Torres, R.C. Self, S. Martinez, M.M.L. Nillos, T. (1996) 'Pyroclastic flows of the June 15, 1991, climactic eruption of Mount Pinatubo', In: Fire and mud: Eruptions and lahars of Mount Pinatubo, Philippines, Newhall CG and Punongbayan RS, *Philippine institute of Volcanology and Seismology* pp 545-570.

Shea, T. Houghton, B.F. Gurioli, L. Cashman, K.V. Hammer, J.E. Hobden, B.J. (2010) Textural studies of vesicles in volcanic rocks: an integrated methodology. *Journal of Volcanology and Geothermal Research* 190(3-4):271-289.

<https://doi.org/10.1016/j.jvolgeores.2009.12.003>

Shea, T. Gurioli, L. Larsen, J.F. Houghton, B.F. Hammer, J.E. and Cashman, K.V. 2010b. Linking experimental and natural vesicle textures in Vesuvius 79AD white pumice. *Journal of Volcanology and Geothermal Research*, 192(1-2), pp.69-84.

Shea, T. Gurioli, L. Houghton, B.F. (2012) Transitions between fall phases and pyroclastic density currents during the AD 79 eruption at Vesuvius: Building a transient conduit model from the textural and volatile record. *Bulletin of Volcanology* 74(10):2363–2381.

<https://doi.org/10.1007/s00445-012-0668-z>.

Shea, T. Leonhardi, T. Giachetti, T. Lindoo, A. Larsen, J. Sinton, J. Parsons, E. (2017) Dynamics of an unusual cone-building trachyte eruption at Pu'u Wa'awa'a, Hualālai volcano, Hawai'i. *Bulletin of Volcanology* 79(4). <https://doi.org/10.1007/s00445-017-1106-z>.

Shepherd, J.B. Aspinall, W.P. Rowley, K.C. Pereira, J. Sigurdsson, H. Fiske, R.S. and Tomblin, J.F. (1979) The eruption of Soufrière volcano, St Vincent April–June

1979. *Nature*, 282(5734), pp.24-28.

Siebert, L. Simkin, T. and Kimberly, P. (2011) *Volcanoes of the World*. Univ of California Press.

Sieron, K. Ferres, D. Siebe, C. Capra, L. Constantinescu, R. Augustín-Flores, J. Zuccolotto, G. Böhnell, H. Connor, L. Connor, C.B. Groppelli, G. (2019) Ceboruco hazard map: part I - definition of hazard scenarios based on the eruptive history. *Journal of Applied Volcanology* 8(9). <https://doi.org/10.1186/s13617-019-0088-2>

Sigmarrsson, O. Vlastélic, I. Andreasen, R. Bindeman, I. Devidal, J.L. Moune, S. Keiding, J.K. Larsen, G. Höskuldsson, A. and Thordarson, T. (2011) Remobilization of silicic intrusion by mafic magmas during the 2010 Eyjafjallajökull eruption. *Solid Earth*, 2(2), pp.271-281.

Signorelli, S. and Carroll, M., 2002. Experimental study of Cl solubility in hydrous alkaline melts: constraints on the theoretical maximum amount of Cl in trachytic and phonolitic melts. *Contributions to Mineralogy and Petrology*, 143(2), pp.209-218.

Singer, B.S. Jicha, B.R. Harper, M.A. Naranjo, J.A. Lara, L.E. Moreno-Roa, H. (2008) Eruptive history, geochronology, and magmatic evolution of the Puyehue-Cordón Caulle volcanic complex, Chile. *Geological Society of America Bulletin* 120(5-6):599-618.
<https://doi.org/10.1130/B26276.1>

Smithsonian Institute, G.V.P. (2013). Ascension (385050) in *Volcanoes of the world*, v. 4.11.0 (08 Jun 2022). Venzke, E (ed.). *Smithsonian Institution*. Downloaded 25 Jul 2022 (<https://volcano.si.edu/volcano.cfm?vn=385050>).
<https://doi.org/10.5479/si.GVP.VOTW4-2013>

Sparks, R.S.J. (1978) The dynamics of bubble formation and growth in magmas: A review and analysis. *Journal of Volcanology and Geothermal Research* 3(1–2):1–37.

[https://doi.org/10.1016/0377-0273\(78\)90002-1](https://doi.org/10.1016/0377-0273(78)90002-1).

Sparks, S.R. Sigurdsson, H. and Wilson, L. (1977) Magma mixing: a mechanism for triggering acid explosive eruptions. *Nature*, 267(5609), pp.315-318.

Sparks, R.S.J., Tait, S.R. and Yanev, Y., 1999. Dense welding caused by volatile resorption. *Journal of the Geological Society*, 156(2), pp.217-225.

Sparks, R.S.J. and Young, S.R. (2002) The eruption of Soufrière Hills Volcano, Montserrat (1995-1999): overview of scientific results. *Geological Society, London, Memoirs*, 21(1), pp.45-69.

Sparks, R.S.J. and Cashman, K.V., 2017. Dynamic magma systems: implications for forecasting volcanic activity. *Elements*, 13(1), pp.35-40.

Stevenson, R.J. and Wilson, L., 1997. Physical volcanology and eruption dynamics of peralkaline agglutinates from Pantelleria. *Journal of Volcanology and Geothermal Research*, 79(1-2), pp.97-122.

Stewart, A.L. McPhie, J. (2006) Facies architecture and Late Pliocene–Pleistocene evolution of a felsic volcanic island, Milos, Greece. *Bulletin of Volcanology* 68(7-8):703-726. <https://doi.org/10.1007/s00445-005-0045-2>

Storey, M. Wolff, J.A. Norry, M.J. Marriner, G.F. (1989) Origin of Hybrid lavas from Agua de Pau volcano, Sao Miguel, Azores. *Magmatism in the Ocean Basins, Geological Society Special Publication* 42:161-180 <https://doi.org/10.1144/GSL.SP.1989.042.01.11>

Stormer, J.r J.C., 1975. A practical two-feldspar geothermometer. *American Mineralogist: Journal of Earth and Planetary Materials*, 60(7-8), pp.667-674.

Sulpizio, R. Mele, D. Dellino, P. and Volpe, L.L. (2005) A complex, Subplinian-type eruption from low-viscosity, phonolitic to tephri-phonolitic magma: the AD 472 (Pollena) eruption

of Somma-Vesuvius, Italy. *Bulletin of Volcanology*, 67(8), pp.743-767.

Suzuki, Y.J. and Koyaguchi, T., 2012. 3-D numerical simulations of eruption column collapse: Effects of vent size on pressure-balanced jet/plumes. *Journal of Volcanology and Geothermal Research*, 221, pp.1-13.

Thomas, R.M.E. and Sparks, R.S.J. (1992) Cooling of tephra during fallout from eruption columns. *Bulletin of Volcanology*, 54(7), pp.542-553.

Tollan, P.M.E. Bindeman, I. and Blundy, J.D. (2012) Cumulate xenoliths from St. Vincent, Lesser Antilles Island Arc: a window into upper crustal differentiation of mantle-derived basalts. *Contributions to Mineralogy and Petrology*, 163(2), pp.189-208.

Toramaru, A. (2006) BND (bubble number density) decompression rate meter for explosive volcanic eruptions. *Journal of Volcanology and Geothermal Research* 154(3-4):303-316. <https://doi.org/10.1016/j.jvolgeores.2006.03.027>

Toramaru, A. Noguchi, S. Oyoshihara, S. Tsune, A. (2008) MND(microlite number density) water exsolution rate meter. *Journal of Volcanology and Geothermal Research* 175(1-2):156-167. <https://doi.org/10.1016/j.jvolgeores.2008.03.035>.

Tuffen, H., Dingwell, D.B. and Pinkerton, H., 2003. Repeated fracture and healing of silicic magma generate flow banding and earthquakes? *Geology*, 31(12), pp.1089-1092.

Valentine, G.A. and Giannetti, B., 1995. Single pyroclastic beds deposited by simultaneous fallout and surge processes: Roccamonfina volcano, Italy. *Journal of volcanology and geothermal research*, 64(1-2), pp.129-137.

Vezzoli, L. Principe, C. Malfatti, J. Arrighi, S. Tanguy, J.C. Le Goff, M. (2009) Modes and times of caldera resurgence: the < 10 ka evolution of Ischia Caldera, Italy, from high-

precision archaeomagnetic dating. *Journal of volcanology and geothermal research*, 186(3-4):305-319. <https://doi.org/10.1016/j.jvolgeores.2009.07.008>

Vona, A. Romano, C. Giordano, D. and Russell, J.K. (2013) The multiphase rheology of magmas from Monte Nuovo (Campi Flegrei, Italy). *Chemical Geology*, 346, pp.213-227.

Wadsworth, F.B. Llewelin, E.W. Vasseur, J. Gardner, J.E. and Tuffen, H. (2020) Explosive-effusive volcanic eruption transitions caused by sintering. *Science advances*, 6(39), p.eaba7940.

Walker, G.P.L., Wilson, C.J.N. and Froggatt, P.C., 1980. Fines-depleted ignimbrite in New Zealand—The product of a turbulent pyroclastic flow. *Geology*, 8(5), pp.245-249.

Walker, G.P.L., Self, S. and Froggatt, P.C., 1981. The ground layer of the Taupo ignimbrite: a striking example of sedimentation from a pyroclastic flow. *Journal of Volcanology and Geothermal Research*, 10(1-3), pp.1-11.

Waters, L.E. and Lange, R.A. (2015) An updated calibration of the plagioclase-liquid hygrometer-thermometer applicable to basalts through rhyolites. *American mineralogist*, 100(10), pp.2172-2184.

Weber, G., Blundy, J., Barclay, J., Pyle, D.M., Cole, P., Frey, H., Manon, M., Davies, B.V. and Cashman, K., 2023. Petrology of the 2020-21 effusive to explosive eruption of La Soufrière volcano, St Vincent: Insights into plumbing system architecture and magma assembly mechanism. Geological Society, London, Special Publications, 539(1), pp.SP539-2022.
Weaver, B. Kar, A. Davidson, J. Colucci, M. (1996) Geochemical characteristics of volcanic rocks from Ascension Island, south Atlantic Ocean. *Geothermics*, 25(4-5):449-470. [https://doi.org/10.1016/0375-6505\(96\)00014-4](https://doi.org/10.1016/0375-6505(96)00014-4)

Webster, J.D. and Rebbert, C.R., (2001) The geochemical signature of fluid-saturated magma determined from silicate melt inclusions in Ascension Island granite xenoliths. *Geochimica et Cosmochimica Acta*, 65(1), pp.123-136.

Whittington, A. Richetm P. Linardm Y. Holtz F (2001) The viscosity of hydrous phonolites and trachytes. *Chemical Geology*, 174(1-3):209-223. [https://doi.org/10.1016/S0009-2541\(00\)00317-X](https://doi.org/10.1016/S0009-2541(00)00317-X)

Wieser, P. Petrelli, M. Lubbers, J. Wieser, E. Kent, A. Till, C. (2021) Thermobar: A critical evaluation of mineral-melt thermobarometry and hygrometry in arc magmas using a new open-source Python3 tool. *Geological Society of America Abstracts with Programs*. Vol 53, No. 6. <https://doi.org/10.1130/abs/2021AM-367080>.